

ANNUAL REPORT

2010

and list of publications



Bayerisches Forschungsinstitut
für Experimentelle Geochemie und Geophysik
Universität Bayreuth

Bayerisches Geoinstitut
Universität Bayreuth
D-95440 Bayreuth
Germany

Telephone: +49-(0)921-55-3700
Telefax: +49-(0)921-55-3769
e-mail: bayerisches.geoinstitut@uni-bayreuth.de
www: <http://www.bgi.uni-bayreuth.de>

Editorial compilation by: Stefan Keyssner and Petra Buchert
Section editors: Andreas Audétat, Tiziana Boffa Ballaran, Leonid Dubrovinsky,
Dan Frost, Florian Heidelbach, Tomoo Katsura, Hans Keppler,
Falko Langenhorst, Catherine McCammon, Nobuyoshi Miyajima,
Dave Rubie, Henri Samuel, Gerd Steinle-Neumann, Nicolas Walte



Staff and guests of the Bayerisches Geoinstitut in July 2010:

Die Mitarbeiter und Gäste des Bayerischen Geoinstituts im Juli 2010:

First row, from left (1. Reihe, v. links) Stefan Keyssner, Davide Novella, Hongzhan Fei, Richard McCormack, Qingguo Wei, Vojtech Vlcek, Mezhoura Oussadou, Ruifang Huang, Li Zhang, Federica Schiavi

Second row, from left (2. Reihe, v. links) Florian Heidelberg, Sushant Shekhar, Coralie Weigel, Gleb Parakhonskiy, Lu Feng, Martha Pamato, Azzurra Zucchini, Mattia Giannini, Antje-Kathrin Vogel, Catherine McCammon, Vincenzo Stagno

Third row, from left (3. Reihe, v. links) Henri Samuel, Alexander Kurnosov, Kilian Pollok, Sven Linhardt, Ryosuke Sinmyo, Yuan Li, Geeth Manthilake, Nobuyoshi Miyajima, Yoichi Nakajima, Heinz Fischer, Holger Kriegel

Fourth row, from left (4. Reihe, v. links) Petra Buchert, Juliane Hopf, Nico de Koker, Mainak Mookherjee, Huaiwei Ni, Alberto Escudero, Diego Bernini, Xiaozhi Yang, Tomoo Katsura, Julien Chantel, Linda Lerchbaumer, Anna Spivak

Fifth row, from left (5. Reihe, v. links) Dmytro Trots, Hans Keppler, Gerd Steinle-Neumann, Razvan Caracas, Patrick Cordier, Vladislav Aleksandrov, David Dolejš, Eran Greenberg, Hubert Schulze, Dan Frost

Sixth row, from left (6. Reihe, v. links) Dennis Harries, Svyatoslav Shcheka, Ulrich Böhm, Oliver Rausch, Detlef Krauße, Volker Pechtold, Falko Langenhorst, Andreas Audétat, Stefan Übelhack, Leonid Dubrovinsky, Dave Rubie

Absent (Es fehlten) Enikő Bali, Tiziana Boffa Ballaran, Uwe Dittmann, Ahmed El Goresy, Geertje Ganskow, Konstantin Glazyrin, Gertrud Gollner, Scott King, Lydia Kison-Herzing, Kurt Klasinski, Suzanne McEnroe, Sergey Ovsyannikov, Clemens Prescher, Wei Sun, Willem van Mierlo, Nico Walte

Contents

Foreword/Vorwort	9/I
1. Advisory Board and Directorship	11
1.1 Advisory Board	11
1.2 Leadership	11
2. Staff, Funding and Facilities	13
2.1 Staff	13
2.2 Funding	13
2.3 Laboratory and office facilities	18
2.4 Experimental and analytical equipment	18
3. Forschungsprojekte - Zusammenfassung in deutscher Sprache	III
3. Research Projects	21
3.1 Earth and Planetary Structure	21
a. Combined effects of plate motion and small-scale convection on mantle stirring efficiency (H. Samuel and S.D. King/Blacksburg)	23
b. The effect of continental lids on mantle convective stirring efficiency (H. Samuel, V. Aleksandrov and B. Deo/Kharagpur)	24
c. Convective stirring efficiency at finite Prandtl number (H. Samuel)	26
d. Adiabatic temperature profiles in the mantle (T. Katsura, in collaboration with A. Yoneda, D. Yamazaki, T. Yoshino and E. Ito/Misasa)	27
e. Subducting slab with pressure- and temperature-dependent thermal properties (P. Maierová and G. Steinle-Neumann)	30
f. The elasticity of lawsonite and the occurrence of low velocity layers (LVL) in subduction zones (J. Chantel, M. Mookherjee and D.J. Frost)	31
g. Composition and stability of hydrous partial melts at 410 km (M. Mookherjee and D.J. Frost)	33
h. Thermal conductivity of MgO periclase at deep mantle pressures: Implications for core-mantle boundary heat flux (N. de Koker)	35
i. Thermodynamics of iron melting to 100 GPa (G. Steinle-Neumann and D. Dolejš/Prague)	36
j. Stability of iron carbides at inner core conditions (M. Mookherjee and G. Steinle-Neumann)	38
k. Fragmentation of metal diapirs in terrestrial magma oceans (H. Samuel, D.C. Rubie and H.J. Melosh/West Lafayette)	40
3.2 <i>Geochemistry</i>	43
a. Oxygen isotopes in the ultra-refractory CAI Efremovka 101,1 and in the early solar nebula (J. Aléon/Orsay, K.D. McKeegan/Los Angeles, A. El Goresy and E. Charon/Paris)	44

b. Sulphide assemblages in primitive EH-3 chondrites ALHA77295, Sahara97072 and Sahara97158 (A. El Goresy, in collaboration with A. Gannoun/Clermont-Ferrand, M. Boyet/Clermont-Ferrand and S. Mostefaoui/Paris)	46
c. REE abundances in primitive EH chondrites (A. Gannoun and M. Boyet/Clermont-Ferrand, A. El Goresy and B. Devouard/Clermont-Ferrand)	49
d. Native Hg, cinnabarite, chalcocite, covellite and copper in the primitive H-3 chondrite Tieschitz: Novel constraints on condensation and accretion processes in the early Solar System (C. Caillet Komorowski/Paris, A. El Goresy, M. Miyahara/Sendai, O. Boudouma/Paris, M. Humayun/Tallahassee, C. Ma/Pasadena and F. Robert/Paris)	51
e. Sulphide mineralogies in CM and CM-like chondrites and their record of early solar system processes (D. Harries and F. Langenhorst)	52
f. Heterogeneous accretion and core-mantle differentiation of the terrestrial planets (D.C. Rubie, D.J. Frost, Y. Nakajima, A.-K. Vogel, in collaboration with F. Nimmo/Santa Cruz, D.P. O'Brien/Tucson, U. Mann/Zürich and H. Palme/Frankfurt)	54
g. The partitioning of volatile elements between metal and silicate at high pressures and temperatures (A.K. Vogel, D.C. Rubie, D.J. Frost and A. Audetat, in collaboration with H. Palme/Frankfurt)	55
h. Silicon and oxygen partitioning between metal, lower-mantle minerals, and silicate-melt during formation of the Earth's core (Y. Nakajima, D.J. Frost and D.C. Rubie)	57
i. Silicate perovskite and the terrestrial noble gas signature (S. Shcheka and H. Keppler)	60
j. The stability of magnesite in the lower mantle and the transition zone as a function of oxygen fugacity (V. Stagno, Y. Tange/Ehime, N. Miyajima, C.A. McCammon, T. Irifune/Ehime and D.J. Frost)	62
k. The oxygen fugacity for carbonate reduction in eclogite assemblages (V. Stagno, C.A. McCammon and D.J. Frost)	64
l. Fe-Mg partitioning between carbonate melts and olivine (D.J. Frost and V. Stagno)	67
m. Iron oxidation state of garnet from upper mantle xenoliths in the Gibeon kimberlite province (Namibia) (M. Longo, P. Nimis, F. Nestola and L. Ziberna/Padua; L. Franz/Basel and C.A. McCammon)	68
n. The oxidation state of mantle wedge garnet peridotites metasomatised by C-bearing subduction fluids (N. Malaspina and S. Poli/Milano; F. Langenhorst)	70
o. Partitioning of halogens between mantle minerals and aqueous fluids (D. Bernini, D. Dolejš/Prague, M. Wiedenbeck/Potsdam and H. Keppler)	72
p. Composition of the bulk oceanic crust and its implications for mineralogical and physical properties of subducting lithosphere (Z. Chemia/Trondheim, D. Dolejš/Prague and G. Steinle-Neumann)	74

q.	Molybdenite saturation in silicic magmas and its use to estimate magmatic fO_2 and fS_2 (A. Audétat, D. Dolejš/Prague, J.B. Lowenstern/Menlo Park)	77
r.	Biogenic nanocrystalline sulphide formation in sediments from the abandoned copper mine Mynydd Parys, Wales (K. Pollok and K.B. Hallberg/Bangor)	80
3.3	<i>Mineralogy, Crystal Chemistry and Phase Transformations</i>	82
a.	An investigation of new mineral of the garnet group bitikleite-(SnFe) $Ca_3SbSnFe^{3+}_3O_{12}$ (I.O. Galuskina and E.V. Galuskin/Sosnowiec, J. Kusz/Katowice, P. Dzierżanowski/Warszawa, K. Prusik/Katowice, V.M. Gazeev/Moscow, N.N. Pertsev/Moscow and L.S. Dubrovinsky)	83
b.	X-ray diffraction study of the inclusions in fibrous diamond (E.M. Smith and M.G. Kopylova/Vancouver, L.S. Dubrovinsky and E.L. Tomlinson/Surrey)	84
c.	Translation interface modulation in NC-pyrrhotites: Direct imaging by TEM (D. Harries, K. Pollok and F. Langenhorst)	85
d.	Mössbauer and X-ray single crystal study of almandine garnet (C.A. McCammon, F. Nestola/Padova and T. Boffa Ballaran, in collaboration with J. Bull and C. Tennant/Christchurch)	86
e.	Crystal chemistry of hibonite as indicator of oxygen fugacities during solar nebula condensation (M. Giannini, T. Boffa Ballaran and F. Langenhorst)	88
f.	Olivine-wadsleyite-pyroxene epitaxy: Element and volatile distributions at the 410 km discontinuity (J.R. Smyth/Boulder, N. Miyajima, G. Huss and E. Hellebrand/Honolulu; D.C. Rubie and D.J. Frost)	90
g.	Solubility of Al, Cr and Si in TiO_2 -rutile at high pressure and high temperature. A comparative study (A. Escudero and F. Langenhorst)	92
h.	An NMR investigation of the Al- and Fe-substitutions in $MgSiO_3$ perovskite (A. Palke/Stanford, D.J. Frost, C.A. McCammon and J.F. Stebbins/Stanford)	94
i.	Phase relations in $MgSiO_3$ - Al_2O_3 system under lower mantle P-T condition (R. Sinmyo, L.S. Dubrovinsky, D.J. Frost and Y. Nakajima)	95
j.	In situ infrared spectra of olivine to 1100 °C (X.-Z. Yang and H. Keppler)	97
k.	High-pressure phonon stability of Fe_2SiO_4 fayalite from first principles calculations (Z. Tang and G. Steinle-Neumann)	98
l.	Structural behaviour of silicate perovskite $(Mg_{0.62}, Fe_{0.38})(Al_{0.36}Si_{0.64})O_3$ at conditions of the Earth lower mantle (L.S. Dubrovinsky, T. Boffa Ballaran, K. Glazyrin, A. Kurnosov, D.J. Frost, N. Dubrovinskaia/Heidelberg, M. Merlini/Milano and M. Hanfland/Grenoble)	99
m.	Structure of an orthorhombic high-pressure Fe_2O_3 polymorph (L.S. Dubrovinsky, K. Glazyrin, A. Kurnosov and T. Boffa Ballaran; N. Dubrovinskaia, P. Schouwink and T. Pippinger/Heidelberg; M. Merlini/Milano and M. Hanfland/Grenoble)	101

n.	Pressure-induced ferrous-ferric transition in iron ions in Fe_{1-x}O wüstite (S.V. Ovsyannikov and L.S. Dubrovinsky; V.V. Shchennikov and M.A. Shvetsova/Yekaterinburg; A. Polian/Paris)	102
o.	Magnetic transitions in Fe_3C (C. Prescher, L.S. Dubrovinsky and C.A. McCammon)	106
3.4	<i>Physical Properties of Minerals</i>	108
a.	Single-crystal X-ray diffraction of Al- and Fe-bearing MgSiO_3 perovskite at pressures of the Earth's lower mantle (T. Boffa Ballaran, A. Kurnosov, K. Glazyrin, M. Merlini/Grenoble and D.J. Frost)	109
b.	High-pressure behaviour of hydrous aluminosilicate phases in the lower mantle (M.G. Pamato, D.J. Frost, T. Boffa Ballaran, F. Heidelbach and N. Miyajima)	110
c.	Compressibility of a super aluminous version of phase D (M.G. Pamato, T. Boffa Ballaran, D.J. Frost, D.M. Trots and A. Kurnosov)	111
d.	High-pressure structural behaviour of $\alpha\text{-Fe}_2\text{O}_3$ up to 25 GPa studied by single-crystal X-ray diffraction and synchrotron radiation (P. Schouwink/Heidelberg, L.S. Dubrovinsky and K. Glazyrin; M. Merlini and M. Hanfland/Grenoble; T. Pippinger and R. Miletich/Heidelberg)	114
e.	Equation of state of α -quartz measured using high-pressure single-crystal X-ray diffraction up to 21.5 GPa (D.M. Trots, A. Kurnosov, T. Boffa Ballaran and D.J. Frost)	115
f.	V_p and V_s measurements of polycrystalline solid solutions at high pressure (J. Chantel and D.J. Frost)	117
g.	Influence of pressure and temperature on the elastic wave velocities of lower mantle perovskite (C.A. McCammon, L.S. Dubrovinsky, K. Glazyrin, M. Mookherjee, R. Sinmyo, O. Narygina/Edinburgh and E. Greenberg/Tel Aviv; I. Sergueev and A. Chumakov/Grenoble)	119
h.	Diffusion of the majorite component in garnet at mantle transition zone conditions (W. van Mierlo, F. Langenhorst, N. Miyajima, D.J. Frost and D.C. Rubie)	120
i.	Single-crystal Ir-Pt interdiffusion in CaIrO_3 post-perovskite (R. McCormack and D.P. Dobson/London; F. Heidelbach; A. Beard, M.W. Ammann and J.P. Brodholt/London)	122
j.	Electrical conductivity of lower crustal minerals (X.-Z. Yang, H. Keppler, C.A. McCammon and H. Ni)	125
k.	Iron oxidation state in $(\text{Mg,Fe})\text{O}$ diffusion couples determined by the flank method (K. Otsuka/New Haven, M. Longo/Padua, C.A. McCammon and S. Karato/New Haven)	126
l.	Mott transition of wüstite at high pressure: the influence of ferric iron (K. Glazyrin, L.S. Dubrovinsky and S. Klotz/Paris)	128
m.	Lattice dynamics of rutile and anatase (V. Vlcek, G. Steinle-Neumann and E. Holbig)	130

3.5	<i>Fluids and their Interaction with Melts and Minerals</i>	132
a.	Nitrogen speciation in mantle fluids (Y. Li, A. Audétat and H. Keppler)	132
b.	Tungsten and molybdenum mobility in subduction zone fluids (E. Bali, A. Audétat and H. Keppler)	135
c.	Molybdenite solubility in aqueous fluids at 600-800 °C, 200 MPa: A synthetic fluid inclusion study (L. Zhang and A. Audétat)	136
d.	The influence of <i>Acidithiobacillus ferrooxidans</i> and <i>Acidithiobacillus thiooxidans</i> on surface morphology and dissolution rates of pyrrhotite (J. Hopf, K. Pollok and F. Langenhorst)	138
e.	Galena dissolution by the acidophilic bacteria <i>Acidithiobacillus ferrooxidans</i> (K. Etzel and K. Pollok)	139
3.6	<i>Physics and Chemistry of Melts and Magmas</i>	141
a.	Water contents of incipient partial melts in equilibrium with peridotite at 6 GPa (D. Novella and D.J. Frost)	142
b.	Electrical conductivity of hydrous basaltic melts: implications for partial melting in the mantle (H. Ni, H. Keppler and H. Behrens/Hannover)	143
c.	Crystallisation kinetics in decompressing magmas and implications for magma dynamics at Stromboli volcano (A. Fortunati and M.R. Carroll/Camerino; H. Keppler)	145
d.	Liquid immiscibility and melting reactions of carbonated mantle peridotite at upper mantle conditions (D. Novella and S. Keshav)	147
e.	Congruent melting of Ca-carbonate in static experiments at 10-21 GPa: significance for the genesis of superdeep diamonds (A. Spivak and Yu. Litvin/Chernogolovka; L.S. Dubrovinsky)	149
3.7	<i>Rheology</i>	151
a.	The effects of stress and water content on the deformation of olivine at high pressure (S. Shekhar, D.J. Frost, N. Walte, N. Miyajima and F. Heidelbach)	152
b.	The effect of aluminium and water on the development of orthopyroxene fabrics (M.A.G.M. Manthilake, N. Miyajima, F. Heidelbach and D.J. Frost)	154
c.	Deformation fabrics at the aragonite-calcite transition (F. Heidelbach and N. Walte)	156
d.	Characterisation of dislocations in dense hydrous magnesium silicate phase A (P. Cordier, A. Mussi and D.J. Frost)	159
e.	Dislocation microstructures of ferropericlase at high pressure and high temperature (N. Miyajima and T. Irifune/Ehime)	160
f.	The development of lattice-preferred orientation in CaPtO ₃ post-perovskite deformed in pure shear (R. McCormack and D.P. Dobson/London, T. Taniguchi/Tsukuba, N. Walte and N. Miyajima)	162

g.	The role of strain rate for grain-scale connectivity of a high-dihedral angle liquid in a crystalline matrix (N. Walte, D.C. Rubie, D.J. Frost and P. Bons/Tübingen)	165
3.8	<i>Metamorphism</i>	168
a.	Fluid-assisted recrystallization in peridotite – natural examples from xenoliths (P. Spacek/Brno and F. Heidelbach)	168
b.	Kaolinite illitization at 300 °C with increasing pressure (M. Mantovani/Sevilla, A. Escudero, A.I. Becerro/Sevilla)	170
c.	A TEM study of shock deformed pyrrhotite from suevite of the Chesapeake Bay Impact Crater, USA (D. Harries, Ch. Mang/Karlsruhe, A. Kontny/Karlsruhe and F. Langenhorst)	172
d.	Natural dissociation of olivine to perovskite and magesiowüstite in a Martian meteorite (M. Miyahara, E. Ohtani and S. Ozawa/Sendai; M. Kimura/Mito; A. El Goresy; T. Sakai, T. Nagase and K. Hiraga/Sendai; N. Hirao and Y. Ohishi/Hyogo)	173
3.9	<i>Materials Science</i>	177
a.	High-pressure synthesis of single crystals of α -boron (G. Parakhonskiy, N. Dubrovinskaia/ Heidelberg and L.S. Dubrovinsky)	177
b.	Pressure-induced isostructural phase transformation in γ -B ₂₈ (N. Dubrovinskaia/Heidelberg, R. Caracas/Lyon, M. Merlini/Milano, M. Hanfland, Y. Filinchuk, D. Chernyshov and V. Dmitriev/Grenoble; E. Zarechnaya and L.S. Dubrovinsky)	179
c.	Thermal EOS of tungsten from single crystal X-ray data (L.S. Dubrovinsky, K. Glazyrin and A. Kurnosov; N. Dubrovinskaia and T. Pippinger/Heidelberg; M. Merlini/Milano and M. Hanfland/Grenoble)	182
d.	First principles phase diagram calculations for the systems MO-M'O with M, M' = Mg, Ca, Sr, Ba, or Cd (O. Adjaoud/Potsdam and G. Steinle-Neumann, in collaboration with B.P. Burton/Gaithersburg and A. van de Walle/Pasadena)	184
e.	P-T phase diagram and structural stability of Pnma-Ti ₂ O ₃ (S.V. Ovsyannikov, L.S. Dubrovinsky, X. Wu/Beijing and N. Dubrovinskaia/Heidelberg)	185
f.	Structural phase transition in Pr _{0.15} Sr _{0.85} MnO ₃ at high pressure (D.P. Kozlenko/Dubna, L.S. Dubrovinsky, N.T. Dang/Dubna and Tula, Z. Jiráček/Prague; E.V. Lukin and B.N. Savenko/Dubna)	189
g.	Elasticity and equation of state of diomignite, Li ₂ B ₄ O ₇ (D.M. Trots, A. Kurnosov, T. Boffa Ballaran and D.J. Frost)	191
3.10	<i>Methodological Developments</i>	193
a.	Portable laser heating system for single crystal X-ray diffraction experiments in diamond anvil cells (L.S. Dubrovinsky and K. Glazyrin; N. Dubrovinskaia/Heidelberg; M. Merlini and M. Hanfland/Grenoble; V.B. Prakapenka/Chicago)	193

b.	Continued development of a synchrotron Mössbauer source and the first results (V. Potapkin, A.I. Chumakov and R. Rüffer/Grenoble; G.V. Smirnov and S.L. Popov/Moscow; L.S. Dubrovinsky and C.A. McCammon)	195
c.	BGI facility for simultaneous measurements of sound velocities and densities of single crystal samples at high pressures: test measurements of α -quartz and pyrope in DAC (A. Kurnosov, D.M. Trots, D.J. Frost and T. Boffa Ballaran)	197
d.	Diamond as a high-pressure gauge up to 2.7 Mbar (N. Dubrovinskaia/Heidelberg, R. Caracas/Lyon, M. Hanfland/Grenoble and L.S. Dubrovinsky)	199
e.	Calibration of the ruby and Sm: YAG pressure gauge up to 120 GPa and 700 K in a diamond anvil cell (Q. Wei and L.S. Dubrovinsky; N. Dubrovinskaia/Heidelberg)	202
f.	Pressure calibration and high-pressure pure shear deformation with the 6-ram press (G. Manthilake, N. Walte and D.J. Frost)	203
g.	The ' <i>quartz-capsule</i> ' – a way to reduce alloying problems with noble metal capsules during hydrothermal experiments (L. Lerchbaumer and A. Audétat)	206
h.	From surface morphology to rates: An automated routine to evaluate converged roughness parameters of heterogeneous surfaces (K. Pollok and T. Chust)	208
i.	StreamV3D, an efficient tool for modeling three-dimensional geodynamic scenarios (H. Samuel)	210
j.	Sparse linear solver using the Schur complement method (V. Aleksandrov and H. Samuel)	212
4.	International Graduate School "Structure, Reactivity and Properties of Oxide Materials"	215
5.	Publications, Conference Presentations, Seminars	219
5.1	Publications (published); Refereed international journals	219
a)	Refereed international journals	219
b)	Popular scientific magazines	226
5.2	Publications (submitted, in press)	226
5.3	Presentations at scientific institutions and at congresses	230
5.4	Lectures and seminars at Bayerisches Geoinstitut	244
5.5	Conference organization	248
6.	Visiting scientists	249
6.1	Visiting scientists funded by the Bayerisches Geoinstitut	249
6.2	Visiting scientists supported by other externally funded BGI projects	250
6.3	Visitors (externally funded)	251

7.	Additional scientific activities	255
7.1	Patent	255
7.2	Theses	255
7.3	Honours and awards	255
7.4	Editorship of scientific journals	255
7.5	Membership of scientific advisory bodies	256
8.	Scientific and Technical Personnel	259
	Index	263

Foreword

International collaboration is one of the strengths of Bayerisches Geoinstitut. The continuous exchange with scientists from Europe, the USA and Japan generates a permanent stream of new ideas that contributes significantly to the success and international reputation of the institute. It is therefore especially pleasing that we are also successful in bringing established scientists to Bayreuth. Prof. Tomoo Katsura, the successor of Dave Rubie, is an internationally-renown scientist who broadens the existing scientific expertise in Bayreuth through his experience in the areas of multianvil technology and applications of synchrotron radiation.

High pressure research in the Earth sciences is strongly coupled to the development of new technologies. This Annual Report contains numerous examples of results that could only be obtained through technological innovations. Two projects through which crystal structures are determined up to 85 GPa and 2300 K are especially noteworthy (see page 99 onwards). Achieving such conditions is only possible through laser heating in the diamond anvil cell. In the past, it was only possible to determine, at most, unit cell parameters using this technology and details of crystal structures could not be determined. The development of a portable laser system with optics that result in an especially low temperature gradient across the sample and long-term laser stability is an essential requisite for the success of these projects. Consequently, a phase transition from Fe_2O_3 to the Rh_2O_3 -II structure has been demonstrated for the first time.

In the Earth's atmosphere, the noble gas xenon is strongly depleted relative to argon so that the Xe/Ar ratio is ten times lower than in chondritic material from which the Earth was formed. A project that is described on page 60 of this Annual Report links the depletion of xenon in the atmosphere with the properties of silicate perovskite in the lower mantle. While perovskite can accept more than 1 weight % argon in its structure, the solubility of xenon in perovskite is negligible. As perovskite crystallised from a magma ocean during the early history of the Earth, an argon-rich reservoir was formed in the lower mantle whereas the original atmosphere was lost as the result of meteorite impacts and ultraviolet radiation. Later degassing of the lower mantle reservoir then released argon, but almost no xenon into the atmosphere. The air that we breathe today may therefore contain a chemical fingerprint that resulted from the crystallisation of a magma ocean 4.5 billion years ago.

Most projects described in this Annual Report were performed using equipment that is available in the Geoinstitut. However, many projects have also used intensive X-rays that are produced at synchrotron sources: in such cases, only sample preparation and data analysis are carried in the institute and the experiments themselves have been performed at facilities such as ESRF in Grenoble. In comparison to synchrotron sources, neutron radiation sources have not been used to much extent in high pressure research, even though there are important advantages. Neutrons can penetrate thick layers of heavy materials with ease and are

particularly suitable for investigating light atoms such as hydrogen that play a major role in the interior of the Earth and other planets. In early 2010 the Bayerisches Geoinstitut was awarded more than two million Euros by the BMBF in order to install a multianvil high-pressure apparatus at the neutron source FRM II at Garching. This will be accomplished over the next three years and will enable samples to be investigated using neutron radiography and neutron diffraction at conditions up to 25 GPa and 3000 °C. This apparatus will be unique world-wide and will be available for use by external users both from the Earth sciences and the material sciences.

As in previous years, and also on behalf of my colleagues, I would like to thank the *Free State of Bavaria* as represented by the *Bayerisches Staatsministerium für Wissenschaft, Forschung und Kunst*, the *President of the University of Bayreuth* as well as the *Kommission für Geowissenschaftliche Hochdruckforschung* of the *Bavarian Academy of Sciences* for their continuing support and strong commitment to the Bayerisches Geoinstitut. We also gratefully acknowledge generous support from external funding agencies, in particular the *Alexander von Humboldt Foundation*, the *European Union*, and the *German Science Foundation*, which have also contributed greatly to the development and success of the Institute.

Bayreuth, February 2011

Hans Keppler

Vorwort

Internationale Kooperation ist eine der Stärken des Bayerischen Geoinstituts. Der ständige Austausch mit Wissenschaftlern aus Europa, den USA und Japan erzeugt einen permanenten Strom neuer Ideen, der wesentlich zum Erfolg und zum internationalen Ansehen des Instituts beigetragen hat. Es ist daher besonders erfreulich, dass es uns immer wieder gelingt, auch etablierte Wissenschaftler nach Bayreuth zu locken. Mit Professor Tomoo Katsura konnte das Geoinstitut einen international renommierten Nachfolger für Dave Rubie gewinnen, der mit seiner Erfahrung auf dem Gebiet der Multi-Anvil-Technologie und der Anwendung von Synchrotronstrahlung die in Bayreuth vorhandene Expertise in hervorragender Weise ergänzt.

Geowissenschaftliche Hochdruckforschung ist stets verknüpft mit der Entwicklung neuer Technologie. Der vorliegende Jahresbericht enthält zahlreiche Beispiele dafür, dass neue Erkenntnisse oft nur durch technologische Innovation gewonnen werden können. Besonders bemerkenswert sind hier zwei Projekte, die sich mit der Bestimmung von Kristallstrukturen bei Drücken bis zu 85 GPa und Temperaturen bis zu 2300 K beschäftigen (Seite 99 ff). Derartige Bedingungen lassen sich nur durch Laser-Heizung in Diamantstempelzellen realisieren. Mit dieser Technologie konnten bisher allenfalls Gitterkonstanten, aber keine Details der Kristallstruktur untersucht werden. Die Entwicklung von tragbaren Laser-Systemen mit einer Optik, die besonders niedrige Temperaturgradienten in der Probe erzeugt und über lange Zeit stabil ist, war eine wesentliche Voraussetzung für diesen Erfolg. Ein Phasenübergang von Fe_2O_3 zur Rh_2O_3 -II-Struktur konnte erstmals *in situ* nachgewiesen werden.

In der Atmosphäre der Erde ist das Edelgas Xenon relativ zu Argon stark verarmt, das Xe/Ar-Verhältnis ist zehnmal kleiner als in chondritischem Material, aus dem die Erde aufgebaut wurde. Eine Arbeit auf Seite 60 dieses Jahresberichts verknüpft die Verarmung von Xenon in der Atmosphäre mit den Eigenschaften von Silikat-Perowskit im unteren Mantel. Während Perowskit bis über 1 Gew.% Argon in seine Kristallstruktur einbauen kann, ist die Löslichkeit von Xenon in Perowskit vernachlässigbar gering. Bei der Kristallisation von Perowskit aus einem Magmenozean in der Frühzeit der Erde bildete sich daher wohl ein Argon-reiches Reservoir im unteren Mantel, während die ursprüngliche Atmosphäre durch Meteorereinschläge und intensive Ultraviolett-Bestrahlung weitgehend verloren ging. Die spätere Entgasung dieses Reservoirs im unteren Mantel setzte dann Argon, aber kaum Xenon in die Atmosphäre frei. Die Zusammensetzung der Luft, die wir atmen, enthält damit möglicherweise heute noch einen chemischen Fingerabdruck der Kristallisation eines Magmenozeans vor 4,5 Milliarden Jahren.

Die Mehrzahl der in diesem Jahresbericht beschriebenen Projekte wurde mit den am Geoinstitut selbst vorhandenen Apparaturen durchgeführt. Viele Experimente nutzen aber auch die intensive Röntgenstrahlung von Synchrotronquellen, so dass nur die Probenvorbereitung und die Analyse der Daten im Haus erfolgt, während die Experimente

selbst beispielsweise an der ESRF in Grenoble ausgeführt werden. Im Vergleich zu Synchrotronquellen werden Neutronenstrahlen bisher nur relativ selten in der Hochdruckforschung angewandt, obwohl Neutronen gegenüber Röntgenstrahlen bedeutende Vorteile haben. Neutronen können auch dicke Schichten von schweren Materialien mühelos durchdringen und sie eignen sich besonders zur Untersuchung leichter Atome wie Wasserstoff, die eine große Rolle im inneren Aufbau der Erde und anderer Planeten spielen. Im Frühjahr 2010 wurden dem Bayerischen Geoinstitut vom BMBF Mittel in Höhe von über zwei Millionen Euro für den Aufbau einer Hochdruckpresse vom Multi-Anvil-Typ an der Forschungsneutronenquelle FRM II in Garching bewilligt. Innerhalb der nächsten drei Jahre wird hier eine Apparatur aufgebaut werden, die die Untersuchung von Proben mittels Neutronen-Beugung und Neutronen-Radiographie bei Drücken bis zu 25 GPa und Temperaturen bis über 3000 °C erlaubt. Diese Apparatur wird weltweit einmalig sein und für externe Nutzer sowohl aus den Geowissenschaften wie auch aus den Materialwissenschaften zur Verfügung stehen.

Wie in den vorangegangenen Jahren möchte ich auch im Namen meiner Kollegen dem *Freistaat Bayern*, vertreten durch das *Bayerische Staatsministerium für Wissenschaft, Forschung und Kunst*, der *Hochschulleitung der Universität Bayreuth* als auch der *Kommission für Geowissenschaftliche Hochdruckforschung der Bayerischen Akademie der Wissenschaften* danken für ihre fortwährende Unterstützung und ihre enge Verbundenheit mit dem Bayerischen Geoinstitut. Wir sind auch sehr dankbar für die großzügige Förderung durch externe Geldgeber, insbesondere durch die *Alexander von Humboldt-Stiftung*, die *Europäische Union* und die *Deutsche Forschungsgemeinschaft*, die ebenfalls wesentlich zur Entwicklung und zum Erfolg des Bayerischen Geoinstituts beigetragen haben.

Bayreuth, im Februar 2011

Hans Keppler

1. Advisory Board and Directorship

1.1 Advisory Board

The *Kommission für Geowissenschaftliche Hochdruckforschung der Bayerischen Akademie der Wissenschaften* advises on the organisation and scientific activities of the institute. Members of this board are:

Prof. Dr. G. BREY	Institut für Geowissenschaften der Johann Wolfgang Goethe-Universität, Frankfurt am Main
Prof. Dr. U. CHRISTENSEN	Max-Planck-Institut für Sonnensystemforschung, Katlenburg-Lindau
Prof. Dr. R. KNIEP	Institut für Chemische Physik fester Stoffe der Max-Planck-Gesellschaft, Dresden
Prof. Dr. H. PALME	Institut für Mineralogie und Geochemie der Universität zu Köln
Prof. Dr. R. RUMMEL	Institut für Astronomische und Physikalische Geodäsie der TU München
Prof. Dr.-Ing. G. SACHS (Chairman)	Lehrstuhl für Flugmechanik und Flugregelung der TU München
Prof. Dr. E. SALJE, FRS, FRSA	Department of Earth Sciences, University of Cambridge
Prof. Dr. H. SOFFEL	Emeritus, Institut für Allgemeine und Angewandte Geophysik der Universität München

The Advisory Board held meetings in Bayreuth (23.04.2010) and in Munich (26.11.2010).

1.2 Leadership

Prof. Dr. Hans KEPPLER (Director)
Prof. Dr. Falko LANGENHORST
Prof. Dr. Tomoo KATSURA

2. Staff, Funding and Facilities

2.1 Staff

At the end of 2010 the following staff positions existed in the Institute:

- Scientific staff *: **13**
- Technical staff: **13**
- Administrative staff: **2**
- Administrative officer: **1**

* Including a tenure-track junior professorship in geodynamic modeling initially funded by *Stifterverband für die Deutsche Wissenschaft* for 6 years, started in 2007.

During 2010, 28 scientific (224 months) positions were funded by grants raised externally by staff members of the institute. In addition 13 long-term scientific positions (103 months) were funded by the resources of the BGI Visiting Scientists' Programme (see Sect. 8) which also supported short-term visits for discussing future projects or presenting research results (see Sect. 6). Positions for 5 Ph.D. students and 1 co-ordinator were funded under the BGI International Graduate School under the Elitenetzwerk Bayern "Structure, Reactivity and Properties of Oxide Materials" (see Sect. 4). 8 scientists (44 months) were supported by personal grants (stipends).

2.2 Funding

In 2010, the following financial resources were available from the Free State of Bavaria:

- Visiting Scientists' Programme: 408.000 €
- Consumables: 391.000 €
- Investment Funding: 137.000 €

The total amount of national/international external funding ("*Drittmittel*") used for ongoing research projects in 2010 was 2.385.000 € (Positions: 1.202.000 €; equipment, consumables and travel grants: 1.183.000 €).

	positions	equipment, consumables, travel grants	total
• ENB	217.000 €	106.000 €	323.000 €
• AvH	92.000 €	22.000 €	114.000 €
• DFG	316.000 €	776.000 € ^{*)}	1.092.000 €
• EU	396.000 €	121.000 €	517.000 €
• BMBF	110.000 €	116.000 €	226.000 €
• Stifterverband	55.000 €	8.000 €	63.000 €
• Others	16.000 €	34.000 €	<u>50.000 €</u>
			2.385.000 €

(ENB = Int. Graduate School „Oxides“ in the Elite Network of Bavaria; AvH = Alexander von Humboldt Foundation; DFG = German Science Foundation; EU = European Union; BMBF = Federal Ministry of Education and Research; Stifterverband = Stifterverband für die Deutsche Wissenschaft; Others: Max-Planck-Gesellschaft, MICINN = Ministerio de Ciencia e Innovación/Gobierno de España, PPP-Frankreich, Industry

^{*)} includes 585.000 € Federal contribution to investment funding (§91B GG)

In the following list only the BGI part of the funding is listed in cases where joint projects involved other research institutions. Principal investigators and duration of the grants are listed in brackets. Total project funding refers to the funding over the entire duration of this project.

Funding institution	Project, Funding	Total Project Funding
BCTC ^{*1)}	(G. Steinle-Neumann, A. v.d. Walle/California Institute of Technology – 1.09. - 6.10) "Ternary solid solutions in mineral physics from ab initio computations" Travel funding: 4.800 € ^{*1)} Bavaria California Technology Center	4.800 €
BMBF	03G0718A (K. Pollok – 10.08 - 9.11) Nachwuchsgruppe "Microstructural Controls on Monosulfide Weathering" (MIMOS) Positions: 3 x E 13/2, each 36 months 241.086 € student assistant, (19,75h/month), 48 months 7.920 € Consumables and travel funding: 57.550 € Overhead: 6.915 € Total funding:	313.471 €
BMBF - DESY	05K10WC1 (L.S. Dubrovinsky – 7.10 - 6.13) "Verbundprojekt: Kernresonante Streutechniken: Entwicklung von Messplätzen zur Charakterisierung von Nanostrukturen, molekularen Schaltern, biologischen Mikroproben und Materie unter extremen Bedingungen mit kernresonanten Streutechniken. Teilprojekt 1" Total funding:	529.670 €
BMBF	05K10WC2 (H. Keppler – 7.10 - 6.13) "Aufbau einer Hochdruckpresse vom Multi-Anvil-Typ für TOF-Neutronenbeugung und Neutronen-Radiographie am FRM II" Total funding:	2.050.078 €
DAAD	(L.S. Dubrovinsky) "Studies of sulphur solubility in hydrothermal conditions"	6.200 €
DFG	Au 314/1-1 (A. Audétat – 9.08 - 8.10) "Fractionation of sulfur, copper and gold in two-phase fluids" Positions: E 13/2, 24 months 68.900 € Consumables and travel funding: 21.000 €	89.900 €
DFG	Bo 2550/4-1 (T. Boffa Ballaran, F. Langenhorst – 2.10 - 1.12) "Crystal chemistry of hibonite as indicator for oxygen fugacities during solar nebula condensation" Positions: E 13/2, 24 months 68.900 € student assistant (57 h/month) 24 months 19.050 € Consumables and travel funding: 22.000 € Overhead: 19.400 €	129.350 €

DFG	Du 393/7-1 (L.S. Dubrovinsky, N.A. Dubrovinskaia – 6.09 - 5.12) "Elasticity of iron and iron-based alloys at conditions of the Earth's and planetary cores" Positions: student assistant (80 h/month), 36 months 23.760 € Consumables and travel funding 42.017 € Publication costs 1.500 € Overhead: 18.600 €	85.877 €
DFG	EV 166/1-1 (M. Evonuk – 11.10 - 10.13) "Core formation in Terrestrial planets via global Rayleigh-Taylor destabilization" 1 position: E 13, 36 months 206.700 € Consumables and travel funding: 6.727 € Publication costs 2.250 € Overhead: 37.100 €	252.777 €
DFG	FR 1555/5-1 (D.J. Frost, C.A. McCammon – 04.10 - 03.11) "Experimental investigation of the redox conditions at which carbonate minerals and melts transform to graphite or diamond in Earth's mantle" 1 position: E 13/2, 12 months 34.450 € Consumables and travel funding: 10.537 € Publication costs 500 € Overhead: 8.100 €	53.587 €
DFG	KE 501/8-1 (H. Keppler – 8.09 - 7.11) "Untersuchungen der Kristallisationskinetik und Gefügeentwicklung von Basalten mit einer neuartigen Moissanit-Sichtzelle" 1 position: E 13, 24 months 137.800 € Consumables and travel funding: 27.690 € Publication costs 800 € Overhead: 32.200 €	198.490 €
DFG	KE 501/9-1 (H. Keppler – 2010 - 2012) "Noble gases in silicate perovskite: Solubility, dissolution mechanism and influence on the equation of state" 1 position: E 13, 36 months 206.700 € Consumables and travel funding: 15.000 € Overhead: 38.300 €	260.000 €
DFG	KO 3958/1-1 (N. de Koker, D.C. Rubie, D.J. Frost – 12.10. - 11.13) "Combining experimental and computational approaches to determine high P and T thermal conductivity of CaGeO ₃ and MgSiO ₃ perovskite" Positions: E 13, 20 months 114.835 € student assistant (57 h/month) 6 months 4.760 € Consumables and travel funding: 6.000 € Overhead: 22.000 €	147.595 €

DFG	La 830/12-1 (F. Langenhorst, A. Deutsch – 2.08 - 11.10) "Mineralogical and geochemical studies of impact melt products from the Chesapeake Bay impact structure" Positions: E 13/2, 2 months 5.740 € Consumables and travel funding: 8.100 €	13.840 €
DFG	La 830/13-1 (F. Langenhorst, A. Woodland, D.J. Frost – 2.08 - 11.10) "Systematics of the post-spinel transition in Fe-bearing compositions" Positions: E 13/2, 10 months 28.710 € Consumables and travel funding: 6.350 €	35.060 €
DFG	La 830/14-1 (F. Langenhorst – 2.08 - 9.14) Gottfried Wilhelm Leibniz-Preis 2007	2.489.000 €
DFG	La 830/15-3 (F. Langenhorst, A. Deutsch – 2.08 - 11.10) "Mineralogical and geochemical studies of impact melt products from the Chesapeake Bay and the Lake Bosumtwi impact structures (ICDP)" Consumables and travel funding: 10.800 €	10.800 €
DFG	Mc 3/16-2 (C.A. McCammon, L.S. Dubrovinsky – 10.09 - 9.12) "High-pressure high-temperature ⁵⁷ Fe Mössbauer spectroscopy in laser-heated diamond anvil cells: Applications for the mineralogy of Earth's lower mantle and core" Positions: student assistant (80 h/month), 36 months 23.760 € Equipment, consumables and travel funding: 30.000 € Overhead: 15.400 €	69.160 €
DFG	Mc 3/17-1 (C.A. McCammon, L.S. Dubrovinsky – 1.10 - 12.12) "Iron-bearing minerals in Earth's lower mantle and coremantle boundary: Development and application of a synchrotron Mössbauer source" Positions: student assistant (80 h/month), 36 months 23.760 € Equipment, consumables and travel funding: 51.935 € Overhead: 14.000 €	89.695 €
DFG	RU 1323/2-1 (D.C. Rubie, D.J. Frost, H. Palme – 4.10 - 3.12) "Conditions, timescales and cosmochemical evolution during the early accretion of terrestrial planets" Positions: E 13/2, 24 months 68.900 € Consumables and travel funding: 16.750 € Overhead: 15.100 €	100.750 €
DFG	SA 2042/2-1 (H. Samuel – 10.10 - 9.13) "The effect of continental plates on convective stirring efficiency" Positions: E 13/2, 36 months 103.350 € student assistant (57 h/month) 12 months 9.525 € Consumables and travel funding: 9.464 € Overhead: 21.200 €	143.539 €

DFG	STE 1105/6-1 (G. Steinle-Neumann – 3.09 - 8.10) DFG SPP 1375 (SAMPLE) "Mineralogical and Dynamic Origin of the South African Superplume" Positions: E13/2, 18 months 51.675 € Consumables and travel funding: 4.654 €	56.329 €
DFG	STE 1105/6-2 (G. Steinle-Neumann, H.-P. Bunge – 9.10 - 8.13) DFG SPP 1375 (SAMPLE) "Mineralogical and Dynamic Origin of the South African Superplume" Positions: ¾ E13, 36 months 155.025 € Consumables and travel funding: 7.200 €	162.225 €
EU	Marie Curie Intra European Fellowships – People "From Planetary to the Nanoscale: Magnetism at the Interface" (F. Langenhorst – 10.09 - 10.11) Positions, consumables and travel funding 231.000 €	231.000 €
EU	Marie Curie Research Training Network "Crust to core: the fate of subducted material" (2.07 - 1.11) G. Steinle-Neumann (coordinator), G. Fiquet (Paris, France), A.I. Beccero (Sevilla, Spain), S. Buiter (Trondheim, Norway), O. Cadek (Prague, Czech Republic), D. Dobson (London, UK), D. Andrault (Clermont-Ferrand, France), P. Jochym (Krakow, Poland), S. Poli (Milan, Italy) and M.W. Schmidt (Zurich, Switzerland) Total funding: 3,3 Mio € BGI funding:	740.000 €
EU	European Research Council (ERC) Advanced Grant No. 227893 (D.J. Frost – 2.09 - 1.14) "Deep Earth elastic properties and a universal pressure scale DEEP" Positions, equipment, consumables and travel funding maximum EU contribution:	2.079.888 €
Stifterverband	Stifterverband für die Deutsche Wissenschaft Junior-Professur Geodynamische Modellierung Positions: W1, 72 months 245.200 € Consumables and travel funding: 120.000 €	365.200 €
PROCOPE	Travel funding (C.A. McCammon, L.S. Dubrovinsky) "Multidisciplinary studies of structures in the deep mantle"	1.588 €

2.3 Laboratory and office facilities

The institute occupies an area of

ca. 1300 m² laboratory space

ca. 480 m² infrastructural areas (machine shops, computer facilities, seminar room, library)

ca. 460 m² office space

in a building which was completed in 1994.

2.4 Experimental and analytical equipment

The following major equipment is available at Bayerisches Geoinstitut:

I. High-pressure apparatus

6x800 tonne independently acting-anvil press (25 GPa, 3000 K)

5000 tonne multianvil press (25 GPa, 3000 K)

1200 tonne multianvil press (25 GPa, 3000 K)

1000 tonne multianvil press (25 GPa, 3000 K)

500 tonne multianvil press (20 GPa, 3000 K)

500 tonne press with a deformation DIA apparatus

4 piston-cylinder presses (4 GPa, 2100 K)

Cold-seal vessels (700 MPa, 1100 K, H₂O), TZM vessels (300 MPa, 1400 K, gas), rapid-quench device

Internally-heated autoclave (1 GPa, 1600 K)

High-pressure gas loading apparatus for DAC

II. Structural and chemical analysis

1 X-ray powder diffractometer

1 X-ray powder diffractometer with furnace and cryostat

Single-crystal X-ray cameras

2 automated single-crystal X-ray diffractometers

High-brilliance X-ray system

Single crystal X-ray diffraction with super-bright source

1 Mössbauer spectrometer (1.5 - 1300 K)

3 Mössbauer microspectrometers

2 FTIR spectrometers with IR microscope

FEG transmission electron microscope, 200 kV analytical, with EDS and PEELS

FEG scanning electron microscope with BSE detector, EDS, EBSD and CL

3 Micro-Raman spectrometers with ultraviolet and visible lasers

Tandem-multipass Fabry-Perot interferometer for Brillouin scattering spectroscopy

JEOL JXA-8200 electron microprobe; fully-automated with 14 crystals, 5 spectrometer configuration, EDX, capability for light elements
193 nm Excimer Laser-Ablation ICP-MS
ICP-AES sequential spectrometer
Water content determination by Karl-Fischer titration
GC/MS-MS for organic analyses
Confocal 3D surface measurement system

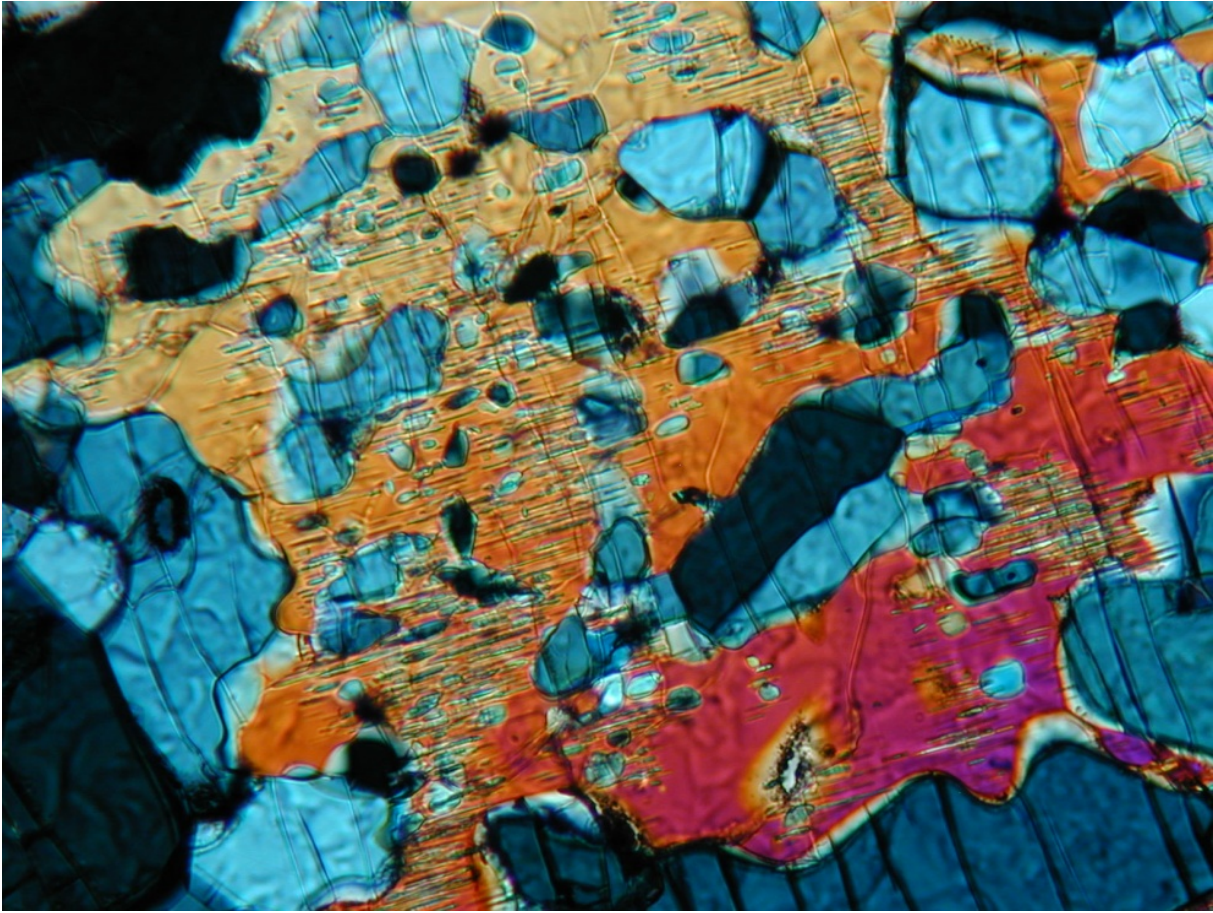
III. *In situ* determination of properties

Diamond anvil cells for powder and single crystal X-ray diffraction, Mössbauer, IR, Raman, optical spectroscopy and electrical resistivity measurements up to at least 100 GPa
Facility for in situ hydrothermal studies in DAC
Externally heated DACs for in situ studies at pressures to 100 GPa and 1200 K
1-atm furnaces to 1950 K, gas mixing to 1600 K, zirconia fO₂ probes
1-atm high-temperature creep apparatus
Gigahertz ultrasonic interferometer with interface to resistance-heated diamond-anvil cells
Heating stage for fluid inclusion studies
Impedance/gain-phase analyser for electrical conductivity studies
Apparatus for in situ measurements of thermal diffusivity at high P and T
Laser-heating facility for DAC
Portable laser heating system for DAC

IV. Computational facilities

9 node linux cluster (2x3.0 GHz Xeon Woodcrest Dual Core, 8 Gb memory), InfiniBand
8 node linux cluster (16x2.83 GHz Xeon 5440 Quad Core, 64 Gb memory), InfiniBand
RAID System (6 + 7 Tb storage)

The Geoinstitut is provided with well equipped machine shops, an electronic workshop and sample preparation laboratories. It has also access to the university computer centre.



Sample of OH-bearing olivine (orange-red) that has been partially transformed experimentally to wadsleyite at 13 GPa and 1400 °C. The large wadsleyite grains (blue) have nucleated incoherently, as previously observed for this transformation. The olivine also contains numerous thin lamellae of wadsleyite ($< 1 \mu\text{m}$ thick) that are oriented with their $[101]$ and $[10\bar{1}]$ directions parallel to the $[100]$ of olivine. Although such transformation textures have been observed previously for the olivine to ringwoodite transformation, this is the first time that transformation to coherent wadsleyite lamellae has been observed. The image is about 100 micrometers across. (Photo by Joseph R. Smyth)

OH-haltiger Olivin (orange-rot) wurde experimentell bei 13 GPa und 1400 °C teilweise in Wadsleyit umgewandelt. Die großen Wadsleyit-Körner (blau) sind inkohärent gewachsen, was für diesen Übergang bereits bei früheren Untersuchungen beobachtet wurde. Olivin weist darüberhinaus zahlreiche dünne Wadsleyit-Lamellen ($< 1 \mu\text{m}$ Durchmesser) auf, deren $[101]$ and $[10\bar{1}]$ -Richtungen parallel zu $[100]$ von Olivin orientiert sind. Derartige Texturen sind zwar schon aus dem Phasenübergang von Olivin nach Ringwoodit bekannt, jedoch ist dies das erste Mal, dass eine kohärente Umwandlungen von Olivin in Wadsleyit beobachtet wurde. Die Länge der unteren Bildkante beträgt ca. 100 Mikrometer. (Foto von Joseph R. Smyth)

3.1 Struktur der Erde und anderer Planeten

Geochemische und geophysikalische Beobachtungen an der Oberfläche von planetaren Körpern können nur interpretiert werden, sofern wir gute Kenntnisse über die Dynamik des Planeteninneren und die physikalischen Eigenschaften der planetaren Materialien unter hohem Druck und hoher Temperatur entwickelt haben. Die Beiträge in diesem Kapitel zeigen, wie mit Hilfe von Experimenten und numerischen Simulationen die Lücke zwischen Beobachtung an der Oberfläche sowie Struktur und Dynamik im Inneren der Erde und anderen erdähnlichen Planeten geschlossen werden kann.

Geochemische Beobachtungen lassen auf einen heterogenen Erdmantel schließen, der jedoch durch Konvektionsvorgänge großräumig durchmischt wird. Daher stehen die verbleibenden kleinräumigen Heterogenitäten im Fokus des Interesses. Das Mischungsverhalten des Erdmantels wird in den ersten drei Beiträgen des Kapitels mit verschiedenen Ansätzen untersucht. Die ersten beiden Beiträge behandeln Mantelkonvektion in Gegenwart von isolierenden Kontinenten und von kleinskaliger Konvektion unterhalb der Lithosphäre. Diese Rahmenbedingungen bewirken eine verstärkte Durchmischung des Erdmantels. In der Gegenwart von Trägheitskräften, wie sie zum Beispiel in Magmenkammern auftreten, ist das Mischungsverhalten eingeschränkt.

Während der Druckverlauf im Erdinneren aufgrund der Dichteverteilung gut verstanden ist, unterscheiden sich Modelle zum Temperaturprofil signifikant. Eine genaue Messung von Phasenübergängen in Experimenten kann dabei helfen, den Temperaturverlauf im Erdinneren zu bestimmen. Der vierte Beitrag dieses Kapitels verwendet Ergebnisse aus neuen Messungen an Phasengleichgewichten im Erdmantel, um eine Adiabate zu konstruieren, die von vorherigen Modellen um mehr als 100 K abweicht.

Die Dynamik und das Verhalten von subduzierten Platten im Erdinneren sind stark von Änderungen der physikalischen Eigenschaften der Materialien als Funktion von Druck und Temperatur abhängig. Diese Veränderungen werden jedoch in den meisten Modellen zur Subduktion vernachlässigt. Ein weiterer Beitrag in diesem Kapitel nutzt experimentell bestimmte Wärmeleitfähigkeiten von Mineralen, um ein thermophysikalisches Modell für verschiedene Gesteinstypen in einer subduzierten Platte zu erstellen. Dieses Modell wird in einem anschließenden Schritt in dynamische Modelle zur Subduktion umgesetzt werden.

In einigen Subduktionszonen treten Schichten mit ungewöhnlich niedrigen Scherwellengeschwindigkeiten auf, die möglicherweise auf der Bildung von Lawsonit, einer wasserhaltigen Mineralphase, beruhen. Die im sechsten Beitrag des Kapitels beschriebenen Untersuchungen der elastischen Eigenschaften von Lawsonit im Labor und in Simulationen sollen hier Klarheit schaffen. Die gewonnenen Daten unterstützen die Interpretation, dass Zonen mit niedrigen Geschwindigkeiten der Erdbebenwellen auf das Auftreten von Lawsonit zurückgeführt werden kann.

Zonen mit niedriger Scherwellengeschwindigkeit und hoher elektrischer Leitfähigkeit in einer Tiefe von 410 km werden in der Regel als partielle wasserhaltige Schmelzen gedeutet. Auftreten und Stabilität einer solchen Schmelzschicht hängen stark von ihrem Auftrieb ab, der wiederum von der Zusammensetzung der Schmelze bestimmt wird. Ein weiterer Beitrag in diesem Kapitel befasst sich mit der petrologischen Untersuchung des CaO-MgO-Al₂O₃-SiO₂-H₂O-Systems und der Bestimmung der Zusammensetzung und Dichte einer partiellen Schmelze im Gleichgewicht mit Mantel-Peridotit. Die dabei entstehende wasserhaltige Schmelze hat eine geringere Dichte als der sie umgebende Mantel und ist damit dynamisch instabil.

Die Wärmeleitfähigkeit von Mineralen des unteren Erdmantels kontrolliert maßgeblich die thermische Entwicklung der Erde. Da die Extrapolation von Daten bis zu Bedingungen des unteren Erdmantels zu großen Unsicherheiten führt, bilden Simulationen der Wärmeleitfähigkeit mit Hilfe der Molekulardynamik einen alternativen Ansatz zur Bestimmung dieser wichtigen Materialeigenschaft. Solche Berechnungen für die Gitterbeiträge zur Wärmeleitfähigkeit von Silikat-Perowskit und MgO werden im achten Beitrag dieses Kapitels vorgestellt; sie erlauben es, für den Wärmefluss vom Erdkern in den Mantel eine Obergrenze von $4.0 \pm 0.5 \text{ Wm}^{-1}\text{K}^{-1}$ anzugeben.

Das Erstarren des inneren Erdkerns aus der Kernflüssigkeit bei hohem Druck spielt ebenfalls eine große Rolle für die thermische Entwicklung der terrestrischen Planeten und die Entstehung eines Magnetfelds durch einen Dynamo. In diesem Zusammenhang ist es wichtig, die latente Wärme bei der Kristallisation zu bestimmen. Experimente hierzu sind schwierig, aber ein thermodynamisches Modell des Phasendiagramms von Eisen kann die latente Wärme entlang der Schmelzkurve in Abhängigkeit vom Druck bestimmen. In einem Beitrag zu diesem Kapitel wird ein derartiges thermodynamisches Modell genutzt, um den Energiebetrag der latenten Wärme in terrestrischen Körpern verschiedener Größen, einschließlich von Mond und Merkur, zu bestimmen.

Argumente aus seismischen und geochemischen Studien deuten darauf hin, dass der Erdkern größere Mengen von Kohlenstoff enthalten könnte, was einen großen Einfluss auf die Massenbilanz des Kohlenstoffs in der Erde hätte. Dabei ist die Eisenkarbid-Phase, die im Gleichgewicht mit Fe im Erdkern stabil ist, von Bedeutung. Der vorletzte Beitrag in diesem Kapitel berichtet über Berechnungen der elektronischen Bandstruktur von zwei Carbiden. Aus den Ergebnissen lässt sich die relative Stabilität von FeC₃-Zementit und einer neu entdeckten Phase mit der Zusammensetzung Fe₇C₃ vorhersagen.

Der letzte Beitrag des Kapitels betrachtet ein Szenario von Kernbildung in terrestrischen Planeten, in dem Eisenkörper durch den Magmaozean absinken. Eine grundsätzliche Frage ist dabei, ob Eisenkörper beim Sinken durch den Magmaozean zerlegt werden und eine Emulsion mit der Silikatschmelze bilden. Mit Hilfe einer Simulation, die finite Volumen verwendet, wurde ein einfaches Kriterium für die Stabilität eines Eisenkörpers abgeleitet. Dieses Kriterium wird von Oberflächenspannung, Trägheitseffekten und viskosen Kräften beeinflusst.

3.2 Geochemie

Die Entstehung des Sonnensystems wurde von chemischen Entwicklungen und Fraktionierungsprozessen begleitet, die in Gesteinen auf der Erde und im Weltall dokumentiert sind. Die Untersuchung dieser Gesteine erlaubt, oft im Vergleich mit Ergebnissen aus experimentellen Forschungen, die frühzeitlichen Prozesse nachzuvollziehen und zu verstehen. Die ersten fünf Beiträge dieses Kapitels befassen sich mit dem ersten dieser frühen Prozesse, der Abkühlung des Sonnennebels, die zur chemischen Aufspaltung in Gaswolke und kondensierte Mineralphasen führte. Zwei dieser Artikel widmen sich Enstatit-Chondrit-Meteoriten, die unter derartig stark reduzierenden Bedingungen (d. h. ohne Verfügbarkeit von Sauerstoff) gebildet wurden, dass sogar Elemente wie Kalzium und Kalium eigene Sulfidminerale ausbilden konnten – Erscheinungen, die im stärker oxidierenden Milieu auf der Erde praktisch unmöglich sind. In diesen Sulfiden reichern sich Elemente mit radiogenen Isotopen an, die für eine Altersbestimmung der Fraktionierungsprozesse dienen können. Die beiden letzten Beiträge zu Meteoriten erläutern, wie bestimmte Paragenesen von Sulfiden und Metallkörnern dazu verwendet werden können, die Bildungsbedingungen während des Endstadiums der Kondensation des Solarnebels einzugrenzen.

Die Entstehung der Erde aus meteoritischer Materie stellt das Thema der folgenden drei Artikel dar. Der erste entwickelt ein Modell für die Akkretion der terrestrischen Planeten aus der Materie in einer radial fraktionierten Sonnenscheibe. Das Modell erlaubt die Vorhersage der Masse der Kerne der inneren Planeten als Funktion des radialen Sonnenabstands und des Eisenanteils im Mantel der Planeten. Die folgenden zwei Beiträge simulieren, wie die Elementverteilung zwischen dem silikatischen Erdmantel und dem Kern aus flüssigem Eisen bei der Entstehung der Erde stattgefunden haben könnte. Es werden Indizien präsentiert, die für eine gleichzeitige Aufnahme von Si und O im Erdkern sprechen, was erklären würde, warum die Dichte des Erdkerns geringer ist als die einer Ni-Fe-Schmelze.

Eine weitere Studie befasst sich mit der Frage, ob Edelgase in Mineralen eingeschlossen sein können, die in dem tiefen Magmenozean der frühen Erdgeschichte auskristallisierten. Es wurde entdeckt, dass in den Mineralen des unteren Erdmantels deutlich mehr Argon als Xenon eingebaut werden kann. Die Freisetzung von Argon aus dem unteren Erdmantel, nachdem die Erde den größten Teils der Ur-Atmosphäre bereits verloren hatte, könnte so eine Erklärung für das hohe Ar/Xe-Verhältnis der heutigen Erdatmosphäre bieten.

Die nächsten drei Projekte betrachten das Auftreten von Karbonatmineralen und -schmelzen im Erdmantel. Im ersten wird gezeigt, dass Karbonate relativ zu Diamant unter den Redox-Bedingungen des unteren Mantels wahrscheinlich nicht stabil sind; die zweite Studie stellt einen vorläufigen Versuch dar, diesen Redox-Übergang Karbonat-Diamant in Eklogiten zu bestimmen. Die dritte Studie stellt eine starke Zunahme im Eisengehalt in Karbonatschmelzen fest, sobald ein gewisser Eisen-Grenzwert überschritten wird. Die abrupte Änderung der Schmelzzusammensetzung ist dem Übergang zwischen karbonatischer und kimberlitischer Schmelze ähnlich und könnte eine Erklärung für den Ursprung dieser Schmelzen im tieferen Erdmantel liefern.

Der Oxidationszustand des Erdmantels ist ein wichtiger Parameter, mit dem sich metasomatische Prozesse nachweisen lassen. Dabei wird die chemische Zusammensetzung von Mantelgesteinen durch Interaktion mit Fluiden oder Schmelzen subtil verändert. Dieses Thema wird in den sich anschließenden Artikeln detailliert untersucht. Ein Projekt untersucht Unterschiede im Oxidationszustand verschiedener Provinzen innerhalb sehr alter Mantel-Lithosphäre unter Südafrika. Der Redoxzustand sehr alter Gesteine, die einen Teil des tiefen Erdmantels oberhalb einer abtauchenden Scholle aus ozeanischer Lithosphäre bildeten, dem sogenannten „Mantelkeil“, steht im Fokus des folgenden Artikels. Der Oxidationszustand dient dazu, Aspekte zur Zusammensetzung der Fluide, die aus der Platte aufsteigen und die die Gesteine metasomatisch alteriert haben, einzugrenzen. Der nächste Artikel beschreibt Untersuchungen zur Verteilung von Halogenen zwischen Mineralen des oberen Erdmantels und Fluiden in Subduktionszonen. Deren Ergebnisse ermöglichen Abschätzungen über das Ausmaß der Fluid/Gestein-Wechselwirkung im Mantelkeil durch Fluide aus Subduktionszonen.

Der dann folgende Artikel stellt eine neue Methode vor, mit der die Gesamtzusammensetzung der ozeanischen Kruste und dem unterlagernden verarmten Mantel aus der Zusammensetzung der am geringsten fraktionierten Basaltgläser von mittelozeanischen Rücken bestimmt wurde. Die Ergebnisse zeigen, dass die ozeanische Kruste „primitiver“ ist als allgemein angenommen und dass der entsprechende verarmte Mantel wenig Granat enthält und daher einen größeren Auftrieb aufweist als bisher angenommen. Der anschließende Beitrag befasst sich mit der Löslichkeit des Sulfidminerals Molybdänit in felsischen Magmen. Dieses Mineral ist ein typischer akzessorischer Bestandteil in kieselsäurereichen Magmen, die bei Intra-Platten-Vulkanismus gebildet wurden. Ein thermodynamisches Modell zur Molybdänit-Löslichkeit erlaubt die Rekonstruktion des magmatischen Redoxzustands und der Schwefelfugazität und deutet darauf hin, dass diese Magmen ursprünglich auch mit dem Eisensulfidmineral Pyrrhotin gesättigt waren.

Der abschließende Beitrag befasst sich mit Biofilmen aus kleinen Drainageabflüssen aus einem aufgelassenen Kupferbergwerk. Es zeigte sich, dass Mikroorganismen als Katalysator für die Ausfällung nanokristalliner Sulfide und amorpher Phasen dienen, welche einen beachtlichen Teil der toxischen Metalle aufnehmen können. Mikroben fördern daher nicht nur die Freisetzung toxischer Metalle (z. B. in Bergwerkshalden), sondern tragen flussabwärts auch zu ihrer Ausfällung bei.

3.3 Mineralogie, Kristallchemie und Phasenumwandlungen

Schon in den vergangenen Jahren wurde an dieser Stelle dargestellt, dass Kenntnisse über Kristallstrukturen von Mineralen und deren Struktur/Eigenschaftsbeziehungen als Funktion von Druck, Temperatur und Beschaffenheit enorm wichtig sind, um Aufbau und dynamische Prozesse im Erdinneren und in anderen Planeten zu verstehen. Die Beiträge dieses Kapitels spannen einen weiten Bogen von der „klassischen“ Mineralogie, d. h. von der Identifizierung und Beschreibung neuer und bekannter Minerale, bis hin zu mineralogischen Untersuchungen bei extremen Bedingungen. Extreme Bedingungen bedeutet in diesem Fall nicht nur hohe

Drücke oder Temperaturen, sondern auch sehr anspruchsvolle Versuchsanordnungen im Labor.

Mineralogen haben mehr als 4400 Minerale katalogisiert, die als Ergebnis einer Mineral-Evolution infolge geochemischer und petrologischer Prozesse angesehen werden können. Zu diesen Prozessen zählen Vulkanismus und Freisetzung von Gasen, partielle Kristallisation und Metamorphose sowie auch Subduktion verschiedener Anteile der Erdkruste und Heraushebung von Gesteinen aus dem Erdinneren. Eine Identifizierung neu entdeckter Minerale (wie im ersten Beitrag beschrieben) oder von Mineralen, die als Einschlüsse in Diamanten auftreten (wie im zweiten Artikel angeführt), liefern uns wertvolle Hinweise auf das geologische Milieu, in dem die Minerale sich gebildet haben. Auf der anderen Seite kann die Bestimmung komplexer kristallographischer Eigenschaften die Strukturen intermediärer Pyrrhotine (dritter Beitrag) oder die asymmetrische Quadrupol-Dublette im Mössbauer-Spektrum eines Almandin-Einkristalls (vierter Artikel) erklären.

Die folgenden fünf Beiträge befassen sich mit der Bestimmung der Bildungsbedingungen verschiedener Minerale hinsichtlich Druck, Temperatur, Sauerstoff- und Wasserfugazität in Abhängigkeit ihrer kristallchemischen Eigenschaften. Der Oxidationszustand von Ti in Hibonit spiegelt die Bedingungen der Sauerstofffugazität im Frühstadium des Sonnennebels wider; Hibonit kondensierte als eines der ersten Minerale aus dem Sonnennebel. Untersuchungen von Wadsleyit-Lamellen und ihres Wirtsminerals Olivin in einem wasserhaltigen, peridotitischen Milieu bei hohen Drücken und Temperaturen ermöglichen uns Einblicke in die Verteilung von Elementen und von Wasser in der Übergangszone im Erdmantel bei 410 km Tiefe. Es wurde auch untersucht, ob die Druckabhängigkeit der Löslichkeit von Al und Cr in Rutil als Geobarometer verwendet werden kann. Lokale Verzerrungen in der Mg-Perowskit-Struktur aufgrund der Fe- und Al-Substitution könnten dagegen mit der NMR-Spektroskopie überprüft werden. Die Al-Substitution wurde bei hohen Drücken und Temperaturen auch untersucht, um den Al_2O_3 -Gehalt von Magnesiumsilikat-Perowskit, der in subduzierter basaltischer Kruste gebildet wurde, zu bestimmen.

Die abschließenden sechs Berichte behandeln das Strukturverhalten von Mineralen unter erhöhten Druck- und/oder Temperaturbedingungen. Bei hohen Temperaturen aufgenommene Infrarot-Spektren von wasserführenden Olivinen ermöglichen ein besseres Verständnis des Lösungsmechanismus von Wasser im oberen Erdmantel. In der Dispersionskurve von α - Fe_2SiO_4 wurde bei ~ 4 GPa eine Phonon-Instabilität entdeckt, die möglicherweise für den Übergang in seine γ -Phase verantwortlich ist. Zum ersten Mal konnten Einkristall-Röntgenbeugungsdiagramme eines Al- und Fe-haltigen Magnesiumsilikat-Perowskits und von Hämatit gleichzeitig bei hohen Drücken und Temperaturen gemessen werden; damit möchte man mit dem Spinübergang verbundene Strukturveränderungen des Perowskit erfassen sowie die Struktur der orthorhombischen Hochdruck-Phase des Hämatits aufklären. Eine Kombination aus Röntgenbeugungs- und thermoelektrischen Kraftmessungen diene dazu, Veränderungen sowohl im $\text{Fe}^{3+}/\text{Fe}^{2+}$ -Verhältnis als auch in der Stöchiometrie von Wüstit bei verschiedenen Drücken zu quantifizieren. Mit der Mössbauer-Spektroskopie wurden zwei magnetische Übergänge in Zementit untersucht, die bei zunehmendem Druck auftreten.

3.4 Physikalische Eigenschaften von Mineralen

Kontinentalverschiebung, Erdbeben und Vulkanausbrüche sind an der Erdoberfläche erkennbare Auswirkungen von Prozessen, die tief im Erdinneren ablaufen. Um diese Prozesse und die Funktionsweise und Struktur des Erdinneren zu verstehen, müssen die relevanten Mantelminerale und deren physikalische Eigenschaften bekannt sein. Die Geschwindigkeiten von Erdbebenwellen können zum Beispiel nur dann in ein Modell des Erdaufbaus umgesetzt werden, wenn die elastischen Eigenschaften und die Kompressibilität der beteiligten Minerale in Abhängigkeit von Druck und Temperatur bekannt sind. Die erforderlichen Kenngrößen werden in Laborexperimenten gewonnen, bei denen die zu untersuchenden Minerale kontrolliert Drücken und Temperaturen ausgesetzt werden, die im tiefen Erdinneren vorliegen. Diese Experimente sind sehr anspruchsvoll, da die Bestimmungen der Mineraleigenschaften *in situ* an geringen Probenvolumina durchgeführt werden müssen, die mit zunehmendem Druck immer kleiner werden. Die kontinuierliche Weiterentwicklung von Versuchsanordnungen sowie die Nutzung von Synchrotrons sind zunehmend wichtig, um Mineraldaten über den tiefsten Teil des Erdinneren zu gewinnen. Dies wird in diesem Kapitel beschrieben.

Die ersten vier Beiträge dieses Kapitels befassen sich mit den Zustandsgleichungen verschiedener Phasen, die entweder für den unteren Erdmantel wichtig sind oder die als Druckindikatoren in Experimenten genutzt werden. Die Druck-Volumen-Daten von Silikat-Perowskit, der Hauptphase des unteren Mantels, konnten bis zu einer neuen oberen Druckgrenze von 75 GPa bestimmt werden; auch können erste Zustandsdaten für eine neue Aluminium-reiche „Phase D“, die möglicherweise für den Transfer von Wasser in den unteren Mantel in Frage kommt, ermittelt werden. Ein weiterer Fortschritt besteht in der präzisen Bestimmung der Kompressibilität des in Diamantstempelzellen genutzten Standardmaterials Quarz bis zu einem neuen Druckmaximum von 21,5 GPa.

Bestimmungen von Kompressions- und Scherwellengeschwindigkeiten mit Hilfe der Ultraschall-Interferometrie und der unelastischen Kernstreuung werden in den folgenden zwei Beiträgen beschrieben. Die Interferometrie-Experimente an unterschiedlichen Granaten zeigen, dass Wellengeschwindigkeiten für Granate mit komplexer Zusammensetzung nicht unmittelbar aus den Geschwindigkeiten der Endglieder einer Mischkristallreihe abgeleitet werden können; vielmehr muss der Einfluss von Elementsubstitutionen im Detail untersucht werden. Die zweite Studie berichtet über Fortschritte bei der Messung von Geschwindigkeiten elastischer Wellen in Silikat-Perowskit unter extremen Bedingungen in einer Diamantstempelzelle. Bei diesen Experimenten wurde erstmals ein neuartiges, tragbares Lasersystem genutzt.

Der abschließende Block von Beiträgen befasst sich überwiegend mit Transporteigenschaften und dem Einfluss von Fe^{3+} auf physikalische Eigenschaften von Mantelmineralen. Zu den wichtigen Ergebnissen zählt, dass Experimente zur Interdiffusion in einem Modellsystem von Post-Perowskit die erwartete große Anisotropie im Diffusionsverhalten dieser Phase bestätigen. Eine andere experimentelle Studie zeigt auf, dass die hohe elektrische Leit-

fähigkeit der Unterkruste schlicht auf die Eigenschaften der Hauptminerale der Kruste, d. h. Plagioklas und Pyroxen, zurückgeführt werden kann. Abgeschlossen wird das Kapitel mit einer interessanten numerischen Studie, die die Stabilität von TiO_2 -Phasen (Anatas gegenüber Rutil) auf der Basis von Dichtefunktional-Berechnungen prognostiziert.

3.5 Fluide und ihre Wechselwirkung mit Mineralen und Schmelzen

Die Atmosphäre und die Ozeane der Erde entstanden durch die Entgasung des Erdinneren. Eine oft vernachlässigte Komponente in diesem System ist Stickstoff. Lange Zeit wurde angenommen, dass praktisch das gesamte Stickstoff-Budget der Erde sich in der Atmosphäre befindet und dass Stickstoff in der Luft keinen Einfluss auf die Entwicklung des Klimas hat. Neuere Arbeiten zeigen jedoch, dass ein hoher Partialdruck von Stickstoff zu einer Verbreiterung der Infrarot-Absorptionsbanden von Treibhausgasen und damit zu einer Erwärmung der Atmosphäre führt. Darüber hinaus gibt es zunehmende Hinweise auf ein tiefes Stickstoff-Reservoir im Erdmantel und für die Rückführung von Stickstoff in den Mantel durch Subduktion. Der erste Beitrag in diesem Kapitel untersucht daher die Stabilität von Stickstoffverbindungen in wasserreichen Fluiden im Erdmantel mit Hilfe von Raman-spektroskopischen Untersuchungen an synthetischen Flüssigkeitseinschlüssen. Die Daten zeigen, dass Ammoniak in Fluiden im oberen Mantel stabil ist, während in Subduktionszonen Stickstoff teilweise zu N_2 oxidiert wird. Das geochemische Verhalten von Stickstoff unterscheidet sich damit grundsätzlich von dem der Edelgase und Abschätzungen aufgrund von N_2/Ar -Verhältnissen in Magmen und vulkanischen Gasen unterschätzen wohl die Größe des Stickstoff-Reservoirs im Mantel.

Hydrothermale Erzlagerstätten sind weltweit die Hauptquelle für Molybdän und Wolfram. Es wurde spekuliert, dass die regionale Konzentration einiger Molybdänlagerstätten verursacht wird durch die Voranreicherung dieses Elements in Subduktionszonen. Zwei Beiträge beschäftigen sich daher mit dem Verhalten von Molybdän und Wolfram. Ein Beitrag untersucht die Mobilität von Mo und W in wasserreichen Fluiden im Erdmantel, während der andere sich mit der Löslichkeit von Molybdänglanz (MoS_2) bei niedrigeren Drücken beschäftigt. Die Daten zeigen, dass in Subduktionszonen Wolfram sehr stark im Fluid angereichert wird, während das Verhalten von Molybdän stärker von den Redoxbedingungen und der Salinität abhängt.

Die letzten beiden Beiträge dieses Kapitels beschäftigen sich mit der Rolle von Bakterien bei der Auflösung von Sulfiden. Es ist mittlerweile allgemein anerkannt, dass viele scheinbar anorganische Prozesse an der Erdoberfläche in Wirklichkeit unter Beteiligung von Mikroorganismen ablaufen, wobei die Mechanismen im Detail oft nicht verstanden sind. Hier wird ein besonders interessantes Experiment beschrieben: Die Gegenwart von Bakterien erhöht die Auflösungsgeschwindigkeit von Pyrrhotin, selbst wenn die Bakterien und der Pyrrhotin von einer semipermeablen Membran getrennt sind. Dies bedeutet, dass nicht das Bakterium selbst, sondern relativ kleine Moleküle, die von ihm freigesetzt werden, die Auflösung von Sulfiden beschleunigen.

3.6 Physik und Chemie von Schmelzen und Magmen

Schmelzprozesse im Erdinneren waren stets ein wichtiger Faktor in der 4,56 Mrd. Jahre alten Entwicklungsgeschichte unseres Planeten. Die Magmenbildung aufgrund partieller Aufschmelzungen und die anschließende Verlagerung in Richtung Erdoberfläche stellen den Hauptmechanismus der chemischen Differenzierung dar. Die Differenzierung ist für die Ausbildung und divergente Entwicklung der ozeanischen als auch der kontinentalen Erdkruste verantwortlich. Die Freisetzung von Magma erfolgt bei Vulkanausbrüchen, die zu den größten Naturgefahren zählen und die durch die Freisetzung vulkanischer Gase die chemische Zusammensetzung der Erdatmosphäre erheblich beeinflussen.

Die Projektbeschreibungen dieses Kapitels spannen einen weiten Bogen über magmatische Prozesse. Im ersten Beitrag werden vorläufige Ergebnisse einer Studie über Phasengleichgewichte in teilgeschmolzenem wasserhaltigem Peridotit vorgestellt. Diese Schmelzen entstehen unter mittelozeanischen Rücken, wobei die Aufschmelzung nur zu einem geringem Grad stattfindet. Die chemische Zusammensetzung sowie der Anteil an Wasser in den entstandenen basaltischen Schmelzen sind wegen der geringen Schmelzanteile experimentell nur schwer zu bestimmen. Die hier beschriebene Methode von „Sandwich“-Experimenten stellt einen brauchbaren Ansatz dar, dieses Problem zu überwinden. Auch der zweite Beitrag befasst sich mit kleinen Teilschmelzen im Erdmantel. Die Bestimmung der elektrischen Leitfähigkeit wasserführender Basaltschmelzen ermöglicht es, den tatsächlich vorhandenen Anteil an Schmelzen in unterschiedlichen Regionen des oberen Erdmantels abzuschätzen. Dazu vergleicht man experimentelle Resultate zur elektrischen Leitfähigkeit im oberen Mantel mit geophysikalischen Messdaten; die Ergebnisse führen zu dem Schluss, dass lediglich 1-2 % wasserhaltiger Schmelze in der Zone der niedrigen seismischen Geschwindigkeiten im oberen Mantel vorhanden ist.

Der dritte Artikel befasst sich mit der Kinetik von Kristallkeimbildung und -wachstum in Magmen des italienischen Vulkans Stromboli. Wenn man das Tempo der Keimbildung und das Wachstum des Mineralbestands der auskristallisierten Lava bestimmt (z. B. an Plagioklas und Klinopyroxen), lassen sich die Gefüge natürlicher Proben hinsichtlich der Dynamik des Ausbruchs interpretieren. Dies bedeutet, dass die Aufstiegsgeschwindigkeiten von Magmen innerhalb des Vulkangebäudes bestimmt werden können. Diese Information ist für die Abschätzung des Gefährdungspotentials eines Vulkans äußerst wertvoll, da die Aufstiegsgeschwindigkeit den explosiven oder nicht explosiven Charakter einer Eruption beeinflusst.

Karbonatite sind relativ seltene magmatische Gesteine, die hauptsächlich aus Karbonatmineralen aufgebaut sind. Lange Zeit war ihre Herkunft im Erdmantel kaum geklärt. Ein möglicher Ursprung wird auf eine Unmischbarkeit von Schmelzen zurückgeführt, d. h. auf eine physische Trennung in eine Silikat- und in eine Karbonatschmelze. Für einen derartigen Mechanismus finden sich weitere Hinweise aufgrund von Schmelzexperimenten zur Bestimmung von Phasengleichgewichten in Schmelzen, die mit karbonatführendem Mantelperidotit in einem vereinfachten System durchgeführt wurden und über die hier

berichtet wird. Der letzte Beitrag dieses Kapitels befasst sich mit dem Zerfall von Kalziumkarbonat bei hohem Druck als Ursprung für Diamanten im Erdmantel, einer Theorie, die in der Fachliteratur vorgestellt wurde. Die in diesem Kapitel präsentierten Ergebnisse stützen diese Hypothese nicht.

3.7 Rheologie

Deformationsprozesse spielen sich in der Erde über einen weiten zeitlichen und räumlichen Skalenbereich ab; zeitlich reichen sie von schnellen Bruchprozessen auf Störungen, die zu Erdbeben führen, bis zu langfristigen tektonischen Plattenbewegungen. Räumlich reicht die Deformation von Versetzungen im Kristallgitter bis zur Bildung ganzer Gebirgsketten. Die Verformung von Gesteinen unter einer angelegten Spannung (d. h. ihre Rheologie) muss daher sowohl als Funktion der Zeit (oder Verformungsrate) als auch der Grössenordnung der Homogenität untersucht werden. Experimentelle Untersuchungen von Deformationsprozessen sind aus zwei Aspekten wichtig: (1) sie erlauben eine Quantifizierung des mechanischen Verhaltens, d. h. des Zusammenhangs von Spannung und Verformungsrate (Fliessgesetz), und (2) produzieren sie Proben mit charakteristischen Mikrostrukturen und physikalischen Anisotropien. Die Kenntnis der Fliessgesetze ist unabdingbar für ein quantitatives Verständnis und die Modellierung von geodynamischen Prozessen in der Erde, während Mikrostrukturen und physikalische Anisotropien dabei helfen, die Gefüge deformierter Gesteine bzw. geophysikalische Beobachtungen (z. B. seismische Anisotropien) sinnvoll zu interpretieren.

Die gegenwärtige experimentelle Ausstattung am Bayerischen Geoinstitut ist daraufhin ausgerichtet, Deformationsexperimente bei möglichst hohen Drücken und Temperaturen durchzuführen und ist weniger gut dazu geeignet, mechanische Parameter (für die Bestimmung von Fliessgesetzen) präzise zu bestimmen. Daher sind die Deformationsuntersuchungen in diesem Kapitel vor allem auf mikrostrukturelle Auswirkungen der plastischen Deformation von Mineralen des Erdinneren hin ausgerichtet. Der Fokus liegt hier auf Abweichungen von bereits bekannten Texturentwicklungen, die durch erhöhten Druck (Olivin), Wassergehalt (Olivin, Orthopyroxen) oder chemische Substitution (Al in Orthopyroxen) entstehen. Das Ziel dieser Untersuchungen ist es, messbare Variationen in der physikalischen Anisotropie zu benutzen, um Informationen über die Verteilung von Wasser oder anderen Elementen im Erdmantel zu gewinnen. Subduktionszonen sind Bereiche intensiver Deformation, in denen neue Minerale unter hohem Druck und (relativ) niedrigen Temperaturen gebildet werden. Diese Minerale und ihr rheologisches Verhalten spielen eine wichtige Rolle bei dem eigentlichen Subduktionsprozess, wie auch bei den damit verbundenen Gebirgsbildungen (insbesondere bei kontinentalen Kollisionen).

Im unteren Erdmantel werden die Konvektionsbewegungen durch die Rheologie der Hauptmineralenkomponenten, Silikatperowskit und Ferroperiklas, bestimmt. Da kontrollierte Deformationsversuche bei den p,T -Bedingungen des unteren Erdmantels gegenwärtig technisch noch nicht durchführbar sind, konzentrieren sich die Untersuchungen auf mögliche

Deformationsmechanismen, wie z. B. Versetzungen und intrakristalline Gleitsysteme in diesen Mineralen. Die basale (D'') Region des unteren Erdmantels ist von besonderem Interesse, da sie geophysikalisch typische Anzeichen einer konzentrierten Deformationszone zeigt (z. B. starke Anisotropien). Deformationsexperimente mit Analogmaterialien des dort vermutlich vorliegenden Post-Perowskits produzieren Texturen, die einige der geophysikalischen Beobachtungen in dieser Zone erklären können.

Die experimentelle Deformation von Mineral-Schmelzgemischen ergibt Mikrostrukturen, die eine Unterscheidung zwischen Domänen erlaubt, die entweder durch die Oberflächenenergie oder die Spannungs-/Verformungsenergie kontrolliert werden und bestimmen, wie leicht sich eine Schmelzphase durch Perkolat von einer festen Phase trennen kann. Dieser Prozess spielt eine entscheidende Rolle in verschiedenen Szenarien für die Bildung des Erdkerns in der frühen Erdgeschichte.

3.8 Metamorphose

Unter Metamorphose versteht man Prozesse, bei denen ursprüngliche Mineralparagenesen in festem Zustand umkristallisieren und sich dabei veränderten Druck- und Temperaturbedingungen ihrer Umgebung anpassen. Metamorphe Gesteine können Informationen über geologische Prozesse liefern, die zum Beispiel in der tiefen Erde oder während gewaltiger Meteoriteneinschläge unter extremen Bedingungen ablaufen und für direkte Untersuchungen nicht zugänglich sind.

Ändert sich die chemische Zusammensetzung der Gesteine während der metamorphen Umwandlung aufgrund von Fluid- bzw. Schmelzzuflüssen, spricht man von Metasomatose. In der ersten Studie werden mikrostrukturelle Veränderungen in einem metasomatisch überprägten Peridotit beschrieben. Charakteristische Merkmale wie eine Formeinregelung der Minerale und neu gewachsene idiomorphe Olivinkristalle konnten mit Fluid-Gesteinsreaktionen im oberen Mantel in Zusammenhang gebracht werden.

Der Prozess der Umbildung von lockeren Sedimenten zu Festgesteinen wird Diagenese genannt; er findet unter vergleichsweise geringen Temperatur- und Druckbedingungen statt. Im zweiten Beitrag werden mineralogische Veränderungen untersucht, die während der Umwandlung des Tonminerals Kaolinit in die Glimmerminerale Illit/Muskovit stattfinden. Diese Reaktion findet bei der Diagenese in sedimentären Becken statt. In der experimentellen Studie wurde der Einfluss des Drucks bei konstant gehaltener Temperatur auf die Illitisierung untersucht.

Thema der beiden abschließenden Beiträge ist die Metamorphose durch Impaktereignisse. Hierbei handelt es sich um sehr kurze, explosionsartige Ereignisse mit intensiver Hitze und hohen Drücken, die durch Meteoriteneinschläge auf der Erde oder anderen Himmelskörpern bewirkt werden. In einem Beitrag wurden Pyrrhotin-Körner aus einem Suevit extrahiert. Suevit ist eine typische Impaktbrekzie (Trümmergestein), das unterschiedlich stark

beanspruchte Auswurfmaterialien und Schmelzanteile enthält. Die Pyrrhotine wurden mit Hilfe der Transmissionselektronenmikroskopie untersucht, und liefern Aufschlüsse zum Einfluss des Impakts auf die Magnetisierung der Minerale. Im letzten Beitrag wird die Zersetzung von Olivin in Impaktschmelzadern einer Meteoritprobe beschrieben. Die Autoren zeigen, dass Teile der Lamellen in Olivin aus amorphisiertem $(\text{Mg,Fe})\text{SiO}_3$ -Perowskit bestehen, einem Mineral, das normalerweise nur unter den Bedingungen des unteren Erdmantels stabil ist.

3.9 Materialwissenschaften

In den vergangenen Dekaden wurden große Fortschritte im Design und Leistungsvermögen von Apparaturen zur Erzeugung hoher Drücke und Temperaturen erzielt. Die Hochdruck-Technik und ihre Anwendungen zur Bestimmung von Volumen, Struktur, elektronischen und magnetischen Eigenschaften von Festkörpern wurden im Laufe der Zeit immer kostengünstiger und alltäglicher, sodass vielversprechende Synthesepfade für neue Gebrauchsmaterialien entwickelt werden konnten. Das Bayerische Geoinstitut ist auf diese anspruchsvolle Erforschung von Materie unter extremen Bedingungen spezialisiert und ist mit seiner modernsten Ausstattung nicht nur auf dem neuesten Stand der Technik sondern entwickelt auch selbst neue Apparaturen und Methoden. In diesem Jahr berichten wir über Untersuchungen an verschiedenen Arten von Feststoffen – Elementen, Oxiden und komplexen Manganiten und Boraten.

Elementares Bor und Bor-reiche Feststoffe sind ein sehr attraktives Forschungsgebiet, da ihre einzigartigen physikalischen Eigenschaften für zahlreiche Verwendungszwecke geeignet sind. Kürzlich wurde am BGI eine Methode zur Synthese einer Hochdruck-/Hochtemperatur-Phase von Bor (B_{28}) mit einer Kombination mehrerer nützlicher Eigenschaften entwickelt: Dieses Material ist superhart, halbleitend und optisch transparent. Der neu synthetisierte Einkristall aus B_{28} wurde mit Ramanspektroskopie und Röntgenbeugung eingehend untersucht, wobei sich ein unerwarteter, gefügeremanenter Phasenübergang zeigte. Eine erste reproduzierbare Hochdruck-Synthese von Einkristallen aus α -Bor bei Bedingungen, die industriell leicht zu handhaben sind, eröffnet neue technologische Perspektiven für dieses halbleitende Material.

Die Mineralogie und die Petrologie teilen als moderne Disziplinen der Erdwissenschaften mit den Materialwissenschaften nicht nur zahlreiche methodische Ansätze wie z. B. physikalische und chemische Methoden zur Synthese und Strukturbestimmung, Überlegungen zur Korrelation von Strukturen und Eigenschaften, Untersuchungen von Materialreaktionen auf Veränderungen bei den thermodynamischen Parametern, Methoden der numerischen Modellierung usw., sondern arbeiten auch auf den gleichen Forschungsgebieten. Oxide, wie Mischkristalle auf der Basis von MgO and Ti_2O_3 (einem typischen Repräsentanten der Sesquioxide), stellen sowohl wichtige Komponenten in petrologischen Systemen als auch interessante Phasen für die Materialphysik dar. Das komplexe Hochdruck-/Hochtemperatur-Verhalten von Ti_2O_3 fügt der Kristallchemie von Sesquioxiden aus Übergangsmetallen eine

neue Dimension hinzu und ist einerseits für die Materialwissenschaften von Bedeutung, trägt aber auch zu unserem Verständnis über das Innere von Riesenplaneten bei.

Die Beziehungen zwischen Struktur und Eigenschaften spielen in den Materialwissenschaften eine elementare Rolle. Zwei neue Beispiele dazu liefern Beobachtungen an druckbedingten Phasenübergängen in Seltenen Erden-Manganiten und Elastizitätsuntersuchungen an Lithiumtetraborat.

3.10 Methodische Entwicklungen

Neue Entwicklungen in experimenteller, analytischer und numerischer Methodik sind das Rückgrat jeglicher wissenschaftlicher Forschung, deren Bedeutung nicht oft genug betont werden kann. Das Bayerische Geoinstitut weist hier eine lange Tradition mit beachtenswerten Erfolgen auf; zahlreiche seiner Innovationen haben Eingang in andere Laboratorien in der ganzen Welt gefunden. Im vergangenen Jahr wurden Fortschritte mit einem tragbaren Laser-Heizsystem für Einkristall-Röntgenbeugungsexperimente in Diamantstempelzellen erzielt, wodurch Kristallstrukturmessungen bei gleichzeitig hohem Druck und hoher Temperatur ermöglicht werden. Weitere Fortschritte gab es bei Mössbauer-Analysen mit energiereicher Synchrotronstrahlung am ESRF in Grenoble. Die Reduzierung des Strahldurchmessers mit Hilfe eines KB-Spiegels erlaubt Mössbauer-Experimente in Diamantstempelzellen bei hohen Drücken und Temperaturen. Die 2009 im BGI aufgebaute Sechs-Stempel-Pressen wurde besonders für Verformungsexperimente weiterentwickelt. Die Zuverlässigkeit des kombinierten Systems aus Brillouin-Streuung und hochauflösender Röntgenbeugung, ebenfalls in Jahre 2009 in Bayreuth eingerichtet, wurde mit Testmessungen an Standardmaterial überprüft. Des Weiteren wird hier über Druckbestimmungen mit Ramanstreuung in Diamantstempelzellen berichtet.

Auf analytischem Gebiet eröffnet der Einsatz von Probenkapseln aus Quarz neue Wege bei der Bestimmung der Konzentrationen von siderophilen Elementen in Fluidphasen. Es wurde eine neue Software entwickelt, mit der sich für zukünftige Kinetikstudien die Oberflächen-Rauigkeit von Mineralen auf der Basis ihrer statistischen Verteilung bestimmen lässt. Schließlich wird ein neuer Ansatz zur numerischen Modellierung scharfer Grenzen bei geodynamischem Fließen beschrieben, die bisher bestehende Einschränkungen überwindet.

3.1 Earth and Planetary Structure

Geochemical and geophysical data obtained at the surface can only be interpreted with a good understanding of the dynamic processes occurring within terrestrial bodies, and their relationships with material properties at relevant pressure and temperature. Using experimental or numerical approaches the contributions in this chapter therefore aim to bridge gaps between surface observations and the structure and dynamics of the interior of Earth and other terrestrial bodies.

While geochemical data suggest that Earth's mantle is heterogeneous, vigorous mantle convection tends to erase heterogeneities. Understanding the survival of mantle heterogeneities is therefore critical in interpreting geochemical observations. The three opening contributions focus on this aspect by investigating the efficiency of mantle mixing in a geodynamic context: infinite Prandtl number convection in the presence of continental lids, small scale sub-lithospheric convection, and finite Prandtl number convection in magma chambers. The main results of the first two contributions are that the presence of continental lids and well-developed small-scale convection can drastically increase stirring efficiency at infinite Prandtl number (*i.e.*, without inertial effects) in the mantle. Inertia effects, likely to occur in magma chambers, on the other hand, significantly reduce the efficiency of convective stirring.

Unlike pressure, current estimates of the temperature profile within the Earth's mantle vary significantly. Using experimentally determined phase relationships in the system $(\text{Mg,Fe})_2\text{SiO}_4$ the next contribution of this chapter determines more precisely an adiabatic profile within the Earth's mantle, which can differ by more than 100 K from previous estimates.

Although subduction dynamics and slab evolution are very sensitive to small changes in physical properties due to temperature, most subduction studies neglect the influence of temperature on thermal properties of the downgoing material. Another contribution to this chapter focuses on taking these aspects into account by determining the thermal conductivity for a multi-component slab with pressure and temperature effects determined in experiments. This work will serve as an input basis for future numerical models of subduction dynamics.

Several subduction zones show the presence of anomalously slow layers with 5-7 % reduction of shear wave velocities, which could be produced by the formation of a hydrous phase (Lawsonite). To investigate the plausibility of such a scenario, one contribution reports experimental and computational results on the elastic properties of this hydrous phase. Elastic moduli suggest that the occurrence of Lawsonite in significant proportions can provide an explanation for the presence of low shear wave velocity anomalies not associated with compressional wave anomalies, as observed in several subduction zones.

The presence of hydrous partial melt in Earth's mantle transition zone is a good candidate for explaining low-shear wave velocities associated with high electrical conductivities at 410 km depth. However, the stability of hydrous partial melts depends on its buoyancy in this region, which is determined by the composition of the melt in equilibrium with the surrounding mantle. One contribution reports experimental results on the CMASH system that were used to derive the composition and the corresponding density of small degrees of partial melt in equilibrium with a peridotitic mantle. The resulting hydrous melt has lower density than the surrounding mantle at 410 km depth.

Thermal conductivity in lower mantle materials is an important physical property that controls the thermal evolution of the Earth. While extrapolating low-pressure experimental data to lowermost mantle conditions can lead to large uncertainties, recently performed first-principle calculations reported in one contribution to this chapter provide a good alternative to experimental approaches. Applying these calculations to an assemblage of MgSiO_3 -perovskite and MgO periclase yields estimates of lattice thermal conductivity in the CMB region and thus allows placing a lower bound value of $4.0 \pm 0.5 \text{ Wm}^{-1}\text{K}^{-1}$ for the heat flux at the base of the Earth's mantle.

The solidification of iron at high pressure plays a key role in the thermal evolution of terrestrial bodies and in generating planetary dynamos. In this context, constraining the latent heat of crystallization is of major importance but remains difficult to determine experimentally at pressures relevant to planetary cores. One contribution presents the results of a thermodynamic model of the iron phase diagram that provide estimates of latent heat along the melting curve of iron as a function of pressure. Such estimates can be used to infer the thermal evolution and the sustainability of dynamos in terrestrial bodies of various sizes, including the Moon and Mercury.

Seismological and geochemical observations suggest that Earth's core may contain significant amounts of carbon. The abundance of C could significantly affect mass balance estimates within the Earth, depending on the phase stability in the Fe-C phase diagram. One contribution explores the relative stability of the Fe_3C cementite phase versus a newly described phase with Fe_7C_3 stoichiometry by means of electronic structure calculations.

The closing contribution to this chapter focuses on a plausible core formation scenario during which iron bodies have sunk through a silicate magma ocean. A fundamental question is whether iron bodies have emulsified as they plunged through the magma ocean. Using a finite volume approach a simple criterion for the stability of iron bodies has been derived. The latter depends on the interplay between surface tension, inertial effects and viscous forces.

a. Combined effects of plate motion and small-scale convection on mantle stirring efficiency (H. Samuel and S.D. King/Blacksburg)

Convection in the Earth’s mantle generates large scale, vigorous motions often thought to be the primary mechanism of mantle stirring. However, additional thermal instabilities may progressively develop below lithospheric plates, leading to smaller scale convective motions. While there is a growing range of evidence supporting the presence of small-scale convection in Earth’s mantle, little is known of its contribution to the mixing of mantle heterogeneities.

We have thus investigated the influence of small-scale convection on mantle stirring efficiency using 2D numerical modeling of infinite *Prandtl* number convection with imposed surface plate motion and temperature and depth dependent viscosity. We measure stirring efficiency using Finite Time Lyapunov Exponents (FTLE) and we vary systematically the plate *Péclet* number, Pe , defined as the ratio of advection time scale based on surface plate velocity to a characteristic diffusion time. Our computational domain has an aspect ratio of 1:3. For moderate Pe , small-scale convection is well developed, leading to an efficient stirring. However, larger Pe numbers do not allow the development of small-scale convection and result in a significantly lower stirring efficiency, although plate motions are faster (Fig. 3.1-1). This indicates that (i) small scale convection contributes significantly to mantle stirring efficiency, (ii) mantle stirring efficiency may spatially vary significantly due to the local magnitude of plate velocity and (iii) the relationship between mantle stirring efficiency and large scale convective motions may be more complex than previously thought.

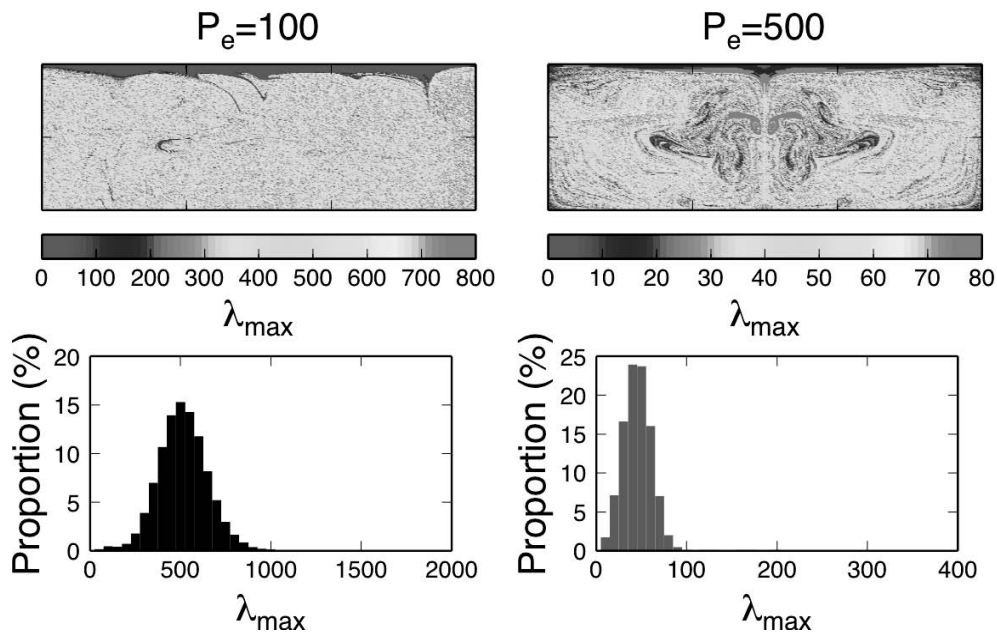


Fig. 3.1-1: Comparison between two numerical experiments with different *Péclet* numbers: $Pe=100$ (slow spreading rate, left) and $Pe=500$ (fast spreading rate, right). Maximum Finite Time Lyapunov Exponents (FTLE) spatial distribution (top) and corresponding histograms (bottom).

Further systematic exploration of the parameter space (Pe , rheological parameters) should help to better quantify and to constrain the role of small-scale convection on mantle stirring efficiency.

b. The effect of continental lids on mantle convective stirring efficiency (H. Samuel, V. Aleksandrov and B. Deo/Kharagpur)

Interpreting surface geochemical data requires understanding the dynamic mechanisms that preserve or erase chemical heterogeneities over geological time. Among these, the presence of continental lids is known to have a first order impact on mantle convective dynamics and heat transfer. Numerical and laboratory experiments have demonstrated that on Earth the dichotomy between continents and oceans can have a first order influence on mantle motions, convective wavelength, heat flow and thermal evolution. One should therefore expect that this also influences the efficiency of convective stirring over billions of years. While a number of studies have estimated mantle mixing times, this effect has not been previously considered.

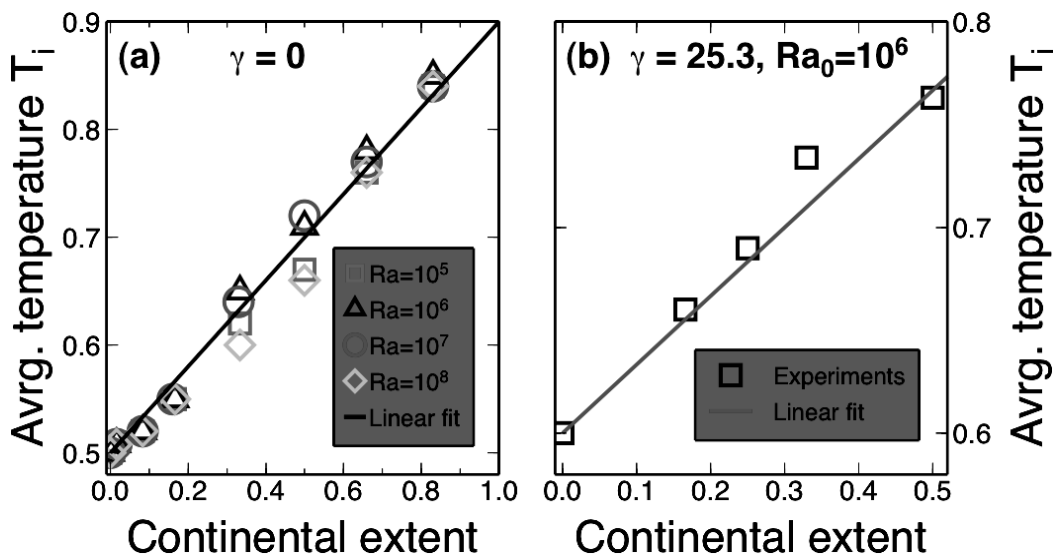


Fig. 3.1-2: Effect of continents on the thermal structure. (a) Average mantle temperature T_i as a function of the continental surface S for various *Rayleigh* numbers and for constant viscosity ($\gamma = 0$). The experimental data is well fitted by a linear expression. (b) Average mantle temperature T_i as a function of the continental surface S for cases with $Ra=10^6$ and $\gamma=25.3$. The experimental trend is well fitted by a linear expression.

We have therefore investigated the influence of continental lids on convective stirring efficiency using numerical experiments at infinite *Prandtl* number, with strongly temperature-dependent viscosity. We find that the presence of continental lids increases mantle temperature (Fig. 3.1-2) and drastically enhance the convective stirring efficiency (Fig. 3.1-3). Furthermore, this increase in stirring efficiency is amplified by the lateral extent of continental lids.

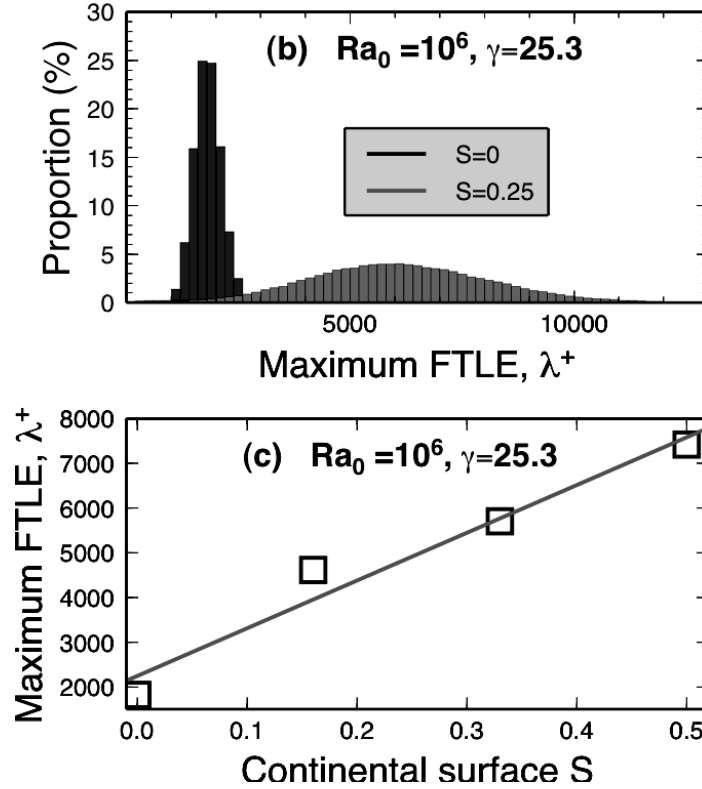


Fig. 3.1-3: Top: Maximum Lyapunov exponent distributions for two numerical experiments with $Ra_0 = 10^6$ and $\gamma = 25.3$: one without a continent ($S = 0$), the other with a continent ($S = 0.25$). Bottom: Average value of the maximum Lyapunov exponents, as a function of the continental lateral extent S , for cases with $Ra_0 = 10^6$ and $\gamma = 25.3$. A linear fit is displayed.

We have developed a simple chaotic mixing model that shows a good agreement with our numerical experiments. Using this model we show that mantle stirring time can be well represented by the following relationship:

$$\tau = a \ln \left(\frac{\delta_0}{\delta} \right) \exp \{ Ra_0 \exp [-\gamma (T_i - 0.5)] \}^{-2/3},$$

where $a = 1.310^7$ My, δ/δ_0 represents the ratio of initial to final size of a given passive heterogeneity. Ra_0 is the reference (surface) *Rayleigh* number, γ the sensitivity of viscosity to temperature (*i.e.*, an activation energy), T_i the dimensionless average mantle temperature.

Using this chaotic mixing model we show that mantle stirring is about 10 times more efficient with continents. These results are valid when accounting for secular changes in mantle convective vigor by combining our chaotic mixing model with mantle thermal evolution derived from parameterized convection models (Fig. 3.1-4). The presence of continents should therefore be taken into account when interpreting the geochemical record.

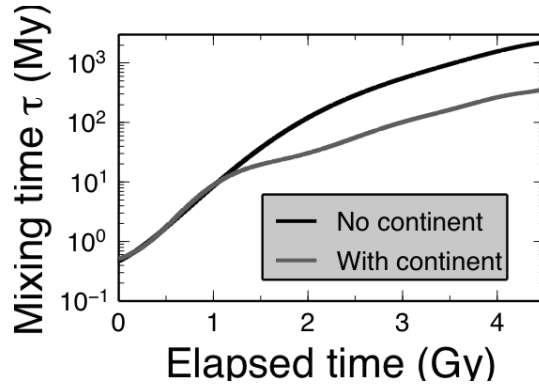


Fig. 3.1-4: Results of the chaotic mixing model for $Ra_0=10^6$. Time evolution of instantaneous mixing times τ for a mantle thermal evolution without a continent (black curve) and a thermal evolution with a continent (grey curve), for $\gamma=37$.

c. Convective stirring efficiency at finite Prandtl number (H. Samuel)

Convective motions in magma chambers play a key role in erasing or preserving mantle heterogeneities. In such a context the low magma viscosities yield significant influence of inertial effects that are otherwise negligible for larger scale solid-state mantle convection. I therefore conducted a series of 2D numerical experiments to investigate and to quantify the effect of inertia on convective stirring efficiency of an iso-viscous Boussinesq fluid, in a domain of aspect ratio 1:2. The *Prandtl* and *Rayleigh* numbers were systematically varied over the ranges $Pr=10^{-2}$ - 10^2 and $Ra=10^5$ - 10^{12} , respectively. Stirring efficiency was quantified using Finite Time Lyapunov Exponents (FTLE). For all values of *Rayleigh* number investigated, increasing inertial effects (*i.e.*, for lower *Pr* numbers), leads to larger scale circulation and reduces the strength and time variability of the flow (Fig. 3.1-5). These effects seem to be more pronounced at higher *Rayleigh* numbers. This resulting combination reduces significantly the convective stirring efficiency, as measured by the FTLE distributions (Fig. 3.1-6).

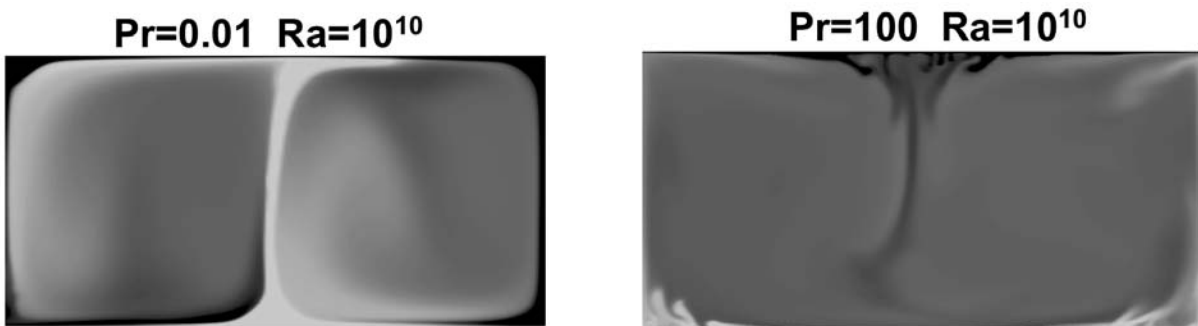


Fig. 3.1-5: Dimensionless temperature fields obtained at statistically steady state for two experiments with $Pr=10^{-2}$ (left) $Pr=100$ (right). For both cases the *Rayleigh* number is $Ra=10^{10}$.

As predicted by mixing theory, I find a good correspondence between chaotic (efficient) and regular (weak) stirring efficiency and the time dependence of the convective motions.

Using analytic mixing theory, the FTLE can be used to estimate convective stirring times within magma chambers of various sizes. Ongoing research will further extend the range of *Rayleigh* number values that could correspond to magma chambers of greater vertical extent. In addition experiments with chemical diffusion will also be conducted in order to take into account the much higher diffusion rates in liquids compared to the solid-state counterpart.

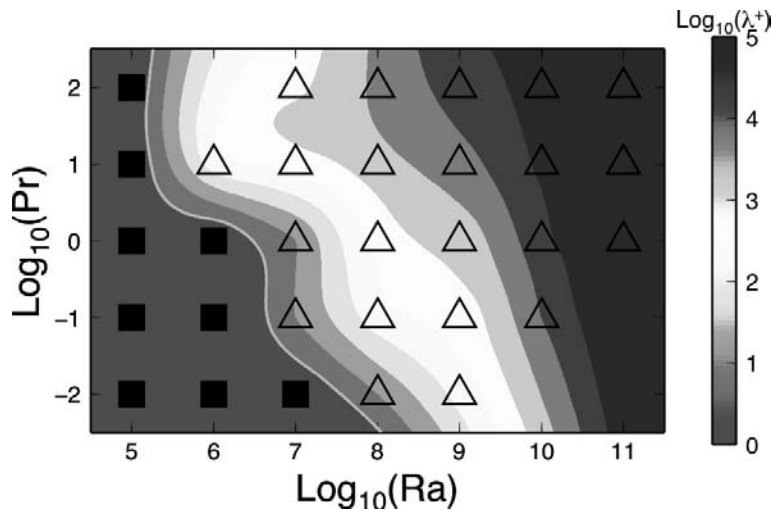


Fig. 3.1-6: Maximum Finite Time Lyapunov Exponent as a function of *Ra* and *Pr*. Triangles indicate experiments where the time dependence of the flow remains, while squares correspond to experiments where negligible time dependence is observed.

d. *Adiabatic temperature profiles in the mantle (T. Katsura, in collaboration with A. Yoneda, D. Yamazaki, T. Yoshino and E. Ito/Misasa)*

Temperature is an essential parameter for understanding the dynamics of the Earth's interior. There is, however, no direct way to measure temperature in the Earth's deep interior. A combination of indirect methods is necessary to estimate the temperature distribution in the deep mantle. The temperature profile in the mantle is considered to be nearly adiabatic because heat should be mainly transported by convection in most part of the mantle due to the small thermal conductivity of the mantle minerals. The adiabatic temperature gradient, $(\partial T/\partial z)_s$, in the Earth is expressed as $(\partial T/\partial z)_s = \alpha g T / C_p$, where T is temperature, z is depth, g is gravitational acceleration, and α and C_p are the thermal expansivity and isobaric heat capacity of the constituent materials, respectively. If we know a temperature at one depth, we can estimate the temperature profile of the mantle using this equation.

Mantle discontinuities could provide such a fix point by comparing the depth of the discontinuity with the pressure of the corresponding phase transition. Recent seismological study suggested that the topography of the 410-km discontinuity is anti-correlated with the shear wave structure in the upper part of the mantle transition zone, and not correlated with the surface tectonic setting. These observations imply that the depth of the 410-km discontinuity is primarily a function of temperature, but not of water and iron contents in the

mantle. For this reason, we first estimate the temperature at the 410-km discontinuity in this study, to obtain a fix point for the temperature profile in the mantle.

Our previous study determined the phase relation of the olivine-wadsleyite transition in the $(\text{Mg,Fe})_2\text{SiO}_4$ system by combining pressure measurement by *in situ* X-ray diffraction and compositional characterization of the recovered samples. However, although the sample pressures were calculated using MgO pressure standard with Matsui scale in the previous study, new pressure scales that explain a wide variety of experimental results are recently proposed (Tange-BM3 and Tange-V scale, respectively). In addition, it is found that the program to calculate pressure based on Matsui scale did not have sufficient precision. Here we have recalculated the phase relations using the Tange-BM3, Tange-V and Matsui scales with higher precision. The recalculated phase boundaries were shifted to lower pressures by $\sim 0.4\text{-}0.5$ GPa.

Recent seismological study suggested that the average depth of the 410-km discontinuity is 409 km. Comparison of this depth with the phase diagrams of the olivine-wadsleyite transition suggests the average temperature at the 410-km discontinuity to be 1830 ± 50 K, which is 70 K higher than previous estimates.

Thermal expansivity and isobaric heat capacities are the physical properties required to calculate the adiabatic temperature gradient. Thermal expansivity at high P-T can be calculated by differentiating the equation of state with respect to temperature. We previously reported high-temperature EoS of Mg_2SiO_4 olivine, wadsleyite, ringwoodite and MgSiO_3 perovskite, respectively, based on the Matsui scale for pressure calculation. Here we recalculated the pressures of the P - V - T data points using the Tange-V scale. The parameters of the equations of state obtained by the recalculation are summarized in Table 3.1-1.

Table 3.1-1: Thermoelastic parameters of mantle minerals. Values with an asterisk are taken from the literature.

	Olivine	Wadsleyite	Ringwoodite	Perovskite
K_T (GPa)	127.4*	169.2*	182 *	261(1)
K	4.4	4.3(1)	4.8(2)	3.8(1)
a_0 ($10^{-5}/\text{K}$)	2.56(1)	2.17(3)	2.45(5)	2.61(2)
a_1 ($10^{-8}/\text{K}^2$)	1.59(2)	1.01(3)	0.91(6)	0.99(3)
δ_T	7.2(3)	5.0(2)	5.6(4)	5.8(2)
θ (K)	760*	814(7)*	830(7)*	1030(20)*
γ_0	0.99(1)	1.15(3)	1.30(3)	1.66(1)
q	2.7(3)	2.2(1)	2.2(2)	1.8(1)
$\partial K_T / \partial T$ (GPa/K)	-0.023(1)	-0.019(1)	-0.025(1)	-0.035(1)
$\partial K_S / \partial T$ (GPa/K)	-0.018(1)*	-0.0175(3)*	-0.0193(9)*	-0.029(2)*

The isobaric heat capacities of olivine, wadsleyite and ringwoodite at high pressures are estimated by correcting those at ambient pressures. For this correction, we assume that the isochoric heat capacities are constant with pressure, and the factor of $1+\alpha\gamma T$ is corrected using the revised equations of state of these minerals. The isobaric heat capacity of perovskite is obtained by multiplying the isochoric heat capacity based on the Debye model with a factor $1+\alpha\gamma T$. The Debye temperature at high P-T was estimated by correcting that at ambient pressure using the equation of state mentioned above. The high-pressure values of the term $1+\alpha\gamma T$ are estimated from the revised equation of state of MgSiO_3 perovskite.

Using these properties, we have estimated the adiabatic temperature gradient and temperature by a step-by-step calculation starting from 410-km depth. The results are shown in Fig. 3.1-7. The adiabatic temperature gradient decreases with increasing depth in the absence of a phase transition. In association with phase transitions it increases abruptly. Although the adiabatic temperature gradient in the upper mantle is usually considered to be 0.3 km/K, it is found that the value of 0.4 km/K is more appropriate. The adiabatic temperature gradient in the upper part of the lower mantle is 0.4 K/km, and decreases to 0.2 K/km at the bottom of the lower mantle. The temperature at the bottom of the mantle transition zone is found to be 1990 ± 50 K, which is 110 K higher than the previous estimation. The temperature at the top of the lower mantle is found to be 1960 ± 50 K. The temperature at 2700 km depth is 2630 ± 60 K, if convective heat transfer still dominates in this region. The temperature at 200 km depth is 1700 ± 50 K. The mantle potential temperature is found to be 1600 ± 40 K.

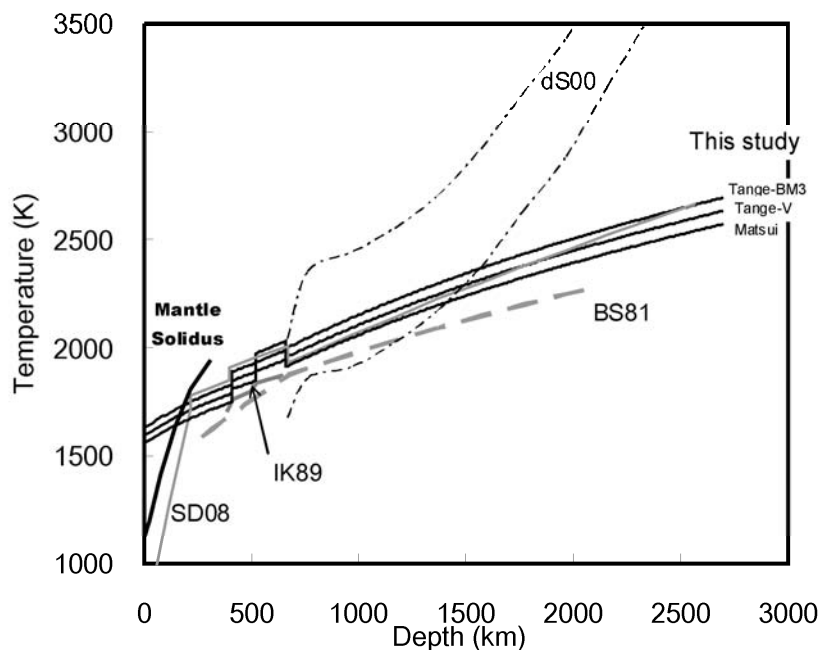


Fig. 3.1-7: Adiabatic temperature distributions in the mantle based on the three equations of state (Tange-BM3, Tange-V and Matsui). Previous estimates are shown for comparison [BS81: Brown and Shankland, 1981; IK89: Ito and Katsura, 1989; dS00: da Silva *et al.*, 2000; SD08: Stacey and Davis, 2008]. The mantle solidus proposed by Hirschmann [2000] is also included.

e. *Subducting slab with pressure- and temperature-dependent thermal properties (P. Maierová and G. Steinle-Neumann)*

Numerical studies of subduction show that it is a highly sensitive system and, due to the non-linearity of the governing equations, minor changes in input parameters may significantly affect its dynamics. Various parametric studies of subduction have been performed examining the influence of rheology, phase transitions and model setup. However, most of them assume constant (or only depth-dependent) thermal properties. At the same time, extensive research has been carried out on thermal properties of minerals at high pressure and high temperature. The data indicate that thermal diffusivity and conductivity are strongly temperature- and pressure-dependent and vary considerably among different mantle phases. According to both computations and experiments, thermal conductivity generally decreases with temperature and increases with pressure. Since the subducting slabs are colder than the surrounding mantle, they should have higher thermal conductivity. This difference may lead to more efficient thermal equilibration of the slabs. The thermal state of the slabs is further influenced by their petrology and by latent heat from phase transitions. These contributions to subduction dynamics warrant further studies by means of numerical modeling.

Current experimental measurements of thermal properties do not reach lower mantle conditions, but computations provide estimates on thermal properties in this region. The results of *ab initio* calculations indicate a significant jump in thermal conductivity at the upper- to lower-mantle transition. However, thermal properties of the lower mantle are still poorly understood and radiative heat transport could play an important role.

Table 3.1-2: Mineral assemblage of simplified petrological models (in mol.%) used for subduction lithologies. UM and TZ are the upper mantle and transition zone, respectively. The lower mantle is represented for the pyrolite composition only (LM).

	ol/wa/ri	cpx/mj	st	pv	pc
basalt		92	8		
harzburgite	80	20			
pyrolite (UM + TZ)	60	40			
pyrolite (LM)				70	30

On the basis of published data we have compiled analytical relationships that approximate pressure- and temperature-dependences of thermal diffusivity and/or conductivity for major mineral phases of the mantle: olivine (ol), wadsleyite (wa), ringwoodite (ri), majorite-garnet (mj), clinopyroxenes (cpx), stishovite (st), perovskite (pv) and MgO periclase (pc). To study the influence of phase assemblage we propose simplified petrological models of the different

slab components and the surrounding mantle: a pyrolite mantle, basalt, and depleted harzburgite (Table 3.1-2). For these mineral assemblages we evaluate thermal conductivity and/or diffusivity using the Hashin-Shtrikman bounds (Fig. 3.1-8). These thermal properties, along with density and heat capacity from thermodynamic mantle models are suitable as an input for numerical models of subduction dynamics.

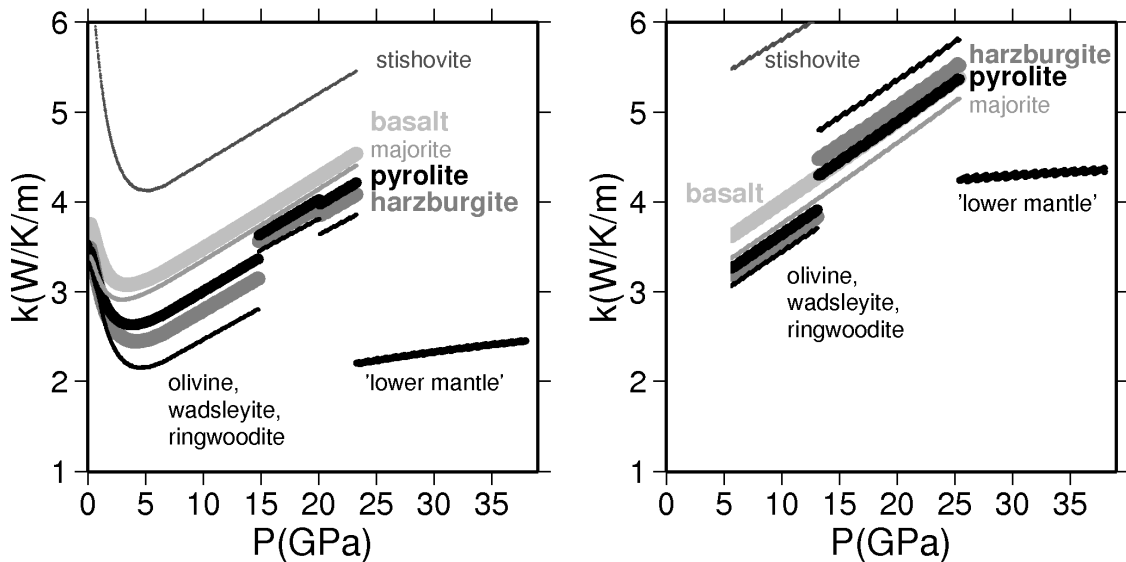


Fig. 3.1-8: Thermal conductivity of mineral phases and phase assemblages in the subducting slab and the surrounding mantle along a representative mantle (left) and slab geotherm (right), neglecting the contributions from clinopyroxene.

f. The elasticity of lawsonite and the occurrence of low velocity layers (LVL) in subduction zones (J. Chantel, M. Mookherjee and D.J. Frost)

As oceanic lithosphere is subducted its constituent minerals undergo a series of phase transformations, instigated mainly by the increasing pressure and temperature. The hydrated oceanic crust undergoes dehydration and eventually transforms to eclogite, a rock containing mainly clinopyroxene and garnet. However, in subduction zones that follow relatively cold geothermal gradients, dehydration may be minimal to depths over 100 km and some transformations may be kinetically hindered. In such subduction zones including, for example, southern Japan a low velocity layer (LVL, 5-7 % slower in V_S) has been observed up to 250 km depth. This anomaly could be caused by the formation of a hydrous layer inside the basaltic portion of the slab, where some thermodynamic simulations have predicted the occurrence of lawsonite-blueschist rocks.

Lawsonite ($\text{CaAl}_2\text{Si}_2\text{O}_7(\text{OH})_2 \cdot \text{H}_2\text{O}$) is a hydrous mineral that can form in the mafic portion of a slab, potentially from H_2O released by the breakdown of serpentine minerals within the underlying ultramafic portions of the slab. Such a process could produce lawsonite rich

horizons (20 % - 30 % volume), which could cause a seismic signal such as observed in the low velocity lenses. However, insufficient data on the lawsonite elasticity do not allow us to test this hypothesis. To determine the elastic properties of lawsonite at high pressure, we have preformed both computational and experimental investigations. We have computed the elasticity of lawsonite using first principles calculations. In addition, we measured the sound velocities of lawsonite up to 8 GPa using ultrasonic interferometry, employing the phase comparison method, in a multianvil apparatus.

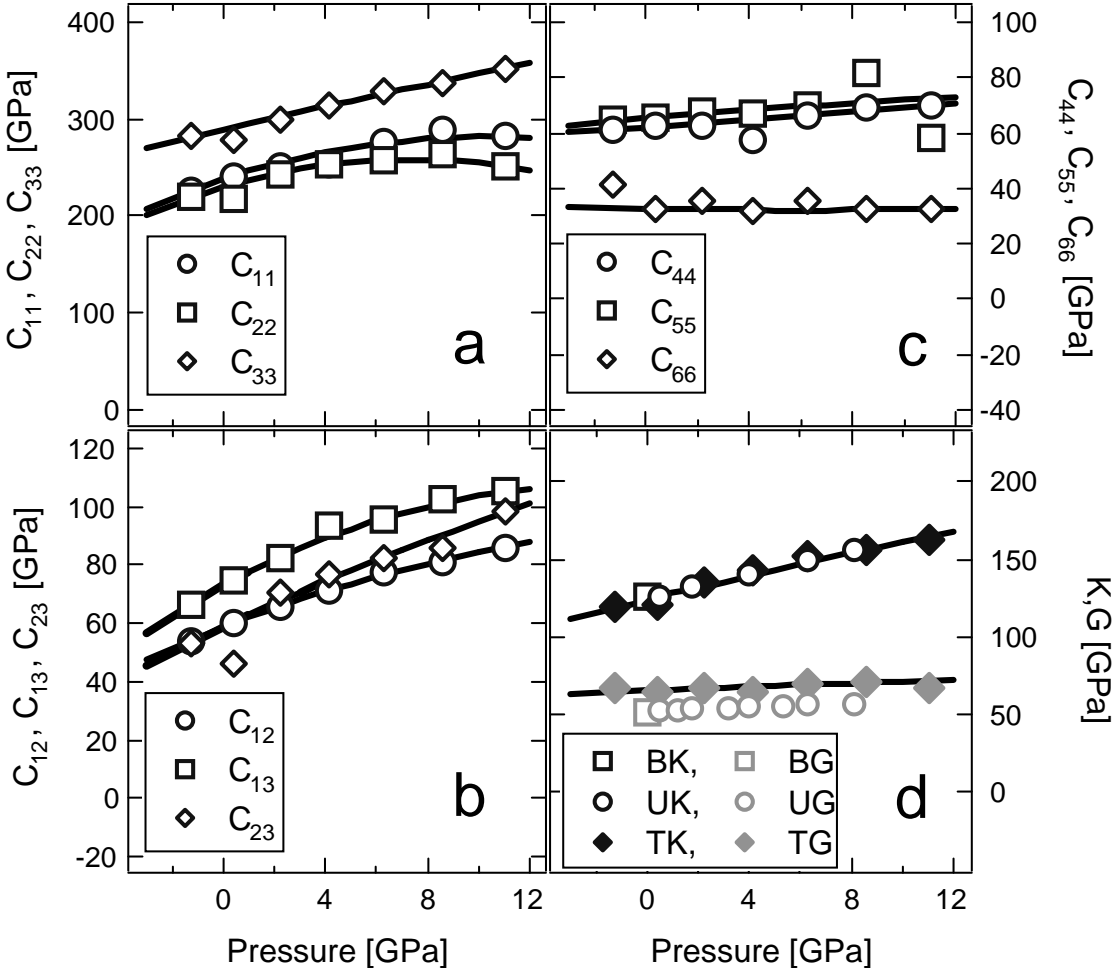


Fig. 3.1-9: Lawsonite elastic constants as a function of pressure, a: the principal components of the elastic constants, b: the diagonal elastic constants, c: the shear elastic constants, d: bulk and shear moduli. Diamonds are the computational results; open circles are the ultrasonic measurements from this study. In d the open squares are Brillouin data from a previous study, circles are ultrasonic measurements and diamonds simulations.

Figure 3.1-9 shows the elastic constants and the aggregate bulk and shear moduli of lawsonite determined by both techniques. With pressure, the difference in computed elastic constants of a similar type (longitudinal, shear, and off-diagonal) increases, and lawsonite is predicted to

become elastically more anisotropic. Computational and experimental bulk, K , and shear moduli, G , are consistent with each other and with a previous experiment performed at room pressure. Figure 3.1-10 shows the systematic relationship between P and S-wave velocity (V_P, V_S) and density for lawsonite and various minerals from the crust and mantle. A subducting basalt will broadly follow the density velocity path indicated by the dashed line, as the plagioclase dominated basalt at low pressures transforms to garnet dominated eclogite by approximately 2 GPa. We observe that the V_P of lawsonite follows this systematic curve with pressure, but V_S remains much lower and follows a shallower gradient. Lawsonite V_S is, therefore, substantially lower than subducted crust at 8 GPa. We estimate that about 25 vol.% lawsonite would be required to lower the V_S of a eclogite-dominated phase-assemblage by 5 %, but its formation would not significantly affect V_P , in agreement with LVL observations.

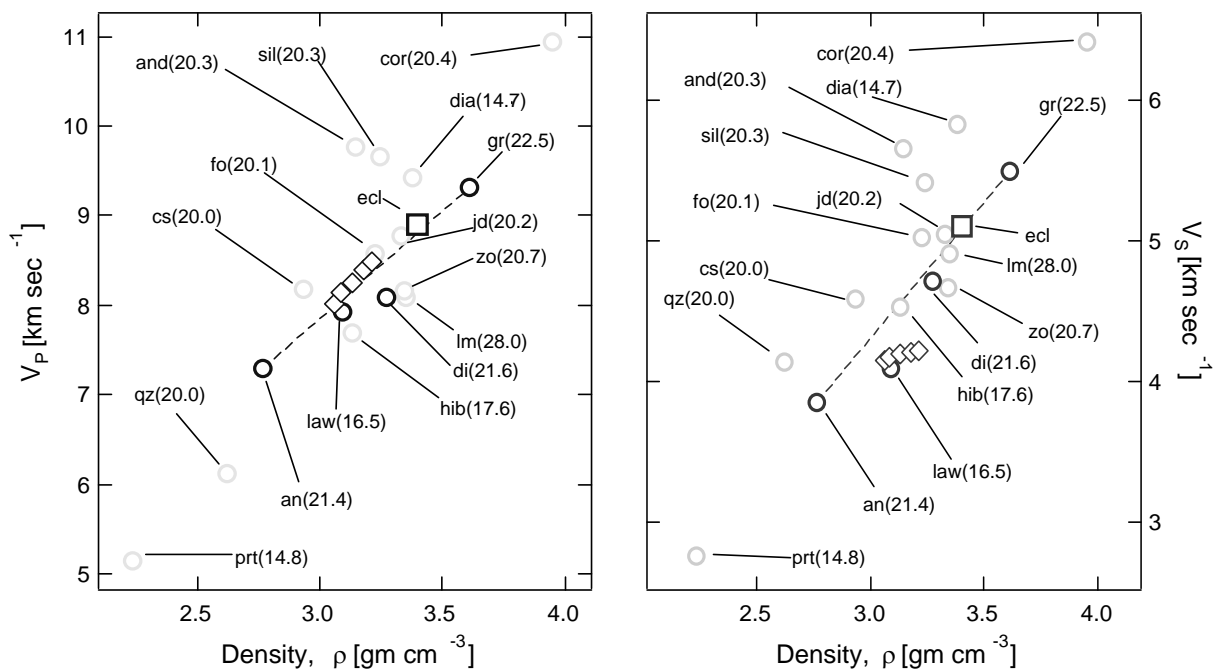


Fig. 3.1-10: Compressional and shear wave velocities of minerals in the $\text{CaO-Al}_2\text{O}_3\text{-SiO}_2\text{-H}_2\text{O}$ system as a function of density. The open-diamonds are our experimental data for lawsonite. The open squares are velocities for eclogite at 200km depth. The mean atomic mass for each phase is shown in brackets.

g. Composition and stability of hydrous partial melts at 410 km (M. Mookherjee and D.J. Frost)

Geophysical observations of low S-wave velocities and high electrical conductivities in the proximity of the 410 km seismic discontinuity have been interpreted as evidence for the presence of silicate partial melt on top of the Earth’s transition zone. It has been suggested that the difference in the water storage capacity of upper mantle versus transition zone

minerals may cause dehydration melting as material up-wells across the 410 km. A key question is whether this hydrous partial melt is neutrally buoyant in the mantle at these conditions. In order to assess this possibility it is important to determine the likely composition of small degree hydrous melts at these conditions and to measure the H₂O contents of mantle minerals coexisting with this melt phase. The composition of a hydrous melt in equilibrium with a mantle peridotite composition has been determined at conditions equivalent to the top of the 410 km seismic discontinuity *i.e.*, 13 GPa and 1800 K.

Sandwich experiments were performed in the Fe-free CMASH system where an “initial-guess” hydrous melt composition was equilibrated with 50 % anhydrous peridotite. Fe-free compositions ensured that H₂O was not lost during the experiments as H₂, because H₂O contents must be determined through mass balance using the starting bulk composition and the resulting compositions of all phases. The resulting melt composition was used to assemble a further melt, which was then equilibrated in the same way. After several iterations it was possible to derive a melt composition that was in equilibrium with a mineral assemblage identical to that observed for anhydrous peridotite at the same conditions: the composition of a small degree partial melt in equilibrium with mantle peridotite (Fig. 3.1-11).

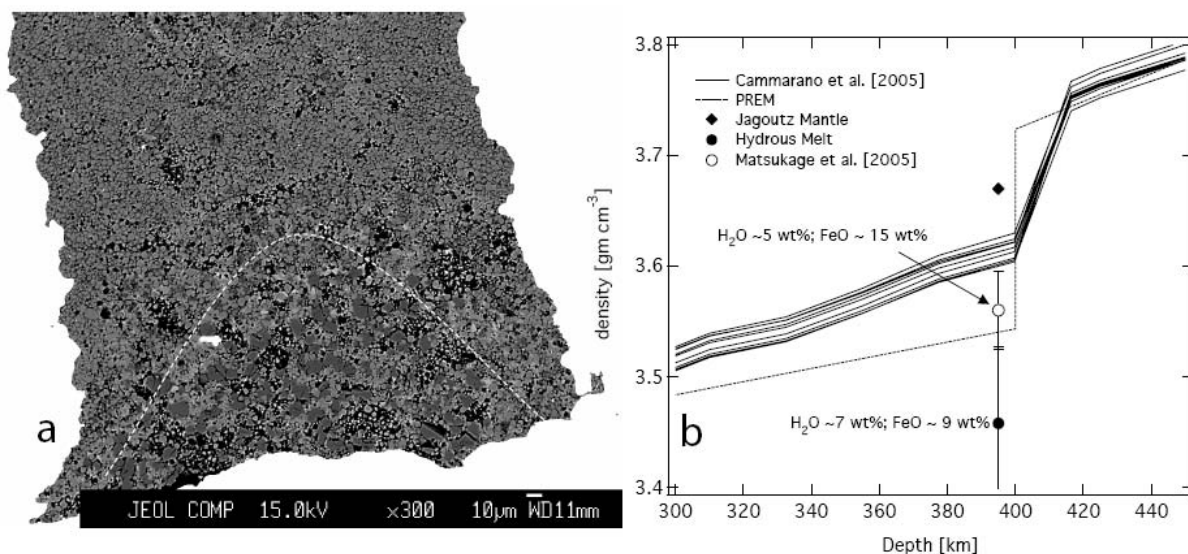


Fig. 3.1-11: a) Backscattered electron image of hydrous partial melt in equilibrium with a solid assemblage of olivine, clino-pyroxene and garnet at 13 GPa and 1800 K; b) Comparison of melt density with the density variation as a function of depth as predicted by PREM. The density of solid upper mantle based on geochemical [Jagoutz] and mineral physics estimates is significantly higher than the density predicted from PREM. Also shown here are the recent density-depth profiles determined by combining mineral physics and seismology data (Cammarano *et al.*, J. Geophys. Res. 110, B01306, 2005). It is evident that the hydrous melt (solid circle) is buoyant at 410 km depth. The previously estimated density (Matsukage *et al.*, Nature 438, 488, 2005) of hydrous melts with 5 wt.% H₂O and 15 wt.% FeO is also shown for comparison.

We performed further experiments to assess the Fe-Mg partitioning between hydrous silicate melt and mineral phases at the same conditions. With the partition coefficients established the composition of the melt phase could be calculated. We found the equilibrium melt to contain 7 wt.% H₂O but to have a lower FeO content of around 9 wt.% than previously assumed values of 15 wt.%. The results of melt density calculations indicate that this melt is buoyant at conditions compatible with the base of the upper mantle (Fig. 3.1-11).

h. Thermal conductivity of MgO periclase at deep mantle pressures: Implications for core-mantle boundary heat flux (N. de Koker)

The thermal conductivity (k) of rocks in the lowermost mantle is critical for evaluating the degree of heat-flux across the core-mantle boundary, and thus gaining an improved understanding of the processes by which the Earth cools. Estimated values of thermal conductivity in the lowermost mantle are very poorly constrained, varying between 4-12 W/m K. This large uncertainty arises partly because thermal conductivity has yet to be measured reliably at lower mantle pressures, but more critically because it is not clear how the existing low-pressure experimental data should be extrapolated to the conditions of the core-mantle boundary. Because first-principles theory is equally robust at ambient and extreme conditions, it is the ideal tool for evaluating the pressure- and temperature-dependence of k , knowledge which can also be used to more confidently extrapolate experimental thermal conductivity values to the lowermost mantle.

We have recently developed and implemented a method by which the lattice thermal conductivity can be accurately computed from first principles using relatively small system sizes and simulation times, obtaining good agreement with low-pressure experimental measurements of k in MgO periclase. Here we report results from a continuation of this work, in that we computed k for periclase at deep mantle pressures.

The k values computed for MgO span a large range of pressures and temperatures, providing the first robust means for testing the appropriate functional form for the pressure-dependence of k in deep mantle minerals. As shown in Fig. 3.1-12, the Debye theory relation

$$k = k_0 \frac{T_0}{T} \left(\frac{\rho}{\rho_0} \right)^g,$$

with

$$g = 3\gamma + 2q - \frac{1}{3},$$

is found to give an excellent description of the pressure-dependence of thermal conductivity in simple oxides. Results further reveal that acoustic modes increasingly dominate thermal

conductivity at high pressure, suggesting that Debye theory will remain a reasonable approximation in more complex compounds.

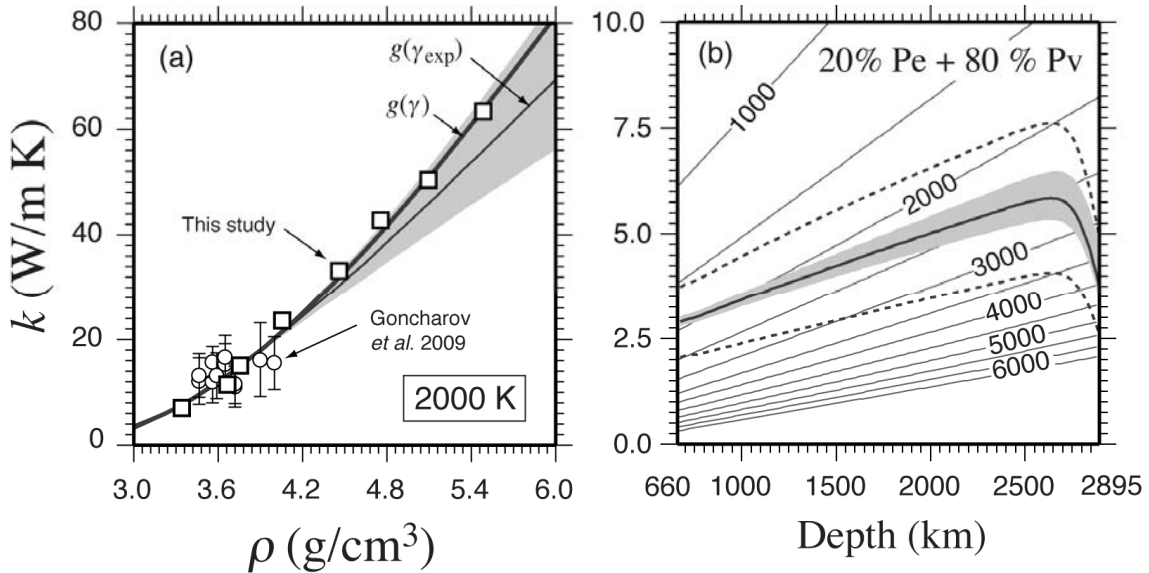


Fig. 3.1-12: (a) Lattice thermal conductivity of MgO periclase computed from first-principles molecular dynamics and (b) Hashin-Shtrikman averaged lattice conductivity of a 20:80 MgO periclase-MgSiO₃ perovskite aggregate for the lower mantle along a mantle adiabat. For MgO the Debye relation based model, constructed using γ and q from these same first-principles calculations, very closely represents the computed values and is within the uncertainty envelope of experimental values.

To estimate the thermal conductivity at the base of the Earth's lower mantle requires knowledge of k in both MgO periclase as well as MgSiO₃ perovskite. Using an experimental estimate of k_0 from the literature, we constructed a Debye theory based model of $k(P,T)$ for MgSiO₃ perovskite. According to these models, an 80:20 mixture of perovskite and periclase would have an aggregate lattice conductivity of 5.9 ± 0.6 W/m K at the top of the D'', and 4.0 ± 0.5 W/m K at its base (Fig. 3.1-12). In the Al and Fe-bearing polycrystalline aggregate, representative of the true mantle, a decrease in lattice conductivity would result from solid solution. If we assume that this decrease is similar in magnitude to the radiative contribution to heat transport, these values indicate that heat-flux from the core is at the lower limit of the range of geophysical estimates.

i. Thermodynamics of iron melting to 100 GPa (G. Steinle-Neumann and D. Dolejš/Prague)

The division of the Earth's core into a solid interior and a liquid envelope has been established by seismological constraints decades ago. The crystallization of the inner core from the outer liquid plays an essential role in the generation of the Earth's magnetic field: the

exclusion of the light elements during freezing contributes buoyancy to convection in the outer core, and the latent heat released contributes to the energy budget of the planetary interior. While experiments are difficult to perform at conditions of the inner core boundary (~ 330 GPa, 5000-7000 K) *ab initio* computations considering both the hcp and liquid iron phases have placed important constraints on these values.

Other terrestrial planets also appear to have a liquid outer core, with geodetic measurements supporting this for the Moon, Mercury, and Mars, with much lower pressure for the center and the core-mantle boundary. The presence of a solid inner core is in question for all these bodies, but appears inescapable due to cooling of the planetary body over geologic time for the Moon and Mercury. For Venus and Mars an inner core may be missing due to a much higher surface temperature and high sulphur content in the core, respectively.

Models for the origin of magnetic fields and thermal evolution of the terrestrial planets can only be advanced if thermodynamic parameters of the liquid and coexisting solid phases of iron are well characterized, especially along the melting curve. Here we have adopted a recently published equation of state with internally consistent parameters for solid and liquid iron in order to explore their relevant thermodynamic properties up to 100 GPa. It is based on a Murnaghan-like pressure-volume equation of state that can readily be inverted for P, providing an easy route to the integration of Gibbs energy. The parametrization closely reproduces the experimentally determined phase equilibria to 100 GPa. We apply the model to compute the entropy and latent heat difference between the solid and liquid phase during transformations from the bcc (δ) to the fcc phase (γ) at ~ 6 GPa and from the fcc to the hcp (ϵ) structure at ~ 60 GPa along the melting curve (Fig. 3.1-13). Entropy is computed by numerical differentiation of the Gibbs energy: $\Delta S = \left(\frac{\partial \Delta G}{\partial T} \right)_p$ and the difference is taken between the liquid and the solid. Latent heat released at crystallization is $\Delta Q = T\Delta S$. Along the univariant solid-liquid curve the latent heat released by cooling shows significant differences, increasing from bcc (~ 14 kJ/mol) through fcc (~ 17 kJ/mol) to the hcp phase (~ 25 kJ/mol).

With central pressure of ~ 5 GPa for the Moon, the liquid phase is in equilibrium with the bcc phase, releasing ~ 14 kJ/mol (250 kJ/kg) at inner core growth, a much smaller value than for the Earth's core. For an approximate core radius of 300 km and an average density of 8100 kg/m³ the solidification of the whole lunar core would release $2.2 \cdot 10^{26}$ J, contributing ~ 1.5 GW to the heat budget of the Moon if homogeneous inner core freezing is assumed over 4.5 Ga. This is a small portion of total current heat flow measured on the Moon on Appollo 15 and 17 sites (15-20 mW/ m², or an integrated heat flow of ~ 760 GW). For comparison on the Earth latent heat of inner core growth could contribute as much as 2 TW out of the ~ 45 TW, an order of magnitude larger fraction.

With ~ 40 GPa at the center of Mercury and the fcc phase in equilibrium with the liquid ~ 17 kJ/mol (300 kJ/kg) are released. The best estimate of the core radius on Mercury is 0.8 of total

planetary radius, *i.e.*, ~ 2000 km. With a higher average density (8500 kg/m^3) due to self-compression, total core crystallization would release $2.1 \cdot 10^{28}$ J.

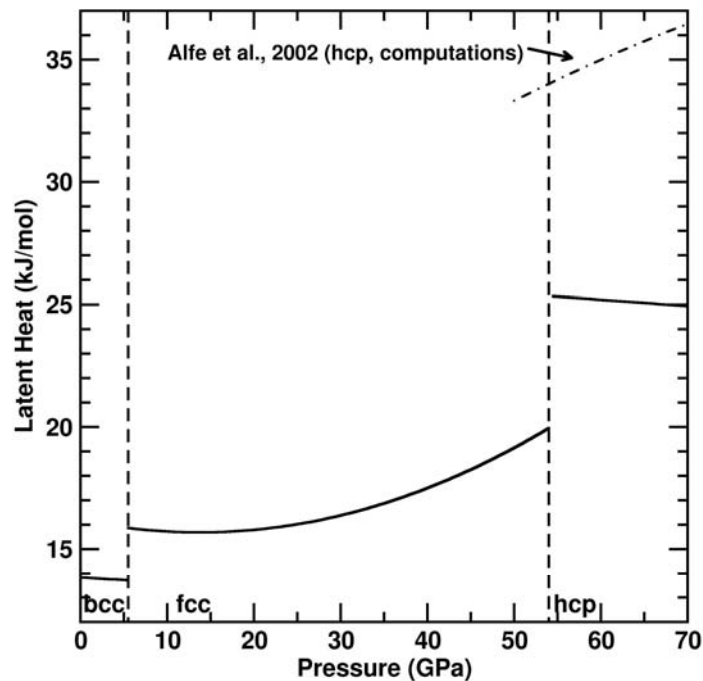


Fig. 3.1-13: Latent heat computed along the melting curve of Fe, *i.e.*, between the liquid and coexisting solid phase. For the liquid-bcc (relevant for the lunar core) and liquid-fcc transition (relevant for the cores of Mars and Mercury) the latent heat released is much smaller than for liquid-hcp at pressures below 70 GPa.

j. *Stability of iron carbides at inner core conditions (M. Mookherjee and G. Steinle-Neumann)*

Comparison of seismological data with experimental measurements on the compressibility of iron shows that the Earth's outer core is lighter than pure iron by 5-10 % and the inner core by 3-7 %, requiring the presence of lighter elements. In exploring various possibilities, it is to be noted that the light element should readily alloy with iron and be cosmochemically abundant. Geochemical arguments suggest that carbon is one of the light alloying elements with concentration between 0.2 wt.% and 4 wt.%. If carbon were the dominant light element in the core, then the core would have orders of magnitude higher carbon budget than the mantle. If carbon were a minor light element, the contribution of the core to the total terrestrial carbon budget would be comparable or smaller to than that of the mantle.

Classically, cementite Fe_3C (6.7 wt.% carbon) has been investigated as a potential carbide phase, coexisting with Fe in the Earth's inner core. However, recently the Fe-C phase diagram has been revisited and extended to higher pressures, and a new phase with Fe_7C_3 stoichiometry has been identified as a stable liquidus phase above 10 GPa. Here we explore

the relative stability of Fe_7C_3 and Fe_3C , considering reactions with bulk composition of 6.7 (Fe_3C) and 8.4 wt.% C (Fe_7C_3), respectively:



We have evaluated the energetics of these reactions with electronic structure calculations, considering Fe_3C cementite, Fe_7C_3 Eckstrom-Adcock carbide, hcp Fe, and diamond. Resulting energy-volume curves were fit with a third order finite strain equation of state. At inner core pressure Fe_7C_3 , Fe_3C and Fe are non-magnetic, hence we have considered non-magnetic energies. At static conditions ($T = 0$ K) the Gibbs energy change associated with the reaction is equivalent to the enthalpy change, ($\Delta H = \Delta E + P\Delta V$).

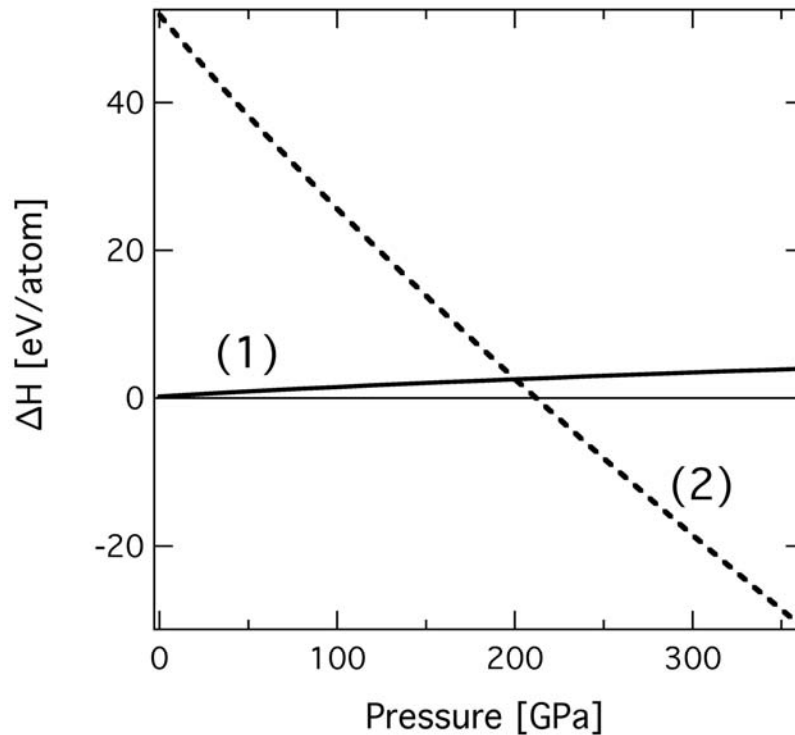


Fig. 3.1-14: Energetics of the reaction (1) $Fe_7C_3 + 2Fe \leftrightarrow 3Fe_3C$ and (2) $3Fe_7C_3 \leftrightarrow 7Fe_3C + 2C$ at static conditions, $T = 0$ K. All calculations are for non-magnetic phases.

For reaction (1) with 6.7 wt.% C, we find that Fe_3C is energetically favored relative to a mixture of Fe and Fe_7C_3 at all pressures (Fig. 3.1-14). This observation does not agree with the recent experimental findings conducted in the iron-carbon systems where Fe_7C_3 is a stable liquidus phase at higher pressures. This discrepancy can be traced to the considerably stiffer bulk modulus computed for hcp iron compared to experiments (Table 3.1-3). The discrepancy between measured and computed values of K_0 is consistent with previous *ab initio* studies,

however. For reaction (2) with bulk 8.4 wt.% C, we find that Fe₃C and C (diamond) is the stable assemblage at lower pressure; above 200 GPa Fe₇C₃ is stabilized over Fe₃C and C. It is likely that temperature or other elements present in the core might affect the relative stability of Fe₇C₃ vs. Fe₃C. The role of temperature could be examined by molecular dynamics simulations or by estimating the vibrational entropy through lattice dynamics. We are undertaking molecular dynamics simulation to incorporate the effects of the temperature.

Table 3.1-3: Equation of state parameters for iron carbides, hexagonal closed packed (h.c.p.) iron and diamond. E₀, V₀, K₀, and K' are zero pressure energy, volume, bulk modulus, and its pressure derivative, respectively. All computations were fit with a third order Eulerian finite strain equation of state.

Phase	Space group	E ₀ (eV/atom)	V ₀ (cc/mol)	K ₀ (GPa)	K'	Reference
Fe ₇ C ₃						
nm	<i>P6₃mc</i>	-8.53	52.82	291	4.5	This work (PBE-PAW)
fm		-8.60	54.81	231	4.4	
exp			55.47	253	3.6	Nakajima <i>et al.</i> 2010
Fe ₃ C						
nm	<i>Pnma</i>	-8.50	21.58	298	4.6	This work (PBE-PAW)
			21.61	317	4.3	Vocadlo <i>et al.</i> 2002
fm		-8.59	22.92	223	3.1	This work (PBE-PAW)
			23.08	229	5.4	Vocadlo <i>et al.</i> 2002
exp			23.37	175	5.2	Scott <i>et al.</i> 2001
Fe (hcp)						
comp	<i>P6₃mmc</i>	-8.37	6.17	296	4.4	This work (PBE-PAW)
			5.90	292	4.4	Steinle-Neumann <i>et al.</i> 1999
exp			6.75	165	5.0	Dewaele <i>et al.</i> 2006
C (diamond)						
comp	<i>Fd3m</i>	-9.06	3.44	434	3.6	This work (PBE-PAW)
exp			3.41	446	3.0	Ocelli <i>et al.</i> 2003

k. Fragmentation of metal diapirs in terrestrial magma oceans (H. Samuel, D.C. Rubie and H.J. Melosh/West Lafayette)

Due to mechanisms such as impact heating, early atmospheric thermal blanketing or radioactive heating, the presence of at least one global magma ocean stage in the early histories of terrestrial planets seems unavoidable. In such a context, a key question is whether (and how much) iron diapirs provided by differentiated impactors have emulsified during their sinking towards the bottom of an early magma ocean. Addressing this problem allows one to put strong constraints on metal-silicate equilibration processes as well as heat distribution within a young terrestrial planet. Previous studies have focused on this question, however no dynamic studies have conducted a systematic exploration of the relevant parameter space corresponding to terrestrial magma oceans.

Using the numerical code *StreamV*, we performed a series of numerical experiments in 3D axisymmetric geometry where we follow the sinking of iron diapirs until they fragment (or not) into smaller bodies. Our models include an accurate treatment of surface tension, inertial effects, stress and composition dependent viscosity, and we investigate systematically the effect of rheological properties and diapir size on the conditions and on the consequences of metal diapir fragmentation in terrestrial magma oceans. The system is governed by the magnitude of the diapir *Prandtl* (Pr) and *Weber* (We) numbers, and the viscous rheology, η . These quantities appear in the dimensionless equation for the conservation of momentum, where we have assumed that velocity and buoyancy are related via *Stokes* law:

$$\rho D_t U = -\nabla p + \frac{1}{Re} \nabla \cdot (\eta (u_{i,j} + u_{j,i})) + \frac{C}{Re} \vec{z} + \frac{1}{We} \kappa \vec{n} .$$

In the above equation, ρ is the density, $U(u_1, u_2, u_3)$ is the velocity vector, p is the dynamic pressure, κ is the curvature of the diapir surface, n the unit normal vector to the diapir surface, C indicates the composition ($C=0$ corresponds to pure silicate, $C=1$ refers to pure iron), and z is a unit vector pointing in the direction of gravity. We have considered Newtonian or power law rheologies that would correspond to either a fully liquid or partially molten magma ocean, respectively.

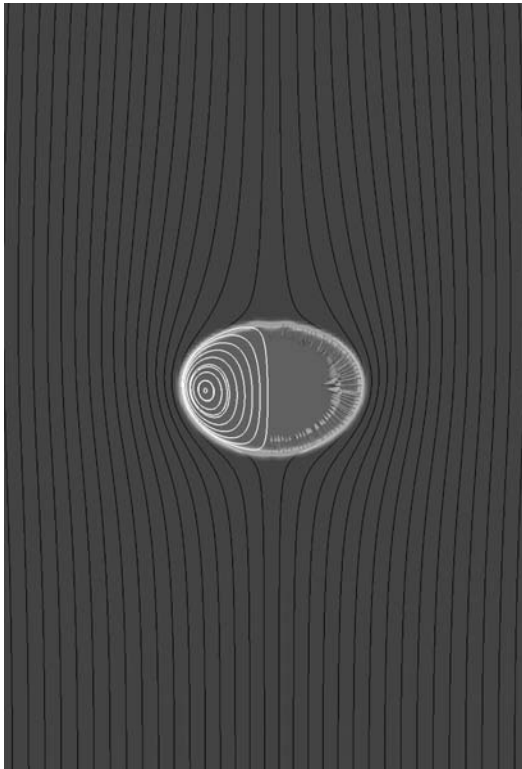


Fig. 3.1-15: Example of a stable diapir at $Re=We=100$ with constant Newtonian viscosity. Selected streamlines outside and within the sinking metal diapir reveal the internal and external flow. The arrows represent the surface tension force acting on the diapir's surface to reduce the interface curvature, preventing breakup.

While increasing inertial effects (larger Re) enhances diapir fragmentation, increasing surface tension forces act against diapir breakup (Fig. 3.1-15) and tend to maintain a spherical shape (Fig. 3.1-15). The condition for diapir breakup therefore depends on the relative magnitude of

We and Re . For Newtonian iso-viscous cases, we find that the stability criterion over the Re and We range investigated is approximately given by:

$$We Re^{1.5} < 4 \cdot 10^4.$$

Above this limit diapirs break up, generally within sinking distances on the order of a few diapir radii (Fig. 3.1-16). On the other hand, for stress dependent rheologies, diapirs rapidly reach a pseudo terminal velocity and may remain stable for large sinking distances (*i.e.*, 10-100 diapir radii) during which their sinking velocity increases gradually. During this phase, the diapir's inertia progressively increases leading to a gradual increase of effective *Reynolds* and *Weber* numbers. This change in We and Re shifts the diapir further towards the critical values leading to break up (Fig. 3.1-17). Our ongoing exploration of the parameter space will allow us to develop scaling relations to better constrain the timing for core formation and metal-silicate equilibration in terrestrial planets and asteroids.

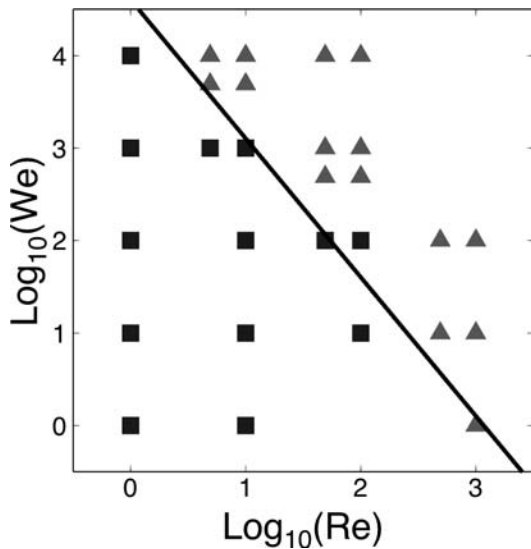


Fig. 3.1-16: Stability diagram (in Re - We space) for dense diapirs sinking through a Newtonian fluid. Each symbol represents a numerical experiment performed with the *StreamV* code. Triangles indicate unstable diapirs while squares indicate stable diapirs. The black line indicates the approximate boundary between stable and unstable diapirs and corresponds to $We Re^{1.5} = 4 \cdot 10^4$.

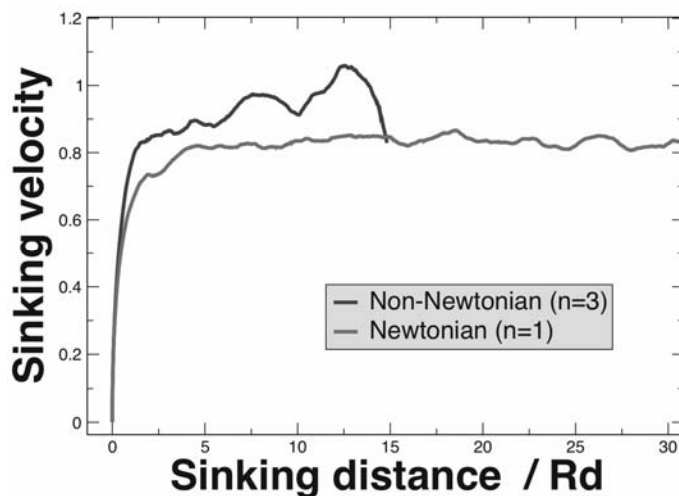


Fig. 3.1-17: Diapir sinking velocity as a function of sinking distance for a Newtonian (light gray) and power law rheology (dark gray). The sudden decrease of velocity for the non-Newtonian case indicates the time at which the diapir breaks up.

3.2 Geochemistry

The events that have shaped the solar system caused chemical changes and fractionations, which are recorded in rocks from the Earth and space. Analysis of these rocks and interpretation, aided often by the results of laboratory experiments, allow these events to be traced and understood. The first five reports in this section examine the earliest of these events, the cooling of the solar nebula, which led to chemical fractionation between nebular gas and condensed mineral phases. Two reports concern enstatite chondrite meteorites that form under such reducing conditions that even elements such as calcium and potassium can form individual sulphide minerals, something which virtually never occurs in the more oxidized environment of the Earth. These sulphides concentrate elements with important radiogenic isotopes, which are useful for tracing the timing of fractionation events. The final two reports on meteorites demonstrate how different assemblages of sulphide and metallic grains can be used to constrain conditions occurring during the final stages of nebula condensation.

The formation of the Earth from meteoritic material forms the subject of the following three contributions. The first of these presents a model for the accretion of the terrestrial planets from a radially fractionated solar disk of material. The model is successful in predicting the variation in core mass as a function of radial distance from the sun for the inner planets and also the iron contents of the planetary mantles. The next two contributions simulate the partitioning of elements between the Earth's silicate mantle and the liquid iron core, which would have occurred as the Earth formed. The second of these presents evidence that Si and O could have simultaneously partitioning into the Earth's core thus explaining why the core density is lower than that of a Ni-Fe liquid.

The following contribution examines whether noble gases could have been trapped in minerals crystallising from a deep magma ocean in the early Earth. The study finds that much larger amounts of Ar can be incorporated in lower mantle minerals than Xe. Degassing of Ar from the lower mantle, after most of the primordial atmosphere was lost, can thus explain the high Ar/Xe ratio of the current Earth's atmosphere.

The next three studies deal with the presence of carbonate minerals and melts in the Earth's mantle. The first finds that carbonates are likely to be unstable with respect to diamond at the redox conditions expected for the lower mantle, while the second is a preliminary attempt to determine the same carbonate-diamond redox transition in eclogite rocks. The third contribution finds a sharp increase in the iron content of carbonate melts once a certain threshold iron content is surpassed. The sharp melt composition change is similar to the transition between carbonate and kimberlitic melts and may help to explain the origin of the latter melts, which form enigmatically in the deep mantle.

The oxidation state of the mantle is an important tool for tracing the occurrence of metasomatism, where mantle rock compositions are subtly changed by the passage of fluids or magmas. This is detailed in the following contributions, the first of which examines

differences in the oxidation state between provinces within the ancient lithospheric mantle beneath south Africa. The second examines the redox state of ancient rocks which formed part of the deep mantle above a subducting slab of oceanic lithosphere, the so called mantle wedge. The oxidation state is used to constrain aspects of the composition of the fluids rising off the slab, which metasomatised these rocks. A further contribution, on a somewhat related theme, examines the partitioning of halogens between upper mantle minerals and subduction zone fluids. These data can be used in conjunction with the Cl/H₂O contents of primitive arc magmas to estimate the extent of fluid/rock interaction of subduction-zone fluids in the mantle wedge

The next study in this section presents a new method for determining the composition of the bulk oceanic crust and underlying depleted mantle from the compositions of least-fractionated mid-ocean ridge basalt glasses. The results are used to demonstrate that bulk oceanic crust is more primitive than commonly assumed and that the corresponding depleted mantle contains less garnet, and is thus more buoyant, than previously assumed. The following contribution examines magma molybdenum concentrations in the presence of the molybdenum sulphide mineral molybdenite, which is a common accessory mineral in silicic magmas formed in within-plate settings. A thermodynamic model for molybdenite solubility allows reconstruction of the magmatic redox state and sulphur fugacity and implies that the magmas must have been originally also saturated in the iron sulphide mineral pyrrhotite.

The final contribution in this section investigates biofilms from small drainage streams that originate within an abandoned copper mine. It is found that microorganisms catalyzed the precipitation of nanocrystalline sulphides and amorphous phases that sequestered a substantial amount of toxic metals. Microbes thus not only promote the release of toxic metals (*e.g.*, in mine wastes), but also help to precipitate them downstream.

a. *Oxygen isotopes in the ultra-refractory CAI Efremovka 101,1 and in the early solar nebula (J. Aléon/Orsay, K.D. McKeegan/Los Angeles, A. El Goresy and E. Charon/Paris)*

Efremovka 101.1 is a unique compact type A Ca-Al-rich inclusion characterized by an ultra-refractory (UR) rare earth element pattern and abundance of UR elements such as Sc and Zr in clinopyroxene. It contains numerous fragments of sinuous texture that were once rims of broken individual CAIs free-floating in the nebula. Many of these sinuous fragments do contain Fe-bearing silicates suggestive of pre-accretionary oxidation events. Among other unique properties it also contains islands of CaTiO₃ perovskite + metal with evidence of late dissolution and replacement by the ultra-refractory Sc- and Zr-rich pyroxene. Secondary alteration (nepheline) is often associated with these mineral associations. A significant portion of the CAI is quenched glass with minute gehlenitic melilite dendrites, which is attributed to the late quench of an impact melt. Finally, E101.1 is fully rimmed by a sequence of monomineralic layers known as Wark and Lovering rim sequence (W-L), which mimics the mineral sequence expected by condensation of a gas of solar composition. Fragments of an olivine-rich accretionary rim remains attached to the W-L rim. SIMS measurements were

conducted according to careful petrographic description, EPMA analyses of individual minerals and classification.

Oxygen isotopes in CAIs are well-known tracers of gas-solid interactions in the proto-solar nebula as they show up to 5 % variations in ^{16}O excess, between a ^{16}O -rich component similar to that measured in the solar wind samples and a ^{16}O -poor component similar to that of the Earth. The exact origin of these variations in CAIs is still debated. It is accepted that they track the change of O isotopic composition of the solar nebular gas, but the details of their recording in CAIs is controversial: solid state diffusion during post-crystallization heating events or liquid state diffusion during melting and crystallization of the inclusions? In order to better understand the mechanism(s) of O isotopic variation in CAIs and to put time constraints on the O-isotope evolution of the solar nebula, we initiated an exhaustive high precision O isotope study of E101.1 by SIMS. 128 individual O-isotope analyses were obtained in the various lithological units of E101.1 using the multicollector IMS 1270 ion microprobe at the University of California Los Angeles.

The results show that O isotopes cover the whole range of variations observed in CAIs between the solar and the planetary isotopic composition. The mineralogical control is similar to that of other CAIs with MgAl_2O_4 spinel being the most ^{16}O -rich mineral and melilite being ^{16}O -depleted. All layers of the W-L rim and the accretionary rims were found to be ^{16}O -rich as commonly observed in other CAIs. The distribution of O isotopes in pyroxene from the sinuous fragments and in host melilite was found to be correlated with mineral chemistry, which demonstrates O-isotope exchange between an ^{16}O -rich melt with a ^{16}O -depleted gas during crystallization. This correlation in pyroxene is observed here for the first time and unequivocally traces the isotopic evolution of the melt during crystallization in the solar nebula (Fig. 3.2-1). Several domains > 200 microns are found in melilite with similar ^{16}O excesses but distinct from each other, which suggests that solid state redistribution of O isotopes also occurred in melilite.

Perovskite grains were found to have variable ^{16}O excesses, which are not correlated with mineral chemistry, thus O-isotopes do not shed light on the origin of the various chemical groups of perovskite grains. By contrast the variations are suggestive of O-isotopic perturbation during the digestion by and crystallization of the UR-pyroxene.

One of the most striking observations was that the UR pyroxene is indeed the most ^{16}O -poor phase, which suggests a late formation in a ^{16}O -poor gas by reaction between perovskite and host melilite. This ^{16}O -poor composition is also found in the associated nepheline and in melt inclusions trapped in metal associated with perovskite. The Fe-rich silicates in the sinuous fragments are ^{16}O -depleted indicating that the oxidizing nebular reservoir encountered by these xenoliths is ^{16}O -poor, a result expected for nebular water. Finally O isotopes in the glassy areas are consistent with closed-system melting and quenching of ~ 50 % sinuous pyroxene and ~ 50 % host melilite, in good agreement with the late impact melting hypothesis.

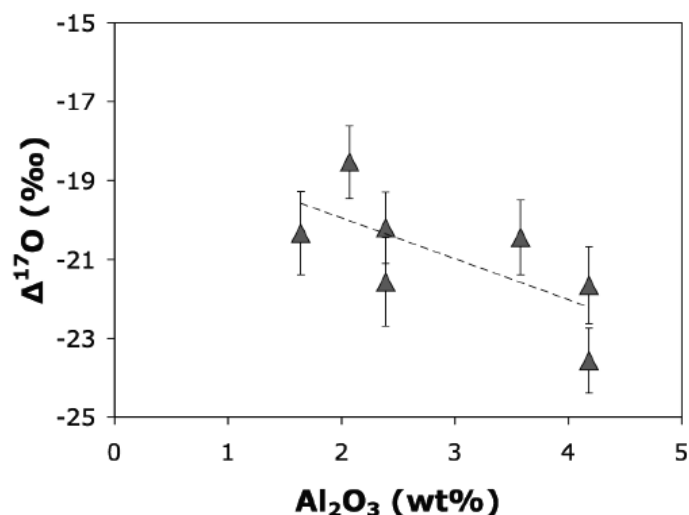


Fig. 3.2-1: O isotopes as a function of pyroxene chemistry demonstrating that O isotope exchange occurred during the crystallization of pyroxene from the CAI liquid in the solar nebula. The most aluminous (*i.e.*, early crystallized) pyroxene grains are the most ¹⁶O-rich.

b. *Sulphide assemblages in primitive EH-3 chondrites ALHA77295, Sahara97072 and Sahara97158 (A. El Goresy, in collaboration with A. Gannoun/Clermont-Ferrand, M. Boyet/Clermont-Ferrand and S. Mostefaoui/Paris)*

The enstatite chondrite group (EC) comprises only 2 % of the chondritic meteorites. Members of this group contain minerals that have condensed and accreted under very reducing conditions ($0.95 > C/O \text{ ratio} < 1.2$). As a consequence of low fO_2 formation many nominally lithophile elements occur as sulphides, including oldhamite (CaS), niningerite (Mg,Fe,Mn)S, troilite (stoichiometric FeS), djerfisherite [(K,Na)₆(Fe,Ni,Cu)₂₆S₂₇Cl], caswellsilverite (NaCrS₂), daubreelite (FeMn)Cr₂S₄ and sphalerite (ZnFeMn)S.

EC are classified into EH and EL, high iron and low iron, respectively. Both subgroups comprise unequilibrated members (EH3 or EL3) and meteorites with higher degrees of equilibration up to EH5-6 or EL-5-6. We have investigated the unequilibrated members of the EH-3 subgroup ALHA77295, Sahara97072 and Sahara97158. Special interest was devoted to the sulphide assemblages, habit of individual oldhamite crystals, mineral association, REE abundances in oldhamite and enstatite, zoning features of niningerite as a sensitive indicator for post-accretionary thermal events and to search for excesses of radiogenic ⁵³Cr* resulting from decay of the short-lived ⁵³Mn isotope ($t_{1/2} = 3.7 \text{ M.a.}$).

We developed a novel petrographic scheme in order to recognize the earliest CaS condensates based on the habit of oldhamite crystals. Idiomorphic crystals with no signs of nebular denudation are considered pristine while anhedral grains likely result from recycling and denudated by collisions in the turbulent gas-dust mixture prior to accretion. Idiomorphic oldhamite crystals occur sequestered in primitive metal sulphide clasts (Fig. 3.2-2a), metal

sulphide clasts subjected to heat events in the solar nebula (Fig. 3.2-2b) or among enstatite crystals in the meteorite matrices. Idiomorphic oldhamite was also encountered once in a chondrule in Sahara97158 thus attesting to its condensation prior to chondrule formation (2-4 M.a. after CAI condensation). An important quest is to check whether asteroidal collisions could have induced selective impact melting and migration of oldhamite from the impacted asteroids leading to selective depletion of CaS in the studied sections, or if the depletion of CaS was simply due to its selective weathering in meteoritic finds, specifically in Antarctic meteorites.

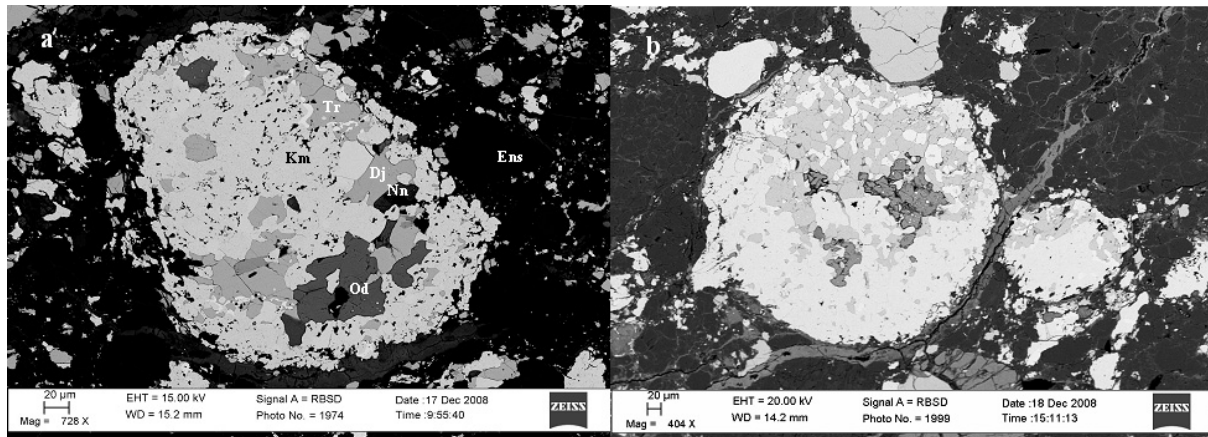


Fig. 3.2-2: Oldhamite-bearing metal-sulphide clasts in the primitive EH-3 chondrite ALHA77295. (a) a primitive fluffy metal-sulphide clast containing clusters of idiomorphic oldhamite crystals (Od), individual ningerite (Nn), djerfisherite (Dj), troilite (Tr) and kamacite (Km) grains. Matrix consists mainly of enstatite (Ens). Individual kamacite grains were decorated with micron-sized enstatite crystallites prior to their accretion in the clast. (b) a metal-sulphide clast with a cluster of idiomorphic oldhamite grains (gray) and a polycrystalline kamacite-troilite intergrowth resulted from recrystallization at high temperature prior to accretion.

The melting point of CaS is 1798° C. Thus any impact melting would not only induce production of liquidus high-pressure assemblages of enstatite (akimotoite or majorite) and plagioclase (lingunite) but also total melting of all sulphides, metals and silicates and production of quenched eutectic sulphide-metal intergrowths as abundantly encountered in shocked L- and H-chondrites. Short-lived isotopic systems like ^{53}Mn - ^{53}Cr would also never withstand impact melting and the isotopic systems would be reset to zero. Our investigations revealed no sign of shock deformation or impact melting in the studied EH-3 chondrites. Hence, impact melting and selective melt migration of oldhamite could comfortably be dismissed.

A further important issue is if the EH-chondrites emerged from one parental asteroid or several proto-asteroids. A key parameter is the chemical composition of ningerite crystals in contact with troilite in conjunction with the experimental investigations in the system MgS-FeS-MnS. Cooling after accretion should lead to normal Fe-Mg zoning in ningerite with

decreasing FeS-contents from their cores to the troilite rim as a result of the decreasing solubility of Fe in niningerite at lower temperatures (Fig. 3.2-3). In contrast, thermal events should invert this trend due to diffusion of Fe from troilite to niningerite at their interface as recorded in niningerite in Yamato-691, Qingzhen and Indarch (Fig. 3.2-3). Furthermore, since cooling or heating of the niningerite-troilite pair does not change the MnS concentration profiles as experimentally demonstrated by Skinner and Luce, niningerite grains with different MnS-contents (lowest 3.56 wt.% in Yamato-9601, highest concentration of 14.63 wt.% in Sahara97158) the variable zoning trends are // to the MgS-FeS join. This is suggestive of different source proto-asteroids (Fig. 3.2-3) with niningerite crystals containing different MnS-contents in the different asteroids. It is expected that shock-induced heating would produce a reversed Fe-Mg zoning trend with hysteresis in the reverse zoning profiles in individual niningerite grains. We did not encounter such hysteresis in any zoning profile in niningerite.

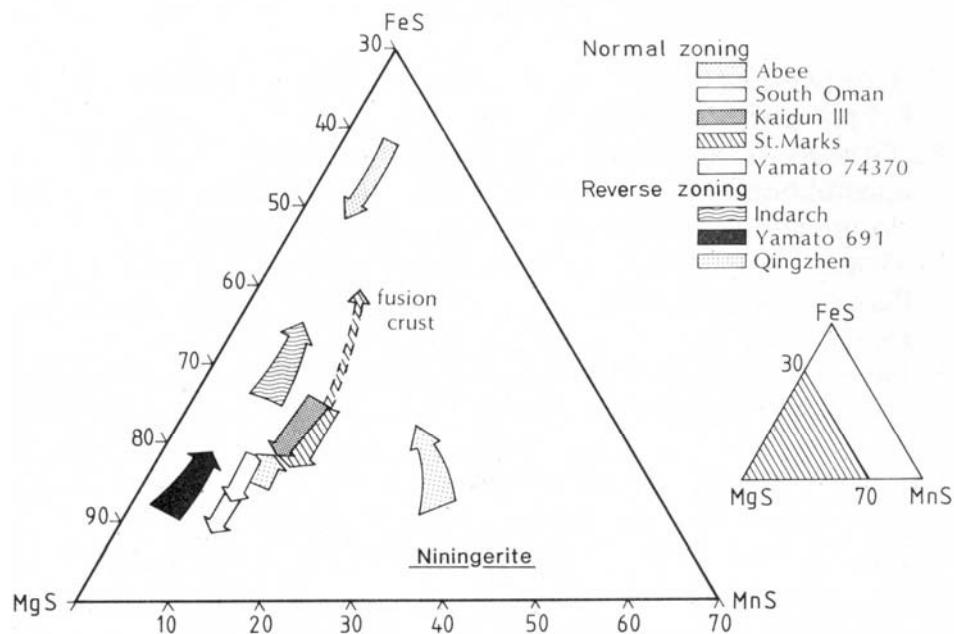


Fig. 3.2-3: MgS-FeS-MnS ternary diagram depicting the zoning trends of numerous niningerite grains from their cores to the troilite-niningerite interfaces in different EH chondrites. All trends plot nearly // to the MgS-FeS join, regardless if the zoning trend is normal or reverse. The zoning arrow at MgS 40 % is from a niningerite encapsulated in a metal sulphide clast in the Qingzhen meteorite. The arrow designating Fusion Crust is the zoning trend in a niningerite in the St. Marks EH4 chondrite that was entrained in the hot fusion crust during passage of St. Marks in Earth's atmosphere.

Figure 3.2-3 demonstrates that the studied EH-3 chondrites very probably emerged from different proto-asteroids with different MnS-contents in niningerite and that these asteroids had different thermal histories after accretion, with none of them being related to shock melting. Study of the ^{53}Mn - $^{53}\text{Cr}^*$ systematics of a 10 μm sphalerite crystal in ALHA77295 by nanoSIMS revealed enormous excesses amounting a $\delta^{53}\text{Cr}^*$ of 1600‰ (Fig. 3.2-4). Such excesses would not have survived any shock-induced heating or melting in the asteroids. The

different MnS-contents and different MgS-FeS zoning trends in niningerite crystals strongly suggests their evolution in different proto-asteroids with different Mn-concentrations and diverse thermal histories.

The homogeneity in the distribution of ^{53}Mn in the early solar system is currently debated among cosmochemists and isotope astrophysicists. The short-lived ^{53}Mn - ^{53}Cr system would reveal stringent constraints in dating early events in the solar system but only if the primordial ^{53}Mn distribution was homogeneous in the solar nebula. Inferred initial $^{53}\text{Mn}/^{55}\text{Mn}$ ratios published up to date vary by 2 orders of magnitude. Our precise nanoSIMS study of the sphalerite in ALHA77295 reveals an $^{53}\text{Mn}/^{55}\text{Mn}$ inferred initial ratio of $6.08 \pm 0.15 \times 10^{-7}$. The $^{55}\text{Mn}/^{52}\text{Cr}$ ratio in the meteoritic sphalerite is quite high thus securing the reliability of the precise datum achieved. In comparison, inferred $^{53}\text{Mn}/^{55}\text{Mn}$ initial ratios in sphalerites measured by SIMS in Indarch revealed values of $3\text{-}5 \times 10^{-6}$. The inferred $^{53}\text{Mn}/^{55}\text{Mn}$ initial ratios in sphalerites in Indarch also vary significantly within individual sphalerite grains. These conflicting results are suggestive of diffusion of Mn and Cr from the sphalerites to neighboring niningerite (Mn) and troilite (Cr), respectively when ^{53}Mn was still extant. Other alternatives are that either the sphalerites solidified at different times corresponding to a time span of 6.3×10^6 years, or ^{53}Mn was heterogeneously distributed in the early solar nebula.

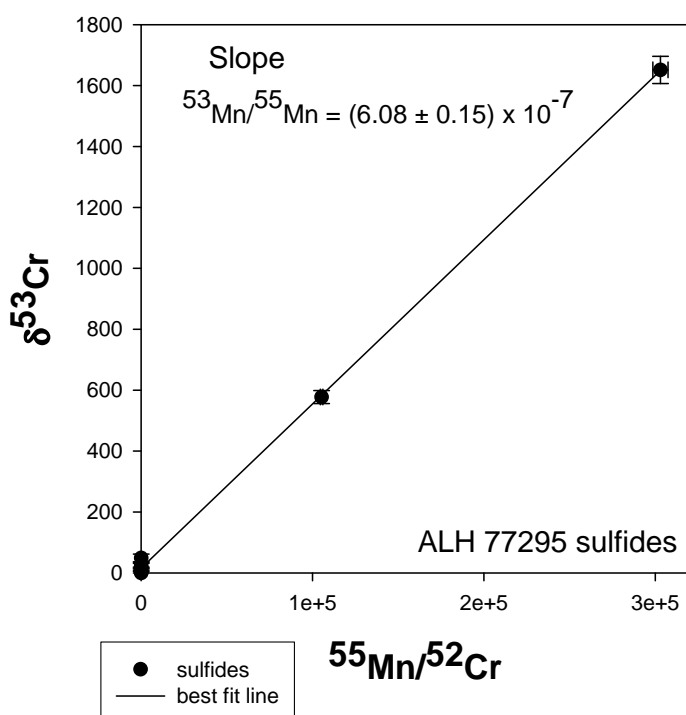


Fig. 3.2-4:
 ^{53}Mn - $^{53}\text{Cr}^*$ isochron measured by nanoSIMS in a $10 \mu\text{m}$ Mn-rich sphalerite grain in the EH-3 chondrite ALHA77295. The inferred $^{53}\text{Mn}/^{55}\text{Mn}$ initial ratio is $6.08 \pm 0.15 \times 10^{-7}$.

c. REE abundances in primitive EH chondrites (A. Gannoun and M. Boyet/Clermont-Ferrand, A. El Goresy and B. Devouard/Clermont-Ferrand)

As detailed in the previous contribution Enstatite chondrites (EC) consist of highly reduced mineral assemblages formed under very low oxygen fugacity conditions where REE are

mainly chalcophile, and concentrated in oldhamite (CaS). The REE inventory of individual minerals in the primitive EH-3 chondrites, Sahara97072 and ALHA77295 were investigated to elucidate their condensation and accretionary mechanisms. This study will also allow us to discuss the REE behaviour in reducing conditions in the solar nebula.

REE concentrations were measured by SIMS and LA-ICPMS. CaS depicts REE enrichments (10-100×C1) and four types of REE patterns were encountered in ALHA77295. The REE distributions cannot be assigned to a specific oldhamite occurrence (matrix, chondrule, metal-sulphide assemblage). The most represented REE pattern is characterized by both slight to large positive Eu and Yb anomalies and is enriched in LREE relative to HREE. The former pattern is present in 97 % of CaS in Sahara97072 (Fig. 3.2-5), suggesting a different source region in the EH3 parent body or different EH asteroids for the two EH3 chondrites. REE concentrations in enstatite grains (MgSiO₃) range between 0.2 to 8×CI. The modal abundance of MgSiO₃ ranges from 60 to 70 % in the bulk meteorites, it is an important REE host next to oldhamite. Most enstatite patterns are characterized by negative Eu and Yb anomalies. Average positive Eu and Yb anomalies observed in most CaS are complimentary to the negative ones in enstatite, thus explaining the flat patterns of the bulk meteorites.

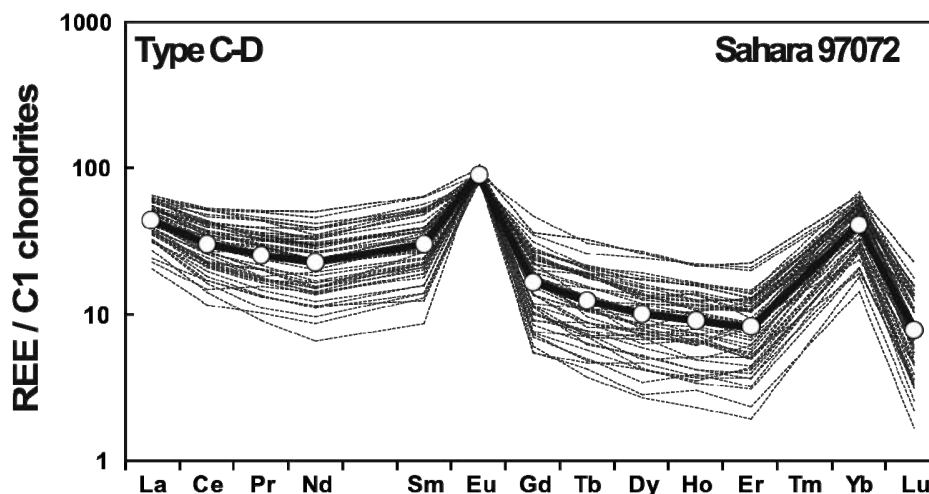


Fig. 3.2-5: CI chondrite-normalized REE patterns for oldhamites from Sahara 97072. Despite the large number of oldhamite grains investigated (n=58) from all petrological types, 97 % of the REE patterns depict positive Eu and Yb anomalies.

Condensation calculations based on cosmic abundances predict that the first CaS condensates should have flat REE patterns with Eu and Yb depletions, since EuS and YbS condense at lower temperature than other REE. However, this pattern is only encountered for enstatite. Although all CaS are enriched in LREE relative to HREE, they have super-chondritic Sm/Nd ratios because like Yb, Sm is slightly enriched relative to neighbouring REE. Our results for EC tend to rule out a previously proposed scenario in which the incorporation of REE (reservoir characterized by a low Sm/Nd ratio) in the Earth's core is used to explain ¹⁴²Nd excesses in terrestrial samples relative to chondrites.

d. *Native Hg, cinnabarite, chalcocite, covellite and copper in the primitive H-3 chondrite Tieschitz: Novel constraints on condensation and accretion processes in the early Solar System (C. Caillet Komorowski/Paris, A. El Goresy, M. Miyahara/Sendai, O. Boudouma/Paris, M. Humayun/Tallahassee, C. Ma/Pasadena and F. Robert/Paris)*

Submicrometer grains of cinnabarite, metallic mercury, chalcocite and covellite were encountered associated with native copper in opaque assemblages in the unequilibrated and unshocked ordinary H3 chondrite “Tieschitz”. Observations were made using a field emission scanning electron microscope on a LN₂ cooled stage in a limited vacuum (Fig 3.2-6). The nature and compositions of the species were determined by electron microprobe and electron backscatter diffraction measurements. Fragile textures consist of alternating rhythmic layering of Cu- and Hg-sulphides with nanometer-sized crystal aggregates of native Cu, containing Hg globules. These textures suggest cold accretion of previously condensed particles. Cu₂S intergrown with HgS indicate equilibration at <<300 °C. The fact that Hg is systematically associated with polycrystalline metallic Cu, the lack of sublimation of Hg or decomposition of HgS, and the absence of any dynamically-induced deformation (twin lamellae //(10-21) in the troilite) all suggest that the native Cu could not have formed as a result of shock of this meteorite, because in this case the high temperatures would have caused the Cu-poor FeNi metal (<30 ppm Cu) to have become homogenized as well.

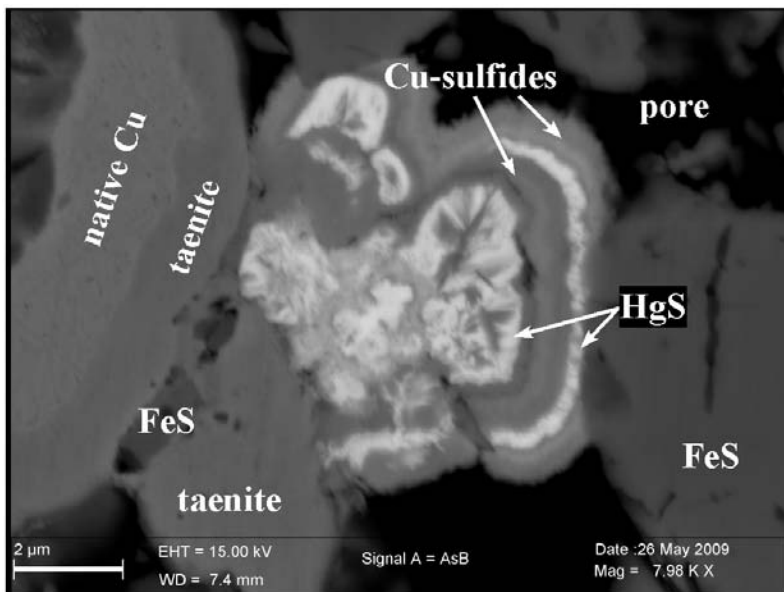


Fig. 3.2-6: Scanning electron microscope image of sulphide and native copper grains in the Tieschitz ordinary chondrite meteorite.

The superchondritic abundance of Hg in the troilite in Tieschitz suggests that tiny condensates were sequestered in the FeS. Electron diffraction patterns also reveal that CuS intimately surrounds HgS, indicating a low-temperature formation before accretion in the parent body of Tieschitz. The existence of Hg-bearing phases is very important to demonstrate the low-temperature condensation of this volatile element whose concentration is highly variable in bulk chondrites without any relation to their metamorphic grade. The presence of this

assemblage shows that it is necessary to reconsider the abundance of Hg in meteorites to understand its cosmochemical behaviour which has been an enigma for 50 years. Tieschitz accreted from a nebular region where low-temperature dust particles were not dispersed, compared to more dynamical regions in which other meteorites lacking Hg and containing higher abundances of low volatile elements were formed. The presence of Hg-bearing phases thus suggests a dense formation environment of Tieschitz.

e. Sulphide mineralogies in CM and CM-like chondrites and their record of early solar system processes (D. Harries and F. Langenhorst)

Assemblages containing iron- and nickel-rich monosulphides such as troilite (FeS), pyrrhotite (Fe_{1-x}S) and pentlandite ((Fe,Ni)₉S₈) are potentially interesting proxies for physicochemical conditions of formation and alteration of planetary materials. Fe deficiency in pyrrhotite is directly related to fS_2 and temperature and can be linked indirectly to fO_2 if certain buffer assemblages (*e.g.*, magnetite) are present.

We sampled sulphides from four Antarctic CM chondrites by the focused ion beam (FIB) technique and studied their mineralogies by analytical transmission electron microscopy (TEM). The CM2 chondrites Yamato-791198 and Yamato-793321 contain pyrrhotite with abundant pentlandite and troilite exsolution (Fig. 3.2-7). In both cases pyrrhotite occurs as strongly twinned 6C superstructure ($\sim Fe_{0.92}S$). The thermally metamorphosed, anomalous CM-like chondrites Yamato-86720 and Belgica-7904 show associations of troilite with metallic (Fe,Ni) and only traces of 6C-pyrrhotite on grain margins. In both meteorites we also found intimate associations of sub-micrometer sized troilite and olivine and interpret them to be thermal breakdown products of PCP (serpentine-tochilinite intergrowths). In Yamato-86720 euhedral hexagonal platelet crystals resembling pyrrhotite found in CI chondrites have been replaced by troilite and iron metal.

The petrologic history of the metamorphosed chondrite grouplet is enigmatic. Narrow clustering of oxygen isotope ratios clearly defines a common origin and places the grouplet on a mass-dependent fractionation line with CI chondrites, pointing to a dehydration of CI-like material. However, textural characteristics are much closer to CM chondrites, with the exception of Yamato-86720, which appears highly altered by aqueous fluids and contains pseudomorphs of CI-like pyrrhotite crystals. On the other hand, this meteorite has virtually no magnetite, which is a typical component of CI chondrites, and contains apparent breakdown products of PCP, which is absent in CI chondrites.

Regarding the normal CM2 chondrites, the precursor of the pentlandite-troilite exsolution assemblages must have formed at temperatures in excess of 140 °C. This is incompatible with aqueous alteration that unlikely exceeded 100 °C (especially in case of Y-791198, which appears little altered compared to other CM chondrites). A possible explanation of the

observed textures is the formation of a homogeneous monosulphide solid solution by solid-gas reaction in the solar nebula at elevated temperature and likely high fS_2 .

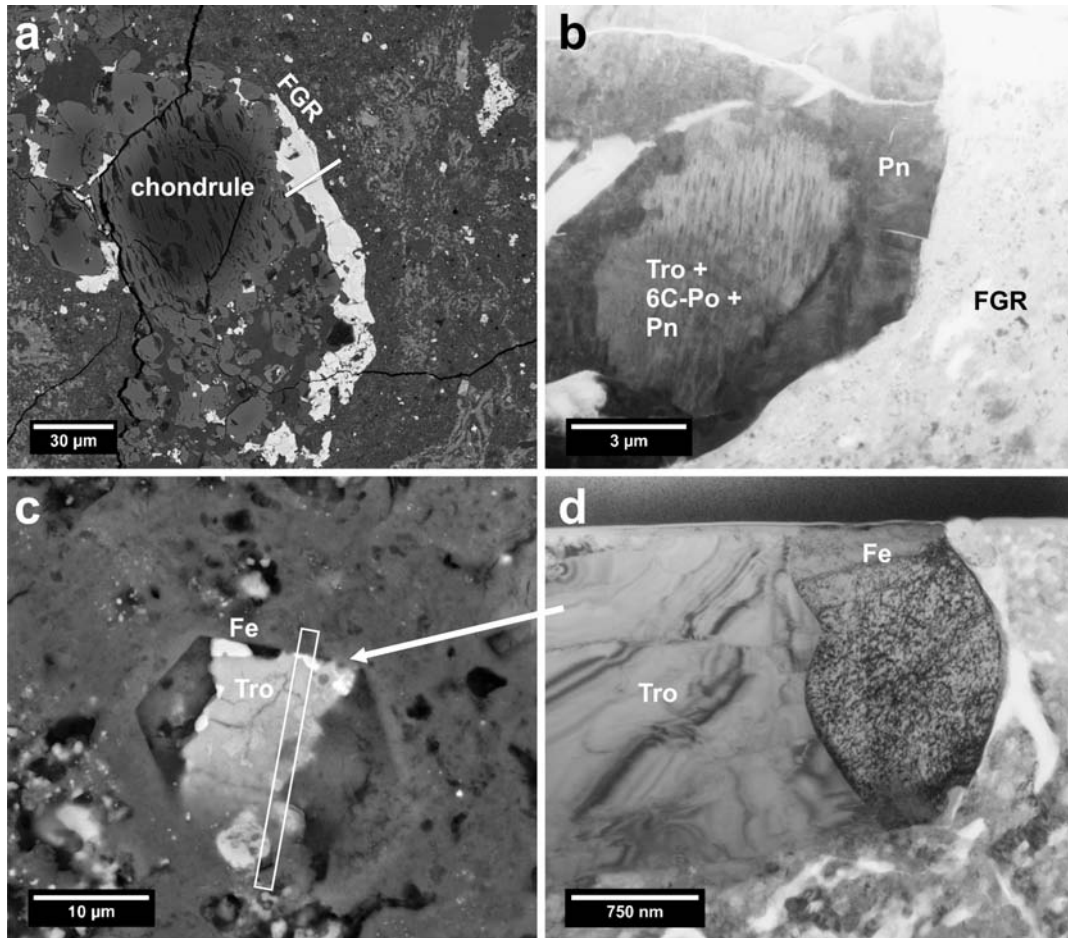
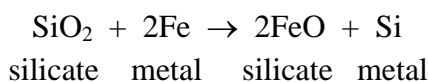


Fig. 3.2-7: (a) Y-791198: SEM-BSE image of sulphide attached to a chondrule margin and surrounded by a fine grained rim (FGR). The white square indicates the location of FIB extraction. (b) BF-TEM image of the FIB section marked in (a). An outer pentlandite (Pn) rim surrounds a core composed of troilite (Tro), 6C-pyrrhotite, and pentlandite. Likely the grain margin served as preferred nucleation site of the first pentlandite exsolution followed by later breakdown of remaining sulphide into Tro, Po and a second generation of Pn. (c) Y-86720: SEM-BSE image of a pseudomorph of Fe sulphide and Fe metal after an euhedral hexagonal platelet crystal. The white square indicates the FIB extraction site. (d) BF-TEM image of the site marked by the arrow in (c). The Fe sulphide is troilite with traces of 6C-pyrrhotite on grain margin to the surrounding matrix. A grain of metallic Fe (6 at.% Ni) is directly attached to the troilite.

Independent of whether the metamorphic CM-like chondrites formed from a CM or CI precursor, the metamorphism must have taken place under reducing, low fS_2 conditions. This led to the conversion of pre-existing pyrrhotite (and likely pentlandite) to troilite and Ni-rich iron metal.

f. *Heterogeneous accretion and core-mantle differentiation of the terrestrial planets (D.C. Rubie, D.J. Frost, Y. Nakajima, A.-K. Vogel, in collaboration with F. Nimmo/Santa Cruz, D.P. O'Brien/Tucson, U. Mann/Zürich and H. Palme/Frankfurt)*

We have developed a new model of core formation that is based on a simplified accretion scenario by which terrestrial planets grow through a series of impacts with smaller differentiated planetesimals and embryos. Each collision involves the impactor's core partially or completely equilibrating in a magma ocean before merging with the planet's proto-core. Compositions of metal and silicate that result from the equilibration process are determined from the bulk composition by a novel approach involving mass balance combined with element partitioning. In the case of the Earth, model parameters (*e.g.*, metal-silicate equilibration pressures and compositions of accreting material) are determined by a least squares fit based on constraints provided by the concentrations of 12 major and trace elements in the Earth's mantle. In order to match the mantle concentrations of the siderophile elements Ni, Co and W, a high degree of disequilibrium is required in the case of large and late impactors: this means that the metallic cores of such impactors only partially re-equilibrated in the magma ocean before merging with the Earth's proto-core. Results also show that accretion of the Earth was heterogeneous: early accreting material was highly-reduced and volatile-poor and later accreted material was relatively oxidized and volatile-rich. Oxygen fugacity increases during accretion by 4-5 log units partly as a consequence of the change in composition of accreting material and partly due to the reaction



This reaction is shifted progressively to the right as the Earth grows because Si dissolves increasingly into core-forming Fe metal alloy as magma ocean depth and metal-silicate equilibration temperatures increase. The consequences are a progressive increase in the FeO content of the Earth's mantle (thus causing oxygen fugacity to increase) and ~ 8 wt.% Si in the Earth's core. According to the present model, the Earth's water inventory was accreted at a late stage, possibly with the "late veneer" after the completion of core formation.

The model is currently being combined with the results of N-body accretion simulations in order to model the evolution of terrestrial planets that form at different heliocentric distances. Preliminary results show that a planet that is located at a heliocentric distance significantly greater than 1 AU (*i.e.*, significantly further from the sun than the Earth) has a smaller core, a lower mantle Mg/Si ratio and a higher mantle FeO concentration compared with the respective values for the Earth (Fig. 3.2-8). The cause of these differences is that a larger proportion of oxidized material is accreted to the high-heliocentric-distance planet compared to the Earth thus resulting in a higher oxygen fugacity and less Si in the core. The trends shown in Fig. 3.2-8 are consistent with the compositions of mantles of the Earth, Mars and possibly Mercury.

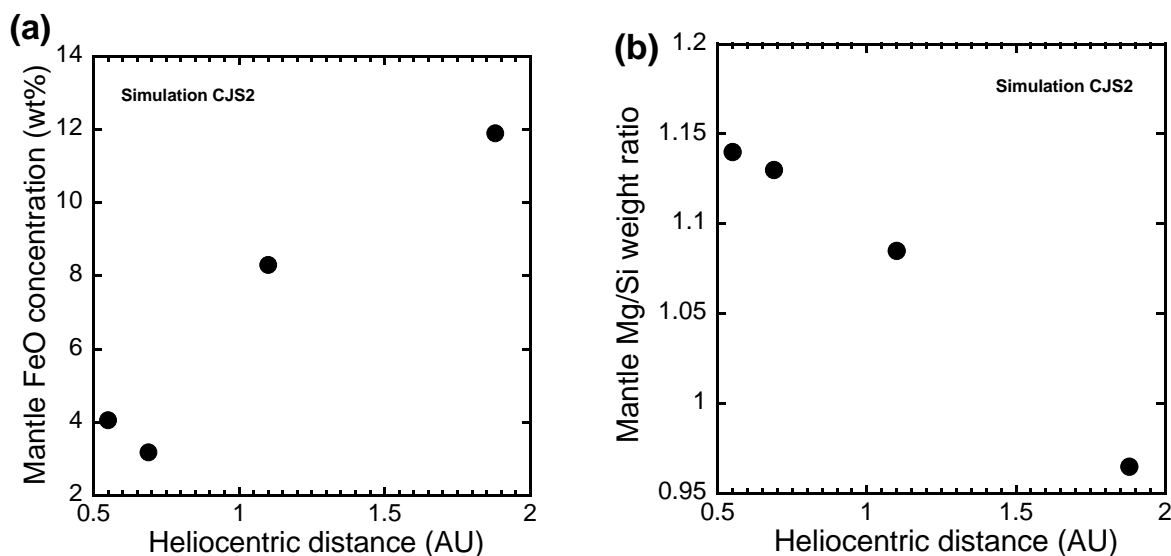


Fig. 3.2-8: (a) Mantle FeO concentrations in four planets that resulted in an N-body accretion simulation that are located at distances from the sun that range from 0.55 to 1.88 AU. The planet at 1.1 AU has a location, mass and mantle FeO concentration comparable to that of the Earth. (b) Mg/Si weight ratios for the four planets shown in (a).

g. *The partitioning of volatile elements between metal and silicate at high pressures and temperatures (A.K. Vogel, D.C. Rubie, D.J. Frost and A. Audetat, in collaboration with H. Palme/Frankfurt)*

One of the most important events in the history of the Earth was the formation of its iron-rich metallic core. It is believed that core formation ended within 100 My after the start of the solar system. However, the processes and conditions that led to the separation of the metallic core from the silicate mantle are not completely understood. Siderophile (metal-loving) element geochemistry can provide answers to these questions.

During the late stages of accretion, the Earth experienced giant impacts with Moon- to Mars-sized bodies that resulted in the melting of a significant part of the Earth and enabled liquid Fe-Ni metal to sink to form the core. The silicate mantle was depleted in siderophile elements because these partitioned strongly into the liquid metal. In recent years, it has been shown that mantle concentrations of non-volatile siderophile elements, such as Ni, Co and W, are consistent with metal-silicate segregation occurring at pressures up to 50 GPa or more – thus indicating the existence of one or more deep magma oceans during the early history of the Earth.

Volatile elements are depleted in the Earth's mantle because of their high volatility, most probably because they failed to condense at high temperatures in the inner part of the solar nebula. However, many of these elements were also depleted by core formation. Studying their metal-silicate partitioning behaviour can therefore provide additional constraints on processes of core formation.

In our project we have chosen the non-volatile elements W, Mo, Co, Ni, the moderately volatile elements P, Cu and Ge and the volatile elements Sn and Pb and are determining their liquid metal - liquid silicate partition coefficients at high pressures and temperatures. We have performed experiments over the pressure range 10.5 GPa to 23 GPa and temperatures between 2273 K and 2673 K using the multianvil apparatus. The oxygen fugacities vary between -2.0 to -2.4 log units relative to the iron-wüstite-buffer (IW). For our starting materials we mixed 3 parts (by weight) silicate (peridotitic composition) with 1 part metal (either (1): 96 wt.% Fe + 1 wt.% of Co, Ni, MoO₃ and W respectively or (2): 95 wt.% Fe + 1 wt.% of P₂O₅, Cu, GeO₂, SnO, and Pb₃O₄ respectively). In one experiment we added 10 wt.% S to the metal phase in order to determine the effect of S on liquid metal/liquid silicate partitioning. During the experiments, the metal segregates from the silicate to form one or more spherical blobs (Fig. 3.2-9), which simplifies the analysis of the two phases. The metal phase of the quenched samples has been analyzed with an Electron Probe Micro-Analyzer (EPMA), whereas siderophile elements in the silicate phase have been measured with a Laser Ablation Inductively Coupled Plasma Mass Spectrometer (LA-ICP-MS). All our experiments have been performed in MgO capsules, which leads to the formation of ferropericlase at the capsule wall and, in some experiments, around the metal blob. This ferropericlase was analyzed with EPMA in order to determine oxygen fugacity relative to the iron-wüstite buffer.

Based on preliminary results, the pressure dependence of the metal-silicate partition coefficient ($D^{\text{met/sil}}$ = concentration of element in metal/concentration in silicate) can be defined for all elements studied. In addition our data clearly show that S affects the partition coefficients of each element by lowering the $D^{\text{met/sil}}$ values. Results for the two volatile elements Sn and Pb are particularly informative. Those elements have been depleted by about the same amount in the Earth's mantle, which requires that their partition coefficients were similar during core formation. However, at low pressures the partition coefficients of these two elements vary by up to several orders of magnitude. Our results show that $D^{\text{met/sil}}$ for Sn and Pb converge with increasing pressure (Fig. 3.2-10), which indicates that equilibration at high pressures (*e.g.*, 30-40 GPa) was necessary to produce the observed mantle concentrations.

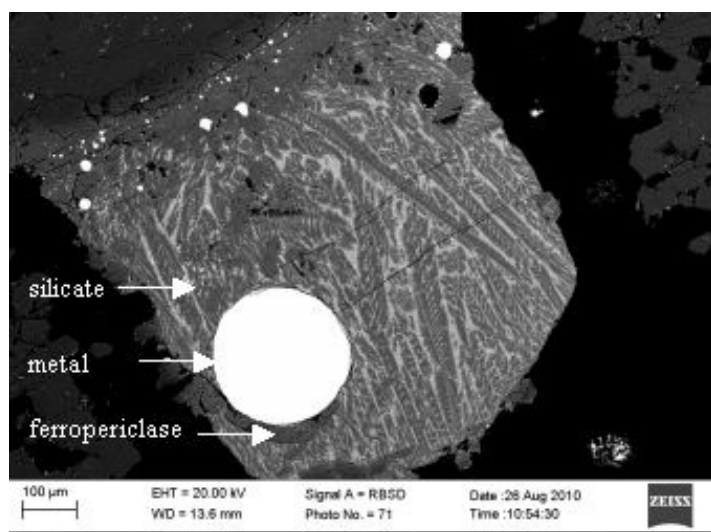


Fig. 3.2-9: SEM-picture of sample S4813 – Set 1, the running conditions are: 10.5 GPa, 2473 K, f_{O_2} : -2,4 log units relative to IW.

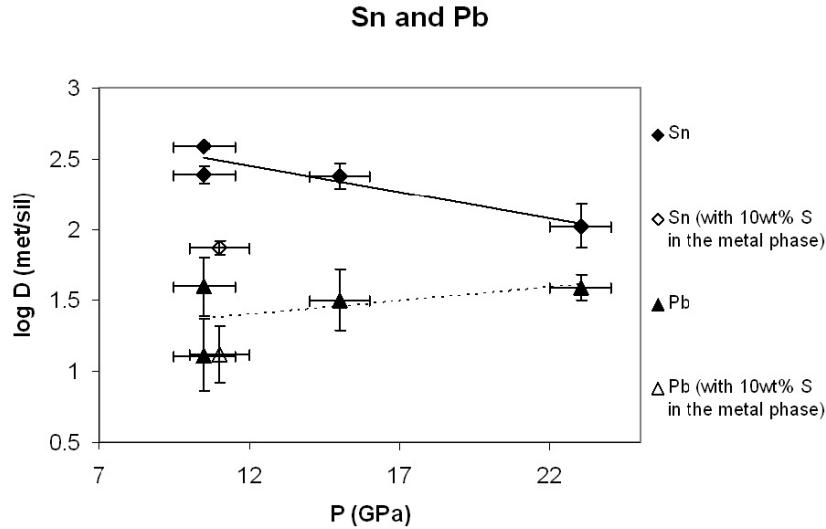


Fig. 3.2-10: Partitioning behaviour of the two volatile elements Sn and Pb. The values for $D^{\text{met/sil}}$ converge with increasing pressure, indicating that equilibration pressures of at least 30-40 GPa were necessary to avoid fractionating these elements in the Earth's mantle.

h. Silicon and oxygen partitioning between metal, lower-mantle minerals, and silicate-melt during formation of the Earth's core (Y. Nakajima, D.J. Frost and D.C. Rubie)

In addition to Fe and Ni, the Earth's core contains one or more light alloying elements in order to explain the 10 % core density deficit. Experimental data on the partitioning behaviour of siderophile elements such as Ni and Co between liquid iron and mantle minerals indicate that pressures of equilibration between core forming metal and the silicate mantle may have been in the range 20-70 GPa. At these conditions the possible candidates for the light elements are Si and O, which might have been supplied from silicate melt and lower mantle minerals at the base of a deep magma ocean. In this study we have investigated Si and O partitioning behaviour between liquid-Fe, (Mg,Fe)SiO₃-perovskite (Pv), ferropericlasite (Fp), and silicate melt.

High-pressure experiments were performed using a Kawai-type multianvil apparatus at 25 GPa and at 2400-2950 K. A starting specimen of metallic Fe (or FeSi alloy) and (Mg,Fe)₂SiO₄ olivine (Fo#70, 90, 95) was packed into an MgO container. Several wt.% of Ni, Co, V, Cr, and W was added in some experiments performed above the silicate solidus (Ni-bearing). The olivine breaks down to form Pv and Fp and melts to silicate-melt and Fp above 2700 K. Chemical analysis was performed with the electron microprobe. Oxygen fugacity in the sample was obtained from the chemical compositions of liquid-Fe and Fp (*i.e.*, relative to the iron-wüstite buffer).

The oxygen distribution coefficient, $K_D = X_{Fe}^{\text{metal}} X_O^{\text{metal}} / X_{FeO}^{\text{Fp}}$, between liquid-Fe and Fp is shown in Fig. 3.2-11a. Our results in the Fe-Pv-Fp system are similar to those previously performed in the Si-free Fe-Fp system at high oxygen fugacity. However, a strong interaction

between O and Si in liquid-metal was observed above the silicate solidus temperature of 2700 K. Fig. 3.2-11b shows the difference of K_D in our Si-bearing system from those in the Fe-Fp system (Frost *et al.*, 2010; J. Geophys. Res., 115, B02202, 2010) as a function of Si concentration of liquid-Fe. The Si content of liquid-Fe increases with decreasing oxygen fugacity. Because oxygen and silicon interact in the liquid, the K_D decreases with Si concentration. The solid line is the fitting result of a thermodynamic model.

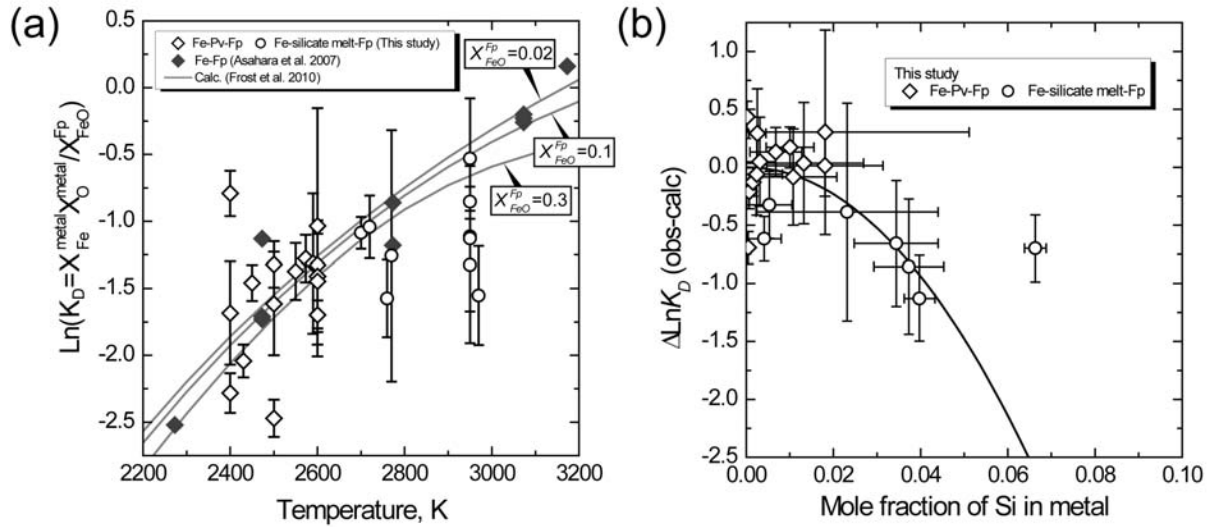


Fig. 3.2-11: (a) Oxygen partitioning between liquid-Fe and ferropericlase at 25 GPa. (a) The distribution partitioning coefficients with previous studies in the Fe-Fp system (Asahara *et al.*, Earth Planet. Sci. Lett., 257, 435, 2007; Frost *et al.*, J. Geophys. Res., 115, B02202, 2010). (b) The difference of oxygen partitioning coefficient between the Fe-Fp-silicate and Fe-Fp system. The difference $\Delta \ln K_D$ was calculated with thermodynamic data for the Fe-Fp system reported by Frost *et al.* (2010). The $\Delta \ln K_D$ decreases with Si concentration in liquid-Fe (solid line).

In order to evaluate the effect of oxygen fugacity on Si partitioning between liquid-Fe and silicate-Pv or -melt, the Si molar partition coefficient $D_{Si}^{metal/silicate} = X_{Si}^{metal} / X_{SiO_2}^{silicate}$ was plotted as a function of fO_2 relative to the iron-wüstite buffer (ΔIW) in Fig. 3.2-11a. The $D_{Si}^{metal/silicate}$ increases with increasing temperature and with decreasing oxygen fugacity. A thermodynamic model was fitted to the present data. The gradient of the slope in Fig. 3.2-12 is -1.00 ± 0.07 , indicating the stoichiometry of the Fe-Si exchange reaction between liquid metal and silica in perovskite, *i.e.*, $Fe^{metal} + SiO_2^{Pv} = FeO^{Fp} + Si^{metal}$.

The silicon partitioning coefficient between liquid metal and silicate melt is shown in Fig. 3.2-12b with previous works. The experimental results are consistent with those in the literature, however, the $D_{Si}^{metal/silicate}$ dependency on oxygen fugacity is much gentler than that expected from the stoichiometry of the Fe-Si exchange reaction. This could be a result of Si and O interaction in Fe liquid. The magnitude of D_{Si} at ΔIW -2.5 where the Fe metal contains

< 1 % O is consistent with that determined by Mann *et al.* (2009; *Geochim. Cosmochim. Acta.*, 73, 7360). With increasing oxygen fugacity and decreasing Si/O mole ratio in metal, the D_{Si} decreases along a curve with a gentler gradient, however, close to -0.5. Interaction between O and Si in the liquid could act to raise the Si content of the melt above that expected from lower temperature experiments where the O content of the melt is lower. However, this interaction would in effect be in the opposite direction from that observed for O partitioning experiments, where the presence of Si lowered the O content of the melt. These conflicting observations could be explained by a model invoking FeO, SiO, Si and Fe species interaction in the metal proposed previously (Frost *et al.*, Annual Report 2009). In the model, SiO speciation is controlled by the internal equilibrium of $FeO^{metal} + Si^{metal} = SiO^{metal} + Fe^{metal}$. Because oxygen in metal increases with increasing oxygen fugacity, SiO increases until Si/O = 1, which corresponds to ΔIW -1.6 in the present study. Under more oxidizing condition, the FeO component becomes dominant due to higher oxygen concentration in the metal, and then Si is more favoured in metal relative to SiO. As a result the Si partitioning coefficient declines toward the Fe-Si exchange reaction curve (broke line in 3.2-12b).

This study shows that oxidation conditions as well as temperature and pressure affect strongly the Si and O partitioning between liquid metal, lower-mantle minerals, and silicate melt. Moreover both elements strongly interact in the metal phase under the high pressures and temperatures at which the Earth's metallic core segregated. In terms of the Earth's core the effect of O in raising D_{Si} at higher oxygen fugacities is likely to be more important than the lowering of the O partition coefficient due to Si, because O concentrations are anyway relatively low in the metal once Si concentrations increase. However, the effect of O interaction to raise D_{Si} may help both O and Si to be the light elements in the core.

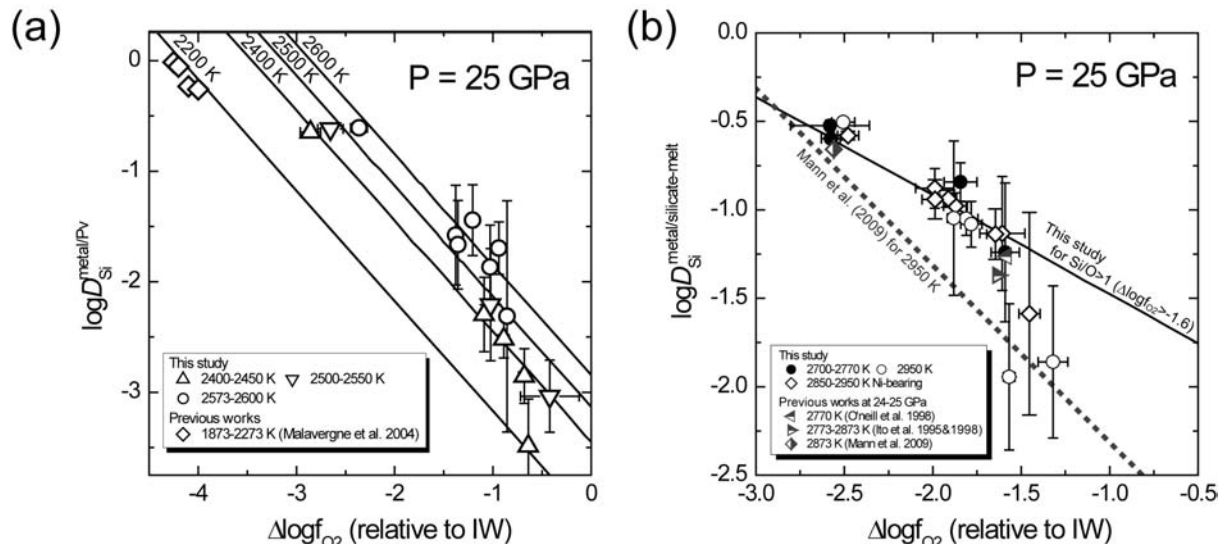


Fig. 3.2-12: Silicon molar partitioning coefficient between liquid-Fe and silicate-perovskite (a) and liquid-Fe and silicate melt (b) as a function of oxygen fugacity relative to the iron-wüstite buffer (IW). (a) The lines show the fitting result to the present data. (b) Our data are plotted with previous studies. The solid line shows the fitting to the data of Si/O>1. The broken line was calculated from the equation of Mann *et al.* (2009; *Geochim. Cosmochim. Acta.*, 73, 7360).

i. Silicate perovskite and the terrestrial noble gas signature (S. Shcheka and H. Keppler)

The relative abundance of noble gases on Earth is very different from the solar abundance pattern. All noble gases are strongly depleted, mostly due to loss to space. However, xenon appears to be particularly depleted on Earth. This cannot be explained by hydrodynamic escape. Moreover, the amount of radiogenic ^{40}Ar that should have been produced over Earth's history is twice larger than the amount actually found in the atmosphere. These observations may be related to trapping of noble gases in some lower mantle reservoir.

Numerous studies on noble gas solubility and noble gas partitioning involving upper mantle minerals demonstrated that noble gases are extremely incompatible. However, the solubility of noble gases in MgSiO_3 perovskite, the main constituent of the lower mantle, has never been measured. We have therefore investigated the solubility of argon and xenon in both pure and Al-bearing magnesium silicate perovskite.

Glasses of appropriate composition were loaded together with 40-80 bars of Ar or Xe into platinum capsules and converted to dense crystalline phases in a 1200t multianvil press at 1200 °C and 10 GPa. Recovered capsules were re-run in a 5000t or in a 1000t multianvil press at 1600-1800 °C and 23-24 GPa for 1 h. Numerous empty cavities indicating saturation of the samples with Ar or Xe were observed in the run products.

Electron microprobe analyses of recovered perovskites show that 0.1-1.3 wt.% of Ar is dissolved in perovskite whereas no Ar was found in other high-pressure minerals (*e.g.*, ringwoodite, majorite, akimotoite, periclase; detection limit 28-40 ppm by weight), except in K-bearing experiments, in which up to 0.5 wt.% Ar was found in phase X (Fig. 3.2-13; simplified formula $\square\text{KMg}_2\text{Si}_2\text{O}_7\text{H}$, with \square = K vacancy). Considerable scattering in the measured Ar content is probably due to release of gas under the electron beam. Perovskite produced in the presence of excess xenon contained numerous cavities. Bubbles slightly below the surface of the polished sample were sometimes still filled by high-density xenon after the experiment and appeared as bright spots in BSE images. However, microprobe analyses of the perovskite host showed xenon contents below detection limit (95-105 ppm by weight). The solubility of xenon in perovskite therefore appears to be orders of magnitude lower than that of argon.

The high solubility of argon in perovskite is probably due to the presence of oxygen vacancies filled by argon. The occurrence of oxygen vacancies in magnesium silicate perovskite is well documented. Microprobe analyses of all Ar-bearing perovskites show a clear deficiency in Si, which for reasons of charge balance requires oxygen vacancies (Fig. 3.2-14). A similar mechanism is expected to occur in phase X, where argon probably fills abundant vacant potassium sites. The low solubility of xenon in perovskite is probably related to its large atomic radius, which makes it unable to occupy the oxygen vacancies.

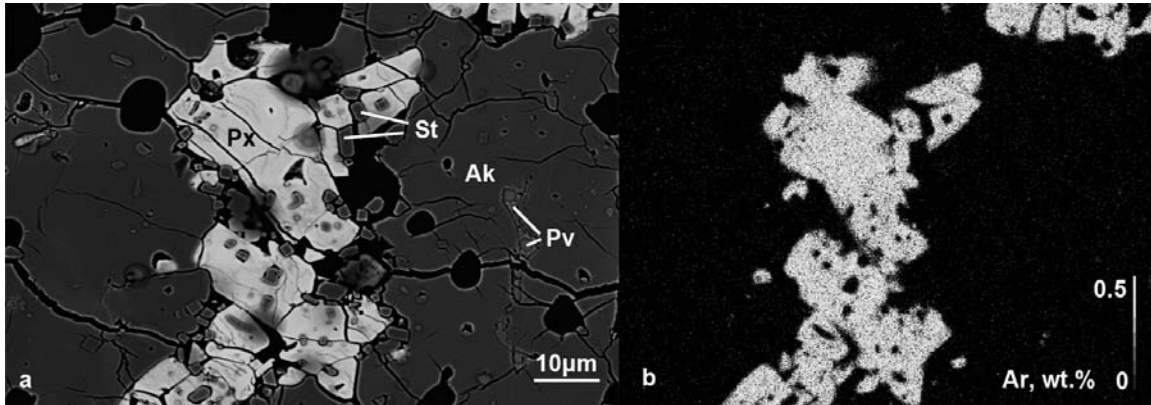


Fig. 3.2-13: (a) BSE image of coexisting phase X (Px), stishovite (St), akimotoite (Ak) and MgSiO₃-perovskite (Pv) grown at T=1800 °C and P>23 GPa, indicating silica-saturated conditions. (b) Argon distribution map of the same area. In this experiment perovskite is not Si-deficient and dissolves no Ar, whereas the vacancy-rich phase X accommodates 0.5 wt.% Ar.

Crystallization of perovskite from a magma ocean at early stages of Earth history may have trapped a significant fraction of primordial argon. However, most xenon degassed to the young primordial atmosphere which was likely lost at some stage due to strong hydrodynamic escape and/or the effects of a giant impact. Therefore, the observed noble gas pattern of the Earth's atmosphere is probably a combination of such massive loss of noble gases during the Hadean and later outgassing of a lower mantle noble gas component enriched in argon but not xenon. Accordingly, a layering in the noble gas content of the mantle is a primary feature, in contrast to the traditional models of noble gas evolution and the noble gas composition of Earth's atmosphere still carries the signature of perovskite fractionation from a magma ocean.

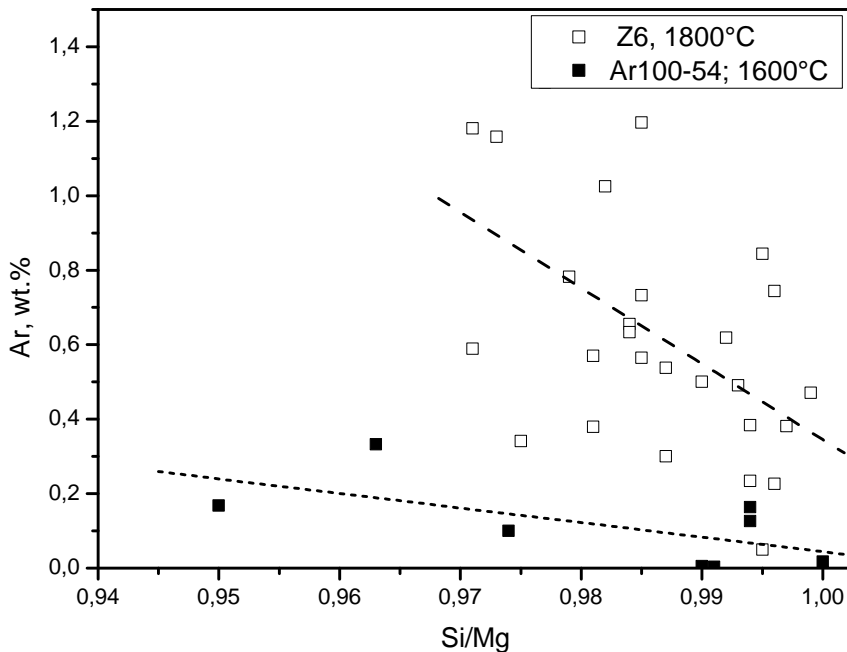


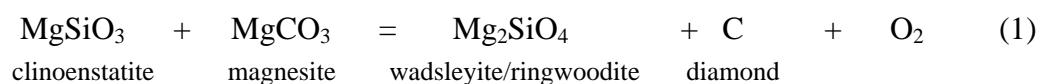
Fig. 3.2-14: Variation of the Ar content in MgSiO₃ perovskite as a function of Si/Mg molar ratio and run temperature. Lines represent linear fits of the data.

j. *The stability of magnesite in the lower mantle and the transition zone as a function of oxygen fugacity (V. Stagno, Y. Tange/Ehime, N. Miyajima, C.A. McCammon, T. Irifune/Ehime and D.J. Frost)*

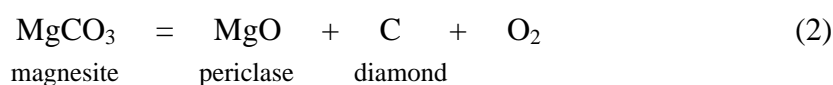
Carbonate minerals have been shown to be thermally stable at pressures compatible with the deep mantle but no experimental data are available to assess the oxygen fugacity at which carbonate minerals would be reduced to diamond. Further, recent studies on natural samples have revealed the occurrence of carbonate phases as inclusions in diamond that are argued to have formed in the transition zone and lower mantle. The aim of this study is to determine the oxygen fugacity at which magnesite will be reduced to diamond in the transition zone and lower mantle. A comparison of this oxygen fugacity with the plausible oxygen fugacity of the mantle is then used to identify the likely host for carbon in the bulk of the mantle.

Experiments were performed in a simplified Fe-Mg-Si-O-C system between 16 and 45 GPa and 1500-1700 °C using multianvil devices available at BGI and at the Geodynamics Research Center (Ehime University, Japan). Chemical analyses of the run products were performed using a Jeol JXA-8200 electron microprobe. Fe³⁺/ΣFe ratios for wadsleyite from 16 GPa and aluminous silicate perovskite from 45 GPa were determined by Mössbauer and Electron Energy Loss Spectroscopy, respectively. At 45 GPa a run was also performed adding Al-bearing glass powder to the mixture, in order to crystallize aluminous magnesium silicate perovskite with a composition similar to that crystallised from pyrolitic bulk compositions reported in the literature.

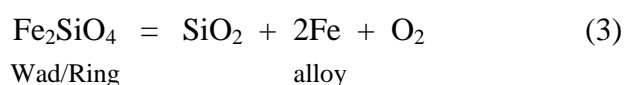
The oxygen fugacity at which magnesite and diamond coexist in the wadsleyite or ringwoodite stability field (410-660 km) is defined by the equilibrium,



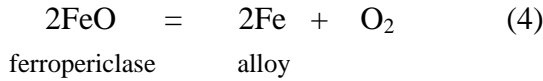
In the lower mantle this oxygen fugacity is defined similarly by the equilibrium,



Although the oxygen fugacity of equilibria (1) and (2) could be calculated using thermodynamic data, uncertainties in equation of state data introduce significant uncertainties into such a calculation. Therefore, 5 wt.% of iridium was added to the starting mixture in order to act as a sliding redox sensor and oxygen fugacities were measured based on the Fe content of Ir-Fe alloy measured after the experiment. The redox sensor in the wadsleyite and ringwoodite stability fields employs the equilibrium,



while at 25 and 45 GPa the $f\text{O}_2$ was measured by using the equilibrium,



Oxygen fugacities in equilibria (3) and (4) were calculated considering the appropriate thermodynamic model for activity-composition relations with the iron end-member component in wadsleyite, ringwoodite, ferropericlase and iron in the alloy determined by chemical composition. An experiment at 45 GPa was performed where Ir metal was replaced in the starting powders by Ni metal. Diamond and magnesite were found to exist in the run products, while Ni metal was completely oxidized and partitioned strongly into ferropericlase.

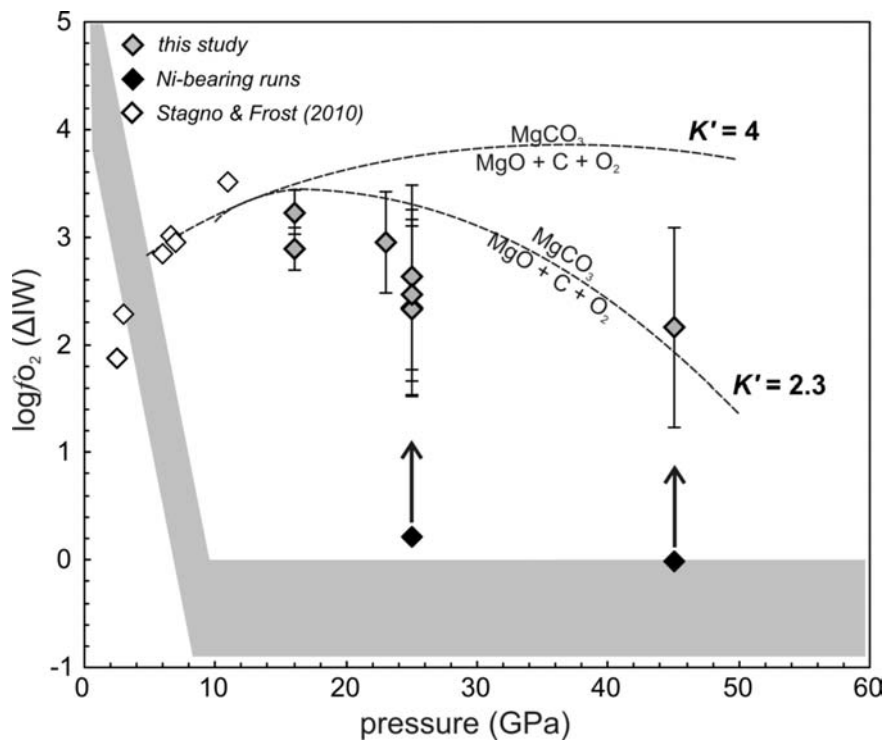


Fig. 3.2-15: The $\log f_{\text{O}_2}$ (normalized to IW) buffered by a diamond and carbonate bearing mantle assemblage is shown as a function of pressure for experiments performed between 1500-1700 °C (grey diamonds). Previous measurements of the carbon-carbonate buffer determined along a mantle adiabat between 3 and 11 GPa are also shown. Black diamonds indicate a lower limit for the carbon-carbonate f_{O_2} implied by the oxidation of Ni metal in experiments containing carbonate and diamond. Dotted curves are thermodynamic determinations of equilibrium (2) made assuming two different values from the literature for K' (pressure derivative of the bulk modulus) of MgCO_3 . The grey shaded region indicates a plausible f_{O_2} of the mantle calculated along a mantle adiabat to 10 GPa.

Figure 3.2-15 shows the experimentally determined f_{O_2} relative to the iron-wüstite oxygen buffer (*i.e.*, ΔIW) at which diamond and magnesite coexist in a bulk silicate Earth composition assemblage to pressures of 45 GPa. For comparison a band showing the plausible f_{O_2} of the mantle is also shown. The f_{O_2} in the lower mantle would be forced to be close to

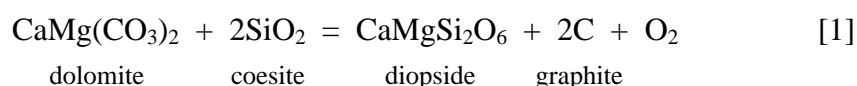
the IW buffer because the perovskite phase that forms the bulk of the lower mantle contains large proportions of ferric Fe even in equilibrium with metallic Fe. The pressure dependence of the fO_2 experimentally determined at which diamond and magnesite coexist was also compared with thermodynamic calculation for the fO_2 of equilibrium (2). A similar pressure trend was found, although the curvature is shown to be dependent on the value of K' (dK/dP) employed for magnesite, of which there is considerable uncertainty in the literature.

Our results show that: a) the fO_2 at which carbon and carbonate coexist in a lower mantle assemblage is approximately 2-3 log units above the iron-wüstite oxygen buffer, which places the lower mantle firmly in the diamond stability field. b) Experiments employing Fe-Ni alloy confirmed complete oxidation of Ni in the presence of magnesite and diamond even at 45 GPa; c) a linear extrapolation of the experimental results shown in Fig. 3.2-15 would result in magnesite being the stable form of carbon coexisting with Fe-Ni metal at an fO_2 below IW at pressures corresponding to the base of the mantle.

k. The oxygen fugacity for carbonate reduction in eclogite assemblages (V. Stagno, C.A. McCammon and D.J. Frost)

Eclogitic xenoliths in kimberlites frequently show evidence of metasomatic events that affect trace rather than major element concentrations. These observations raise important questions concerning the preservation of diamonds during oxidizing metasomatic events, the effectiveness of carbonate melts as metasomatic agents, as well as the efficiency of the subducting oceanic crust to bring carbonate down into the mantle. Although previous experimental studies provided useful information on carbonate stability and melting relations in eclogitic reservoirs, it is also important to determine the oxygen fugacity at which carbonate (solid or melts) turns into elemental carbon in typical mantle eclogitic assemblages in order to elucidate carbon storage in the mantle and the mechanism for diamond formation. The aim of this study is, therefore, to investigate the $Fe^{3+}/\Sigma Fe$ ratios of garnets and clinopyroxenes within eclogitic rocks buffered by carbon/carbonate assemblages as function of pressure and temperature and to determine the oxygen fugacity at which solid and liquid carbonate coexists with elemental carbon in eclogitic assemblages.

The equilibrium between elemental carbon and carbonate under subsolidus conditions in an eclogite composition can be described by the equilibrium,



The oxygen fugacity buffered by this equilibrium (given the abbreviation DCDG) can be calculated from thermodynamic data, but there are uncertainties surrounding the thermodynamic properties of dolomite and such calculations cannot, therefore, be performed

effectively above the solidus of a carbonated eclogite. Therefore, we require an assemblage that enables us to measure the oxygen fugacity buffered by carbon/carbonate equilibria in eclogitic assemblages. Only at oxygen fugacities above those buffered by DCDG can carbonate be stable in eclogite rocks.

For all experiments a MORB composition is employed in the system $\text{SiO}_2\text{-Al}_2\text{O}_3\text{-MgO-FeO-CaO-Na}_2\text{O-C}$. A first set of experiments were performed at 3 GPa adding natural kyanite to the starting glass composition. In a second set of experiments the starting composition was doped with 10 % TiO_2 and FeTiO_3 in order that both rutile and ilmenite were stabilized as observed in some experiments on natural eclogite compositions. All experiments contained Ir metal in order that Fe-Ir alloy could be used as a sliding redox sensor.

First results showed crystallization of the main silicate phases represented by an omphacitic clinopyroxene and garnet solid solution from the starting glass (Fig. 3.2-16). Small grains of coesite were observed that imply silica saturation. Carbon is present in the run products both as graphite and solid or liquid carbonate solid solution. Further, the partitioning of Fe-Mg between garnet and clinopyroxene is in agreement with previous studies. In kyanite-bearing experiments a Ca-rich carbonate melt, similar to previous studies on eclogites, was observed, however rutile-bearing experiments produced a melt dominated by FeCO_3 which was far more Fe-rich than expected in eclogite compositions.

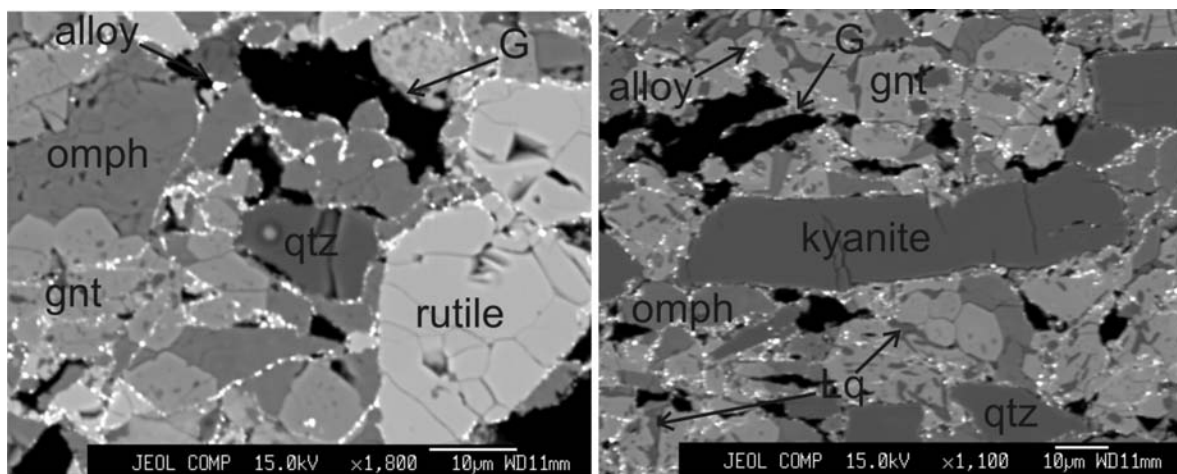


Fig. 3.2-16 : Left) recovered sectioned run product from 3 GPa/950 °C after 42 hr showing a Ti-bearing assemblage with rutile. Right) Run at 3 GPa/950 °C showing a mineral assemblage after 120 hr with kyanite. Notes: quartz (qtz), garnet (gnt), graphite (G), liquid (Lq) and the iron-iridium alloy (bright phase).

In experiments containing kyanite the oxygen fugacity fixed by the coexistence of graphite and carbonate minerals or melts can be calculated from the equilibrium,



The oxygen fugacity in Ti-bearing assemblage is calculated from,



The oxygen fugacity calculated using these equilibria is compared in Fig. 3.2-17, which also shows determinations of the DCDG [1] and EMOG buffers from thermodynamic data. EMOG defines the same buffering equilibria as DCDG in peridotite rocks (see previous contribution). The results from the kyanite bearing eclogite assemblage indicate a lower oxygen fugacity for the carbonate-graphite equilibrium than predicted from thermodynamic data. These experiments produced melts that were most consistent with those from previous experiments. Results from rutile bearing experiments are consistent with the thermodynamic calculation for DCDG, however, these melts were very Fe rich and not at all similar to those expected in eclogite assemblages. We conclude that the $f\text{O}_2$ determined for the kyanite assemblage was more likely to reflect that of the graphite-carbonate melt transition in eclogite rocks.

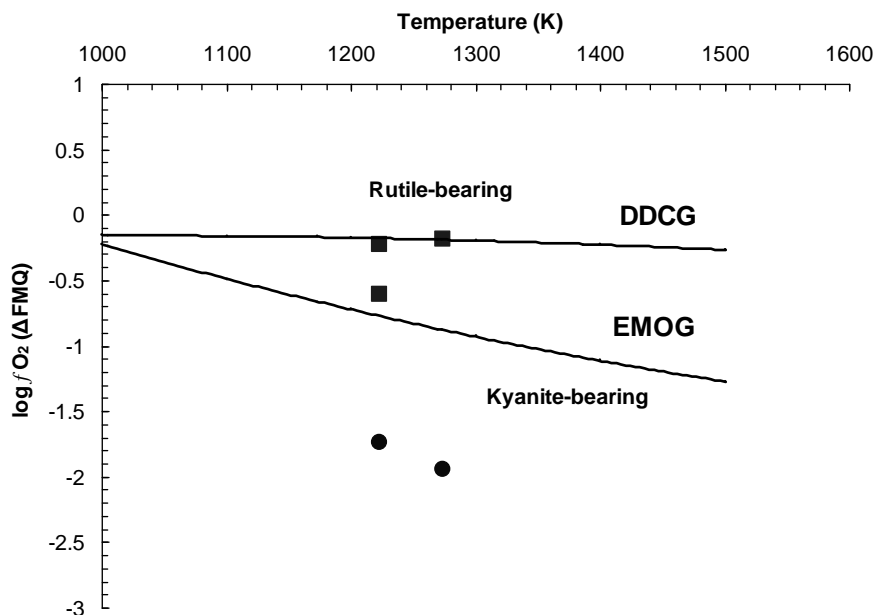


Fig. 3.2-17: Oxygen fugacities calculated from kyanite (circles) and rutile (squares) bearing eclogite experiments using equilibria [2] and [3] respectively. Values are compared with calculations of the DCDG equilibrium [1] from thermodynamic data and the determination of the EMOG buffer from a previous study. Uncertainties propagated from compositional measurement are of the order of 0.2 log units.

Complementary experiments will be performed to enable the $\text{Fe}^{3+}/\Sigma\text{Fe}$ ratios of garnet and clinopyroxene to be determined within an eclogite composition where the oxygen fugacity is buffered by the presence of elemental carbon and carbonate minerals or melts. Results of these experiments will show whether ferric iron components are stabilized within garnet and clinopyroxene as a function of pressure and temperature. This will provide the basis for

determining whether with increasing pressure during subduction there will be a tendency for carbonate minerals to reduce in eclogitic rocks as a result of pressure favouring the formation of Fe^{3+} components in garnet and clinopyroxene. Similarly the point at which diamonds would become oxidized to carbonate minerals and melts in upwelling regions of the mantle that have eclogitic compositions will be examined.

1. Fe-Mg partitioning between carbonate melts and olivine (D.J. Frost and V. Stagno)

Carbonate melts may be important metasomatic agents in the mantle and might be formed as incipient melts beneath mid ocean ridges. As melt inclusions from mantle rocks, carbonates are quite rare, however, and their existence is mainly implied from their expected metasomatic effects. This scarcity can be explained by the numerous reactions that they can undergo with mantle minerals that makes their long-term isolation as inclusions relatively improbable. As a result experimental studies to determine their likely composition at mantle conditions are important for tracing their influence.

We have performed experiments to measure the Fe-Mg partitioning between carbonate melts and olivine between 3 and 6 GPa and at 1200-1400 °C. In some experiments multi-chamber Re-capsules were spark eroded such that carbonate-olivine mixtures with different Fe/Mg ratios could be equilibrated separately in a single experiment. Melts had a Ca/(Ca+Mg) ratio of approximately 0.3.

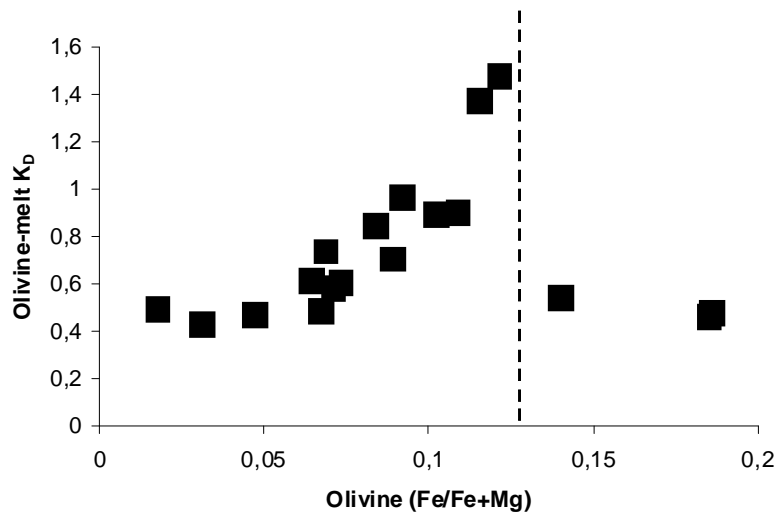


Fig. 3.2-18: The olivine-melt K_D ($[\text{Fe}_{\text{ol}} \cdot \text{Mg}_{\text{melt}}] / [\text{Fe}_{\text{melt}} \cdot \text{Mg}_{\text{ol}}]$) for carbonate-rich melts as a function of olivine molar Fe/(Fe+Mg) ratio. Experiments performed between 3 and 6 GPa and 1200-1400 °C. Vertical dashed line indicates a jump in the K_D with olivine Fe content, which also coincides with an increase in the Si-content of the melt.

Figure 3.2-18 shows the olivine-melt K_D ($[\text{Fe}_{\text{ol}} \cdot \text{Mg}_{\text{melt}}] / [\text{Fe}_{\text{melt}} \cdot \text{Mg}_{\text{ol}}]$) for carbonate-rich melts as a function of olivine Fe/(Fe+Mg) ratio or Fe#. Very little variation of K_D with pressure or

temperature occurs, however, there is a strong variation of K_D with the Fe content of olivine. Carbonate-melts in equilibrium with mantle-like olivine have high values of K_D , which implies very low melt Fe contents. However, beyond an olivine Fe# of approximately 0.12 a jump in K_D occurs, which is also coincident with a rapid increase in the SiO₂ content of the melt from below 5 wt.% to over 20 wt.%. The transition is also marked by larger degrees of melting. A series of experiments at 6 GPa and 1400 °C have helped to define this transition, which is similar to that which occurs between carbonate and kimberlite with increasing temperature. One consequent model for the formation of kimberlite magma could be as a result of the migration of carbonate melts from refractory Fe-poor mantle into more iron-rich regions where the rapid increase in melt proportion allows percolation and migration. Liquid immiscibility between the two melts at the olivine content of the apparent transition cannot be excluded.

m. Iron oxidation state of garnet from upper mantle xenoliths in the Gibeon kimberlite province (Namibia) (M. Longo, P. Nimis, F. Nestola and L. Ziberna/Padua; L. Franz/Basel and C.A. McCammon)

The Gibeon Kimberlite Province of southern Namibia is located between Keetmanshoop and Mariental, and contains more than 75 group 1 kimberlites. Such “off-craton” kimberlites are apparently non-diamondiferous, unlike the older “on-craton” kimberlites of the adjacent Kaapvaal craton. The P-T conditions of crystallization have been previously estimated, giving a restricted pressure range (3.8-4.6 GPa), which corresponds to a depth of origin ranging between 100 and 140 km. A temperature gradient can be recognized, even at similar depths. In particular, the lowest temperatures were registered by coarse equant texture kimberlites; whereas the highest temperatures have been registered by the mosaic-porphyroclastic ones. In contrast to the nearby Kaapvaal craton, in the Gibeon xenoliths the “cold” coarse equant peridotites are relatively enriched garnet lherzolites with low modal orthopyroxene content; whereas the “hot” mosaic-porphyroclastic peridotites are depleted garnet harzburgites with high modal orthopyroxene contents. So far, geothermobarometric studies on the Gibeon Kimberlite Province have neglected the oxidation state of Fe. Previous studies have showed that the application of different geothermometers (*i.e.*, opx-gnt versus cpx-opx equilibria) on the same suite of samples shows a consistent variation. Such differences may be due to transient heating at specific depths or during short-lived residence of the xenoliths in a shallower magma chamber. In order to provide insight into possible causes of this behaviour, we studied the iron oxidation state of garnets from Namibia and calculated the oxygen fugacities.

Nineteen garnets from garnet peridotites were selected from the Gibeon Townsland 1 pipe, representative of the three different kimberlite texture types (coarse equant, porphyroclastic and mosaic-porphyroclastic). Samples were measured using the electron microprobe at the Bayerisches Geoinstitut to determine the Fe³⁺/ΣFe ratio using the flank method (see previous BGI Annual Reports). Samples examined in this study show a narrow variation in iron composition ΣFe (wt.%) between 5 and 6.5 % and the Fe³⁺/ΣFe ratio measured by the flank method varies roughly between 5 and 10 % (Fig. 3.2-19). Oxygen fugacities were determined

using the olivine-orthopyroxene-garnet oxybarometer, and results show that oxygen fugacities are between -1.4 and -3.3 $\Delta\log fO_2$ (FMQ). There is no obvious correlation between fO_2 and texture (Coarse, Porphyroclastic, Mosaic Porphyroclastic) and our results show generally more oxidized conditions to those from the on-craton Kapvaal samples, even at similar depths (Fig. 3.2-20). Most of the samples do not show heterogeneity in major element analysis, except for samples KGG-55 and KGG-62a. Preliminary results for those two samples show a variation of flank method ratio from core to rim, suggesting possible zoning in Fe^{3+} content. Further studies are underway to determine if there is a systematic relation between Fe^{3+} content and the variation in geothermometry results, as well as to elucidate the process that has produced more uniformly oxidized xenoliths in the Namibian samples compared to those from Kapvaal.

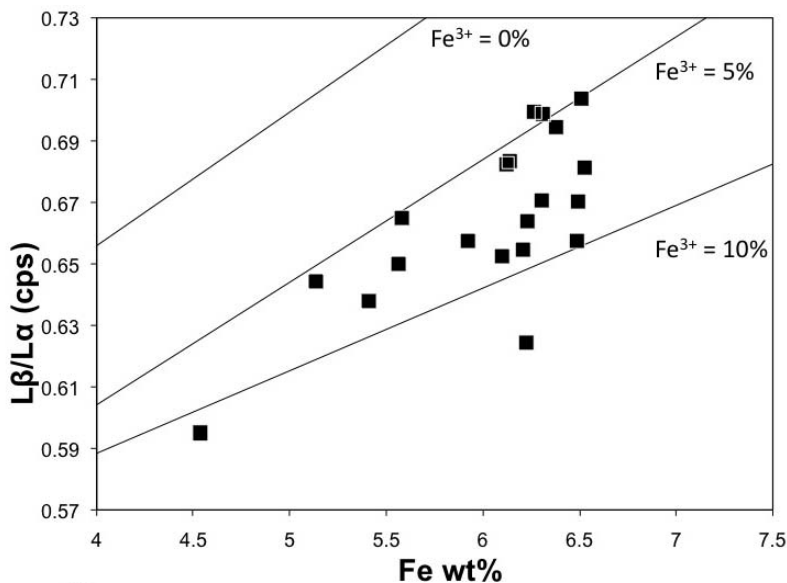


Fig. 3.2-19: $L\beta/L\alpha$ ratio as a function of ΣFe (wt.%) for the suite of garnets from Namibia. The white curves represent lines of equal $Fe^{3+}/\Sigma Fe$ concentration.

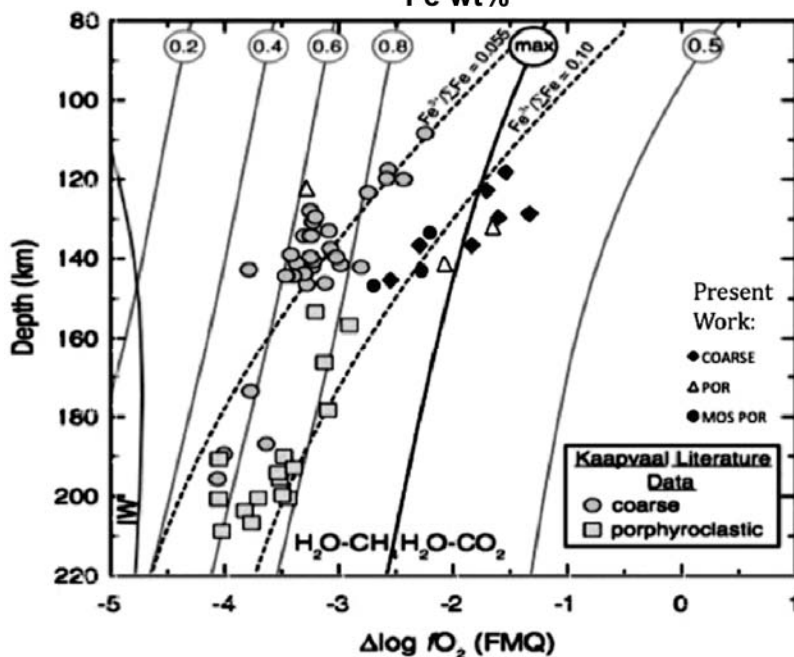


Fig. 3.2-20: Depth – fO_2 relationship for peridotite xenoliths from the present work compared with previously studied peridotite xenoliths for localities in the Kapvaal craton, excluding Kimberley. There is an observable correlation of texture (coarse and porphyroclastic) with depth in the Kapvaal region; whereas results

so far show no correlation with depth in the Namibian region (present work).

n. *The oxidation state of mantle wedge garnet peridotites metasomatised by C-bearing subduction fluids (N. Malaspina and S. Poli/Milano; F. Langenhorst)*

Volatiles in the Earth's mantle affect its rheological properties, melting relations and major and trace element transport. At subduction zones, volatile transfer from the slab to the mantle wedge is accomplished by fluid phases enriched in COH components released during dehydration, partial melting and/or decarbonation reactions in the slab lithologies. The coexistence of hydrates, carbonates and C polymorphs down to 200 km depth in subduction environments indicates that in the deep mantle the composition of C-saturated COH fluids closely relates to the oxidation state of the system. Determination of the iron oxidation state of metasomatic minerals (*e.g.*, garnet) thus provides an essential information regarding the composition of the metasomatic fluids, such as those responsible for diamond formation.

We studied the metasomatised garnet websterites from Bardane (Western Gneiss Region, Norway), a unique example of hydrate-carbonate-bearing mantle rocks affected by subduction fluid infiltration at ultrahigh pressure, in the stability fields of diamond and majorite. These samples represent slices of former Archean transition zone mantle that upwelled, melted and accreted to a thick cratonic lithosphere, where it cooled until the Middle Proterozoic (stages M1-M2). During the subsequent Caledonian to Scandian subduction cycle (stage M3) these depleted mantle rocks were dragged into deep portions of the supra-subduction mantle wedge, where the episodic/progressive infiltration of crustal fluids at increasing depth enhanced crystallisation of diamond and of majoritic garnet. We studied the peak (M3) mineral assemblage garnet + orthopyroxene + olivine ± clinopyroxene ± phlogopite, where garnet composition becomes majoritic with a PT increase from 3 to 6.5 GPa and 800-1000 °C. Majoritic garnet contains polyphase inclusions with daughter Cr-spinel + phlogopite/K-amphibole + dolomite/magnesite + graphite/diamond. They witness a close relation between COH-fluid/mineral interaction and the oxidation state of the rock. We determined the fO_2 in the M3 assemblage starting from Fe^{3+} analyses in majoritic garnet, measured by the electron microprobe using the “flank method” at the University of Milano.

To check the quality of $Fe^{3+}/\Sigma Fe$ measurements in peridotitic garnets with relatively low total iron content we used pyrope-rich garnets from orogenic mantle peridotites (Sulu UHP belt, China) as additional standards, whose $Fe^{3+}/\Sigma Fe$ ratio was cross-calibrated by electron energy-loss spectroscopy (EELS) at the Bayerisches Geoinstitut (Fig. 3.2-21). The fO_2 values obtained for the Bardane mantle wedge garnet websterites are up to 2 log units lower than the FMQ buffer and plot on the continuation of a trend extending from arc lavas to mantle wedge garnet peridotites equilibrated at 4-5 GPa (Fig. 3.2-22). The determination of oxygen fugacity of the hydrate-carbonate-bearing M3 mineral association enabled us to estimate the speciation of slab-derived metasomatic COH fluids responsible for polyphase inclusion formation. Such fluids are mixtures of silicates and H_2O+CO_2 , where water is the dominant species of the COH component. The peculiar composition of majorite-hosted diamond-bearing polyphase inclusions from Bardane and the speciation of its COH component point to an “oxidised” silicate-rich aqueous fluid contaminant from the subducted slab to the mantle wedge.

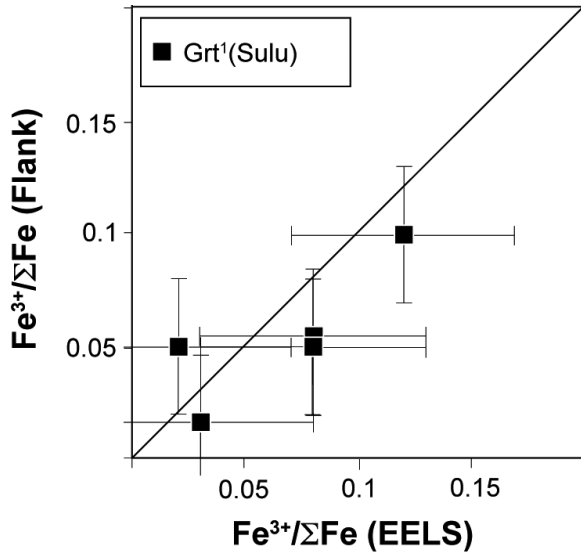


Fig. 3.2-21: $\text{Fe}^{3+}/\Sigma\text{Fe}$ determined by the “flank method” and EELS in garnet grains from mantle wedge peridotites of the UHP Sulu Belt (Eastern China) used as additional standards. The error bars refer to $\sigma=3\%$ and $\sigma=5\%$ in the “flank method” and EELS $\text{Fe}^{3+}/\Sigma\text{Fe}$ respectively, for $\Sigma\text{Fe}<8\text{wt.}\%$.

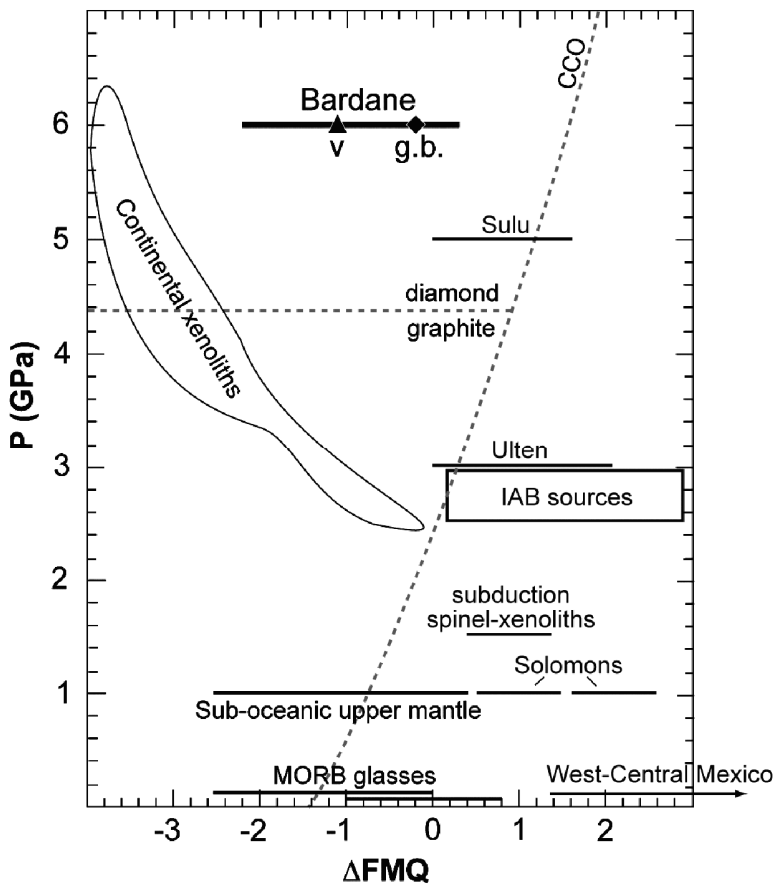


Fig. 3.2-22: Ranges and average values of ΔFMQ ($\log f_{\text{O}_2 \text{ sample}} - \log f_{\text{O}_2 \text{ FMQ}}$) for the M3-3 grain boundary (g.b.) and vein (v) majoritic garnets plotted as a function of pressure. They are compared with different mantle domains from literature: garnet peridotite xenoliths from subcratonic lithospheric mantle (curved white area on the left side of the plot), orogenic mantle wedge garnet peridotites from the Ulten Zone (Italian Central Alps) and the UHP Sulu Belt, subduction related spinel peridotite xenoliths, Mid Ocean

Ridge (MORB) glasses and sub-oceanic upper mantle. Note the negatively correlated trend between mantle wedge garnet peridotites, arc lavas from west-central Mexico and from Solomon, and island arc basalt (IAB) sources, which is parallel to the ΔFMQ decrease of continental xenoliths with pressure. The CCO oxygen buffer ($\text{C} + \text{O}_2 = \text{CO}_2$), calculated at an average $T=900\text{ }^\circ\text{C}$, and the graphite-diamond transition at the maximum M3 temperature conditions ($1000\text{ }^\circ\text{C}$), are also indicated for reference.

o. *Partitioning of halogens between mantle minerals and aqueous fluids (D. Bernini, D. Dolejš/Prague, M. Wiedenbeck/Potsdam and H. Keppler)*

Fluorine and chlorine are minor constituents in the upper mantle and are traditionally considered to be hosted mainly by hydrous phosphates or silicates. However, no systematic attention has been paid to the possibility of incorporating halogens in nominally anhydrous silicates. This is particularly relevant for the release of halogens during dehydration reactions in the subducting lithosphere. The chlorine and fluorine contents of mantle serpentinites are two to three orders of magnitude higher than their concentrations in the primitive mantle, and it is not clear whether this difference is simply due to a contrasting availability of accessory phosphates or hydrous silicates, or whether there is also some control *via* halogen incorporation in nominally anhydrous rock-forming silicates. If nominally anhydrous rock-forming silicates were able to incorporate fluorine or chlorine to the extent comparable to hydroxyl solubility, they would become the most important reservoir of halogens on the planet .

In order to understand the global geochemical cycle of halogens, we performed phase equilibrium experiments in the system forsterite-enstatite-pyrope-H₂O with added MgCl₂ or MgF₂, and measured the solubility of halogens in these minerals. The composition of the fluid phase and the corresponding fluid-mineral partition coefficients were calculated by mass balance. Experiments were performed in an end-loaded piston cylinder apparatus at 1100 °C and 2.6 GPa. Starting materials were mixtures of Mg(OH)₂, Al(OH)₃ and SiO₂, or anhydrous silicate glasses synthesized from MgO, Al₂O₃ and SiO₂. Major element compositions of the minerals were measured with a JEOL JXA-8200 electron microprobe, whereas the F and Cl concentrations in forsterite, enstatite and pyrope were measured by a Cameca ims 6f SIMS instrument at the Geoforschungszentrum Potsdam.

The chlorine solubility in forsterite, enstatite and pyrope is very low (0.2-0.9 ppm) and is independent of the fluid salinity (0.3-40 wt.% Cl). This suggests that an intrinsic saturation limit in these minerals is reached already at very low Cl concentrations. Chlorine is therefore exceedingly incompatible in upper mantle minerals, and the corresponding fluid/mineral partition coefficient are solely a function of fluid salinity: $D_{Cl}^{fl/min}$ increases from $4.5 \cdot 10^3$ to $1.6 \cdot 10^6$ as the fluid salinity changes from 0.3 to 40 wt.% Cl. The overall fit including all three mineral phases is described by the following power law:

$$D_{Cl}^{fl/min} = 27860 X_{Cl}^{1.06}$$

where X_{Cl} is the fluid salinity in wt.% Cl (Fig. 3.2-23a). The fluorine solubility is 16-31 ppm in enstatite and 24-52 ppm in pyrope, again independent of fluid salinity. Forsterite dissolves 246-267 ppm F up to a fluid salinity of 1.6 wt.% F, after which it is replaced by minerals of the humite group. The partition coefficient between aqueous fluid and nominally anhydrous minerals, $D_F^{fl/min}$ increases from ~ 8 to $5.8 \cdot 10^3$ as the fluid salinity increases, as follows.

$$D_F^{\text{fl/min}} = 226.31 X_F^{1.10}$$

where X_F is the fluid salinity in wt.% F (Fig. 3.2-23b). At high fluorine contents in the system, humite group minerals containing fluorine concentrations of 2.6 wt.% in clinohumite, 3.6 wt.% in humite, 4.6-6.7 wt.% chondrodite, and 11.4 wt.% in norbergite were observed. Partition coefficients of fluorine for the humite group minerals range from $8.4 \cdot 10^0$ to $5.8 \cdot 10^3$. The coexistence of two humite group minerals in several runs yields the fluorine-hydroxyl partition coefficients $D^{\text{hum/chum}} = X_F^{\text{hum}} / X_F^{\text{chum}} = 1.10$ and $D^{\text{no/cho}} = 0.98$. These results indicate negligible fractionation of fluorine between humite-group pairs at 1100 °C and 2.6 GPa.

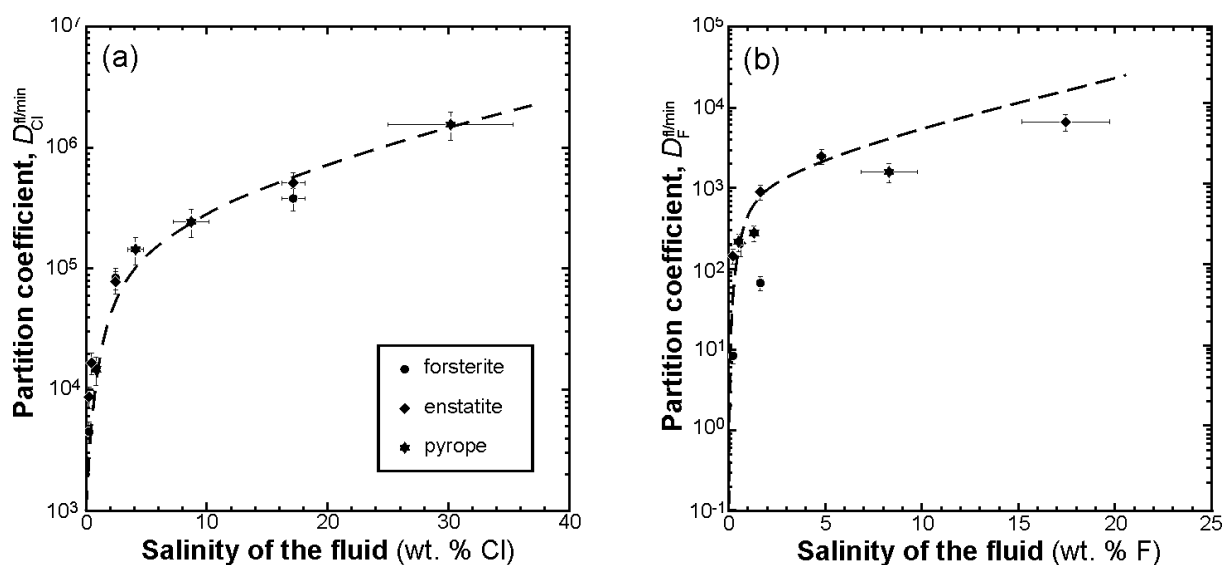


Fig. 3.2-23: Partition coefficients of chlorine (a) and fluorine (b) between aqueous fluids and minerals.

Overall, the fluorine solubility in forsterite and garnet is comparable to that of hydroxyl, which would be consistent with the charge-coupled substitution $\text{MgO}_2 \leftrightarrow \square\text{F}_2$ in forsterite, and fluorination of oxygen polyhedra and charge balance by local chemical defects in pyrope. In Al-bearing enstatite the fluorine solubility is much lower than that of hydroxyl, revealing that the substitution $[\text{SiO}]^{2+} \leftrightarrow [\text{AlF}]^{2+}$ is ineffective. The decrease in chlorine solubility by four orders of magnitude when compared to fluorine is consistent with increasing lattice strain.

Partition coefficients of chlorine between aqueous fluid and minerals are approximately three orders of magnitude higher than those for hydroxyl. Consequently, protracted fluid flow from subducting slab through the mantle wedge will lead to more efficient sequestration of H_2O into the nominally anhydrous minerals and thus to a gradual increase in the fluid salinity. Simple mass balance calculations reveal that subduction zone fluids containing 0.24 to 4.25 wt.% Cl ($\text{Cl}/\text{H}_2\text{O} \sim 0.002$ to 0.05) had to interact with the overlying mantle wedge in order to

produce the elevated Cl/H₂O ratios (0.02 to 0.14), which are typical of primitive melt inclusions from arc magmas (Fig. 3.2-24). To produce this increase, the rock-fluid ratios may have been as high as 4300, but these values represent minimum estimates because the fluid released from the subducted slab is assumed to equilibrate with completely dry bulk assemblage. If the nominally anhydrous minerals already contain some H₂O, then the process becomes less efficient, and even higher rock-fluid ratios are required to produce the Cl/H₂O content of arc magmas. Considering an average thickness of the oceanic crust of 7 km and ~ 1 wt.% fluid loss during dehydration, a fluid flux, $f = 70 \text{ m}_{\text{fl}}^3 \text{ m}_{\text{rock}}^{-2}$ through the slab-mantle wedge interface can be estimated. Characteristic length scales of fluid-rock interaction above this interface can be calculated from the relation between the fluid flux and estimated rock/fluid ratio (ϕ): $f = L/\phi$. For the maximum Cl/H₂O values of arc magmas, the rock-fluid ratio resulting from Cl/H₂O values of global subduction outflux is 1300, thus leading to a migration distance of ~ 90 km, which is comparable to subarc mantle wedge thickness. These calculations suggest that diffusive fluid flow from the subducted slab into the melting regions in the wedge is sufficient to pervasively metasomatize the mantle and produce the characteristic volatile signature of arc magmas.

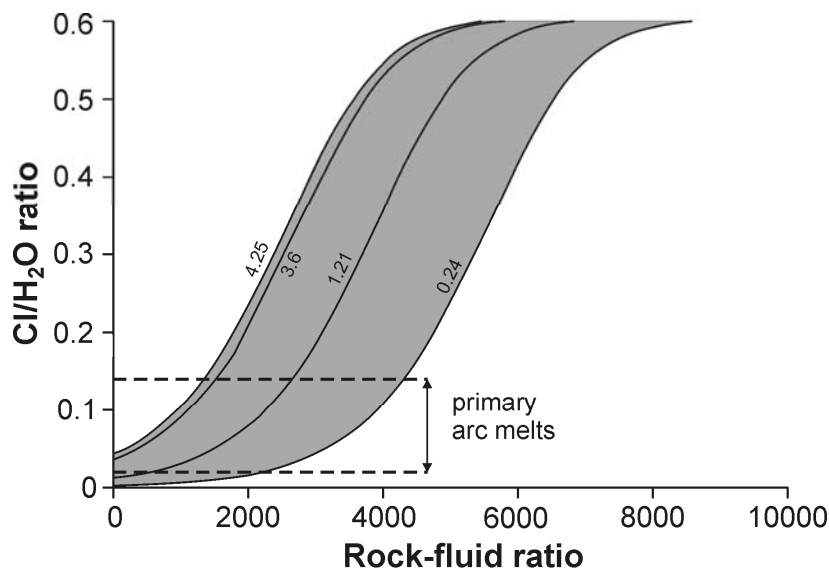


Fig. 3.2-24: The rock-fluid ratio vs. Cl concentration in aqueous fluid illustrating the progressive increase in the fluid salinity as the amount of the rock that interacted with the fluid along the flow path increased. The four different curves refer to four different initial salinities (0.24,

1.21, 3.6, and 4.25 wt.% Cl). Range of the Cl concentrations in the aqueous fluids infiltrating the arc melting region is shown for comparison.

p. *Composition of the bulk oceanic crust and its implications for mineralogical and physical properties of subducting lithosphere (Z. Chemia/Trondheim, D. Dolejš/Prague and G. Steinle-Neumann)*

Extraction of basaltic magmas at mid-ocean ridges is one of the main differentiation processes on Earth, and it has important bearings on crustal evolution, plate dynamics, especially

subduction and the possible detachment of basalt and underlying depleted mantle (DM) during sinking of the slab through the mantle. A good characterization of the oceanic crust composition and the complementary depleted peridotitic mantle is hence of critical importance in determining phase equilibria and physical properties of subducting lithosphere. The chemical composition of the bulk oceanic crust is often approximated by mid-ocean ridge basalt (MORB) composition, but intrusive gabbros and cumulates also contribute significantly to the oceanic lithosphere. Furthermore, the composition of the DM is neither known nor accessible, but it may be estimated based on mass balance constraints imposed by melt-solid equilibria. We propose a simple mass balance approach, which allows us to estimate compositions of the bulk oceanic crust and depleted peridotite in a self-consistent manner and link them to the primitive pyrolite model.

The overall composition of the bulk oceanic crust (BOC) is taken to be represented by primary partial melt in equilibrium with the mantle peridotite, which has not undergone any subsequent fractionation. We evaluate a set of 7629 major-element data of mid-ocean ridge glasses for incompatible element concentrations and Mg/Fe ratios, which indicate the degree of fractionation. In detail, we calculate the Mg/Fe ratio of olivine in equilibrium with the melt (glass) composition using a distribution coefficient of $D_{ol/liq}^{Fe/Mg} = 0.3$.

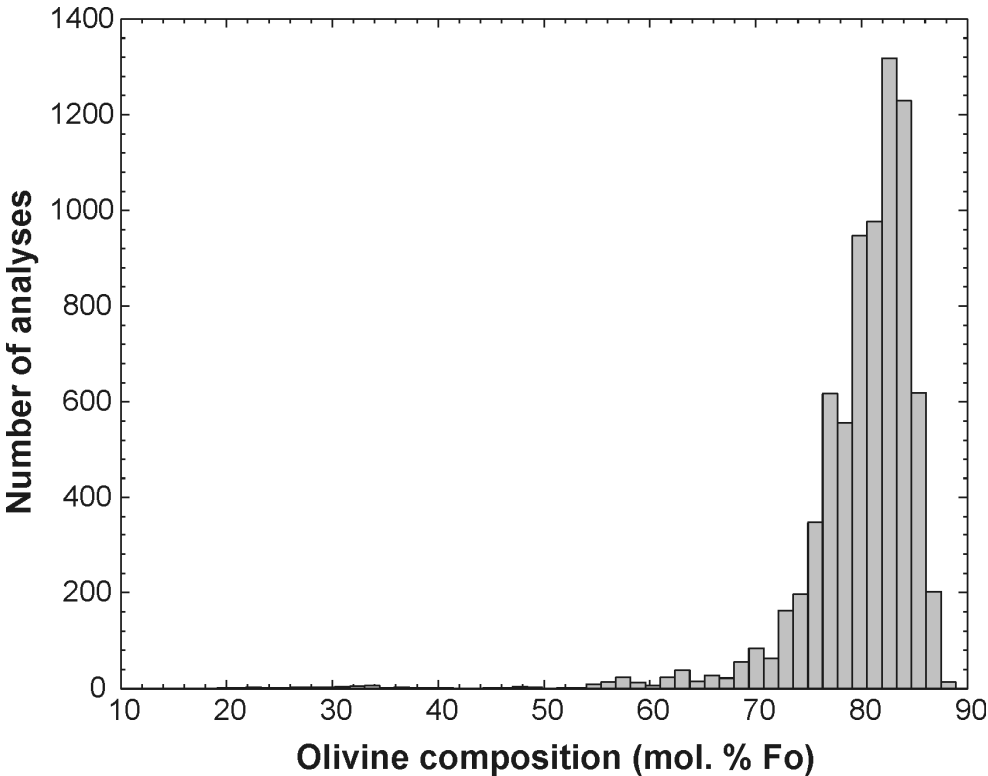


Fig. 3.2-25: Frequency histogram of mid-ocean ridge glasses indicating compositions equilibrium olivine. The data set commences at Fo₉₂ (primary melts in equilibrium with primitive mantle) and it evolves towards lower Fo contents as a result of subsequent fractionation.

Recalculated olivine compositions show lognormal distribution with a mean at Fo₈₃, and a steady decrease toward Fo₆₀ (Fig. 3.2-25). This indicates that the predominant portion of mid-ocean ridge melts (glasses) has undergone substantial fractionation of olivine ± pyroxene. Only glasses in equilibrium with olivine Fo₈₈₋₉₁ are considered to be primary melts (Fig. 3.2-26), and their average composition taken as representing the bulk oceanic crust (Table 3.2-1).

In order to calculate the complementary composition of DM, we use the mass balance, $X_i^{PM} = F \cdot X_i^{BOC} + (1 - F) \cdot X_i^{DM}$, where PM refers to primitive mantle, and F represents the degree of partial melting. Enrichment factors between BOC and PM were computed for all major oxides, and their highest values indicate the most incompatible elements (Na – 4.85, P – 4.05, Al – 3.82, Ti – 3.33). Since Na₂O is perfectly incompatible in olivine and orthopyroxene, its enrichment factor has been inverted to obtain the degree of partial melting, $F = 0.206$. This value is in agreement with previous geochemical estimates of the extent of partial melting beneath the mid-ocean ridges. The resulting composition of DM, obtained by mass balance, is listed in Table 3.2-1.

Table 3.2-1. Composition of the depleted mantle and bulk oceanic crust

wt. %	SiO ₂	TiO ₂	Al ₂ O ₃	Cr ₂ O ₃	FeO	MnO	MgO	CaO	Na ₂ O	K ₂ O	P ₂ O ₅
DM	43.73	0.079	1.19	0.484	8.17	0.129	45.09	1.11	0.00	0.027	0.004
BOC	49.94	0.670	17.01	-	7.61	0.159	9.78	12.96	1.75	0.037	0.086
MORB (PH87)	49.51	0.900	16.75	0.070	8.05	0.140	9.74	12.50	2.18	0.065	0.095
MORB (H88)	50.75	1.625	15.35	-	10.49	-	7.62	11.37	2.69	0.107	-
MORB-MAR (K04)	49.83	1.106	16.25	-	9.69	0.140	8.64	11.71	2.91	0.050	0.080
MORB-EPR (K04)	50.22	1.472	15.81	-	9.52	0.160	7.59	12.20	2.76	0.130	0.130

References: PH87 – Presnall and Hoover (1987; CMP 87, 170), H88 – Hofmann (1988;EPSL, 90, 297), K04 – Klein (2004; Treatise of Geochemistry, 3.13, 433).

Our bulk oceanic crust estimate is more primitive than all average mid-ocean ridge basalts. In detail, BOC contains slightly more MgO, CaO and Al₂O₃, and significantly less FeO and Na₂O. This corresponds to a lower abundance of Ca-rich plagioclase and diopside, and elevated contents of orthopyroxene at low pressures. At high pressures, the oceanic crust is expected to contain less omphacitic clinopyroxene in favour of garnet. The depleted mantle contains 3-4 times less Al₂O₃ when compared to pyrolite estimates commonly employed in calculations of phase equilibria and physical properties of subducting oceanic mantle. Consequently, suboceanic DM will contain only negligible amounts of garnet; combined with elevated *Mg#* this contributes to lower density and greater buoyancy.

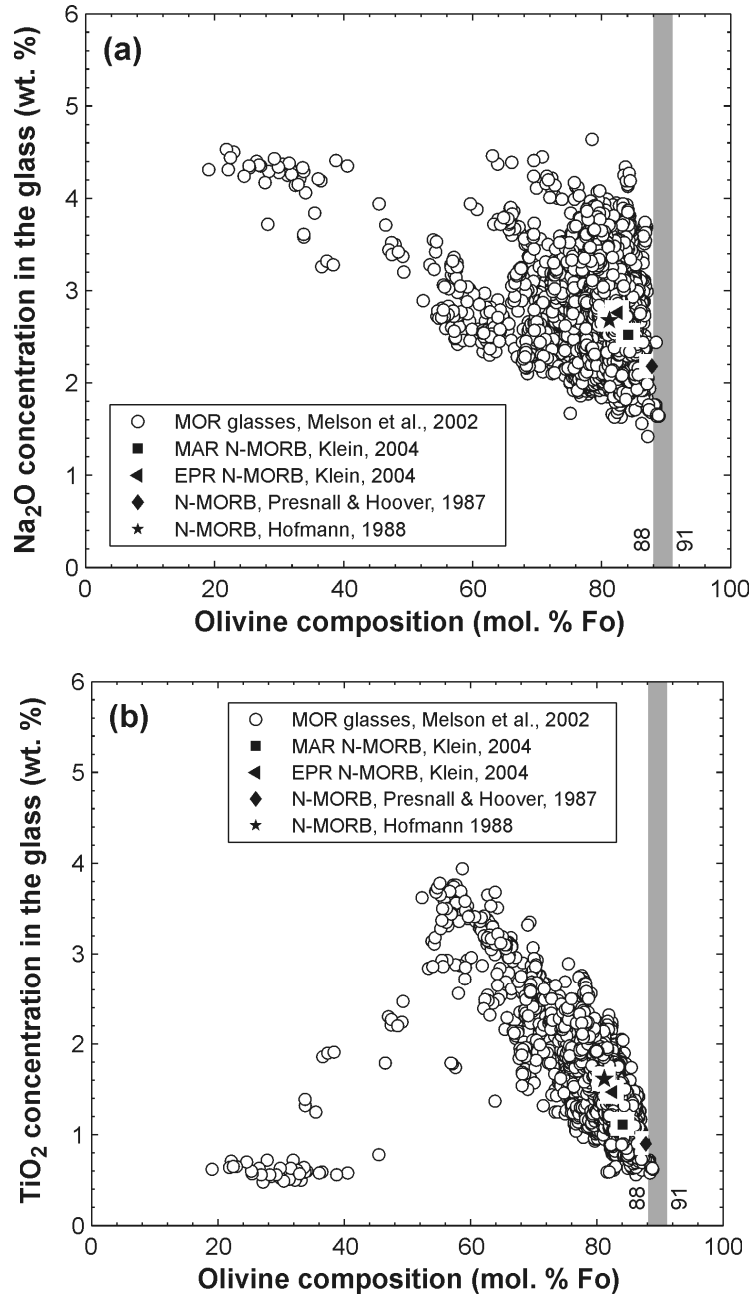


Fig. 3.2-26: Concentrations of Na₂O (a) and TiO₂ (b) in mid-ocean ridge glasses plotted as a function of equilibrium olivine composition. A few well-constrained data points correspond to primitive mantle melts. MORB estimates are significantly richer in incompatible elements, corresponding to 20-40 % crystal fractionation.

q. *Molybdenite saturation in silicic magmas and its use to estimate magmatic fO_2 and fS_2 (A. Audéat, D. Dolejš/Prague, J.B. Lowenstern/Menlo Park)*

Sulphur-rich minerals in intermediate to silicic magmas exert the most important control on the distribution of chalcophile elements during magma evolution. In addition, they provide

information about the fugacities of sulphur (fS_2) and oxygen (fO_2) during magmatic differentiation and crystallization. These intensive thermodynamic parameters are crucial for interpreting solubilities and saturation limits for sulphide phases in silicate melts, including those that are dissolved in the form of oxide species.

Molybdenite (MoS_2) was identified as an accessory magmatic phase in 13 out of 27 silicic magma systems examined worldwide. The molybdenite occurs as small ($<20 \mu m$), triangular or hexagonal platelets included in quartz phenocrysts. Some molybdenite inclusions have droplets of glassy silicate melt attached to them, providing unambiguous proof of their magmatic origin. Laser-ablation ICP-MS analyses of coeval melt inclusions reveal that molybdenite-saturated rhyolite melts contain 1-13 ppm Mo and have geochemical signatures typical of within-plate granites. In contrast, arc-associated rhyolites are rarely molybdenite-saturated, despite similar Mo concentrations. A thermodynamic model devised to investigate the effects of T , fO_2 and fS_2 on molybdenite solubility reproduces the measured Mo concentrations in molybdenite-saturated samples well if the magmas are assumed to have been additionally saturated in pyrrhotite and magnetite (Fig. 3.2-27), but provides a poor fit if fS_2 is assumed to have been constant relative to iron sulphide buffers.

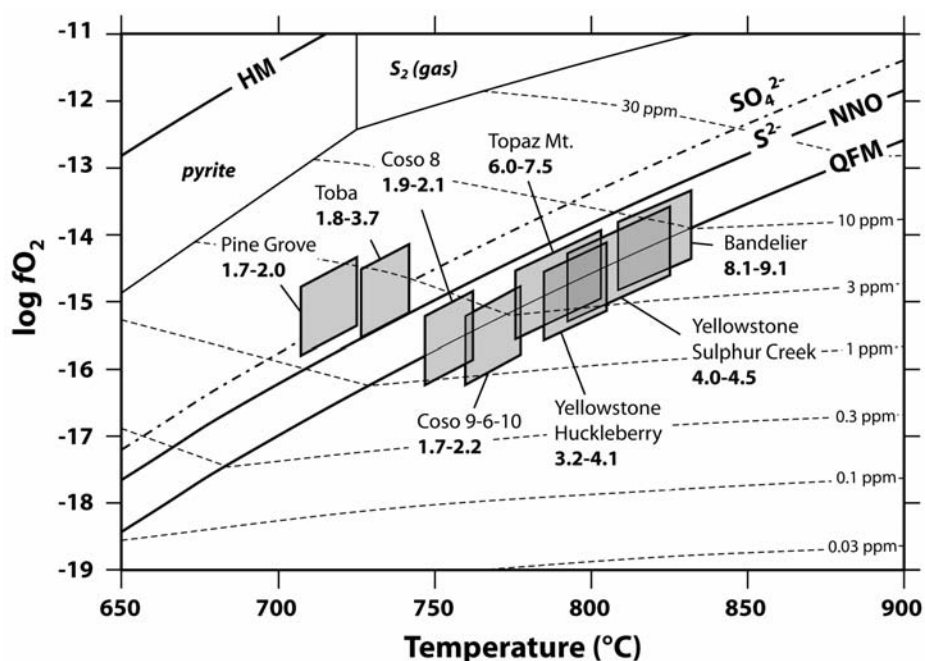


Fig. 3.2-27: Estimated T - fO_2 conditions of molybdenite saturated magmas (grey boxes) and measured Mo concentrations in silicate melt inclusions (bold values next to boxes). Thermodynamically predicted molybdenite solubility isopleths for magmas saturated in molybdenite, pyrrhotite and magnetite/fayalite are shown as dashed lines. Also shown are the stability fields of pyrite and S_2 gas, and the position of common fO_2 buffers (HM – hematite-magnetite; NNO – NiNiO; QFM – quartz-fayalite-magnetite)

While magnetite was present in all molybdenite-saturated magmas, petrographic evidence for pyrrhotite saturation was found in only a few of them only. However, noting that molybdenite

solubility isopleths in $\log f\text{O}_2$ vs. $\log f\text{S}_2$ space are very closely spaced (Fig. 3.2-28), this pattern implies that our samples must have been at (or very close to) pyrrhotite saturation. In the example of the Pine Grove magma, which is known: (1) to have been saturated in molybdenite and magnetite, (3) to have crystallized at $\sim 715^\circ\text{C}$ and $\log f\text{O}_2 = -14.5$ to -15.5 (based on Fe-Ti-oxide thermobarometry and the calculated zircon saturation temperature of this melt), and (3) to have contained 1.7-2.0 ppm Mo dissolved in the silicate melt (based on LA-ICP-MS analysis of melt inclusions), the measured Mo content of the melt fits the solubility predicted by thermodynamic calculations only if $f\text{S}_2$ was buffered close to the pyrrhotite-magnetite buffer. If $f\text{S}_2$ was just 0.5 log units above or below this buffer, the observed Mo concentration in the melt should have been a factor of two lower or higher, respectively. Using the same procedure we demonstrate that all molybdenite-bearing magmas have been at (or close to) pyrrhotite saturation. This finding greatly simplifies reconstruction of magmatic $f\text{O}_2$ and $f\text{S}_2$ when temperature and the Mo concentration in the melt is known. The latter two parameters may be constrained by LA-ICP-MS analysis of melt inclusions, with temperature being estimated *via* zircon saturation thermometry. The combination of petrographic identification of molybdenite saturation and LA-ICP-MS analysis of melt inclusions thus provides a means to reconstruct magmatic $f\text{O}_2$ and $f\text{S}_2$. Most importantly, this method can also be applied in slowly crystallized or intrusive rocks, for which these parameters are very difficult to constrain otherwise because Fe-Ti oxides and sulphides are either destroyed or re-equilibrated.

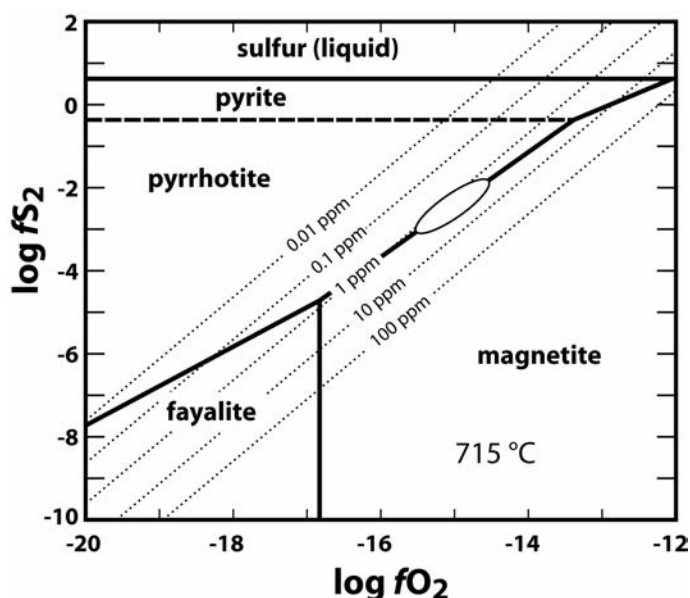


Fig. 3.2-28: Isothermal $f\text{S}_2$ vs. $f\text{O}_2$ plot at 715°C showing predicted molybdenite solubilities (dotted isopleths) and stability fields of pyrite, pyrrhotite, fayalite and magnetite. The white ellipse indicates the reconstructed crystallization conditions of the molybdenite-saturated Pine Grove tuff based on magnetite-ilmenite $f\text{O}_2$ barometry and a Mo melt content of 1.7-2.0 ppm. The combined $f\text{O}_2$ barometry and Mo melt content implies an $f\text{S}_2$ buffered near the pyrrhotite-magnetite buffer.

If pyrrhotite saturation is independently assumed, $f\text{O}_2$ can be estimated from measured Mo and Zr concentrations of melt inclusions (with the latter providing the information on melt temperature) in Fig. 3.2-27. The corresponding $f\text{S}_2$ is then obtained by intersecting the reconstructed $f\text{O}_2$ with the magnetite-pyrrhotite buffer line.

r. Biogenic nanocrystalline sulphide formation in sediments from the abandoned copper mine Mynydd Parys, Wales (K. Pollok and K.B. Hallberg/Bangor)

Abandoned mine sites are well known to cause short- and long-term effects on the environment. One aspect is the microbial catalyzed weathering of sulphides which produces acidic sulphate-rich surface waters and mobilizes toxic metals. The transport paths of these metals (*e.g.*, Cu, Zn, Pb) depend highly on whether they are bound by adsorption (*e.g.*, on iron oxides or clays) or as colloidal particle (with a certain size distribution) and how this binding reacts to varying biogeochemical conditions. For example, biofilm communities in stream sediments can facilitate the microbial reduction of sulphate by sulphate-reducing bacteria which leads to the precipitation of metal sulphides and thus to a natural retention of toxic metals.

Here, we present first results on such a biogenic sulphide formation in sediments close to an adit of an abandoned copper mine in Mynydd Parys, Wales, for which operation ended about 100 years ago. The acid mine drainage stream itself is about 0.5 m wide by about 30 cm deep, and flows out of the adit at a rate of about 0.5 m³/min. The water has a pH of 2.4 and contains about 65 mg/L Zn, 40 mg/L Cu, 19 mg/L Mn, and 600 mg/L Fe. A sample was taken in August 2009 from the sediment of the stream, approximately 2 cm below the surface, and consists of mainly ochrous material and some biofilm. During storage at 4 °C the sample turned increasingly black indicating active sulphide formation facilitated by sulphate-reducing bacteria.

Powder XRD indicates the presence of mackinawite and potentially sphalerite but the patterns are dominated by quartz and kaolinite peaks. STEM-EDX maps (Fig. 3.2-29 a-d) were used to locate the sulphides in order to study their morphological characteristics and grain sizes. Sphalerite occurs as round polycrystalline aggregates as revealed by electron diffraction (Fig. 3.2-29 e) with a wide size distribution from a few hundred nm down to a few nm and significantly binds arsenic. Abundant shaggy aggregates with a size of 100-300 nm consist of polycrystalline mackinawite (Fig. 3.2-29f). The individual crystals are in the range of 5-10 nm as revealed by HRTEM. However, other morphologies of mackinawite (round and platy aggregates) which in part cover the microorganisms have been observed as well. Furthermore, an amorphous phase with elevated contents of Cu, Pb, and As but with no Zn was found.

Two conclusions are evident from the analysis of sulphides formed in acid mine drainage soils. Firstly, nanocrystalline phases are abundantly formed by the reaction of metals in solution with dissolved sulphide produced by microorganisms. These phases are considered to be more reactive than larger crystals of the same minerals and might be potentially bio-available. However, information about the condition at which they form, how long they persist and how they interact with natural waters and sediments is largely missing. Secondly, the sampling of soil with biological activity is a challenge because separating soil from the buffering solution causes changes in the phase assemblage over time. On the other hand it

shows the promising ability of adapted soil microbial community for bioremediation of acid mine drainage waters.

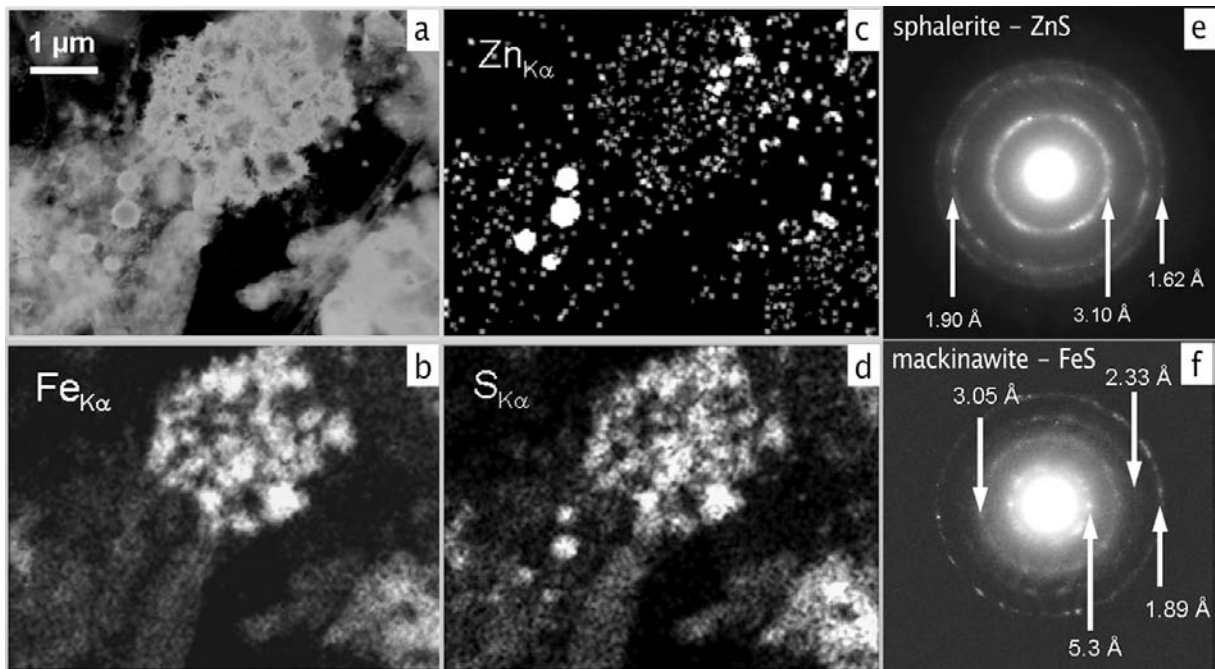


Fig. 3.2-29: (a) STEM dark field image of sediment slurry with newly formed sulphides from an adit of the abandoned copper mine in Mynydd Parys, Wales. (b-d) Iron, zinc and sulphur element map, respectively. (e,f) Electron diffraction pattern of polycrystalline sphalerite and mackinawite, respectively, with characteristic d values.

3.3 Mineralogy, Crystal Chemistry and Phase Transformations

As we have demonstrated over the years, knowledge of the crystal structure of minerals and how their structure-properties relations change as a function of pressure, temperature composition is essential for understanding the structure and dynamics of the Earth and other planets. The contributions collected in this section cover a wide range of studies from “traditional” mineralogy, *i.e.*, identification and characterisation of new and old minerals to mineralogy at extreme conditions, where for extreme conditions we can consider not only high pressures or temperatures, but also very challenging experimental set ups.

Mineralogists have catalogued more than 4400 mineral species on the Earth which can be considered a result of mineral evolution dependent on a sequence of geochemical and petrological processes, including volcanism and degassing, fractional crystallisation and metamorphism, as well as due to subduction of chemically diverse crustal materials and uplift of rocks from the Earth’s interior. Identification of minerals whether new as in the first contribution or present as inclusions in diamond as in the second one, can give precious information on the geological environment which led to their formation. In the other hands characterisation of crystallographic complexities can give a better understanding of the structures of intermediate pyrrhotites (third contribution) or the asymmetric quadrupole doublet in Mössbauer spectra of single-crystal of almandine (fourth contribution).

Knowledge of the crystal chemistry of different minerals has been used in the next five contributions to constrain the conditions of pressure, temperature, oxygen and water fugacities at which they had formed. The oxidation state of Ti in hibonite can be related to the oxygen fugacity conditions of the early solar nebula in which this mineral was one of the first to condense. Characterisation of wadsleyite lamellae and of the olivine grains which host them in a hydrous peridotite-composition subjected at high pressure and high temperature can give insights into the element and water distribution at the 410 km discontinuity. The pressure dependence of the solubility of Al and Cr in rutile has been studied as possible geobarometer, whereas the local distortion of the magnesium perovskite structure due to Al and Fe substitution may be addressed by a NMR spectroscopy. Al substitution in perovskite has also been studied at high pressure and temperatures in order to constrain the Al₂O₃ concentration in magnesium silicate perovskite formed in subducted basaltic crust.

Finally, the last six contributions deal with the structural behaviour of minerals at non-ambient conditions. High-temperature IR spectra of hydrous olivines have been collected to better understand water dissolution in olivine in the upper mantle. A phonon instability has been found at ~ 4 GPa in the dispersion curve of α -Fe₂SiO₄ which may be responsible for its transition to the γ phase. For the first time, single-crystal diffraction data have been collected for an Al- and Fe-bearing magnesium silicate perovskite and hematite both at high pressure and temperature to address possible structural changes associated to the spin transition in the former and to resolve the structure of the high-pressure orthorhombic phase of the latter. A combination of X-ray diffraction with thermoelectric power measurements has been used to quantify the changes both in the Fe³⁺/Fe²⁺ ratio and in the stoichiometry of wüstite under pressure, whereas Mössbauer spectroscopy has been used to characterise two magnetic transition occurring with increasing pressure in cementite.

a. An investigation of new mineral of the garnet group bitikleite-(SnFe) $\text{Ca}_3\text{SbSnFe}^{3+}_3\text{O}_{12}$ (I.O. Galuskina and E.V. Galuskin/Sosnowiec, J. Kusz/Katowice, P. Dzierzanowski/Warszawa, K. Prusik/Katowice, V.M. Gazeev/Moscow, N.N. Pertsev/Moscow and L.S. Dubrovinsky)

A new garnet, bitikleite-(SnFe), was discovered in altered carbonate xenolith confined to the Upper Chegem caldera situated at the interfluves of Chegem and Kenstanty (right affluent of the Baksan River) Rivers, Kabardino-Balkaria, North Caucasus, Russia. Bitikleite-(SnFe) is the third garnet of the bitikleite series from the Upper Chegem caldera with the common crystal chemical formula $\text{Ca}_3\text{SbR}^{4+}\text{R}^{3+}_3\text{O}_{12}$, $\text{R}^{4+} = \text{Zr}, \text{Sn}^{4+} \dots$; $\text{R}^{3+} = \text{Al}, \text{Fe} \dots$. The new garnet bitikleite-(SnFe) forms a solid solution with toturite $\text{Ca}_3\text{Sn}_2\text{Fe}_2\text{SiO}_{12}$, kimzeyite $\text{Ca}_3\text{Zr}_2\text{Al}_2\text{SiO}_{12}$, kerimasite $\text{Ca}_3\text{Zr}_2\text{Fe}_2\text{SiO}_{12}$, schorlomite $\text{Ca}_3\text{Ti}_2\text{Fe}_2\text{SiO}_{12}$, bitikleite-ZrFe $\text{Ca}_3\text{SbZrFe}_3\text{O}_{12}$ and bitikleite-SnAl and also uranian garnet - elbrusite-(Zr) $\text{Ca}_3\text{U}^{6+}\text{ZrFe}^{2+}\text{Fe}^{3+}_2\text{O}_{12}$.

Bitikleite-(SnFe) consists of crystals up to 50 μm in size in the kumtyubeite zone of skarns; these zones are located in the intimate vicinity of the ignimbrite contact. The bitikleite-(SnFe) crystals are inhomogeneous, they contain kerimasite zones and elbrusite-(Zr) overgrowths and have a fragmentary poikilitic structure.

Bitikleite-(SnFe) crystallizes in the typical garnet space-group, $Ia\bar{3}d$ with $a = 12.536(3) \text{ \AA}$ (single crystal data) and its structure is close to that of the synthetic garnet $\text{YCa}_2\text{SbFe}_4\text{O}_{12}$ [$a = 12.521(1) \text{ \AA}$].

Raman spectra of bitikleite-(SnFe) are analogous to those of kimzeyite, kerimasite, bitikleite-(ZrFe) and bitikleite-(SnAl) (Fig. 3.3-1).

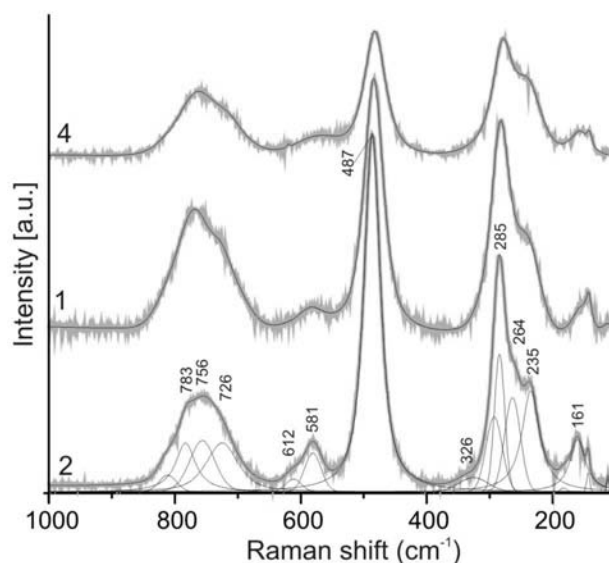


Fig. 3.3-1: Raman spectra of garnets: 1 – Zr-bearing bitikleite-(SnFe), 2 – Zr-free bitikleite-(SnFe), 4 – U-bearing bitikleite-(SnFe).

Bitikleite-(SnFe) was registered under the number IMA2010-064 in the Commission on New Minerals, Nomenclature and Classification (CNMNC) of the International Mineralogical Association (IMA), deadline for voting this mineral in the *CNMNC IMA* will be on December, 31, 2010.

b. *X-ray diffraction study of the inclusions in fibrous diamond (E.M. Smith and M.G. Kopylova/Vancouver, L.S. Dubrovinsky and E.L. Tomlinson/Surrey)*

Fibrous diamond is a variety of diamond that is cloudy or opaque due to the presence of millions of sub-micron-sized inclusions. The inclusions can be mineral inclusions (*e.g.*, olivine) or fluid inclusions, which later crystallize daughter minerals (*e.g.*, H₂O-CO₂ fluid, mica, and carbonate). Electron microprobe, infrared spectroscopy, SIMS, ICPMS, and FIB-TEM have been used to study the inclusions in fibrous diamond.

In our investigation, we used transmission-geometry X-ray diffraction (XRD) to examine the inclusion contents in fibrous diamonds. XRD is a quick and non-destructive technique, which gives a superior measure of bulk mineralogy, potentially making it a powerful complementary tool. The XRD patterns were collected at BGI with a RIGAKU FR-D high-brilliance source, OSMIC Inc. Confocal Max-Flux optics, and a SMART APEX 4K CCD area detector.

Judging from mineral chemistry and the visual appearance of the two-dimensional diffraction patterns (diffraction spots or rings in Fig. 3.3-2), the identified minerals were divided into three groups: suspected daughter minerals in fluid inclusions, mineral inclusions, and secondary phases or contaminants. All samples were expected to contain abundant daughter minerals in fluid inclusions. However, only 9 out of the 38 analyzed diamonds yielded diffraction patterns for phases that are likely to be daughter minerals (see for example the pattern reported in Fig. 3.3-2). Twelve of the samples gave no pattern besides diamond itself. These results were later reproduced using synchrotron X-rays at the APS facility in Chicago.

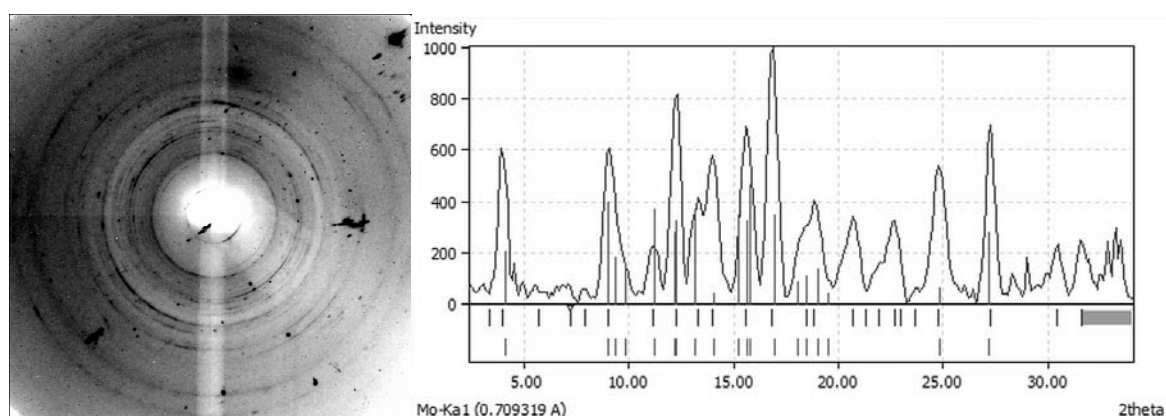


Fig. 3.3-2: An example of a daughter mineral in silicic fluid inclusions in a fibrous diamond. The diffraction pattern (left) for a stationary fibrous diamond and integrated profile (right) are dominated by diffraction rings for a mica mineral (upper ticks). Reference lines for celadonite ($K(Mg,Fe,Al)_2(Si,Al)_4O_{10}(OH)_2$) are shown.

The lack of XRD response from fluid inclusions cannot be explained by attenuation of the diffracted X-rays, therefore we can expect either that the amount of mineral material in the fluid inclusions is too small to be detected using XRD or that, despite some evidence from the TEM images and electron diffraction, the fluid inclusions contain amorphous or dissolved matter instead of crystalline minerals. The next step will be to better quantify the detection limit of the XRD setups used.

c. Translation interface modulation in NC-pyrrhotites: Direct imaging by TEM (D. Harries, K. Pollok and F. Langenhorst)

The crystallographic complexity of ‘hexagonal’ or ‘intermediate’ pyrrhotites (Fe_{1-x}S with $0.125 > x > 0.080$) is a long-standing and challenging problem. Integral (*e.g.*, 5C) and non-integral NC type structures found within this group at ambient temperatures are characterized by sharp but complicated electron diffraction patterns, which were found to be interpretable in terms of a translation interface modulation (TIM) superstructure. Dark-field transmission electron microscopy (TEM) images (Fig. 3.3-3) obtained using superstructure reflections show dense arrangements of stripes which can be interpreted as arrays of closely spaced anti-phase domain boundaries (APB). The displacement vector at the interface is $R = 1/8[001]$ of a metrically hexagonal 4C superstructure cell and the involved translations are solely confined to the Fe sublattice. The vacancy arrangement of the APB-free monoclinic 4C-pyrrhotite serves as a base of the TIM superstructure and therefore NC structures can be regarded as two

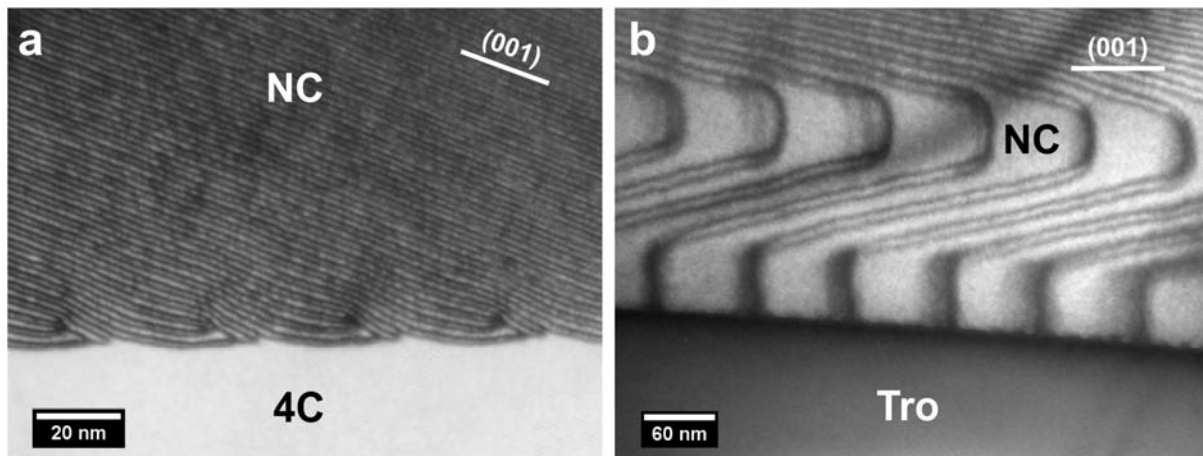


Fig. 3.3-3: (a) DF-TEM image using pyrrhotite superstructure reflections of the interface between exsolution lamellae of 4C-pyrrhotite and NC-pyrrhotite matrix. The NC portion shows dark stripes relating to anti-phase domain boundaries (APBs) that terminate in eight-fold node structures. The 4C portion is free of APBs. (b) Superstructure DF-TEM image of the interface between troilite (Tro) and NC-pyrrhotite showing strongly bending APBs likely in response to a chemical gradient developed during exsolution.

super-imposed ordering phenomena relating to the arrangements of individual vacancies and APBs, respectively. APBs are chemically non-conservative and govern the higher Fe/S ratios of intermediate NC-pyrrhotites. If oriented strictly parallel to (001) the APBs can be regarded as completely filled Fe double layers within the 4C stacking sequence. However, direct imaging of APBs shows waviness and variable disorder on mesoscopic scales, yielding essentially aperiodic structures. A high degree of self-organization among APBs has been observed within supposed diffusion profiles around exsolved troilite lamellae and along interfaces with 4C-pyrrhotite, where complicated eight-fold node arrangements occur. Our TEM observations indicate that all NC-type pyrrhotites can be treated by the TIM approach and that the concepts of polytypism and polysomatism in pyrrhotite are not fully capable in representing the observed structural complexities.

d. *Mössbauer and X-ray single crystal study of almandine garnet (C.A. McCammon, F. Nestola/Padova and T. Boffa Ballaran, in collaboration with J. Bull and C. Tennant/Christchurch)*

It has long been known that Mössbauer measurements of single crystal almandine garnet often exhibit an asymmetric quadrupole doublet – a somewhat surprising result in a cubic crystal. Some questions arise: can one account for the observed asymmetry in terms of previously measured Mössbauer parameters and known crystallography and, what extra information might be obtained from a single crystal study? Calculations in answer to the first of these questions were effected in a previous study by our group, but never confirmed experimentally. The second question required for its answer, ideally, an end member almandine crystal of adequate size for Mössbauer data collection. Typically end-member almandine crystals, or synthetic crystals, are rather small with diameters not exceeding a few mm. “End-member” crystals, moreover, are often solid solutions with (usually) pyrope and frequently contain small amounts of ferric iron that interfere with the predominant ferrous-iron quadrupole doublet.

The theoretical angular dependence of reduced intensity ratio, $I_1/(I_1+I_2)$, was calculated based on the electric-field-gradient and mean-squared-displacement tensors that were constructed from hyperfine parameters from earlier polycrystalline Mössbauer studies and X-ray-determined atomic displacement parameters. Calculations were made for each of six Laue class 222 symmetry-related sites occupied by Fe^{2+} in the garnet structure, which were then summed, since all six sites contribute to the same quadrupole doublet. The composite “theory” curve is a sinusoidal-type curve with 180° periodicity. The curve maxima, at 180° intervals correspond to the crystal [0 0 1] and [1 0 0] axes. The anisotropy in the curve derives completely from anisotropy in the msd tensor or, equivalently, anisotropy in the recoilless fractions. An isotropic msd tensor leads to an invariant “curve” with reduced intensities 0.5 for all crystal orientations. The total intensity, averaged over the six sites, is also invariant and depends only on the trace of the msd matrix since the off-diagonal elements of the msd matrix

average to zero over the six sites. There exists a recoilless fraction matrix with the same eigenvectors as the msd matrix. If one inputs this matrix in the above calculations, the invariant value of the total intensity at each orientation is just $\frac{1}{3}$ x the trace of the input recoilless-fraction matrix.

The current experimental study followed the acquisition from Wrangell Island, Alaska of a large, maximum dimension ~ 2 cm, almandine crystal with excellent dodecahedral morphology. Following earlier treatment of a near end-member crystal kindly supplied by A. Woodland, a slice was cut perpendicular to the [1 0 1] direction and doubly polished to a final thickness of 150 μm . For Mössbauer data collection a single circle goniometer mounted on a brass collimator at 45° to the gamma-beam direction was constructed. Rotation of the goniometer results in the gamma beam tracing out a right circular cone in the crystal. Special directions on the cone surface are the [0 0 1] and [1 0 0] crystal directions. Spectra were collected on a conventional spectrometer at intervals of 20° over the full 360° of rotation. The experimental reduced intensities obtained from Voigt profile fits, with error bars at the 2-sigma level, are shown in the Fig. 3.3-4. Interestingly the points match quite well earlier data collected by the milliprobe technique (BGI Annual Report 2006). In addition, the observed angular dependence of total intensities was invariant (within error) and the periodicity exactly 180° . By matching the periodicity to the calculated curve, as in the figure, it can be assured that any derived Mössbauer parameters are well defined in the chosen crystal axis system.

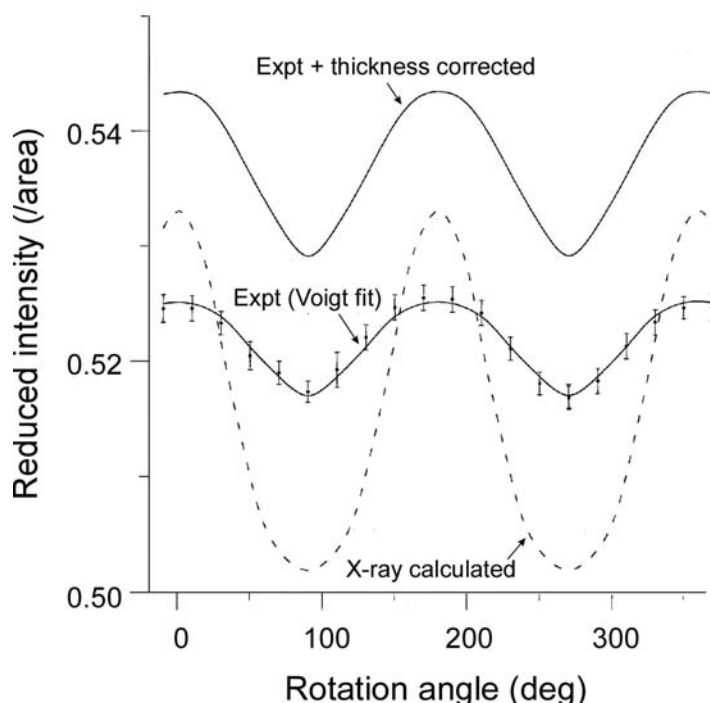


Fig. 3.3-4: Calculated and observed reduced intensities for Wrangell almandine crystal; the “X-ray calculated” curve is based on X-ray determined atomic displacements and magnetically perturbed Mössbauer measurements at 4.2 K.

The first important result of these measurements is that the anisotropy in the reduced intensities is unequivocal. It follows that the mean-squared displacement or, equivalently the recoilless fraction principal values are also anisotropic. A consequence of this is that the Goldanski-Karyagan effect *may* be observed in polycrystalline samples. Secondly, examination of the line widths shows that, within error, they are *angular independent* but, the width of the lower line exceeds that of the upper by around 9.6 %. The consequences are two-fold. The angular invariance of the line widths means that the anisotropy in reduced areas is dependent only on the fractional dips, since for Lorentzians $Area = (\pi/2) \times FWHM \times fractional\ dip$. The second consequence is that the plot of (non-thickness corrected) reduced intensities is shifted vertically downwards by 0.016 units; the anisotropy in the plot is unchanged. This is interpreted as implying that, in addition to anisotropy in the msd tensor, there is present spin-spin relaxation in the lower, $m = \pm 3/2 \leftrightarrow \pm 1/2$ nuclear transition. Both effects will influence the spectra of polycrystalline spectra of almandine. For example, in natural almandine polycrystalline spectra, the lower velocity peak is observed invariably to be the broader.

e. Crystal chemistry of hibonite as indicator of oxygen fugacities during solar nebula condensation (M. Giannini, T. Boffa Ballaran and F. Langenhorst)

Chondritic meteorites are representative samples of primordial matter in the solar system. They are characterized by the presence of chondrules (small spherical droplets of molten or partially molten minerals), Fe-Ni alloys and sulfides, refractory Calcium-Aluminium-rich Inclusions (CAIs), amoeboid olivine aggregates and fine-grained matrix material. In particular, CAIs are believed to be the first condensates of the solar nebula since they yield the oldest measured ages of the solar system. They consist mainly of melilite, spinels, perovskite, hibonite, diopside, metal, anorthite and olivine. Although corundum (Al_2O_3) is predicted to be the first major oxidic phase to condensate from a hot solar gas, it is found rarely in CAI inclusions; instead the most Al-rich phase found in CAIs is hibonite and it has been postulated that this mineral is either the primary condensate instead of corundum or replaced corundum at lower temperatures.

Hibonite has the structure of the magnetoplumbite group minerals with general formula $AM_{12}O_{19}$ and space group symmetry $P6_3/mmc$. It is based on 10 layers of close-packed oxygen atoms perpendicular to the c axis of the hexagonal cell with a sequence which can be expressed as “*chhhcchhhc*” where c stands for cubic and h for hexagonal close-packed layers. The large A atoms (mainly Ca in the case of hibonite) occupy two of these layers in a 12-fold coordinated site, whereas the M ions are distributed over five different sites: three with octahedral, one with tetrahedral and one with bipyramidal coordination. A variety of cations is accommodated by the mineral hibonite, which usually deviates significantly from the ideal end-member composition ($CaAl_{12}O_{19}$) due to significant amounts of divalent as well as trivalent and pentavalent cations occupying the M sites. In particular, meteoritic hibonite can

incorporate up to 7 wt.% of Ti into its structure in different oxidation states, which may allow the estimation of the oxygen fugacity, fO_2 , at which the mineral has equilibrated.

This project aims at experimentally determining the cation distribution and valence state of titanium in synthetic hibonite and its dependence on temperature, oxygen fugacity and composition in order to provide a quantitative calibration for the oxygen fugacity analysis of meteoritic hibonite. This may allow to better constrain the conditions at which CAIs formed and evolved.

Polycrystalline hibonites have been synthesized with a typical ceramic method, starting from the corresponding oxide mixtures heated at 1600 °C for 4 to 10 hours in air or under controlled oxygen fugacity in a gas mixing furnace using a CO/CO₂ flux. These products have been used as starting material to synthesize single crystal hibonite through a “hot-pressing” method using the piston cylinder apparatus. Synthetic runs have been performed at 15 kbars in a temperature range from 1300 °C to 1550 °C for 4 to 24h. Single crystals with maximum dimensions of up to 200µm have been obtained so far for one Ti-rich composition, and a complete set of intensity data has been collected using a Kappa geometry Xcalibur diffractometer equipped with a CCD detector. Structural refinements performed on this data collection suggest that the titanium atoms may be located in the structure of hibonite at the M4 site, which is a trigonally distorted octahedron occurring in face-sharing pairs. Variation in the cation-oxygen bond distances between pure hibonite and terrestrial hibonite correlates well with the site assignment for titanium and also suggests that the magnesium atoms may be located at the tetrahedral M3 site (Fig. 3.3-5).

The valence state of titanium has been measured with electron energy loss spectroscopy (EELS) using a Philips CM20 scanning TEM, operating at 200 keV, equipped with Gatan PEELS 666 parallel electron spectrometer. The calibration technique used is based on spectral features and intensities of the L_{32} white lines of Ti. The advantage of this technique is that the Ti^{3+}/Ti^{4+} ratio can be determined directly with high lateral resolution at the nano-scale.

The Ti^{3+}/Ti^{4+} ratio has been determined for hibonites with the same composition ($CaAl_{11.22}Mg_{0.36}Ti_{0.42}O_{19}$) but synthesized and/or equilibrated at different fO_2 . Two of these samples are considered now: a polycrystalline hibonite synthesized in air and a single crystal which has experienced reducing conditions due to the piston cylinder assembly ($fO_2 \approx 8$). In the sample synthesized in air, the 40 % of titanium is present in the structure as Ti^{3+} ; this amount increases to 60 % for the sample re-equilibrated at low fO_2 . These data suggest that the Ti^{3+} concentration in synthetic hibonite depends not only on the redox conditions at which it is synthesized but also on the crystal chemistry, *i.e.*, the cation site where Ti is located. Even at very oxidizing conditions the substitution mechanism $Mg^{2+} + Ti^{4+} = 2Al^{3+}$ is not unique and some $Ti^{3+} = Al^{3+}$ substitution takes place. A possible reason for this may be the repulsion between highly-charged cations in the face-sharing octahedra which can be reduced if some of the Ti atoms are trivalent instead of tetravalent.

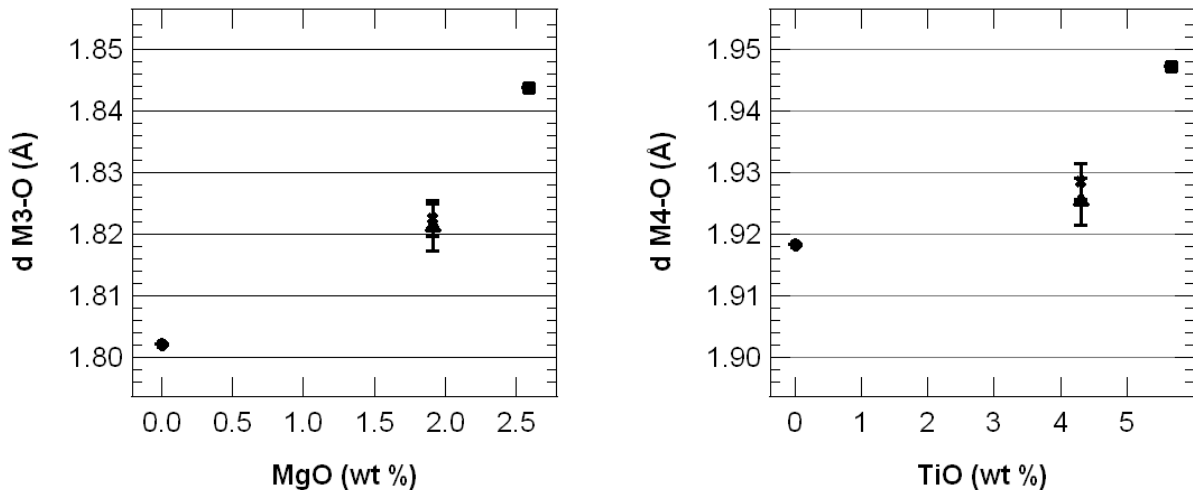


Fig. 3.3-5: Cation-oxygen bond distances for M3 and M4 sites plotted against Mg and Ti content respectively. Triangle and cross: present work; circle: synthetic end-member hibonite from Hofmeister, A. M. (2004), *Geoch. et Cosmoch. Acta* 68(22), 4721; square: natural hibonite from Bermanec, V., D. *et al.* (1996), *Can. Min* 34: 1287.

f. Olivine-wadsleyite-pyroxene epitaxy: Element and volatile distributions at the 410 km discontinuity (J.R. Smyth/Boulder, N. Miyajima, G. Huss and E. Hellebrand/Honolulu; D.C. Rubie and D.J. Frost)

We have synthesized hydrous peridotite-composition samples at 13 GPa and 1400 °C with co-existing coarse grains (~ 100 micrometer) of olivine, wadsleyite, clinoenstatite, and melt in a multianvil press. The olivine grains contain fine-scale lamellae of wadsleyite and clinoenstatite that likely resulted from small temperature fluctuations during the four-hour experiment. Major-element compositions were determined by electron microprobe and H contents by secondary ion mass spectroscopy (SIMS). The olivine is about Fo₉₃ in composition and contains about 650 ppm by weight H₂O. The wadsleyite is about Fo₈₇ in composition and contains about 1650 ppm by weight H₂O. The clinoenstatite is about En₉₃ in composition and contains about 440 ppm H₂O. A back-scattered electron image of the exsolution texture is shown in Fig. 3.3-6.

High resolution transmission electron microscopy of the lamellae and host show that the olivine and wadsleyite share their close-packed oxygen planes so that the wadsleyite lamellae are nearly planar and perpendicular to the [1 0 0] of olivine (Fig. 3.3-7). The wadsleyite lamellae thus have their [1 0 1] and [1 0 -1] directions parallel to the [1 0 0] of olivine. Additionally, a second orientation relation with the [001] of olivine parallel to [100] of wadsleyite is also found as incoherent blebs of wadsleyite in olivine. The coexisting melt phase quenched to a feathery mass of mostly wadsleyite crystals. Neither a quenched glass phase nor a nominally hydrous phase was observed.

Although olivine-spinel epitaxy has been reported previously, olivine-wadsleyite epitaxy has not. The lamellae indicate that the olivine-wadsleyite transformation can proceed effectively

by coherent mechanisms that could potentially preserve lattice preferred orientation. The observed rapid inversion from olivine to wadsleyite means that metastable preservation of olivine below 410 km is unlikely under slightly hydrous conditions. The distribution of H among the nominally anhydrous phases implies that dehydration of peridotites by partial melting is inefficient so that complete dehydration of subducting slabs is unlikely or impossible.

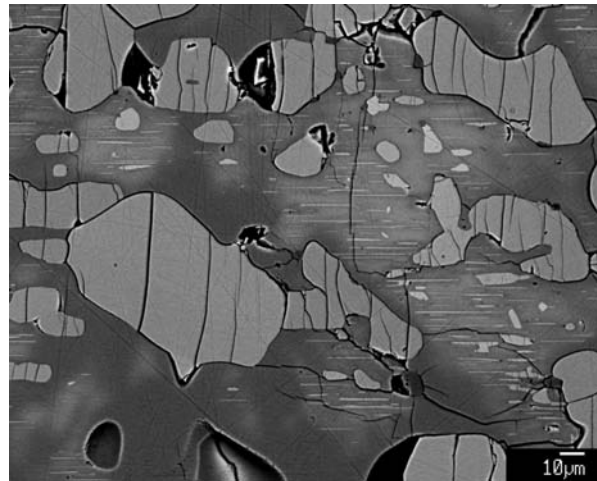


Fig. 3.3-6: Backscattered electron image of exsolution texture of wadsleyite (bright) from olivine (darker). The 410 km discontinuity in the Earth is thought to be due to the olivine to wadsleyite transformation. Wadsleyite is capable of incorporating several times the water mass of the Earth's oceans and may play an important role in the water balance of the planet. The wadsleyite (bright rounded grains and lamellae) are richer in Fe and H relative to the darker olivine.

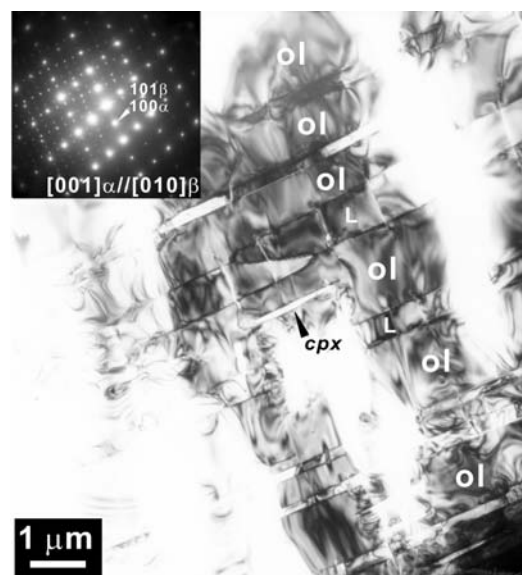


Fig. 3.3-7: TEM image and diffraction pattern of the olivine-wadsleyite intergrowth (ol: olivine, L: wadsleyite, cpx: clinoenstatite).

g. Solubility of Al, Cr and Si in TiO₂-rutile at high pressure and high temperature. A comparative study (A. Escudero and F. Langenhorst)

Titanium dioxide (TiO₂) has been intensively studied for a few decades due to both basic and applied interests in material science and geosciences. On one hand, TiO₂ is widely used due to its photoconductive and catalyst characteristics in both research and industrial applications, on the other hand, rutile is a common accessory mineral in metamorphic and plutonic igneous rocks. The trace element geochemistry of rutile provides useful information on provenance, temperature, pressure, and ages. There are several indications that the solubility of certain tri- and quadrivalent cations increases with pressure. For instance, exsolutions of corundum and spinel have been reported in rutile from kimberlites and diamondiferous eclogites from South Africa and natural SiO₂-rich rutile has been found in nature. In this experimental study we have tested whether the solubility of Al, Cr, and Si in rutile could be used as potential geobarometer.

To study the aluminium, chromium and silicon solubility in rutile, high-pressure/high-temperature multianvil experiments have been performed from 0.5 to 3 GPa and 1300°C in a piston cylinder and from 5 to 10 GPa and 1300°C in a 1200 tonne MA8 Kawai-type multianvil press. The samples have been characterised by XRD, ²⁷Al MAS-NMR, ²⁹Si MAS-NMR, SEM and EDX-TEM.

XRD and NMR data indicate two different mechanisms for the trivalent cations incorporation in rutile, which have also been observed at atmospheric pressure. The main mechanism of solubility is the substitution of Ti⁴⁺ by Al³⁺ or Cr³⁺ on normal octahedral sites (substitutional), plus the formation of oxygen vacancies. At higher pressures, Al³⁺ and Cr³⁺ are also incorporated into octahedral interstices of the rutile structure, although this mechanism is much less important. The incorporation of Al³⁺ or Cr³⁺ into these interstices at higher pressures (> 2.5 GPa in the Al system and > 1 GPa in the Cr system, both at 1300 °C) reduces the rutile symmetry, which transforms from tetragonal to orthorhombic. This symmetry change gives rise to a microstructure consisting of [110] twins, which can be observed in Fig. 3.3-8A.

On the contrary, the behaviour of the Si-TiO₂ system is completely different. There are neither appreciable changes in the unit cell parameters nor in the symmetry or microstructure of Si-doped rutile with pressure up to 7 GPa. A normal Si-doped rutile grain synthesised at 7 GPa and 1300 °C is shown in Fig. 3.3-8B.

The variation in the Al, Cr and Si solubility in rutile with pressure is shown in Fig. 3.3-9. In general, the solubility of all dopants in rutile increases with pressure. However the incorporation of the trivalent cations into TiO₂ is much more efficient than that observed in the Si-doped system. High pressure enhances drastically the solubility of both Al₂O₃ and Cr₂O₃ in TiO₂. Rutile is able to accommodate up to 9.8 % in weight of Al₂O₃ at 7 GPa and 1300 °C with respect to the 1.22 % in weight at atmospheric pressure. A similar behaviour has been observed for Cr-doped rutile. Both NMR and EDX data indicate that the solubility of Si in rutile at high pressure and 1300 °C is extremely low: only about 0.5 % in weight of SiO₂ is incorporated into the rutile structure at 7 GPa.

We can, therefore, suggest that both the incorporation of Al^{3+} and Cr^{3+} into rutile could be used as potential geobarometers, whereas the SiO_2 solubility in rutile, inspite of increasing with pressure, is not sensitive enough to act as a useful pressure calibrant.

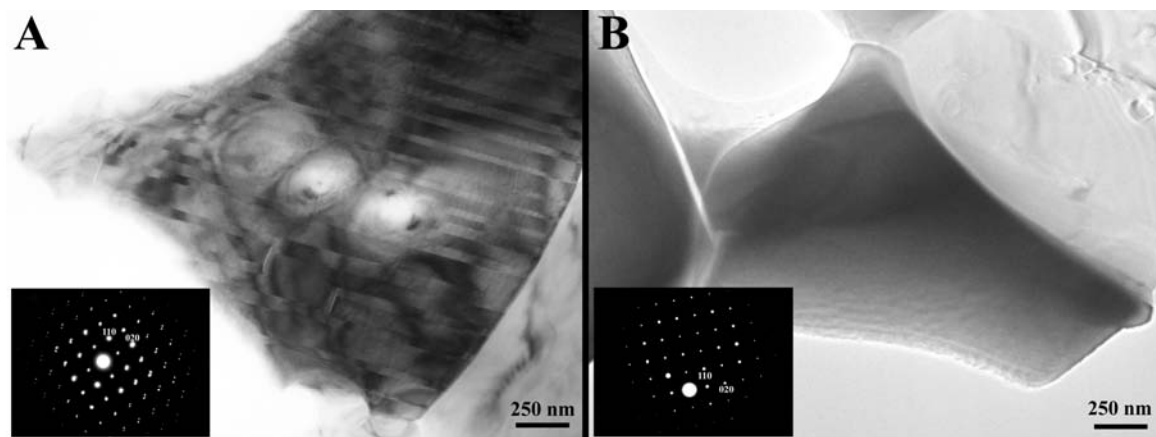


Fig. 3.3-8: A) Bright field TEM micrograph of a Cr-doped rutile grain, showing a microstructure consisting of twins. Al-doped rutile grains show a similar microstructure. B) Bright field TEM micrograph of a Si-doped rutile grain. Both samples were synthesised at 7 GPa and 1300 °C. Both images were taken along the rutile [001] zone axis.

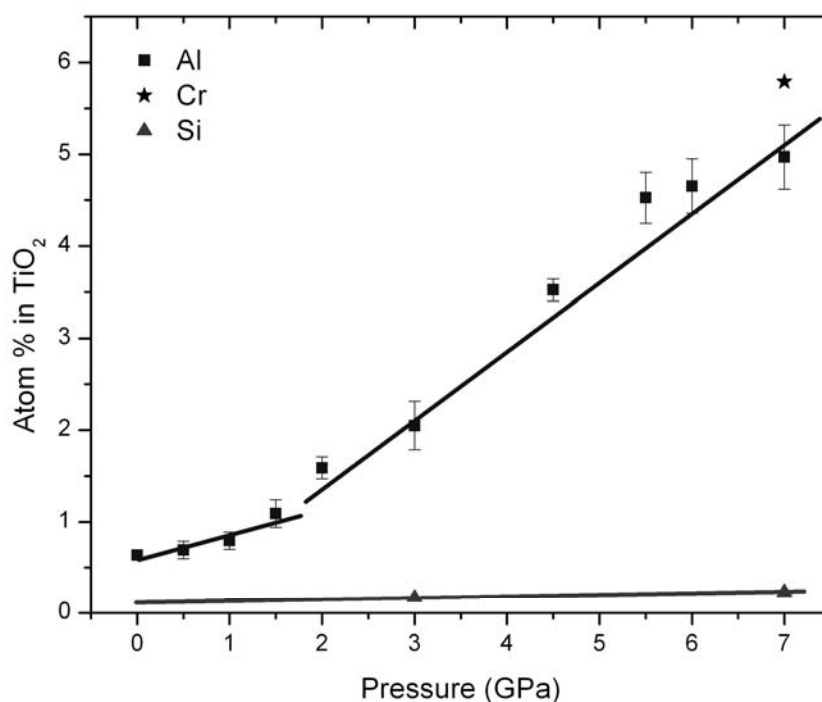


Fig. 3.3-9: Solubility of Al, Cr and Si in rutile versus pressure at 1300 °C. Data have been obtained from EDX analyses on the TEM on rutile single crystals. The standard deviation of the measurements is also shown. The straight lines are only intended as guides to the eye.

h. *An NMR investigation of the Al- and Fe-substitutions in MgSiO₃ perovskite (A. Palke/Stanford, D.J. Frost, C.A. McCammon and J.F. Stebbins/Stanford)*

Perovskite-structured MgSiO₃ (henceforth, perovskite) is thought to comprise the bulk of the lower mantle along with ferropericlase (MgO). In the perovskite structure Si⁴⁺ occupies octahedral “B” sites while Mg²⁺ occupies larger twelve-coordinated “A” sites. Perovskite is also thought to be the host phase for most of the Al and much of the Fe in the lower mantle. Previous Nuclear Magnetic Resonance (NMR) studies have been performed on Al-bearing, Fe-free perovskite; however, the presence of Fe³⁺ in perovskite can have a profound effect on the incorporation of Al³⁺ and vice versa. Computational studies indicate that the most energetically favorable substitution mechanism is for Al³⁺ to replace Si⁴⁺ at the B site with Fe³⁺ replacing Mg²⁺ at an adjacent A site. NMR spectroscopy is a valuable tool for investigating the local atomic environments and short-range ordering of such substitutions. Furthermore, at relatively small concentrations of paramagnetic species (Fe²⁺ and/or Fe³⁺) we have been able to collect high-resolution NMR spectra.

Silicate glasses of composition (Mg_{1-x}Fe_x)(Si_{1-x}Al_x)O₃ (x=0.01, 0.025) were synthesized with 99 % ²⁹Si-enriched SiO₂ and 95 % ⁵⁷Fe-enriched Fe₂O₃ starting materials and subsequently converted to aluminous-pyroxene in a 1200 tonne MA8 Kawai-type multianvil press at 8 GPa and 1200 °C. The pyroxenes and one additional glass of similar composition with x=0.05 were subsequently converted to perovskite at 26 GPa and 1900 °C. The synthesis runs were characterized by Raman spectroscopy. ²⁷Al and ²⁹Si NMR as well as Mössbauer spectroscopy are currently under way and further characterization of these samples by XRD and EPMA are planned.

The ²⁹Si NMR spectrum for the (Mg_{0.99}Fe_{0.01})(Si_{0.99}Al_{0.01})O₃ pyroxene used in the perovskite synthesis is shown in Fig. 3.3-10. The two main peaks are at -80.6 and -83.2 ppm in agreement with previous studies. There are five additional low-intensity peaks from +37.1 to -96.5 ppm labeled as “c.s.” in Fig. 3.3-10. The peaks at +37.1 and -43.5 ppm are almost certainly contact-shifted peaks caused by an interaction between the ²⁹Si nucleus with the magnetic moment of the unpaired electrons on a nearby iron atom. The other “c.s.” peaks are in the possible range of tetrahedral ²⁹Si chemical shifts but given the absence of other phases seen in the Raman spectra, we can expect these peaks to be likely contact-shifted peaks as well. Variable temperature NMR studies are planned in order to clearly make this distinction. The ²⁹Si NMR spectrum for perovskite synthesized from this pyroxene is shown in Fig. 3.3-11. A sharp peak is found at -191.6 ppm consistent with previous NMR studies on pure phase perovskite. In addition, a broad peak is seen at -81.1 ppm. The identity of this peak is, as of yet, unknown. However, this peak is in the same position as both MgSiO₃ glass and crystalline MgSiO₃ pyroxene. Though it is much broader than the two peaks expected for pyroxene, if there is extreme structural disorder or excessive partitioning of iron into a pyroxene phase this could cause significant broadening of these peaks into one broad resonance. One alternative hypothesis is that this peak is due to amorphization of perovskite upon crushing (despite the fact that the material was crushed at liquid nitrogen temperature). XRD experiments are planned to detect the possible presence of a pyroxene phase. ²⁹Si NMR spectra have been collected on three perovskite compositions (x = 0.01, 0.025, and 0.05) and

^{27}Al and Mössbauer spectra are currently being collected which, it is hoped, will provide further information on the substitution mechanisms involved in the incorporation of Al and Fe into perovskite.

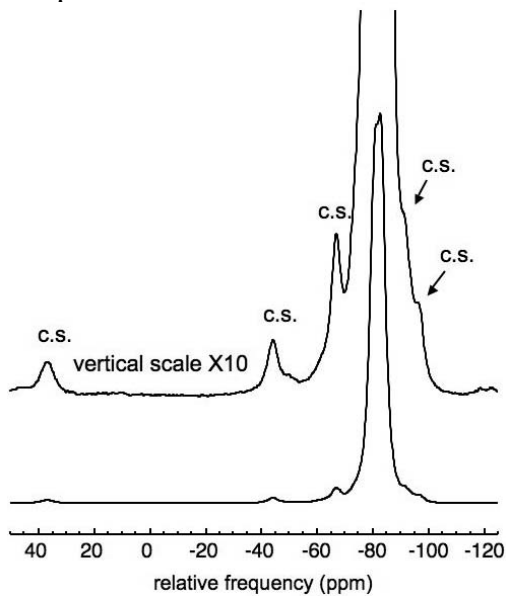


Fig. 3.3-10: ^{29}Si NMR spectrum of a high-pressure pyroxene of composition $(\text{Mg}_{0.99}\text{Fe}_{0.01})(\text{Si}_{0.99}\text{Al}_{0.01})\text{O}_3$ collected at a field of 14.4 T using a pulse delay of 0.01 s and a spinning speed of 20kHz. The two spectra are identical with the upper spectrum having 10X vertical exaggeration.

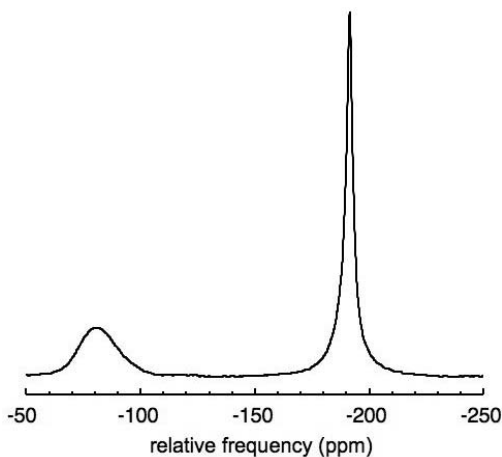


Fig. 3.3-11: ^{29}Si NMR spectrum of a perovskite of composition $(\text{Mg}_{0.99}\text{Fe}_{0.01})(\text{Si}_{0.99}\text{Al}_{0.01})\text{O}_3$ collected at a field of 14.4 T using a pulse delay of 0.01 s and a spinning speed of 20kHz.

i. Phase relations in $\text{MgSiO}_3\text{-Al}_2\text{O}_3$ system under lower mantle P-T condition (R. Sinmyo, L.S. Dubrovinsky, D.J. Frost and Y. Nakajima)

Aluminium is the fourth most abundant cation in the Earth's mantle, and plays an important role in the phase relations and physical properties of lower mantle minerals. However, experimental/theoretical studies on the phase relations of the $\text{MgSiO}_3\text{-Al}_2\text{O}_3$ system at lower mantle condition are limited. Theoretical calculations predicts that the maximum solubility of Al_2O_3 in perovskite is approximately 15 wt.% in the $\text{MgSiO}_3\text{-Al}_2\text{O}_3$ system at 30-80 GPa and 2000 K. In addition, the stability field of MgSiO_3 -rich perovskite decreases, with respect to corundum, with decreasing temperature in this system. Although poorly constrained as a function of pressure and temperature the Al_2O_3 concentration in perovskite in subducted basaltic crust will strongly influence the mineral proportions within such rocks in the lower mantle.

We have examined phase relations in the $\text{MgSiO}_3\text{-Al}_2\text{O}_3$ system at lower mantle conditions using high-pressure and -temperature experiments. For starting material, 75 wt.% MgSiO_3 + 25 wt.% Al_2O_3 and 50 wt.% MgSiO_3 + 50 wt.% Al_2O_3 compositional gels were used. A Kawai-type multi-anvil press was used for high-pressure and -temperature generation. The sample was loaded into Re capsule and then packed into an MgO container. LaCrO_3 was used as a heater. Pressure and temperature conditions were 27 GPa at 1873 K and 2073 K. The recovered sample was chemically analyzed by using a scanning electron microscope (Fig. 3.3-12).

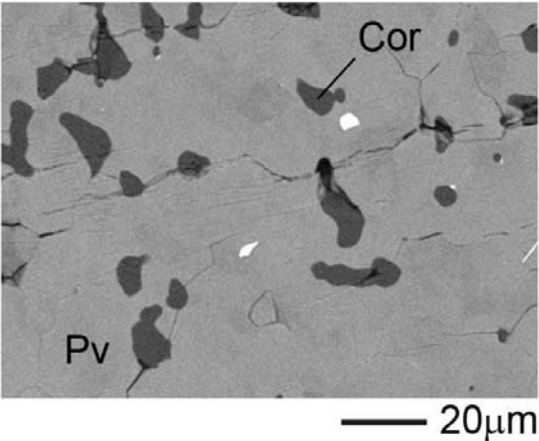


Fig. 3.3-12: Back-scattered electron image of the sample recovered from 27 GPa and 2073 K. Small dark grains are corundum while the matrix is perovskite.

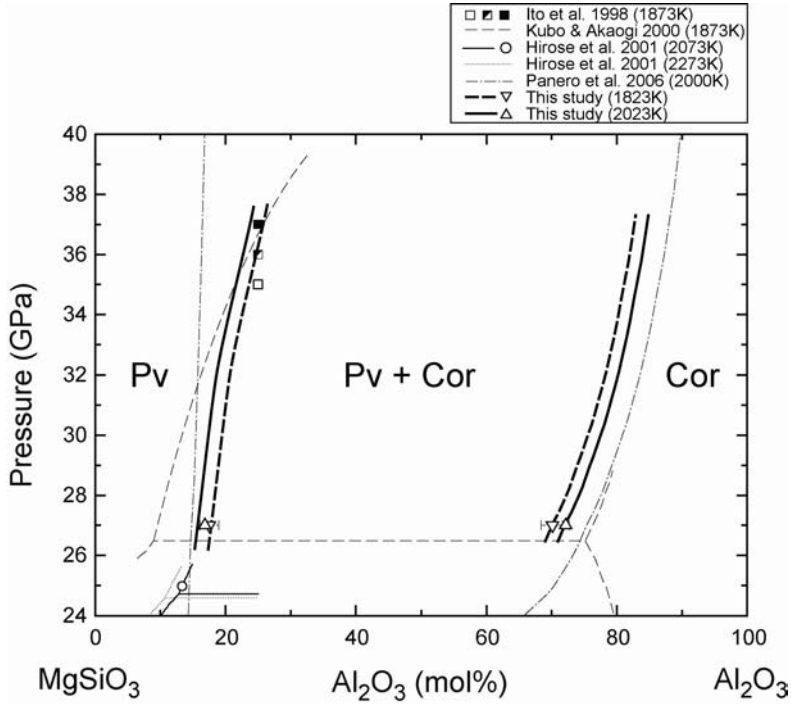


Fig. 3.3-13: Phase diagram of the $\text{MgSiO}_3\text{-Al}_2\text{O}_3$ system at high pressure. The boundary between perovskite and perovskite + corundum stability field was estimated from the results of Hirose *et al.* (2001; EPSL 184, 567), Ito *et al.* (1998; GRL 25, 821) and this study. Literature curves are calculated from the results of Kubo & Akaogi (2000; PEPI 121, 85), and Panero *et al.* (2006; EPSL 252, 152).

j. *In situ* infrared spectra of olivine to 1100 °C (X.-Z. Yang and H. Keppler)

Olivine is the major constituent of the upper mantle. The presence of minor amounts of water as H-related defects in the structure of olivine has a strong effect on the electrical conductivity, rheology and many other properties of the upper mantle; it may even be essential for triggering plate tectonics on Earth. The incorporation mechanism of water in olivine is critical for understanding water solubility and the effects of water on physical properties. Models for the dissolution of water in olivine have been derived mostly from infrared spectra. Recent studies have shown that at least four different mechanisms may be important for the water dissolution in olivine, which could be assigned to Si vacancies, Mg vacancies, Ti-clinohumite-like point defects and trivalent cations. The room temperature infrared spectra of olivine have been used to infer the D/H isotopic fractions between coexisting minerals at mantle conditions, the silica activity in the mantle and also as a tool in diamond exploration. However, this only makes sense if the room temperature spectra of olivine reflect those at mantle conditions. H is very mobile at high temperature and its position may change even during very fast quench. We therefore studied the infrared spectra of olivine at high temperatures.

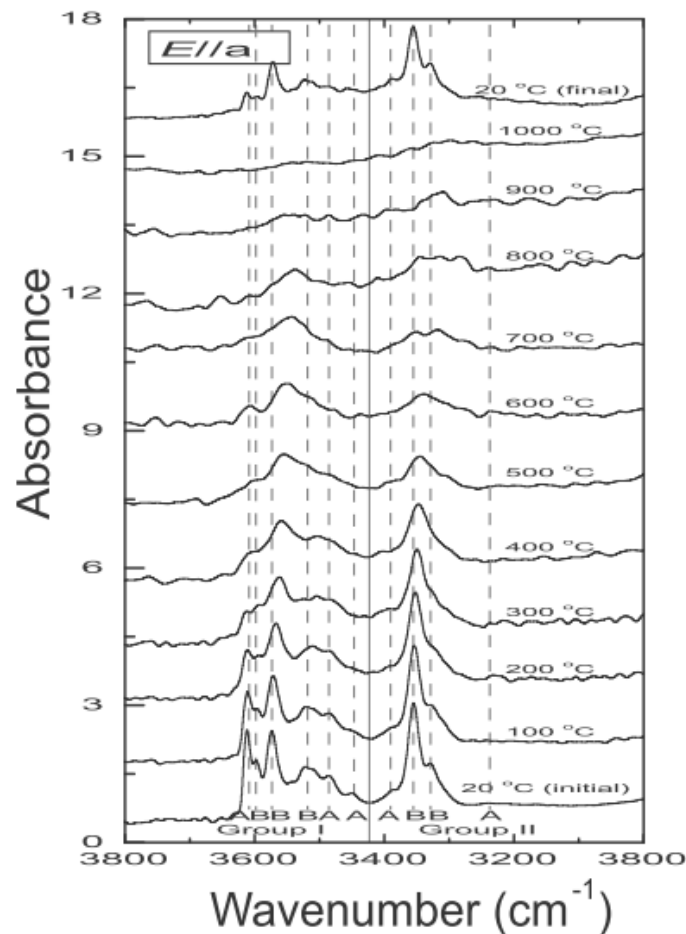


Fig. 3.3-14: Polarized *in situ* infrared spectra of olivine at high temperatures (*E//a*)

Hydrous samples were prepared by annealing oriented San Carlos olivines at 3 GPa and 1100 °C in a piston cylinder apparatus. The *in situ* infrared spectra at high temperatures were measured in a micro-heating stage (with Ar and 2 % H₂ as buffer). The results show that the annealed olivines reproduce almost all the important bands observed in natural samples (Fig. 3.3-14), and the spectra at high temperatures are significantly different from those at room temperature due to band broadening, shifting and overlap. The spectra show that even at the highest temperatures studied, there are still two well-separated groups of OH bands centered between 3200 and 3300 cm⁻¹ and between 3500 and 3600 cm⁻¹, respectively. The distinction between group I ($\nu > 3450$ cm⁻¹) and group II bands ($\nu < 3450$ cm⁻¹) is therefore still meaningful at upper mantle temperatures. However, a prominent band at 3612 cm⁻¹ already loses intensity by 100 °C and nearly disappears by 300 °C, suggesting that it corresponds to a particular H environment that only formed during cooling of the sample and that it is not stable at high temperature. A similar band is prominent in many olivines from mantle xenoliths and previously it has sometimes been assigned to OH group surrounding Si vacancies. Our data suggest that structural models of water dissolution in olivine derived from infrared spectra at ambient conditions may not be fully applicable for the upper mantle.

k. *High-pressure phonon stability of Fe₂SiO₄ fayalite from first principles calculations (Z. Tang and G. Steinle-Neumann)*

Fayalite (Fe₂SiO₄) is the Fe-endmember of the olivine solid solution that dominates the mineralogy of the Earth's upper mantle to a depth of 410 km. For Mg₂SiO₄ phase transitions to high-pressure polymorphs occur at ~ 12.5 GPa (β) and ~ 15 GPa (γ), both of which are spinel-type structures. Fayalite, by contrast, transforms directly to the γ -phase, and does so at much lower pressure (~ 3 GPa at room temperature). This difference in phase behaviour has not been understood on a fundamental level.

While Mg₂SiO₄ has been studied extensively by density functional theory (DFT)-based computations, there is only a small number of studies on Fe₂SiO₄ due to its electronic and magnetic structure. Fe₂SiO₄ shows Mott-insulator like behaviour that is not readily captured by standard implementations of DFT using either the local density (LDA) or generalized gradient approximation (GGA) to the exchange and correlation potential. For describing strongly correlation systems such as Fe₂SiO₄, the DFT+U approach is typically employed with the Hubbard repulsion parameter U describing the on-site Coulomb interaction. Also, fayalite is anti-ferromagnetic (afm) with a Néel temperature of 65 K, showing non-collinear magnetic interactions. The nature of magnetic interaction in fayalite is ambiguous based on neutron diffraction data, but DFT+U computations have established that the collinear approximation to one structure (afmI) is energetically favored over the other (afmII) at ambient conditions.

Here we explore the energetics of the two collinear afm configurations over a wide unit cell volume to examine the energetics of the afm structures. We use the GGA+U formulation with U=4.5 eV and Hund's exchange J=0.9 eV, consistent with previous works on Fe₂SiO₄.

Computations were performed with the Projector Augmented Wave method as implemented in Vienna *ab initio* simulation package. In agreement with previous computations we find the afmI structure stable over the afmII structure, with the energy difference between them increasing with compression.

In addition we have computed the phonon dispersion curves for both afm structures using the direct method as implemented in the PHONON code. We find the afmII structure has unstable phonon modes even at ambient pressure volume, and the afmI structure shows a soft mode at the X (1/2,0,0) – S (1/2,1/2,0) branch of the Brillouin zone boundary (Fig. 3.3-15a). At very modest compression (~ 4 GPa) this soft mode becomes unstable (Fig. 3.3-15b). The unstable phonon mode could be responsible for the transition of α -Fe₂SiO₄ to the γ phase that occurs in experiments in the range of 2-4 GPa. It precedes a possible elastic instability (representative of phonon modes at the zone center) that has been observed in strongly non-linear decrease of elastic constants above 5 GPa.

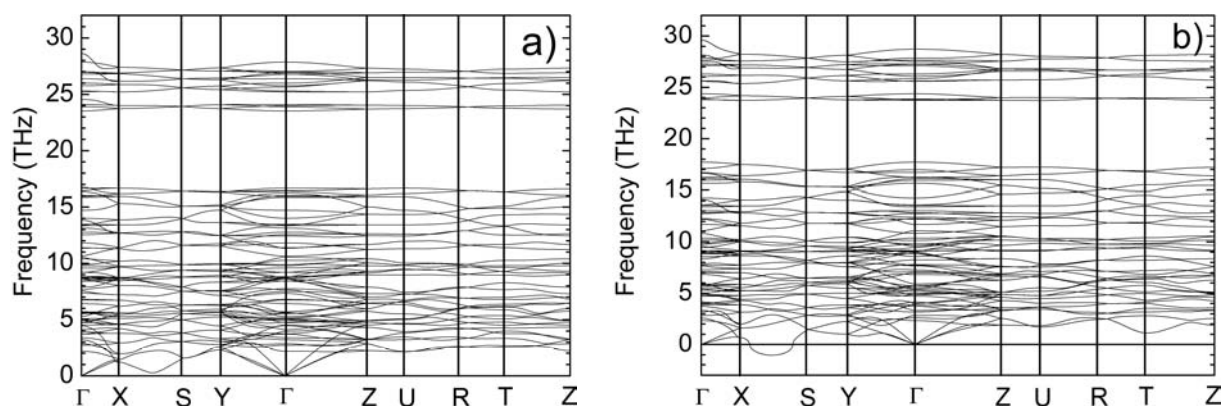


Fig. 3.3-15: Computed phonon dispersion curves of α -Fe₂SiO₄ in the afmI structure at (a) a unit cell volume of 314 Å³ close to the zero pressure; and (b) a unit cell volume of 308 Å³ corresponding to ~ 4 GPa.

1. Structural behaviour of silicate perovskite (Mg_{0.62}Fe_{0.38})(Al_{0.36}Si_{0.64})O₃ at conditions of the Earth lower mantle (L.S. Dubrovinsky, T. Boffa Ballaran, K. Glazyrin, A. Kurnosov, D.J. Frost, N. Dubrovinskaia/Heidelberg, M. Merlini/Milano and M. Hanfland/Grenoble)

Iron and aluminium bearing magnesium silicate perovskite (Mg,Fe,Si,Al)O₃ is the most abundant material on the Earth because it is likely to be the main component of the lower mantle. For decades the structure and properties of silicate perovskite have been the focus of mineral physics research, but so far single crystal structural data are available only for its pure magnesium end-member MgSiO₃ perovskite at ambient temperature and pressures up to 10 GPa. Iron and aluminium could significantly affect properties of silicate perovskite, especially due to electronic transitions in Fe²⁺ and Fe³⁺. So far only limited information based on powder X-ray diffraction data about the crystal-chemical effect of spin changes in ferrous iron is

available. Using a multianvil apparatus we synthesized single crystals of $(\text{Mg}_{0.62}, \text{Fe}_{0.38})(\text{Al}_{0.36}\text{Si}_{0.64})\text{O}_3$ silicate perovskite containing predominantly Fe^{3+} ($\text{Fe}^{2+}/\Sigma\text{Fe}\sim 7(3)\%$) and studied them in a DAC loaded with Ne as pressure transmitting medium. Experiments were performed at the ID9 beamline of the ESRF synchrotron facility. The maximum pressure reached was 85 GPa both at ambient temperature and at 2050(100) K. The sample was first compressed at ambient temperature to about 30 GPa with steps of ~ 4 GPa between the data-collection runs, and then heated to the desired temperature in the stability field of silicate perovskite. After each heating cycle the laser power was gradually released, the pressure increased, and the measurements were repeated. At each pressure-temperature point we were able to collect 50 to 70 unique reflections and refine the silicate perovskite structure to R1 below 8.5 %.

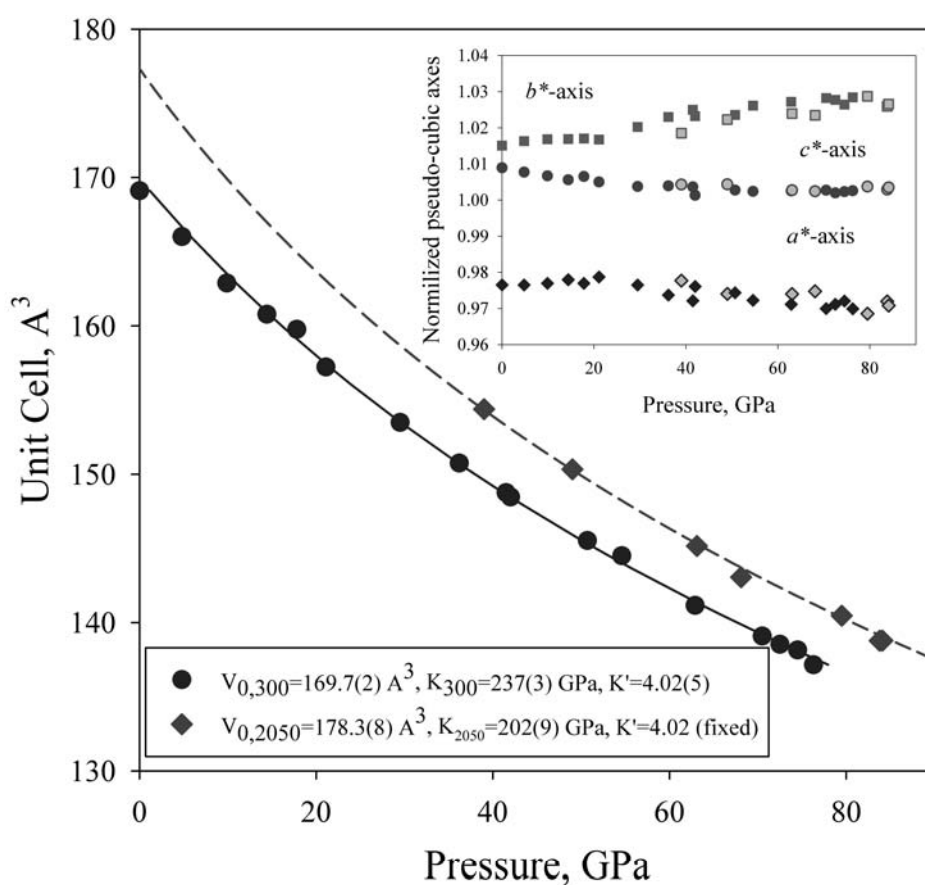


Fig. 3.3-16: Pressure-volume data of $(\text{Mg}_{0.62}, \text{Fe}_{0.38})(\text{Al}_{0.36}\text{Si}_{0.64})\text{O}_3$ silicate perovskite obtained by means of single-crystal X-ray diffraction experiments in a laser-heated DAC. Uncertainties in the volume and in the pressure (determined from the lattice parameters of Ne) are within the symbols. Continuous curves are the fits of the experimental data using a 3rd order Birch-Murnaghan equation of state for ambient temperature and for 2050(100) K. The insert shows the variation with pressure and temperature (filled symbols – ambient temperature, open – 2050(100) K) of the normalized pseudo-cubic axes of orthorhombic perovskite ($a^* = a/\sqrt{2} (V/4)^{-1/3}$, $b^* = b/\sqrt{2} (V/4)^{-1/3}$, and $c^* = c/2 (V/4)^{-1/3}$; a, b, c , and V are the unit cell parameters and the cell volume, respectively).

The fit of the room temperature pressure – volume data using a third order Birch-Murnaghan equation of state (Fig. 3.3-16) gives the bulk modulus ($K_{300}=237(5)$ GPa) which is significantly lower than the bulk modulus of pure magnesium or Fe^{2+} -bearing silicate perovskite (250-264 GPa). The bulk modulus further decreases to 202(9) GPa at 2050(100) K (assuming the value of K' = 4.02 as obtained at ambient temperature). These results are in qualitative agreement with previous publications. Similarly to the behaviour of ferrous silicate perovskite, the molar volume, lattice parameters, the mean bond distances of the (Si,Al) O_6 octahedra and (Mg,Fe) O_8 -polyhedra do not demonstrate any sign of irregular changes which could be related to high-spin – low-spin (HS-LS) crossover. However, close inspection of the variation of B-O1-B and B-O2-B tilt angles (B=Si,Al) with pressure shows that at ambient temperature above ~ 60 GPa the response of (Si,Al) O_6 -octahedral network on compression changes. It is worth noting, however that the high-temperature high-pressure data relevant to conditions of the Earth lower mantle does not show any changes in the compressional behaviour of Fe^{3+} -bearing silicate perovskite at any pressure.

m. *Structure of an orthorhombic high-pressure Fe_2O_3 polymorph (L.S. Dubrovinsky, K. Glazyrin, A. Kurnosov and T. Boffa Ballaran; N. Dubrovinskaia, P. Schouwink and T. Pippinger/Heidelberg; M. Merlini/Milano and M. Hanfland/Grenoble)*

At ambient pressure trigonal hematite $\alpha\text{-Fe}_2\text{O}_3$ (space group $R\bar{3}c$) is a wide-gap antiferromagnetic insulator and can be considered as an archetype of a *Mott*-insulator. Due to its significance in the solid state and mineral physics, the high-pressure behaviour of Fe_2O_3 has been intensively investigated. On compression at ambient temperature above 50 GPa it undergoes a sluggish structural phase transition into a phase with an orthorhombic symmetry. The same phase has been reported to appear upon heating above about 30 GPa. The exact structure of the orthorhombic phase remains, however, controversial. Two structural models have been proposed – that of the high-pressure Rh_2O_3 -II-type structure (space group $Pbna$, #60) and the orthorhombic perovskite-type structure (space group $Pbnm$, #62). While the Mössbauer spectroscopic data seems to support the Rh_2O_3 -II-type structure, the powder diffraction data collected by different groups at different synchrotron facilities over the last several decades were not able to unambiguously assign the structural type.

We compressed a single crystal of hematite Fe_2O_3 in a DAC loaded with Ne as pressure transmitting medium to 25.6(5) GPa and collected the X-ray diffraction data in 40° ω -scans with a 0.5° step at the ID9 beamline of the ESRF synchrotron facility. After integration of the collected intensity data we obtained 45 unique reflections for the refinement of the four structural parameters of hematite ($R\bar{3}c$) which resulted in a discrepancy index $R1 = 4.5\%$ (Table 3.3-1). Upon heating to 2200(100) K the pressure increased to 34.0 (5) GPa, the quality of the crystal decreased, but we still could collect 26 unique reflections with which we could refine the hematite structure with a 8.7 % discrepancy factor (Table 3.3-1). Laser-heating at 40.4(5) GPa and 2300(100) K resulted in the appearance of a new set of reflections.

All 50 unique reflections of this set were indexed with an orthorhombic unit cell with lattice parameters $a=4.855(1)$ Å, $b=5.039(2)$ Å, and $c=7.187(2)$ Å. The space group suggested by the CrysAlis® software was *Pbna*. This assignment is consistent with the Rh₂O₃-II-type structure, and indeed, the 10 structural parameters related of this structure type could be refined with a discrepancy factor $R1 = 5.2$ %. In contrast, the orthorhombic perovskite structural model (space group *Pbnm*, 11 refined structural parameters) gives a discrepancy factor four times larger, $R1 = 20.5$ %, Table 3.3-1). The orthorhombic phase can be quenched at high pressure, therefore a further data collection was performed at 37.3(4) GPa and room temperature from which 58 unique reflections were successfully integrated. These could be refined in the Rh₂O₃-II-type structure with a discrepancy factor $R1 = 4.9$ %; but gave a very poor $R1 = 17.6$ % for the orthorhombic perovskite structural model (Table 3.3-1). Thus, the single crystal X-ray diffraction data unambiguously demonstrate that hematite transforms to the Rh₂O₃-II-type structured phase upon laser-heating at about 40 GPa. Although the reflections of the Rh₂O₃-II-type structure could be recorded on compression at ambient temperature up to at least 60 GPa, the quality of the crystals decreased with pressure and single-crystal structural refinements were therefore not performed.

Table 3.3-1: Results of single crystal structural refinement of Fe₂O₃ at different pressures and temperatures.

<i>P</i> (GPa)	<i>T</i> (K)	Structure-type	Space Group	R1 %	Lattice parameters			
					<i>a</i> , Å	<i>b</i> , Å	<i>c</i> , Å	<i>V</i> , Å ³
25.6(2)	298	Hematite	$\bar{R}3c$	4.5	4.898(2)		13.196(10)	45.70(1)
34.0(5)	2200(100)	Hematite	$\bar{R}3c$	8.7	4.906(3)		13.171(10)	45.75(2)
40.4(5)	2300(100)	Rh ₂ O ₃ -II	<i>Pbna</i>	5.2	4.855(1)	5.039(1)	7.187(2)	43.96(1)
40.4(5)	2300(100)	Orthorhombic Perovskite	<i>Pbnm</i>	20.5	4.855(1)	5.039(1)	7.187(2)	43.96(1)
37.3(4)	298	Rh ₂ O ₃ -II	<i>Pbna</i>	4.9	4.823(1)	5.009(1)	7.161(4)	43.25(1)
37.3(4)	298	Orthorhombic Perovskite	<i>Pbnm</i>	17.6	4.823(1)	5.009(1)	7.161(4)	43.25(1)

n. *Pressure-induced ferrous-ferric transition in iron ions in Fe_{1-x}O wüstite (S.V. Ovsyannikov and L.S. Dubrovinsky; V.V. Shchennikov and M.A. Shvetsova/Yekaterinburg; A. Polian/Paris)*

Compression of solids modifies their crystal and electron band structures and related properties. There are also subtle effects of pressure, like for instance, the introduction of different kinds of defects or modification of structure of native defects, which are not detected by conventional structural techniques, although they may strongly influence the magnetic, transport and optical properties. In a case of one of the lower mantle constitutions, namely, wüstite, (Fe_{1-x}O) the pressure-induced changes documented by different research groups are

strongly controversial. A possible reason is a not properly-understood behaviour of iron-related point and cluster defects as well as the stoichiometry of the defect rock-salt-(RS) structure of wüstite. Neutron diffraction data suggest that the number of empty octahedral sites is twice that of iron deficiency (x), hinting that the fraction of iron at the interstitial tetrahedral sites is close to x . The Fe^{3+} ions in Fe_{1-x}O are proposed to be randomly distributed. The defect structure of Fe_{1-x}O was believed to be a source of its high inelasticity. Analysis of a plenty of samples revealed the direct relationships between the stoichiometry of Fe_{1-x}O and its lattice parameter a (a (Å) = $3.856 + 0.478 \times (1-x)$) and its thermopower value S via the $\text{Fe}^{3+}/\text{Fe}^{2+}$ ratio

$$(S = k/|e| \times \ln(2 \times (\text{Fe}^{3+}/\text{Fe}^{2+})_{\text{oct}} + A) \quad \text{Eq. 1}$$

where e is the electron charge, k the Boltzmann's constant, and A is a small shift that is related to an 'entropy of transport term'. Normally, samples recovered from high pressure (except those recovered from both high P and high T) exhibit reduced lattice parameter that might hint either at possible decrease in the iron content (and hence increase in the $\text{Fe}^{3+}/\text{Fe}^{2+}$ ratio) or at very high inelasticity. The thermopower method in a combination with high pressure was never applied to wüstite but it may be used to detect changes in the polaron conductivity (hopping between Fe^{2+} and Fe^{3+} ions on the octahedral sites) under pressure.

To resolve the puzzle of high-pressure properties of wüstite, we applied structural, optical and transport methods aiming to measure experimentally the changes both in the $\text{Fe}^{3+}/\text{Fe}^{2+}$ ratio and in the stoichiometry of wüstite under pressure. The investigations were performed on a quasi-single-crystalline wüstite ingot ($a = 4.303(4)$ Å, and estimated composition $\text{Fe}_{0.935}\text{O}$). Structural and spectroscopic methods were employed at ambient conditions only, to characterize the sample before and after the high-pressure experiments. The thermopower value of wüstite was measured under pressure up to 20 GPa.

The X-ray diffraction patterns of the samples after the high-pressure experiments show an expected shift with respect to the starting material indicating a reduced lattice parameter (Fig. 3.3-17). However, further pressure cycles up to 15-22 GPa of the recovered samples resulted in an unchanged lattice parameter close to $a = 4.2833(8)$ Å; with an estimated value of $x = 0.107(2)$. Although, the amount of iron in the wüstite lattice is decreasing, we do not observe any enhancement of the reflections of $\alpha\text{-Fe}$ in the recovered samples, but on the contrary their weakening (insets in Fig. 3.3-17). Such a 'dissolution' of iron in FeO under pressure has been often observed, and there has been a long-standing conjecture that applied pressure 'stabilizes' the non-equilibrium wüstite lattice to 15 GPa by creating clustered iron. A simple explanation of this contradiction consists in a shredding of the iron clusters, and for this reason structural techniques probing long-range order are unable to detect the iron.

For 'ambient' thermopower values ($\sim +80 \pm 5$ $\mu\text{V}/\text{K}$) (Fig. 3.3-18) the calculations found that the $\text{Fe}^{3+}/\text{Fe}^{2+}$ ratio and the stoichiometry are respectively higher by ~ 0.04 and lower by \sim

0.01 than expected for $\text{Fe}_{0.935}\text{O}$ (Fig. 3.3-18). Increasing pressure enhances the $\text{Fe}^{3+}/\text{Fe}^{2+}$ ratio to 0.35 at 17.5 GPa (Fig. 3.3-18b). Charge balance conservation suggests that iron is leaving the lattice and thereby the material gradually shifts to a less stoichiometric composition with $x \approx 0.115$ at 17.5 GPa (Fig. 3.3-18b), in agreement with the structural data. Although the HP treatment of all the samples investigated leads eventually to consistent compositions (Fig. 3.3-18a), the difference between the data collected in different experiments points out that the rate of stoichiometry alteration depends on the details of the compression procedure. One can recognize in the data a tendency to stabilization of the thermopower to a value above $S \sim 20$ – $25 \mu\text{V/K}$ (Fig. 3.3-18a) suggesting a limit of pressure-tuned stoichiometry as $x \approx 0.125$ (Fig. 3.3-18b).

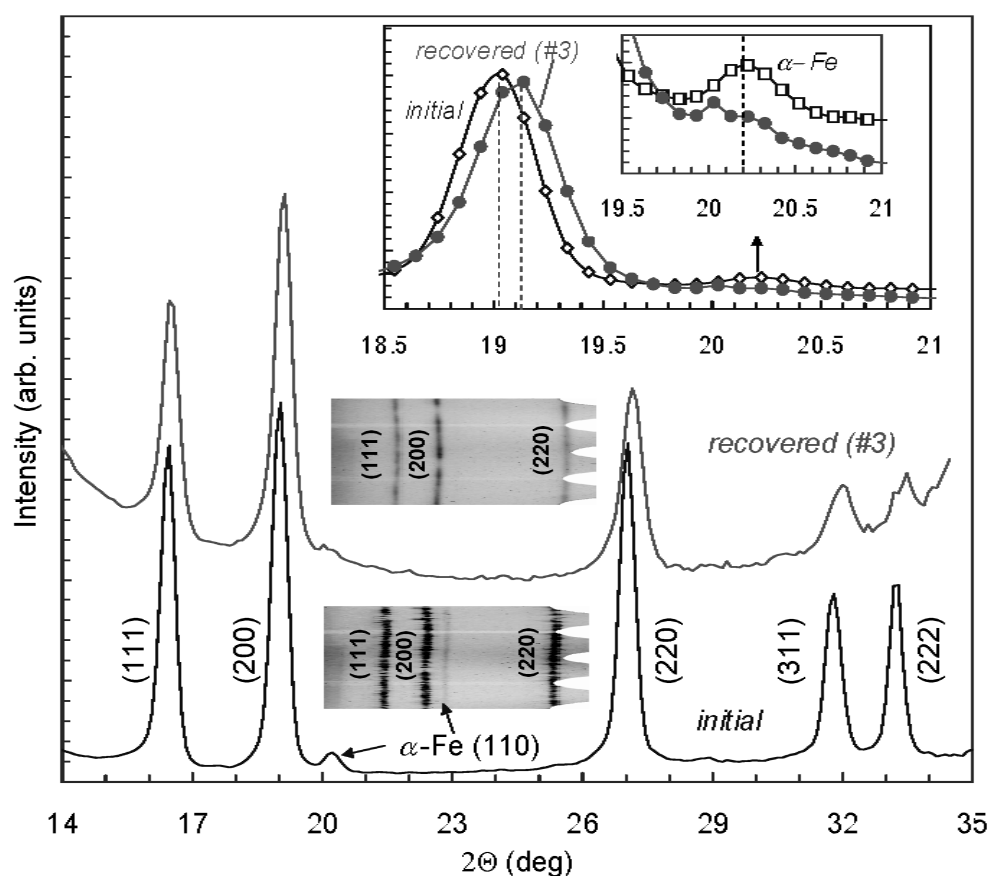


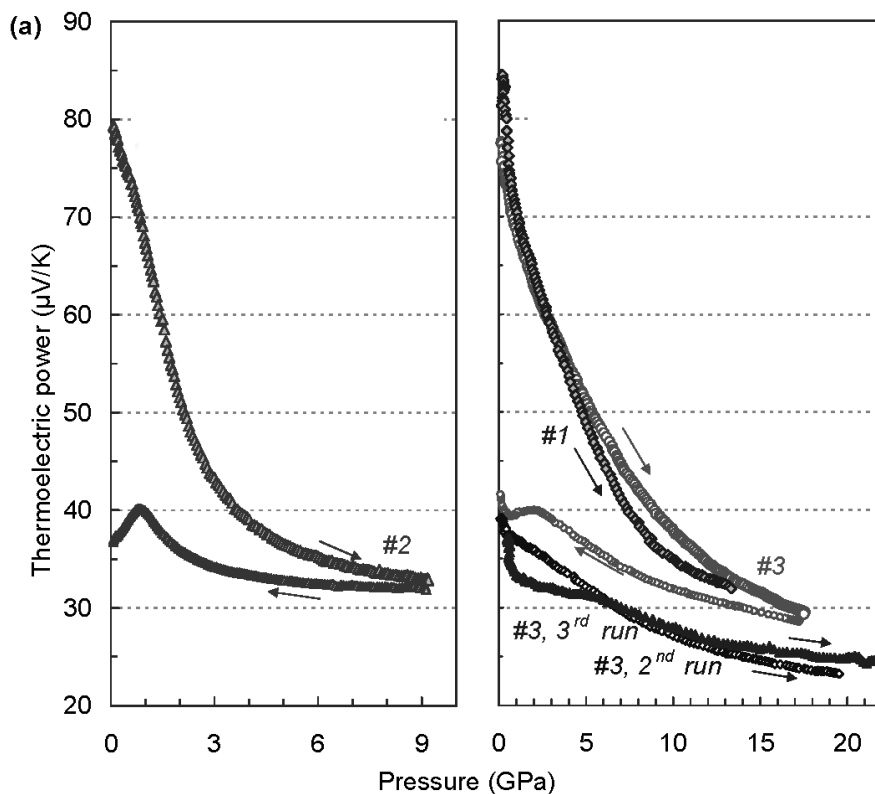
Fig. 3.3-17: An example of X-ray diffraction pattern of a wüstite crystal before and after the high-pressure experiment. The latter exhibits shifts in the positions of the peaks related to Fe_{1-x}O . The upper inset shows the 18.5 – 21° range in more details. The two insets near the diffraction patterns are azimuth patterns. The height covers a full range, 0 – 360° , and the width corresponds to a 2θ range of ~ 12 – 28 deg.

A former study on diffusivity of Fe in Fe_{1-x}O found a dependence on x : at 800°C the diffusion coefficient D strongly diminishes when x increases from ~ 0.05 to ~ 0.1 . To explain

this fact it was proposed that Fe ions diffuse by exchanging sites with ‘free mobile vacancies’, and increasing vacancy concentration enhances short-range defect-defect interactions and favors defect clusters formation, in which vacancies are ‘much less mobile’. *Hypothetical extrapolation* of these data to ‘ $D \rightarrow 0$ ’ gives $x \sim 0.15$, *i.e.*, close to our estimation of a limit of the stoichiometric shift under pressure ($x \sim 0.125$). Therefore, a ‘stabilization’ of FeO under pressure may mean a defect-clusters-related restriction in iron migration that prevents both further leaving/coming of iron into the lattice, and a decomposition of FeO into iron and Fe₃O₄.

In summary, we showed that a typical composition (Fe_{0.935}O) after pressure cycling up to ~ 20 GPa eventually shifts to \sim Fe_{0.89}O. Since, ‘effective’ properties of materials depend on their mesostructure, this could explain the controversial and puzzling high-pressure properties that are ascribed to ‘ideal’ wüstite. In particular, this explains, a strong scattering of bulk modulus data, the high inelasticity, and the differences in the high-pressure phases, a possibility of acquisition of magnetic properties under pressure, and many other things.

It is worthy mentioning that this year after the publication of our work [S.V. Ovsyannikov *et al.* Phys. Rev. B, 81, 060101 (R) (2010)] a team from the Geophysical Lab (CIW, Washington, D.C.) also claimed some ‘ferroic’ transition in FeO under pressure [Y. Ding, Z. Cai, J. Chang, R.J. Hemley, W.L. Mao, and H.-K. Mao, Nanoscale diffraction imaging study of the high-pressure ferroic transition in FeO, *Phys. Rev. Lett.* 2010, submitted].



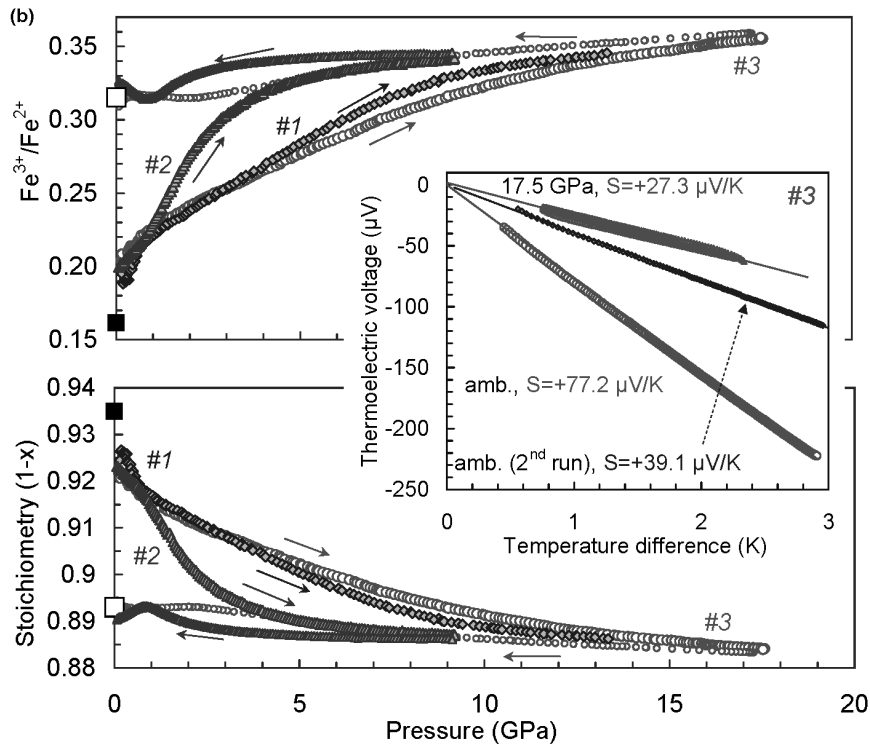


Fig. 3.3-18: (a) Pressure dependencies of the thermoelectric power of wüstite (Fe_{1-x}O) measured in two different cells; and (b) $\text{Fe}^{3+}/\text{Fe}^{2+}$ ratio and the stoichiometry of wüstite calculated according to the thermoelectric power. The filled and open squares at ambient pressure are respectively the starting and ending values determined by Eq. 1. The inset gives examples of the thermopower determination from a linear slope of a thermoelectric voltage on a temperature difference across sample #3.

o. *Magnetic transitions in Fe_3C (C. Prescher, L.S. Dubrovinsky and C.A. McCammon)*

Cementite (Fe_3C) in the orthorhombic structure (Pnma) is a metallic ferromagnet and transforms to the paramagnetic state at a Curie temperature of 483 K at ambient pressure. It is classified as an Invar material due to its nearly vanishing thermal expansion coefficient below T_c . Carbon atoms occupy interstitial sites in a hexagonal close packed structure of iron atoms. The structure leads to different iron sites with slightly different magnetic moments.

Carbon is one of the candidate light elements for the Earth's core, and Fe_3C was even proposed to be the major inner core component. This hypothesis inspired many experimental and computational investigations of this material. However, the transition from the ferromagnetic state to the paramagnetic or nonmagnetic state is still highly debated, and the proposed transition pressures vary from 5 to 68 GPa.

We conducted diamond anvil cell experiments up to 88 GPa with a Fe^{57} enriched Fe_3C sample. Neon was used as pressure transmitting medium to ensure hydrostatic conditions. The changes in magnetic order and physical state of iron were detected by Mössbauer spectroscopy.

Mössbauer spectroscopy shows a two stage loss of magnetism in Fe_3C . At 10 GPa there is a second order transition from the ferromagnetic to the paramagnetic state, as seen by a vanishing magnetic hyperfine splitting in the Mössbauer spectra (Fig. 3.3-19), and at around 24 GPa the material loses all of its magnetic moment due to a spin transition, as seen by a change in slope of the central shift in respect to pressure (Fig. 3.3-20).

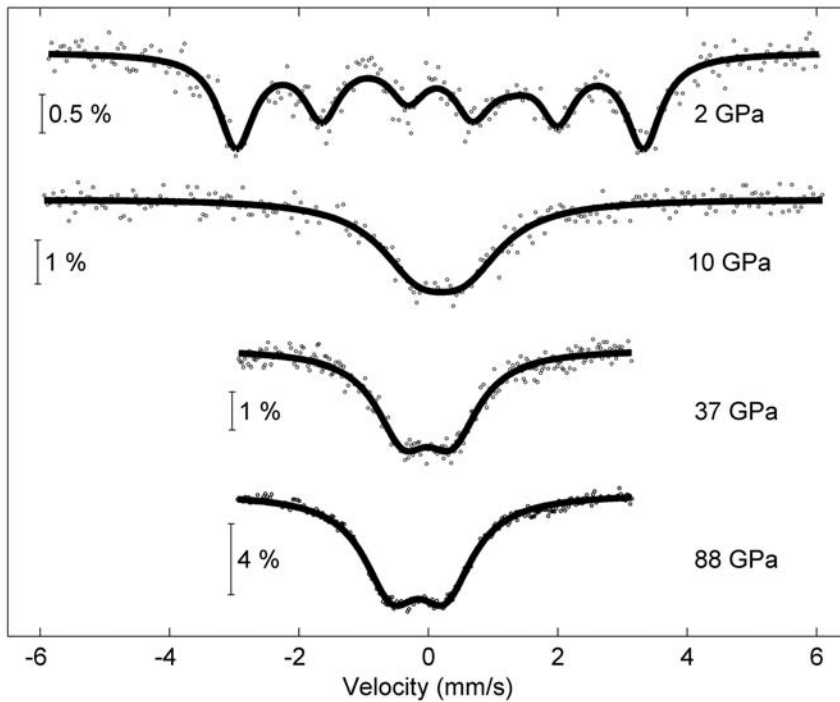


Fig. 3.3-19: Mössbauer spectra of Fe_3C at selected pressures showing the loss of magnetic hyperfine splitting around 10 GPa.

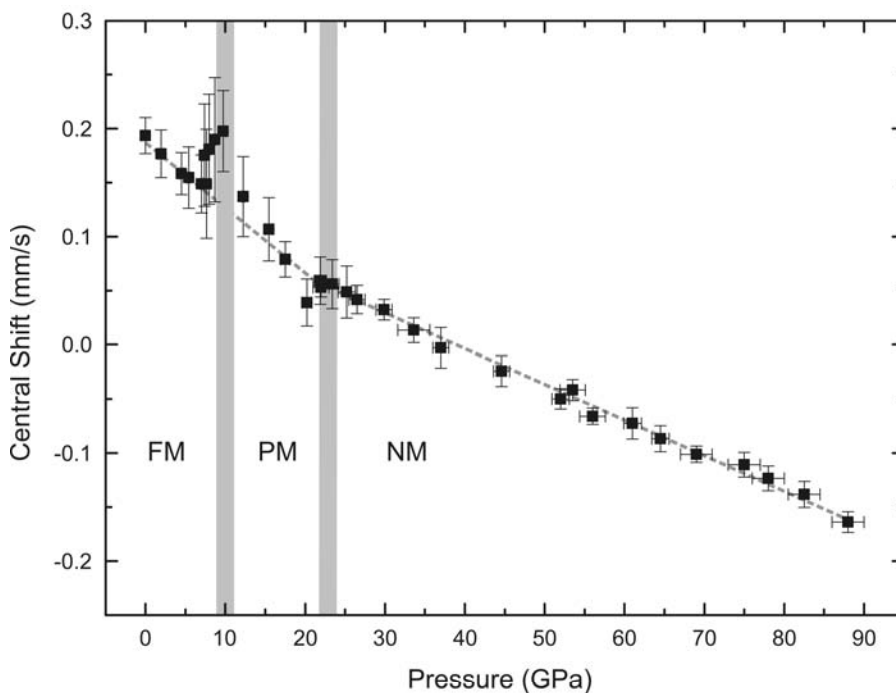


Fig. 3.3-20: Central shift as a function of pressure for Fe_3C . A transition from the ferromagnetic (FM) to paramagnetic (PM) state occurs at 10 GPa and at above 23 GPa Fe_3C becomes non-magnetic (NM) due to a spin transition.

3.4 Physical Properties of Minerals

Plate motions, earthquakes and volcanic eruptions are surface expressions of processes taking place in the deep Earth's interior. An interpretation of these phenomena and an understanding of the functioning and structure of the Earth's interior is largely based on the knowledge of the relevant minerals and their physical properties. The velocities of seismic waves, created by earthquakes, can only be converted into a structural model of the Earth's interior, if the elastic and compressional properties of the relevant minerals are known as function of pressure and temperature. Such data is provided by controlled laboratory experiments that allow to compress and heat minerals to the pressures and temperatures prevailing in the deep Earth's interior. These experiments are very demanding, because measurements of the mineral properties have to be carried out *in situ* on sample volumes that become increasingly small with increasing pressure. Continuous developments of experimental setups and the use of synchrotron sources are commonly required to obtain the mineral data for the deepest part of the Earth's interior, as is illustrated in this chapter.

The first four contributions of this chapter present equation-of-state data for phases either relevant for the Earth's lower mantle or useful for pressure calibration. The *P-V* data on silicate perovskite, the major phase of the lower mantle, are extended to a new pressure limit of 75 GPa and first equation of state data are presented for a new aluminous phase D that could potentially transport water into the lower mantle. The determination of the compressibility of quartz, which is widely used as internal standard material, up to a pressure of 21.5 GPa is a further advancement presented in this chapter.

Measurements of sound and shear wave velocities using ultrasonic interferometry and nuclear inelastic scattering are reported in the next two contributions. The first investigation on various garnets demonstrates that the wave velocities for complex garnet compositions can not be directly inferred from endmember data and requires detailed study of the effect of substitutions. The second study reports the progress in determining the elastic wave velocities of silicate perovskite at high pressure and temperature in a diamond anvil cell that is coupled with a newly designed portable laser heating system.

The final block of contributions to this chapter focuses largely on transport properties and the effect of Fe^{3+} on the physical properties of mantle minerals. Important results are, for example, that interdiffusion experiments on a post-perovskite model system corroborate the expected large anisotropy in diffusivity of post-perovskite. In another experimental study, it is shown here that the high electrical conductivity of the Lower crust could be simply accounted for by the properties of the main crustal phases, *i.e.*, plagioclase and pyroxenes. The chapter is completed with a computational study, which predicts the stability of TiO_2 phases (anatase vs. rutile) on the basis of density functional theory calculations.

a. *Single-crystal X-ray diffraction of Al- and Fe-bearing MgSiO₃ perovskite at pressures of the Earth's lower mantle (T. Boffa Ballaran, A. Kurnosov, K. Glazyrin, M. Merlini/Grenoble and D.J. Frost)*

Perovskite structured compounds form the bulk of the Earth's lower mantle and are among the most widely used crystal structures in technological applications due to the variety of physical properties arising from their structural phase transitions. It is therefore not surprising that the stability and structural changes of perovskites are an ongoing subject of investigation. The aristotype perovskite structure, space group $Pm\bar{3}m$, consists of a three-dimensional framework of perfectly regular and untilted corner-sharing octahedra, BX₆, within the cavity of which lie the A cations in 12-fold coordination. At ambient conditions most perovskite structures exhibit a lower symmetry due to octahedral tilting and cation displacements with respect to the cubic aristotype. Several studies have been focused on the temperature behaviour of different perovskites and different phase transformations to higher symmetry phases have been successfully described in terms of a change in the tilting pattern of effectively rigid octahedra. Pressure, on the other hand, has been found to give rise to a small but significant amount of compression of the BX₆ octahedra. Such structural studies cover a limited pressure range and therefore cannot be used to infer the structural state of MgSiO₃ perovskite at pressures of the Earth's lower mantle (20 -120 GPa), for which either *ab initio* calculations or structural data from high-pressure powder diffraction experiments, which suffer from large uncertainties, have to be relied on. Knowledge of the real structural state of MgSiO₃ phases at pressures of the lower mantle is, however, crucial not only to better constrain the physico-chemical properties of the Earth's interior but also to understand the structural instability, which leads to the perovskite to post-perovskite phase transition.

A MgSiO₃ perovskite sample containing Fe and Al was synthesized at 25 GPa and 1300 °C from a ground mixture of oxides and hydroxides with a bulk composition similar to that found in experiments on mid ocean ridge basalt compositions. Microprobe analysis, Mössbauer spectroscopy and single crystal X-ray diffraction were used to characterize the resulting perovskite crystals. High-pressure experiments at room temperature were performed with a 10 x 10 x 10 μm³ single-crystal using a rhenium gasket pre-indented to a 50 μm thickness and with a 100 μm hole mounted on a membrane diamond anvil cell (DAC) loaded with He as pressure transmitting medium and a ruby chip as internal pressure standard. X-ray diffraction data were collected at different pressures up to 75 GPa at the European Synchrotron Radiation Facility (ESRF, Grenoble, France), on beam line ID-09. The *P-V* data show no discontinuity up to the maximum pressure reached and the clear curvature of the normalised stress, F_E , vs Eulerian strain, f_E plot implies that a 4nd order Birch-Murnaghan (BM-IV) equation of state (EoS) is needed to correctly fit the data. The calculated EoS parameters are the following: $V_0 = 168.972 (5) \text{ \AA}^3$, $K_0 = 230.0 (8) \text{ GPa}$, $K' = 5.70 (16)$ and $K'' = -0.11 (1) \text{ GPa}^{-1}$. Pressure induces a major shearing of the octahedral site as indicated by the changes of the O-B-O angles; in particular the O2-B-O2 angle of the basal octahedral plane decreases from 90.8° to 90° (regular octahedron) at about 50 GPa and decreases steadily to a value of 89° at 75 GPa.

A recent investigation of the perovskite to post-perovskite phase transition suggests that the repulsion between inter-octahedral anions driven closer by octahedral tilting destabilises the perovskite structure when $V_A:V_B < 4$, however such interpretation requires the assumption of rigid octahedra. The variation of the $V_A:V_B$ ratio of our sample is shown in Fig. 3.4-1. Above 50 GPa the $V_A:V_B$ ratio appears to be independent of pressure suggesting that the shearing of the basal octahedral plane and not the octahedral tilting is the major distortion mechanism at elevated pressures. We, therefore, suggest that the structural instability leading to the transformation to the post-perovskite structure is related to the collapsing of the octahedral framework, due to the large distortion of the octahedra and not simply due to anion-anion repulsion.

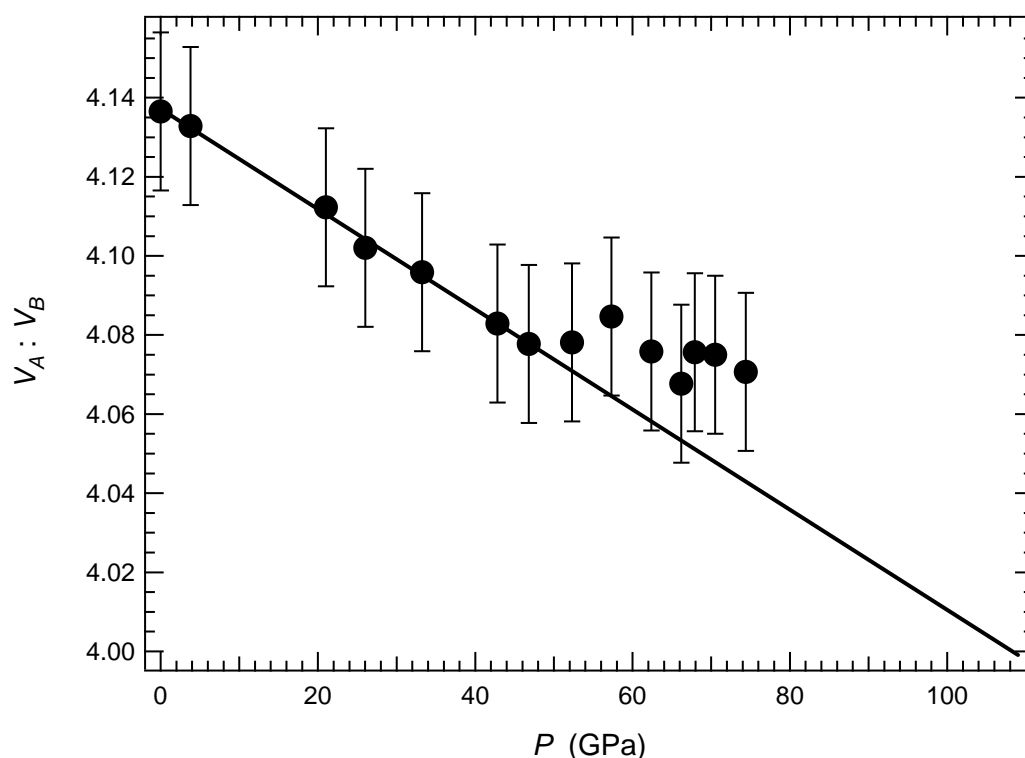


Fig. 3.4-1: Variation as a function of pressure of the $V_A : V_B$ ratio of Al-, Fe-bearing $MgSiO_3$ perovskite.

b. High-pressure behaviour of hydrous aluminosilicate phases in the lower mantle (M.G. Pamato, D.J. Frost, T. Boffa Ballaran, F. Heidelbach and N. Miyajima)

Water is transported and recycled into the Earth's interior by hydrous minerals in descending slabs and the amount of water that ultimately reaches the deep Earth in the subduction process is thus likely governed by the stability of high-pressure hydrous phases. As water plays an important role in mantle dynamics and planetary evolution, the study of the structure and stability of possible hydrous high-pressure phases in subducting slabs is of crucial importance.

A number of hydrous phases have been experimentally synthesized at pressures and temperatures compatible with subduction zone conditions in peridotites, basalts and sediment compositions. In the system MgO-SiO₂-H₂O (MHS), different dense hydrous magnesium silicates (DHMS) have been synthesized. Phase D (MgSi₂O₆H₂ ideal formula) is the densest (3.4 g/cm³) hydrous high-pressure phase; it is stable up to 50 GPa. Very recently, a new Al form of phase D (Al-phase D), containing up to 50 wt.% Al₂O₃, was synthesized in a simplified basaltic bulk composition at lower mantle conditions. The high-temperature stability of this new modification of phase D suggests that this phase may be an important host for water within portions of subducting oceanic crust in the Earth's lower mantle. No phase with a similar structure has been previously reported, therefore we conducted a high-pressure and high-temperature study in the simplified system Al₂O₃-SiO₂-H₂O with the main purpose of determining the extent to which the partitioning of Al into Al-phase D affects the stability of this phase.

In order to investigate the stability of this new Al-phase D, multianvil experiments at pressures ranging from 22 to 26 GPa and temperatures from 1050 to 1600 °C were performed. Two starting compositions, referred to mixture 1 (19.24 wt.% Al₂O₃, 55.5 wt.% AlOOH and 25.27 wt.% SiO₂) and mixture 2 (13.59 wt.% Al₂O₃, 39.27 wt.% AlOOH and 47.15 wt.% SiO₂), were prepared by mixing SiO₂, Al₂O₃ and Al(OH)₃ in different proportions.

The run products were characterized by means of X-ray powder diffraction, scanning electron microscopy (SEM), transmission electron microscopy (TEM) and the chemical compositions were determined by electron microprobe analysis (EMPA).

In this study, we report for the first time the synthesis of a new form of phase D containing up to 57 wt.% Al₂O₃ and totally Mg and Fe free. The stoichiometry of Al-phase D varies as a function of temperature and starting composition employed. In the silica-rich composition (mixture 2), phase D has been found in equilibrium with stishovite and phase Egg, whereas in an alumina-rich composition (mixture 1) it is found in coexistence with stishovite and δ AlOOH. The new Al-phase D is stable, together with stishovite, at least up to 1600 °C and 26 GPa, conditions compatible with normal mantle adiabat at the top of the lower mantle.

The HP-HT occurrence of Al hydrous phases investigated in this study, in particular Al-phase D, together with stishovite, suggests that they may act as important carriers of water in the deep lower mantle.

c. Compressibility of a super aluminous version of phase D (M.G. Pamato, T. Boffa Ballaran, D.J. Frost, D.M. Trots and A. Kurnosov)

Phase D (MgSi₂O₆H₂ ideal formula) is one of the most important phases among the dense hydrous magnesium silicates (DHMS). It is the densest (3.5 g/cm³) among the DHMS and the

only phase where Si is found only in octahedral coordination. The high pressure-temperature stability of phase D has been investigated in the simple system MgO-H₂O-SiO₂ (MHS) and it has been found to be stable at lower mantle conditions up to 50 GPa, eventually persisting to a depth of approximately 1250 km.

Phase D has trigonal symmetry with space group *P*-31*m*. The crystal structure is based on a hexagonal closed packed array of oxygen atoms and is composed of alternating MgO₆ and SiO₆ octahedra layers stacked along the *c*-axis. Mg occupies the M1 site (1*a* Wyckoff position) and Si the M2 site (2*d*). In the SiO₆ octahedral layer, each octahedron shares three edges with others to form brucite-like layers with one of the three octahedral sites, corresponding to the 1*b* Wyckoff position being vacant. In the MgO₆ octahedral layers two of three octahedral sites, corresponding to the 2*c* Wyckoff position (M3), are vacant. Very recently (see annual report 2009), a new Al form of the dense hydrous magnesium silicate phase D (Al-phase D), containing up to 50 wt.% Al₂O₃, was synthesized in a simplified basaltic bulk composition at lower mantle conditions. In Al-phase D, the substitution of Al for Mg and Si gives rise to a more complex structure with Al/Si disorder and with partial occupancy of the M3 site, which is vacant in Mg-phase D. Given the difference in crystal structure we may expect a different high-pressure behaviour of Al-phase D with respect to Mg-phase D.

In order to determine the compressibility and equation of state parameters of this new variant of phase D, high-pressure single crystal X-ray diffraction measurements were performed. The evolution of the unit-cell volumes of two crystals of Al-phase D (s4430x3 and s4430x8), up to 13.6 GPa, is reported in Fig. 3.4-2. The data show a smooth, continuous trend, indicating that there is no phase transition within the pressure range investigated. The pressure-volume data were fitted using a third-order Birch-Murnaghan equation of state, yielding $V_0 = 84.22(2) \text{ \AA}^3$, $K_0 = 149(2) \text{ GPa}$ and $K' = 7.1(5)$ for the first crystal (s4430x3) and $V_0 = 84.67(1) \text{ \AA}^3$, $K_0 = 153(2) \text{ GPa}$ and $K' = 6.4(5)$ for the second crystal (s4430x8). Al-phase D is less compressible than the Al-Fe bearing phase D ($K_0 = 137(3) \text{ GPa}$, $K' = 6.3(3)$) and is as compressible as the Mg-phase D ($K_0 = 166(3) \text{ GPa}$, $K' = 4.1(3)$). The compression of Al-phase D is anisotropic with axial compressibilities showing an *a*:*c* ratio of 1.00:1.34 (Fig. 3.4-3). The axial anisotropy of Al-phase D is smaller than that of Mg-phase D and Al-Fe bearing phase D. Thereby, the *c* axis of Al-phase D is stiffer than that of the other two phases. This is likely due to the partial occupancy of the M3 sites in Al-phase D, since the incorporation of cations in a crystal site that is normally vacant may contribute to the stiffening of the *c* axis of Al-phase D, reducing in this way the axial anisotropy.

The high pressure and temperature stability of Al-phase D investigated in this study together with its high bulk modulus indicate that this phase is stable at lower mantle conditions and may be an important host phase for water transportation in descending slabs to the Earth's deep mantle.

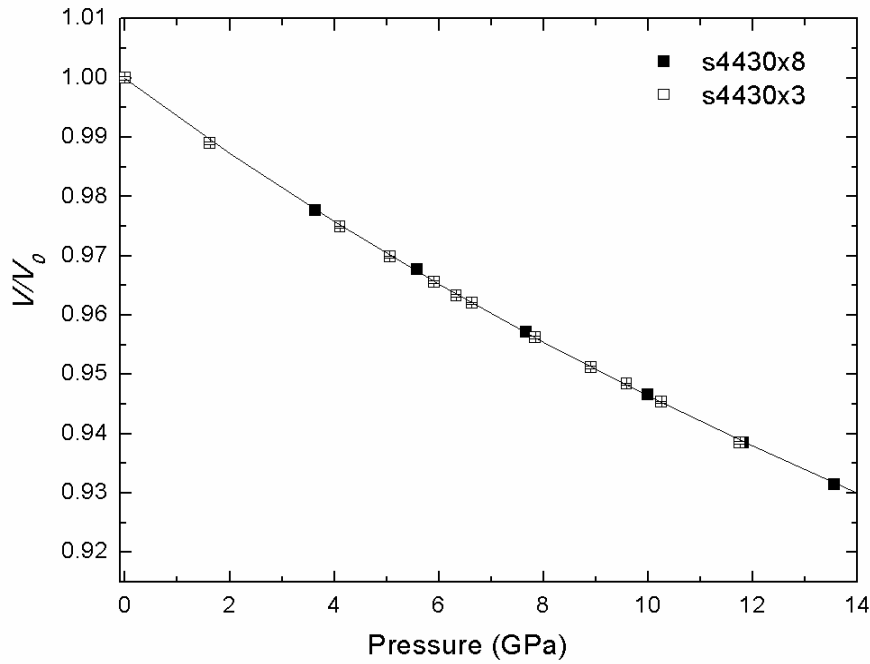


Fig. 3.4-2: Evolution of the unit-cell volumes (normalized volumes) as a function of pressure. Open symbols: crystal s4430x3; filled symbols: crystal s4430x8. The solid curve represent the least square fit to a 3rd order Birch-Murnaghan equation of state. The standard deviations are within the size of the symbols.

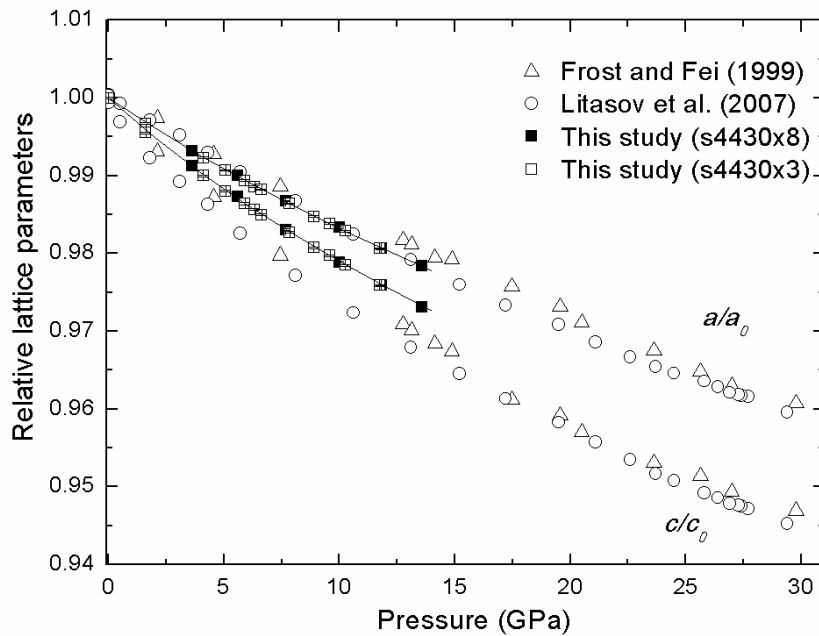


Fig. 3.4-3: Variation of relative lattice parameters (a/a_0 and c/c_0) as a function of pressure. Filled and open squares: Al-phase D (this study); open triangles: Mg-phase D (Frost D.J. and Fei Y., Phys. Chem. Miner. 26, 415, 1999.); open circles: Al-Fe bearing phase D (Litasov K.D., Ohtani E., Suzuki A., Funakoshi K., Phys. Chem. Miner. 34, 159, 2007).

d. *High-pressure structural behaviour of α -Fe₂O₃ up to 25 GPa studied by single-crystal X-ray diffraction and synchrotron radiation (P. Schouwink/Heidelberg, L.S. Dubrovinsky and K. Glazyrin; M. Merlini and M. Hanfland/Grenoble; T. Pippinger and R. Miletich/Heidelberg)*

The majority of transition metal sesquioxides (M₂O₃: M=Al, Ti, V, Cr, Fe) adopt the corundum structure (*R*-3c), forming compounds with great importance in mineralogy and technology due to their electric and magnetic properties. Among these, Fe₂O₃ hematite is particularly relevant to geosciences and also very interesting to solid state physics as it can be considered an archetype Mott-Insulator, antiferromagnetic between the Morin temperature (260 K) and the Néel temperature (955 K). Considering that iron is one of the most abundant elements in the Earth's mantle it is essential to understand in detail the high-pressure as well as the high-temperature behaviour of iron bearing compounds as well as of trivalent iron in general. Fe₂O₃ is a well studied compound. Numerous experimental PXRD as well as theoretical works have been conducted, special effort has been spent on clarifying its high-pressure phase transition. Only recently, the high-pressure phase was identified unambiguously. However, no single-crystal data exist at pressures higher than 50 kbar, up to date.

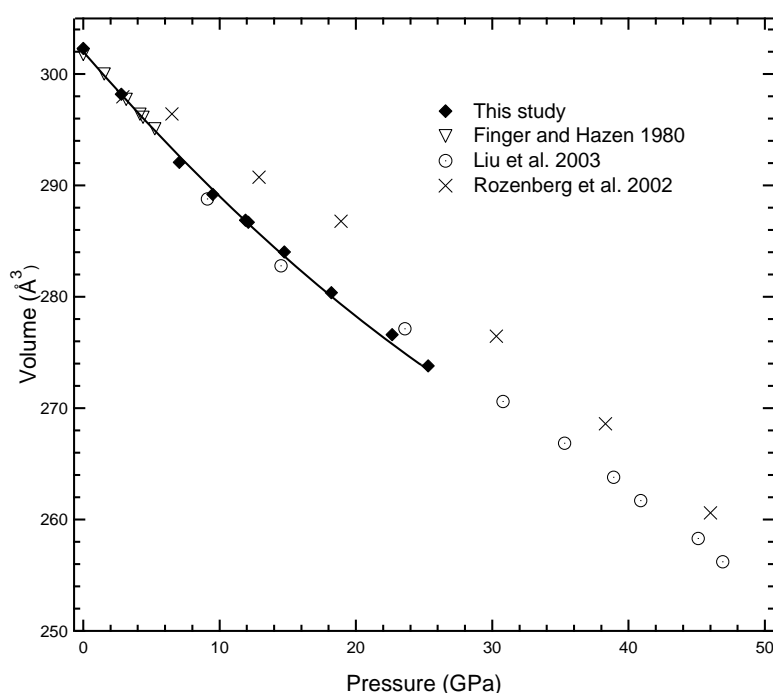


Fig. 3.4-4: Normalised unit cell volume of hematite. The solid line represents a fit of a 2nd order Birch-Murnaghan equation of state to the data points determined in this study. Esd's are smaller than symbols.

In this study synchrotron radiation was used to collect high-pressure data up to 25 GPa on a synthetic Fe₂O₃ single-crystal sample. Neon was loaded into a diamond anvil cell (DAC) to

provide quasi-hydrostaticity throughout the investigated pressure range. 10 data points were collected, which allowed for accurate refinements of structural parameters and the determination of bulk as well as axial compressibilities (Fig. 3.4-4). Moduli were extracted from the fit of a Birch-Murnaghan equation of state, which was truncated at second order according to finite strain analysis. The fit yields $K_0=207(3)$, $K_{a0}=751(17)$ and $K_{c0}=492(8)$, respectively, reflecting the 1.5 times stiffer a -axis. The octahedral bulk modulus of FeO_6 is virtually identical to the bulk modulus K_0 . The pressure dependency of structural parameters shows that there are two competing mechanisms that counteract compression, *i.e.*, face-sharing of dimers of octahedra supporting c and the distorted HCP (hexagonal close packing) in (0001), which stabilizes the a -axis. Hematite was found to compress quite uniformly, showing just slight changes of distortion parameters at higher pressures. This is contradictory to earlier results, which might be due to the better hydrostatic environment of Neon loaded cells (as opposed to Argon loaded cells) and due to the superior nature of single-crystal data, minimizing sample and data evaluation problems commonly encountered when handling powder samples.

e. Equation of state of α -quartz measured using high-pressure single-crystal X-ray diffraction up to 21.5 GPa (D.M. Trots, A. Kurnosov, T. Boffa Ballaran and D.J. Frost)

In the last decade quartz has been used as internal pressure standard in high-pressure single-crystal X-ray diffraction up to 10 GPa thanks to very precise and accurate measurements of its unit-cell lattice parameters. Several powder and single crystal diffraction investigations have also been performed above 10 GPa in different pressure media, but the results reported are discordant. These investigations were mainly focused on the search for new high-pressure polymorphs of SiO_2 and on its pressure induced amorphisation above 21 GPa. Given the very precise compressibility data present in the literature up to 10 GPa, quartz is an ideal choice for testing the performance of our new high-brilliance diffractometer system at least up to the amorphisation pressure. We have therefore decided to determine precisely unit-cell parameters of α - SiO_2 in the entire pressure range of its existence using quartz single-crystals which are normally too small to be measured in a conventional diffractometer.

A quartz crystal with dimensions of approximately $35 \times 30 \times 15 \mu^3$ was loaded in the Boehler-Almax diamond anvil cell with helium pressure medium, which is believed to generate the most hydrostatic conditions. The 8-position centering of diffraction maxima were performed on a Huber single crystal diffractometer coupled with an ultra high intensity rotating anode X-ray source and multilayer optics. The ruby fluorescence shift calibrated in helium pressure medium was used for pressure calibration. The variation of the unit-cell volume of quartz as a function of pressure is shown in Fig. 3.4-5. The quasi-hydrostaticity of the helium pressure medium was monitored by measuring the full width at half maximum (FWHM) of several diffraction peaks and an example is shown in the inset of Fig. 3.4-5. No significant

broadening is observed in the investigated pressure range confirming the absence of non-hydrostatic conditions which would lead to very pronounced increases in the mosaic spread of α -quartz and hence in the widths of the diffraction peaks. At 21.5 GPa the diffraction peaks of α -quartz disappear, however diffraction spots were still observable using an Xcalibur diffractometer equipped with a CCD detector, suggesting that a transformation to another crystalline phase and not amorphisation has occurred. The structure of this phase is still under investigation.

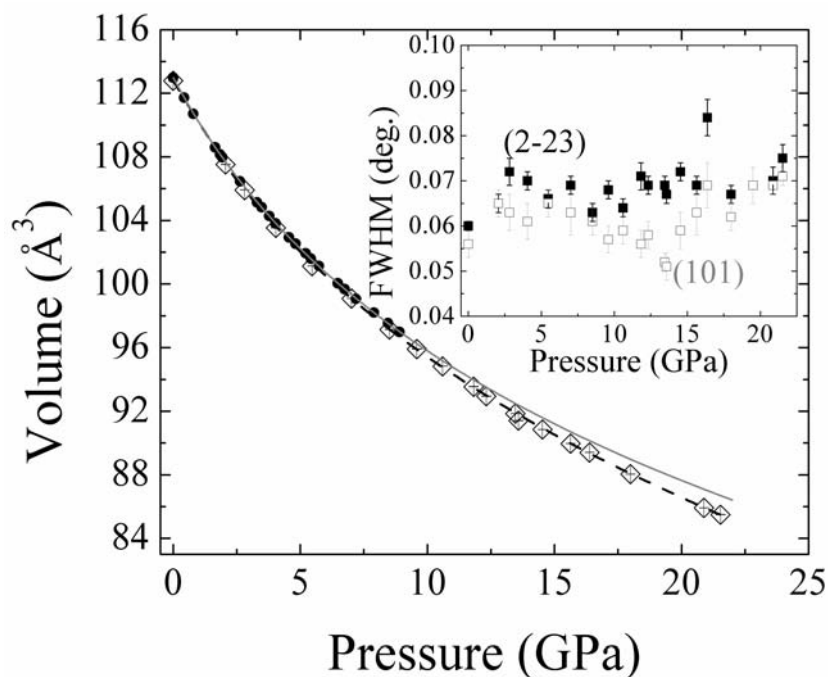


Fig. 3.4-5: Variation of the unit-cell volume of α -SiO₂ measured by single crystal X-ray diffraction. Open diamonds: this study; filled circles: Angel *et al.* (J Appl Crystallogr, 30, 461, 1997). Solid and dashed lines correspond to the description of data by III- (J Appl Crystallogr, 30, 461, 1997) and IV- (our data) order BM-EoS, respectively. Inset: variations in the width of the (101) and (2-23) reflections as a function of pressure in our experiment.

A careful analysis of the normalised stress, F_E vs. Eulerian strain, f_E plot constructed for our data and for the precise data collected by Angel *et al.* (J Appl Crystallogr, 30, 461, 1997) (Fig. 3.4-6) reveals that the two sets of data are in agreement, however in order to describe the compressibility of quartz for the whole pressure range between room pressure and 21 GPa, a IV-order Birch-Murnaghan equation of state (BM-IV EoS) needs to be used. The resulting BM-IV EoS parameters obtained from the fit of our P - V data are the following: $V_0 = 112.79(2) \text{ \AA}^3$, $K=36.4(7) \text{ GPa}$, $K'=6.6(4)$ and $K''=-0.69(14) \text{ GPa}^{-1}$. The need of a higher order EoS to describe the compressibility of quartz up to 21 GPa is likely the primary reason for the discrepancy between EoS parameters present in the literature, which have been calculated using III-order BM EoS also for data above 10 GPa.

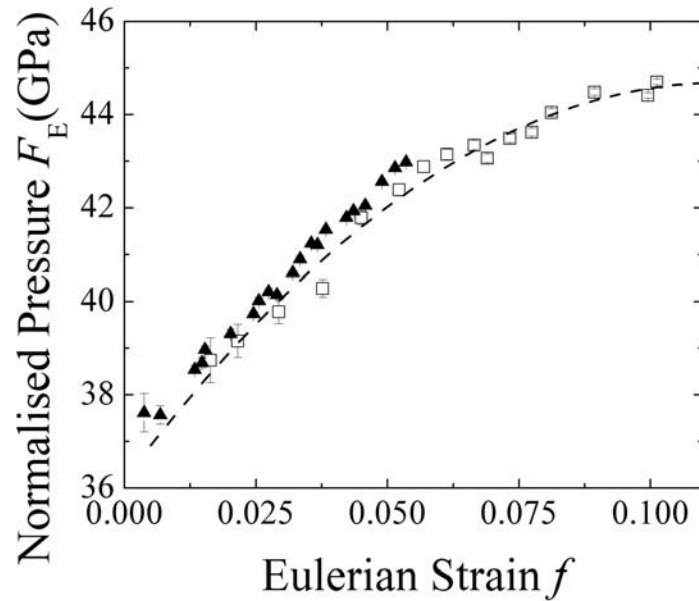


Fig. 3.4-6: Normalised stress, F_E vs. Eulerian strain, f_E plot. Open squares: this study; filled triangles: Angel *et al.* (J Appl Crystallogr, 30, 461, 1997). The two set of data can be fitted together only by means of IV-order BM EoS.

f. V_p and V_s measurements of polycrystalline solid solutions at high pressure (J. Chantel and D.J. Frost)

The most accurate method to investigate the mineralogy and chemistry of the mantle at depths greater than 150 km is through the analysis of compressional (P) and shear (S) seismic waves and comparison with the same velocities calculated for expected mineral assemblages. Regional variations in seismic wave velocities could originate from either chemical or thermal heterogeneities and experimental measurements of mineral wave velocities at high pressures and temperatures are required to differentiate between these causes. Chemical heterogeneities in the mantle are potentially developed through the subduction of basaltic oceanic crust. In the transition zone a major difference between rocks formed from subducted basaltic crust and typical ultramafic mantle will be the proportion and chemistry of the mineral garnet, with the former being composition mainly of garnet at these conditions. MORB and peridotitic garnets will differ in the proportions of Ca, Fe and majoritic component with the former being richer in all components except majorite. Most models use partial derivatives of elastic properties with respect to composition to determine the elastic properties of complex garnet compositions in the mantle. However most of these derivatives with respect to composition are determined from studies on single chemical variants and very few measurements of the elastic properties of complex garnets expected in the mantle exist.

We have systematically investigated the effect of chemical variations on seismic wave velocities of garnets up to transition zone conditions by studying the effects of Ca, Fe and

majoritic substitutions on the elasticity of pyrope. In addition, however, we have synthesized garnets at transition zone conditions with compositions expected from both subducted basaltic material and typical ultramafic mantle. We employ ultrasonic MHz interferometry to measure adiabatic elastic properties of these hot pressed garnet samples through travel time measurements of P and S sound wave velocities. The measurements performed in the multianvil apparatus employ a buffer rod to transmit the ultrasound to the center of the octahedral assembly. Experiments are performed using an 18mm octahedral sample assembly with 11 mm tungsten carbide cube truncations. Experiments were performed up to 18 GPa in a 5000 tons press. Since an intense in-house X-ray source is not available for pressure determination, we perform experiments only at room temperature and employ *in situ* measurements of resistance changes in metal alloy wires to the calibrate pressure.

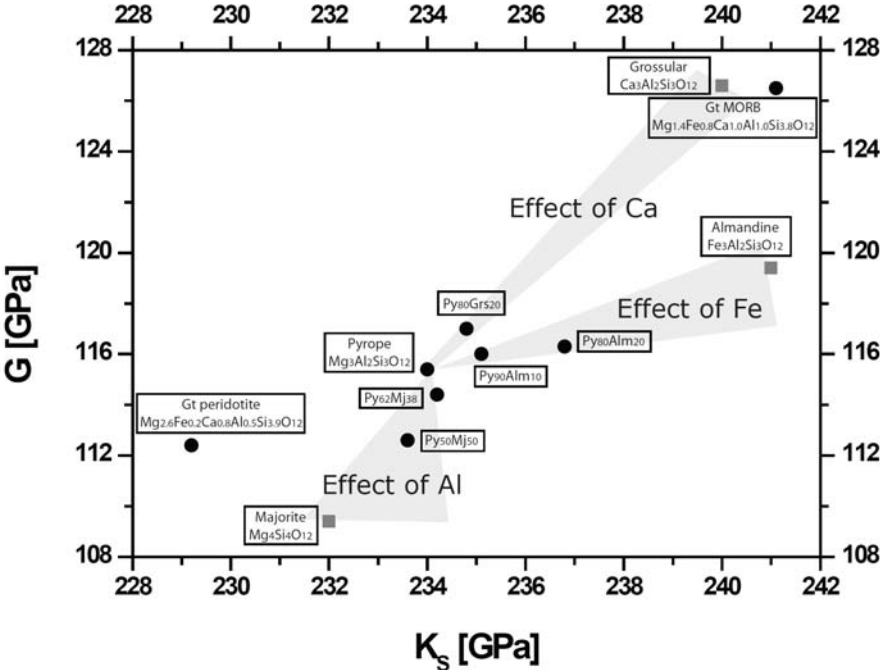


Fig. 3.4-7: Shear (G) and Bulk (K_s) moduli of polycrystalline hot pressed garnet aggregates measured at 16 GPa using ultrasonic interferometry in the multianvil device. Shaded regions show directions of major substitutions resulting from the addition of Fe, Ca and Mg + Si to the pyrope end member. Garnets typical of peridotite (Gt peridotite) and mid ocean ridge basalt (Gt MORB) compositions at transition zone conditions are also shown but their elastic properties do not correspond to a clear substitutional trend or simple vector addition. Grey squares are end-member.

Experimental results for shear and bulk moduli determined at 16 GPa and room temperature are summarized in Fig. 3.4-7. Our data indicate that the partial substitutions of Ca, Fe and Mg + Si into pyrope result in moduli changes in 3 distinct directions, which are consistent with the changes expected from literature measurements on the end-member garnets. These results

are consistent with a linear relationship between each chemical substitution and the elastic properties, along the entire range of each substitution. However, the elastic constants of MORB and peridotitic garnet are inconsistent with a summation of partial molar derivatives of the elastic properties with respect to composition, if data from the three individual substitutions are used. Although peridotitic garnets have a significant majoritic garnet component, there is no substitution that can obviously account for the lower K_s of these samples. Similarly, the elastic properties of MORB garnet should reflect only a small proportion of Ca and Fe substitution into pyrope but the resulting elastic properties of MORB garnet are similar to those of the grossular end member. One possible explanation is that the elastic properties of complex garnets are affected by other substitutions that are not considered, such as the Fe-majorite substitution ($\text{Fe}_4\text{Si}_4\text{O}_{12}$), or that strongly non-linear elastic property effects arise when two or more substitutions are present. Most models for determining seismic velocities from mineral assemblages assume a linear combination of partial derivative elastic properties in proportion to the abundance of the particular substitution. Our results imply this is unlikely to lead to a correct prediction of the properties of garnets with complex compositions, unless more detailed studies of the effects of multiple substitutions are made.

g. Influence of pressure and temperature on the elastic wave velocities of lower mantle perovskite (C.A. McCammon, L.S. Dubrovinsky, K. Glazyrin, M. Mookherjee, R. Sinmyo, O. Narygina/Edinburgh and E. Greenberg/Tel Aviv; I. Sergueev and A. Chumakov/Grenoble)

In the dominant chemical system of the Earth's mantle, $\text{MgO-SiO}_2\text{-Al}_2\text{O}_3\text{-FeO-Fe}_2\text{O}_3$, the perovskite structure is the most stable host over a wide range of pressure and temperature conditions, constituting up to 80 % of the lower mantle. The ability of iron to adopt multiple valence and spin states can drastically change the physical and chemical properties of lower mantle perovskite from those of the endmember composition MgSiO_3 , which can have significant implications for the modelling of lower mantle properties and dynamics. Nuclear resonance methods offer a unique opportunity for studying both the electronic and dynamic properties of iron compounds, and nuclear inelastic scattering (NIS) in particular allows the determination of elastic wave velocities for direct comparison with bulk geophysical data. Over the past few years our group has been systematically studying varying compositions of iron-containing silicate perovskite using NIS at room temperature, and more recently, at high temperature using a portable laser heating system.

We performed NIS measurements in laser-heated diamond anvil cells, coupled with nuclear forward scattering to determine spin populations and X-ray diffraction to observe crystal structures. All nuclear resonance synchrotron experiments were performed on beamline ID18 at the European Synchrotron Radiation Facility in Grenoble, France. The Debye model could be applied to the NIS data in conjunction with known equations of state of the different silicate perovskite compositions in order to determine the mean Debye sound velocity, and

hence the compression (V_p) and shear (V_s) wave velocities. The variation of all elastic wave velocities with pressure shows a consistent variation for all compositions studied (shown in Fig. 3.4-8 for V_s). The influence of temperature on V_s appears to be relatively small for all perovskite compositions studied, similar to results for ferropericlase. Preliminary analysis suggests that the temperature derivatives of the shear moduli of iron-containing silicate perovskites are similar to values for garnet-majorite, which as already noted in the literature are significantly lower than values for other dominant mantle minerals. The reduced influence of temperature on the shear velocity of the dominant mineral of the lower mantle may have important implications for the interpretation of fast and slow regions in seismic tomography data.

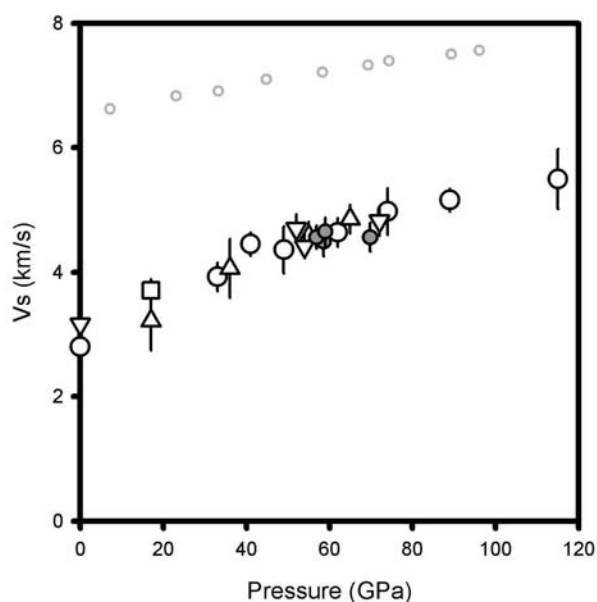


Fig. 3.4-8: Variation of V_s with pressure for different compositions of silicate perovskite as measured using nuclear inelastic scattering. Open symbols indicate data taken at room temperature, while solid grey symbols refer to high-temperature data. Compositions are as follows: MgSiO_3 (small grey circles) [data from Murakami *et al.* 2007, EPSL 256: 47-54], $\text{Mg}_{0.88}\text{Fe}_{0.12}\text{SiO}_3$ (triangles), $\text{Mg}_{0.85}\text{Fe}_{0.15}\text{Si}_{0.95}\text{Al}_{0.05}\text{O}_3$ (square), $\text{Fe}_{0.18}\text{Mg}_{0.82}\text{SiO}_3$ (large black circles), $\text{Mg}_{0.58}\text{Fe}_{0.42}\text{Si}_{0.66}\text{Al}_{0.34}\text{O}_3$ (inverted triangles).

h. *Diffusion of the majorite component in garnet at mantle transition zone conditions (W. van Mierlo, F. Langenhorst, N. Miyajima, D.J. Frost and D.C. Rubie)*

Majorite ($\text{Mg}_4\text{Si}_4\text{O}_{12}$) is a high pressure polymorph of enstatite (MgSiO_3) and possesses the garnet structure. End-member majorite is only stable above 17 GPa, however since it forms a solid-solution with the other natural garnets it can be present as component at lower pressures in natural garnet. The amount of majorite component in garnet, and therefore the amount of enstatite that can be dissolved in garnet, increases with increasing pressure. Therefore, majoritic garnet is thought to constitute up to 40 vol.% of the transition zone of the Earth's mantle, making it the second most abundant phase after the high-pressure polymorphs of

olivine, wadsleyite and ringwoodite. Subducted oceanic crust might even consist of 80 vol.% of majoritic garnet. The transport properties of this majoritic garnet phase however, are not well understood. Since non-polymorphic reactions in dry systems are often transport-limited, determining the diffusivity of the majorite component in garnet may provide additional constraints on the time-scales on which reactions proceed in the Earth's mantle.

Diffusion experiments have been conducted in a multianvil apparatus with diffusion couples made of polished cylinders of natural single crystal Dora Maira pyrope ($\text{Py}_{93}\text{Alm}_5\text{Gr}_2$) and synthetic majoritic garnet ($\text{Py}_{55}\text{Mj}_{45}$) enclosed in a platinum capsule. Next to the pyrope – majoritic garnet diffusion couples, also one experiment with an almandine – pyrope diffusion couple (15 GPa, 1500 °C) was investigated. Two sets of runs were performed with the pyrope – majoritic garnet diffusion couples, the first set of five runs at 15 GPa between 1400 °C and 1900 °C and the second set of three runs at 1800 °C between 12 and 20 GPa. The duration of the experiments was dependent on exact pressure and temperature conditions, but was between 2 and 24 hours. After recovery of the run products, the capsule was cut perpendicular to the diffusion couple interface and then further prepared for TEM and electron microprobe analyses. TEM specimens were thinned to electron transparency by Ar ion-milling or using a FIB/SEM to cut thin films across the diffusion interface. Since all obtained diffusion profiles were too short to be measured by electron microprobe, *i.e.*, in the order of hundreds of nanometers, all the diffusion profiles were measured using TEM in combination with an EDS system.

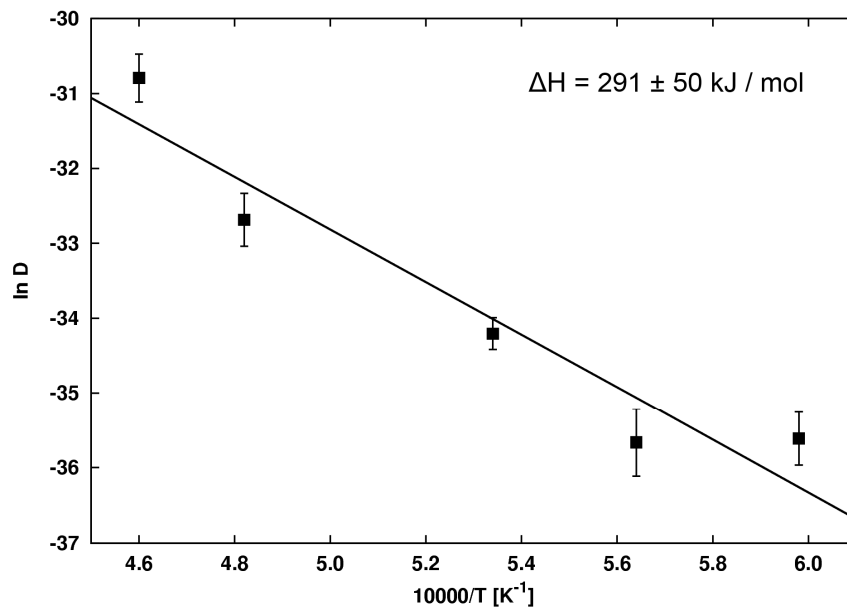


Fig. 3.4-9: The diffusivity of the majorite component in garnet as function of temperature for the pyrope – majoritic garnet diffusion couples at 15 GPa.

The experiments show that diffusion of the majorite component in garnet is slow and comparable in magnitude with silicon tracer diffusivity in wadsleyite and ringwoodite. From the first set of pyrope – majoritic garnet diffusion couples at constant pressure, we determined

the activation enthalpy of diffusion at 15 GPa to be 291 ± 50 kJ mol (Fig. 3.4-9), with a pre-exponential factor of 2.3×10^{-7} cm² s⁻¹. Comparing the results of the experiments with the pyrope – almandine couples with those of the pyrope – majoritic garnet samples also show that diffusion of Mg and Fe is 2 - 3 orders of magnitude faster than that of the majorite component, and that of Ca 1 – 2 order of magnitude faster. From the experiments done at constant temperature (1800 °C) we determined the activation volume for diffusion of the majorite component to be 3.3 ± 0.1 cm³ mol⁻¹ (Fig. 3.4-10), which is significantly lower than that for Mg tracer diffusivity (8 ± 1 cm³ mol⁻¹) determined by Chakraborty and Rubie (1996). We also determined from this data an activation energy of diffusion of 241 ± 54 kJ mol⁻¹, which is similar to previously determined activation energy for Mg tracer diffusion in garnet.

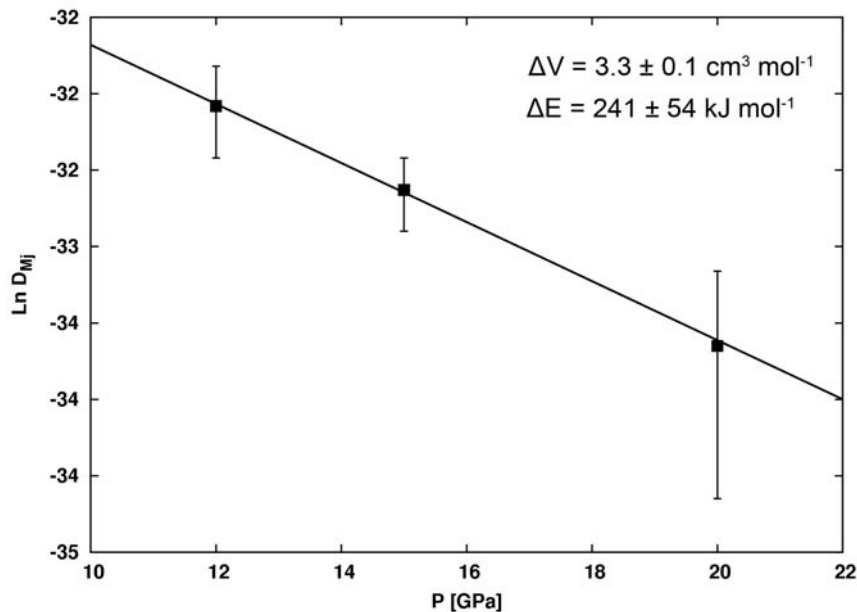


Fig. 3.4-10: The diffusivity of the majorite component as function of pressure at 1800 °C.

i. Single-crystal Ir-Pt interdiffusion in CaIrO₃ post-perovskite (R. McCormack and D.P. Dobson/London; F. Heidelbach; A. Beard, M.W. Ammann and J.P. Brodholt/London)

Diffusion is an important process in the lower mantle, exerting control over the rheological properties of deep mantle minerals. A recent study suggested, based on first principles calculations, that the anisotropy in the diffusivity of the lower mantle MgSiO₃ post-perovskite phase is extremely high. They predict the diffusivity in the *a*-direction to be six to eight orders of magnitude higher than that in the *b*- and *c*-directions. We have performed experiments to determine if a measurable anisotropy is in fact present in a post-perovskite phase. For this study we measured Ir-Pt interdiffusion in single crystals of the low-pressure post-perovskite analogue CaIrO₃.

Experiments were performed using diffusion couples consisting of single crystals of CaIrO₃ post-perovskite in a fine grained matrix of CaPtO₃ post-perovskite. The samples were

compressed to 4 GPa in a multianvil press and then heated to the target temperature and maintained at that temperature long enough to allow diffusion to proceed to a measurable level. Diffusion profiles in recovered samples were measured by electron microprobe (Fig. 3.4-11). The orientation of the crystallographic axes in the single crystals was determined using Electron Backscatter Diffraction (EBSD). The appropriate equations for diffusion in an infinite composite medium were convolved with a Gaussian function to account for structure in the electron beam. The resultant curve was then fitted to the measured diffusion profiles (Fig. 3.4-12). This fit returns values for diffusivity of Ir in the matrix and in the single crystal.

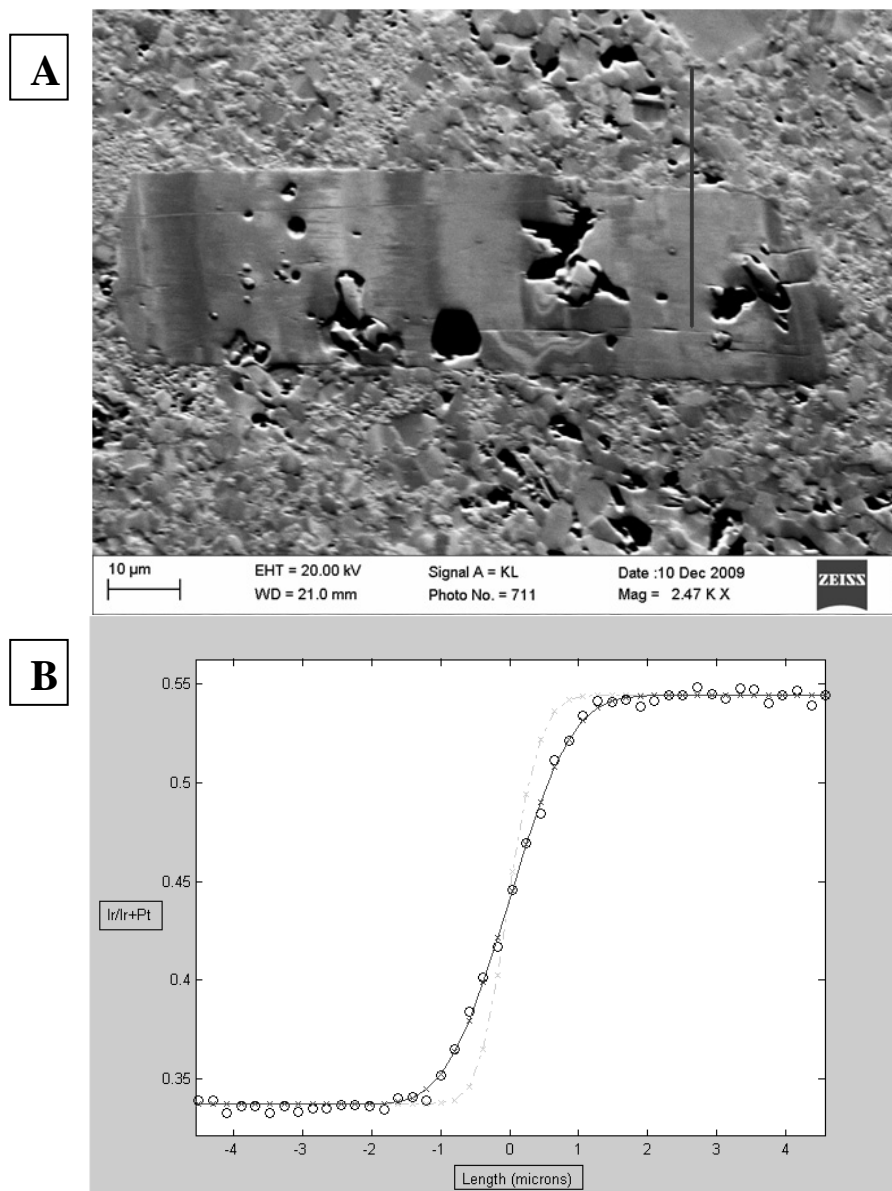


Fig. 3.4-11: Orientation contrast image of one CaIrO_3 single crystal annealed in CaPtO_3 at 1000 $^\circ\text{C}$ for 4 hours. The position of the profile in B is indicated by the black line. **B**: Ir diffusion profile, expressed as $\text{Ir}/(\text{Ir}+\text{Pt})$, (black circles). The fitted curve (Dark line) comprises a diffusion component (Light dotted line) and a Gaussian convolution to account for structure in the electron beam.

The non-perpendicular angle of the interface between the single crystal and the matrix (leading to artificially lengthened profiles) was corrected for by plotting the measured values for diffusivity in the matrix, which should be constant for all orientations at a given P,T condition, and finding the minimum value. This corresponds to the value that would be measured if the interface were perpendicular. The ratio of this value to the measured matrix diffusivity in any particular diffusion profile was then used to correct the measured diffusivities in the crystal to what they would be if the interface were perpendicular at that point.

The corrected diffusivities thus obtained were convolved with the crystallographic orientation in order to determine the diffusion tensor for CaIrO_3 . Our experiments give the relative speed of diffusion in the axial directions as $D_a > D_b > D_c$ in this system (Fig. 3.4-12). In addition we have performed *ab initio* simulations of the activation energy for migration of iridium in CaIrO_3 . These simulations agree in giving $D_a > D_b > D_c$. Preliminary experimental results give Arrhenius parameters of Ir-Pt interdiffusion in the axial directions of CaIrO_3 of:

$$\begin{array}{ll} D_0(a) = 26.6(15)e+6 \text{ m}^2/\text{s}; & H^*(a) = 581(81) \text{ kJ/mol} \\ D_0(b) = 27.5(13)e+3 \text{ m}^2/\text{s}; & H^*(b) = 527(17) \text{ kJ/mol} \\ D_0(c) = 2.8(1)e+2 \text{ m}^2/\text{s}; & H^*(c) = 483(9) \text{ kJ/mol} \end{array}$$

More experiments remain to be performed to verify these results. The uncertainties are large due to the fact that these data were only calculated using three experiments and would be expected to improve substantially as more data are added.

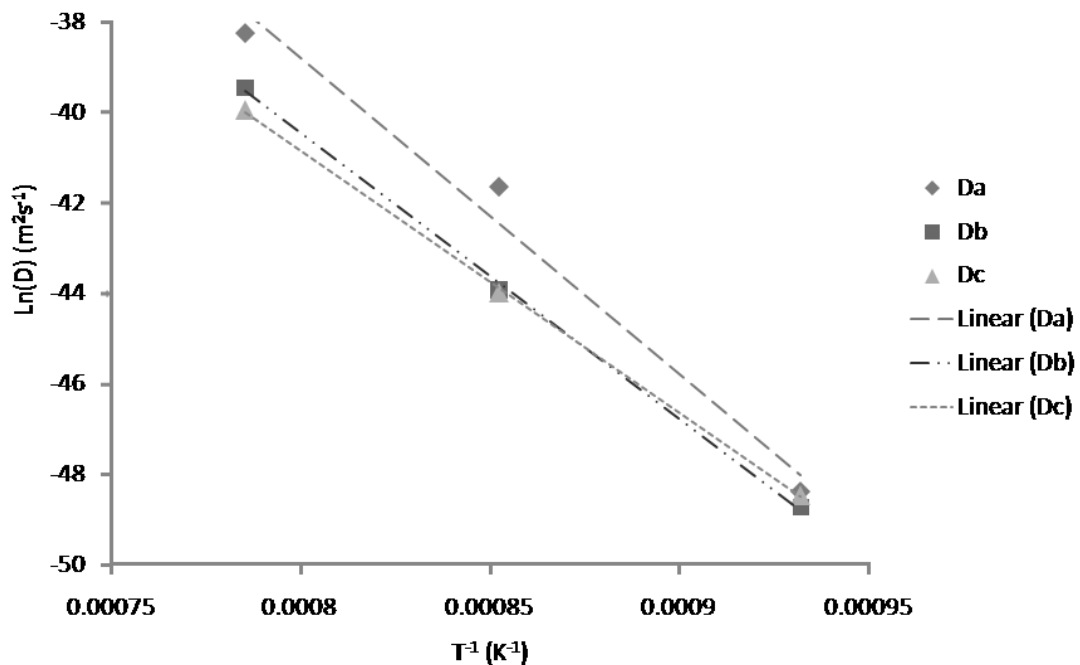


Fig. 3.4-12: Arrhenius plot for diffusion in the axial directions in CaIrO_3 . Diffusion in the b- and c- axial directions is very similar while diffusion in the a-direction is substantially higher.

j. Electrical conductivity of lower crustal minerals (X.-Z. Yang, H. Keppler, C.A. McCammon and H. Ni)

The high electrical conductivity in the lower continental crust has been recognized for more than three decades, however, the possible origin remains a controversial issue. Understanding the conductivity anomaly may provide insights into the composition, structure and rheology of the lower crust and of the tectonics of the whole continent.

We have measured the electrical conductivity of lower crustal clinopyroxene, orthopyroxene and plagioclase separated from fresh mafic xenolith granulites from north China, with particular emphasis on the effect of water content. Samples with different water contents were prepared using a 1-atm gas-mixing furnace, rapid quench cold-seal vessels and a piston cylinder apparatus. The electrical conductivity was analyzed with a Solarton-1260 impedance/gain phase analyzer in the frequency range of 10^6 -0.01 Hz in an end-loaded piston cylinder apparatus. For pyroxenes, the oxygen fugacity was buffered by Ni-NiO. The sample assembly for the conductivity measurement is illustrated in Fig. 3.4-13.

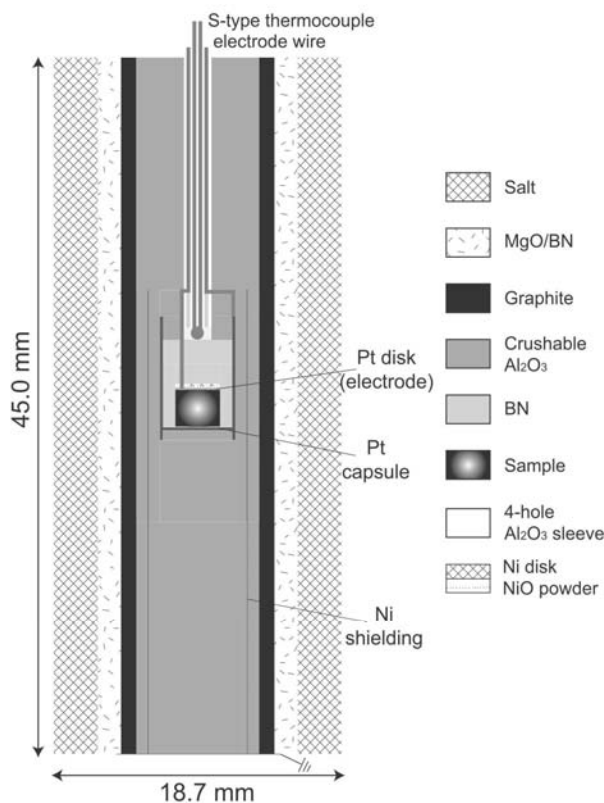


Fig. 3.4-13: Sample assembly for the conductivity measurement.

The results show that the electrical conductivity of lower crustal minerals can be significantly enhanced by the presence of minor amounts of water in the mineral structure, ranging from < 100 to hundreds of ppm depending on temperature and composition, to a comparable level as that measured by geophysical deep sounding techniques (*e.g.*, 10^{-4} to 10^{-1} S/m for most

regions: Fig. 3.4-14). Accordingly, the high electrical conductivity in the lower crust may mostly be accounted for by the main mineral phases themselves, without the widespread presence of other highly conductive materials such as fluids, melts or hydrous minerals. The difference of conductivity between pyroxenes and plagioclase at similar conditions (*e.g.*, temperature, pressure and water content) may explain the conductivity anisotropy observed in some regions of the lower crust, if plagioclase and clinopyroxene occur in separate bands as often observed in lower-crustal granulite xenoliths. Our results imply that the ductile deformation and flow of the lower crust may be mainly controlled by the viscosity of the minerals at high temperature and elevated water content, rather than by the effects of fluids or melts.

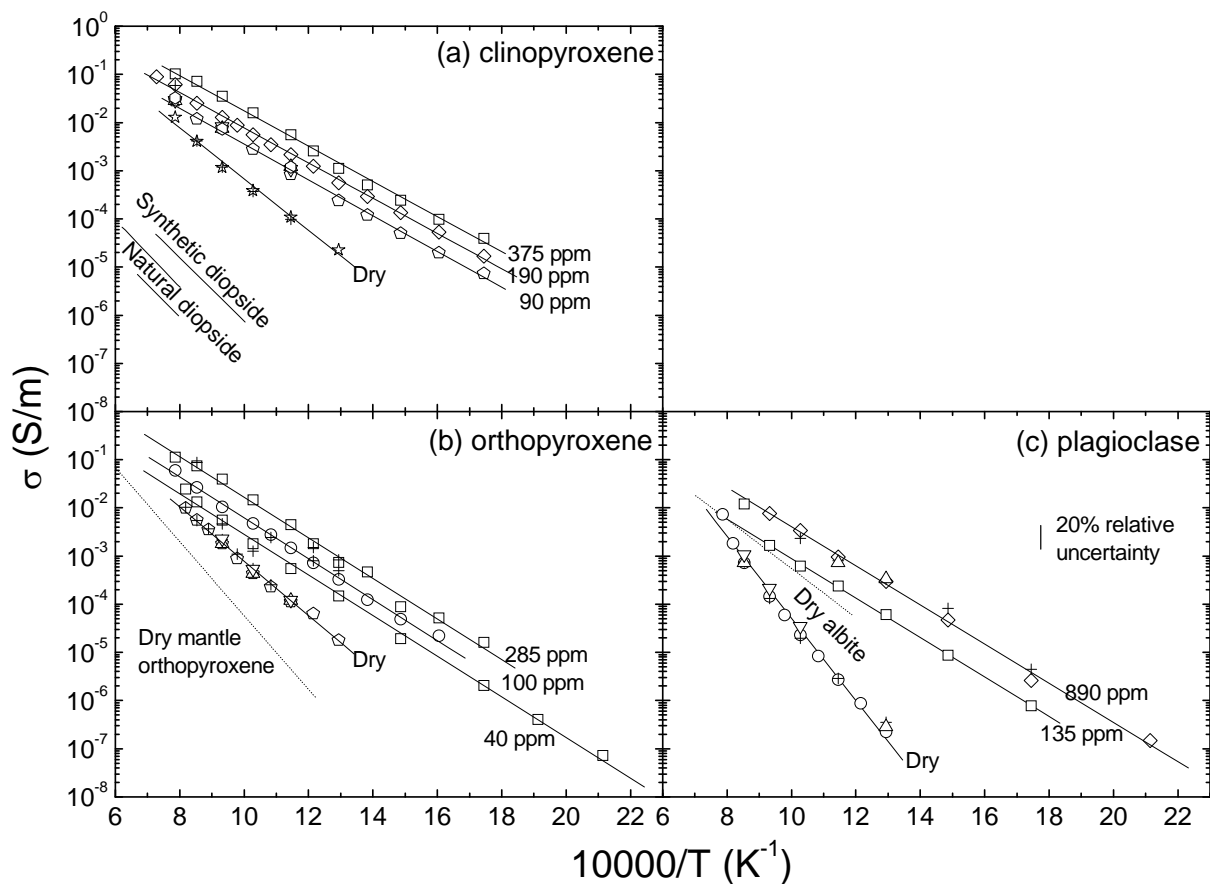


Fig. 3.4-14: Electrical conductivity of lower crustal (a) clinopyroxene, (b) orthopyroxene and (c) plagioclase. Data were obtained at 12 kbar.

k. *Iron oxidation state in (Mg,Fe)O diffusion couples determined by the flank method (K. Otsuka/New Haven, M. Longo/Padua, C.A. McCammon and S. Karato/New Haven)*

The small amounts of Fe^{3+} dissolved in (Mg,Fe)O ferropericlase, the second most abundant phase in the lower mantle, affect various transport properties such as atomic diffusion, electrical conductivity, and rheology as well as phase relations and element partitioning. Since

the $\text{Fe}^{3+}/\sum\text{Fe}$ ratio in (Mg,Fe)O changes by orders of magnitude with variation of thermochemical conditions such as oxygen fugacity, chemical composition, temperature, and pressure, it is important to explore the solubility of Fe^{3+} in a wide range of conditions relevant to the lower mantle.

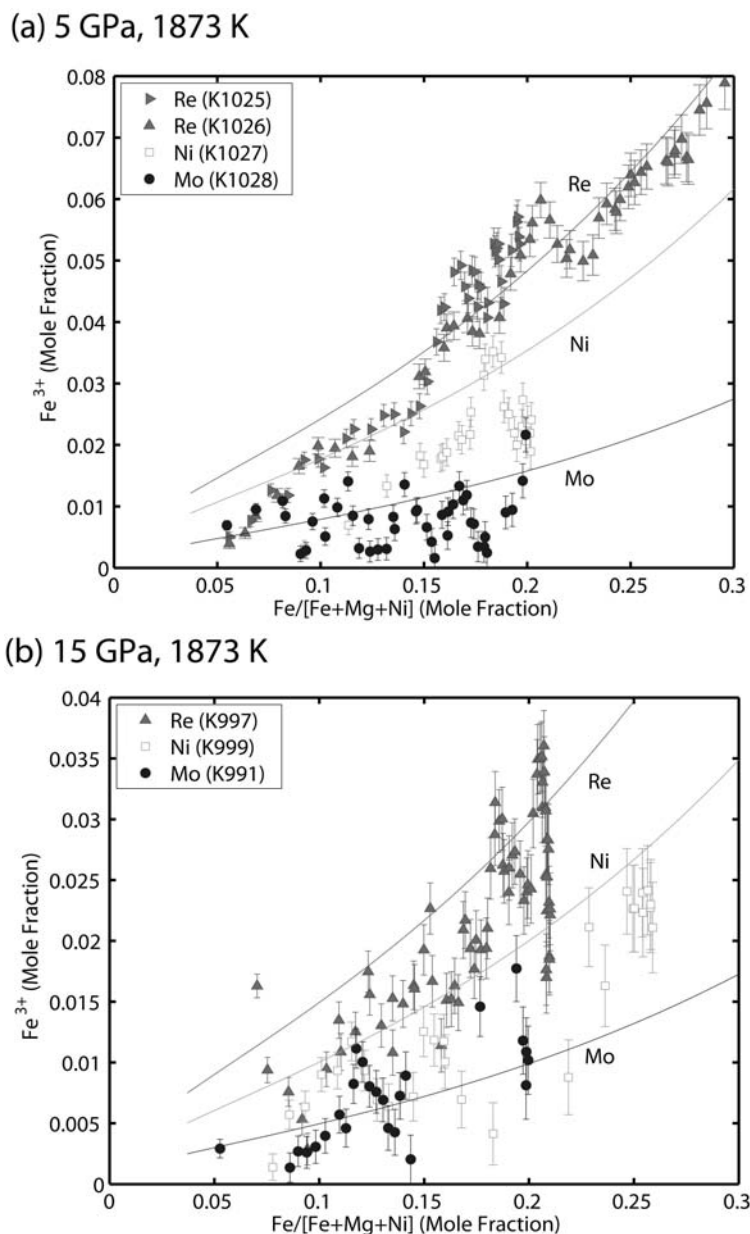


Fig. 3.4-15: The Fe^{3+} solubility in (Mg,Fe)O determined using the flank method plotted against the $\text{Fe}/(\text{Fe}+\text{Mg}+\text{Ni})$ mole fraction obtained at 1873 K and (a) 5 GPa and (b) 15 GPa. The oxygen fugacity decreases in the order Re, Ni and Mo.

Here, we performed high-pressure and high-temperature experiments on Mg and Fe interdiffusion in (Mg,Fe)O to investigate Fe^{3+} solubility over a broader range of the Mg/(Mg+Fe) ratio than previously reported. The (Mg,Fe)O diffusion couples, consisting of

MgO and (Mg,Fe)O single crystals, were annealed at 1673-1873 K and 5-15 GPa under the control of oxygen fugacity by metal and oxide solid-state buffers (Re-ReO₂, Ni-NiO, or Mo-MoO₂). Annealing duration was determined such that diffusion flow of Fe³⁺ reached a steady state but that of Mg and Fe did not. We applied the flank method using a standard electron microprobe to investigate the Fe³⁺ content along Mg-Fe interdiffusion profiles. Compared with other techniques such as Mössbauer spectroscopy and electron energy loss spectroscopy, the flank method has advantages of relatively high spatial resolution (down to a few microns) and large spatial coverage (more than mm), which makes it suitable to determine the Fe³⁺ content in diffusion couples.

Figure 3.4-15 shows the Fe³⁺ content obtained in this study. The Fe³⁺ content increases with increasing oxygen fugacity and Fe/(Fe+Mg+Ni) ratio, while it decreases with pressure and temperature at fixed oxygen fugacity. Our results are reasonably consistent with previous high-pressure results for constant Mg/(Mg+Fe) ratios as well as for the compositional dependence at room pressure. We thus conclude that the Fe³⁺ content in (Mg,Fe)O diffusion couples reaches chemical equilibrium at the local chemical composition of Fe, Mg, and Ni under externally defined conditions of oxygen fugacity, pressure, and temperature.

1. Mott transition of wüstite at high pressure: the influence of ferric iron (K. Glazyrin, L.S. Dubrovinsky and S. Klotz/Paris)

Being a model system for Mott transitions, wüstite (Fe_{1-x}O) is of great importance in solid state physics. At ambient conditions Fe_{1-x}O is paramagnetic (PM) and crystallizes in the cubic NaCl structure. However, cooling to temperatures below 200 K promotes a transition to an antiferromagnetic structure (AFM) with spins aligned along the [111] direction. The magnetic transition is accompanied by a transformation of the wüstite structure from cubic (C) to rhombohedral (RH) symmetry. In a previous study of Fe_{1-x}O (x=0.062) we have shown that the magnetic and structural transitions do not occur at the same temperature and the application of pressure results in an even more complicated behaviour. The higher the pressure is, the larger is the difference between the critical temperatures of the transitions. This study addresses the so-far unknown influence of ferric iron on the Mott transition in wüstite at high pressure.

We performed low temperature scans of Fe_{1-x}O (x=0.075) at the neutron powder diffraction D20 beam line ILL, Grenoble, France. The scans were collected at three different pressures (0 GPa, 4.8 GPa, 9 GPa). Data refinement was done as in our previous study, using the Fullprof software package for Rietveld analysis. This yields values of unit cell parameters and magnetic moment of iron in the antiferromagnetic state. Figure 3.4-16 shows an excerpt of powder diffraction patterns collected at 4.8 GPa. The arrows mark the beginning of magnetic (upper part) and structural transitions (lower part) determined from the Rietveld analysis. The results of our experiments are summarized in Fig. 3.4-17. Despite the slight difference in

ferric iron content, the two wüstites studied show transitions at significantly different temperatures and pressures, suggesting a very strong influence of the ferric iron content on Mott transitions.

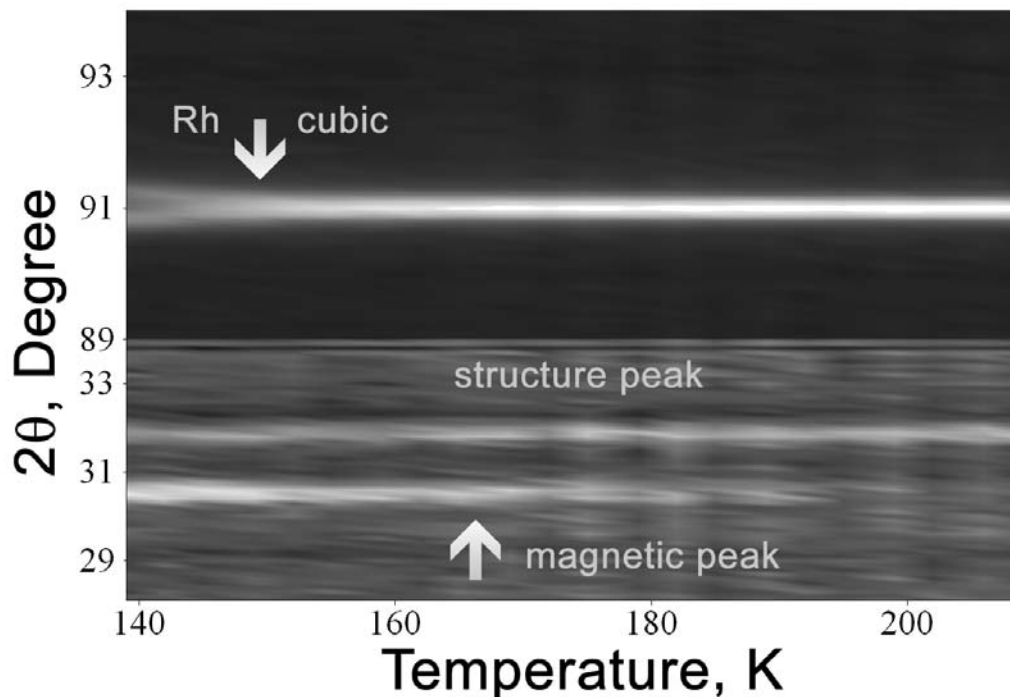


Fig. 3.4-16: Maps of powder diffraction patterns at different 2theta angles. Arrows mark the beginning of structural (upper) and magnetic transition (lower).

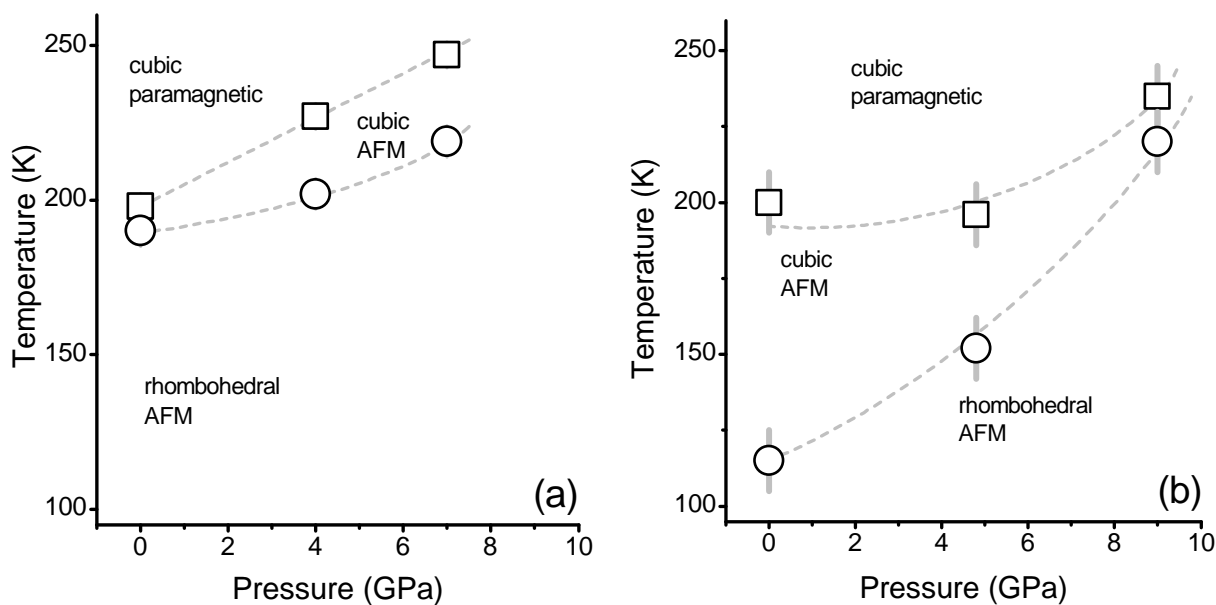


Fig. 3.4-17: Comparison of phase diagrams for two wüstite Fe_{1-x}O compositions: (a) $x=0.062$, (b) $x=0.075$.

m. Lattice dynamics of rutile and anatase (V. Vlcek, G. Steinle-Neumann and E. Holbig)

At ambient conditions TiO_2 can be stable as rutile (spacegroup $P4_2/mnm$, with 2 formula units in the unit cell, $Z=2$), but also anatase ($I4/amd$, $Z=4$) and brookite ($Pcab$, $Z=8$) both synthetically and naturally as accessory minerals in rocks. Anatase and brookite convert to rutile at higher pressures and temperatures. Rutile has been confirmed as the stable phase by drop solution calorimetry. However, density functional theory-based all-electron calculations consistently predict anatase stable over rutile in the ground state.

Here we explore the influence of vibrational contributions to the Helmholtz free energy in order to test whether they can account for the discrepancy between calorimetry and ground state computations. We compute the full phonon dispersion curves for both rutile and anatase using the linear-response method as implemented in the abinit software. We explore the structure and the phonon dispersion curves for both the local density (LDA) and generalized gradient approximations (GGA) to the exchange and correlation potential. Static energies, zero pressure volumes (V_0), and structural parameters are evaluated with the all-electron projector-augmented wave (PAW) method, while current limitations of the abinit software only allow linear-response calculations with pseudopotentials (PS).

For evaluation of dynamical matrix, the Born effective charges and the dielectric tensor were determined. Both polymorphs show high values of dielectric constant that are in reasonable agreement with experimental values and Born effective charges are much bigger than the nominal charges. The high effective charges can be understood in terms of modified bond hybridization during displacement: during the movement of a cation away from an anion the electrons are transferred to the negative atoms.

From the dynamical matrix the normal mode eigenfrequencies were calculated for both rutile and anatase using GGA and LDA (Fig. 3.4-18). For anatase both approximations yield similar results. However, only LDA provides relevant data for rutile, and GGA computations exhibit soft modes for one of the B_{1g} branches at $q \rightarrow 0$, suggesting a displacive phase transformation to the CaCl_2 structure. This is caused by different zero pressure volumes from the PAW and PS calculations. When the volume is increased to V_0 obtained from the PS calculations the frequency value becomes real. This indicates that phonons in rutile are very sensitive to structural parameters.

The phonon contribution to the Helmholtz free energy can be evaluated by integration over all the modes through the phonon density of states. The phonon free energy drops as entropy increases with temperature. When phonon energies are combined with static ground state calculation the Helmholtz free energy for both polymorphs at very low temperatures is very similar, with anatase being slightly more stable than rutile (Fig. 3.4-19). With increasing temperature anatase becomes more favored. Since the difference is very small, the anharmonic behaviour of rutile lattice even at low temperatures most probably stabilizes the structure and further reduces the free energy.

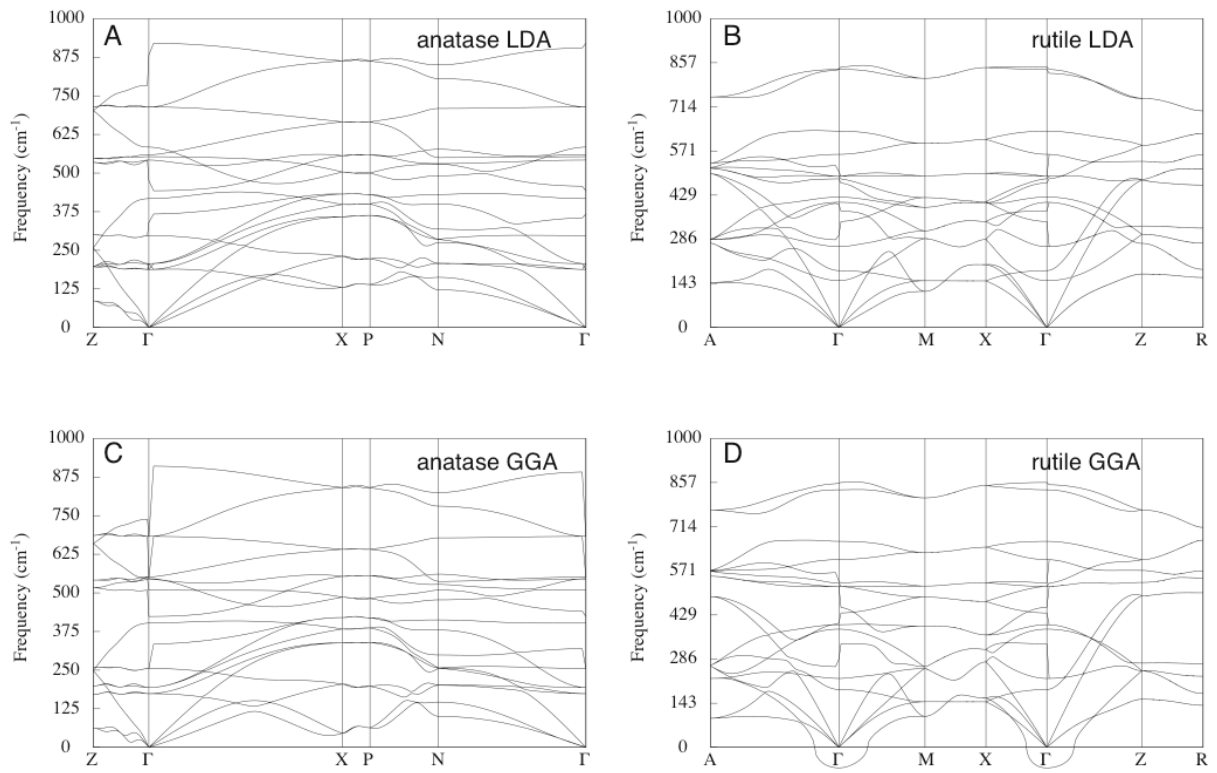


Fig. 3.4-18: Phonon dispersion curves calculated for anatase (left column) and rutile (right column), with the local density (LDA, first row) and generalized gradient approximations (GGA, second row) to exchange and correlation.

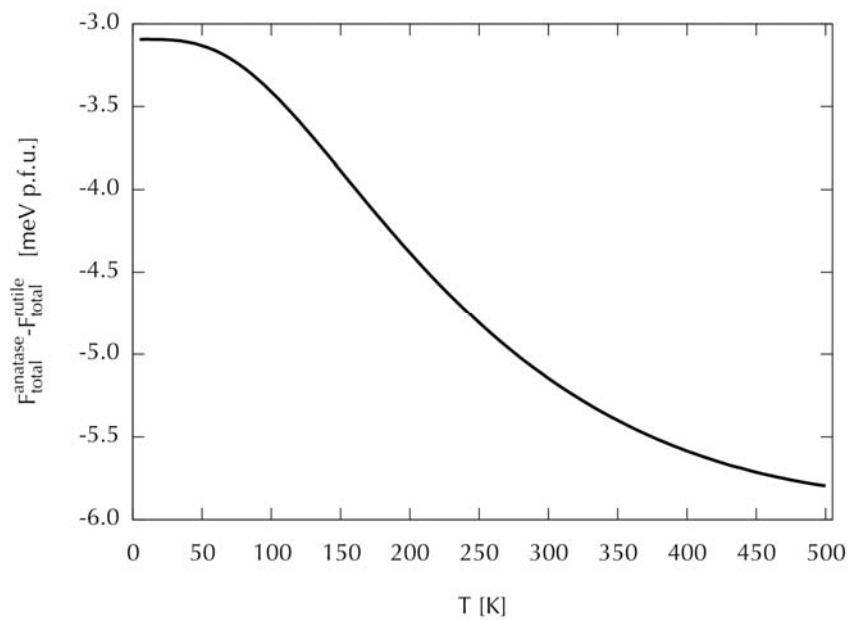


Fig. 3.4-19: Helmholtz free energy difference between rutile and anatase at their respective static zero pressure volume.

3.5 Fluids and their interaction with melts and minerals

The Earth's atmosphere and oceans formed by the degassing of Earth's interior. An often-neglected component in this system is nitrogen. For a long time, it was believed that the behaviour of nitrogen is very simple, with most of the nitrogen budget of our planet residing in the atmosphere, where N_2 was considered to be a purely inert component. However, recent work has shown that the nitrogen partial pressure indirectly contributes to the greenhouse effect by broadening the spectral lines and therefore enhancing the infrared absorption of greenhouse gases. Moreover, there is increasing evidence for the existence of a deep nitrogen reservoir in the mantle and for recycling of nitrogen into Earth's interior in subduction zones. The first contribution in this chapter therefore focuses on the speciation of nitrogen in mantle fluids using Raman spectroscopy of synthetic fluid inclusions. The data show that ammonia is the stable form of nitrogen in aqueous fluids throughout most of the upper mantle, while in subduction zones, nitrogen is partially oxidized to N_2 . One implication of these data is that the mantle abundance of nitrogen based on N/Ar ratios in magmas and volcanic gases is likely underestimated.

Hydrothermal deposits are the world's most important source of molybdenum and tungsten. It has been speculated that the regional concentration of some molybdenum deposits is due to some pre-enrichment of this element during subduction zone processes. Two contributions therefore focus on the behaviour of molybdenum and tungsten, one by looking at Mo and W mobility in aqueous fluids at mantle pressures, while the other one calibrates molybdenite (MoS_2) solubility at lower pressures relevant for the formation of hydrothermal ore deposits. The data show that under subduction zone conditions, in particular tungsten very strongly partitions into aqueous fluids, while the behaviour of molybdenum is more sensitive to redox conditions and fluid salinity.

The last two contributions of this section study the role of bacteria in the dissolution of sulfide minerals. It is now generally recognized that many seemingly inorganic processes occurring on Earth's surface are mediated by microorganisms, but the mechanisms are not always well understood. A particularly interesting experiment is described here: The presence of bacteria enhances the dissolution rate of pyrrhotite even if bacteria and pyrrhotite are separated by a semi-permeable membrane. This implies that not the bacterium itself, but relatively small molecules released from it are responsible for accelerating the dissolution of sulfides.

a. Nitrogen speciation in mantle fluids (Y. Li, A. Audétat and H. Keppler)

Nitrogen speciation in fluids controls the nitrogen exchange between Earth's atmosphere, crust, and mantle. NH_3 released from the Earth's young mantle into the atmosphere may have been an important ingredient for the abiotic synthesis of organic compounds and the origin of life. In addition, NH_3 is a strong greenhouse gas that could resolve the faint young Sun paradox. Minerals in Earth's interior may be a major reservoir for nitrogen, with NH_4^+ substituting for K^+ .

Until now, little is known about the nitrogen species in fluids in Earth's deep interior. We therefore conducted a systematic study of nitrogen speciation in aqueous fluids as a function of pressure, temperature and oxygen fugacity by trapping N-H-O fluids as fluid inclusions in minerals (pre-cracked San Carlos olivine or HF-etched Brazil quartz). Experiments were carried out in a piston cylinder apparatus with a $\sim 11\text{ mol/L}$ solution of NH_3 in water as starting material. The temperatures and pressures ranged from 600 to 1300 °C and from 15 to 30 kbar, to simulate conditions typical for the upper mantle and for subduction zones. A double capsule technique was used to control oxygen fugacity by three different buffers (Fe-FeO, Co-CoO, Ni-NiO).

The recovered olivine or quartz crystals with fluid inclusions were polished for Raman micro-spectroscopic measurements. All the Raman spectra showed that at the conditions investigated, N_2 and/or NH_3 are the only detectable nitrogen species (Fig. 3.5-1). The NH_3 concentration in the quenched aqueous solution at room temperature was calibrated by measuring the Raman spectra of a series of solutions of known concentration. With increasing NH_3 concentration, the ratio of the height of the sharp NH_3 peaks to the area of the entire complex Raman signal in the 3000-3500 cm^{-1} range increases and this relationship was used for calibration (Fig. 3.5-2). NH_3 concentration in the vapor phase was estimated using Henry's Law; the N_2 concentration in the fluid was calculated by mass balance.

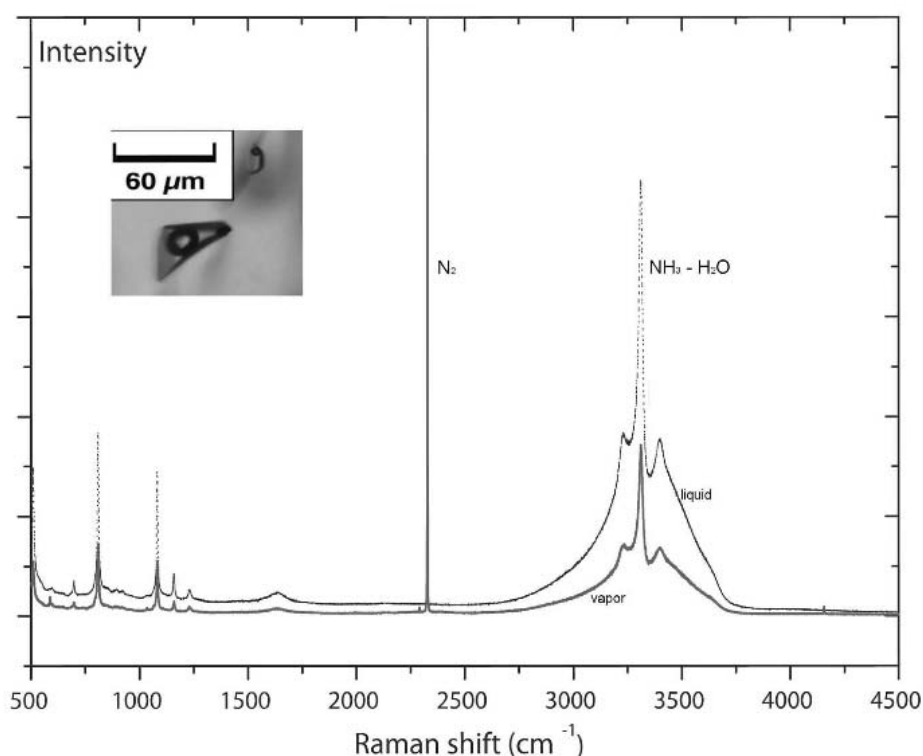


Fig. 3.5-1: A representative synthetic fluid inclusion in quartz and its Raman spectrum at ambient conditions. The fluid inclusion was trapped at 700 °C, 1.5 GPa and Ni-NiO buffer conditions. The N_2 peak is located at 2331 cm^{-1} , whereas the strongest peak of the aqueous $\text{NH}_3\text{-H}_2\text{O}$ complex is around 3336 cm^{-1} . N_2 is mainly stored in the vapor phase, NH_3 in the liquid phase.

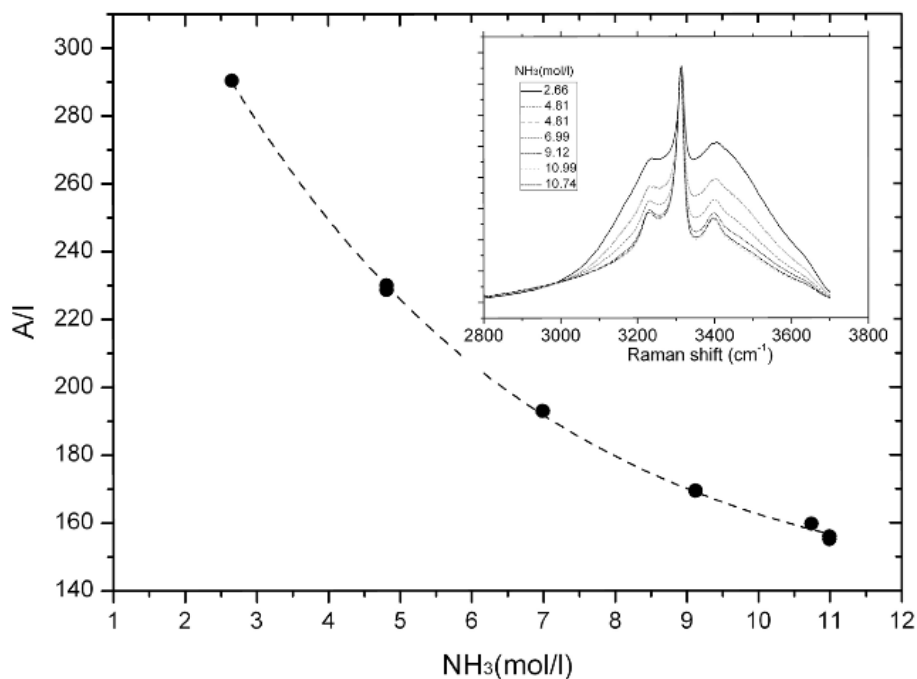


Fig. 3.5-2: The calibration curve used to determine NH₃ concentration (mol/l) from Raman spectra of aqueous solutions at ambient conditions. Plotted is the ratio of peak area A in the 3000-3500 cm⁻¹ region over the peak height I of the strongest peak of NH₃ as function of NH₃ concentration. The insert shows the Raman spectra used for calibration.

The equilibrium $N_2 + 3 H_2 = 2 NH_3$ can be described by the equilibrium constant

$$K = \frac{x_{NH_3}^2}{x_{N_2} f_{H_2}^3} \quad (3.5-1)$$

where x are molar fractions and f_{H_2} is hydrogen fugacity. The experiments at 1.5 GPa with different oxygen buffers show a linear relationship between $\ln K$ and $1/T$ (temperature in Kelvin; Fig. 3.5-3).

The preliminary results of this study imply that nitrogen in subduction zone fluids, in particular for cool geotherms, is mostly present as NH₃. Therefore, nitrogen should behave similar to K, as NH₄⁺ readily substitutes for K⁺. Nitrogen is probably partially subducted into the deep mantle and partially returned into the shallow arc mantle. The NH₃ ascending in fluids from subduction zones into the overlying mantle partially decomposes into H₂ and N₂ due to increasing temperature and decreasing pressure. Since nitrogen behaves as an atmophile element only in the form of N₂, but not in the form of NH₃, the nitrogen abundance of the bulk silicate Earth based on N/Ar ratios in fluids and magmas must be underestimated. Our results also suggest that NH₃ may be a major nitrogen species released into the Hadean's atmosphere from the Earth's young and very reduced mantle.

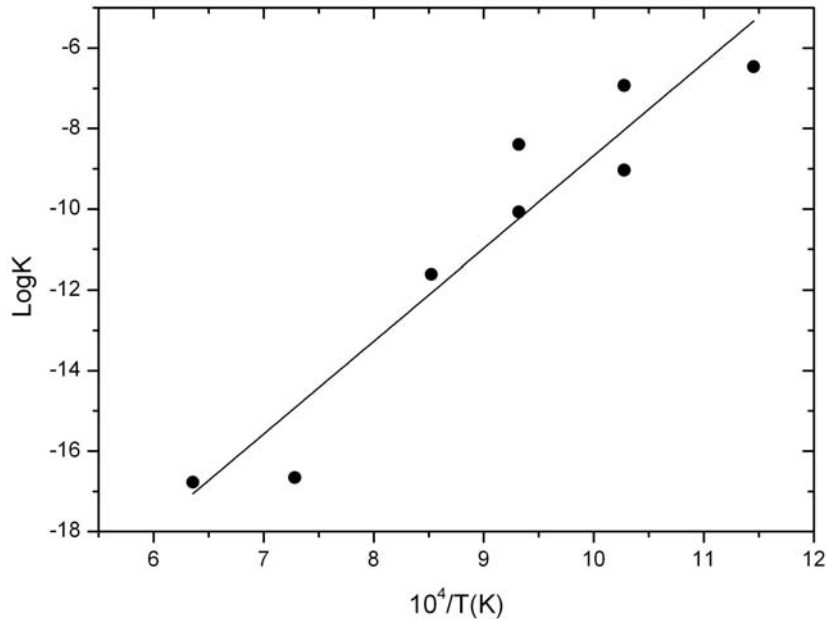


Fig. 3.5-3: The equilibrium constant K for the reaction $N_2 + 3 H_2 = 2 NH_3$ at 1.5 GPa.

b. Tungsten and molybdenum mobility in subduction zone fluids (E. Bali, A. Audétat and H. Keppler)

High precision W- and Mo-analyses of island arc lavas confirm that both W and Mo can be mobilized by subduction zone fluids, although their relative enrichment can be decoupled. The decoupling might be related to (1) initially different Mo/W ratios in the subducted component; (2) the presence or absence of residual sulfides in the source region that might sequester Mo but not W during melting; (3) or a different redox-sensitivity of W and Mo mobility in aqueous fluids. Our study focuses on this last possibility.

We carried out W- and Mo-oxide solubility experiments at 26.1 kilobars, 600 to 800 °C, at fO_2 conditions ranging from -5.09 to +1.94 logarithmic units relative to the FMQ buffer, and fluid salinities between 2 and 20 wt.% NaCl_{equiv.} Fluids were trapped as synthetic fluid inclusions in quartz and analyzed by Laser-Ablation-ICP/MS. We also investigated whether the incorporation mechanism of these elements in mantle minerals changes as a function of these variables.

W-oxide solubility is high and nearly independent on the NaCl content of the fluid at 800 °C (Fig. 3.5-4a), suggesting that W did not dissolve as chloride complexes. In contrast, the solubility of Mo-oxide is doubled (Fig. 3.5-4a) over the same salinity range. Both W- and Mo-oxide solubility depends strongly on fO_2 , although to a different extent in different fO_2 regimes (Fig. 3.5-4a). W-oxide solubility increases strongly with fO_2 from the IW (iron-wüstite) to the Co-CoO buffer, whereas between Co-CoO and Re-ReO₂ there is a further, but less significant increase. In contrast, Mo-oxide solubility increases more than an order of magnitude in the latter fO_2 interval. According to the relationship between Mo-oxide solubility and fO_2 , Mo seems to be dissolved in the fluid phase dominantly as Mo⁶⁺. The

relationship between W-oxide solubility and fO_2 can be explained by the change of oxidation state of W in the solid phase and the dissolution mechanisms. At reducing conditions, WO_2 is the stable form of W-oxide. The exponent of 0.229 in the equation of Fig. 3.5-4b would suggest that W at these conditions dissolved in a W^{4+}/W^{6+} mixed valence state in the fluid. At more oxidizing conditions W-oxide recrystallized to a Na-W bronze with a composition of $Na_{0.14-0.17}WO_3$. At these conditions, W dissolved in the fluid phase probably mostly as W^{6+} .

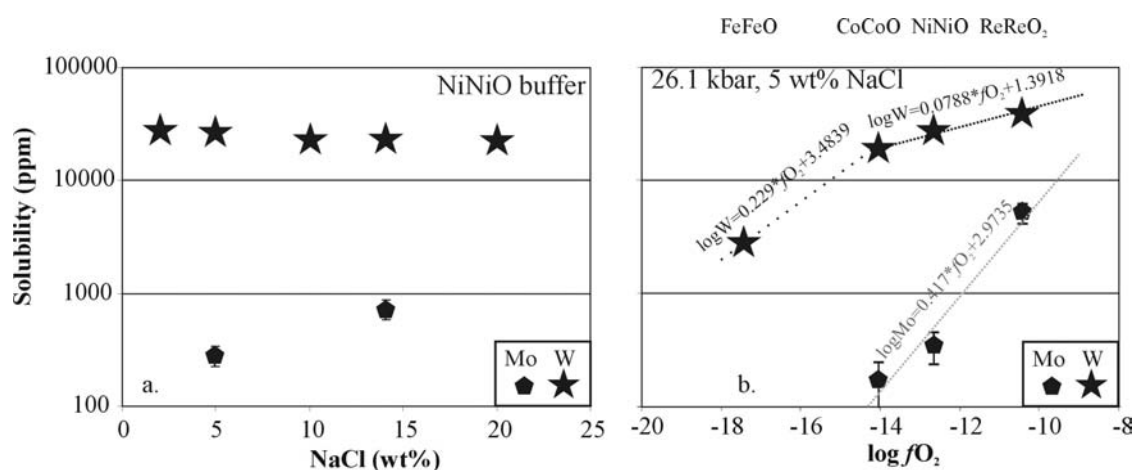


Fig. 3.5-4: Solubility of W- and Mo-oxide at 800 °C and 26.1 kbar. (a) Solubility as a function of fluid salinity studied at Ni-NiO buffer conditions. (b) Solubility as a function of oxygen fugacity at constant salinity of 5 wt.% $NaCl_{equiv}$. Equations in figure (b) show the relationship between solubility and oxygen fugacity, in which the concentrations of W and Mo are in molality.

In a separate set of experiments, we crystallized upper mantle minerals in the presence of excess Mo- or W-oxide. These experiments show that clinopyroxene is the major host of W and Mo in the mantle, except maybe if sulphides are present. The maximum solubility of W and Mo in clinopyroxenes was 60 and 30 ppm, respectively, independent of oxygen fugacity at 1000 °C and 26.1 kbar. This means that fluid/(bulk mantle) partition coefficients for both Mo and W are very high. In particular for W, the partition coefficient is independent of fluid salinity and it is only slightly affected by oxygen fugacity under the relatively oxidizing conditions that usually prevail in subduction zones. Therefore, W abundance could be a powerful tracer for the fraction of fluid absorbed in the zone of melting. The Mo/W ratio, on the other hand, is particularly sensitive to oxygen fugacity and to a smaller degree to fluid salinity.

c. Molybdenite solubility in aqueous fluids at 600-800 °C, 200 MPa: A synthetic fluid inclusion study (L. Zhang and A. Audétat)

Although the general principles of Mo enrichment in molybdenite deposits are relatively well understood, little is known about the mechanism of molybdenum transport in hydrothermal

fluids, especially at high temperature and pressure. Most previous experimental studies were performed in sulfur-free systems, but the recent discovery of molybdenite (MoS_2) saturation in many barren and ore-forming magmas implies that Mo-transport in hydrothermal fluids is controlled by the solubility of molybdenum sulfide over their entire evolution from magmatic to hydrothermal ore-forming conditions. It is thus necessary to constrain molybdenum solubility in sulfur-bearing systems and to understand the main controlling parameters.

We have conducted MoS_2 solubility experiments in aqueous solutions containing 2-20 wt.% NaCl and 0-2 M HCl at 600-800 °C, 200 MPa, and various f_{O_2} - f_{S_2} conditions imposed by mineral buffers. Quartz pieces with a rough surface containing deep, narrow etch channels were used to trap the fluid inclusions. For each experiment, 1-3 mg MoS_2 , 20-30 mg mineral buffers, an etched quartz piece and 100-150 ml NaCl (-HCl) solutions spiked with ~ 400 ppm Rb and Cs were loaded into Au or Pt capsules. All experiments were performed in rapid-quench hydrothermal autoclaves. After an initial period of equilibration for 1-7 days, the quartz pieces were cracked *in situ* by dragging the capsule rapidly to the cold end of the autoclaves and then moving it back to the hot end, where it was kept for another 2-4 days to allow the cracks to be healed. Two different types of fluid inclusions were obtained in this way (Fig. 3.5-5): “Primary” inclusions that formed relatively early (before the *in situ* cracking) due to quartz growth over the etched quartz surface, and “refilled” inclusions that were re-opened during the *in situ* cracking and thus contain fluid trapped after a known equilibration time.

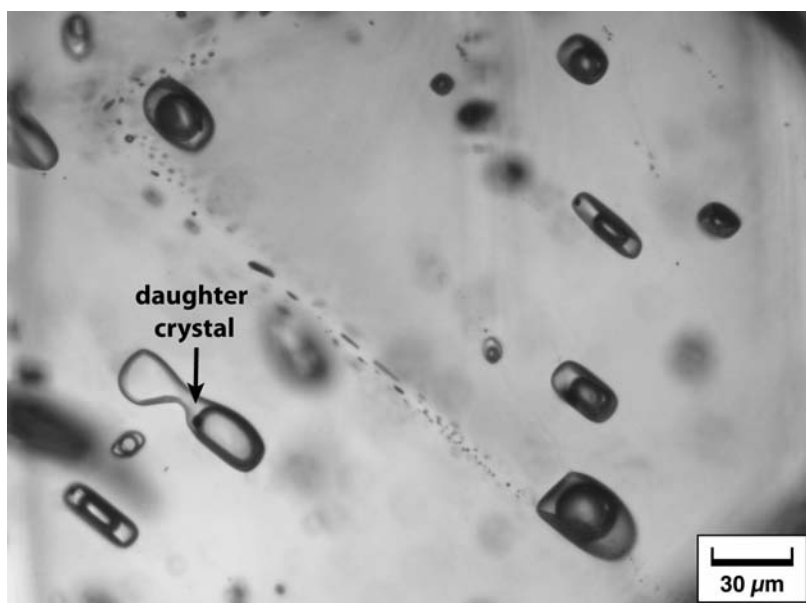


Fig. 3.5-5: Synthetic inclusions in quartz, produced at 800 °C and 200 MPa. The inclusion on the lower right was intersected by a crack during the *in situ* cracking and thus represents a refilled inclusion. Also visible are small opaque precipitates (daughter crystals) in some of the inclusions.

The major and trace element contents of both the primary and refilled inclusions were analyzed by LA-ICP-MS, using a 193 nm Excimer Laser (Coherent) attached to an Elan DRC-e (Perkin Elmer) instrument. NIST SRM 610 glass was used as external standard, whereas the Cs concentration of the starting fluid was used as internal standards.

Our LA-ICP-MS data suggest that the refilled inclusions provide the most reliable and reproducible results, with primary inclusions showing comparable compositions in some runs, but significantly lower and variable metal concentrations in other runs. The measured Mo concentrations in primary inclusions range from 5 to 3000 ppm and increase with increasing temperature, NaCl concentration and oxygen fugacity, but decrease with increasing sulfur fugacity. Our data can be fitted by the following equation:

$$\log C_{Mo} = 0.464 \log fO_2 - 0.426 \log fS_2 + 0.731 \log C_{NaCl} - 0.342 (1000/T) + 3.777 \quad (3.5-2)$$

where C_{Mo} and C_{NaCl} are the concentrations of Mo and NaCl in mol/kg, T is given in Kelvin, and fO_2 and fS_2 are oxygen and sulfur fugacity in bar. Corresponding isopleths in the $\log fO_2$ - fS_2 diagram at 800 °C / 200 MPa and a fluid salinity of 8 wt.% NaCl are shown in Fig. 3.5-6. Importantly, the equation fits very well both our and Cao's (1989) data, suggesting that it is valid over a wide range of P-T- fO_2 - fS_2 -X. Thus, if applied to Mo concentrations measured in natural fluid inclusions, our molybdenite solubility model can be used to provide constraints on the fO_2 and fS_2 conditions of ore formation.

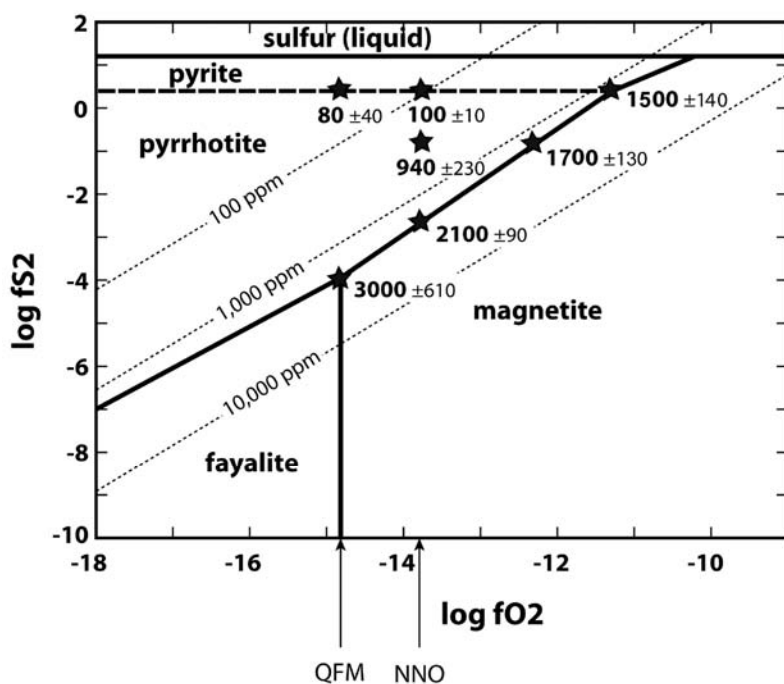


Fig. 3.5-6: Measured molybdenite solubility as a function of oxygen and sulfur fugacity at 8 wt.% NaCl, 800 °C / 200 MPa (stars). Dashed lines represent fitted solubility isopleths in ppm by weight based on equation 3.5-2.

d. *The influence of Acidithiobacillus ferrooxidans and Acidithiobacillus thiooxidans on surface morphology and dissolution rates of pyrrhotite (J. Hopf, K. Pollok and F. Langenhorst)*

Pyrrhotite ($Fe_{1-x}S$) is an abundant sulfide mineral in natural rocks and mine wastes. Microbes can significantly accelerate its rate of oxidation and thereby enhance the production of sulfuric acid, causing environmental problems known as Acid Mine Drainage (AMD). To

study the influence of microorganisms on the dissolution rates and to examine the mechanisms of dissolution, we performed dissolution experiments on well-polished pyrrhotite cubes in the presence of the two acidophilic species *Acidithiobacillus ferrooxidans* (*A.f.*, Fe- and S-oxidizing bacterium) and *Acidithiobacillus thiooxidans* (*A.t.*, S-oxidizing bacterium).

The polished pyrrhotite surfaces were dissolved in abiotic and biotic oxidation experiments under acidic conditions. Surface morphology of abiotic/biotic altered pyrrhotite surfaces was measured by 3D confocal surface microscopy (μ Surf) and scanning electron microscopy (SEM) at various reaction times (7, 14 and 28 days).

These experiments reveal that *A.f.* distinctly augments the oxidation of pyrrhotite and particularly favors the dissolution of troilite (FeS) lamellae, which are embedded in the Fe-deficient pyrrhotite matrix. *A.f.* develops a whitish biofilm on the pyrrhotite surfaces, whereas *A.t.* does not form a visible biofilm. After washing (biofilm removal), both strains show cell residues on the surface. *A.t.* shows a stronger cell adhesion on the surface than *A.f.* Contrary to observations of bacterial pyrite oxidation both bacterial strains show no preferred orientation for cell attachment on the pyrrhotite surface. To investigate the impact of biofilm formation on mineral dissolution, experiments were performed with cells separated from the mineral using a dialysis capsule. These experiments revealed a slower increase in surface roughness compared to free cells, indicating that bacterial substances below 20.000 Dalton (molecular weight of molecules) and not the bacterial cells itself are actively involved in the dissolution process of pyrrhotite. Troilite lamellae dissolve to a similar extent in both biotic experiments, but not in the control experiment.

Pyrrhotite dissolution rates in this work were determined by measuring the volume of mineral removed from the surface by using μ Surf measurements. The total rate for pyrrhotite dissolution is lowest for the control experiment with 2.6×10^{-9} mol/(m²×s) and highest for the *A.f.* experiment with free cells (1.8×10^{-8} mol/(m²×s)). Free cell experiments show high initial rates of pyrrhotite dissolution decreasing with time. The encapsulated cells yielded low initial reaction rates, which continuously increased up to slightly higher rates than for free cells after 28 days. Since biofilms prevent the direct contact between the surrounding media and the sulfide surface, this may lead to a reduced efficiency of surface oxidation/dissolution.

e. Galena dissolution by the acidophilic bacteria *Acidithiobacillus ferrooxidans* (K. Etzel and K. Pollok)

Acidithiobacillus ferrooxidans is an iron- and sulphur-oxidizing bacterium, which is frequently found on waste heaps of processed sulphured ores. It is well known to catalyse the oxidation of sulphides resulting in acid mine drainage, production of sulphuric acid, and the release of high concentrations of metals into ground and surface waters. However, the release of hazardous elements is not only controlled by the reactivity of the primary sulphides and the

activity of the bacteria involved, but also by the formation of secondary mineral assemblages. Secondary phases can influence the dissolution kinetics of the primary sulphide via coating or adsorption. The dissolution of galena is closely related to the formation of secondary phases with low solubility (*e.g.*, anglesite), which can partly passivate the reactive surface.

In this study, the dissolution of three, natural galenas by the acidophilic bacteria *Acidithiobacillus ferrooxidans* has been investigated. Microprobe analyses of galena samples yield variable amounts of trace elements (*e.g.*, Ag, Sb), between < 1 and up to 8 wt.%. For biotic dissolution experiments, galena was milled and wet-sieved resulting in powders with a defined grain size of 40 to 50 μm with a BET surface areas of 0.064-0.073 m^2/g . Powders were sterilized using ethanol and ultraviolet light for 30 minutes. Cultures of *Acidithiobacillus ferrooxidans* cells were grown in 50 ml 9k medium (0.1 g/l KCl, 0.65 g/l $\text{KH}_2\text{PO}_4 \cdot 3\text{H}_2\text{O}$, 3 g/l $(\text{NH}_4)_2\text{SO}_4$, 0.5 g/l $\text{MgSO}_4 \cdot 7\text{H}_2\text{O}$, 0.01 g/l $\text{Ca}(\text{NO}_3)_2 \cdot 4\text{H}_2\text{O}$; acidified to pH 2 with H_2SO_4) and supplemented with 0.5 g sterilized galena powders. Flasks were incubated at 30 $^\circ\text{C}$ on a rotary shaker for 3, 6, 10, 15, 21 and 28 days. Crystalline phases and solutions were analyzed and quantified using XRD (Rietveld), SEM, TEM, ICP-OES and ICP-MS techniques.

In all experiments, dissolution of galena and formation of the secondary phases anglesite (PbSO_4), jarosite ($\text{KFe}_3(\text{SO}_4)_2(\text{OH})_6$) and native sulphur were observed. Secondary phases form rims around galena grains and were also found as fine-grained suspensions in the solutions. The proportion of secondary phases varies for the different galenas and their amount increases with time. However, the dominating secondary phase in all experiments is anglesite. The samples show dissolution rates between 2.9 and 3.8×10^{-8} $\text{mol}/(\text{m}^2\text{s})$. The highest rates were found for the galena containing the highest amount of silver and antimony. This is in strong contrast to abiotic experiments, where the galena with highest trace element amounts shows slowest dissolution rates. Chemical analyses of the solutions yield for all experiments a constant amount of lead (< 4 ppm), however, for the trace element enriched galena, antimony concentrations increased with time up to 15 ppm.

With this experimental study, we showed that sulphide-oxidizing bacteria, such as *Acidithiobacillus ferrooxidans*, affect the dissolution of galena and thus the mobilization of hazardous metals. Similar to abiotic dissolution, time resolved experiments with *Acidithiobacillus ferrooxidans* show no passivation of galena surfaces. However, bacteria influence both the proportion and texture of secondary phases. In contrast to abiotic experiments, dissolved lead does not only precipitate as secondary anglesite rims around galena grains, but also as fine-grained anglesite in solutions.

3.6 Physics and Chemistry of Magmas and Melts

Melting in the Earth's interior has played an essential role in the evolution of the planet throughout its 4.56 billion year history. The formation of magma by partial melting and its subsequent transport towards the Earth's surface is the main mechanism by which chemical differentiation occurs. Such differentiation is responsible for the formation and evolution of both oceanic and continental crust. The eruption of magma at the Earth's surface results in volcanism, one of the major natural hazards that also has a major effect on the chemistry of the Earth's atmosphere due to the release of volcanic gases.

The contributions presented in this section cover a range of aspects with respect to magmatic processes. The first contribution presents preliminary results of a phase equilibrium study of partial melting of hydrous mantle peridotite. Such melting occurs under mid oceanic ridges and involves very small degrees of melting. The composition and water contents of the resulting basaltic melts are of great interest but are very difficult to determine experimentally because of the very small melt fractions. The method reported below, utilizing "sandwich" experiments, represents a viable experimental approach to solving this problem. The second contribution is also concerned with small degrees of partial melting in the Earth's mantle. By measuring the electrical conductivity of hydrous basaltic melts, the fraction of melt that is actually present in various regions of the upper mantle can be estimated. This is done by comparing the experimental results with geophysical measurements of the electrical conductivity of the upper mantle and leads to the conclusion that as little as 1-2 % of hydrous melt is present in the low-velocity zone of the upper mantle.

The third contribution is concerned with the kinetics of nucleation and growth of crystals in magmas of the Stromboli volcano in Italy. By measuring the rates of nucleation and growth of the constituent minerals of crystallised lavas (*e.g.*, plagioclase and clinopyroxene), the textures of the natural samples can be interpreted in terms of eruption dynamics. This means that the rates of ascent of magmas within a volcanic edifice can be determined. Ultimately such information is valuable for estimating volcanic hazards because the magma ascent rate is linked to whether or not an eruption is explosive.

Carbonatites are relatively rare magmatic rocks that consist mainly of carbonate minerals. Their origin in the Earth's mantle has, for many years, been rather uncertain. One likely origin involves their formation by liquid immiscibility – *i.e.*, the physical separation of silicate liquid and carbonate liquid. Further evidence for this mechanism is provided by phase equilibrium melting experiments performed on carbonated mantle peridotite in a simplified system, as reported below. The final contribution in this section is concerned with the decomposition of calcium carbonate at high pressure being a source of diamonds in the Earth's mantle, as proposed in the literature. This hypothesis is not supported by the results that are reported here.

a. Water contents of incipient partial melts in equilibrium with peridotite at 6 GPa (D. Novella and D.J. Frost)

The onset of adiabatic melting in the mantle beneath mid oceanic ridges is thought to first occur through the formation of small degree H₂O-rich melts. Small degree melts produced from mantle with a relatively low bulk H₂O content still have the potential to strip trace elements from larger regions of the mantle compared to dry melting processes. Their presence may also be responsible for the low viscosity of the asthenospheric mantle and for the regular metasomatism of the lithospheric mantle. In this regard, the compositions of incipient melts in mantle peridotite containing low amounts of bulk water are very important. The depth for the onset of melting in upper mantle peridotite can be determined as a function of the bulk rock H₂O content from knowledge of the mineral/melt partition coefficients of H₂O and information on the effect of H₂O on the mantle solidus. Water solubility in upper mantle nominally-anhydrous minerals (NAMs) has been determined in a very large number of studies carried out in the last decades. However, in these studies, mineral H₂O contents were established through coexistence with fluid/melt phases that had unknown compositions, particularly with respect to H₂O content. Many previous studies were performed in simplified chemical systems where the H₂O activity of the melt was likely higher than in realistic mantle melts, which contain additional mainly incompatible elements.

The aim of this study is to determine the chemical composition and H₂O content of small fraction hydrous melts that form by melting a hydrous, upper mantle peridotite, in a complex chemical system (11 components) at adiabatic temperatures and high pressures. Sandwich experiments are performed in a multianvil apparatus, using a double-capsule technique. In our setup, an inner AuPd capsule containing different proportions of mantle peridotite and hydrous-basaltic melt is contained in an outer PtRh capsule. Between the two capsules, hydrous-basaltic powder is packed, surrounding the inner capsule, with the purpose of buffering H₂O activity and oxygen fugacity at levels similar to those of the inner capsule. With this technique, the water content of incipient hydrous melt was investigated at a pressure of 6 GPa and a temperature compatible with a mantle adiabat at this depth (1400°C).

In the first part of the study a basaltic melt, with a composition taken from the literature and containing 7 wt.% H₂O, was sandwiched between layers of peridotite. H₂O was added to the basalt by mixing hydroxides with a previously synthesized glass. After equilibration the recovered phase assemblage consisted of forsterite + clinopyroxene + garnet with a relatively small fraction of melt that was not sufficiently significant to separate into analyzable melt pockets. In a second series of experiments, a higher initial basalt H₂O content was employed (12 wt.%) and the melt was sandwiched with 50 wt.% peridotite. The resulting experiment is shown in Fig. 3.6-1 where a large melt pool, which has crystallized on quenching, is in equilibrium with orthopyroxene, clinopyroxene and garnet. As a result of reaction with the sandwiching peridotite the melt has evolved from containing 10 wt.% MgO to 20 wt.% MgO and mass balance indicates a melt H₂O content of 8.5 wt.%. The melt composition, however,

is not saturated in olvine so in further experiments the determined melt composition will be fabricated and further equilibrated with 50 wt.% peridotite. Over a series of experimental iterations, taking the resulting melt and equilibrating it again with peridotite, the melt composition should evolve to attain equilibrium with a sub-solidus peridotite mineralogy.

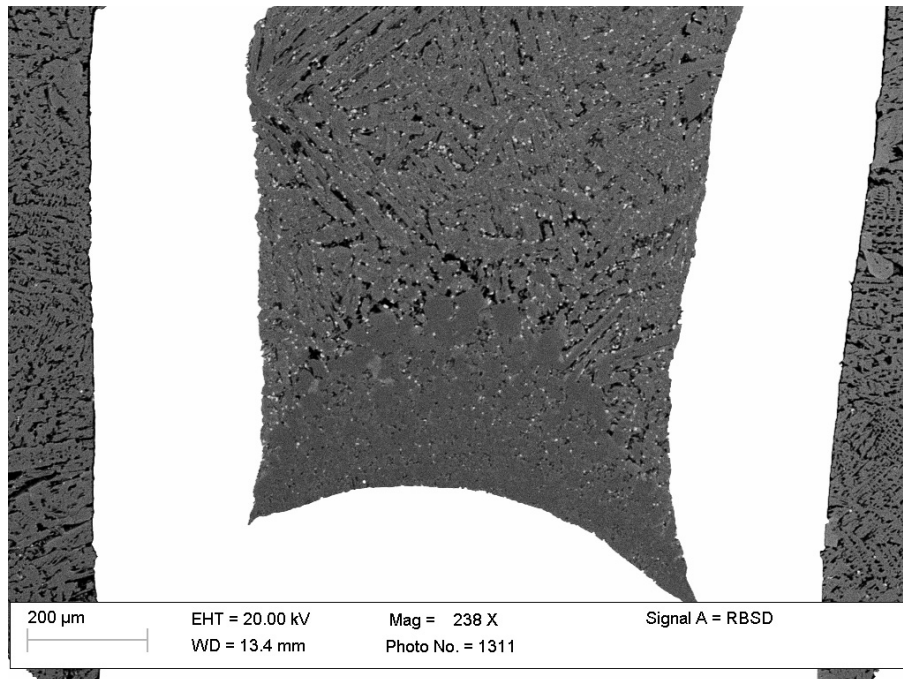


Fig. 3.6-1: Backscattered electron (BSE) image showing the run product of an experiment performed at 6 GPa and 1400 °C. In this experiment a representative dry mantle peridotite composition was equilibrated with a basalt containing 12 wt.% water. The recovered charge shows the presence of quenched melt in equilibrium with a lower portion of ortho-, clino-pyroxene and garnet. Melt from the surrounding double capsule can be seen at either side of the inner capsule.

b. Electrical conductivity of hydrous basaltic melts: implications for partial melting in the mantle (H. Ni, H. Keppler and H. Behrens/Hannover)

Magnetotelluric studies have revealed regions with high electrical conductivities (> 0.1 S/m) in the Earth's uppermost asthenosphere, which correspond approximately to the seismic low-velocity zone (LVZ) at 70-220 km depths. Furthermore, electrical conductivity shows a marked anisotropy in the oceanic LVZ, with higher values in the direction of plate spreading. These phenomena have been attributed to the presence of either hydrated olivine, carbonatite melts, or silicate melts.

We investigated the electrical conductivity of both H₂O-bearing (0-6 wt.% H₂O) and CO₂-bearing (0.5 wt.% CO₂) Fe-free basaltic melts at 2 GPa and 1473-1923 K in a piston cylinder

apparatus. H₂O contents of starting glasses were analyzed by both Karl Fischer Titration and FTIR. A glass tube of 4 mm length was bracketed by a Pt rod of 0.5 mm diameter (the inner electrode) and a Pt₉₅Rh₅ tube of 3.2 mm inner diameter (the outer electrode). The two electrodes were connected to a Solartron 1260 impedance analyzer using Pt wires of 0.35 mm diameter. Temperature was monitored using a Pt-Pt₉₀Rh₁₀ thermocouple, which was not involved in the circuit for conductivity measurements. The impedance contribution from the Pt wires was evaluated by a short-circuit experiment. Samples maintained their shape after experiments but showed some H₂O loss. Conductivities acquired during the first heating cycle, which are least affected by H₂O loss, are presented here.

Electrical conductivity of basaltic melt depends on temperature and H₂O content (Fig. 3.6-2) according to $\log \sigma = 2.172 - (860.82 - 204.46 w^{0.5}) / (T - 1146.8)$, where σ is the electrical conductivity in S/m, T is the temperature in K, and w is the H₂O content in wt.%. The effect of small amounts of CO₂ (on the order of 0.5 wt.%) on electrical conductivity is negligible compared to the effect of H₂O. The positive effect of water on conductivity is attributed to enhanced Na mobility and is more pronounced than that for felsic silicate melts. The conductivity of basaltic melt with > 6 wt.% H₂O approaches that of carbonatite melt.

Our results can be used to infer the melt fraction in a partial molten mantle. In a mantle with 125 ppm water and for a bulk water partition coefficient of 0.006 between minerals and melt, 2 % of melt would account for the observed electrical conductivity of 0.1 S/m in the LVZ (Fig. 3.6-3). However, for plausible higher water contents and stronger partitioning of water into the melt or melt segregation in tube-like structures, even less than 1 % of hydrous melt may be sufficient to produce the observed conductivity.

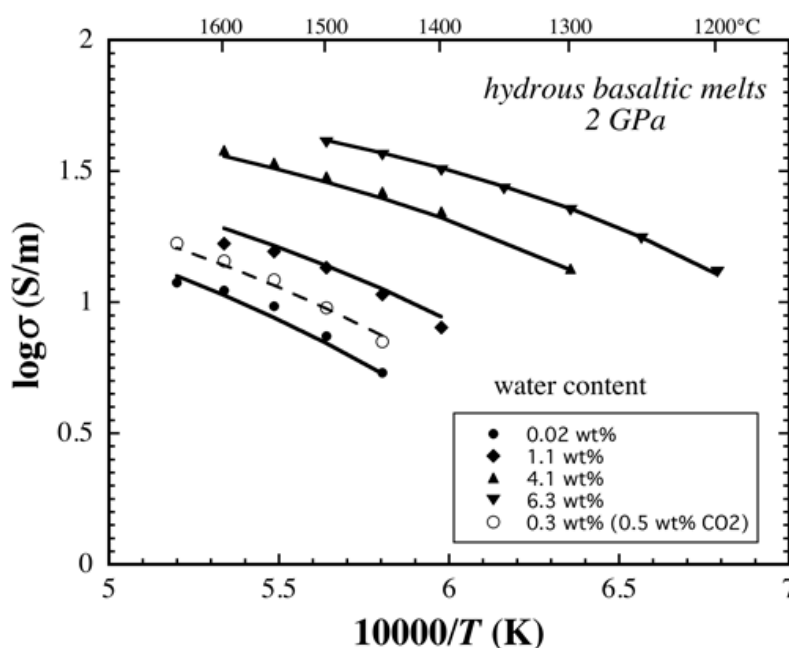


Fig. 3.6-2: Electrical conductivity of volatile-bearing basaltic melts at 2 GPa.

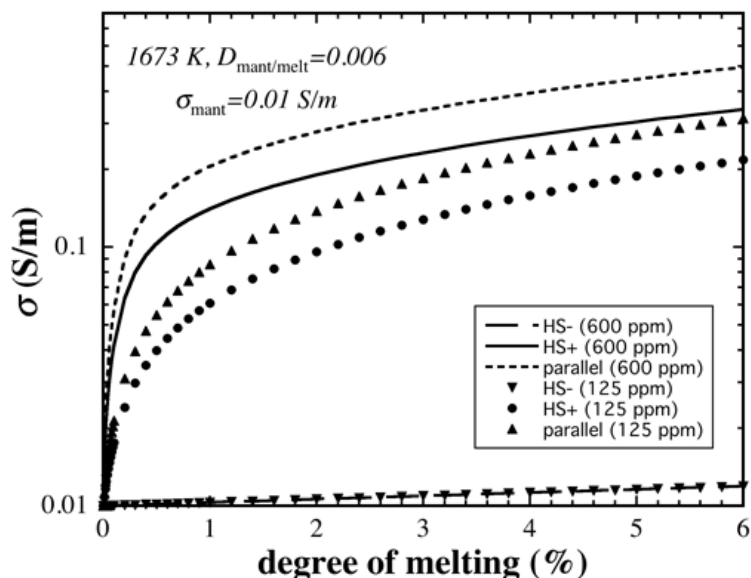


Fig. 3.6-3: Evolution of electrical conductivity of the mantle (with 600 ppm or 125 ppm H₂O) with increasing degree of partial melting, based on the Hashin and Shtrikman lower bound (HS-), Hashin and Shtrikman upper bound (HS+), and the parallel model. The conductivity of the mantle without any partial melting is 0.01 S/m.

c. Crystallisation kinetics in decompressing magmas and implications for magma dynamics at Stromboli volcano (A. Fortunati and M.R. Carroll/Camerino; H. Keppler)

Textural observations and data on phase compositions for natural samples can provide invaluable insights into magmatic processes, their timescales, and the dynamics of magmatic systems. In order to make full use of such observations, especially kinetic/timescale aspects that are of interest for magma dynamics, we must have quantitative data on the rates of crystal nucleation and growth under appropriate P-T-X conditions. These data, combined with studies of crystal size distributions (CSDs) may be used to constrain the times involved in the production of observed phenocryst populations. Furthermore, interpretation of the temporal significance of differences in groundmass crystallization is aided by knowledge of crystal nucleation and growth rates and may provide important constraints on the timescales of magma ascent within the crust.

Crystal growth is induced by undercooling of magmas and in this study we have paid particular attention to undercooling produced by decompression and water loss, as invariably occurs in ascending hydrous magmas; the initial work has concentrated on plagioclase and clinopyroxene growth in magmas from the Stromboli volcano.

Decompression experiments on a primitive basaltic sample from Stromboli (PST9 + 2 wt.% H₂O) have been performed using rapid-quench TZM pressure vessels, at a temperature of 1075 °C and in the pressure range 100-5 MPa. Each experiment involved initially holding the

sample at 100 MPa, 1075 °C for 4 hrs, after which samples were rapidly decompressed and allowed to stay at the final pressure (75, 50, 25, 10, 5 MPa) for times of 0.5, 1, 2, 4, and to 8 hrs before quenching. This procedure allows us to quantify crystal growth and nucleation rates as a function of time.

The quenched samples were analyzed by SEM and resulting BSE images (e.g., Fig. 3.6-4) were used to quantify crystal nucleation and growth rates as a function of time and imposed undercooling; lower final pressure corresponds to greater undercooling due to the negative dP/dT slope of the plagioclase liquidus in hydrous systems. Preliminary results for plagioclase growth rates (Fig. 3.6-5) show that they decrease by as much as an order of magnitude ($\sim 10^{-7}$ to 10^{-8} cm/sec) as the experimental duration increases from 0.5 to 8 hrs. We suggest that this mainly reflects the closer approach to equilibrium in longer duration experiments.

The observed plagioclase compositions in experiments at 5-10 MPa final pressure are very similar to those observed in natural scoria produced on a daily basis at the Stromboli volcano. This suggests that much of the plagioclase crystal growth occurs at relatively shallow depths within the conduit. However, as noted by previous workers, the natural plagioclases (as well as clinopyroxenes) show complex zoning patterns, including clear periods of resorption and later overgrowth of new material. Experiments in progress should help to quantify the possible range of P-T-time conditions needed to produce the observed textures. Comparison of measured growth rates with CSD studies of Stromboli samples are consistent with minimum residence times in the conduit on the order of 3-4 weeks; such times are minimum estimates because they do not take into account the abundant textural evidence for periods of dissolution for some members of the crystal population.

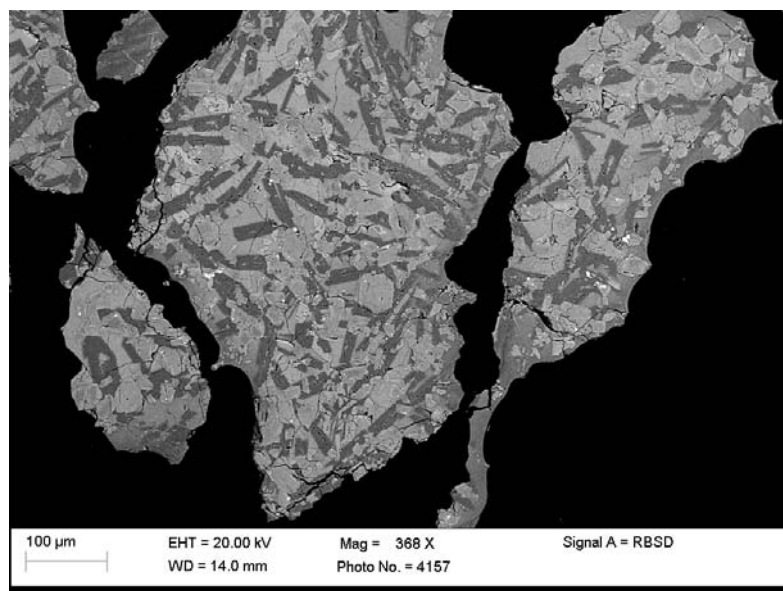


Fig. 3.6-4: Backscattered electron image of the experiment at 1075 °C and 5 MPa for 4 hours. Large dark grey phases are plagioclase, lighter greys are clinopyroxene and glass (~ 40 % plagioclase, 30 % clinopyroxene, 25 % melt, 5 % Fe-Ti oxides).

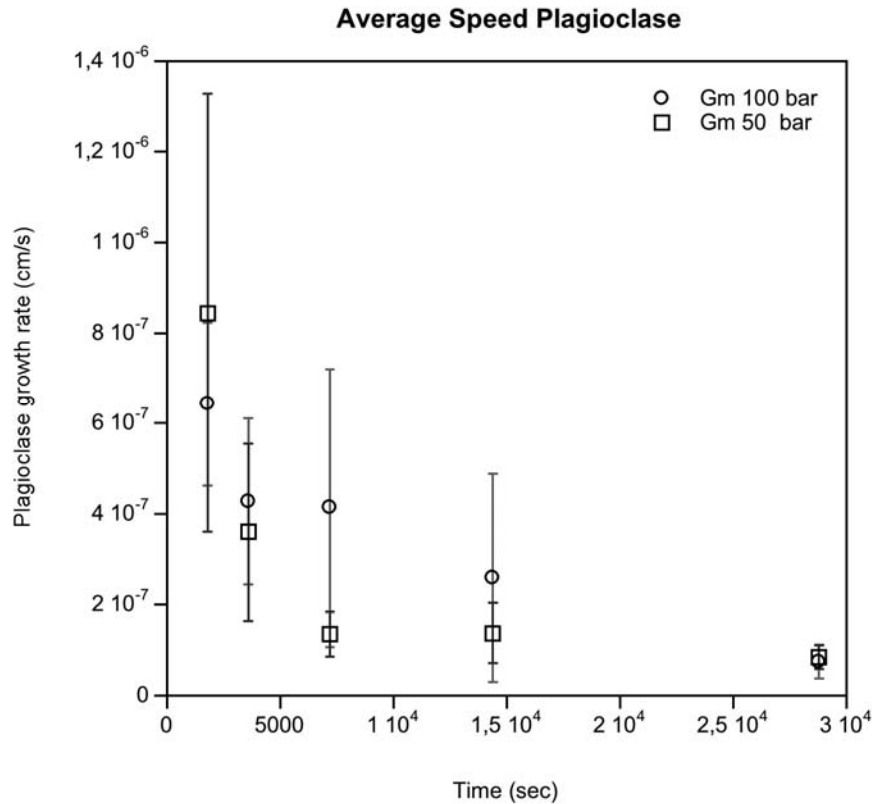


Fig. 3.6-5: Average growth rate of plagioclase at 1075 °C and 10.5 MPa.

d. *Liquid immiscibility and melting reactions of carbonated mantle peridotite at upper mantle conditions (D. Novella and S. Keshav)*

Calcio-carbonatites are unusual magmas that consist of CaO, MgO, some FeO and Na₂O, with the rest being CO₂. These magmas are thought to have their origin(s) in the Earth's mantle. Owing to their specific physical attributes, such as low dihedral angle and low viscosity, are considered to be important magmas at various depths in the Earth for a number of melt-rock interactions including modal and cryptic metasomatism recorded in mantle specimens. While the mantle origin of these magmas has been accepted, the genesis mechanisms that produce calciocarbonatites are still debated. Different models for the genesis of carbonatites have been discussed, and liquid immiscibility, in particular, has been proposed to play an important role in the production of these magmas. A large number of experimental studies undertaken in the past, on both simplified or complex systems, have determined the extent of immiscibility between carbonatitic and silicate melt, in alkali-bearing systems. In alkali-free systems, microprobe data regarding such liquid-liquid separation has never been reported. However, in a study aimed at investigating the melting behaviour of carbonated peridotite at 2-3 GPa, we obtained preliminary results in the system CaO-MgO-Al₂O₃-SiO₂-CO₂ (CMAS-CO₂) that suggested liquid immiscibility as a possible mechanism for the formation of calciocarbonatites in an alkali-free system (see BGI Annual Report 2009).

To strength support for our preliminary study, we present the results of about 40 new melting experiments in the system CMAS-CO₂, and couple them to certain aspects of theoretical petrology. Experiments were conducted at pressures of 2-3 GPa and temperatures of 1325-1550 °C, using a piston cylinder apparatus.

Run products consisting of six phases have been used to evaluate melting reactions. For the sake of brevity, we present two examples to demonstrate what melting reactions look like in such experimental and theoretical investigations. For instance, an experiment performed at 2.2 GPa and 1460 °C produced forsterite (fo) + orthopyroxene (opx) + clinopyroxene (cpx) + spinel (sp) + carbonatitic melt (carb) + silicate liquid (sil), an univariant situation in a five component system. This allows us to calculate the reaction for the vapor absent curve [shown as (vap)]:



Similarly, an experiment at 2 GPa/1425 °C resulted in a univariant phase assemblage consisting of fo + cpx + sp + carb + sil + vapor, which allows us to write the following reaction for the the opx absent line [shown as (opx)]:



It can be seen that the melting reactions are of peritectic type, with forsterite being produced upon melting. Therefore, based on our new experimental data set, the position of the carbonated peridotite solidus ledge, and the lower pressure (< 2.1 GPa) part of the vapour-bearing solidus, all in the system CMAS-CO₂, we have deduced how these reactions could be described. The results of this exercise are shown in Fig. 3.6-6, in which the reactions were

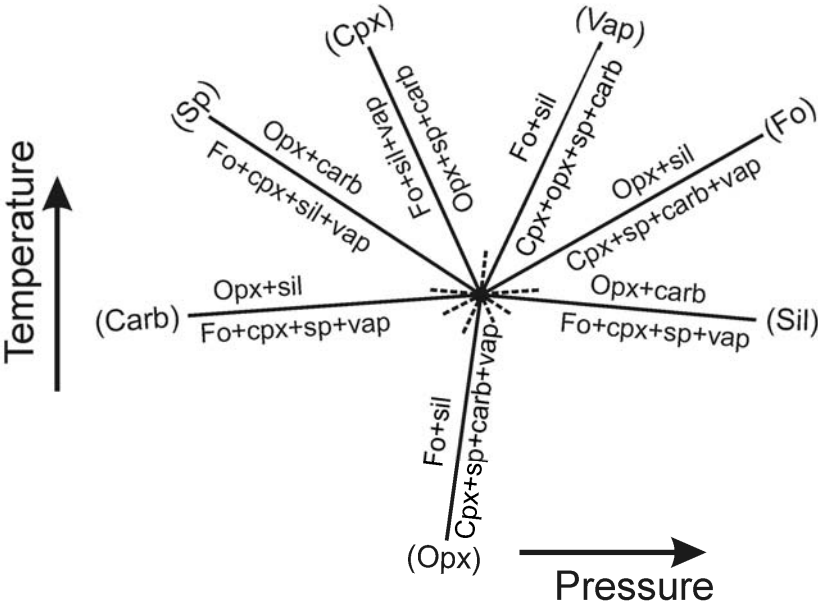


Fig. 3.6-6: Schreinemakers analysis of reactions in the CMAS-CO₂ system displayed as a T-P projection Abbreviations are as follows: fo - forsterite; opx – orthopyroxene; cpx – clinopyroxene; sp – spinel; vap – vapor; carb – calciocarbonatitic melt; sil – carbonated-silicate melt. The phase absent in each reaction is shown in parentheses. Dashed lines are metastable extensions of the stable univariant reactions.

computed using the methods of F.A.H. Schreinemakers. The topological relations shown in Fig. 3.6-6 are entirely consistent with the experimentally known phase relations along the carbonated peridotite solidus ledge, and experimental data characterized by the presence of two liquids and the absence of opx.

Based on the experimental observations reported here, liquid immiscibility is further supported as the process responsible for the formation of primary calciocarbonatites in an alkali-free system, at pressures and temperatures such as those investigated in this study.

e. Congruent melting of Ca-carbonate in static experiments at 10-21 GPa: significance for the genesis of superdeep diamonds (A. Spivak and Yu. Litvin/Chernogolovka; L.S. Dubrovinsky)

Calcium carbonate is probably one of the main carbonate components in diamond-forming lithologies at conditions of the transition zone and lower mantle. It has been proposed in the literature that decomposition of calcium carbonate in the upper mantle and transition zone could provide carbon for the formation of diamonds. The main aim of this project was to evaluate this hypothesis by investigating experimentally the conditions of chemical stability and the P-T field of congruent melting of CaCO_3 at 10-30 GPa.

$\text{Ca}^{13}\text{CO}_3$ was used as the starting material for the experiments. Carbonate containing the ^{13}C isotope was necessary for the purpose of identifying possible carbon phases. Experiments were carried out in laser-heated diamond anvil cells (LH-DAC) at pressures in the range 11-22 GPa and at temperatures of 1500-3500 K. Raman spectra of temperature-quenched samples were collected using a LabRam system (632 nm He-Ne excitation laser).

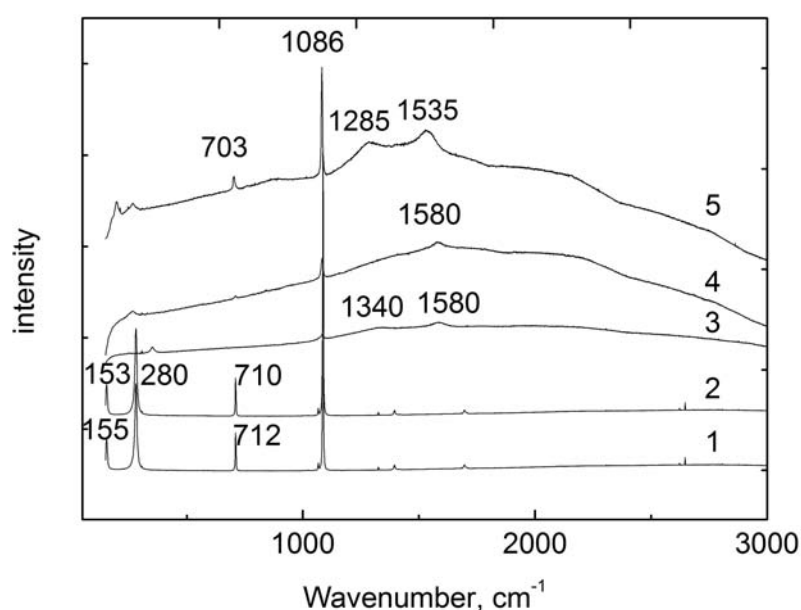


Fig. 3.6-7: Raman spectra of samples: 1. CaCO_3 at room pressure and temperature; 2. $\text{Ca}^{13}\text{CO}_3$ at room pressure and temperature; 3. $\text{Ca}^{13}\text{CO}_3$ at 21 GPa and 3500 K; 4. $\text{Ca}^{13}\text{CO}_3$ at 20 GPa and 3500 K; 5. $\text{Ca}^{13}\text{CO}_3$ at 11 GPa and 3500 K.

It was found that melting of CaCO_3 is congruent in static experiments at 20-21 GPa. In contrast, in experiments at 11 GPa, Ca-carbonate decomposes and graphite rich in the carbon ^{13}C isotope crystallised. Raman spectra of this sample show characteristic peaks of graphite (^{13}C) at 1535 cm^{-1} and 1285 cm^{-1} (Fig. 3.6-7).

Thus, the field of congruent melting of Ca-carbonate is broad, lies between 20-21 GPa and 2300-3500 K and is in agreement with the CaCO_3 phase diagram calculated from shock-experiment data. Our results indicate that decomposition of CaCO_3 alone can not provide a source for diamond formation at conditions of the Earth's upper mantle and transition zone.

3.7 Rheology

Deformation in the Earth occurs over a wide range of scales, both in time and space; in time it ranges from the rapid movements on faults causing earthquakes to the long durations of plate tectonic movements. Spatially it spans the submicroscopic movement of dislocations in a crystal lattice to the formation of whole mountain ranges. The response of rocks to an applied stress (*i.e.*, their rheology) therefore needs to be understood both as a function of time (or strain rate) and scale of homogeneity. Experiments can help in the understanding of deformation processes in two ways: 1) they allow to determine the mechanical behaviour, *i.e.*, stress-strain rate relationships (flow laws), and 2), they produce samples with characteristic microstructures and physical anisotropies. Flow laws are needed for a quantitative understanding and modeling of geodynamic processes in the Earth, whereas microstructures and physical anisotropies help in the interpretation of deformation fabrics of natural rocks and geophysical observations (*e.g.*, seismic anisotropy) respectively.

The experimental equipment presently available at the Geoinstitut is designed to perform deformation experiments at high pressures and temperatures and less well suited to determine mechanical parameters (*i.e.*, for the derivation of experimental flow laws). Therefore deformation studies are focussing on the microstructural effects of deformation of minerals present in the Earth's interior. The focus here is on deviations in textural development, that may be caused by increased pressure (olivine), water content (olivine, orthopyroxene) or chemical substitution (Al in orthopyroxene). The motivation in these studies is that detectable variations in physical anisotropy may be used to gain information about the distribution of water or other elements in the mantle. Subduction zones are regions of intense deformation where new minerals are formed under high pressure (relatively) low temperature conditions. These minerals and their rheology are important for the understanding of the subduction process itself and the connected mountain building processes (especially in the case of continental collisions).

In the lower mantle, convective flow is governed by its main constituents, ferropericlaase and silicate perovskite. Since controlled deformation experiments at lower mantle conditions are presently not feasible, studies focus on the possible deformation mechanisms, such as dislocations and slip systems under pressure and temperature. The basal (D'') region of the lower mantle is particularly interesting since geophysically it exhibits features of an intense deformation zone (*e.g.*, strong anisotropies). Experimental deformation studies of analogue materials of its main mineral, post-perovskite, produce textural results which may explain some of the observed geophysical features.

Lastly, the experimental deformation of mineral-melt mixtures yields microstructures that allow to distinguish surface- and stress/strain-energy controlled domains, which determine how easily an intergranular melt can separate from the surrounding rocks. This is an important process in core formation scenarios of the early Earth.

a. *The effects of stress and water content on the deformation of olivine at high pressure (S. Shekhar, D.J. Frost, N. Walte, N. Miyajima and F. Heidelbach)*

Crystallographic preferred orientation developed in olivine due to shearing in the mantle is thought to be the prominent reason behind seismic anisotropy in the upper mantle. Seismic anisotropy in the upper mantle can be observed up to a depth of 350 km with a marked drop in the strength of anisotropy seen around 250 km. Studies on natural rock samples from the mantle and deformation experiments performed on olivine have revealed that olivine deforms mainly through dislocation creep with Burgers vectors parallel to the [100] crystallographic axis under low-pressure conditions (up to 3 GPa). Under similar pressures, evidence of [001] slip has been reported due to the presence of water.

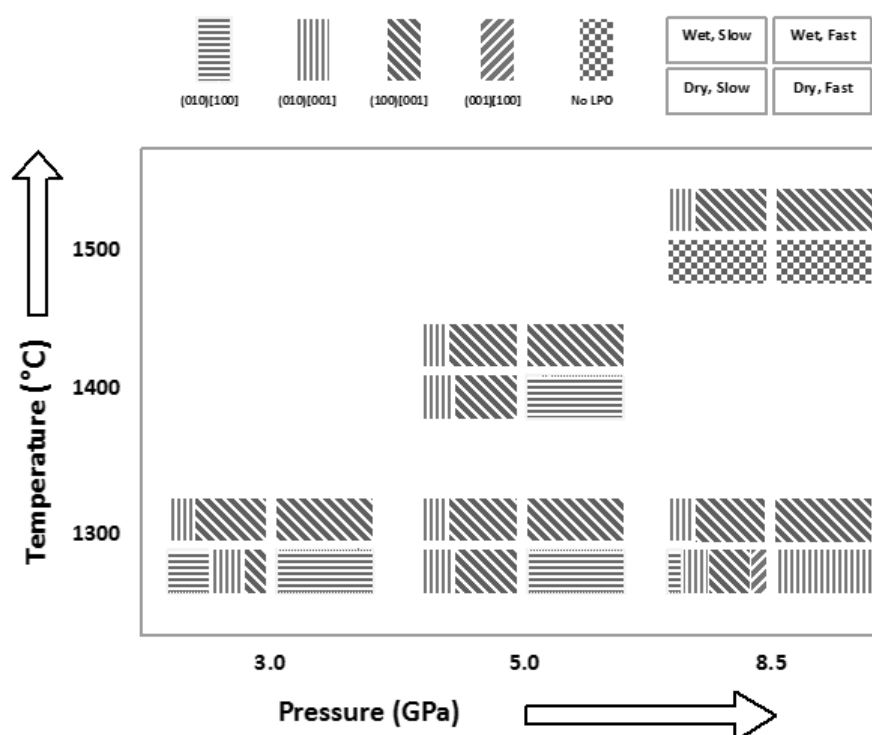


Fig. 3.7-1: Summary of fabrics observed in San Carlos olivine deformed under dry and wet conditions at different strain rate. Experiments were performed between 3 to 8.5 GPa and 1300 °C to 1500 °C; a key for the different experimental conditions (dry/wet, slow/fast) is shown in the top right corner; the width of the individual fabric symbols indicates the number of grains of different orientation components, but it is not drawn to scale.

In order to understand the deformation mechanism in olivine at pressures greater than 3 GPa, we have performed experiments using the deformation DIA multi-anvil apparatus. The DIA consists of 6 square faceted anvils that compress a cubic high-pressure assembly. The deformation DIA possesses two vertically acting opposing inner rams, which can be operated independently of the main compressive force to deform the sample assembly. The

experimental setup consists of a hot-pressed sample of polycrystalline dry San Carlos olivine 0.2 mm cut from a 1.2 mm diameter core at 45°. This slice is sandwiched between alumina pistons also cut at 45° in simple shear geometry. Experiments have been performed at 3, 5 and 8 GPa at a deformation anvil strain rate between $1.0 \times 10^{-4} \text{ s}^{-1}$ to $2.5 \times 10^{-5} \text{ s}^{-1}$ and temperatures between 1300-1500 °C under dry and water rich condition. Deformed samples were cut normal to the shear plane and parallel to the shear direction. Then the sample was polished and analyzed using electron back scattered diffraction (EBSD) to identify the crystallographic preferred orientation (CPO).

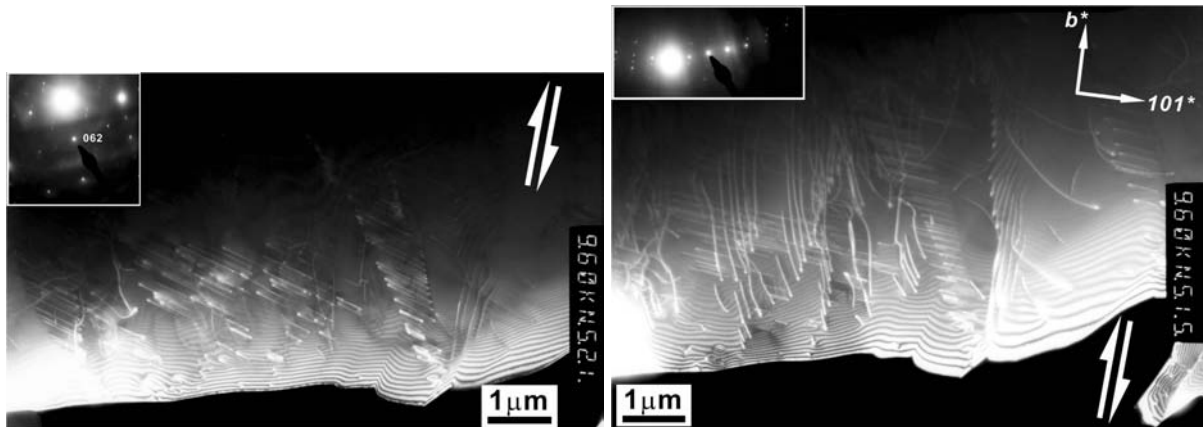


Fig. 3.7-2: 8 GPa and 1550 °C; only [001] dislocations are visible (left image) and both [100] & [001] dislocation are visible along sub-grain boundaries (right image)

Our results (Fig. 3.7-1) indicate that stress and water content have profound effect on the olivine slip system. Under water rich and high stress conditions, the CPO is dominated by (100)[001] indicating slip on that system. Under dry conditions, samples deformed at a relatively higher strain rate (high stress) showed similarly evidence of the (010)[001] slip system.

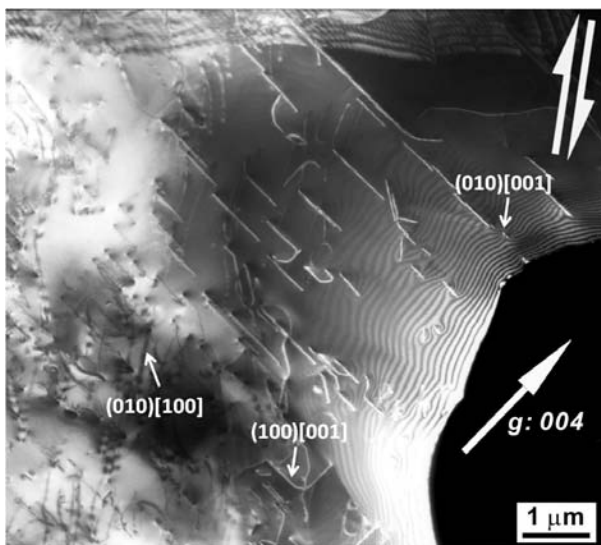


Fig. 3.7-3: TEM image of dry San Carlos olivine sample deformed at 8 GPa, 1300 °C at strain rate of 2.5×10^{-5} . Sample shows (010)[001], (100)[001] and (010)[100] slip systems active.

Observations mentioned above are true irrespective of the pressure under which experiments were performed. Samples deformed under relatively lower stresses show a variety of fabrics that include (010)[100], (010)[001], (100)[001] and (001)[100] slip systems (Fig. 3.7-2) but (010)[100] and (001)[100] slip systems appear to contribute very little to the overall fabric under water rich conditions.

TEM observations have been made on several of the recovered samples in order to correlate the developed CPO with the action of specific dislocations. Samples deformed at 8 GPa and 1200 °C show straight edge dislocations normal to the diffraction vector, $g: 004$. Whereas, experiments performed at 1400 °C and 8 GPa resulted in very few visible sub grains in the SEM orientation contrast image and only very weak CPO could be observed. TEM study on this sample shows that [001] & [100] edge dislocations were co-activated in climb-configuration which resulted in no perceptible CPO (Fig. 3.7-2). Dry sample deformed at a slower strain rate ($2.5 \times 10^{-5} \text{ s}^{-1}$, 8 GPa, 1300 °C) shows (010)[001], (100)[001] and (010)[100] slip systems active (Fig. 3.7-3).

b. *The effect of aluminium and water on the development of orthopyroxene fabrics (M.A.G.M. Manthilake, N. Miyajima, F. Heidelbach and D.J. Frost)*

Pyroxenes are the second most abundant mineral phase in the upper mantle and are a major constituent of mafic and ultramafic rocks such as peridotites and pyroxenites. It is estimated that the typical upper mantle contains up to 40 % pyroxenes, where 20-30 % of them are orthopyroxene. Despite the large abundance, relatively few studies have investigated the fabric development of orthopyroxenes in comparison to the large number of experimental and theoretical studies on olivine. Recent studies have shown that aluminous orthopyroxene can dissolve up to ~ 7000 ppmw of water, which is likely to influence the deformation behaviour. It is therefore important to investigate the effect of chemical variants such as the presence of alumina and water on the fabric development in orthopyroxene.

Deformation experiments were carried out in simple shear geometry in a deformation-DIA apparatus using 8-6 assembly configuration at 1.5 GPa and 1100 °C. Samples used in these experiments were MgSiO_3 enstatite, aluminous enstatite (5 and 10 wt.% Al_2O_3) and hydrous aluminous enstatite (10 wt.% Al_2O_3 , 1800 ppmw and 4700 ppmw H_2O), synthesized in the piston cylinder apparatus at 1.5 GPa and 1100 °C. Samples were deformed at strain rates of $5 \cdot 10^{-4} \text{ s}^{-1}$ and $3 \cdot 10^{-5} \text{ s}^{-1}$ with total strains (γ) of approximately 1.2.

Electron backscattered diffraction analysis (Fig. 3.7-4) shows that in all samples slip along the [001] axis is dominant, independent of the chemical composition. This observation can easily be understood from the crystal structure, as [001] in orthopyroxene is the shortest compared to other possible Burgers vectors. However, the dominant slip plane changes depending on the composition. In MgSiO_3 enstatite, the dominant slip plane is (100), whereas in aluminous

enstatite, (010) is strongly aligned with the macroscopic shear plane indicating slip. With changing water contents in aluminous enstatites, both (010) and (100) planes coexist together and at the highest water contents examined, the dominant slip plane reverted back to (100).

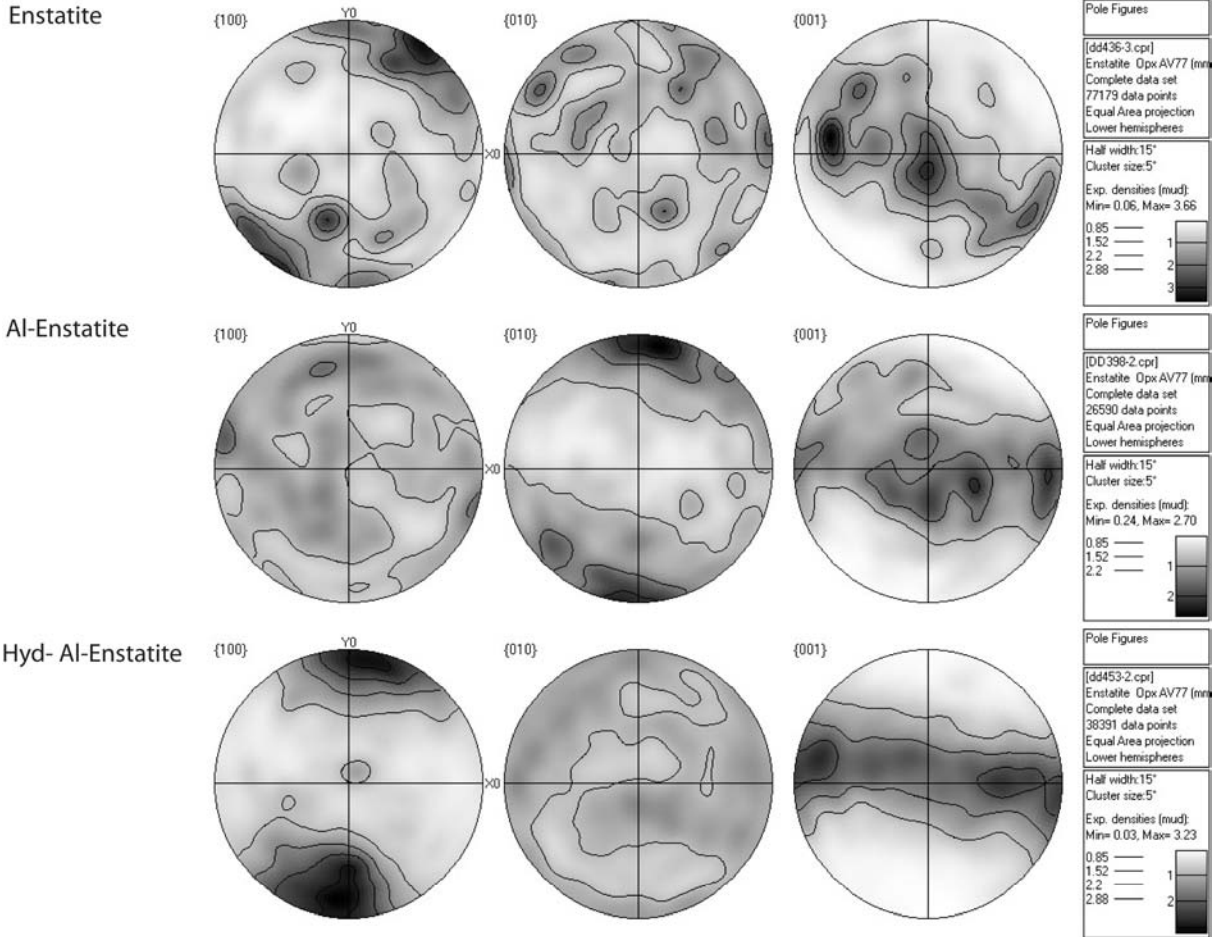


Fig. 3.7-4: Pole figures showing the lattice-preferred orientation of enstatite, aluminous orthopyroxene and hydrous aluminous orthopyroxene; shear plane is horizontal, shear sense is sinistral; lower hemisphere, equal area projections.

Dislocation microstructures of selected samples were studied using a transmission electron microscope. Glide on the (100)[001] slip-system in $MgSiO_3$ enstatite implied by EBSD measurements could be confirmed due to the high activity of [001] dislocations on the (100) plane (Fig. 3.7-5a), but no direct evidence was found for the (010)[001] slip-system in aluminous enstatite. However, in aluminous enstatite [001] dislocations were found to occur on the {210} plane (Fig. 3.7-5b), which corresponds to one of the cleavage planes of the orthopyroxene structure and is the first observation of such behaviour reported for orthopyroxenes in general.

Change of the dominant slip plane with Al incorporation and subsequent hydration can be explained by crystal chemistry of aluminous orthopyroxene. Al occupancy mostly occurred at

M1 and T2 sites forming stronger covalent bonds which make it harder to slip along (100). With hydration in which the protons are most likely positioned in the O1B-O2B edge resulting a decrease of relative strength of (100), which may transform the slip system back to (100)[001].

Seismic anisotropy calculated for both MgSiO_3 enstatite and hydrous aluminous enstatite indicate maximum anisotropy for V_p of 1.3 % and it is 2.1 % for aluminous enstatite. The shear wave splitting reached 1.8 % for MgSiO_3 enstatite, 1.15 % for hydrous aluminous enstatite and 1.7 % for aluminous enstatite. This result shows that the contribution to the seismic anisotropy from orthopyroxene is not significantly large, unless the anisotropy caused by olivine is weak.

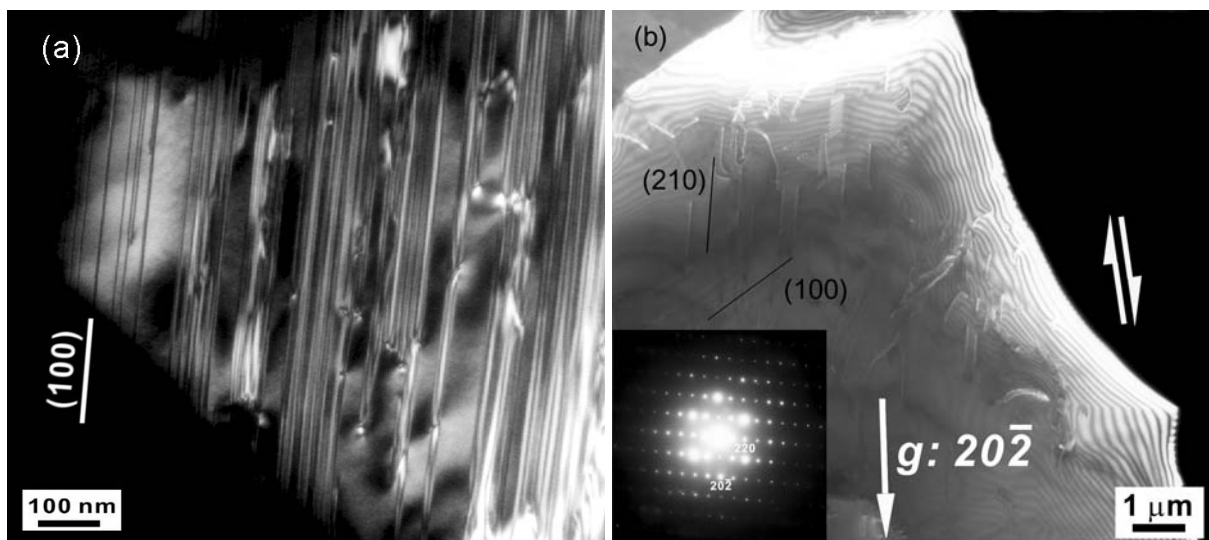


Fig. 3.7-5: (a) Dark field electron micrograph of showing stacking-faults connected through partial dislocations parallel to (100) in enstatite crystal. (b) Weak-beam Dark field electron micrograph showing [001] dislocations gliding on {210} in aluminous orthopyroxene. Note the weak contrast of dislocations in (100).

c. Deformation fabrics at the aragonite-calcite transition (F. Heidelbach and N. Walte)

Aragonite (CaCO_3) is the orthorhombic high-pressure modification of trigonal calcite and is formed in carbonaceous sedimentary sequences that undergo deep subduction. Structurally similar to calcite, it is likely one of the weaker components in the subducting slab and thus accommodating large strains during the subduction process. Little is known about the deformation microstructures and textures of aragonite since aragonite-calcite transformation is a reconstructive phase transition such that aragonite is rarely preserved in exhumed subducted terranes. However, aragonite deformation fabrics may be still inherited in the calcite microstructures in exhumed material. We deformed aggregates of aragonite at 3 GPa and 800 °C in the D-DIA multianvil press in order to produce deformation fabrics that may be similar

to those in natural aragonite mylonites and then annealed them statically in the stability field of calcite.

We performed experiments in different deformation geometries (axial compression, simple shear) and analyzed the fabrics with SEM-EBSD. The starting material was produced by pressurizing (3 GPa) and heating (800 °C) Carrara marble for up to five days in the piston cylinder press. The long run durations were needed to produce a sufficiently large grain size ($\sim 10 \mu\text{m}$) in the starting material. The deformation experiments were carried with strain rates of 10^{-4} sec^{-1} in axial compression and reached strains of 30-40 %, sufficient to produce a characteristic fabric. A series of deformed samples was decompressed after deformation into the calcite stability field (2 GPa, 800 °C) and left there statically for varying amounts of time (2 minutes to 3 hours) and then quenched.

Samples deformed in axial compression show a roughly axisymmetric CPOs characterized by $\{100\}$, $\{001\}$ and $\{101\}$ fiber components with a strong alignment of $\{010\}$ perpendicular to the compression direction. Grains show a flattened shape compatible with the overall strain and abundant twins as well as subgrain structures. Twin lamellae on $\{011\}$ are ubiquitous in all deformed samples.

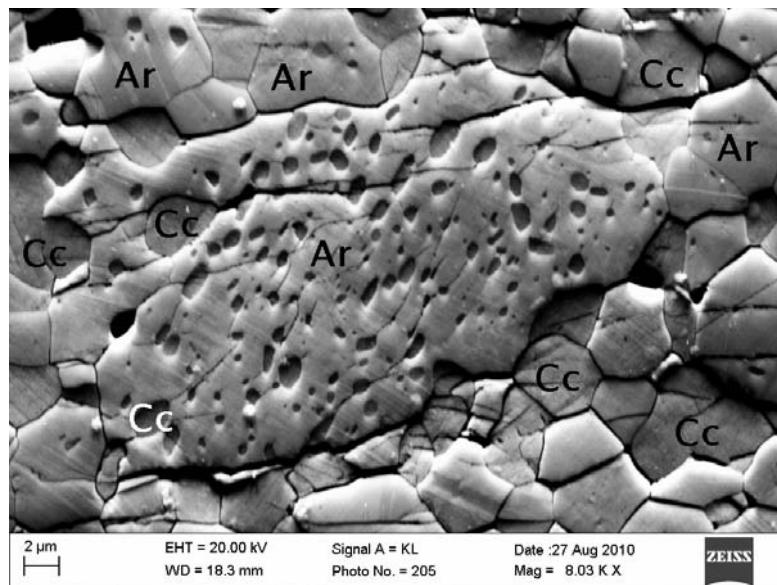


Fig. 3.7-6: SEM orientation contrast micrograph of an aragonite sample annealed for three hours in the calcite stability field; note that calcite (Cc) appears both intracrystalline as well as on grain boundaries of aragonite (Ar).

After the transformation new calcite grains appear intragranular as submicron sized nuclei inside aragonite as well as greater than a micron size grains along grain boundaries or triple junctions of the aragonite grains (Fig. 3.7-6). With longer durations in the calcite stability field also clusters of calcite grains develop. For neither type of new calcite grains a epitaxial

orientation relationship with the enclosing or neighboring aragonite grains could be detected. The amount of calcite transformation can only be roughly estimated due to temperature gradients in the assembly: ~ 5 % after 15 minutes and ~ 30 % after 3 hours. Aragonite CPOs are basically preserved (Fig. 3.7-7 top) during the partial transformation in the calcite stability field. Only the {001} alignment appears to vanish after 3 hours of transformation. The newly formed calcite has a weak CPO with broad concentrations of {001} and {108}/{018} near the compression axis ((Fig. 3.7-7 bottom).

Aragonite samples show grain shape preferred orientation and CPOs indicative of dislocation creep and twinning on (011). CPOs display an alignment of (100), (001) and (101) in the compression plane/shear plane making them likely to be intracrystalline slip planes. The (100) plane, which shows the strongest alignment corresponds structurally to the basal plane of calcite. The [010] direction is aligned perpendicular to the compression direction and parallel to the shear direction respectively indicating that **b** (as shortest lattice repeat) may serve as a Burgers vector in intracrystalline slip.

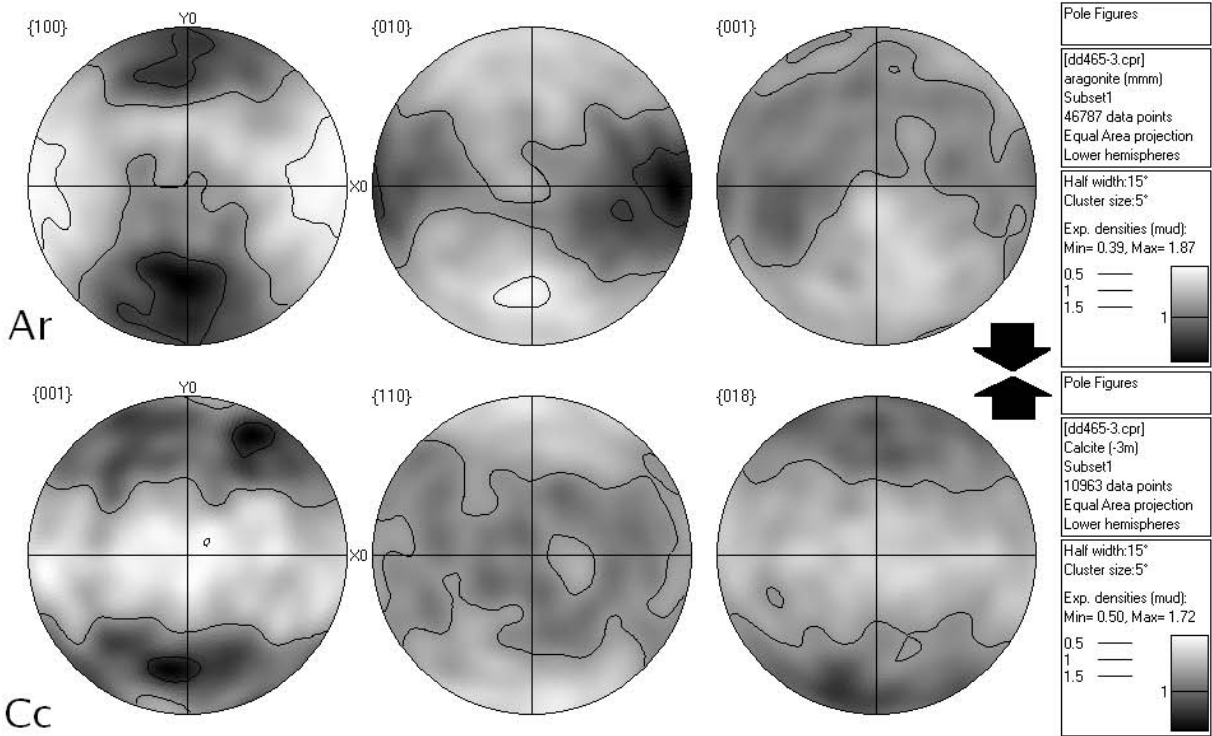


Fig. 3.7-7: Pole figures of aragonite (top) and calcite (bottom) of an aragonite sample annealed for three hours in the calcite stability field.

Invoking a shear mechanism during the phase transition the **b** direction corresponds to the **a** axis of the calcite structure. Based on this mechanism one could expect that calcite inherits some of the aragonite fabric. However, neither intracrystalline nuclei nor the newly formed grains along boundaries and at triple points of the aragonite grain structure yield a systematic

orientation relationship between aragonite and calcite. Nevertheless calcite displays a weak CPO with an alignment of the basal {001} and the {108}/{018} planes the latter being the e-twins) subparallel to the compression axis. This could be caused by remanent stresses in the sample during back-transformation (*i.e.*, preferred growth under stress).

d. Characterisation of dislocations in dense hydrous magnesium silicate phase A (P. Cordier, A. Mussi and D.J. Frost)

Hydrous phases play a major role in the dynamics of subduction zones. Besides being potential carriers for water, serpentines can accommodate large deformations and have a large impact on the seismicity of subducted slabs. Beyond ca. 200 km depth, serpentines are not stable any more, but several dense hydrous magnesium silicate (DHMS) phases (the so-called “alphabet” phases) are potential carriers for transporting water at great depths. However, nothing is known about the mechanical properties of these phases. We have studied the plastic properties of phase A, which is the first DHMS to appear after the serpentine destabilization.

The crystal lattice of $Mg_7Si_2H_6O_{14}$ phase A is hexagonal (space group $P6_3$), with $a = 7.86 \text{ \AA}$ and $c = 9.57 \text{ \AA}$. The structure is composed of weakly-distorted, close-packed layers of oxygen atoms and hydroxyl groups, with an ABCB sequence, along the c axis (1/2 of the octahedral interstice sites are filled by Mg atoms and 1/4 of the tetrahedral interstice sites are filled by Si atoms). The sample has been synthesized from high-purity oxides (MgO , SiO_2 and $Mg(OH)_2$) at 11 GPa and 900 °C during 240 min. The resulting specimen of phase A has been further deformed at 11 GPa and 700 °C during 45 min.

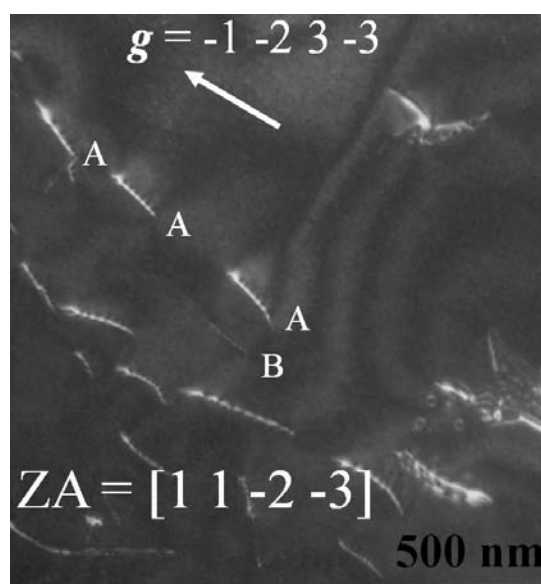


Fig. 3.7-8: TEM micrograph in weak-beam dark-field conditions ($ZA =$ zone axis, $g =$ diffraction vector); dislocations labeled A are $\pm 1/3[2\bar{1}\bar{1}3]$ and the dislocation labeled B is $\pm 1/3[2\bar{1}\bar{1}0]$.

After deformation, the sample was mechanically polished down to a 20 μm thickness, then ion sputtered with an argon ion beam, at liquid nitrogen temperature in order to reduce the irradiation damage (phase A is extremely sensitive to irradiation). Subsequently, the thin foil was studied in Lille with a Philips[®] CM30 transmission electron microscope (TEM) operated at 300 kV. The analyses have been performed in low illumination conditions and with a Gatan[®] cold stage (liquid nitrogen), in order to slower beam damage. The grain size of phase A is in average $50 \pm 10 \mu\text{m}$. Dislocations are observed in most of the grains (only the smallest grains might be free from dislocations). They are usually entangled, and the dislocation density is of the order of 10^{13} m^{-2} . Some subgrain boundaries have been observed suggesting that diffusion is active.

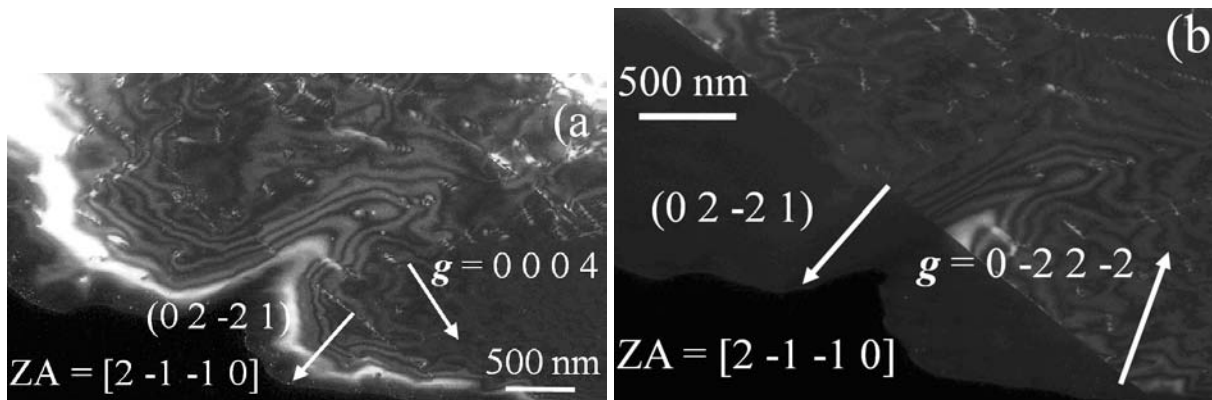


Fig. 3.7-9: TEM micrograph in weak-beam dark-field conditions (ZA = zone axis, g = diffraction vector); diffraction vectors $g = 0004$ (a) and $0\bar{2}2\bar{2}$ (b) reveal a $(0\bar{2}\bar{2}1)$ twin plane.

We have characterized $1/3\langle 2\bar{1}\bar{1}0 \rangle$ and $1/3\langle 2\bar{1}\bar{1}3 \rangle$ perfect dislocations, with approximately the same proportions (Fig. 3.7-8). No evidence of $[0001]$ dislocations has been noticed, even if the elastic energy of such dislocations is lower than the one of $1/3\langle 2\bar{1}\bar{1}3 \rangle$ dislocations. Furthermore, no evidence of basal slip system has been noticed, which is uncommon for hexagonal lattice. Moreover, some $(0\bar{2}\bar{2}1)$ twins were observed (Fig. 3.7-9).

e. Dislocation microstructures of ferropericlase at high pressure and high temperature (N. Miyajima and T. Irifune/Ehime)

The rheological behaviour of silicate perovskite and ferropericlase at high pressure and temperature are indispensable for discussing dynamics of the Earth's lower mantle. Deformation of plastically weaker ferropericlase ((Mg,Fe)O) than coexisting silicate perovskite is likely to be responsible for bulk strain of the rock, if it develops a sufficient grain connectivity in a fabric development at high temperature. Particularly, lattice preferred

orientations (LPO) of the polycrystalline ferropericlase can be important to explain observed seismic anisotropies in the bottom of Earth's lower mantle, so called "D" layer". For understanding deformation mechanisms to create a LPO pattern, dislocation microstructures of ferropericlase under lower mantle conditions are very important, because dislocation creep mechanisms could become one of dominant deformation mechanisms in the D" layer. In order to discuss the influence of pressure on the active slip system in ferropericlase, we report dislocation microstructures of ferropericlase synthesized at different pressures of 0, 15 and 44 GPa, by using TEM.

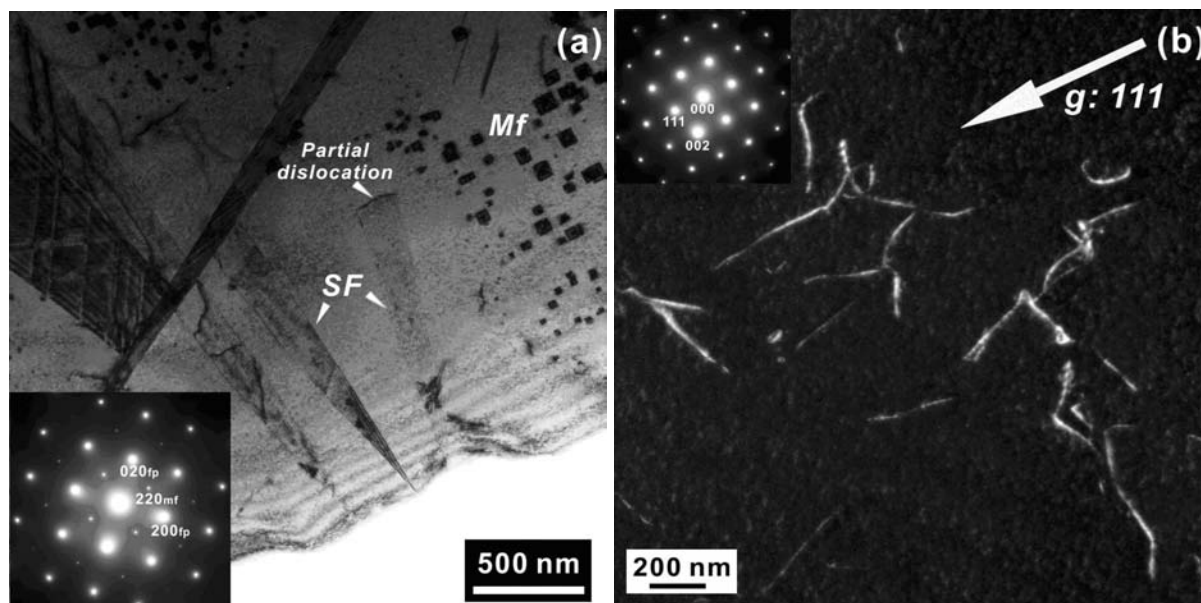


Fig. 3.7-10: TEM micrographs of ferropericlase synthesized (a) at ambient pressure (courtesy sample from S.D. Jacobsen/Evanston, USA), (b) at 15 GPa and ~ 2100 K (from M. Longo/Padova, Italy). The insets are selected area diffraction patterns indicating the nearest zone axis.

Bright-field TEM image (Fig. 3.7-10a) shows the dislocation textures of ferropericlase synthesized at ambient pressure and high temperature. Partial dislocations with stacking faults were nucleated during thermal annealing, whereas a high density of perfect dislocations was also artificially activated by sample polishing process before Ar-milling. Cubic-shaped impurities are epitaxial magnesian ferrite. In the ferropericlase synthesized at 15 GPa and about 2100 K, curved dislocations with $\mathbf{b} = 1/2 [110]$ are tangled on the $(1\bar{1}0)$ plane (Fig. 3.7-10b).

In a pyrolite mineral assemblage recovered from 44 GPa and 2073 K, MgSiO_3 perovskite (MgPv) contained a few dislocations and ferropericlase displayed a high density of dislocations (Fig. 3.7-11). In more detail, straight long screw dislocations with $\mathbf{b} = 1/2[1\bar{1}0]$ were nucleated on the (110) and/or $(11\bar{1})$ planes (Fig. 3.7-11a) and the other dislocations with $\mathbf{b} = 1/2[01\bar{1}]$ was along the (011) plane (Fig. 3.7-11b) in the same grain.

Dislocation microstructures of ferropericlase synthesized at high temperatures and different pressures from 0 to 44 GPa were compared in the TEM images. High-pressure samples indicate that an active slip system of $1/2\langle 110 \rangle\{110\}$ in (Mg,Fe)O, consistent with previous studies at lower pressures, although ambient pressure samples shows unusual partial dislocations with stacking faults. The characteristic textures of straight screw dislocations along a specific crystal orientation in the highest pressure sample strongly imply that the Peierls friction for movement of $1/2\langle 110 \rangle$ dislocations in (Mg,Fe)O increases with increasing pressure.

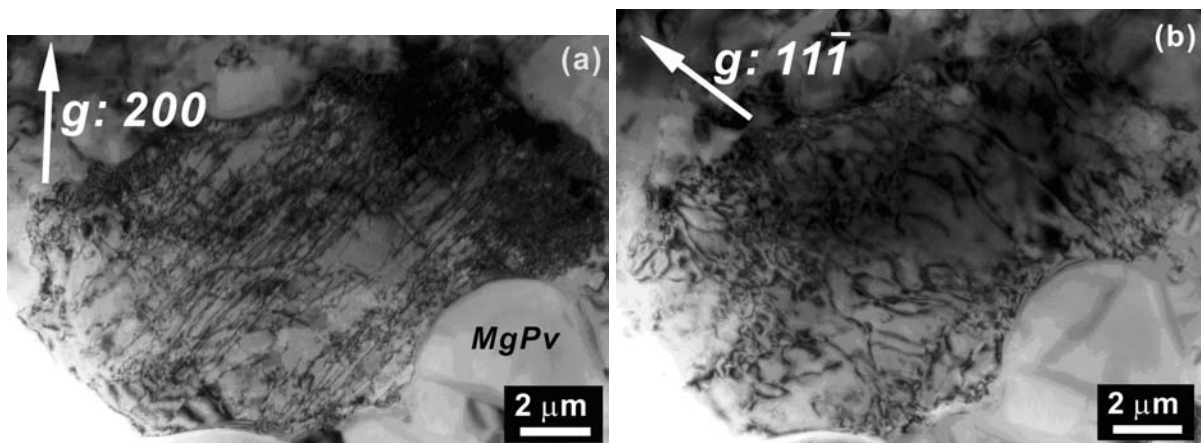


Fig. 3.7-11: Bright field TEM micrographs of ferropericlase in a pyrolite mineral assemblage recovered from 44 GPa and 2073 K. (a) $1/2[1\bar{1}0]$ dislocations on the (110) and/or (111) planes are visible with diffraction condition of $g = 200$ (b) $1/2[01\bar{1}]$ dislocation on the (011) plane are visible with $g = 11\bar{1}$. The TEM foil orientation was close to the [011] zone axis.

f. *The development of lattice-preferred orientation in CaPtO_3 post-perovskite deformed in pure shear (R. McCormack and D.P. Dobson/London, T. Taniguchi/Tsukuba, N. Walte and N. Miyajima)*

Knowledge of the deformation mechanism of post-perovskite is important for interpreting observed seismic anisotropy in the lowermost part of the mantle (D''). Experiments on post-perovskite MgSiO_3 and the low-pressure analogue material CaIrO_3 yield different textures, leaving the interpretation of the observed seismic signatures unclear. Here we present results of deformation experiments on CaPtO_3 post-perovskite which has been suggested to be a better analogue to MgSiO_3 . Post-perovskite CaPtO_3 deforms by glide of [100] dislocations on the (010) plane, consistent with previous experiments on CaIrO_3 . In addition, strong textures can rapidly develop in the presence of a weak minority phase, supporting the recent suggestion that the D'' reflector might be due to a rapid generation of texture in post-perovskite.

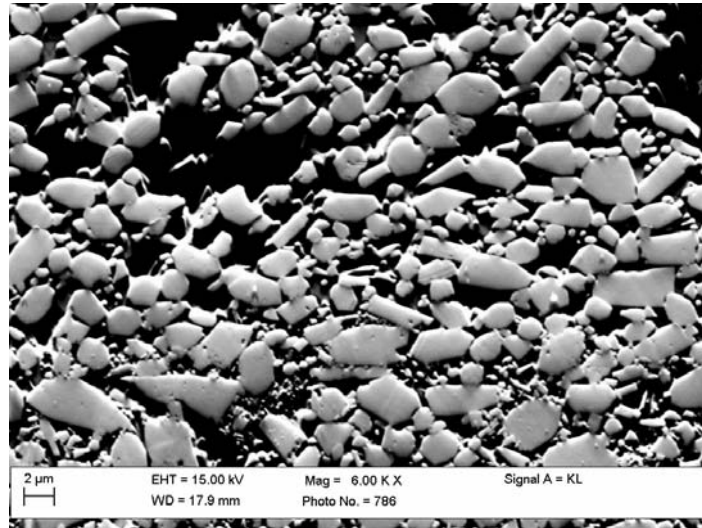


Fig. 3.7-12: Orientation contrast image of CaPtO_3 (plus $\text{Ca}_x\text{Pt}_3\text{O}_4$) deformed in pure shear at 1073 K and $6 \times 10^{-5} \text{ s}^{-1}$. The $\text{Ca}_x\text{Pt}_3\text{O}_4$ forms the interstitial fine-grained material and originally filled many of the cavities in the section. Crystals of CaPtO_3 show little internal deformation and have their long morphological axes (corresponding to the crystallographic a-axis) oriented perpendicular to the compression direction.

Pre-synthesised CaPtO_3 containing up to 20 % of an impurity phase ($\text{Ca}_x\text{Pt}_3\text{O}_4$) were deformed in the deformation-DIA multianvil at 4 GPa and 1073 or 1273 K. The cell arrangement was similar to previous d-DIA experiments except that the furnace used here was a 75 μm thick inconel foil to ensure that the sample was not reduced by reaction with the furnace; no evidence of platinum reduction was observed in any of the recovered samples. After hydrostatic compression the sample was heated to the temperature of interest and allowed to sinter for up to 30 minutes before starting the deformation phase of the experiment. Once the sample was sintered the cell was deformed by advancing the two anvils at either end of the furnace such that the cubic pressure medium shortened at a rate of $9.3 \times 10^{-6} \text{ s}^{-1} < \dot{\epsilon} < 5.6 \times 10^{-5} \text{ s}^{-1}$. This corresponded to sample strain rates of $1.59 \times 10^{-5} \text{ s}^{-1} < \dot{\epsilon} < 1.12 \times 10^{-4} \text{ s}^{-1}$. Samples were deformed to total strains of $0.18 < \epsilon < 0.36$ after which experiments were terminated by simultaneously stopping the deformation and quenching the temperature. The pressure was then slowly released, being careful that the distance between the two axial anvils remained constant, hence no further strain was imparted to the sample during decompression.

Figure 3.7-12 shows an orientation contrast image of CaPtO_3 with 20 % impurity phase, deformed at 1073 K and $6.2 \times 10^{-5} \text{ s}^{-1}$; results are the same for deformation at 1273 K. Post-perovskite grains are idiomorphic with elongation in the crystallographic a-direction of ~ 3 times the b- and c-directions; grains are typically $< 6 \mu\text{m}$ long and 1-2 μm wide. Grains are oriented with their long axes perpendicular to the direction of maximum stress and there is little evidence of internal deformation, with euhedral to subhedral grain shapes and no

variability of forward scattered electron intensity within grains. This suggests that grain-boundary sliding might have played an active role in the deformation, possibly enhanced by the presence of the sub-micron impurity phase on the grain boundaries. This is supported by the observation that experiments with smaller amounts of the impurity phase ($\sim 10\%$) showed more internal strain in CaPtO_3 and a weaker texture for comparable amounts of strain. Electron back-scattered diffraction of the CaPtO_3 shows very clear LPO development (Fig. 3.7-13) with (010) poles oriented parallel to the compression direction and (100) producing a girdle perpendicular to the compression direction.

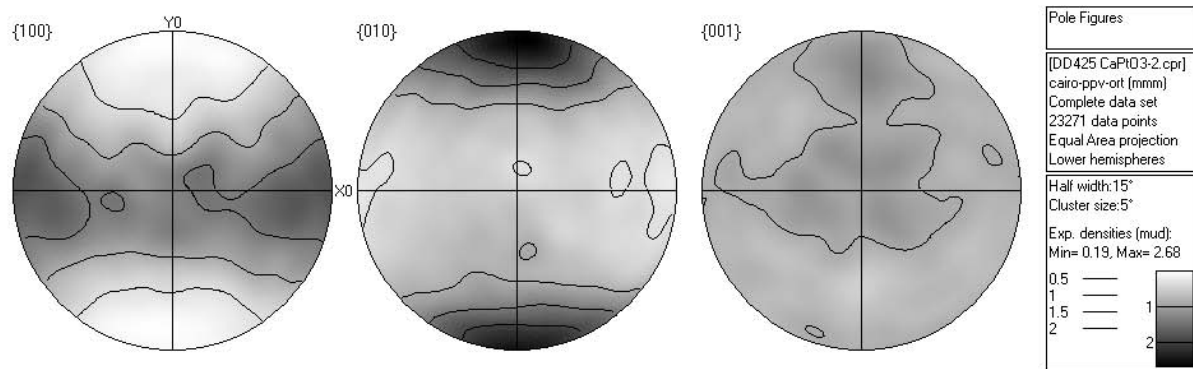


Fig. 3.7-13: Pole figure plot of CaPtO_3 from the experiment shown in figure 3.7-11; compression direction is vertical in both figures; equal area, lower hemisphere projection.

The dominance of [100] dislocations and the strong LPO development with (010) poles in the compression direction, and (100) poles in a girdle, suggests that CaPtO_3 post-perovskite was deforming by glide of [100] dislocations on a (010) glide plane. This is consistent with deformation textures previously observed in CaIrO_3 post-perovskite, but there is some difference in the deformation mechanisms. Previous experiments in CaIrO_3 deformed in simple shear at 1473 K to high strains of $\epsilon=0.5$ showed irregular grain-boundaries suggesting that grain-boundary migration was significant in the iridate phase. Thus the present results, which show clear texture generation but idiomorphic crystals and rare sub-grains, might have had insufficient strain to show significant grain-boundary migration. The presence of a fine-grained (sub-micron) impurity phase further promoted sliding of grain boundaries over their migration. The shape of CaPtO_3 grains, which are elongated in the crystallographic a-direction, combined with grain-boundary sliding would also enhance generation of the a-girdle texture in axial compression and might, therefore, have contributed to the rapid generation of texture in the present experiments.

The presence of MgO in the lower-mantle assemblage might promote rapid texture generation at the onset of strain in a manner similar to that observed here, and as suggested recently as a cause for the D'' reflector. Furthermore, in the presence of an impurity phase idiomorphic grain shapes appear to be preserved during deformation. For CaPtO_3 any shape preferred

orientation developed during deformation will reinforce the lattice preferred orientation generated by slip on [100](010); this is true for CaIrO_3 which also tends to grow with an elongation along the crystallographic a-axis. It remains to be seen if silicate post-perovskite develops grain-shape anisotropy but we note here that fluoride post-perovskites show a strong elongation in the a-direction, suggesting that this might be ubiquitous to post-perovskite-structured materials. Elongation in the a-direction would tend to enhance texture generation for any glide plane at a high angle to (100).

g. *The role of strain rate for grain-scale connectivity of a high-dihedral angle liquid in a crystalline matrix (N. Walte, D.C. Rubie, D.J. Frost and P. Bons/Tübingen)*

Core-mantle differentiation of small planetesimals has been suggested to be initiated by deformation-assisted segregation of molten Fe-S through a crystalline peridotite matrix. An important factor for melt percolation is whether an interconnected melt-network is established at a given melt fraction, dihedral angle, and strain rate. In this study we used two different approaches to investigate high dihedral angle melt interconnectivity. (i) High-pressure axial compression experiments on olivine-FeS melt (initial melt fraction ca. 3 vol.%, dihedral angle $\sim 75^\circ$) and olivine-Au melt (initial melt fraction ca. 4 vol.%, dihedral angle $\sim 150^\circ$) were performed at strain rates of 10^{-3} s^{-1} to 10^{-6} s^{-1} . (ii) Analogue experiments with norcamphor- H_2O (dihedral angle ca. 85°) were performed in an optical *in situ* shear apparatus that allows a continuous observation of the evolving solid-liquid microstructure.

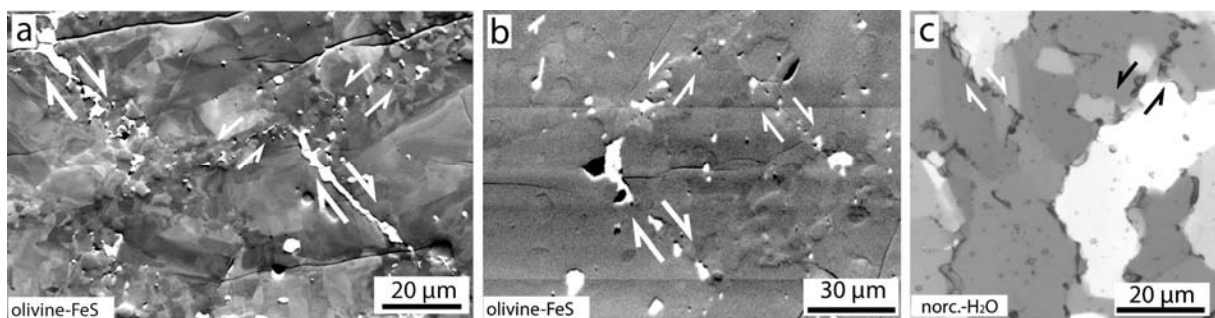


Fig. 3.7-14: Olivine-FeS (a-b) and norcamphor- H_2O (c) deformation experiments at a high strain rate of $\geq 10^{-4} \text{ s}^{-1}$. Deformation is localized into small shear zones that are oriented along elongated melt pockets.

Both the olivine-FeS/Au melt experiments and the analogue experiments reveal a similar range of liquid-matrix interactions as a function of the strain-rate and the dihedral angle. At a “high” strain-rate above $\sim 10^{-4} \text{ s}^{-1}$ the analogue experiments and the olivine-FeS melt experiments are characterized by melt/liquid lubricated shear zones (Fig. 3.7-14). The zones are formed by an elongation and interconnection of liquid pockets that allow grain boundary sliding and strain localization, which leads to limited segregation with a final melt fraction of

ca. 2 vol.%. Melt pocket shape is dominated by stress and strain, hence, the deformation regime is termed stress/strain dominated. At a “low” strain-rate of $\sim 10^{-5} \text{ s}^{-1}$ or below, melt pockets in both analogue and d-DIA experiments are generally little elongated and are not oriented in linear arrays (Fig. 3.7-15). Melt pockets are passively moving within the deforming matrix and no melt interconnectivity is established. Here, the melt pocket shape is mainly determined by surface tension that acts against elongation, hence, the deformation regime is termed surface tension dominated deformation regime. Both regimes are separated by a broad transition regime in which melt pockets are influenced both by deformation and surface tension.

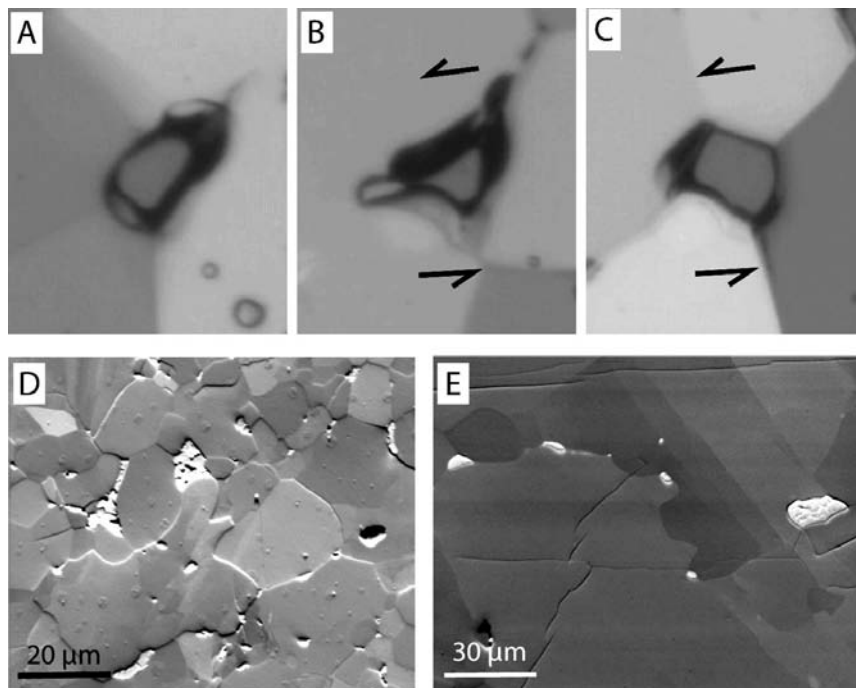


Fig. 3.7-15: Deformation experiments at low strain rates. (a-c) Surface tension prevents elongation of liquid pocket in a norcamphor-H₂O analogue experiment at $1 \times 10^{-6} \text{ s}^{-1}$. (d-e) Olivine-FeS melt experiments at 1200 °C, $2 \times 10^{-6} \text{ s}^{-1}$ (d) and at 1400 °C, $6 \times 10^{-6} \text{ s}^{-1}$. Melt pocket shape in (d) is dominated by grain-growth; at higher temperatures, circular melt pockets pin migrating grain boundaries (e).

To determine whether deformation in undifferentiated planetesimals may lead to interconnection, the experimental results need to be extrapolated to realistic natural conditions with lower strain rates (10^{-12} - 10^{-14} s^{-1}) and larger grain and melt pocket sizes (in the mm range). This is done by balancing differential stresses and surface tension; it turns out that melt pocket radius r is connected to the strain rate by $r \propto \dot{\epsilon}^{-1/n}$ with an exponent $n = 3.5$ for dislocation creep (Fig. 3.7-16). Extrapolation of our results suggest that a high dihedral angle solid-melt system (differentiation under very reducing conditions) will deform in the surface tension dominated regime, thereby limiting the potential for interconnection. A moderate

dihedral angle solid-melt system (oxidizing sulphur-rich conditions) may deform in the stress dominated regime, hence, interconnection and limited melt segregation is possible, leaving a few percent of melt stranded in the matrix.

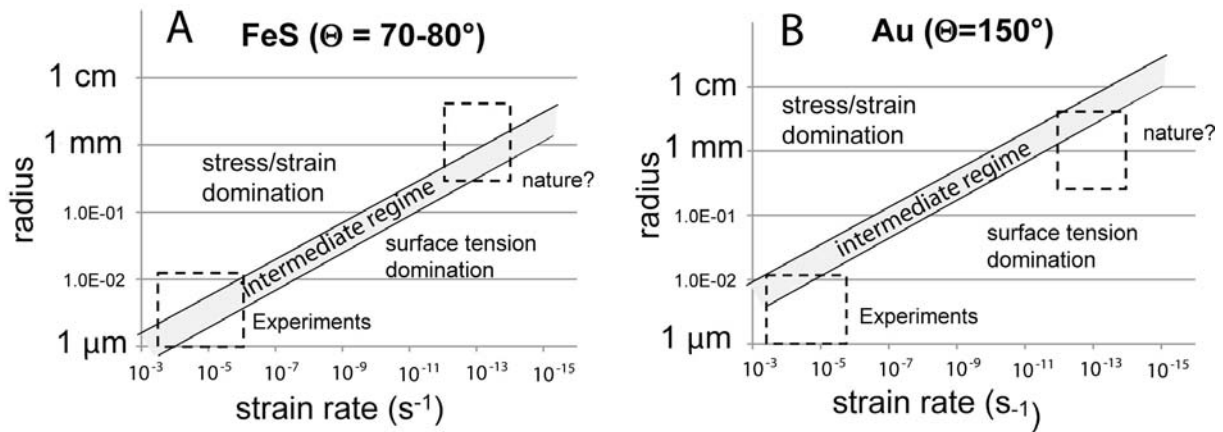


Fig. 3.7-16: Deformation regimes in olivine-FeS metal melt (a) and olivine-Au melt (b). In the stress dominated regime melt interconnection occurs and limited segregation is possible. In the surface tension dominated regime melt pockets remain separate and segregation is unlikely.

3.8 Metamorphism

Metamorphism denotes solid-state processes, in which a primary mineral phase assemblage recrystallizes and equilibrates to new pressure and temperature conditions. Subsequent investigation of these metamorphic assemblages often allows gaining information of geological processes that occur under extreme conditions that are difficult to examine directly, *e.g.*, in the deep Earth or during large meteorite impacts.

If the bulk chemical composition of rocks is altered during metamorphic reactions by fluid or melts flux, the process is called metasomatism. The first contribution presents an investigation of microstructural changes that took place in metasomatised peridotites. Characteristic features such as shape preferred orientations and idiomorphic crystal shapes of olivine could be linked to upper mantle fluid-rock interactions.

The process that is responsible for transforming sediments into sedimentary rocks is called diagenesis, and takes place at comparably low temperatures and pressures. The second contribution explores the mineralogical changes that turn the clay mineral kaolinite into illite/muscovite, a reaction that is commonly used for tracing the progress of diagenesis in sedimentary basins. In this study the effect of pressure variation for the illitisation at a constant temperature was explored.

The topic of the last two contributions is shock metamorphism, short bursts of intense heat and pressure that accompany meteorite impacts on planets or planetary bodies. For the third contribution pyrrhotite minerals were extracted from suevite, a rock that formed from ejected and partially molten material during a large meteorite impact, and investigated by transmission electron microscopy, to determine the effect of the impact on the mineral magnetization. In the final contribution olivine dissociation reactions are described that are found in or close to impact melt-veins in a meteorite. The authors provide evidence that part of the lamellar intergrowth may represent amorphized $(\text{Mg,Fe})\text{SiO}_3$ perovskite, a mineral that is normally only stable under lower mantle conditions.

a. *Fluid-assisted recrystallization in peridotite – natural examples from xenoliths (P. Spacek/Brno and F. Heidelbach)*

It is widely accepted that mantle peridotites may contain a significant amount of fluid phase in a broad sense, including volatile fluids *sensu stricto* and melts. Since the fluids have first order effect on transport properties of grain boundaries, they might play a very important role during the deformation of the mantle. In natural samples the deformation mechanisms of minerals, and hence the rheological properties of the rocks, are inferred from their deformation microfabrics. In peridotites the correct interpretation of olivine microfabric is a crucial issue.

A high melt content related to magmatic processes in the shallow lithosphere is often observed in xenoliths of spinel peridotites found in basaltic lavas. Inclusions of volatile fluids are extremely abundant in some of these samples, too. Therefore, xenoliths are suitable material to study the interaction between peridotite and fluids.

The presence of fluid at grain boundaries usually enhances the exchange rate of elements between the crystal grains, and may lead to specific modes of recrystallization, which differ from the fluid-free system. Unequivocal indicators of the presence of fluids during recrystallization may be chemical variations at grain boundary regions or crystallization of phases enriched in some elements which are not present in the old phases. Such chemical transformations are abundant and they are generally called “metasomatism” in petrology. However, the fluids do not always leave compositional fingerprints in the recrystallized regions. In many samples we observe strong indications of fluid-assisted recrystallization with both old and new grains having identical chemical composition within the resolution limits of standard microprobe analysis. In these cases only specific microstructures indicate the former presence of fluids, such as the formation of near-perfect idiomorphic olivine grains (“tablet olivine”) growing at the expense of old olivine grains (Fig. 3.8-1).

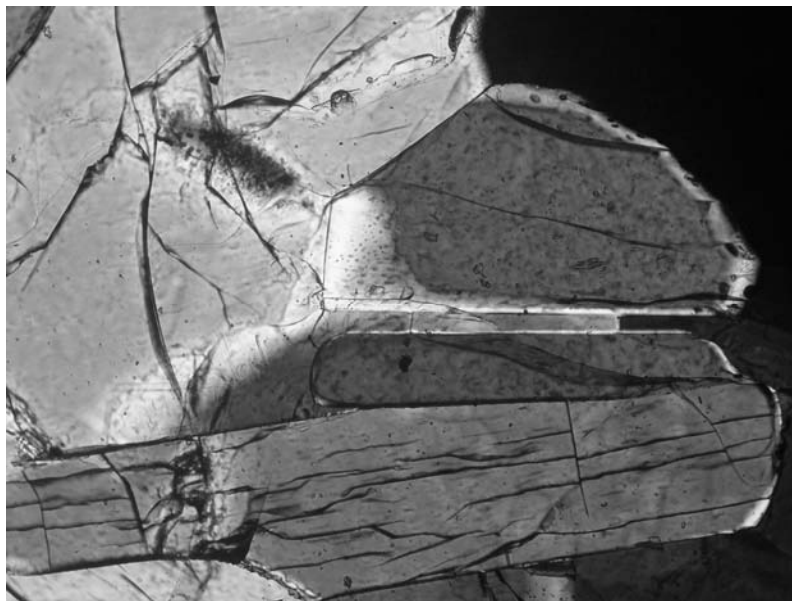


Fig. 3.8-1: Photomicrograph of recrystallized olivine grains with well developed crystal faces growing at the expense of older strained olivine grains. Fluid inclusions are common at grain boundaries. Crossed polarized light, image width is 0.785 mm.

Generally, we are interested in two kinds of processes – (1) fluid/rock interaction in ductile regime with dynamic recrystallization, and (2) the role of fluids during annealing of the rock in static conditions or in the brittle regime of deformation. In our study we analyse the microstructural relations between the original and recrystallized olivine grains in the samples with both static and dynamic fluid-assisted recrystallization. The results will be combined to

explain the development of specific lattice- and shape preferred orientations (LPO and SPO) and to find the common rules for these processes.

The preliminary analyses indicate the potentially important role of preferential development of (010) crystal faces in olivine with fluid-wetted grain boundaries. The microstructural observations indicate several mechanisms of LPO and SPO development in the recrystallized grains (Fig. 3.8-2): a) selective exaggerated growth of some small grains with orientations inherited from the host grains, b) tendency of recrystallized grains to align their larger crystal faces by passive rotation into orientations suitable for grain boundary sliding, and c) oriented growth of recrystallized grains along systems of preferred microfractures.

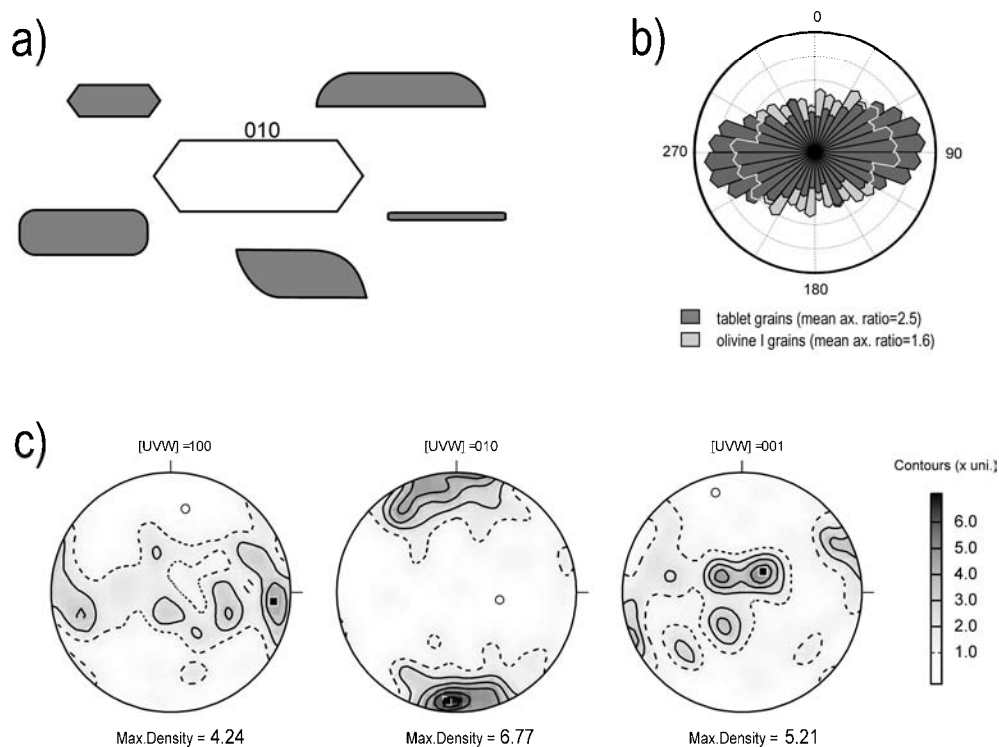


Fig. 3.8-2: Idealized olivine crystal shapes (a), SPO of grain boundaries (b), and LPO (c) of recrystallized „tablet“ grains of olivine in xenolith from Lutyňa.

b. Kaolinite illitization at 300 °C with increasing pressure (M. Mantovani/Sevilla, A. Escudero, A.I. Becerro/Sevilla)

One of the important reactions producing illite as a consequence of burial diagenesis is the illitization of kaolinite, which has been investigated extensively in both natural systems and experimental conditions. Experimental illitization of kaolinite in aqueous solutions containing K^+ has been the subject of study for a number of years since the synthesis of muscovite from kaolinite and KOH solutions at 300 °C. Most of the studies report results on the kinetics of kaolinite illitization, the influence of Na^+ and Mg^{2+} ions on the kaolinite illitization and the

transformation in high molar KOH solutions at low temperatures. All these studies analyse the influence of temperature, chemistry, pH and solid/liquid ratio on the illitization process. However, the reactions are conducted in autoclaves or hydrothermal reactors that generate an internal pressure corresponding to the water vapour pressure at each temperature. The use of this type of reactors, therefore, hinders carrying out the experiments at any other pressure value.

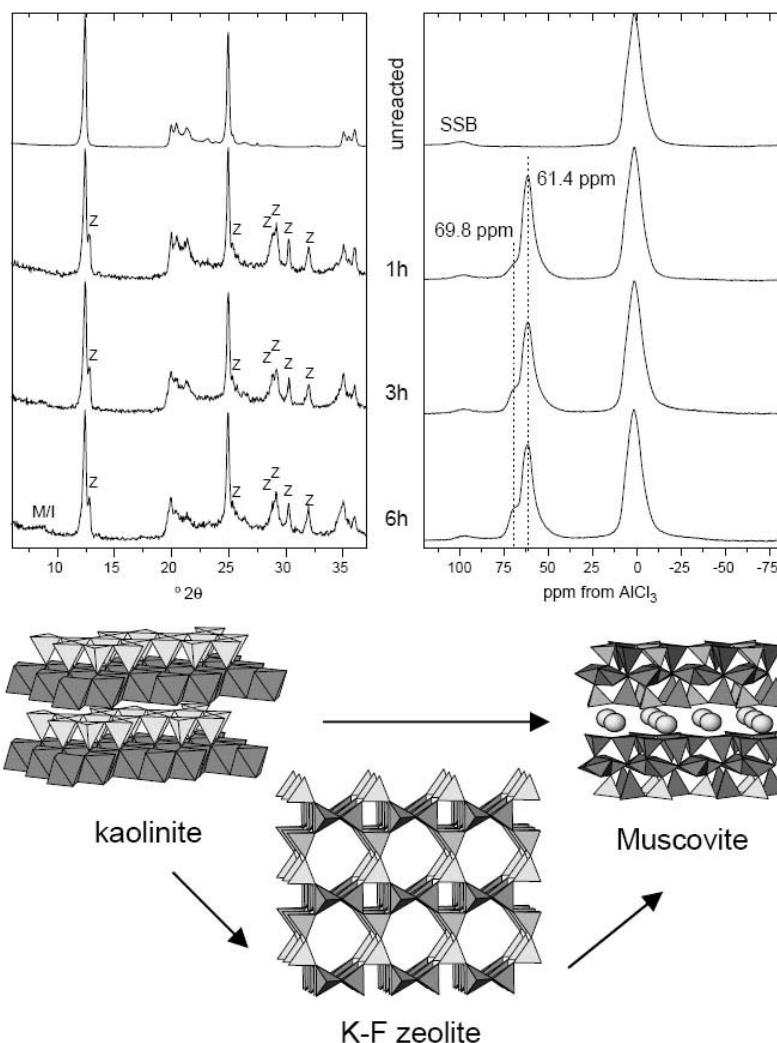


Fig. 3.8-3: XRD patterns (top left) and ^{27}Al MAS NMR spectra (top right) of kaolinite before and after hydrothermal reaction in 2.85 M KOH solution at 300 °C and 1000 bar for 1, 3 and 6 h. M/I: muscovite/illite. Z: K–F zeolite. SSB = Spinning Side Band. Bottom: Polyhedral representations of the crystal structures of kaolinite, muscovite and K–F zeolite.

The aim of the present study is to understand the influence of pressure on the progress of kaolinite illitization. The formation of illite via illitization of kaolinite takes place at an intermediate burial depth of 3–4 km, where pressure can reach values of some 100 MPa (~ 1000 bars). Experiments with powdered kaolinite in KOH (2.85M) solution were carried out

in cold-seal pressure vessels at 300 °C and pressures of 500 bars to 3000 bars. The reaction products were analysed using long and short range order techniques: X-ray diffraction spectroscopy has been used to track the formation of new crystalline phases and ²⁹Si and ²⁷Al MAS NMR spectroscopy have informed of the presence of small crystallites of new phases not detected with XRD. SEM and TEM have been used to analyse the morphology of the reaction products.

The XRD patterns showed a direct transformation of kaolinite into illite/muscovite (I/M) with increasing pressure. However the ²⁷Al MAS-NMR spectra showed, in addition to the I/M resonances, the presence of signal at 60.9 ppm, that should correspond to an intermediate phase, invisible to XRD. A new series of experiments at 300 °C and 1000 bars for 1, 3, 6 hours was carried out to look for a direct evidence of such intermediate phase. XRD and ²⁷Al MAS NMR data of these samples are shown in Fig. 3.8-3. Between 1 and 6 hours of treatment it was clearly observed a well resolved series of reflections of a new crystalline phase called zeolite F. The ²⁷Al signal at 60.9 ppm observed in the spectra must correspond, therefore, to zeolite F nuclei. The pattern after 3 h reaction also showed the presence of a broad reflection of muscovite/illite at 8.7° 2θ, which increased in intensity with time. The typical reflections of kaolinite were still present after 6 h reaction. In conclusion, Kaolinite transforms into I/M when submitted to hydrothermal treatment at increasing pressure, with the formation of an intermediate phase called zeolite F, although coherent diffraction domain size is very small to be detected by XRD.

c. A TEM study of shock deformed pyrrhotite from suevite of the Chesapeake Bay Impact Crater, USA (D. Harries, Ch. Mang/Karlsruhe, A. Kontny/Karlsruhe and F. Langenhorst)

Rock magnetic properties of the suevites obtained from drillings into the Chesapeake Bay impact crater, USA are predominantly related to pyrrhotite and magnetite. We extracted a pyrrhotite sample from a polished thin section of suevite from the Eyreville drill hole by focused ion beam (FIB) preparation and analyzed it by analytical transmission electron microscopy (TEM) in order to elucidate impact related features that may influence the magnetic properties. The analyzed pyrrhotite shows distinct shock related features in form of densely arranged stacking faults and is clearly of a pre-impact origin. Although the measured *c* lattice constant is consistent with a 4C-pyrrhotite composition, SAED pattern reveal superstructure reflections that partially deviate from the 4C structure and do not match any known pyrrhotite superstructure (Fig. 3.8-4). These reflections probably indicate a superstructure related to Fe vacancy reordering in response to the strongly shock faulted sulfur sublattice of the pyrrhotite structure. The structural changes have a direct effect on the Curie temperature, which is shifted from the typical value of 315 °C to about 360 °C. As the suevites experienced pressures between 10 - 35 GPa pyrrhotite most likely lost its initial magnetization and is now carrying a shock remanent magnetization. The investigated pyrrhotite grain was found in a state of partial replacement by marcasite, indicating the action of hydrothermal fluids in the cooling suevite deposits.

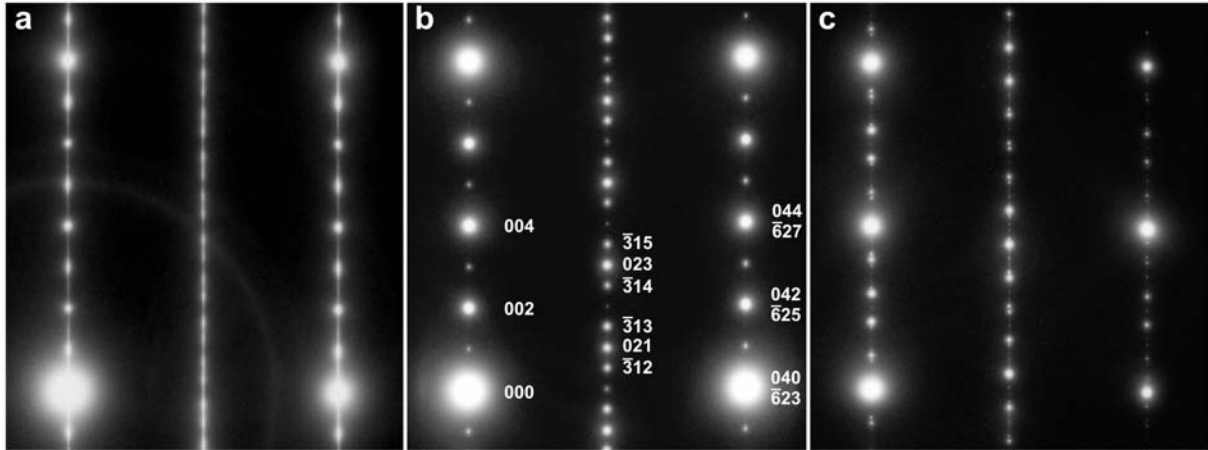


Fig. 3.8-4: Selected area electron diffraction patterns of different pyrrhotites. (a) Shocked pyrrhotite from suevite of the Chesapeake Bay Crater. Reflections are diffuse but still show clear intensity maxima. The rows of the fundamental NiAs type reflections are similar to 4C-pyrrhotite, but the central row is distinct even if twinning is taken into account. For comparison: (b) Unshocked, twinned 4C-pyrrhotite from Nyseter Gruva, Norway. (c) Unshocked NC-pyrrhotite ($N = 4.84$) from the same locality as (c).

d. *Natural dissociation of olivine to perovskite and magnesio-wüstite in a Martian meteorite (M. Miyahara, E. Ohtani and S. Ozawa/Sendai; M. Kimura/Mito; A. El Goresy; T. Sakai, T. Nagase and K. Hiraga/Sendai; N. Hirao and Y. Ohishi/Hyogo)*

High-pressure and -temperature experiments indicate that olivine transforms to its high-pressure polymorphs wadsleyite and ringwoodite, with increasing pressure and temperature and finally dissociates to $(\text{Mg,Fe})\text{SiO}_3$ -perovskite (Pv) + magnesio-wüstite (Mw). Its dissociation mechanism is important to understand the dynamics of the Earth's interior because it affects physical and chemical properties. Since the dissociation was discovered experimentally, many people have been looking for the decomposition reactions in natural samples. However, the dissociation of olivine has never been reported from any natural samples so far. Therefore, the dissociation mechanism of olivine in natural samples is still debated.

We carefully scanned olivine grains in the Martian meteorite, Dar al Gani (DaG) 735 with a FE-SEM and laser micro-Raman spectroscopy. Here we report the first evidence for the dissociation of olivine at high-pressure and -temperature condition induced by a dynamic event on Mars.

DaG 735 studied here consists mainly of olivine (Fa_{34-41}) phenocrysts and a fine-grained matrix. The matrix consists mainly of pigeonite, augite, orthopyroxene, plagioclase glass (maskelynite), merrillite and chromite. There is a shock vein in the DaG 735. The dissociation

texture of olivine was observed in olivine grains adjacent to the shock vein and in olivine fragments entrained in the shock vein. The dissociation textures can be divided into two types; (1) a fine-grained granular ($< \sim 100$ nm) type and (2) a coarse-grained ($< \sim 1.0$ μm) granular type. The fine-grained granular textures are always found adjacent to the shock vein. Only fine-grained granular textures were observed in the olivine fragments entrained in the shock vein. Raman spectra corresponding to pyroxene-glass (~ 665 cm^{-1}) (and minor olivine) were obtained from these dissociation textures. The bulk chemical compositions of these dissociation constituents (Fa_{38-40}) obtained by EPMA are identical to those of the original olivine (Fa_{38-41}).

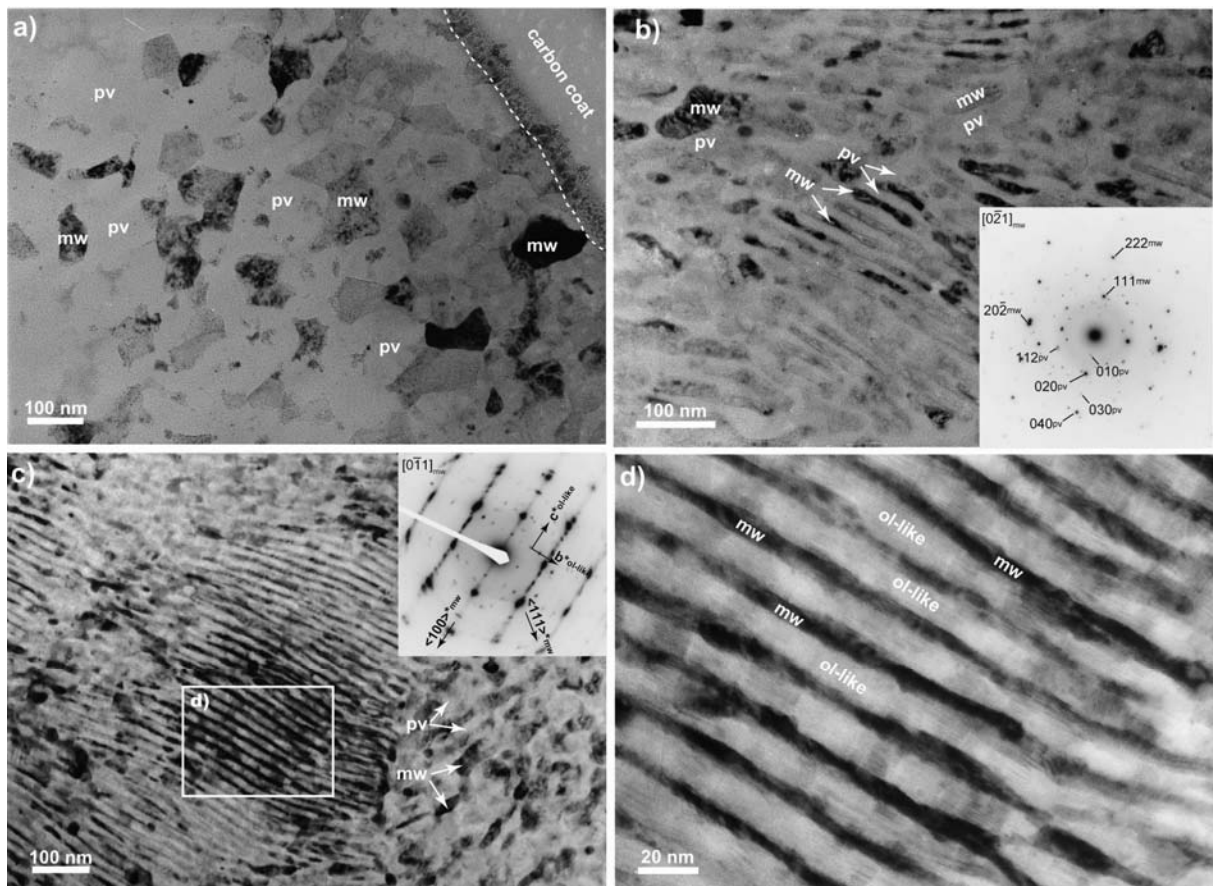


Fig. 3.8-5: TEM images of dissociated olivine. a) equigranular $(\text{Mg,Fe})\text{SiO}_3$ -perovskite (pv) and magnesiowüstite (mw), b) A fragment consisting of alternating $(\text{Mg,Fe})\text{SiO}_3$ -perovskite and magnesiowüstite laminae between granular $(\text{Mg,Fe})\text{SiO}_3$ -perovskite and magnesiowüstite. SAED patterns correspond to granular magnesiowüstite and $(\text{Mg,Fe})\text{SiO}_3$ -perovskite ($b = 4.95(5)$ \AA , a - and c -axes could not be determined.), c) A fragment consisting of alternating magnesiowüstite and olivine-like mineral ($b = 9.92(14)$ and $c = 4.75(4)$ \AA , a -axis could not be determined.) with pyroxene composition. SAED patterns show $\langle 100 \rangle_{\text{Mw}} // (001)_{\text{Ol-like}}$. Granular magnesiowüstite and $(\text{Mg,Fe})\text{SiO}_3$ -perovskite surround the fragment, d) High-Resolution TEM image of a box in c) depicting alternating magnesiowüstite and olivine-like phase.

Slices of the olivine dissociation assemblage were prepared by a FIB system and studied at both a TEM and STEM equipped with an EDS. TEM images show that the fine-grained granular parts consist of equigranular Mw and poorly-crystallized (or amorphous) material (Fig. 3.8-5a). The chemical composition of the poorly-crystallized material is $(\text{Mg,Fe})\text{SiO}_3$. Although clinopyroxene, majorite and akimotoite are candidates for such a composition, they occur in shocked meteorites usually in a crystalline state. Hence, it is unlikely that the glass with the $(\text{Mg,Fe})\text{SiO}_3$ composition represents any of the three phases mentioned above. In rare cases, we could record weak diffraction patterns from the poorly-crystallized materials, which disappeared within ~ 30 second after electron beam irradiation. Nonetheless, we could record some diffraction patterns, which are similar to those of perovskite (Fig. 3.8-5b). We could calculate only a lattice parameter of the b -axis ($4.95(5) \text{ \AA}$) with the diffraction patterns, which appears to be the b -axis value of $(\text{Mg}_{0.75},\text{Fe}_{0.25})\text{SiO}_3\text{-Pv}$ ($4.9330(6) \text{ \AA}$). We anticipate that the poorly-crystallized material was $(\text{Mg,Fe})\text{SiO}_3\text{-Pv}$ prior to amorphization. The chemical compositions obtained by STEM-EDS indicate that iron is more enriched in Mw than in $(\text{Mg,Fe})\text{SiO}_3\text{-Pv}$.

The coarse-grained granular parts include fragments (a dimension $< \sim 0.5 \mu\text{m}$) that are characterized by lamellar intergrowth (Figs. 3.8-5b-d). Many vitrified $(\text{Mg,Fe})\text{SiO}_3\text{-Pv}$ and Mw grains exist in the interstices of the fragments although their dimensions are much smaller than those described above (Fig. 3.8-5a). The bulk compositions of the fragments are similar to those of the original olivine. Two different layers are alternatively stacked in the lamella. Selected electron diffraction (SAED) patterns and the semi-quantitative analyses indicate that the lamellae are alternating Mw and poorly-crystallized material with a composition of $(\text{Mg,Fe})\text{SiO}_3$. We assume that the latter is vitrified $(\text{Mg,Fe})\text{SiO}_3\text{-Pv}$. In some cases, we encounter a crystallographically olivine-like layer stacked with Mw instead of the expected vitrified $(\text{Mg,Fe})\text{SiO}_3\text{-Pv}$ layer. The semi-quantitative compositions of the olivine-like layers appear to be $(\text{Mg,Fe})\text{SiO}_3$. Although olivine with a $(\text{Mg,Fe})\text{SiO}_3$ composition was previously reported from a shock vein of Tenham L6 chondrite, its detail are still unclear. Alternating akimotoite and Mw lamellae or ringwoodite were previously reported as metastable phases during dissociation of ringwoodite or olivine to $\text{Mw} + (\text{Mg,Fe})\text{SiO}_3\text{-Pv}$. The olivine with $(\text{Mg,Fe})\text{SiO}_3$ composition may be a metastable phase as well. Polycrystalline olivine assemblages and olivine fragments appear with increasing distance from the shock vein. Their compositions (Fa_{39-43}) are identical to the original olivine.

The dissociation mechanisms of olivine or ringwoodite to $\text{Mw} + (\text{Mg,Fe})\text{SiO}_3\text{-Pv}$ was previously studied using high-pressure generating devices. Micro-textural evolution from lamellar into equigranular, similar to the sequence of textures encountered here, was previously observed with increasing temperature but at constant pressure conditions. The micro-textural evolution observed in DaG 735 is due to the decreasing thermal gradient into the olivine grain during a dynamic event; *i.e.*, the portion adjacent to the shock vein is the hottest. It is likely that polycrystalline olivine breakdown assemblages kinetically favor grain-boundary nucleation and growth mechanism, leading to form granular texture (Figs. 3.8-5a-

b). Conversely, olivine fragments favor the intra-crystalline mechanism, which would be initiated with defects such as stacking faults and micro-pipes, leading to form lamellar texture (Figs. 3.8-5b-d). When temperature is high enough, only equigranular texture would evolve (Fig. 3.8-5a).

The partitioning coefficients, $K^{Pv/Mw} = [FeO/MgO]_{Pv}/[FeO/MgO]_{Mw}$, between (Mg,Fe)SiO₃-Pv and Mw in equigranular and lamellar textures are ~ 0.15 and ~ 0.78, respectively. The difference between the equigranular and lamellar textures is evident. The partitioning coefficient increases with increasing temperature at constant pressure. The partitioning coefficient between members of the lamellar texture is extremely high. Even if the phase transformation was completed, equilibrium was not achieved in the lamellar texture, as a result of the short duration of the high-pressure and -temperature event. Atomic diffusion would be delayed compared to the phase transformation, especially in case of the lamellar texture. Alternatively, $K^{Pv/Mw}$ might depend strongly on temperature at constant pressure conditions.

3.9 Materials Science

The past decades have brought great progress in the design and capability of apparatus for generating high pressures and high temperatures. High pressure has consequently become a more common and progressively less expensive method for tuning the volume, structure, electronic and magnetic properties, etc. of solids in fundamental physics experiments, as well as providing promising synthesis routes for new applied materials. Bayerisches Geoinstitut is involved in highly sophisticated and challenging research on materials at extreme conditions, and not only maintains state-of-the-art equipment but also develops new apparatus and methods. This year we report the results of studies of various classes of solids – elements, oxides, and complex manganites and borates.

Elemental boron and boron-rich solids are attractive materials for researchers because of their unique physical properties which are suitable for numerous applications. Recently a method of synthesis was developed at BGI of a high-pressure high-temperature phase of boron (B_{28}) which combines a number of useful properties – superhard, semiconducting and optically transparent. The newly grown single crystals of B_{28} were used for detailed Raman spectroscopy and single crystal X-ray diffraction studies which revealed an unexpected isostructural transformation. The first reproducible high-pressure synthesis of single crystals of α -boron at conditions readily accessible to industry opens up new technological perspectives for this semiconducting material.

The Earth science disciplines of modern mineralogy and petrology share with materials science not only the methodological approaches (*e.g.*, physical and chemical methods of synthesis and characterisation of materials, search for correlations between structures and properties, studies of the response of materials to changes of thermodynamic parameters, methods of theoretical modelling, etc.), but also the topics of investigations. Oxides, such as solid solutions based on MgO and Ti_2O_3 (a typical representative sesquioxide), are important components of petrological systems, as well as interesting phases for materials physics. The complex high-pressure high-temperature behaviour of Ti_2O_3 adds a new dimension to the crystal chemistry of transition metal sesquioxides and may be significant not only for materials science, but also for understanding the interiors of the giant planets.

The relation between structure and properties plays a basic role in materials science. Two new examples of its importance are provided by the observation of pressure-induced transformations in rare-earth manganites and studies of the elasticity of lithium tetraborate.

a. *High-pressure synthesis of single crystals of α -boron (G. Parakhonskiy, N. Dubrovinskaia/Heidelberg and L.S. Dubrovinsky)*

Elemental boron and boron-rich phases are attractive materials for researchers because of their unique physical properties which make them suitable for a number of applications. There are two polymorphs of pure crystalline boron that can be synthesised at ambient pressure: α -

rhombohedral boron and β -rhombohedral boron, where the latter is the most easily available modification and can be purchased or relatively easily synthesised in a chemical laboratory. Recently a new high-pressure high-temperature boron phase, orthorhombic γ -B₂₈, was synthesised.

Of all boron modifications, α -boron has the simplest structure. It consists of boron icosahedra arranged in a simple rhombohedral unit cell with $Z=12$. Single crystals of α -boron are difficult to obtain. So far they have been synthesised at ambient pressure primarily through either a pyrolytic decomposition of BI₃ on a tantalum, tungsten and boron nitride surface heated at 800-1000 °C, or by crystallising amorphous boron from a platinum melt. Only three laboratories have been able to obtain single crystals of α -B, and the last reliably documented synthesis was performed nearly 50 years ago by R. Naslain at the University of Bordeaux. The unavailability of single crystals of α -boron is the main reason that their properties have been so far insufficiently studied. In particular, experimental data on the electron density distribution in α -boron is lacking and the nature of bonding has so far only been described based on powder diffraction data. In general, the question of which phase is the ground state of boron is still open and theoretical predictions of bonding, properties and phase relations in the boron system require verification.

We obtained single crystals of pure α -boron starting from β -boron, a synthesis path which has not been reported in the literature so far. Synthesis was performed in a 1000-tonne (Hymag) and 1200-tonne (Sumitomo) multianvil hydraulic press at various pressure-temperature conditions (6-11 GPa and 1200-1600 °C). Highly crystalline β -B (99.995 wt.% purity, grain size < 1000 micron) purchased from Chempur was used as a boron source material. Either pure boron or a mixture of B and Pt powders was loaded into a gold capsule made from metallic tubes. The high-pressure assemblies 18/11 or 25/15 with LaCrO₃ or graphite furnaces were used. Tiny crystals (Fig. 3.9-1) extracted from the capsule were identified as α -B using Raman spectroscopy (Fig. 3.9-2) and confirmed using X-ray diffraction. The colour of the crystals varied from light red to deep red and yellowish depending on the size of the crystals and the experimental synthesis conditions.

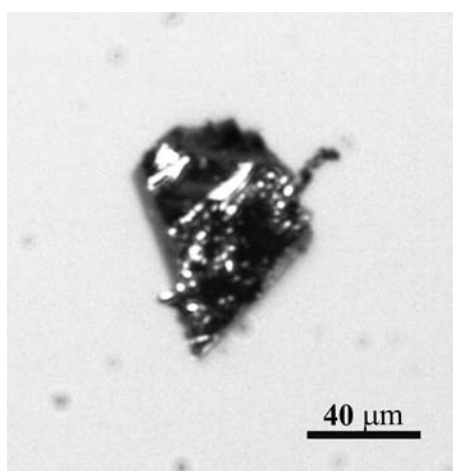


Fig. 3.9-1: Single crystal of α -boron.

The synthesised α -boron is a result of recrystallization from a boron-platinum melt at high pressures and high temperatures. The melting point of pure boron is 2300 °C, but the boron-platinum system is known to have a low melting eutectic that results in a considerable decrease of the melting temperature even at high pressure, with the possibility for α -B synthesis at temperatures as low as 1200 °C. Thus, in a series of experiments we have shown the feasibility of obtaining single crystals of α -boron of good quality at high pressures and high temperatures, and for the first time single crystals of α -boron were synthesised from β -boron as a starting material.

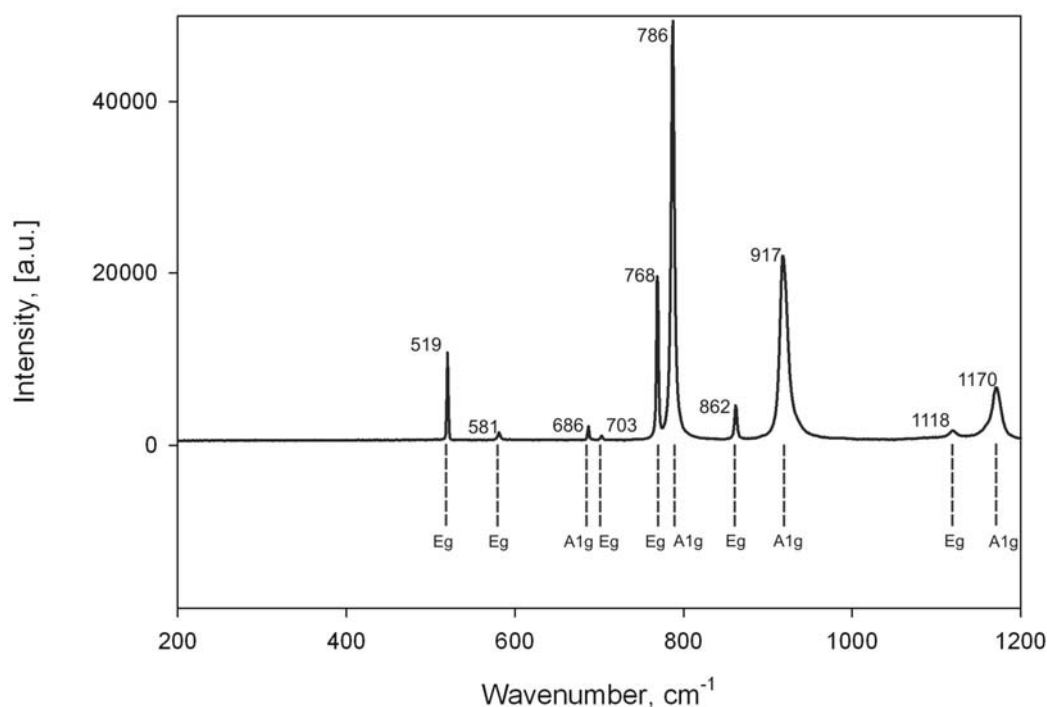


Fig. 3.9-2: A typical Raman spectrum obtained from α -boron synthesised at high pressures and temperatures.

b. *Pressure-induced isostructural phase transformation in γ -B₂₈ (N. Dubrovinskaja/Heidelberg, R. Caracas/Lyon, M. Merlini/Milano, M. Hanfland, Y. Filinchuk, D. Chernyshov and V. Dmitriev/Grenoble; E. Zarechnaya and L.S. Dubrovinsky)*

Elemental boron and boron-rich compounds have been given particular scientific and technological attention because of their specific physical properties: high melting temperatures, a wide energy band gap, high hardness, strong absorbance of neutrons, etc. The structures of these materials are based on icosahedral units as a common feature, and even high pressure does not destroy the rigid units: the recently described high-pressure boron phase γ -B₂₈ consists of B₁₂ icosahedra typical for rhombohedral α - and β -boron. Pure boron crystallises as a γ -B₂₈ phase with *Pnmm* space group at pressures above 8.5 GPa and temperatures higher than 1500 °C. The structure consists of B₁₂ icosahedra and B₂ dumbbells linked covalently (Fig. 3.9-3), and contains 28 atoms in the unit cell. The γ - B₂₈ phase was

demonstrated to be stable to at least 30 GPa and 2000 K; however experimental information about the high-pressure behaviour of the γ -B₂₈ phase has been limited until recently.

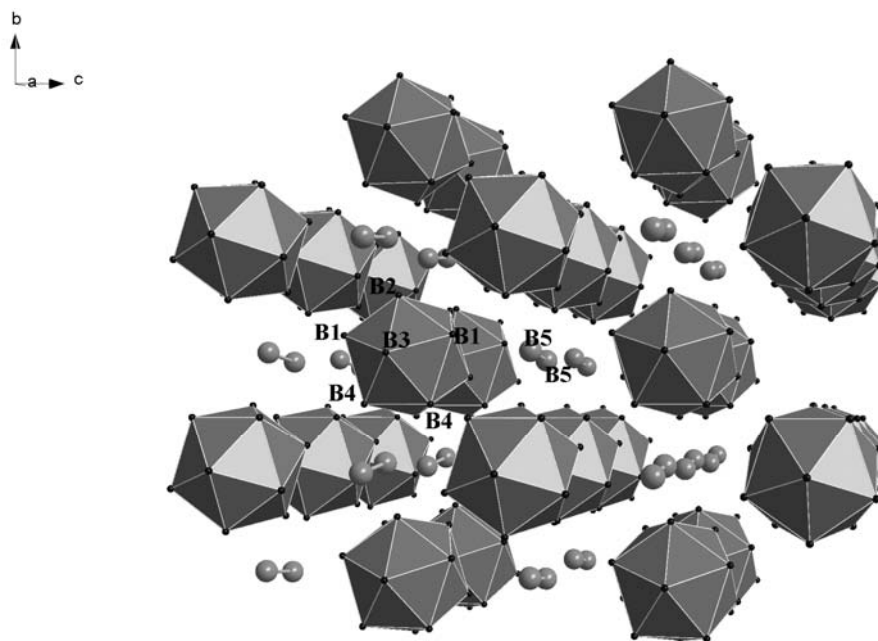


Fig. 3.9-3: Crystal structure of γ -B₂₈.

Here we present results of a high-pressure Raman spectroscopic study of γ -B₂₈ up to 105 GPa and single-crystal X-ray diffraction to over 65 GPa. Single crystals and polycrystalline aggregates of γ -B₂₈ were grown at high pressure and high temperature using a large volume press. Diamond anvil cell experiments were conducted at BGI or at ESRF using diamond anvils with culets of 300 μm , 250 μm or 120 μm in diameter. Gaskets made of rhenium (in the Raman spectroscopy experiments) or steel (in single crystal X-ray diffraction experiments) were indented to a thickness of about 50 μm and holes with diameters of 100 μm or 80 μm were drilled in the centre. Small isometric pieces of the high-pressure boron phase synthesised in a multianvil apparatus were loaded into the gasket holes along with ruby spheres which served as pressure markers. Ne or He was used as a pressure transmitting medium and were loaded at 1.4 kbar (all single crystal X-ray diffraction experiments were performed in a He pressure medium). Single- and double-sided laser annealing was performed on samples compressed in a Ne pressure medium at pressures above 20 GPa at temperatures up to 2000 K.

Raman spectroscopy was performed on single crystals (with typical dimensions of $\sim 5 \times 5 \times 25 \mu\text{m}^3$) and polycrystalline aggregates of the B₂₈ phase. Measurements were performed with LabRam and Dilor XY (DILOR GmbH) systems with a resolution better than 2 cm^{-1} . The 632.8 nm line of a He-Ne laser and 514 nm of an Ar laser were used for the excitation with a power at the sample position of 15 mW to 50 mW. The positions of Raman peaks were determined by processing experimental data using PeakFit© v4.12 software. Single-crystal X-

ray diffraction data were collected at ID09a, ESRF, at 293 K using a MAR555 Image Plate detector, radiation with a wavelength of 0.4143 Å, and a crystal-to-detector distance of 399 mm. 120 frames in the omega scanning range of -30 - +30° were collected (0.5° scanning step size) with an exposure time of 1 s. The data were processed using the CrysAlis software (Oxford Diffraction 2006; CrysAlis RED, version 1.171.31.8, Oxford Diffraction Ltd., Abingdon, Oxfordshire). Crystal structure refinements on integrated intensities were carried out using Jana2006 software.

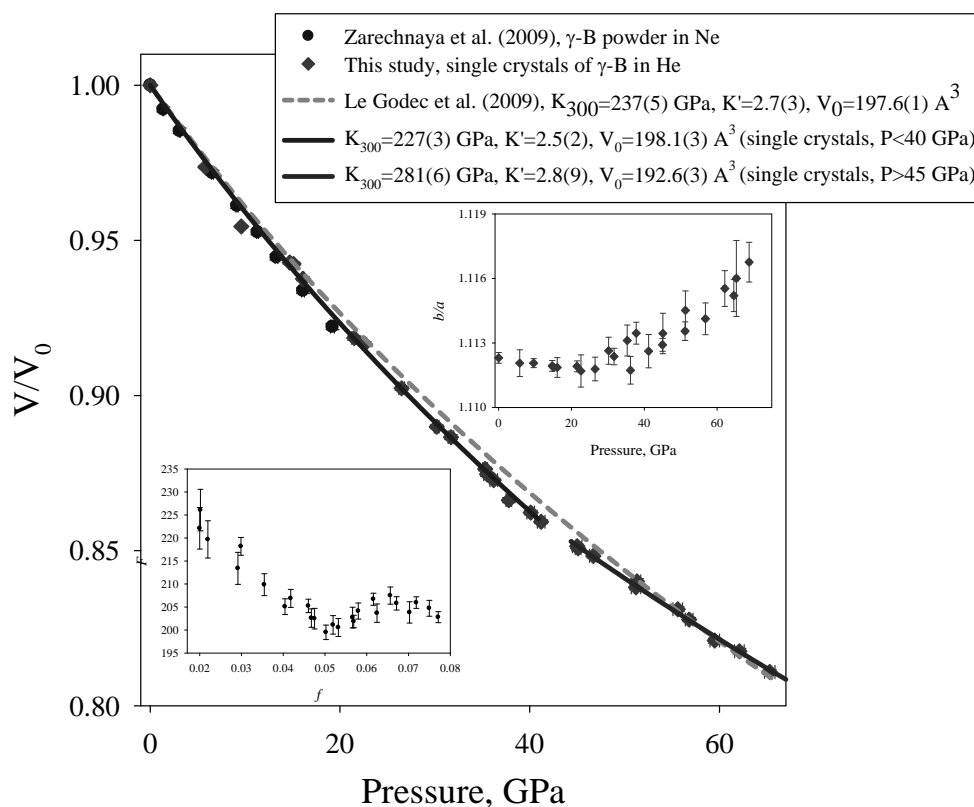


Fig. 3.9-4: The relative unit cell volume of γ -B₂₈ as a function of pressure (diamonds – single crystal data from this study; circles – our powder diffraction data; lines are fits with a 3rd order Birch-Murnaghan (BM3) equation of state, and the dashed line is from literature data based on powder X-ray diffraction to 70 GPa). Inserts show the variation of the ratio of the lattice parameters b/a as a function of pressure and a F - f plot (normalized stress vs. Eulerian strain).

Both the Raman and the single crystal X-ray diffraction studies revealed the existence of *two states* of γ -B₂₈ with a pronounced difference in their vibrational and compressional properties (Fig. 3.9-4). The abrupt change of the properties occurs at pressures \sim 40 GPa. However, neither symmetry nor structure was observed to change in this pressure range. We conclude, therefore, that B₂₈ undergoes an *isostructural* phase transformation (ISPhT). ISPhTs are particular cases of isosymmetric transformations and include discontinuous isostructural transitions and crossovers. They are rare, intriguing phenomena in solids often associated with a significant volume collapse, giant magneto-elastic coupling, or negative thermal expansion.

Boron is an element in the second row of the Periodic Table and the conventional mechanisms of the ISPhT in its crystal structure are highly unlikely (indeed, theoretical calculations do not indicate any significant changes of band structure of γ -B₂₈ to at least 100 GPa). At the same time γ -B₂₈ is a quasimolecular material. A detailed single-crystal X-ray diffraction study conducted at ambient pressure revealed strong polar-covalent bonding with an electron density excess at B2 and B4 atoms (which belong to the B₁₂ icosahedra) and an electron density deficit at B5 atoms (which form B₂ dumbbells) (Fig. 3.9-3). This suggests that the ISPhT in γ -B₂₈ can be a result of changes in the electron density distribution between boron atoms and/or bonds; in other words, changes in the character of chemical bonding.

c. Thermal EOS of tungsten from single crystal X-ray data (L.S. Dubrovinsky, K. Glazyrin and A. Kurnosov; N. Dubrovinskaia and T. Pippinger/Heidelberg; M. Merlini/Milano and M. Hanfland/Grenoble)

High-pressure research depends critically on pressure standards. The common requirements for a pressure standard are a simple crystal structure giving few diffraction lines, the absence of phase transitions at high pressures and temperatures, and a relatively high chemical stability. Tungsten easily satisfies these conditions and its accurate equation of state at ambient temperature has already been measured based on single crystal compression experiments up to above 150 GPa. There are theoretical predictions of the thermal equation of state (EOS) of tungsten, but experimental static compression data at high temperature are lacking. We determined lattice parameters of tungsten single crystals compressed in a Ne pressure transmitting medium (which can be used also as an internal pressure standard; Fig. 3.9-5). Because of the simple body-centred cubic structure with just two atoms per unit cell, usually only 3 to 5 powder diffraction lines can be measured in high-pressure experiments and X-ray energies up to 40 keV; whereas using a single crystal, 8 to 16 diffraction peaks were recorded and individually integrated after refining the beam centre position.

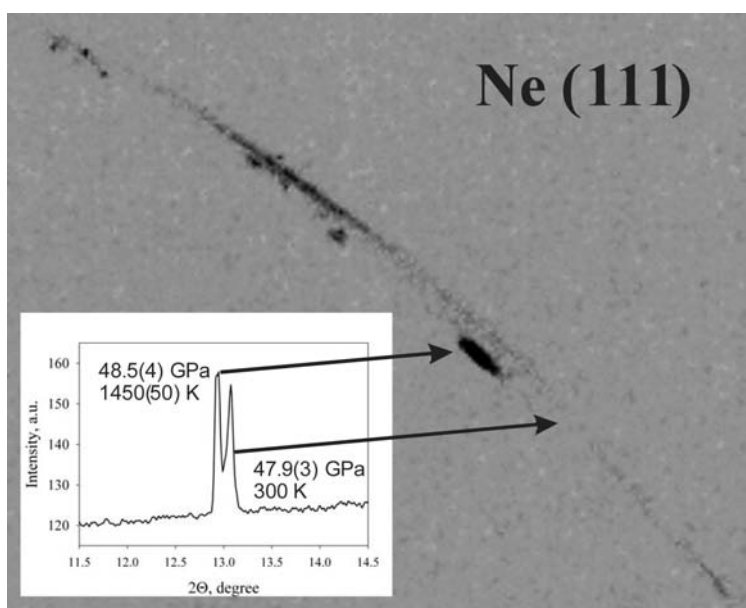


Fig. 3.9-5: Splitting of the Ne (111) line during heating at 48 GPa.

The fit of eighteen P - V data points collected at ambient temperature and pressures between 4.5 GPa and 46.6 GPa using a 3rd order Birch–Murnaghan EOS gave a bulk modulus of $K_{300}=304(2)$ GPa and a pressure derivative of $K'=4.1(2)$ in good agreement with literature data (Fig. 3.9-6, Table 3.9-1). The data collected during laser heating were evaluated using a previously described formalism. In particular, we used the following formula to describe our experimental data:

$$P=1.5 K_{T,0} [(V_{T,0}/V)^{7/3}-(V_{T,0}/V)^{5/3}] [1-0.75 (4- K'_{T,0})\{ (V_{T,0}/V)^{2/3}-1\}], \quad (9.1)$$

where $K_{T,0}$, $K'_{T,0}$, and $V_{T,0}$ are the bulk modulus, its pressure derivative, and the volume of the unit cell at zero pressure and temperature T (in K), respectively. The bulk modulus can be expressed as

$$K_{T,0}=1/(b_1+b_2T+b_3T^2), \quad (9.2)$$

while the unit cell volume $V_{T,0}$ is given by the following equation:

$$V_{T,0}=V_0\exp(\alpha_1*(T-T_0)+ \alpha_2*(T^2-T_0^2)/2- \alpha_3(1/T-1/T_0)), \quad (9.3)$$

where V_0 is the unit cell volume at zero pressure and b_i and α_i are fitted parameters.

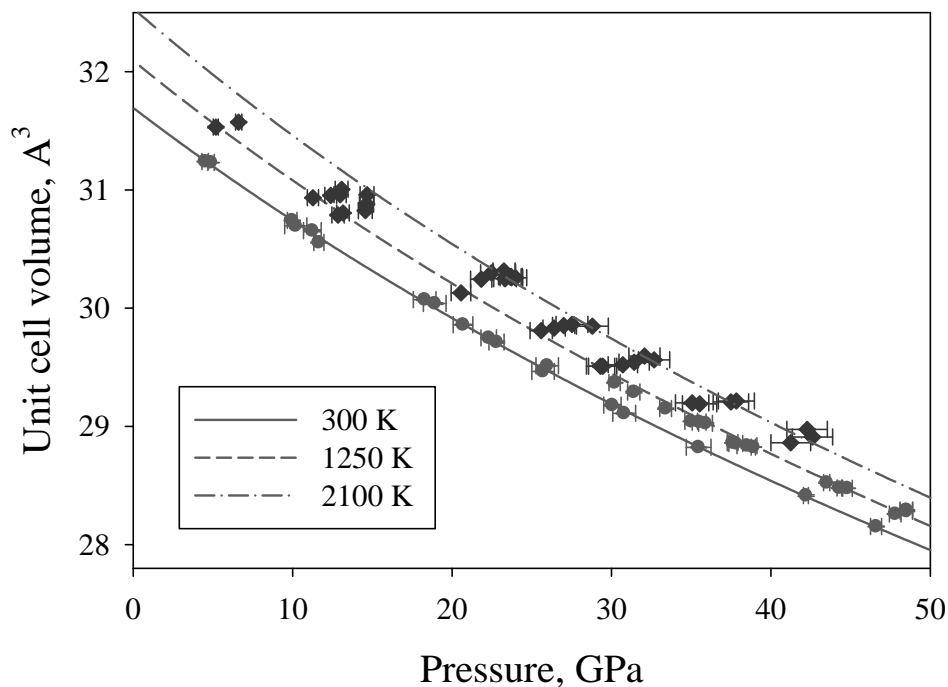


Fig. 3.9-6: Unit cell volume of tungsten measured at different pressures and temperatures. The data points shown by circles were used to fit a thermal equation of state with Ne as a pressure gauge as described by Eqs. (9.1-9.3). The pressures corresponding to the data points shown by diamonds and for the curves were determined using the fitted thermal EOS parameters.

Table 3.9-1: Thermoelastic parameters of tungsten (Eqs. 9.1-9.3)

$V_0, \text{\AA}^3/\text{mol}$	31.69(2)
$K'_{300,0}$	4.09(33)
$\alpha_1, 10^{-5} \text{ K}^{-1}$	1.37(1)
$\alpha_2, 10^{-9} \text{ K}^{-2}$	-0.74(2)
$\alpha_3, \text{ K}$	1.098(3)
$b_1, 10^{-3} \text{ GPa}^{-1}$	3.168(28)
$b_2, 10^{-7} \text{ K}^{-1} \text{ GPa}^{-1}$	2.800(25)
$b_3, 10^{-11} \text{ K}^{-2} \text{ GPa}^{-1}$	-3.66(3)

d. *First principles phase diagram calculations for the systems MO-M'O with M, M' = Mg, Ca, Sr, Ba, or Cd (O. Adjaoud/Potsdam and G. Steinle-Neumann, in collaboration with B.P. Burton/Gaithersburg and A. van de Walle/Pasadena)*

The alkaline-earth oxides and CdO have similar valence configurations and crystallise in the rock-salt structure. These materials have attracted significant attention recently, and have been studied both experimentally and theoretically because of their importance in a wide range of industrial applications from catalysis to microelectronics. While the end-member compositions have been widely studied, the solid solutions between them are largely unexplored and provide an interesting perspective for higher melting temperatures and physical properties. In addition to industrial applications the solubility of the other M^{2+} ions in MgO is of significance for the Earth's mantle.

First-principles (FP) computations, in which properties of materials are derived from quantum mechanics, are particularly interesting because they allow for the exploration of new materials even before a procedure to synthesise them has been devised. A FP calculation seeks to determine the properties of a material without relying on any experimental input, starting solely from the knowledge of the atomic number of the constituents. The cluster expansion (CE) formalism is increasingly used as a valuable tool for predicting and interpreting thermodynamic effects in a wide class of materials and problems, including precipitation, solubility limits, ionic diffusion and chemical ordering. We have used the Alloy Theoretic Automated Toolkit (ATAT) which combines FP calculations and the CE formalism and takes in account configurational contributions to free energy. Our calculations predict asymmetric miscibility gaps in the all six systems (Fig. 3.9-7).

Even in the simplest case of a harmonic crystal, the vibrational energy as a function of atomic arrangement can have a strong effect on the phase diagram. In the present work, we have investigated the phase diagrams of MgO-CaO, MgO-CdO, CaO-SrO, SrO-BaO, MgO-SrO and CaO-BaO solid solutions. In the ATAT vibrational contributions to free energy are taken into account by a transferable force constant approach. Here we find that this approach fails

for systems with large size mismatch between the M and M' ions (MgO-SrO and CaO-BaO). For the other systems the vibrational contribution to the free energy considerably changes the miscibility gap at high temperature and the consolute temperature (the maximum temperature of the miscibility gap) is reduced, improving the agreement with available experimental data. For the MgO-based solid solutions (MgO-CaO, MgO-CdO, MgO-SrO) the M' ions are soluble in MgO only at very high temperatures.

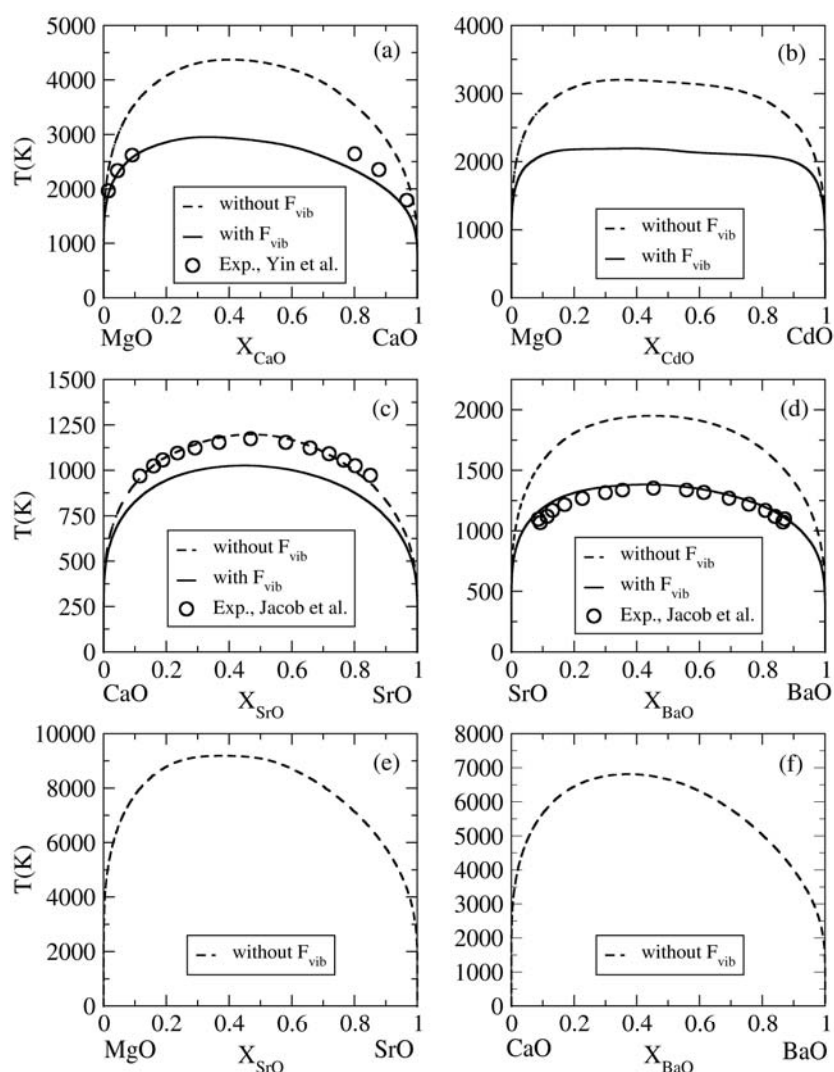


Fig. 3.9-7: Calculated phase diagrams for the systems: (a) MgO-CaO, (b) MgO-CdO, (c) CaO-SrO, (d) SrO-BaO, (e) MgO-SrO, and (f) CaO-BaO. Solid and dashed curves are performed with and without F_{vib} , respectively. Open circles show experimental data.

e. *P-T phase diagram and structural stability of $Pnma\text{-Ti}_2\text{O}_3$ (S.V. Ovsyannikov, L.S. Dubrovinsky, X. Wu/Beijing and N. Dubrovinskaia/Heidelberg)*

Titanium oxides have attracted attention due to their potential technological importance. At ambient conditions sesquioxides normally adopt a corundum-type structure. High-pressure studies (*e.g.*, in Al_2O_3 , Fe_3O_3 , etc.) revealed transitions to a post-corundum phase (presumably

of Rh_2O_3 (II)-type) and then to a CaIrO_3 -type. A U_2S_3 -type structure was considered as a potential endpoint of the above transition sequence in the pressure range up to 3-4 Mbar. Very recently it was shown that other sesquioxides of both ‘transient’ (such as Sc_2O_3 and Ti_2O_3) and heavier cation masses (such as In_2O_3) deviate from the proposed sequence. Thus, a new phase found in Ti_2O_3 has been refined with $Pbnm$ symmetry (standard notation – $Pnma$) and the Th_2S_3 structural type, and this phase appeared to be quenchable to ambient conditions. Likewise, phases of Sc_2O_3 and In_2O_3 have been refined in the Gd_2S_3 -type structure. Further compression of sesquioxides, and in particular the new phases, could lead to the discovery of a new transition sequence(s).

Very recently two research groups, our team at BGI and a team at ISSP (Tokyo), independently synthesised a new golden polymorph of Ti_2O_3 with the Th_2S_3 -type structure ($Pnma$ space group). We investigated the structural, optical, transport and other properties of $Pnma$ phases at high pressure and high temperature and report some of these results below.

After a series of HP-HT synthesis runs in a multianvil press and *in situ* high-pressure studies in diamond anvil cells we were able to determine for the first time a P - T phase diagram of Ti_2O_3 (Fig. 3.9-8). This diagram relates the three currently known phases of Ti_2O_3 and shows that the transition to the $Pnma$ phase is possible after a transition from the original corundum to the distorted corundum phase that is characterised by a different c/a ratio. If the distorted corundum phase is neglected in lattice dynamics calculations one obtains a transition pressure (3 GPa) to the $Pnma$ phase that is too low.

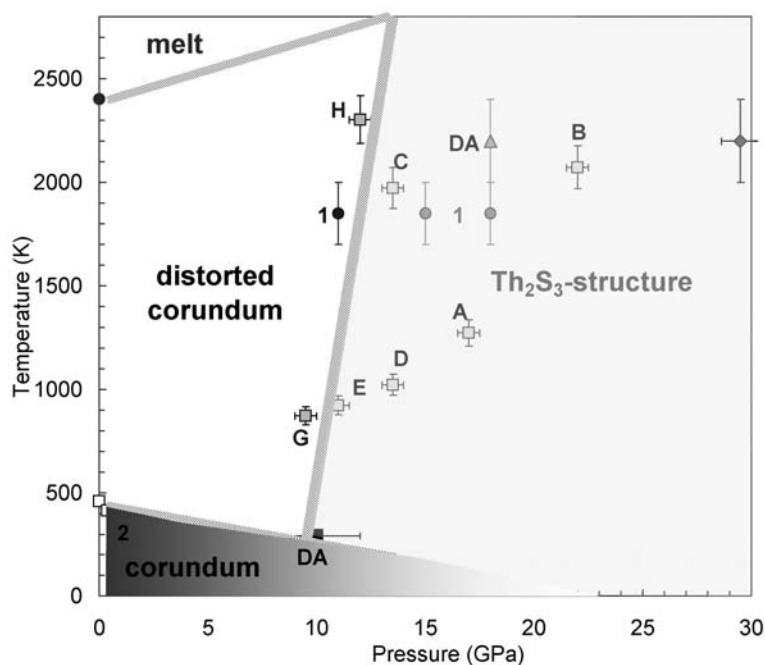


Fig. 3.9-8: Proposed P - T phase diagram of Ti_2O_3 . Different symbols correspond to different experimental runs conducted by our group and those from the literature.

In several *in situ* high-pressure runs of $Pnma$ - Ti_2O_3 to 50-75 GPa we established that the $Pnma$ phase is stable up to 80 GPa and 2200 K (Fig. 3.9-9). Comparative structural and optical studies on samples of $Pnma$ - Ti_2O_3 synthesised at different P - T conditions did not

reveal any essential differences. For instance, the Raman spectra of the *A-E* samples are almost identical (Fig. 3.9-10), and the only difference between them consists in a minor softening of the frequencies (by 2-3 cm^{-1}) in samples synthesised at higher temperatures (~ 2000 K). This behaviour may be due to a strong variation in sample mesostructure: at the higher temperatures of ~ 2000 K the starting micrograins of 1-3 μm in diameter grow into single crystallites of ~ 10 -20 μm in diameter, hence reducing internal stresses in the crystallites. The pressure evolution of the Raman spectra showed the structural stability of the *Pnma* phase (Fig. 3.9-11), in agreement with the structural data (Fig. 3.9-8).

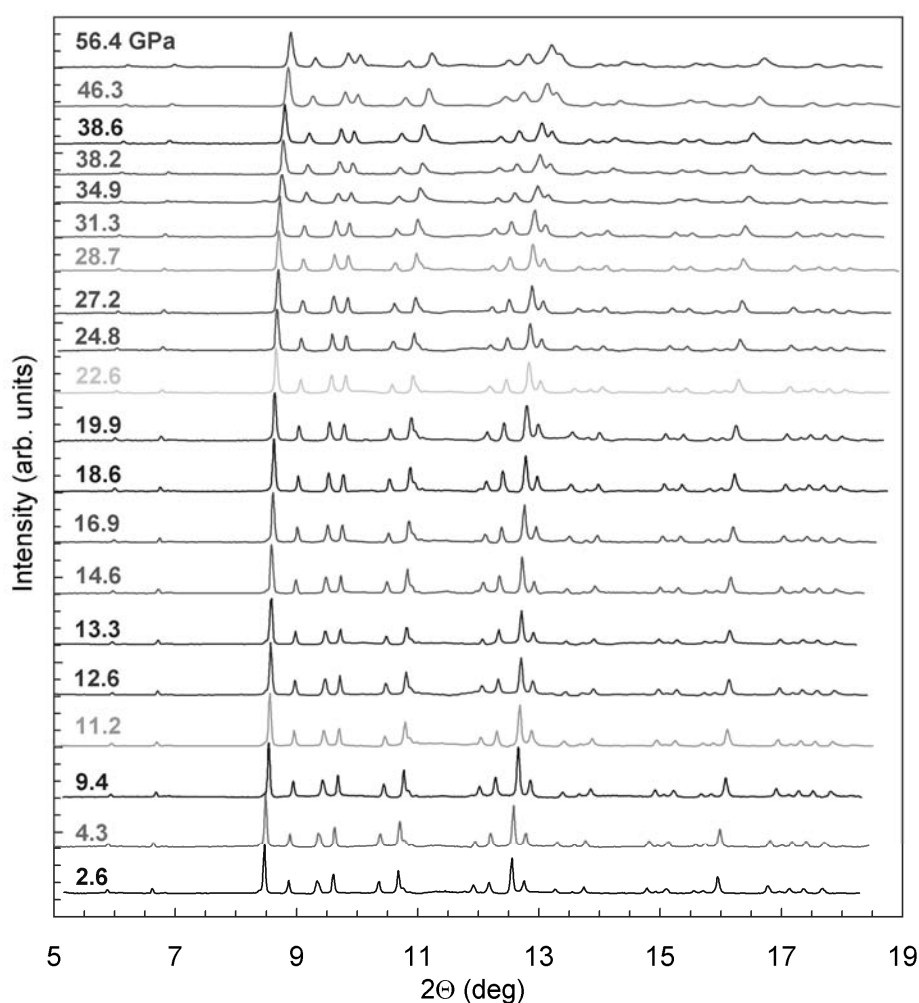


Fig. 3.9-9a: Evolution of X-ray diffraction patterns of *Pnma*- Ti_2O_3 under pressure.

Electrical resistivity measurements established the semiconducting character of electrical conductivity in the *Pnma* phase and revealed a narrow energy gap below 0.1-0.2 eV. Theoretical calculations of the density of states also found a gap of about 0.1-0.2 eV. However, direct probing of the electron band structure with mid- and near-infrared absorption spectroscopy could not detect the edge of absorption down to 0.08 eV.

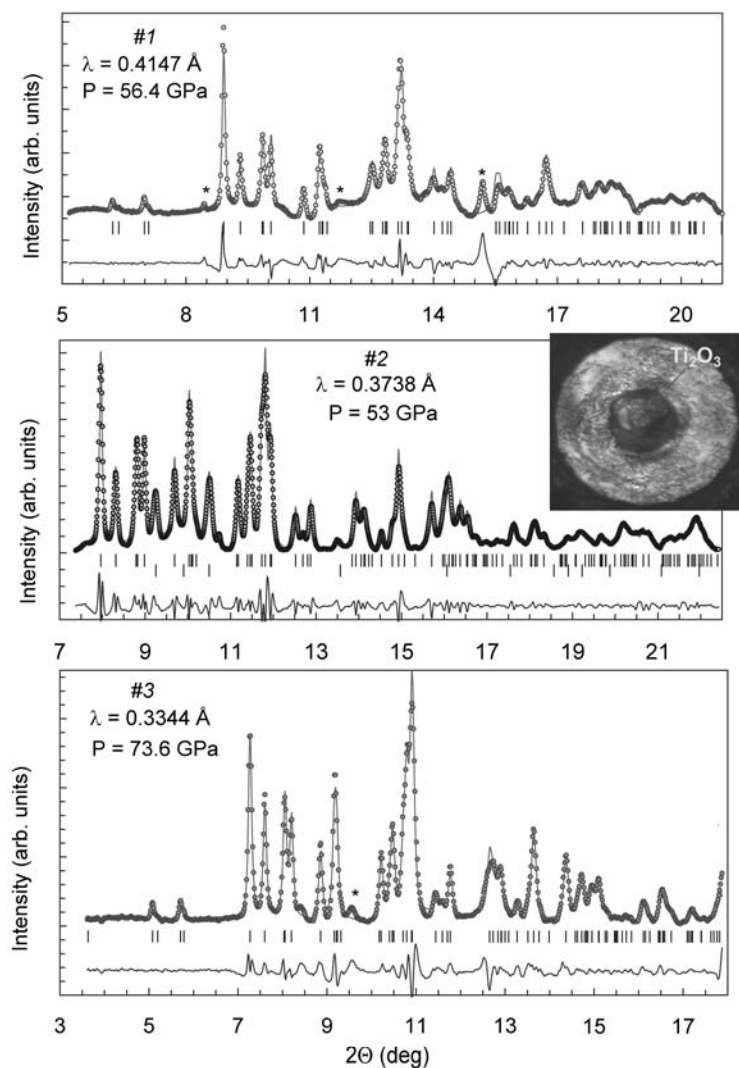


Fig. 3.9-9b: Examples of refinement of X-ray diffraction patterns of Ti_2O_3 in the $Pnma$ space group for samples at different pressures.

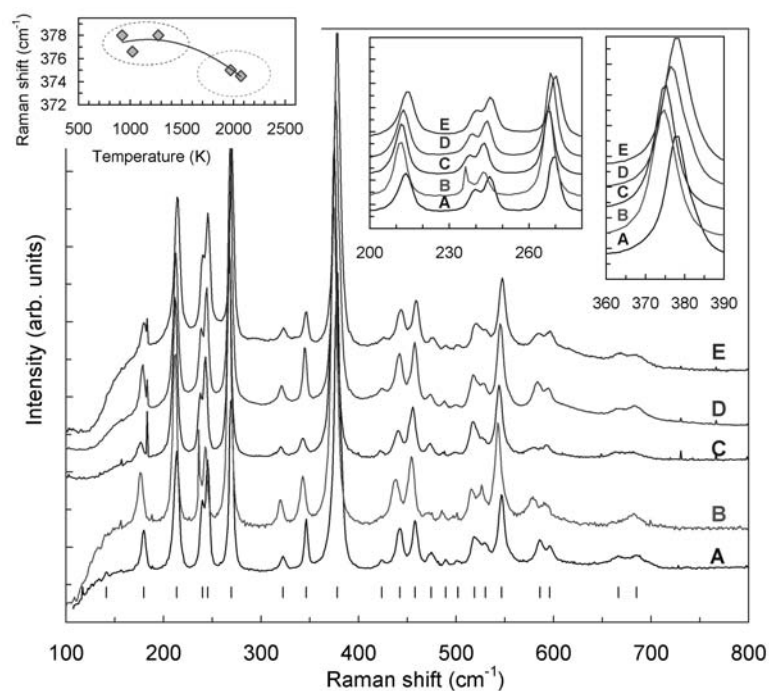


Fig. 3.9-10: Raman spectra of several samples of $Pnma$ - Ti_2O_3 . The left inset shows the dependence of wave number of the strongest peak on synthesis temperature. The right insets show regions of the main plot at a larger scale.

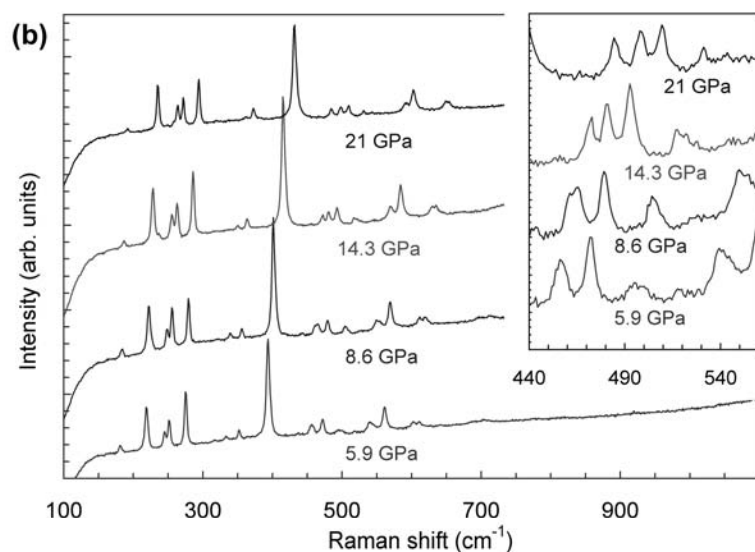
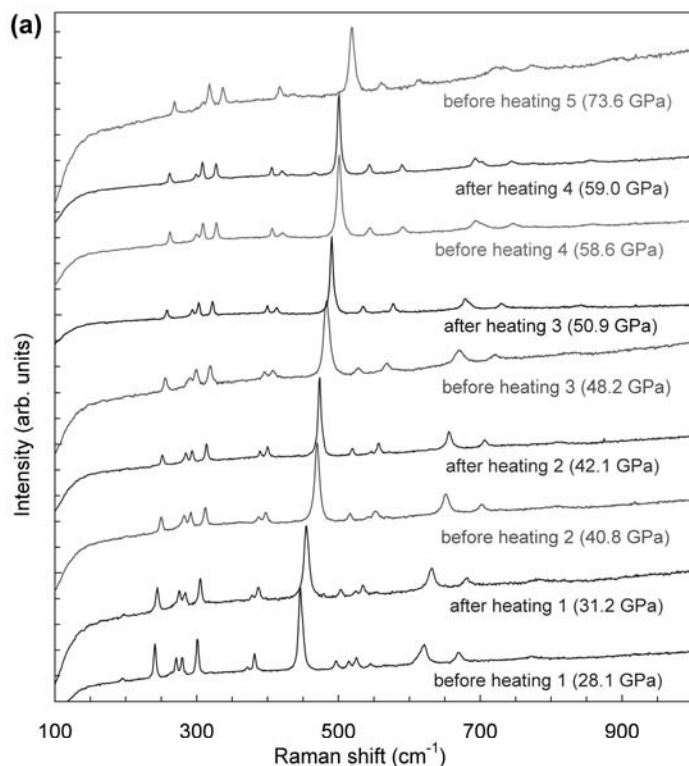


Fig. 3.9-11: Raman spectra of *Pnma*-Ti₂O₃ under high pressure before and after laser heating: (a) up to 74 GPa, (b) less than 22 GPa.

f. *Structural phase transition in Pr_{0.15}Sr_{0.85}MnO₃ at high pressure (D.P. Kozlenko/Dubna, L.S. Dubrovinsky, N.T. Dang/Dubna and Tula, Z. Jiráček/Prague; E.V. Lukin and B.N. Savenko/Dubna)*

Manganites of perovskite type $Ln_{1-x}A_xMnO_3$ (Ln – lanthanum or rare earth element, A – alkaline earth element) exhibit rich magnetic and electronic phase diagrams depending on the type of Ln and A elements and their ratio. The properties of manganites depend to a large extent on the balance between ferromagnetic (FM) interactions mediated by itinerant charge

carriers (double-exchange mechanism) and superexchange interactions between localised spins of manganese ions, which are generally antiferromagnetic (AFM). The FM double exchange is usually stronger than AFM superexchange for doping levels $x < 0.5$, while for higher x values the AFM superexchange interaction becomes dominant. Recently it was found that application of high pressure also leads to various modifications of the magnetic structure of $\text{Pr}_{1-x}\text{Sr}_x\text{MnO}_3$ manganites, $x \sim 0.5$. While previous studies of $\text{Pr}_{1-x}\text{Sr}_x\text{MnO}_3$ were mainly focused at the $x \sim 0.5$ region, high-pressure behaviour of compounds with larger x values in the vicinity of the boundary between C-type and G-type AFM states of the magnetic phase diagram still remains unclear. In the present study, we have investigated the crystal structure of $\text{Pr}_{0.15}\text{Sr}_{0.85}\text{MnO}_3$ manganite using X-ray diffraction at pressures up to 55 GPa.

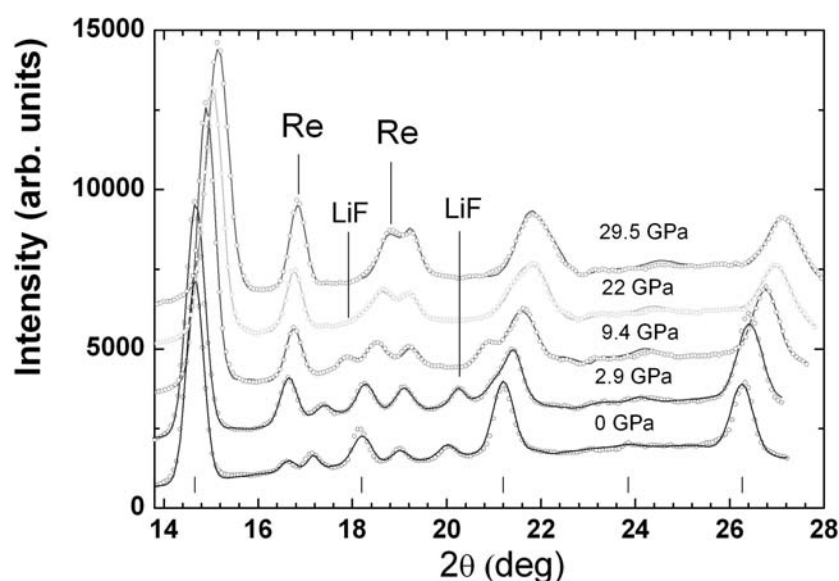


Fig. 3.9-12: X-ray diffraction patterns of $\text{Pr}_{0.15}\text{Sr}_{0.85}\text{MnO}_3$ measured at room temperature and the indicated pressures and processed using the Rietveld method. The experimental points, calculated profiles and Bragg peak positions (for the cubic phase at ambient pressure) are shown. The diffraction peaks from LiF added for pressure calibration and the Re gasket are also marked.

The X-ray diffraction patterns of $\text{Pr}_{0.15}\text{Sr}_{0.85}\text{MnO}_3$ at selected pressures and ambient temperature are shown at Fig. 3.9-12. At ambient conditions, the cubic phase with space group $Pm\bar{3}m$ was observed. At pressures above 2 GPa a splitting of the diffraction peak (200) at $2\theta = 21.2^\circ$ was observed, indicating a structural transition to a phase with lower symmetry. From analysis of experimental data using the Rietveld method, it was found that the high-pressure phase of $\text{Pr}_{0.15}\text{Sr}_{0.85}\text{MnO}_3$ has tetragonal $I4/mcm$ symmetry, which is a consequence of a MnO_6 octahedral tilt of the $00c'$ type. The unit cell of this structure is quadrupled with respect to the simple perovskite subcell (lattice parameters $a_t \approx a_p\sqrt{2}$ and $c_t \approx 2a_p$). The volume compressibility data of the tetragonal high-pressure phase were fitted using a third-

order Birch–Murnaghan equation of state. The calculated values of the bulk modulus, its pressure derivative and the unit cell volume corresponding to ambient pressure for the tetragonal phase of $\text{Pr}_{0.15}\text{Sr}_{0.85}\text{MnO}_3$ are $B_0 = 225(8)$ GPa, $B' = 4(1)$ and $V_0 = 223.4(8)$ Å³, respectively.

g. Elasticity and equation of state of diomignite, $\text{Li}_2\text{B}_4\text{O}_7$ (D.M. Trots, A. Kurnosov, T. Boffa Ballaran and D.J. Frost)

Natural $\text{Li}_2\text{B}_4\text{O}_7$ (mineral name diomignite) has been found as small (< 30 µm) anhedral or euhedral crystals in fluid inclusions in spodumene. It has been suggested that the presence of diomignite in Li- and B-rich rare-element pegmatites, in particular in Tanco pegmatite, may be partially responsible for accumulation/precipitation of rare-metal ores and gem minerals. Moreover, the recent technological interest in lithium tetraborate $\text{Li}_2\text{B}_4\text{O}_7$ has been motivated by its excellent prospects for use in non-linear optical and piezoelectric devices. Despite the mineralogical and technological interest in $\text{Li}_2\text{B}_4\text{O}_7$, its high-pressure behaviour is not well constrained. Amorphisation has been observed at 17 GPa by means of high-pressure Raman scattering; whereas the elastic behaviour was studied using ultrasonic wave velocity measurements at pressures < 1 GPa. Based on these latter measurements which indicated a shear mode softening with pressure, a possible phase transition was suggested to occur at about 3.2 GPa.

In the present study single crystal diffraction experiments were performed on $\text{Li}_2\text{B}_4\text{O}_7$ up to 8 GPa in order to determine whether it undergoes any phase transformation and to obtain accurate and precise equation of state parameters. Because $\text{Li}_2\text{B}_4\text{O}_7$ is composed of very light atoms with small scattering power, it is difficult to carry out experiments with diffractometer systems equipped with conventional X-ray sources. We found that by using a high-brilliance rotating anode X-ray source combined with multilayer optics we can obtain a significant increase in the signal to noise ratio and perform experiments on very small and/or very light materials without the need of a synchrotron radiation source. The P -unit cell data collected for lithium tetraborate $\text{Li}_2\text{B}_4\text{O}_7$ (space group $I4_1cd$) revealed no phase transitions up to 8.3 GPa. The pressure evolution of the unit cell volume of the $I4_1cd$ structure has been described using a third-order Birch-Murnaghan equation of state (BM-EoS) with the following parameters: $V_0 = 923.21(6)$ Å³, $K_0 = 45.6(6)$ GPa and $K' = 7.3(3)$ (Fig. 3.9-13). A linearised BM-EoS was used to fit the axial compressibilities with the following EoS parameters: $a_0 = 9.4747(3)$ Å, $K_{0a} = 73.3(9)$ GPa, $K'_a = 5.1(3)$ and $c_0 = 10.2838(4)$ Å, $K_{0c} = 24.6(3)$ GPa, $K'_c = 7.5(2)$ for the a and c axes, respectively. The elastic anisotropy of $\text{Li}_2\text{B}_4\text{O}_7$ is very large with a zero pressure compressibility ratio $\beta_c/\beta_a = 3.0(1)$. The compressibility of $\text{Li}_2\text{B}_4\text{O}_7$ obtained in our study is significantly larger than that estimated from ultrasonic wave velocity experiments performed only below 1 GPa, and is in general agreement with other compressibility values available in the literature.

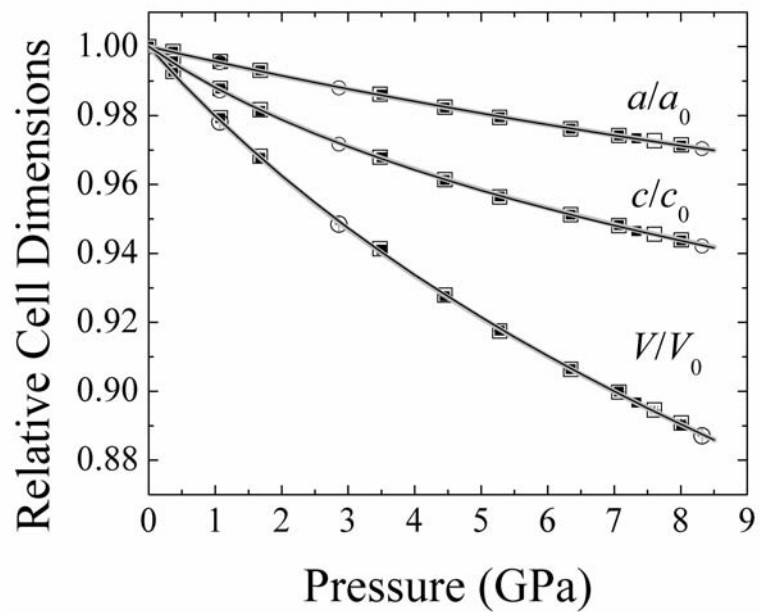


Fig. 3.9-13: Variation of the relative unit-cell volume and lattice parameters of $\text{Li}_2\text{B}_4\text{O}_7$ measured using single crystal X-ray diffraction.

3.10 Methodological Developments

New developments in experimental, analytical and numerical techniques form the backbone of any scientific research. Hence their importance cannot be overemphasized. The Bayerisches Geoinstitut has a long tradition of participating at the highest level in this discipline, with many of its innovations having been adapted by labs worldwide. The design, fabrication and testing of new experimental, analytical and numerical methods is a time-consuming challenge that requires a high technical and financial support, both of which is provided at the Bayerisches Geoinstitut. In the last year, new development was made in a portable laser heating system for single crystal X-ray diffraction experiments in diamond anvil cells, which renders it possible to study crystal structures at simultaneous high pressures and temperatures. Continuous efforts were made for the intense synchrotron Mössbauer source at ESRF. In the last year, the reduction of beam size by a KB mirror was installed to allow high P-T Mössbauer experiments in diamond anvil cells. The 6-ram multianvil apparatus installed in 2009 was continuously developed especially for deformation experiment. The reliability of the combination system of Brillouin spectroscopy and high-brilliance X-ray diffraction installed in 2009 was examined by test measurement for standard materials. Techniques for pressure measurement of diamond anvil cell using Raman scattering are also reported here.

The development in the analytical field is to measure the concentration of siderophile elements and sulfur in fluid phases using a quartz capsule. Another is the development of software to characterize mineral surface roughness on basis of statistical parameterization for future application to kinetic studies. Finally, a new approach is described for the numerical modeling of sharp boundaries in geodynamic flow that overcomes previous limitations.

a. *Portable laser heating system for single crystal X-ray diffraction experiments in diamond anvil cells (L.S. Dubrovinsky and K. Glazyrin; N. Dubrovinskaia/Heidelberg; M. Merlini and M. Hanfland/Grenoble; V.B. Prakapenka/Chicago)*

There are two major methods of heating in diamond anvil cells (DAC) – laser and electric heatings. X-ray powder diffraction experiments under electric (external) heating in DACs can generate temperatures up to 1200 K at pressures over 250 GPa. However, single crystal X-ray diffraction studies are limited to about ~1000 K. Laser heating techniques in DACs cover a wide pressure-temperature field – above 250 GPa and up to 3500 K. Recent advantages in on-line laser heating techniques result in significant improvement of reliability of *in situ* X-ray powder X-ray diffraction studies in laser-heated DACs that become routine at a number of synchrotron facilities including specialized beam-lines at the 3rd generation synchrotrons. However, so far all existing DAC laser-heating systems cannot be used for single crystal X-ray diffraction experiments, aimed not only determining lattice parameters, but also at measuring intensity data for structural refinements. The reason is that the laser beam enters

the cell at a fixed angle in all existing DAC laser-heating facilities. A partial rotation of the DAC, which is required in monochromatic single crystal X-ray diffraction experiments, results in the loss of the target. It may be even dangerous if the powerful laser light starts to scatter in arbitrary directions by the diamond anvils. In order to overcome this problem, we have modified a portable laser heating system according to our own design.

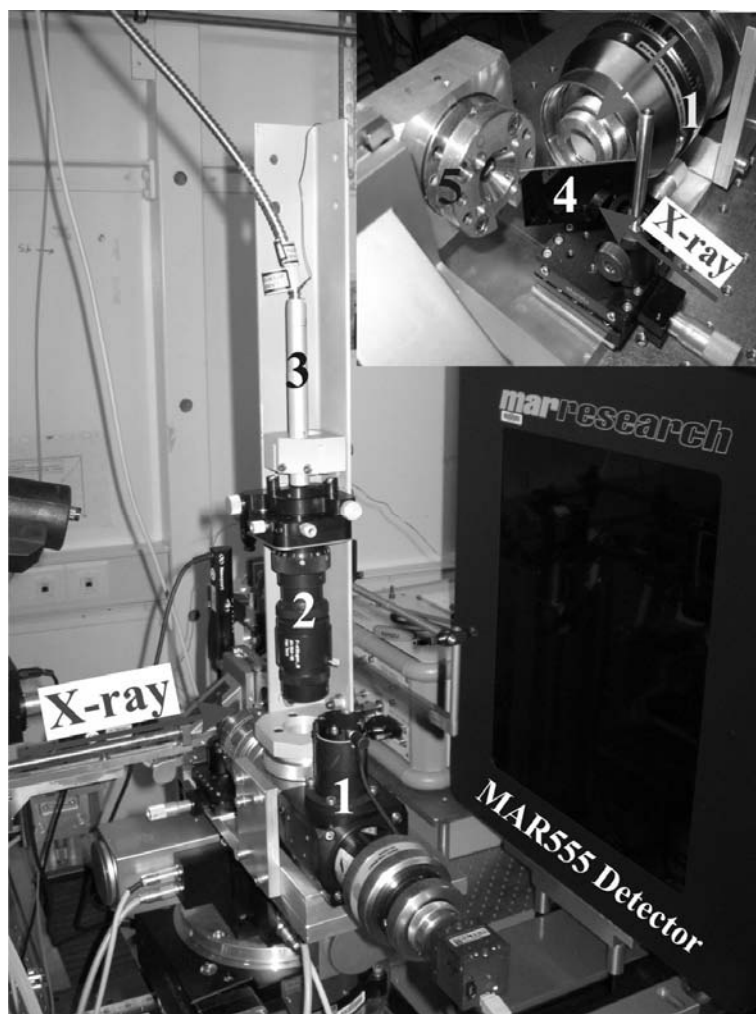


Fig. 3.10-1: Universal laser-heating head (UniHead) with a π -shaper mounted for single crystal X-ray diffraction experiments in diamond anvil cell at ID09a beam-line at ESRF (Grenoble). 1: UniHead; 2: π -shaper; 3: the optical fiber connected to the 100 W laser light source; 4: the silver-coated carbon mirror; 5: the diamond anvil cell. Gray arrow in inset shows the direction of the laser beam.

The system consists of two major components – the source of laser light (100 W SPI100 Modulated High Power Fiber Laser) and the universal laser-heating head (UniHead) (Fig. 3.10-1). The functions of the UniHead in the portable laser heating system are (1) to focus the incoming laser beam on the sample within the DAC, (2) to provide high magnification imaging of the sample in the DAC with coaxial illumination, and (3) to give access for the

multi-wavelength spectroradiometry for temperature measurements. The output of the SPI100 laser has a Gaussian shape with a diameter of ~ 3 mm at $1/e^2$ and is focused down to ~ 25 μm at FWHM. However, use of the π -shaper (Fig. 3.10-1) increases the beam size to ~ 40 μm and creates a flat top beam. Due to the modular construction, the portable laser heating system can be used in various modifications, namely, for heating samples in an independently standing DAC or in a cell coupled directly to UniHead - in a “direct” (the optical axis of the DAC and the UniHead axis coincide) or “right angle” (at 90° between the optical axis of the DAC and that of the UniHead) geometry. In the following experiments performed at the ID09a beam line at the ESRF synchrotron facility, we employed the UniHead in the “right angle” geometry with a carbon mirror mounted from the side of the incident X-ray beam (inset in Fig. 3.10-1). The X-ray scattering from glassy carbon, is blocked by the DAC’s body and does not introduce any features into the X-ray diffraction profiles. In the “right angle” geometry, the DAC and the UniHead mounted on a common general platform were rotated simultaneously and ω -scans (necessary for single crystal X-ray diffraction experiments) were realised without loss of the focusing of the laser. In the present configuration we used ω -scans in the range of -30 to $+10$ degrees with a 0.5° step size.

We have demonstrated the application of this system for simultaneous high-pressure and high-temperature single crystal diffraction studies using three examples – accurate measurements of the lattice parameters of tungsten single crystals at pressures up to 43 GPa and 2500 K, and high-pressure high-temperature structural behaviour of hematite Fe_2O_3 up to 40 GPa and 1800 K and silicate perovskite $(\text{Mg}_{0.62}\text{Fe}_{0.38})(\text{Al}_{0.36}\text{Si}_{0.64})\text{O}_3$ up to 88 GPa and 2500 K.

b. Continued development of a synchrotron Mössbauer source and the first results (V. Potapkin, A.I. Chumakov and R. Rüffer/Grenoble; G.V. Smirnov and S.L. Popov/Moscow; L.S. Dubrovinsky and C.A. McCammon)

We have constructed an intense Synchrotron Mössbauer Source (SMS) at beamline ID18 of the European Synchrotron Radiation Facility (ESRF). The source has convenient in-line geometry and high intensity. It can work in any mode of the storage ring operation. Our previous work (see BGI Annual Report 2009) demonstrated that a high-quality energy-domain Mössbauer spectrum of a standard-calibration single-line absorber can be collected over a period of only 10 minutes. Its source line is roughly two and one half times wider than the ^{57}Fe natural line. However, the beam size in that system was quite large and roughly one cm in diameter. For geophysical studies, beam focusing should be realized by further development of the apparatus in order to study samples at high pressure and eventually high temperature.

In order to reduce the beam size while retaining a large portion of the X-ray intensity, we installed Kirkpatrick-Baez mirrors in the experimental hutch, resulting in a beam diameter of

10-15 microns with a throughput of 60 %. Through careful adjustment of the geometry, the small size of the beam could be maintained also during vibration of the $^{57}\text{FeBO}_3$ crystal (the Mössbauer source). Initial tests were made using a diamond anvil cell (DAC) containing ^{57}Fe , followed by measurements of DACs containing $^{57}\text{Fe}_3\text{O}_4$ and $^{57}\text{Fe}_2\text{O}_3$, each at 70 GPa. For these experiments high quality spectra could be collected within 10 minutes.

In order to demonstrate the application of the SMS to geophysical studies, we chose a project that would be otherwise impossible to carry out using conventional Mössbauer spectroscopy – the nature of high-pressure spin transitions of Fe^{3+} in lower mantle perovskite. Such transitions are important to lower mantle properties and dynamics because of their potential effect on density, elasticity, transport and rheological properties; however they are expected to occur only at high pressures (> 50 GPa), in which sample sizes are inevitably small. Furthermore, although Mössbauer spectroscopy is an excellent method to detect the presence of iron spin transitions, the smaller influence of the atomic environment of Fe^{3+} on hyperfine parameters compared to Fe^{2+} means that a high signal-to-noise ratio is required to detect changes in spin state.

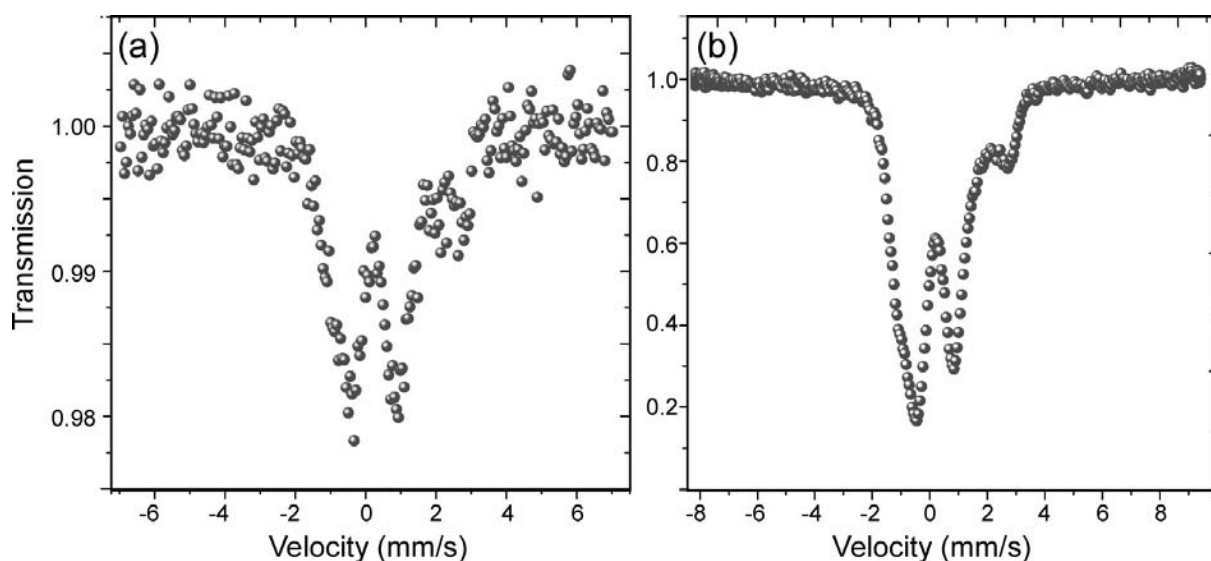


Fig. 3.10-2: Comparison of two Mössbauer spectra of the same DAC loaded with $(\text{Mg}_{0.6}^{57}\text{Fe}_{0.4})(\text{Si}_{0.7}\text{Al}_{0.3})\text{O}_3$ perovskite at 94 GPa: (a) using conventional Mössbauer spectroscopy at Bayerisches Geoinstitut collected over one week; (b) using SMS at ID18, ESRF collected over 10 minutes.

We loaded a sample of $(\text{Mg}_{0.6}^{57}\text{Fe}_{0.4})(\text{Si}_{0.7}\text{Al}_{0.3})\text{O}_3$ perovskite containing approximately 80 % Fe^{3+} into a DAC. SMS spectra were collected at roughly 10 GPa pressure intervals during compression to nearly 100 GPa, and each spectrum measurement took approximately 10 minutes. At the end of the synchrotron experiment, the DAC was returned to Bayerisches

Geoinstitut and a conventional Mössbauer spectrum was collected for comparison (Fig. 3.10-2). The measurement time for the BGI system (left) was around one week (~ 10080 minutes), compared to only 10 minutes for the ESRF system (right), around three orders of magnitude lower. At the same time, the spectral quality of the SMS spectrum is vastly superior to that of the conventional spectrum, and enables resolution of the individual sub-spectra. Preliminary analysis of the sequence of ten SMS spectra as a function of pressure suggests that nearly all Fe^{3+} occupies the A-site and shows no spin transition as a function of pressure. However, there may be a small proportion of Fe^{3+} on the B-site which undergoes a high-spin to low-spin transition above 50 GPa.

c. BGI facility for simultaneous measurements of sound velocities and densities of single crystal samples at high pressures: test measurements of α -quartz and pyrope in DAC (A. Kurnosov, D.M. Trots, D.J. Frost and T. Boffa Ballaran)

A Brillouin spectroscopy system has been recently built up at BGI. Due to the combination of the system with a high intensity X-ray source, the system opens a new area for *in situ* studies of materials under extreme conditions. With this system, it is now possible to measure sound velocities and densities of materials simultaneously as a function of pressure and temperature. These data will lead to new pressure scales, as the current scales are still essentially based on dynamic shock-wave data. The experimentally determined density-velocity relationships will also provide essential information for understanding seismic observations and modeling the composition and evolution of the Earth. So far such measurements were possible only at the synchrotron facilities, namely, APS and SPring-8.

The facility consists of a six-pass Brillouin spectrometer combined with a high intensity X-ray generator, rotating anode, with Mo $K\alpha$ radiation. A Verdi laser with wave length of 532 nm at power of 0.3-0.5 mW is used for excitation of Brillouin scattering. The central part for both sub-systems (X-ray and Brillouin) is a 4-circle Huber diffractometer. The diamond anvil cell is mounted on a goniometric head to perform both single crystal X-ray diffraction and Brillouin scattering measurements simultaneously. The Brillouin setup is designed to enable the adjustment of both collecting and focusing optics without disturbing the scattering geometry and to preserve alignment of the sample (this is especially important for high temperature measurements).

The BGI Brillouin system uses the forward 80° scattering geometry where incident and scattered angles are equal (symmetric platelet geometry). This simplifies the Brillouin equation and allows calculation of the elastic constants without knowledge of refractive index.

Here we report results of two test single-crystal Brillouin measurements. The first measurement was conducted on a natural iron-bearing pyrope-rich garnet at ambient pressure and temperature in a DAC. A reference measurement was conducted using a well-proven

Brillouin system at GFZ Potsdam in order to examine reliability of our system. The sample plate was oriented on the (110) plane, and polished, with diameter of 125 μm and thickness of 20 μm . No pressure medium was used in this experiment. The second measurement was conducted for a single crystal of α -quartz at a pressure of 3 GPa and room temperature with various orientation to the axis of DAC for comparison with literature data. The crystal was oriented on the (1000) plane, and polished, with a diameter of 35 μm and thickness of 70 μm . The sample with a ruby chip was loaded into a 200 μm Re gasket sample chamber of a 90° symmetric diamond anvil cell with a pressure medium of a mixture of methanol–ethanol–water in proportions of 16:3:1.

The Brillouin spectrum of the pyrope sample is shown in Fig. 3-10-3. Pyrope displays only a small elastic anisotropy at ambient pressure, so different orientations were measured to reduce the error in velocity determination, then the data for different χ were averaged. Our velocities are in excellent agreement (less than 1 % difference) with velocities measured at GFZ Potsdam on the same sample (see table). On the other hand, they are about 4 % lower than velocities of pyrope measured by Univ. Illinois [Sinogeikin and Bass, *PEPI*, 2000]. The most probable reason for this difference is differences in sample composition: The natural iron-containing pyrope in this study, whereas a pure Mg end-member pyrope was used by Shinogeikin and Bass [2000].

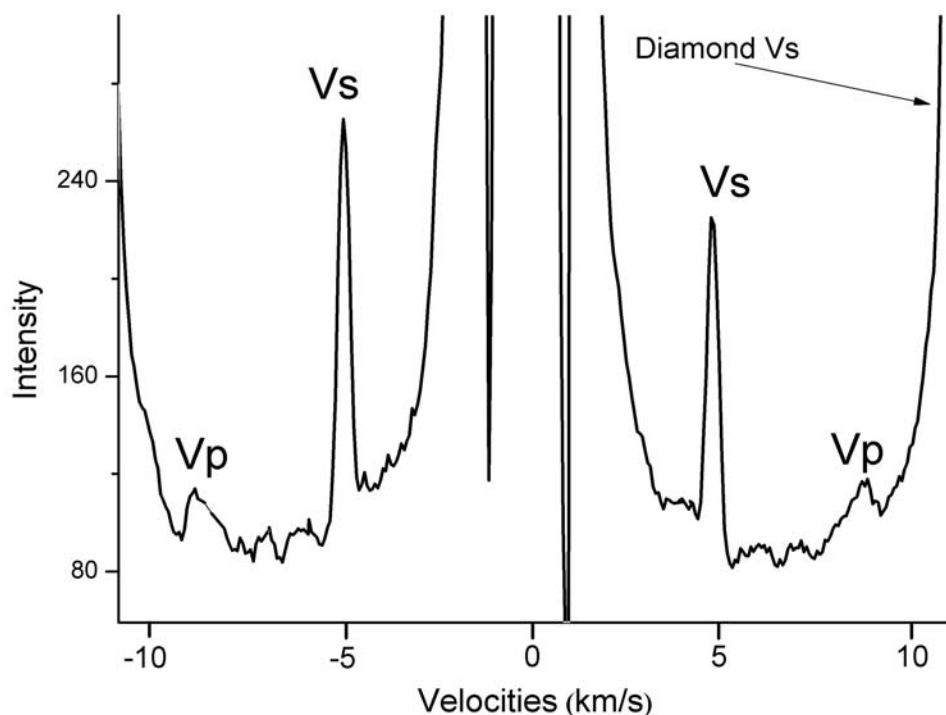


Fig. 3.10-3: An example of a Brillouin spectrum of natural pyrope collected using the BGI Brillouin system in a diamond anvil cell at ambient conditions.

Table 3.10-1: Sound velocities of pyrope in DAC at ambient conditions. The errors are in the range of 1 % for all measurements.

Laboratory	BGI	GFZ	Univ. Illinois
Sample	Natural pyrope		Synthetic pure pyrope
V _p , km/s	8.87	8.78	9.12
V _s , km/s	4.96	4.95	5.13

The single crystal diffraction data of α -quartz are presented in another contribution. Here we present an example of simultaneous measurement of the sound velocities as a function of χ -angle measured at high pressure in DAC (Fig. 3.10-4).

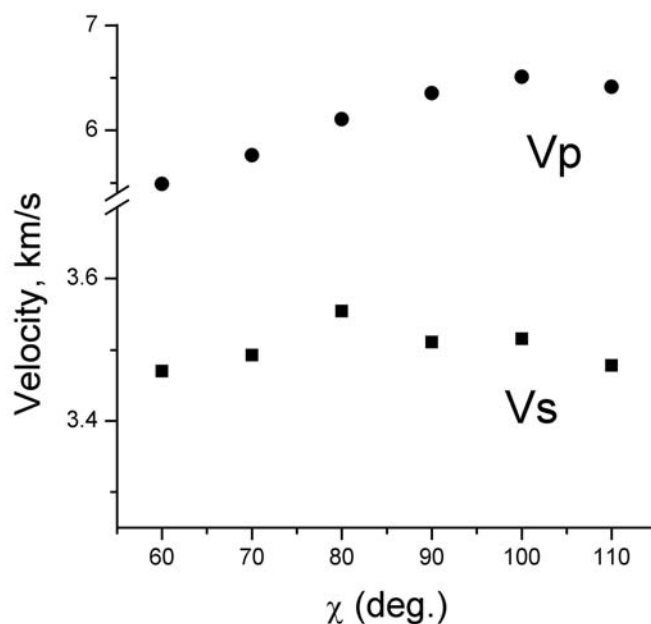


Fig. 3.10-4: Longitudinal and transverse wave velocities of α -quartz sample as a function of χ at 3.0 GPa and room temperature.

d. *Diamond as a high-pressure gauge up to 2.7 Mbar (N. Dubrovinskaia/Heidelberg, R. Caracas/Lyon, M. Hanfland/Grenoble and L.S. Dubrovinsky)*

Diamond anvil cell (DAC) technique has become a very important method of studying behaviour of materials under pressure in various fields of research ranging from physics to biology and geosciences. Optical methods to determine pressure in DAC experiments are

based on calibrated pressure dependence of the fluorescence or Raman shift of suitable materials. The Raman frequency of the LTO optical phonon of diamond has been long since recognised as a good pressure marker for the diamond anvil cell experiments, because of stability of diamond at ultra-high pressures.

There are at present two ways how diamond is used as a pressure gauge. One is that a chip of a single crystal of diamond is loaded into a DAC and pressure is monitored on the Raman shift recorded from this crystal. The other is that Raman signals from a center of the culet of a diamond anvil itself is used employing the existing correlation between the high-frequency edges of the Raman band with the normal stress at the culet face. The Raman shift is previously calibrated against pressure using known equations of state (EOS) of metals that were obtained *in situ* X-ray diffraction measurements. Both of the above mentioned methods have their advantages and drawbacks. In the former method, direct compression of the diamond chip in a DAC above 20-30 GPa almost in all pressurization media is a difficult experimental task because of a bridging effect. A helium pressurization medium allowed reaching pressure of 140 GPa in experiments with the diamond chip at room temperature. However, utilizing He in a DAC used for laser heating can result in experimental failure as at elevated temperatures because He diffuses into the diamond anvils and embrittles them. In the latter method, the Raman spectra reflect the whole range of stress states of the diamond anvil and are characterised by the steep edges at both high- and low-frequency sides. Although it was shown that there is a universal correlation between the edge frequency and the sample pressure due to the elastic response of the culet face of the diamond anvil to the normal stress, there is an ambiguity in determination of the edge frequency and its uncontrollable change due to the different experimental designs and setups including various culet shapes and sizes, crystallographic orientation of anvils, pressure media, types of materials under investigation, etc.

In the present work, we have proposed a new design of DAC experiments that could help to overcome some of the problems mentioned above. In particular, we offer an *in situ* method of synthesis of diamond micro-crystals for their further use as a diamond gauge in the course of the same experiment. The proposed method involves laser heating of hydrocarbons, which serve as a source of carbon, *in situ* in a DAC. For this purpose a tiny drop of a mixture of a metal powder (for example, Pt) and hydrocarbons is loaded into a DAC (Fig. 3.10-5). Metals are used as heat absorbers for heating the surrounding hydrocarbons. Upon heating at any pressure above about 15 GPa the hydrocarbons transform into diamond. The lattice parameter of diamonds recovered to ambient conditions ($a=3.5668(5)$ Å, average of five independent experimental runs) and parameters of the equation of state ($K_{300} = 445(10)$ GPa, $K' = 4.1(1)$ measured on decompression from 120 GPa) coincide with the literature data within precision of measurements, which confirms the purity of synthesized material. Paraffin and cyclododecane have been tested so far, with equal success. As our X-ray diffraction experiments showed that Pt captures hydrogen releasing under decomposition of hydrocarbons. The diamond microcrystals synthesised *in situ*, *i.e.*, “being born” in a DAC, are very tiny, and therefore, they do not cause a problem of bridging between anvils up to very high pressures. This situation is unlike the chips of diamond single crystals loaded into DACs

as pressure sensors in the hitherto conventionally designed DAC experiments. These microcrystals can be used as a pressure gauge up to ultra-high pressures in various pressure media.

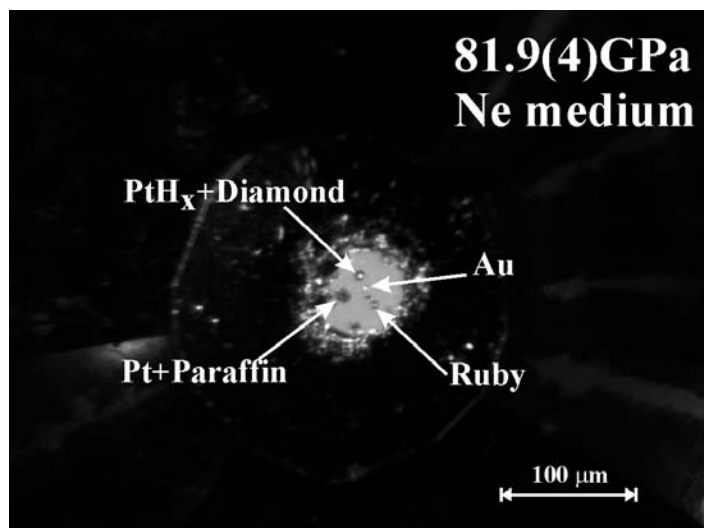


Fig. 3.10-5: A photograph of the pressure chamber of a DAC containing Au and ruby (used as known pressure markers), as well as two drops of a mixture of Pt and paraffin (used for *in situ* diamond synthesis) in a Ne pressure medium in the experiment at about 82 GPa. Laser heating of one of the drops of the Pt and paraffin mixture resulted in synthesis of diamond and platinum hydride (PtH_x) confirmed by *in situ* synchrotron X-ray diffraction and Raman spectroscopy.

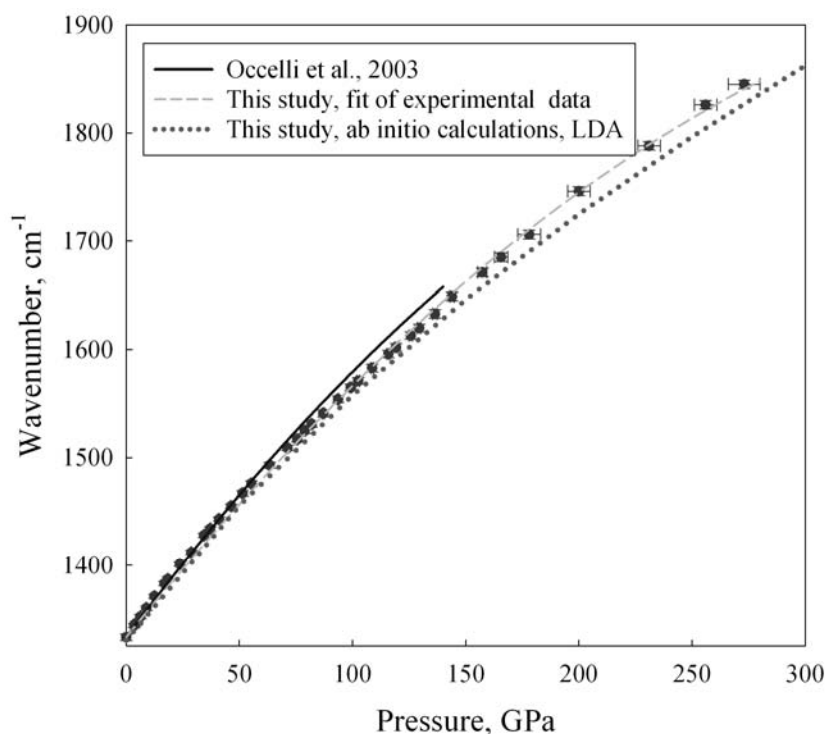


Fig. 3.10-6: Raman frequency of the LTO optical phonon of diamond versus pressure up to 270 GPa ($\omega(P)=1333+2.610(21) * P-2.750(11)*10^{-3}*P^2$; P in GPa, ω in cm⁻¹) in comparison with experimental literature data of Ocelli *et al.* (see Ref. 10), blue line up to 140 GPa) and the results of our *ab initio* calculations (dotted line). Error bars are either shown or within the dots.

In a series of experiments in Ne pressure medium, we first examined a feasibility of *in situ* synthesis of diamond microcrystals and then calibrated the Raman shift vs pressure measured by Ruby fluorescence technique and EoS of gold (Fig. 3.10-6). The calibration curve of the

Raman shift vs pressure is extended up to 270 GPa and experimental results are compared with those of *ab initio* calculation. The present results agree with the previous experimental study and *ab initio* calculation within 4 % of errors.

e. Calibration of the ruby and Sm: YAG pressure gauge up to 120 GPa and 700 K in a diamond anvil cell (*Q. Wei and L.S. Dubrovinsky; N. Dubrovinskaia/Heidelberg*)

In diamond anvil cell (DAC) experiments, fluorescence and Raman spectra of various materials have been used as a pressure gauge. Well-known examples are ruby, samarium doped yttrium-aluminium garnet Sm:YAG, diamond and cubic boron nitride. Relationship of frequency of the R1 ruby fluorescence line to pressure and temperature were previously studied up to 15 GPa and about 1000 K. The effect of temperature on the pressure-induced frequency shift of Sm:YAG fluorescence lines was previously investigated up to 25 GPa, which suggests that its temperature-dependence is almost negligible. However, so far there are no calibrations of the ruby and Sm YAG pressure gauges in a megabar pressure range at high temperatures. We used the LO and TO Raman shifts of cubic boron nitride (cBN), which was calibrated as a function of pressure and temperature in previous works, in order to study the pressure-temperature dependence of ruby and Sm:YAG fluorescence lines at pressures up to 120 GPa and temperatures up to 700 K.

In three independent experiments, small pieces of cBN, Sm:YAG, and ruby were loaded into diamond anvil cells equipped with anvils with flat working surfaces of 250 μm or 120 μm (beveled) in diameter. Rhenium gaskets with initial thickness of 200 μm were pre-pressed to 20-30 μm , and holes of 120 or 80 μm in diameter were drilled in the center of the indentation. Ne was loaded at pressure of about 1.5 kbar as a pressure transmitting medium. The whole-heating assembly developed in BGI was employed, and a Pt/Pt-10%Rh thermocouple was used for temperature measurement. Raman and fluorescence spectra were collected with Dilor XY triple spectrometer (Ar laser, x50 objective with a long working distance, a CCD detector cooled with liquid-nitrogen).

We collected over 100 data points for R1 and R2 ruby fluorescence lines, S1 and S2 fluorescence lines of Sm:YAG, and LO and TO Raman shifts of cBN at pressures up to 120 GPa and temperatures up to 700 K. Particularly, the ruby R1 fluorescence line was found to be a function of pressure and temperature described by the following equations (Fig. 3.10-7):

$$P = \frac{a}{b} \left[\left(\frac{\lambda}{\lambda_T} \right)^b - 1 \right],$$

$$a = a_{300} + a_1 * (T - 298),$$

$$b = b_{300} + b_1 * (T - 298) + b_2 * (T - 298)^2$$

$$\lambda_T = \lambda_{300} + \lambda_1 * (T - 298), \tag{1}$$

where P is pressure in GPa, λ_T is the wave length of fluorescence in nm, $a_{300}=1914.8$ GPa, $a_1 = 0.6223$ GPa/K, $b_{300} = 9.28$, $b_1 = -0.0024$ K⁻¹, $b_2 = -8.21 \cdot 10^{-7}$ K⁻², $\lambda_{300} = 694.2$ nm, $\lambda_1 = 0.00628$ nm/K

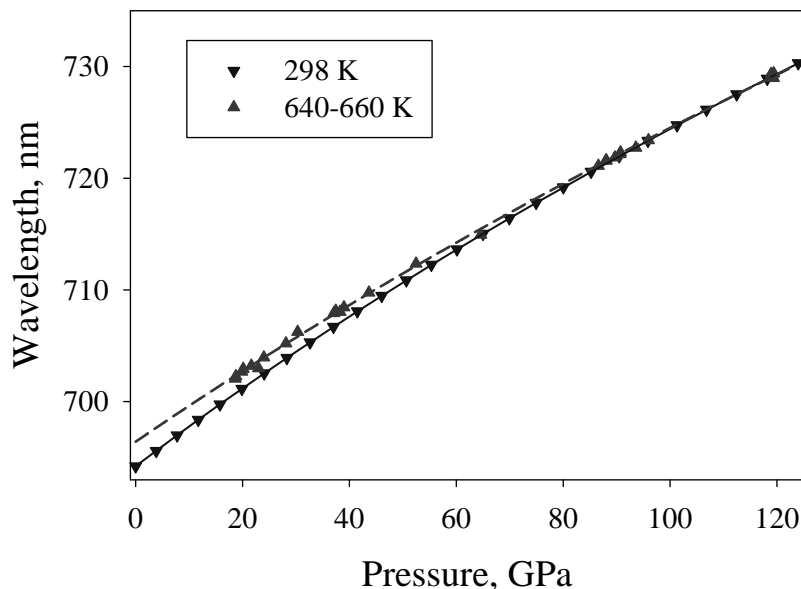


Fig. 3.10-7: Position of the R1 ruby fluorescence line at ambient temperature (inverted triangles) and at 640-660 K (triangles) as a function of pressure determined from the position of LO and/or TO Raman peaks of cBN. Lines are calculated using Eq. (1) with the values for 300 K and 650 K isotherms.

f. Pressure calibration and high-pressure pure shear deformation with the 6-ram press (G. Manthilake, N. Walte and D.J. Frost)

The 6-ram multianvil press is designed to apply high loads on an inner cubic high-pressure chamber while maintaining a high level of symmetry in the applied strain. The inner chamber can contain either a second stage of 8 hard inner anvils or a cubic pressure assembly. The device consists of six 8 MN hydraulic rams aligned at right angles. The hydraulic system with independent pumps allows the oil pressure in each hydraulic ram to be controlled independently. The position of each anvil attached to the rams is measured using a linear encoder and controlled to within 0.2 micrometers. It is therefore possible to compress the cubic chamber while maintaining a highly precise cubic geometry, which is essential if sintered diamond inner anvils are compressed. The open design of the press provides optimal access to the high-pressure region for neutron diffraction experiments.

The anisotropic expansion of the press frame under load creates asymmetry in the position of the vertical versus horizontal rams. This difference in frame expansion cannot be accounted for by measurements of the ram positions using the linear encoders because these measure the position of the ram relative to the press frame. However, the asymmetry in the frame

expansion can be measured by compressing an edge cut cube made of copper, which is designed to form a cube without forming gaskets up to high loads. Differences in the distances between the faces of the recovered cube after compression can be used to assess the geometry of the compressed chamber. A correction can be applied during the compression to correct for the differences in press frame expansion by driving in the horizontal rams further than those in the vertical direction. This correction is also a non linear function of load which can be accounted for using software. The resulting differences in cube dimensions are shown in Fig. 3.10-8, which shows them to be in general less than 20 microns up to loads of 1000 tonnes. Further refinement is hindered only by the accuracy to which the recovered cube dimensions can be determined.

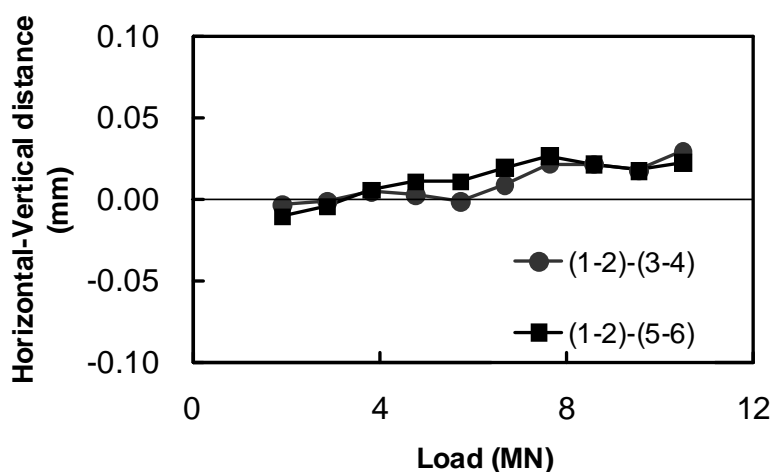


Fig. 3.10-8: Differences between copper cube dimensions measured in the two horizontal directions compared to the vertical direction in a series of experiments performed up to 1000 tonnes. A perfect cubic compression would give values of zero, however, differences are generally less than 20 microns.

In order to perform experiments with cubic sample assemblies, a requisite for deformation experiments, a 6-6 two-stage anvil setup similar to the approach adopted by Ehime University is also used here. The sample is placed in a set of six second-stage anvils that are guided by an aluminium or steel cage (Fig. 3.10-9). The whole setup is placed between the six main anvils of the press. The main advantage of adding second stage anvils is that different sample sizes can be used without time consuming changes of the main anvils in the press. The sample cubes are made out of fired pyrophyllite (at 700 °C or 1000 °C) to remove crystal-bound water and to enhance pressure efficiency. Water-free pyrophyllite is self-gasketing and has a good neutron transparency that makes it a prime candidate for later neutron diffraction experiments at FRM II in Garching.

Room temperature bismuth pressure calibrations have been performed for 6/4 and 8/6 assemblies (assembly edge length/anvil truncation length in mm) (Fig. 3.10-9). Considering that a combined load of only 0.8-1.2 MN (out of a pressure reserve of up to 24 MN) was

sufficient to reach ~ 8 GPa in 6-mm assemblies, pressure generation and/or sample sizes can be significantly enhanced in the future by the use of larger second stage anvils and a harder grade of tungsten carbide.

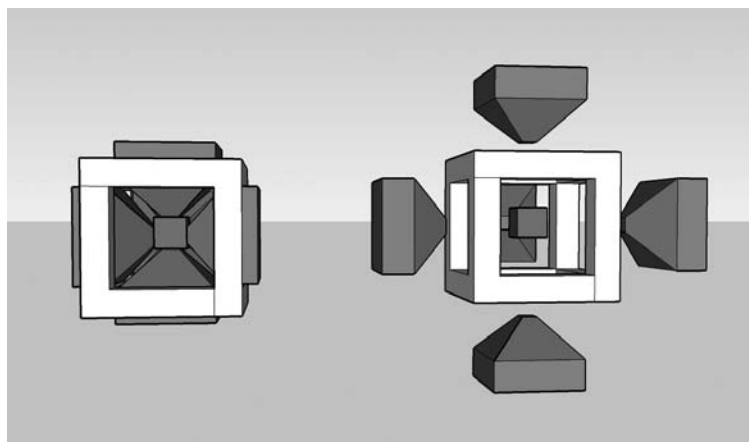


Fig. 3.10-9: Experimental setup for cubic sample assemblies. The cage with the six second stage anvils is placed between the first stage anvils. The base diameter of the anvils is 20 mm for 8 mm and 6 mm sample cubes.

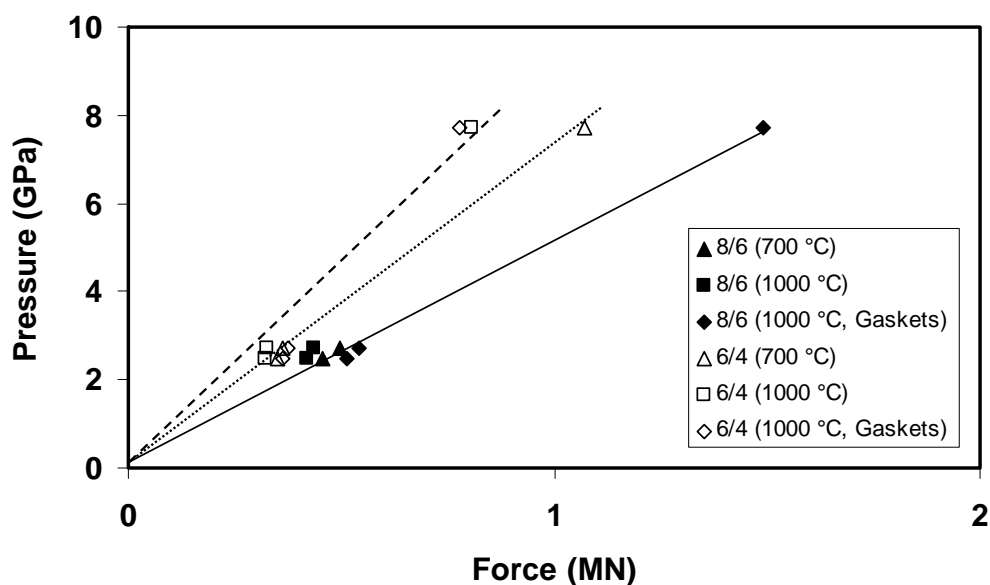


Fig. 3.10-10: Room temperature bismuth calibration for cubic 8/6 and 6/4 assemblies. The pyrophyllite cubes were either fired at 700 °C or 1000 °C to remove crystal-bound water. Note that the use of Teflon gaskets caused a lower efficiency at lower pressures (2.5 and 2.7 GPa) but a slightly higher efficiency at higher pressures (7.7 GPa).

Conventional high-pressure deformation devices such as the deformation-DIA induce deformation by uniaxial compression of the assembly that results either in axial compression

of a cylindrical sample or in simple shear if bevelled pistons are used in the assembly. The independent control of all six anvils in the new press allows to apply more complex deformation geometries such as pure shear, *i.e.*, deformation is induced by two perpendicular anvil pairs that are simultaneously driven into and out of the sample ($\sigma_1 - \sigma_3$ plane), while the 3rd anvil pair is held constant (σ_2) and controls the mean pressure in the sample. The position control of all anvils allows an unprecedented precision in strain and strain rate control in the press. Pure shearing tests with significant sample shortening showed that the shortening set by the anvil movement is transferred to efficient length changes of the samples.

g. *The ‘quartz-capsule’ – a way to reduce alloying problems with noble metal capsules during hydrothermal experiments (L. Lerchbaumer and A. Audétat)*

A common method for studying mineral solubility and partitioning in fluids at high pressures and temperatures is to trap aliquots of these fluids during the experiment in form of synthetic fluid inclusions and subsequently analyze their content at ambient conditions. In most cases, these experiments are performed by loading a piece of quartz (as host for the fluid inclusions), SiO₂-glass, buffer minerals plus the fluid into a noble metal capsule (Au, Pt, AgPd). The sample is then equilibrated for several days at high pressures and temperatures, with the timing of fluid inclusion formation being either unconstrained or being controlled by *in situ* cracking. In most applications the noble metal capsule does not interact with the charge, and any compositional variations observed in the synthesized fluid inclusions can be ascribed to disequilibrium with respect to the dissolving minerals or to an external fO_2 -buffer.

However, in charges containing both copper and sulphur, none of the commonly used noble metals are inert: Au has a strong tendency to take up Cu, whereas both Pt and AgPd tend to react with S. This does not just influence the amount of copper and sulfur dissolved in the fluid, but also affects fO_2 because *e.g.*, Cu^(I) dissolved in the fluid transforms into Cu⁽⁰⁾ during alloying, with the result that the remaining charge gets oxidized.

A couple of approaches have been tested to reduce these problems: (1) using gold capsules that were coated with a thin layer of copper metal at its inner walls, (2) using gold capsules alloyed with 5 wt.% copper (Au₉₅Cu₀₅), and (3) using a quartz liner inside the noble metal capsule. The first two methods efficiently prevent the loss of copper, but they bring along several other disadvantages: the capsule material reacts with the fluid to produce copper sulphides which again results in changes of fO_2 , fS_2 and pH.

After several modifications the setup with the quartz liner turned out to be the most promising (Fig. 3.10-11). In this approach, an etched piece of natural quartz is loaded together with fluid (and buffer minerals if necessary) into a cylindrical container drilled out of single-crystal synthetic quartz. This container is then closed with a plug of SiO₂-glass and a cap of single-crystal synthetic quartz. The whole assembly is then sealed into a gold capsule. During

isobaric heating the density of the loaded fluid decreases, with the result that part of it escapes from the container into the flexible space between the container and Au capsule. However, once the run temperature (600-800 °C) is reached the SiO₂ glass quickly recrystallizes and forms a sealing cap on the container which stops the fluid from escaping. Since the system is thus closed, no interactions between the fluid and the metal-capsule should take place. This hypothesis is confirmed by comparing the elemental concentrations in the starting solution with those in the fluid inclusions that have formed during the run (Fig. 3.10-12). The element concentrations measured in the fluid inclusions in the run product are identical with those of the starting solution within 14 % for Na, Cu, Cs, Pb and Co, 15 % for S and 25 % for Ag. The slightly higher concentrations of S and Ag in the fluid inclusions can be explained by the fact that these two elements were loaded as solids (in contrast to all other elements), thus their mass could increase relatively to the mass of fluid remaining in the capsule due to expulsion of fluid into the surrounding gold capsule during heating.

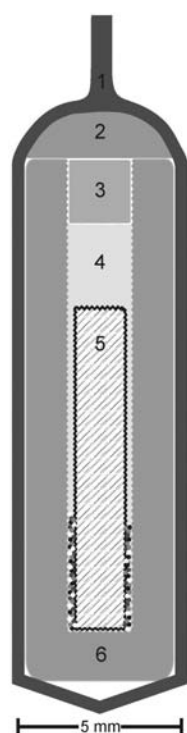


Fig. 3.10-11: The new assembly with 1:Au-capsule; 2:synthetic quartz lid; 3:SiO₂ glass plug; 4:fluid with buffer minerals (small dots); 5:etched core of natural quartz; 6:synthetic quartz liner.

Also in two-phase fluid systems the use of the quartz capsule method leads to a major improvement of reproducibility: the relative standard deviations are 60-100 % for runs performed in simple gold capsules and only 6-15 % in similar runs performed in the quartz capsules. Note that the quartz capsule method has also some disadvantage: it does not allow initiating fluid inclusion formation after a given time of pre-equilibration, and therefore it may not be possible to buffer fO_2 externally. However, by using internal fO_2 buffers and etched rather than pre-cracked quartz cores, this problem can be solved. Thus, hydrothermal runs with fluids containing both sulphur and copper are now doable with this quartz capsule method.

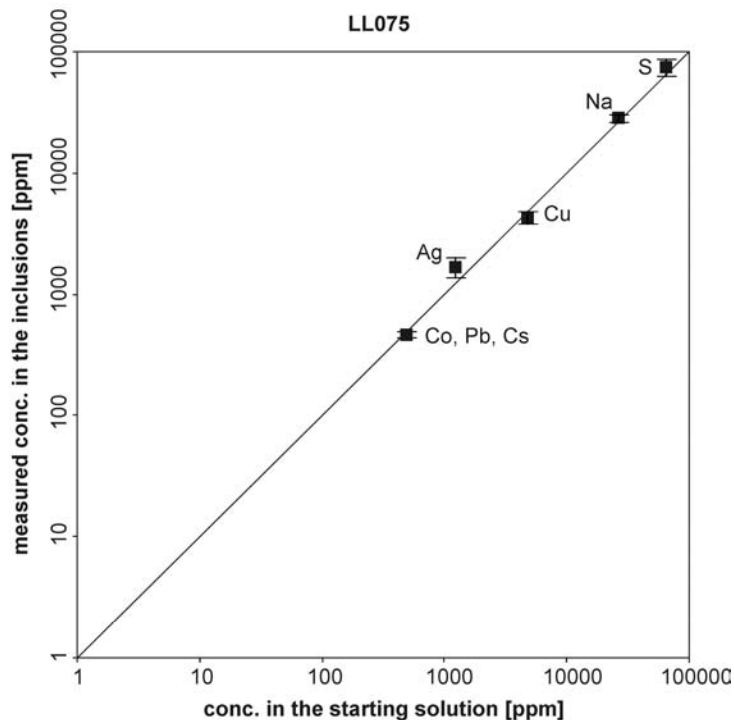


Fig. 3.10-12: Comparison of the element concentrations in the starting solution with the concentrations in the fluid inclusions generated during the run. The p - T conditions are 700 °C and 1500 bar.

h. *From surface morphology to rates: An automated routine to evaluate converged roughness parameters of heterogeneous surfaces (K. Pollok and T. Chust)*

In geochemical studies, rates are usually determined from dissolution studies (either flow through or batch experiments) using a size fraction of ground and sieved starting material by measuring the change in fluid chemistry as a function of time. The surface area of the starting material is commonly determined by the BET method and used as a constant to normalize rates. Recently, topographic methods have been introduced to directly measure dissolution rates and surface roughness and offer new insights into the reaction mechanisms and surface reactivity. Furthermore, it permits a systematic determination of surface roughness parameters. As statistical quantities, roughness parameters are strongly dependent on the field of view of the used technique or the sampling size. The concept of ‘converged roughness parameter’ was shown to be very useful to characterize certain surface building blocks by employing recurrent (squared) bisections of the measuring field with an edge length of a . A surface parameter is defined as converged when a flat slope is found in the convergence graph (roughness parameter versus edge length a). Converged parameters intrinsically depend on the choice of ‘representative’ areas for their analysis. Furthermore, artificial measuring points may lead to an overestimation of roughness parameters. Here, we present the newly developed program ROUGHNECK, which calculates a number of surface roughness parameters from topographic data as function of sampling size allowing to analyze and visualize roughness parameter distributions.

The program ROUGHNECK utilizes the common Surface Data Format (SDF) as input and output file format which can be produced by any metrological technique measuring surface

topography. Our input files produced by a confocal measurement system consist of 984x984 points representing a 160x160 μm field of view. For this study a quality criteria of a minimum of 99 % of measured points was used for the topographic data. The residual non-measured points were linearly interpolated. The following 3D roughness parameters are implemented so far: the *roughness average* S_a , the *root-mean-square roughness* S_q , the *peak-to-peak height* S_z , the *ten-point-height* S_{10z} , the *root-mean-square-gradient* S_{dq} , the *surface-skewness* S_{sk} , the *surface-kurtosis* S_{ku} , and the *surface area ratio* F . The program uses freely selectable edge lengths for the desired sampling area, which is moved pixel by pixel over the entire field of view (Fig. 3.10-13a). The surface area ratio, $F=A_{3D}/A_{2D}$, which describes the surface area of a three dimensional surface normalized by the two dimensional (projected) surface, is used as an example parameter to illustrate the statistical procedure. A perfectly flat surface will result in $F=1$, while a rough surface results in $F>1$. This parameter is a so-called hybrid surface parameter because it does not mainly depend on the amplitude but is more sensitive to the high frequency modulations of the surface as it is measured by the slope between adjacent surface points.

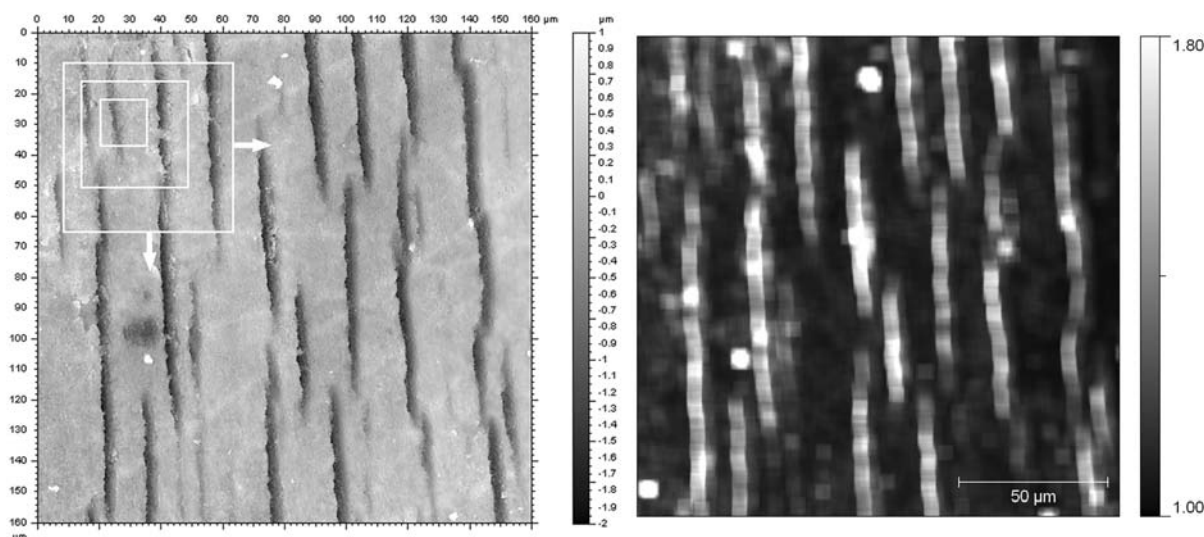


Fig. 3.10-13: (a) Surface of pyrrhotite after biologically enhanced dissolution after 28 days measured by confocal microscopy. The squares illustrate the principle of roughness parameter calculation as function of sampling size by a systematical movement of the sampling area performed with ROUGHNECK. (b) Spatial distribution of F values for a squared sampling size with edge length $a=4 \mu\text{m}$. High F values (~ 1.6) can be found at the positions of the lamellae. Very high F values originate from overlying particles, but they do not alter the converged roughness parameter determined from the histogram (Fig. 3.10-14a).

ROUGHNECK has been used to calculate the converged F parameters of the biologically dissolved pyrrhotite surface with abundant troilite exsolution lamellae as function of reaction time. The distribution of roughness parameters (here frequency N vs. F) can be plotted as histogram by applying discrete bins (Fig. 3.10-14a). The maxima of the distributions show the roughness value for a significant portion of the measured surface. For heterogeneous surfaces,

a number of maxima may indicate various components with different surface roughness. In general, the maximum F value increases with increasing sampling area. Figure 3.10-14b shows a convergence graph for the pristine and reacted pyrrhotite surfaces. At small scale ($a=1$ to $10\ \mu\text{m}$), the first maxima represent only the roughness of the pyrrhotite matrix which dissolves slower than the troilite lamellae. At larger scale ($a=15$ to $100\ \mu\text{m}$) the F value includes contributions from both because the spacing between the lamellae is smaller than the edge length of the sampling area. The graph shows that surface roughness is mainly affected by the deepening of troilite lamellae which represent the reactive sides of dissolution. The output data for every sampling area can also be visualized providing a spatial roughness parameter distribution (Fig. 3.10-13b). This is particularly useful if certain surface components, like the locations of the reacted troilite lamellae, represent only a small portion of the entire surface and are hence not well represented in the histogram. From the roughness distribution image ($a=4\ \mu\text{m}$) a roughness parameter for the troilite lamellae of 1.6 can be determined. In turn, the imaged surface roughness also validates that the parameter distribution (Fig. 3.10-14a) is not sensitive for artifacts like overlying particles or inaccurately measured surface points.

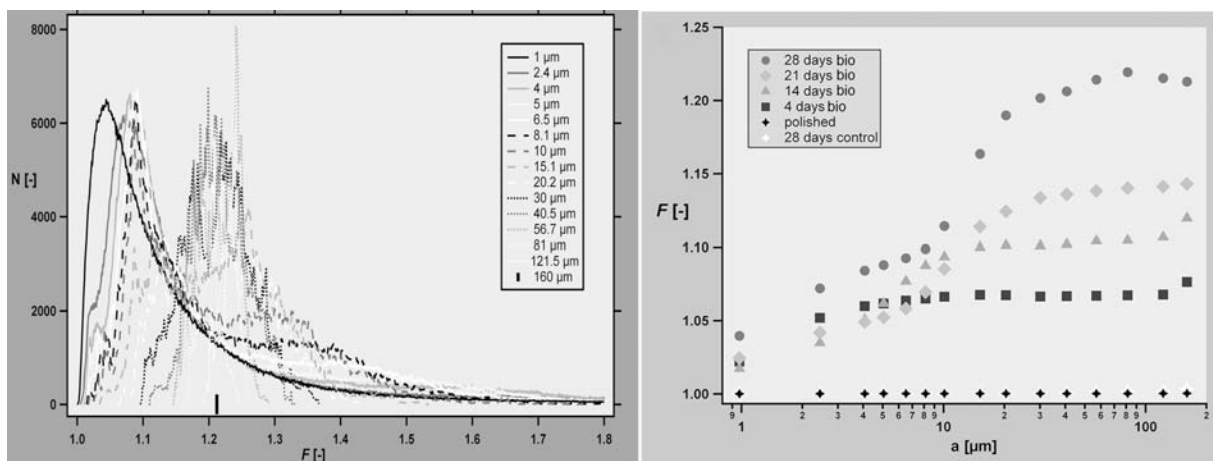


Fig. 3.10-14: (a) F value distributions for various squared sampling areas with a given edge length. With increasing sampling size the maximum of the curves is shifted to higher F values. However, the transition from low values around 1.05-1.1 to values around 1.2 is clearly visible and used in the convergence graph (Fig. 3.10-13a). For some curves (*e.g.*, $a = 4\ \mu\text{m}$) up to 3 maxima can be located indicating the heterogeneity of surface components. (b) Evolution of F as function of the edge length of the squared sampling area calculated for fresh and reacted pyrrhotite surfaces. F at larger sampling size ($> 10\ \mu\text{m}$) is controlled by the deepening of troilite lamellae.

i. StreamV3D, an efficient tool for modeling three-dimensional geodynamic scenarios (H. Samuel)

A numerical code to model thermo-chemical, multi-component flow in three-dimensional space was developed here in complement to the 2D frame previously reported (see BGI

annual report 2008) *StreamV3D*. This major evolution from 2D to 3D was performed by replacing the stream function with a primitive variable formulation where the pressure and the velocity are directly calculated by solving effectively the mass and momentum equations, using a SIMPLER algorithm. The set of discretized Stokes equations is solved with various sparse openMP/MPI parallel direct solvers (superLU, MUMPS, or PARDISO libraries) or with a robust iterative conjugate gradient or multigrid method for cases with a large number of points. A basic MPI parallel domain decomposition was implemented using a *Schwartz* additive method. This will further be improved using the more efficient *Schur* complement domain decomposition method (see 3.10-j). The code can handle sharp and large variations (typically orders of magnitude across a single grid cell) in rheological parameters, transport properties and density. The conservation of energy (or the conservation of any other scalar quantity) uses the same finite volume formulation as in *StreamV*. In addition, higher order accurate advection schemes have been implemented, such as fifth order WENO scheme and third order TVD for the time discretization. Furthermore, robust methods such as the tracer-in-cell and the particle level set methods have also been fully implemented and benchmarked, and allow accurate modeling of multi-component flows or the presence of surface tension.

Deviatoric stress contributions

◆ P, S _{xx} , S _{zz}	$\tau_{ijk}^{xx} = 2\eta_{ijk} \frac{U_{i+1,jk} - U_{ijk}}{\Delta x}$	$\tau_{ijk}^{xy} = \eta_{ijk} \left(\frac{U_{ijk} - U_{ij-1k}}{\Delta y} + \frac{V_{ijk} - V_{i-1jk}}{\Delta x} \right)$
● V _z	$\tau_{ijk}^{yy} = 2\eta_{ijk} \frac{V_{ij+1k} - V_{ijk}}{\Delta y}$	$\tau_{ijk}^{xz} = \eta_{ijk} \left(\frac{U_{ijk} - U_{ijk-1}}{\Delta z} + \frac{W_{ijk} - W_{i-1jk}}{\Delta x} \right)$
● V _x		
■ e _{xz} , S _{xz}	$\tau_{ijk}^{zz} = 2\eta_{ijk} \frac{W_{ijk+1} - W_{ijk}}{\Delta z}$	$\tau_{ijk}^{yz} = \eta_{ijk} \left(\frac{V_{ijk} - V_{ijk-1}}{\Delta z} + \frac{W_{ijk} - W_{ij-1k}}{\Delta y} \right)$

Staggered Grid

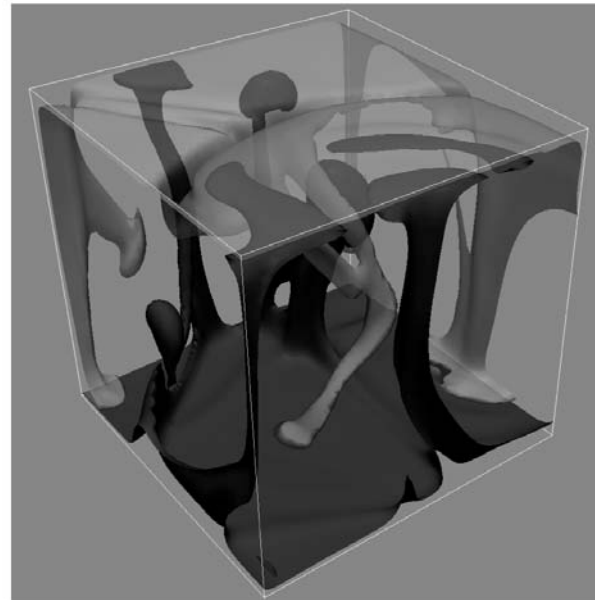
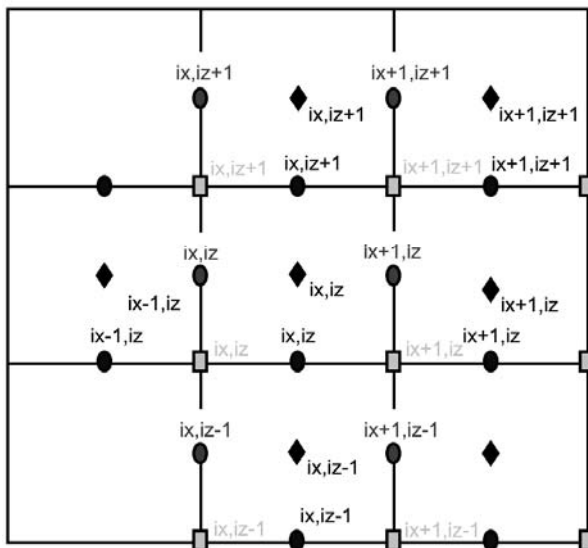


Fig. 3.10-15: Schematic standard staggered grid used in *StreamV3D* to discretize the governing conservation equations (mass, momentum, energy and composition) with a finite volume method and example of vigorous thermal convection on a 60^3 grid.

The code is designed to be used for modeling a great variety of 3D geodynamic scenarios such as vigorous thermo-chemical convective flows with continental and/or oceanic plates, non axisymmetric thermo-chemical plumes, subduction dynamics or *Rayleigh-Taylor* flows. Although the current version can model infinite *Prandtl* number flows, inertial, finite *Prandtl* number effects will be incorporated, using a linear multi-step *Adams-Bashforth* method for temporal discretisation. As in the 2D version non-linear convective terms and viscous terms in the momentum equation will be discretized separately to achieve a better numerical stability and accuracy. Given an appropriate grid resolution, this formulation will allow modeling compressible flow at all speeds, including shock waves.

j. Sparse linear solver using the Schur complement method (V. Aleksandrov and H. Samuel)

Modeling accurately three-dimensional geodynamic problems requires solving large sparse systems of equations, for which convergence with widely used “*optimum*” iterative solvers (*e.g.*, multigrid) can often be problematic, in particular in the presence of large variations in material properties. On the other hand, available sparse direct solvers are more robust but require prohibitive amounts of memory and execution time. A fast, robust and memory efficient sparse linear solver based on the algorithm of *Schur* complement domain decomposition was therefore developed. The method is well suited to solve boundary value problems such as the Laplace equation in a rectangular domain. The solver function, which is implemented in Fortran, could also support other elliptic operators and general domains. The Laplace equation is discretized by a second order finite differences scheme, which in three dimensions takes the form:

$$u_{i+1,j,k} + u_{i-1,j,k} + u_{i,j+1,k} + u_{i,j-1,k} + u_{i,j,k+1} + u_{i,j,k-1} - 6u_{i,j,k} = 0.$$

The indices of the nodes are then reordered by decomposing the domain into several equal-sized, non-overlapping sub-domains and interface, assigning the highest indices to the nodes belonging to the interface (Fig. 3.10-16). With this ordering, the linear system is rewritten in the following block form:

$$\begin{bmatrix} A_{00} & 0 & 0 & \cdots & 0 & A_{0p} \\ 0 & A_{11} & 0 & \cdots & 0 & A_{1p} \\ 0 & 0 & A_{22} & \cdots & 0 & A_{2p} \\ \vdots & \vdots & \vdots & \ddots & \vdots & \vdots \\ 0 & 0 & 0 & \cdots & A_{p-1p-1} & A_{p-1p} \\ A_{p0} & A_{p1} & A_{p2} & \cdots & A_{pp-1} & A_{pp} \end{bmatrix} \begin{bmatrix} x_0 \\ x_1 \\ x_2 \\ \vdots \\ x_{p-1} \\ x_p \end{bmatrix} = \begin{bmatrix} b_0 \\ b_1 \\ b_2 \\ \vdots \\ b_{p-1} \\ b_p \end{bmatrix}$$

where p is the number of subdomains, $A_{00}, A_{11}, \dots, A_{p-1, p-1}$ are square matrices of order equal to the number of nodes of the corresponding domain, and A_{pp} is a square matrix of order equal to the number of nodes of the interface – we shall refer to this order as *Schur* size.

The algorithm performs block Gaussian elimination to cancel the last row that involves calculation of a *Schur* complement matrix and its analogous transformation to the right-hand side according to the following formulas:

$$A'_{pp} = A_{pp} - \sum_{i=0}^{p-1} A_{pi} A_{ii}^{-1} A_{ip}, \quad b'_p = b_p - \sum_{i=0}^{p-1} A_{pi} A_{ii}^{-1} b_i$$

As a result, the elimination yields a linear system for the interface unknowns $A'_{pp} x_p = b'_p$, which is called *Schur* system and A'_{pp} is called the *Schur* matrix. By back substitution using the formula: $A_{ii} x_i = b_i - A_{ip} x_p$ for $i = 0, 1, 2, \dots, p-1$ the remaining unknowns are calculated. Since each domain is coupled only with a part of the interface, the matrices $A_{0p}, A_{1p}, \dots, A_{p-1p}$ contain zero columns (when there are four equal subdomains as shown in Fig. 3.10-16 the number of the zero columns is approximately half of the *Schur* size). The algorithm takes into account this fact to reduce the memory usage. The resulting *Schur* matrix is solved with either the ScaLAPACK library or the stabilized bi-conjugate gradient method (BiCGstab(1)).

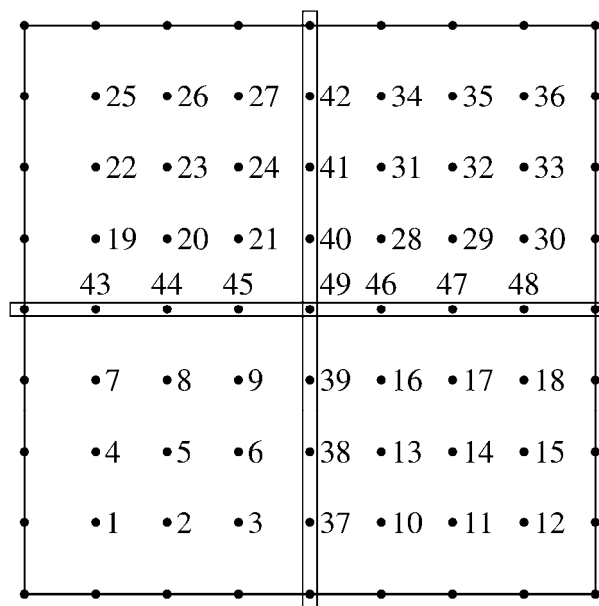


Fig. 3.10-16: Ordering of the nodes of four subdomains and the interface. Consecutive indices are assigned to the nodes of each sub-domain. The highest indices are assigned to interface nodes.

Overall the method is a robust and fast approach for solving sparse linear systems arising from boundary value problems for elliptic partial differential equations. It demonstrates

smaller memory usage during the factorization. For example with 90^3 nodes if MUMPS is used directly on the problem then the needed memory for the LU factors is about 1 GB whereas the *Schur* complement method requires as low as 300 MB (Fig. 3.10-17). The memory savings would allow larger geophysical problems to be solved on even shorter times when the BiCGstab is used. Our ongoing efforts will further decrease the computational cost associated with the *Schur* matrix by optimizing the bi-conjugate gradient solver.

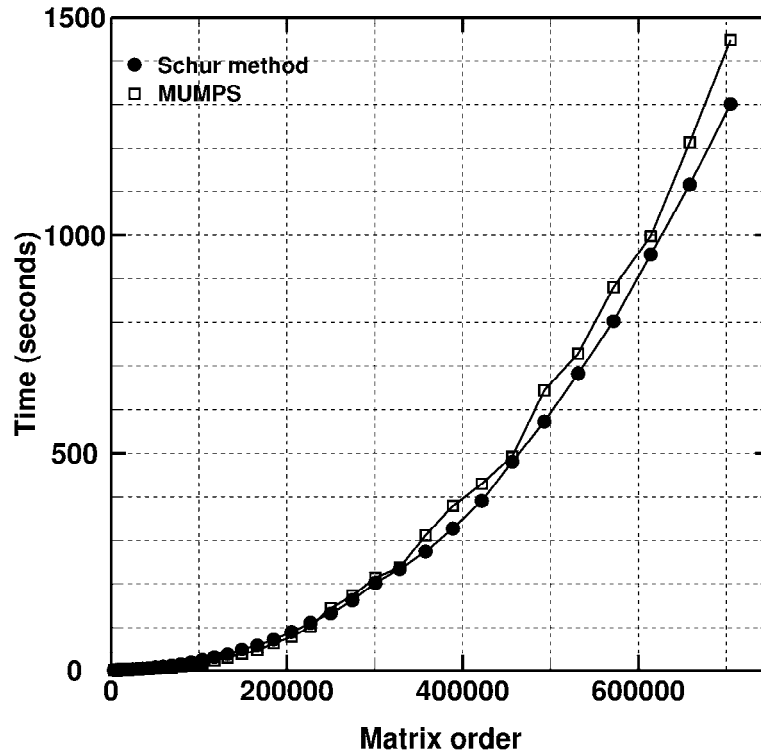


Fig. 3.10-17: Time performance of the linear solver with the *Schur* complement domain decomposition compared with the MUMPS library. Both binaries were compiled with the Intel compiler and executed on the BGI cluster using eight processors.

4. International Graduate School – Elitenetzwerk Bayern/Elite Network of Bavaria "Structure, Reactivity and Properties of Oxide Materials" (OXIDES)

The interdisciplinary Graduate School is funded by the State of Bavaria and it encompasses three cooperating institutes: Bayerisches Geoinstitut (BGI), Institute of Inorganic Chemistry I (AC I), both in Bayreuth, and the Fraunhofer Institute for Silicate Research (ISC) in Würzburg. These institutes provide their experimental and analytical facilities, complementary expertise in basic and applied research, and commitment to capitalize on synergies as well as international contacts to other leading research institutes all over the world.

The Graduate School is chaired by Prof. Dr. Hans Keppler/BGI and it includes twelve other faculty members and one coordinator. Enrollment in 2010 was eleven doctoral students on a full-time basis at all three institutes (BGI, AC I, ISC) and, in addition, sixteen doctoral students have associate status in the school which provides them with full access to all educational activities. Research projects include physical and chemical properties of oxides and mineral assemblages and mineral/melt interactions at P-T conditions of the deep Earth, synthesis and investigation of new layer silicates, polymer coatings, transition metal oxides and polyoxometalates as well as the development of new methods in NMR crystallography.

During 2010, three students have graduated:

- | | |
|--|--|
| <i>Olga Narygina</i>
(M.Sc. 2006, Jekaterinburg)
on 18.03.2010 | Investigation of the properties of iron-bearing alloys and silicates and their implications for the Earth's lower mantle and core
<u>Supervisor:</u> Prof. L. Dubrovinsky

Dr. Narygina took a post-doctoral position at the University of Edinburgh/UK |
| <i>Geertje Ganskow</i>
(Dipl. Geol. 2006, Jena)
on 18.05.2010 | The effect of iron on the stability, water content and compressibility of mantle silicates - implications for a hydrous Martian interior
<u>Supervisor:</u> Prof. F. Langenhorst

Dr. Ganskow took a post-doctoral position at the Brown University in Providence/Rhode Island, USA |
| <i>Evgeniya Zarechnaya</i>
(M.Sc. 2004, Moscow)
on 23.07.2010 | The 5 th element - a new high-pressure/high-temperature allotrope
<u>Supervisor:</u> Prof. L. Dubrovinsky

Dr. Zarechnaya became a research scholar at Harvard University in Cambridge/MA., USA |

Two new students were accepted by the doctoral program:

Tina Örtel
(Dipl. Bau.-Ing. 2009, Weimar)
since 11.01.2010

Reactivity of inorganic nanoparticles in ultra-high performance concrete
Supervisors: Dr. C. Gellermann, Prof. G. Sestl

Davide Novella
(M.Sc. 2010, Bayreuth)
since 16.04.2010

Silicate mineral and melt interactions with reduced volatile phases in the Earth's mantle
Supervisors: Dr. Frost, Prof. H. Keppler

Five new associate students were accepted to the doctoral program:

Mattia Giannini
(M.Sc. 2009, Pavia)
since 15.02.2010

Crystal chemistry of hibonite as indicator for oxygen fugacities during solar nebula condensation
Supervisors: Dr. T. Boffa Ballaran, Prof. F. Langenhorst

Hongzhan Fei
(B.Sc. 2008, Hangzhou)
since 15.04.2010

Experimental studies on the rheology of ringwoodite
Supervisor: Prof. T. Katsura

Bashar Diar-Bakerly
(M.Sc. 2009, Aleppo)
since 01.07.2010

Surface modification of kaolinite using different catechols to improve its chemical and physical properties
Supervisor: Prof. J. Breu

Martin Schieder
(M.Sc. 2010, Bayreuth)
since 01.11.2010

Mesostructuring of Isopolyoxometalates
Supervisor: Prof. J. Breu

Martha Pamato
(M.Sc. 2010, Bayreuth)
since 01.11.2010

Elasticity of mafic crust in the lower mantle
Supervisor: Prof. L. Dubrovinsky, Dr. T. Boffa Ballaran

Descriptions of some of the student research projects are listed in Chapter 3 of this yearbook. Students also gave presentations at major international meetings in 2010. The list of presentations and publications may be found in Chapter 5.

As part of program requirements, all students undergo an intensive training program, in addition to their research project, that encompasses lectures, short courses, research colloquium, doctoral seminar, seminars by invited leading experts and weekend seminars on soft skills such as scientific writing, ethics and team work. Invited speakers from overseas and

Europe gave 10 lectures during the last year and presented novel experimental techniques and current research results.

The following courses and seminars were offered by ENB in 2010:

- Doctoral seminar, Bronnbach; Graduate School Oxides (Univ. Bayreuth, ISC Würzburg), 31.01.-01.02.2010
- Short course on "*Microstructural Characterization with TEM/SEM methods*", 22.-25.03.2010, Bayerisches Geoinstitut, Prof. F. Langenhorst
- Industrial site visit - ESK Ceramics, Kempten, Germany, 15.-16.04.2010
- Short course on "*Equilibrium and transport properties of high-temperature systems*", 02.-04.08.2010, Bayerisches Geoinstitut, Dr. David Dolejš (Prague)
- Soft skills short course on "*Scientific Writing*", 04.-05.10.2010, Bayerisches Geoinstitut, Kempkes & Gebhardt Organisationsberatung (Köln)

Two students (*V. Stagno*, *D. Bernini*), the speaker and the coordinator of the graduate school, *Prof. H. Keppler* and *Dr. F. Heidelberg* participated in the Graduation Ceremony of the Elite Network of Bavaria with the State Minister *Dr. W. Heubisch* in Munich on October 7, 2010. One OXIDES student (*V. Stagno*) gave an oral presentation of his research.



Furthermore, students of the graduate school participated in several external short courses/seminars during 2010.

Students and members of the graduate program received international awards for their research; these awards are listed in section 7.3.

Dr. Olga Narygina (3rd from right) received the Bernd-Rendel-Prize of the German Research Foundation (DFG) for her excellent research on material behaviour under extreme pressures and temperatures of the Earth's mantle and core.



Detailed information on the Graduate School "Structure, Reactivity and Properties of Oxide Materials" can be found at <http://www.uni-bayreuth.de/elitenetzwerk/oxides>.

5. Publications, Conference Presentations, Seminars

5.1 Publications (published)

Supplement to **2009** (papers published at the end of 2009):

MOOKHERJEE, M.; STEINLE-NEUMANN, G. (2009): Detecting deeply subducted crust from the elasticity of hollandite. *Earth and Planetary Science Letters* 288, 349-358

2010

a) Refereed international journals

ALVARO, M.; NESTOLA, F.; BOFFA BALLARAN, T.; CAMARA, F.; DOMENEGHETTI, M.C.; TAZZOLI, V. (2010): High-pressure phase transition of a natural pigeonite. *American Mineralogist* 95, 300-311

ASKER, C.; KARGEN, U.; DUBROVINSKY, L.; ABRIKOSOV, I.A. (2010): Equation of state and elastic properties of face-centered-cubic Fe-Mg alloy at ultrahigh pressures from first-principles. *Earth and Planetary Science Letters* 293, 130-134

AUDÉTAT, A.; BALI, E. (2010): A new technique to seal volatile-rich samples into platinum capsules. *European Journal of Mineralogy* 22, 23-27

AUDÉTAT, A. (2010): Source and evolution of molybdenum in the porphyry Mo(-Nb) deposit at Cave Peak, Texas. *Journal of Petrology* 51, 1739-1760

BASYUK, T.; VASYLECHKO, L.; FADEEV, S.; BEREZOVETS, V.; TROTS, D.; NIEWA, R. (2010): Phase and structural behaviour of the PrAlO_3 - SmAlO_3 system. *Acta Physica Polonica A* 117, 98-103

BLÄSS, U.W.; LANGENHORST, F.; MCCAMMON, C.A. (2010): Microstructural investigations on strongly stained olivines of the Chassignite NWA 2737 and implications to its shock history. *Earth and Planetary Science Letters* 300, 255-263

BOFFA BALLARAN, T.; FROST, D.J.; MIYAJIMA, N.; HEIDELBACH, F. (2010): The structure of a super-aluminous version of the dense hydrous magnesium silicate phase D. *American Mineralogist* 95, 1113-1116

BORISOV, A.; MCCAMMON, C. (2010): The effect of silica on ferric/ferrous ratio in silicate melts: An experimental study using Mössbauer spectroscopy. *American Mineralogist* 95, 545-555

BRAEUNLING, D.; PECHER, O.; TROTS, D.M.; SENYSHYN, A.; ZHEREBTSOV, D.A.; HAARMANN, F.; NIEWA, R. (2010): Synthesis, crystal structure and lithium motion of Li_8SeN_2 and Li_8TeN_2 . *Zeitschrift für anorganische und allgemeine Chemie* 636, 936-946

CARACAS, R.; BOFFA BALLARAN, T. (2010): Elasticity of $(\text{K},\text{Na})\text{AlSi}_3\text{O}_8$ hollandite from lattice dynamics calculations. *Physics of the Earth and Planetary Interiors* 181, 21-26

- CERNIK, R.J.; DUBROVINSKY, L.; FREER, R.; THRALL, M. (2010): An *in situ* high pressure-high temperature powder diffraction study of the formation of a precursor phase of bismuth manganite. *Ceramics International* 36, 2315-2321
- CHAREEV, D.; KURNOSOV, A.; DUBROVINSKY, L.; NARYGINA, O.; GAVRILENKO, P.; ZARECHNAYA, E.; DUBROVINSKAIA, N.; LITVIN, Y.; OSADCHIL, E. (2010): New synthetic high-density nickel sulfide: A plausible component of the Earth's core and terrestrial planets. *Doklady Earth Sciences* 432, 771-774
- COMODI, P.; BOFFA BALLARAN, T.; ZANAZZI, P.F.; CAPALBO, C.; ZANETTI, A.; NAZZARENI, S. (2010): The effect of oxo-component on the high-pressure behavior of amphiboles. *American Mineralogist* 95, 1042-1051
- DE KOKER, N.; STIXRUDE, L. (2010): Theoretical computation of diffusion in minerals and melts. – In: ZHANG, Y.; CHERNIAK, D. (Eds.): *Reviews of Mineralogy and Geochemistry Volume 72: Diffusion in Minerals and Melts*, 971-996
- DE KOKER, N. (2010): Structure, thermodynamics, and diffusion in $\text{CaAl}_2\text{Si}_2\text{O}_8$ liquid from first-principles molecular dynamics. *Geochimica et Cosmochimica Acta* 74, 5657-5671
- DE KOKER, N. (2010): Thermal conductivity of MgO periclase at high pressure: Implications for the D" region. *Earth and Planetary Science Letters* 292, 392-398
- DÉGI, J.; ABART, R.; TÖRÖK, K.; BALI, E.; WIRTH, R.; RHEDE, D. (2010): Symplectite formation during decompression induced garnet breakdown in lower crustal mafic granulite xenoliths: mechanisms and rates. *Contributions to Mineralogy and Petrology*, 159, 293-314
- DOS SANTOS-GARCIA, A.J.; AREVALO-LOPEZ, A.M.; FERNANDEZ-SANJULIAN, J.; ALARIO-FRANCO, M.A.; FROST, D. (2010): Synthesis, structural and magnetic disordering in the $\text{IrSr}_2\text{RECu}_2\text{O}_{8+x}$ family of metalo-cuprates by HP+HT oxidation. *High Pressure Research* 30, 17-23
- EL GORESY, A.; DUBROVINSKY, L.; GILLET, Ph.; GRAUP, G.; CHEN, M. (2010): Akaogiite: An ultra-dense polymorph of TiO_2 with the baddeleyite-type structure, in shocked garnet gneiss from the Ries Crater, Germany. *American Mineralogist* 95, 892-895
- FERROIR, T.; DUBROVINSKY, L.; EL GORESY, A.; SIMIONOVICI, A.; NAKAMURA, T.; GILLET, Ph. (2010): Carbon polymorphism in shocked meteorites: Evidence for new natural ultrahard phases. *Earth and Planetary Science Letters* 290, 150-154
- FROST, D.; ASAHARA, Y.; RUBIE, D.C.; MIYAJIMA, N.; DUBROVINSKY, L.S.; HOLZAPFEL, C.; OHTANI, E.; MIYAHARA, M.; SAKAI, T. (2010): Partitioning of oxygen between the Earth's mantle and core. *Journal of Geophysical Research – Solid Earth* 115, B02202, doi: 10.1029/2009JB006302
- GALADÍ-ENRÍQUEZ, E.; DÖRR, W.; ZULAUF, G.; GALINDO-ZALDÍVAR, J.; HEIDELBACH, F.; ROHRMÜLLER, J. (2010): Variscan deformation phases in the southwestern Bohemian Massif: new constraints from sheared granitoids. *Zeitschrift der Deutschen Geologischen Gesellschaft* 161, 1-23
- GANSKOW, G.; BOFFA BALLARAN, T.; LANGENHORST, F. (2010): Effect of iron on the compressibility of hydrous ringwoodite. *American Mineralogist* 95, 747-753
- GAVRILENKO, P.; BOFFA BALLARAN, T.; KEPPLER, H. (2010): The effect of Al and water on the compressibility of diopside. *American Mineralogist* 95, 608-616

- GUILLAUME, C.L.; SERGHIOU, G.; THOMSON, A.; MORNIROLI, J.P.; FROST, D.J.; ODLING, N.; JEFFREE, C.E. (2010): Correlation between structural and semiconductor metal changes and extreme conditions materials chemistry in Ge-Sn. *Inorganic Chemistry* 49, 8230-8236
- IRIFUNE, T.; SHINMEI, T.; MCCAMMON, C.; MIYAJIMA, N.; RUBIE, D.; FROST, D. (2010): Iron partitioning and density changes in pyrolite in Earth's lower mantle. *Science* 327, 193-195
- ITO, E.; YAMAZAKI, D.; YOSHINO, T.; FUKUI, H.; ZHAI, S.; SHATZKIY, A.; KATSURA, T.; TANGE, Y.; FUNAKOSHI, K. (2010): Pressure generation and investigation of the post-perovskite transformation in MgGeO_3 by squeezing the Kawai-cell equipped with sintered diamond anvils. *Earth Planetary Science Letters* 293, 84-89
- ITO, E.; YOSHINO, T.; YAMAZAKI, D.; SHATSKIY, S.; SHAN, S.; GUO, X.; KATSURA, T.; HIGO, Y.; FUNAKOSHI, K. (2010): High pressure generation and investigation of the spin transition of ferroperricite ($\text{Mg}_{0.83}\text{Fe}_{0.17}\text{O}$). *Journal of Physics: Conference Series* 215 (1), 012099, doi: 10.1088/1742-6596/215/1/012099
- JUHIN, A.; MORIN, G.; ELKAIM, E.; FROST, D.J.; FIALIN, M.; JUILLOT, F.; CALAS, G.; (2010): Structure refinement of a synthetic knorringite, $\text{Mg}_3(\text{Cr}_{0.8}\text{Mg}_{0.1}\text{Si}_{0.1})_2(\text{SiO}_4)_3$. *American Mineralogist* 95 (1), 59-63
- KARKI, B.B.; BHATTARAI, D.; MOOKHERJEE, M.; STIXRUDE, L. (2010): Visualization and analysis of structural and dynamical properties of simulated hydrous silicate melt. *Physics and Chemistry of Minerals* 37, 103-117
- KEPLER, H. (2010): The distribution of sulfur between haplogranitic melts and aqueous fluids. *Geochimica et Cosmochimica Acta* 74, 645-660
- KOPYLOVA, M.; NAVON, O.; DUBROVINSKY, L.; KHACHATRYAN, G. (2010): Carbonatitic mineralogy of natural diamond-forming fluids. *Earth and Planetary Science Letters* 291, 126-137
- KOZLENKO, D.P.; DANG, N.T.; JIRAK, Z.; KICHANOV, S.E.; LUKIN, E.V.; SAVENKO, B.N.; DUBROVINSKY, L.S.; LATHE, C.; MARTIN, C. (2010): Structural and magnetic phase transitions in $\text{Pr}_{0.15}\text{Sr}_{0.85}\text{MnO}_3$ at high pressures. *The European Physical Journal B*, 77, 407-411
- LIN, J.-F.; MAO, Z.; YAVAS, H.; ZHAO, J.; DUBROVINSKY, L. (2010): Shear wave anisotropy of textured hcp-Fe in the Earth's inner core. *Earth and Planetary Science Letters* 298, 361-366
- MALASPINA, N.; SCAMBELLURI, M.; POLI, S.; VAN ROERMUND, H.L.M.; LANGENHORST, F. (2010): The oxidation state of mantle wedge majoritic garnet websterites metasomatised by C-bearing subduction fluids. *Earth and Planetary Science Letters* 298, 417-426
- MANTOVANI, M.; ESCUDERO, A.; BECERRO, A.I. (2010): Effect of pressure on kaolinite illitization. *Applied Clay Science* 50, 342-347
- MAO, Z.; JACOBSEN, S.D.; JIANG, F.; SMYTH, J.R.; HOLL, C.M.; FROST, D.J.; DUFFY, T.S. (2010): Velocity crossover between hydrous and anhydrous forsterite at high pressures. *Earth and Planetary Science Letters* 293, 250-258

- MCCAMMON, C.; DUBROVINSKY, L.; NARYGINA, O.; KANTOR, I.; WU, X.; GLAZYRIN, K.; SERGUEEV, I.; CHUMAKOV, A. (2010): Low-spin Fe²⁺ in silicate perovskite and a possible layer at the base of the lower mantle. *Physics of the Earth and Planetary Interiors* 180, 215-221
- MECKLENBURGH, J.; HEIDELBACH, F.; MARIANI, E.; MACKWELL, S.; SEIFERT, F. (2010): Rheology and microstructure of (Ca_{0.9},Sr_{0.1})TiO₃ perovskite deformed in compression and torsion. *Journal of Geophysical Research* 115, B05204, doi: 10.1029/2009JB006520
- MIKHAILOVA, D.; NARAYANAN, N.; GRUNER, W.; VOSS, A.; SENYSHYN, A.; TROTS, D.M.; FUESS, H.; EHRENBERG, H. (2010): The role of oxygen stoichiometry on phase stability, structure, and magnetic properties of Sr₂CoIrO_{6-δ}. *Inorganic Chemistry* 49, 10348-10356
- MIKHAILOVA, D.; NARAYANAN, N.; VOSS, A.; EHRENBERG, H.; TROTS, D.M.; RITTER, C.; ECKERT, J.; FUESS, H. (2010): Solid solution Sr₂Sc_{1+x}Re_{1-x}O₆ with a perovskite-like structure: Phase transitions and magnetic properties. *European Journal of Inorganic Chemistry* 8, 1196-1206
- MIKHAILOVA, D.; SARAPULOVA, A.; VOSS, A.; THOMAS, A.; OSWALD, S.; GRUNER, W.; TROTS, D.M.; BRAMNIK, N.N.; EHRENBERG, H. (2010): Li₃V(MoO₄)₃: A new material for both Li extraction and insertion. *Chemistry of Materials* 22, 3165-3173
- MINCH, R.; EHM, L.; WINKLER, B.; KNORR, K.; PETERS, L.; DUBROVINSKY, L.; DEPMEIER, W. (2010): High-pressure behavior of otavite (CdCO₃). *Journal of Alloys and Compounds* 508, 251-257
- MINCH, R.; DUBROVINSKY, L.; KURNOSOV, A.; EHM, L.; KNORR, K.; DEPMEIER, W. (2010): Raman spectroscopic study of PbCO₃ at high pressures and temperatures. *Physics and Chemistry of Minerals* 37, 45-56
- MIYAHARA, M.; OHTANI, E.; KIMURA, M.; EL GORESY, A.; OZAWA, S.; NAGASE, T.; NISHIJIMA, M.; HIRAGA, K. (2010): Coherent and subsequent incoherent ringwoodite growth in olivine of shocked L6 chondrites. *Earth and Planetary Science Letters* 295, 321-327
- MIYAJIMA, N.; HOLZAPFEL, C.; ASAHARA, Y.; DUBROVINSKY, L.; FROST, D.J.; RUBIE, D.C.; DRECHSLER, M.; NIWA, K.; ICHIHARA, M.; YAGI, T. (2010): Combining FIB milling and conventional Argon ion milling techniques to prepare high-quality site-specific TEM samples for quantitative EELS analysis of oxygen in molten iron. *Journal of Microscopy* 238, 200-209
- MIYAJIMA, N.; NIWA, K.; HEIDELBACH, F.; YAGI, T.; OHGUSHI, K. (2010): Deformation microtextures in CaIrO₃ post-perovskite under high stress conditions in a laser heated DAC. *Journal of Physics: Conference Series* 215, 012097 doi: 10.1088/1742-6596/215/1/012097
- MOOKHERJEE, M.; KARATO, S. (2010): Solubility of water in pyrope-rich garnet at high pressure and temperature. *Geophysical Research Letters* 37, L03310
- MORARD, G.; KATSURA, T. (2010): Pressure-temperature cartography of Fe-S-Si immiscible system. *Geochimica et Cosmochimica Acta* 74(12), 3659-3667

- MUSSI, A.; CORDIER, P.; MAINPRICE, D.; FROST, D.J. (2010): Transmission electron microscopy characterization of dislocations and slip systems in K-lingunite: Implications for the seismic anisotropy of subducted crust. *Physics of Earth and Planetary Interiors* 182, 50-58
- NAKASHIMA, D.; OTT, U.; EL GORESY, A.; NAKAMURA, T. (2010): Heavily fractionated noble gases in an acid residue from the Klein Glacier 98300 EH3 chondrite. *Geochimica et Cosmochimica Acta* 74, 5134-5149
- NARAYANAN, N.; MIKHAILOVA, D.; SENYSHYN, A.; TROTS, D.M.; LASKOWSKI, R.; BLAHA, P.; SCHWARZ, K.; FUESS, H.; EHRENBERG, H. (2010): Temperature and composition dependence of crystal structures and magnetic and electronic properties of the double perovskites $\text{La}_{2-x}\text{Sr}_x\text{CoIrO}_6$ ($0 \leq x \leq 2$). *Physical Review B* 82, 024403
- NARYGINA, O.V.; KANTOR, I.Y.; MCCAMMON, C.A.; DUBROVINSKY, L.S. (2010): Electronic state of Fe^{2+} in $(\text{Mg,Fe})(\text{Si,Al})\text{O}_3$ perovskite and $(\text{Mg,Fe})\text{SiO}_3$ majorite at pressures to 81 GPa and temperatures to 800 K. *Physics and Chemistry of Minerals* 37, 407-415
- NARYGINA, O.; DUBROVINSKY, L.S.; MIYAJIMA, N.; MCCAMMON, C.A.; KANTOR, I.Y.; MEZOUAR, M.; PRAKAPENKA, V.B.; DUBROVINSKAIA, N.A.; DMITRIEV, V. (2010): Phase relations in Fe–Ni–C system at high pressures and temperatures. *Physics and Chemistry of Minerals*, doi 10.1007/s00269-010-0396-x
- NAZZARENI, S.; COMODI, P.; BINDI, L.; DUBROVINSKY, L. (2010): The crystal structure of gypsum-II determined by single-crystal synchrotron X-ray diffraction data. *American Mineralogist* 95, 655-658
- NESTOLA, F.; BOFFA BALLARAN, T.; ANGEL, R.; ZHAO, J.; OHASHI, H. (2010): *In situ* high-pressure behaviour of Ca-bearing silicates: the effect of divalent and trivalent 3d-transition elements. *American Mineralogist* 95, 832-838
- OTSUKA, K.; MCCAMMON, C.A.; KARATO, S.-I. (2010): Tetrahedral occupancy of ferric iron in $(\text{Mg,Fe})\text{O}$: Implications for point defects in the Earth's lower mantle. *Physics of the Earth and Planetary Interiors* 180, 179-188
- OVSYANNIKOV, S.V.; SHCHENNIKOV, V.V. (2010): High-pressure routes in the thermoelectricity or how one can improve a performance of thermoelectrics. *Chemistry of Materials* 22, 635-647
- OVSYANNIKOV, S.V.; SHCHENNIKOV, V.V.; SHVETSOVA, M.A.; DUBROVINSKY, L.S.; POLIAN, A. (2010): Tuning of the stoichiometry of Fe_{1-x}O wüstite by compression. *Physical Review B* 81, 060101 (R) (rapid communication)
- OVSYANNIKOV, S.V.; SHCHENNIKOV, V.V.; KARKIN, A.E.; POLIAN, A.; BRIOT, O.; RUFFENACH, S.; GIL, B.; MORET, M. (2010): Pressure cycling of InN to 20 GPa: *in situ* transport properties and amorphization. *Applied Physics Letters* 97, 032105
- OVSYANNIKOV, S.V.; WU, X.; SHCHENNIKOV, V.V.; KARKIN, A.E.; DUBROVINSKAIA, N.; GARBARINO, G.; DUBROVINSKY, L. (2010): Structural stability of a golden semiconducting orthorhombic polymorph of Ti_2O_3 under high pressures and high temperatures. *Journal of Physics – Condensed Matter* 22, 375402
- ROZENBERG, G.Kh.; PASTERNAK, M.P.; XU, W.M.; DUBROVINSKY, L.; HANFLAND, M. (2010): Crystallographic transitions related to high-pressure magnetic and electronic phenomena in Fe-based compounds. *High Pressure Research* 30, 238-251

- RUSKOV, T.; SPIROV, I.; GEORGIEVA, M.; YAMAMOTO, S.; GREEN, H.; MCCAMMON, C.; DOBRZHINETSKAYA, L. (2010): Mössbauer spectroscopy studies of the valence state of iron in chromite from the Luobusa massif of Tibet. *Journal of Metamorphic Geology* 28, 551-560
- SAMUEL, H.; TACKLEY, P.J.; EVONUK, M. (2010): Heat partitioning in terrestrial planets during core formation by negative diapirism. *Earth and Planetary Science Letters* 290, 13-19
- SAMUEL, H.; EVONUK, M. (2010): Modeling advection in geophysical flows with particle level sets. *Geochemistry Geophysics Geosystems* 11, Q08020, doi: 10.1029/2010GC003081
- SATA, N.; HIROSE, K.; SHEN, G.; NAKAJIMA, Y.; OHISHI, Y.; HIRAO, N. (2010): Compression of FeSi, Fe₃C, Fe_{0.95}O, and FeS under the core pressures and implication for light element in the Earth's core. *Journal of Geophysical Research* 115, B09204, doi: 10.1029/2009JB006975
- SCHIAVI, F.; WALTE, N.; KONSCHAK, A.; KEPLER, H. (2010): A moissanite cell apparatus for optical *in situ* observation of crystallizing melts at high temperature. *American Mineralogist* 95, 1069-1079
- SCHOLLENBRUCH, K.; WOODLAND, A.B.; FROST, D.J. (2010): The stability of hercynite at high pressures and temperatures. *Physics and Chemistry of Minerals* 37, 137-143
- SERGHIOU, G.; GUILLAUME, C.L.; JEFFREE, C.E.; THOMSON, A.; FROST, D.J.; MORNIROLI, J.P.; ODLING, N. (2010): Imaging of mixing and reaction in group IV systems recovered from high pressures and temperatures. *High Pressure Research* 30, 44-50
- SHATSKIY, A.; BORZDOV, Y.M.; YAMAZAKI, D.; LITASOV, K.D.; KATSURA, T.; PALYANOV, Y.N. (2010): Aluminum nitride crystal growth from AlN–Al system at 6.0 GPa and 1800 °C. *Crystal Growth and Design* 10(6), 2563-2570
- SHATSKIY, A.; YAMAZAKI, D.; BORZDOV, Y.; MATSUZAKI, T.; LITASOV, K.D.; COORAY, T.; FEROT, A.; ITO, E.; KATSURA, T. (2010): Stishovite single crystal growth and application to silicon self-diffusion measurements. *American Mineralogist* 95, 135-143
- SHIRYAEV, A.A.; ZUBAVICHUS, Y.V.; MCCAMMON, C.; VELIGZHANIN, A.A. (2010): Iron in fibrous diamonds from different localities: X-ray absorption and Mössbauer data. *Russian Geology and Geophysics* 51, 1262-1266
- SINMYO, R.; HIROSE, K. (2010): The Soret diffusion in laser-heated diamond-anvil cell. *Physics of the Earth and Planetary Interiors* 180, 172-178
- STAGNO, V.; FROST, D.J. (2010): Carbon speciation in the asthenosphere: Experimental measurements of the redox conditions at which carbonate-bearing melts coexist with graphite or diamond in peridotite assemblages. *Earth and Planetary Science Letters* 300, 72-84, doi: 10.1016/j.epsl.2010.09.038
- TARANTINO, S.; ZEMA, M.; BOFFA BALLARAN, T. (2010): Crystal structure of columbite at high pressure. *Physics and Chemistry of Minerals* 37, 769-778

- TRONCHE, E.J.; KAN, M.V.; VRIES, J.D.; WANG, Y.; SANEHIRA, T.; LI, J.; CHEN, B.; GAO, L.; KLEMME, S.; MCCAMMON, C.A.; WESTRENN, W.V. (2010): The thermal equation of state of FeTiO₃ ilmenite based on *in situ* X-ray diffraction at high pressures and temperatures. *American Mineralogist* 95, 1708-1716
- TROTS, D.M.; SENYSHYN, A.; SCHWARZ, B.C. (2010): Low temperature structural variations and molar heat capacity of stolzite, PbWO₄. *Journal of Solid State Chemistry* 183, 1245-1251
- VLCEK, V.; ČÍŽEK, J.; DRAHOKOUPIL, J.; VALENTA, J.; MIYAJIMA, N.; SKÁLA, R. (2010): Defects in CaF₂ caused by long-time irradiation and their response to annealing. *Philosophical Magazine* 90, 2749-2769
- WEIGEL, C.; MCCAMMON, C.; KEPPLER, H. (2010): High-temperature Mössbauer spectroscopy: A probe for the relaxation time of Fe-species in silicate melts and glasses. *American Mineralogist* 95, 1701-1707
- WU, X.; HOLBIG, E.; STEINLE-NEUMANN, G. (2010): Structural stability of TiO₂ at high pressure in density-functional theory based calculations. *Journal of Physics: Condensed Matter* 22, 295501
- WU, X.; STEINLE-NEUMANN, G.; NARYGINA, O.; MCCAMMON, C.; DUBROVINSKY, L. (2010): *In situ* high-pressure study of LiNbO₃-type FeTiO₃: X-ray diffraction and Mössbauer spectroscopy. *High Pressure Research* 30, 395-405
- WU, X.-P.; ZHANG, B.-H.; XU, J.-S.; KATSURA, T.; ZHAI, S.-M.; YOSHINO, T.; MANTHILAKE, G.; SHATSKIY, A. (2010): Electrical conductivity measurements of periclase under high pressure and high temperature. *Physica B: Condensed Matter* 405, 53-56
- WU, X.; QIN, S.; DUBROVINSKY, L. (2010): Structural characterization of the FeTiO₃-MnTiO₃ solid solution. *Journal of Solid State Chemistry* 183, 2483-2489
- XU, W.M.; ROZENBERG, G.; PASTERNAK, M.P.; KERTZER, M.; KURNOSOV, A.; DUBROVINSKY, L.; PASCARELLI, S.; MUNOZ, M.; VACCARI, M.; HANFLAND, M.; JEANLOZ, R. (2010): Pressure-induced Fe ↔ Cu cationic valence exchange and its structural consequences: High-pressure studies of delafossite CuFeO₂. *Physical Review B* 81, 104110
- YE, Y.; SMYTH, J.R.; HUSHUR, A.; MANGHNANI, M.H.; LONAPPAN, H.; DERA, P.; FROST, D.J. (2010): Crystal structure of hydrous wadsleyite with 2.8 % H₂O and compressibility to 60 GPa. *American Mineralogist* 95, 1765-1772
- YOSHIASA, A.; ITO, T.; SUGIYAMA, K.; NAKATSUKA, A.; OKUBE, M.; KUROSAWA, M.; KATSURA, T. (2010): A peculiar site preference of B in MgAl_{2-x}B_xO₄ (x = 0.0, 0.11 and 0.13) spinel under high-pressure and high-temperature. *Zeitschrift für Anorganische und Allgemeine Chemie* 636 (3-4), 472-475
- YOSHINO, T.; MATSUZAKI, T.; SHATSKIY, A.; KATSURA, T. (2010): Effect of water on electrical conductivity of olivine aggregates with implications for electrical structure in the upper mantle. *Earth and Planetary Science Letters* 288, 291-300
- YOSHINO T.; LAUMONIER M.; MCISAAC, E.; KATSURA, T. (2010): Electrical conductivity of basaltic and carbonatite melt-bearing peridotites at high pressures: Implications for melt distribution and melt fraction in the upper mantle. *Earth and Planetary Science Letters* 295 (3-4), 593-602

- YOSHINO, T.; KATSURA, T.; YAMAZAKI, D.; ITO, E. (2010): Electrical conductivity of mantle peridotite at the uppermost lower mantle condition. *Journal of Physics: Conference Series* 215 (1), 012102, doi: 10.1088/1742-6596/215/1/012102
- ZARECHNAYA, E.; DUBROVINSKAIA, N.; CARACAS, R.; MERLINI, M.; HANFLAND, M.; FILINCHUK, Y.; CHERNYSHOV, D.; DMITRIEV, V.; DUBROVINSKY, L. (2010): Pressure-induced isostructural phase transformation in gamma-B-28. *Physical Review B* 82, 184111
- ZARECHNAYA, E.; DUBROVINSKAIA, N.; DUBROVINSKY, L.; FILINCHUK, Y.; CHERNYSHOV, D.; DMITRIEV, V. (2010): Growth of single crystals of B-28 at high pressures and high temperatures. *Journal of Crystal Growth* 312, 3388-3394
- ZHAI, S.M.; KANZAKI, M.; KATSURA, T.; ITO, E. (2010): Synthesis and characterization of strontium-calcium phosphate γ -Ca_{3-x}Sr_x(PO₄)₂ (0 ≤ x ≤ 2). *Materials Chemistry and Physics* 120, 348-350
- ZHANG, Y.; NI, H. (2010): Diffusion of H, C, and O components in silicate melts. *Review in Mineralogy and Geochemistry* 72, 171-225
- ZHANG, Y.; NI, H.; CHEN, Y. (2010): Diffusion data in silicate melts. *Review in Mineralogy and Geochemistry* 72, 311-408

b) Popular scientific magazines

- POLLOK, K.; HARRIES, D.; HOPF, J.; ETZEL, K.; SCHEITER, D.; CHUST, T.; HOHELLA, M.F., JR.; HELLIGE, K.; PEIFFER, S.; HALLBERG, K.; LANGENHORST, F. (2010): Microstructural controls on monosulphide weathering and heavy metal release (MIMOS). – In: MÜNCH, U.; DRANSCH, W. (Eds.): *Mineral Surfaces – From Atomic Processes to Industrial Applications*, GEOTECHNOLOGIEN Science Report 16, 182-197

5.2 Publications (submitted, in press)

- AUDÉTAT, A.; DOLEJS, D.; LOWENSTERN, J.B.: Molybdenite saturation in silicic magmas: occurrence and petrological implications. *Journal of Petrology* (submitted)
- AUDÉTAT, A.; LOWENSTERN, J.B.: Melt inclusions. – In: TUREKIAN, K.K.; HOLLAND, H.D. (Eds.): *Treatise on Geochemistry, Volume 12* (submitted)
- BALI, E.; AUDETAT, A.; KEPPLER, H.: The mobility of U and Th in subduction zone fluids: an indicator of oxygen fugacity and fluid salinity. *Contributions to Mineralogy and Petrology* (in press), doi 10.1007/s00410-010-0552-9
- BINDER, B.; KEPPLER, H.: The oxidation state of sulfur in magmatic fluids. *Earth and Planetary Science Letters* (in press)
- BLÄß, U.; LANGENHORST, F.; MCCAMMON, C.: Microstructural investigations on strongly stained silivines of the Chassignite NWA 2737 and implications for its shock history. *Earth and Planetary Science Letters* (in press)

- ESCUADERO, A.; MIYAJIMA, M.; LANGENHORST, F.: Microstructure, composition and P-T conditions of rutile from diamondiferous gneiss of the Saxonian Erzgebirge, Germany. *European Journal of Mineralogy* (submitted)
- ESCUADERO, A.; LANGENHORST, F.: Aluminium incorporation in rutile (TiO₂) at high pressure. *Journal of Solid State Chemistry* (submitted)
- ESCUADERO, A.; TSUNO, K.; LANGENHORST, F.: Phase relations in the TiO₂ – Al₂O₃ system at pressures up to 10 GPa. Solubility of Al in rutile at high pressure and high temperature. *Chemistry of Materials* (submitted)
- FABIAN, K.; MIYAJIMA, N.; ROBINSON, P.; MCENROE, S.A.; BOFFA BALLARAN, T.; BURTON, B.P.: Chemical and magnetic properties of rapidly cooled metastable ferri-ilmenite solid solutions: I. Fe-Ti order transition in quenched synthetic Ilm 60. *Geophysical Journal International* (submitted)
- GANNOUN, A.; BOYET, M.; EL GORESY, A.; DEVOIRE, B.: REE and actinide microdistribution in Sahara 97072 and ALHA 77295 EH 3 chondrites. *Geochimica et Cosmochimica Acta* (submitted)
- GANNOUN, A.; BOYET, M.; RIZOT, H.; EL GORESY, A.: ¹⁴⁶Sm-¹⁴²Nd systematics of enstatite chondrites converges toward a terrestrial composition. *Proceedings of the National Academy of Sciences* (submitted)
- GLAZYRIN, K.; MCCAMMON, C.; DUBROVINSKY, L.; SCHOLLENBRUCH, K.; MERLINI, M.; HANFLAND, M.: Novel behavior of magnetite at high pressure. *Physical Review Letters* (submitted)
- GREENBERG, E.; DUBROVINSKY, L.S.; MCCAMMON, C.; ROUQUETTE, J.; KANTOR, I.; PRAKAPENKA, V.; ROZENBERG, G.K.; PASTERNAK, M.P.: Pressure-induced structural phase transition of the iron end-member of ringwoodite (γ -Fe₂SiO₄) investigated by X-ray diffraction and Mössbauer spectroscopy. *American Mineralogist* (submitted)
- HAMMOUDA, T.; CHANTEL, J.; DEVIDAL, J-L.: Apatite solubility in carbonatitic liquids and trace element partitioning between apatite and carbonatite at high pressure. *Geochimica et Cosmochimica Acta* (in press)
- HAMMOUDA, T.; ANDRAULT, D.; KOGA, K.T.; KATSURA, T.; MARTIN, A.: Ordering in double carbonates and implications for processes at subduction zones. *Contributions to Mineralogy and Petrology* (in press)
- HARRIES, D.; POLLOK, K.; LANGENHORST, F.: TEM evidence for translation interface modulation in NC-pyrrhotites: A general structural model. *American Mineralogist* (submitted)
- HELLIGE, K.; POLLOK, K.; LARESE-CASANOVA, P.; PEIFFER, S.: Pathways of ferrous iron mineral formation upon sulfidation of lepidocrocite surfaces. *Geochimica et Cosmochimica Acta* (submitted)
- JACOBSEN, S.D.; LIU, Z.; BOFFA BALLARAN, T.; LITTLEFIELD, E.F.; EHM, L.; HEMLEY, R.J.: Effect of H₂O on upper mantle phase transitions in MgSiO₃: is the depth of the seismic X-discontinuity an indicator of mantle water content? *Physics of the Earth and Planetary Interiors* (in press)
- KATSURA, T.; YONEDA, A.; YAMAZAKI, D.; YOSHINO, T.; ITO, E.: Adiabatic temperature profile in the mantle. *Physics of the Earth and Planetary Interiors* (in press)

- KEEFNER, J.W.; MACKWELL, S.J.; KOHLSTEDT, D.L.; HEIDELBACH, F.: Dependence of the creep of dunite on oxygen fugacity: Implications for viscosity variations in Earth's mantle. *Journal of Geophysical Research* (in press)
- LONGO, M.; MCCAMMON, C.; JACOBSEN, S.: Iron oxidation state in (Mg,Fe)O using the flank method: I. Calibration. *Contributions to Mineralogy and Petrology* (submitted)
- MALASPINA, N.; LANGENHORST F.; POLI, S.; FUMAGALLI, P.; TUMIATI, S.: Fe³⁺ partitioning between garnet and pyroxenes in ultrahigh pressure mantle wedge peridotites from Sulu (China). *American Mineralogist* (submitted)
- MANTHILAKE, M.A.G.M.; DE KOKER, N.; FROST, D.J.: Thermal conductivity of CaGeO₃ perovskite at high pressure. *Geophysical Research Letters* (submitted)
- MANTOVANI, M.; ESCUDERO, A.; BECERRO, A.I.: Influence of OH⁻ concentration on the illitization of kaolinite at high pressure. *Applied Clay Science* (in press)
- MATSUZAKI, T.; HAGIYA, K.; SHATSKIY, A.; MATSUI, M.; KATSURA, T.: Crystal structure of anhydrous K-phase X, K_{2.13}(Mg_{1.91}Cr_{0.02})Si₂O₇ synthesized at 16 GPa and 1700 °C. *Journal of Mineralogical and Petrological Sciences* (in press)
- MITTAL, R.; MISHRA, S.K.; CHAPLOT, S.L.; OVSYANNIKOV, S.V.; GREENBERG, E.; TROTS, D.; DUBROVINSKY, L.; SU, Y.; BRUECKEL, Th.; MATSUISHI, S.; HOSONO, H.; GARBARINO, G.: Synchrotron X-ray diffraction study of BaFe₂As₂ and CaFe₂As₂ at high pressures up to 56 GPa at ambient and low-temperatures down to 33 K. *Physical Review B* (submitted)
- PRESNALL, D.C.; GUDFINNSSON, G.H.: Oceanic volcanism from the low-velocity zone – without plumes. *Journal of Petrology* (in press)
- MIYAHARA, M.; OHTANI, E.; OZAWA, S.; KIMURA, M.; EL GORESY, A.; SAKAI, T.; NAGASE, T.; HIRAGA, K.; HIRAO, N.; OHISHI, Y.: Natural dissociation of olivine to perovskite and magensio-wüstite in a Martian meteorite. *Proceedings of the National Academy of Sciences* (submitted)
- MOOKHERJEE, M.; NAKAJIMA, Y.; STEINLE-NEUMANN, G.; GLAZYRIN, K.; WU, X.; DUBROVINSKY, L.; MCCAMMON, C.A.; CHUMAKOV, A.: High pressure behavior of iron carbide (Fe₇C₃) at inner core conditions. *Journal of Geophysical Research* (in press)
- NAKAJIMA, Y.; TAKAHASHI, E.; SATA, N.; NISHIHARA, Y.; HIROSE, K.; FUNAKOSHI, K.; OHISHI, Y.: Thermoelastic property and high-pressure stability of Fe₇C₃: Implication for iron-carbide in the Earth's core. *American Mineralogist* (submitted)
- NAKASHIMA, D.; OTT, U.; EL GORESY, A.; NAKAMURA, T.: Heavily fractionated noble gases in an acid residue from the KLE 98300 EH3 chondrite. *Earth and Planetary Science Letters* (in press)
- NALIBOFF, J.; LITHGOW-BERTELLONI, C.; RUFF, L.; DE KOKER, N.: The effects of lithospheric thickness and density structure on Earth's stress field. *Geophysical Journal International* (submitted)
- NARYGINA, O.; DUBROVINSKY, L.; MIYAJIMA, N.; MCCAMMON, C.A.; KANTOR, I.Y.; MEZOUAR, M.; PRAKAPENKA, V.B.; DUBROVINSKAIA, N.; DMITRIEV, V.: Phase relations in the Fe-Ni-C system at high pressures and temperatures: Implications for the Earth's core. *Physics and Chemistry of Minerals* (in press)

- NARYGINA, O.; DUBROVINSKY, L.S.; MCCAMMON, C.A.; KURNOSOV, A.; KANTOR, I.Y.; PRAKAPENKA, V.B.; DUBROVINSKAIA, N.A.: X-ray diffraction and Mössbauer spectroscopy study of *fcc* iron hydride FeH at high pressures and implications for the composition of the Earth's core. *Earth and Planetary Science Letters* (submitted)
- NESTOLA, F.; BOFFA BALLARAN, T.; KOCH-MÜLLER, M.; BALIC-ZUMA, T.; TARAN, M.; OLSEN, L.; PRINCIVALLE, F.; SECCO, L.; LUNDEGAARD, L.: New accurate compression data for γ -Fe₂SiO₄. *Physics of the Earth and Planetary Interiors* (in press)
- NI, H.; KEPPLER, H.; MANTHILAKE, M.A.G.M.; KATSURA, T.: Electrical conductivity of dry and hydrous albite glasses and liquids at high pressure. *Contributions to Mineralogy and Petrology* (in press)
- NI, H.; KEPPLER, H.; BEHRENS, H.: Electrical conductivity of hydrous basaltic melts: implications for partial melting in the upper mantle. *Contributions to Mineralogy and Petrology* (in press)
- NI, H.; DE KOKER, N.: Thermodynamics, diffusion and structure of NaAlSi₂O₆ liquid at deep mantle conditions: A first-principles molecular dynamics study. *Journal of Geophysical Research* (submitted)
- NIWA, K.; MIYAJIMA, N.; OHGUSHI, K.; GOTOU, H.; YAGI, T.: *In situ* observation of shear stress-induced perovskite to post-perovskite phase transition in CaIrO₃ and the development of its deformation texture in a diamond-anvil cell up to 30 GPa. *Physics and Chemistry of Minerals* (submitted)
- OVSYANNIKOV, S.V.; DUBROVINSKY, L.: High-pressure high-temperature synthesis of Cr₂O₃ and Ga₂O₃. *High Pressure Research* (in press)
- POLLOK, K.; PUTNIS, C.V.; PUTNIS, A.: Mineral replacement reactions in solid solution-aqueous solution systems: Volume changes, reactions paths and end-points using the example of model salt systems. *American Journal of Science* (submitted)
- QUI, N.V.; SCHOLZ, P.; KRECH, T.; KELLER, T.; POLLOK, K.; ONDRUSCHKA, B.: Multiwalled carbon nanotubes oxidized by UV/H₂O₂ as catalyst for oxidative dehydrogenation of ethylbenzene. *Catalysis Communications* (in press), doi: 10.1016/j.catcom.2010.11.007
- SCHILLING, J.; WU, F.-Y.; MCCAMMON, C.; WENZEL, T.; MARKS, M.A.; PFAFF, K.; JACOB, D.; MARKL, G.: The compositional variability of eudialyte-group minerals (EGM). *Mineralogical Magazine* (submitted)
- SHATSKIY, A.; LITASOV, K.D.; TERASAKI, H.; KATSURA, T.; OHTANI, E.: Performance of semi-sintered ceramics as pressure transmitting media up to 30 GPa. *High Pressure Research* (in press)
- SHATSKIY, A.; BORZDOV, Yu.M.; LITASOV, K.D.; OHTANI, E.; KHOKHRYAKOV, A.F.; PALYANOV, Yu.N.; KATSURA, T.: Pressless split-sphere apparatus equipped with scaled-up Kawai-cell for mineralogical studies at 10-20 GPa. *American Mineralogist* (in press)
- SUN, N.; STIXRUDE, L.; DE KOKER, N.; KARKI, B.B.: First principles molecular dynamics simulations of diopside (CaMgSi₂O₆) liquid to high pressure. *Geochimica et Cosmochimica Acta* (submitted)

- SUSHILA, S.; SCHOLZ, P.; POLLOK, K.; ONDRUSCHKA, B.; BATRA, V.S.: Application of industrial waste based catalysts for total oxidation of propane. *Chemical Engineering Journal* (in press), doi: 10.1016/j.cej.2010.11.024
- PETTKE, T.; OBERLI, F.; AUDÉTAT, A.; WIECHERT, U.; HEINRICH, C.A.: Quantification of transient signals in multiple collector inductively coupled plasma mass spectrometry: Accurate lead isotope ratio determination by laser ablation of individual fluid inclusions. *Journal of Analytical Atomic Spectrometry* (in press)
- RUBIE, D.C.; FROST, D.J.; MANN, U.; ASAHARA, Y.; TSUNO, K.; NIMMO, F.; KEGLER, P.; HOLZHEID, A.; PALME, H.: Heterogeneous accretion, composition and core-mantle differentiation of the Earth. *Earth and Planetary Science Letters* (in press), doi: 10.1016/j.epsl.2010.11.030
- TANG, Z.; STEINLE-NEUMANN, G.: Magnetic structure of Fe₂SiO₄ spinel from electronic structure and lattice dynamics calculations. *Physical Review B* (submitted)
- TROTS, D.M.; KURNOSOV A.; VASYLECHKO, L.; BERKOWSKI, M.; BOFFA BALLARAN, T.; FROST D.J. (2010): Elasticity and equation of state of Li₂B₄O₇. *Physics and Chemistry of Minerals* (submitted)
- TSUNO, K.; FROST, D.J.; RUBIE, D.C.: Effect of nickel and sulphur on the partitioning of oxygen between ferropericlase and liquid Fe alloy at high pressures and temperatures. *Physics of the Earth and Planetary Interiors* (submitted)
- WALTE, N.; RUBIE, D.C.; BONNS, P.; FROST, D.J.: Deformation of a crystalline aggregate with a small percentage of high-dihedral-angle melt: Implications for core-mantle differentiation during planetary formation. *Earth and Planetary Science Letters* (submitted)
- XIONG, X.; KEPPLER, H.; AUDÉTAT, A.; HUAIWEI, N.; SUN, W.; LI, Y.: Partitioning of Nb and Ta between rutile and felsic melt and the fractionation of Nb/Ta during partial melting of hydrous metabasalt. *Geochimica et Cosmochimica Acta* (submitted)
- YANG X.; KEPPLER, H.: *In situ* infrared spectra of OH in olivine to 1100 °C. *American Mineralogist* (submitted)
- YANG X.; KEPPLER, H.; MCCAMMON, C.; NI, H.; XIA, Q.; FAN, Q.: The effect of water on the electrical conductivity of lower crustal clinopyroxene. *Journal of Geophysical Research* (submitted)

5.3 Presentations at scientific institutions and at congresses

- ADJAOUD, O.; STEINLE-NEUMANN, G.; BURTON, B.P.; VAN DE WALLE, A.: 12.-16.09.2010, Psi-k Conference 2010, Berlin, Germany: "First principles phase diagram calculations for the systems MO-M'O with M, M' = Mg, Ca, Sr, Ba, or Cd"
- ALEKSANDROV, V.; SAMUEL, H.: 06.-08.10.2010, Geodynamics Workshop, Münster, Germany: "The Schur complement method and solution of large-scale geophysical problems"
- ALEKSANDROV, V.; SAMUEL, H.: 15.-17.11.2010, c2c Subduction Workshop, Mariánské Lázně, Czech Republic: "The Schur complement method and solution of large-scale geophysical problems"

- ALÉON, J.; MCKEEGAN, K.; EL GORESY, A.; CHARON, E.: 26.-30.07.2010, 73rd Annual Meeting of the Meteoritical Society, New York, USA: "Oxygen isotopes in the ultra-refractory CAI Efremovka 101,1 and the solar nebula"
- AUDÉTAT, A.; DOLEJS, D.; LOWENSTERN, J.B.: 11.-14.04.2010, EMPG XIII, Toulouse, France: "Molybdenite saturation in silicic magmas"
- AUDÉTAT, A.; DOLEJS, D.; LOWENSTERN, J.B.; SUN, W.; LI, Z.: 15.06.2010, Leibniz Universität Hannover, Institut für Mineralogie, Hannover, Germany: "The behaviour of molybdenum in magmatic and hydrothermal environments: evidence from nature and experiments"
- BALI, E.; AUDÉTAT, A.; KEPPLER, H.: 11.-14.04.2010, EMPG XIII, Toulouse, France: "The mobility of U and Th in subduction zone fluids – an indicator of oxygen fugacity and fluid salinity"
- BALI, E.; AUDÉTAT, A.; KEPPLER, H.: 21.-27.08.2010, IMA2010, Budapest, Hungary^{*2}: "Tungsten mobility in subduction zones – a high P-T synthetic fluid inclusion study", Abstract CD
- BASYUK, T.; FADEEV, S.; BEREZOVETS, V.; TROTS, D.; HOFFMANN, S.; NIEWA, R.; VASYLECHKO, L.: 29.08.-02.09.2010, European Crystallographic Meeting ECM-26 and 12th European Powder Diffraction Conference (EPDIC XII), Darmstadt, Germany: "Crystal structure behaviour prediction in the $\text{RAlO}_3\text{-R}'\text{AlO}_3$ system"
- BLÄß, U.; LANGENHORST, F.; MCCAMMON, C.: 21.-27.08.2010, IMA2010, Budapest, Hungary^{*2}: "Origin of strong staining of olivine in the Martian meteorite Northwest Africa 2737"
- BLÄß, U.; MCCAMMON, C.; LANGENHORST, F.: 19.-22.09.2010, 88th Annual DMG Meeting, Münster, Germany^{*3}: "Resulting implications from the shock-induced formation of metallic iron in olivines of NWA 2737"
- BOFFA BALLARAN, T.; KURNOSOV, A.; GLAZYRIN, K.; MERLINI, M.; FROST, D.J.: 10.-11.11.2010, Workshop 'Synchrotron Radiation in Earth, Space & Planetary Science – Exploiting the UK's newest facility', Diamond Light Source, Didcot, U.K. (*invited*): "Structural distortion of Al,Fe-bearing MgSiO_3 perovskite at pressures of the Earth's lower mantle"
- BOFFA BALLARAN, T.: 03.-04.09.2010, European Crystallographic Meeting, Satellite Workshop 'Methods of High-Pressure Single-Crystal X-ray Diffraction', Darmstadt, Germany (*invited*): "Equations of state"
- BOFFA BALLARAN, T.; KURNOSOV, A.; GLAZYRIN, K.; MERLINI, M.; FROST, D.J.: 24.-29.07.2010, American Crystallography Association Annual Meeting, Chicago, USA: "Structural behaviour of $(\text{Mg,Fe}^{3+})(\text{AlSi})\text{O}_3$ perovskite at pressures of the Earth's lower mantle"
- BOFFA BALLARAN, T.; FROST, D.J.; PAMATO, M.G.; MIYAJIMA, N.; HEIDELBACH, F.: 02.-07.05.2010, EGU 2010, Vienna, Austria^{*1}: "A super-aluminous phase D stable within subducting oceanic crust in the Earth's lower mantle", Geophysical Research Abstracts 12, EGU2010-10077-1, 2010
- BOLFAN-CASANOVA, N.; FEROT, A.; MUNOZ, M.; PASCARELLI, S.; MCCAMMON, C.A.: 13.-17.12.2010, AGU Fall Meeting, San Francisco, USA^{*4}: "Ferric iron and water incorporation in wadsleyite at 410-km depth", Abstract DI23C-05, 2010

- CAILLET-KOMOROWSKI, C.; EL GORESY, A.; MIYAHARA, M.; BOUDOUMA, O.; HUMAYUN, M.: 26.-30.07.2010, 73rd Annual Meeting of the Meteoritical Society, New York, USA: "HgS, Hg metal, Cu₂S and native Cu in opaque assemblages in a primitive H3 chondrite: Novel constraints for early solar system condensation and accretion episodes"
- CHANTEL, J.; FROST, D.J.: 30.-31.01.2010, 2010 Weekend Seminar ENB Graduate School 'Oxides', Bronnbach, Germany: "Vp and Vs measurements of polycrystalline garnet solid solutions to pressures of 16 GPa"
- CHANTEL, J.; FROST, D.J.: 11.-14.04.2010, EMPG XIII, Toulouse, France: "Vp and Vs measurements of polycrystalline garnet solid solutions to pressures of 16 GPa"
- CHANTEL, J.; FROST, D.J.: 01.-02.06.2010, c2c Network Meeting, Trondheim, Norway: "Vp and Vs measurements of polycrystalline garnet solid solutions to pressures of 16 GPa"
- CHANTEL, J.; FROST, D.J.: 01.-02.07.2010, International Meeting Marie Curie Network, Torino, Italy: "Measurements of elastic properties of silicates at mantle conditions"
- CHANTEL, J.; FROST, D.J.; MOOKHERJEE, M.: 27.-30.09.2010, HERCULES Short courses, ESRF, Grenoble, France: "Vp and Vs measurements of polycrystalline garnet solid solutions to pressures of 16 GPa"
- CHANTEL, J.; FROST, D.J.; MOOKHERJEE, M.: 27.-30.09.2010, DESY High Pressure Workshop, Lüneburg, Germany: "Vp and Vs measurements of polycrystalline garnet solid solutions to pressures of 16 GPa"
- CHANTEL, J.; MOOKHERJEE, M.; FROST, D.: 13.-17.12.2010, AGU Fall Meeting, San Francisco, USA^{*4}: "Low velocity layer (LVL) in subduction zones: elasticity of lawsonite", Abstract MR22A-04, 2010
- CHEMIA, Z.; DOLEJS, D.; STEINLE-NEUMANN, G.: 02.-07.05.2010, EGU 2010, Vienna, Austria^{*1}: "Thermal effects of metamorphic reactions in a three-component slab", Geophysical Research Abstracts 12, EGU2010-5768, 2010
- CHUST, T.; STEINLE-NEUMANN, G.; BUNGE, H.-P.: 02.-07.05.2010, EGU 2010, Vienna, Austria^{*1}: "Combined mantle convection and mineral physics simulation", Geophysical Research Abstracts 12, EGU2010-6161, 2010
- CORDIER, P.; MUSSI, A.; FROST, D.J.: 13.-17.12.2010, AGU Fall Meeting, San Francisco, USA^{*4}: "Transmission electron microscopy characterization of the plastic mechanisms of phase A", Abstract MR22A-05, 2010
- DE KOKER, N.: 10.-12.03.2010, 3. Berichtskolloquium of the DFG SPP 1236 'Structures and characteristics of crystals at extremely high pressures and temperatures', Oberursel, Germany: "Thermal conductivity of MgO periclase at deep mantle condition"
- DE KOKER, N.: 30.04.2010, ETH Zurich, Institut für Geophysik, Zurich, Switzerland: "Thermal conductivity in the deep Earth: Constraints from first principles simulation"
- DE KOKER, N.: 01.-02.06.2010, c2c Network Meeting, Trondheim, Norway: "Thermal conductivity of MgO periclase at high pressure: Implications for the D"
- DE KOKER, N.: 02.09.2010, Theory Seminar, Fritz-Haber-Institut der Max-Planck-Gesellschaft, Berlin, Germany (*invited*): "Computations of thermal conductivity using equilibrium first-principles molecular dynamics"
- DE KOKER, N.: 12.-16.09.2010, Psi-k Conference 2010, Berlin, Germany: "Computations of thermal conductivity using equilibrium first-principles molecular dynamics"

- DE KOKER, N.: 11.-14.10.2010, CECAM Workshop 'Computational Mineral Physics: Applications to Geophysics', ETH Zurich, Switzerland (*invited*): "Melting at extreme conditions: Insights from first principles molecular dynamics, 11.-14.10.2010"
- DE KOKER, N.: 15.-17.11.2010, c2c Subduction Workshop, Mariánské Lázně, Czech Republic: "Thermal conductivity of MgO periclase at high pressure: Implications for the D""
- DE KOKER, N.: 11.-12.12.2010, MSA Short Course on 'Diffusion in Minerals and Melts', Napa Valley, California, USA (*invited*): "Insights into chemical diffusion in silicate minerals and melts from first-principles simulations"
- DE KOKER, N.; STEINLE-NEUMANN, G.; VLCEK, V.: 13.-17.12.2010, AGU Fall Meeting, San Francisco, USA ^{*4}: "Electrical and thermal conductivity of liquid iron at core pressures and temperatures: results from first-principles molecular dynamics", Abstract MR14A-03, 2010
- DUBROVINSKY, L.: 10.-12.03.2010, 3. Berichtskolloquium of the DFG SPP 1236 'Structures and characteristics of crystals at extremely high pressures and temperatures', Oberursel, Germany: "Single crystal diffraction in a laser heated diamond anvil cell"
- DUBROVINSKY, L.; DUBROVINSKAIA, N.: 27.06.-02.07.2010, Gordon Research Conference 'Research at High Pressure', Holderness, New Hampshire, USA (*invited*): "New old boron based materials"
- DUBROVINSKY, L.; NARYGINA, O.; MCCAMMON, C.; DUBROVINSKAIA, N.: 21.-27.08.2010, IMA2010, Budapest, Hungary ^{*2} (*keynote lecture*): "Effect of carbon and hydrogen on phase relations in Fe-Ni system at high pressures and temperatures"
- DUBROVINSKY, L.; MCCAMMON, C.; GLAZYRIN, K.; NARYGINA, O.; MERLINI, M.; KANTOR, I.; HANFLAND, M.; CHUMAKOV, A. (*invited*): 29.08.-02.09.2010, European Crystallographic Meeting ECM-26 and 12th European Powder Diffraction Conference (EPDIC XII), Darmstadt, Germany: "Interplay between structural and electronic behavior in iron bearing Earth lower mantle minerals"
- DUBROVINSKY, L.; NARYGINA, O.; MCCAMMON, C.; GLAZYRIN, K.; PASCARELLI, S.; HANFLAND, M.; KANTOR, I.; PRAKAPENKA, V.: 19.-22.09.2010, 88th Annual DMG Meeting, Münster, Germany ^{*3}: "Mineral physics of chemically homogeneous spin transition zone in Earth's lower mantle"
- EL GORESY, A.; MIYAHARA, M.; OZAWA, S.; OHTANI, E.; GILLET, Ph.; BECK, P.; MONTAGNAC, G.: 26.-30.07.2010, 73rd Annual Meeting of the Meteoritical Society, New York, USA: "Liquidus high-pressure assemblages in shocked Martian shergottites: Constraints to equilibrium peak-shock pressures and consequences to radiometric ages"
- EL GORESY, A.: 28.10.2010, Tohoku University, Institute of Mineralogy, Petrology and Mineral Deposits, Sendai, Japan: "Heterogeneous and none-equilibrium accretion of primitive EH-3 chondrites in the reduced region of the solar nebula"
- EL GORESY, A.: 12.11.2010, Tohoku University, Institute of Mineralogy, Petrology and Mineral Deposits, Sendai, Japan: "REE abundances in oldhamite, enstatite and niningerite in primitive EH-3 chondrites: Genetic implications"

- ESCUADERO, A.: 13.-17.09.2010, CSIC Postgraduate Course 'Structure determination of Real Solids. Nuclear Magnetic Resonance Technique', Universidad de Sevilla, Instituto de Ciencia de Materiales de Sevilla, Spain (*invited*): "Magnetic interactions in solid state. Magic angle spinning", "Dmfit: a program to simulate and fit NMR spectra"
- ESCUADERO, A.; LANGENHORST, F.: 19.-22.09.2010, 88th Annual DMG Meeting, Münster, Germany^{*3}: "Solubility of Al, Cr and Si in TiO₂-rutile at high pressure and high temperature. A comparative study", Abstract Volume, 79
- FABIAN, K.; ROBINSON, P.; MCENROE, S.A.; HEIDELBACH, F.: Experimental study of the magnetic signature of basal-plane anisotropy in hematite. Springer Monograph, IAGA Proceedings
- FENG, L.; MIYAHARA, M.; LIN, Y.; OHTANI, E.; EL GORESY, A.; NAGASE, T.; HU, S.: 26.-30.07.2010, 73rd Annual Meeting of the Meteoritical Society, New York, USA: "First evidence for multi shock events on the L chondritic parent body"
- FROST, D.J.: 11.01.2010, University of Utrecht, The Netherlands: "Cycling and detection of volatiles in the mantle"
- FROST, D.J.: 14.-15.10.2010, Workshop for Extreme Conditions Research in a Large Volume Press at PETRA III, Lüneburg, Germany: "Geoscience in the multianvil employing neutron based techniques"
- FROST, D.J.; MOOKHERJEE, M.: 19.-22.09.2010, 88th Annual DMG Meeting, Münster, Germany^{*3}: "The composition and buoyancy of hydrous partial melt at conditions of the 410 km seismic discontinuity", Abstract volume 107
- FROST, D.J.; MOOKHERJEE, M.: 02.-07.05.2010, EGU 2010, Vienna, Austria^{*1}: "The formation and chemistry of low degree hydrous partial melt on top of the transition zone", Geophysical Research Abstracts 12, EGU2010-10953, 2010
- FROST, D.J.; TSUNO, K.; RUBIE, D.C.; NAKAJIMA, Y.: 13.-18.06.2010, Goldschmidt 2010, Knoxville, USA: "Si and O in the Earth's core and their effects on the metal-silicate partitioning of other siderophile elements", Geochimica et Cosmochimica Acta 74 (11), Supplement 1, A308
- FUJI-TA, K.; KATSURA, T.; ICHIKI, M.; YOSHINO, T.; KOBAYASHI, T.; OGAWA, Y.: 23.-28.05.2010, Japan Geoscience Union Meeting 2010, Chiba City, Japan: "Electrical conductivity variation of hydrous mineral and rock associated with dehydration"
- GANNOUN, A.; BOYET, M.; EL GORESY, A.; DEVOUARD, B.: 26.-30.07.2010, 73rd Annual Meeting of the Meteoritical Society, New York, USA: "REE abundances in individual oldhamite, niningerite, and enstatite in several EH3 chondrites: Genetic implications"
- GIANNINI, M.; BOFFA BALLARAN, T.; LANGENHORST, F.: 27.-30.10.2010, Joint Meeting: 'Paneth Kolloquium' & 'The first 10 million years of the solar system', Nördlingen, Germany: "Crystal chemistry of hibonite as indicator for oxygen fugacities during solar nebula condensation"
- GUO, X.; YOSHINO, T.; KATSURA, T.; YAMAZAKI, D.; SHAN, S.; ITO, E.: 23.-28.05.2010, Japan Geoscience Union Meeting 2010, Chiba City, Japan: "*In situ* infiltration experiments of basalt - San Carlos olivine couple based on the electrical resistance measurements"

- HARRIES, D.; POLLOK, K.; LANGENHORST, F.: 30.-31.01.2010, 2010 Weekend Seminar ENB Graduate School 'Oxides', Bronnbach, Germany: "Transmission Electron Microscope (TEM) insights into the modulated structure of pyrrhotite"
- HARRIES, D.; POLLOK, K.; LANGENHORST, F.: 08.-12.02.2010, Short Course on 'Microstructures and Physico-Chemical Properties of Earth and Planetary Materials', Verbania, Italy: "Microstructural self-organisation in the modulated structure of pyrrhotite: Direct observations by TEM"
- HARRIES, D.; POLLOK, K.; LANGENHORST, F.: 21.-27.08.2010, IMA2010, Budapest, Hungary^{*2}: "Self-organisation in the modulated structure of pyrrhotite: Direct observations by TEM"
- HARRIES, D.; POLLOK, K.; LANGENHORST, F.: 19.-22.09.2010, 88th Annual DMG Meeting, Münster, Germany^{*3}: "Translation interface modulation in pyrrhotite: Structural self-organisation observed by transmission electron microscopy"
- HARRIES, D.; LANGENHORST, F.: 27.-30.10.2010, Joint Meeting: 'Paneth Kolloquium' & 'The first 10 million years of the solar system', Nördlingen, Germany: "A FIB-TEM study of sulfide mineralogies in CM chondrites"
- HEIDELBACH, F.; WALTE, N.: 19.-22.09.2010, 88th Annual DMG Meeting, Münster, Germany^{*3}: "Deformation fabrics of aragonite under high pressure and temperature"
- HEIDELBACH, F.: 08.12.2010, Universität Freiberg, Geologisches Institut, Freiberg, Germany: "Experimental constraints on the plastic deformation and anisotropy of mantle minerals"
- HOFFMANN, S.; VASYLECHKO, L.; TROTS, D.; YOSHIMURA, M.: 20.-22.09.2010, 15. Vortragstagung der Fachgruppe 'Festkörperchemie und Materialforschung' der Gesellschaft Deutscher Chemiker, Berlin, Germany: "Thermal expansion of Al₆Ti₂O₁₃ between 20 K and 1173 K"
- HOPF, J.; POLLOK, K.; LANGENHORST, F.: 04.-05.10.2010. 9th Symposium on remediation 'Microbial Impact on Element Mobility', Friedrich-Schiller-University Jena, Germany: "Comparison of surface morphology and cell adhesion mechanisms of pyrrhotite in the presence of *Acidithiobacillus ferrooxidans* and *Acidithiobacillus thiooxidans*"
- IRIFUNE, T.; SHINMEI, T.; MCCAMMON, C.; MIYAJIMA, N.; RUBIE, D.; FROST, D.: 23.-28.05.2010, Japan Geoscience Union Meeting 2010, Chiba City, Japan: "Phase relations, Fe partitioning, and density changes in pyrolite under the lower mantle P-T conditions"
- KATSURA, T.; YONEDA, A.; YAMAZAKI, D.; YOSHINO, T.; ITO, E.: 02.-07.05.2010, EGU 2010, Vienna, Austria^{*1}: "Adiabatic temperature profile in the mantle", Geophysical Research Abstracts 12, EGU2010-2364, 2010
- KATSURA, T.; YONEDA, A.; YAMAZAKI, D.; YOSHINO, T.; ITO, E.: 23.-28.05.2010, Japan Geoscience Union Meeting 2010, Chiba City, Japan: "The adiabatic temperature profile in the mantle"
- KATSURA, T.: 26.06.2010, Johann Wolfgang Goethe-Universität Frankfurt/M., Institut für Geowissenschaften, Frankfurt/M., Germany: "High P-T *in situ* X-ray diffraction in a multianvil apparatus"
- KATSURA, T.: 09.07.2010, DESY, HASYLAB, Hamburg, Germany: "Introduction of the multianvil beam line BL04B1 at SPring-8"

- KATSURA, T.: 14.-15.10.2010, Workshop for Extreme Conditions Research in a Large Volume Press at PETRA III, Lüneburg, Germany: "In situ X-ray observations by combination of a multianvil apparatus and highly brilliant monochromatic X-rays"
- KATSURA, T.; YONEDA, A.; YAMAZAKI, D.; YOSHINO, T.; ITO, E.: 05.-07.11.2010, 2010 TANDEM Symposium on Deep Earth Mineralogy, Wuhan, China: "Adiabatic temperature profiles in the mantle"
- KATSURA, T.: 01.12.2010, Charles University in Prague, Faculty of Mathematics and Physics, Prague, Czech Republik: "Adiabatic temperature profiles in the mantle"
- KEPPLER, H.: 11.01.2010, IMPMC Paris: "Volatiles in Earth's mantle"
- KEPPLER, H.: 30.04.2010, University of Edinburgh, Center of Extreme Conditions, Edinburgh, U.K.: "Volatiles in Earth's mantle"
- KEPPLER, H.: 20.05.2010, ETH Zurich, Switzerland: "Volatiles in Earth's mantle"
- KEPPLER, H.: 13.-17.12.2010, AGU Fall Meeting, San Francisco, USA^{*4} (invited): Bowen Lecture: "Volatiles in Earth's interior", Abstract V22A-02, 2010
- KOMAREK, A.C.; REUTHER, M.; LORENZ, T.; COUSSON, A.; BOURREE, F.; TROTS, D.; BAEHTZ, C.; MORGENROTH, W.; BRADEN, M.: 29.08.-02.09.2010, European Crystallographic Meeting ECM-26 and 12th European Powder Diffraction Conference (EPDIC XII), Darmstadt, Germany: "Metal-insulator transitions in RE_{1-x}M_xTiO₃: evidence for charge order-stabilizing an insulating phase"
- LANGENHORST, F.: 02.02.2010, Universität Leipzig, Germany: "Kristallchemie, Realstruktur und Ordnungsphänomene in Perowskiten"
- LANGENHORST, F.: 08.-12.02.2010, Short Course on 'Microstructures and Physico-Chemical Properties of Earth and Planetary Materials', Verbania, Italy: "Down to the nanoscale: Structural and chemical properties of minerals as obtained from TEM, STEM, EDX and EELS"
- LANGENHORST, F.: 25.-27.06.2010, Nördlingen 2010: 'The Ries Crater, the Moon, and the Future of Human Space Exploration, Nördlingen, Germany: "Shock metamorphism at the Ries and implications for lunar rocks and martian meteorites"
- LANGENHORST, F.: 28.10.2010, Clemens-Winkler-Kolloquium, Freiberg, Germany: "Minerale unter Schock – Impaktereignisse in Natur und Experiment"
- LERCHBAUMER L.; AUDÉTAT A.: 02.-07.05.2010, EGU 2010, Vienna, Austria^{*1}: "Partitioning of copper in a two phase fluid system at 600 °C and 700 bar – a study on synthetic fluid inclusions", Geophysical Research Abstracts 12, EGU2010-2862-1, 2010
- MAIEROVA, P.; STEINLE-NEUMANN, G.; CADEK, O.: 13.-17.12.2010, AGU Fall Meeting, San Francisco, USA^{*4}: The effect of a realistic thermal diffusivity on numerical model of a subducting slab", Abstract DI31A-1935, 2010
- MALASPINA, N.; SCAMBELLURI, M.; POLI, S.; VAN ROERMUND, H.L.M.; LANGENHORST, F.: 02.-07.05.2010, EGU 2010, Vienna, Austria^{*1}: "Silicate-rich aqueous fluids sources for diamond crystallisation in deep mantle wedge", Geophysical Research Abstracts 12, EGU2010-8083, 2010
- MALASPINA, N.; SCAMBELLURI, M.; POLI, S.; VAN ROERMUND, H.L.M.; LANGENHORST, F.: 13.-15.09.2010, 89th Meeting of the 'Societa' Italiana Mineralogia e Petrologia' (SIMP), Ferrara, Italy: "Slab-to-mantle "oxidation" transfer: insights from diamond-bearing majoritic garnets (Western Norway)", Plinius 36

- MANTHILAKE, M.A.G.M.; DE KOKER, N.; FROST, D.J.: 11.-14.04.2010, EMPG XIII, Toulouse, France: "Thermal diffusivity of CaGeO₃ perovskite"
- MANTHILAKE, M.A.G.M.; DE KOKER, N.; FROST, D.J.: 14.-15.10.2010, Workshop for Extreme Conditions Research in a Large Volume Press at PETRA III, Lüneburg, Germany: "Thermal conductivity of CaGeO₃ perovskite at high pressure"
- MANTHILAKE, M.A.G.M.: 08.-09.11.2010, Workshop on Continental Lithospheric and Asthenospheric Anisotropy, School of Cosmic Physics, Dublin Institute for Advanced Studies, Dublin, Ireland: "Laboratory studies of electrical conductivity and deformation and their application to dynamics of the mantle"
- MANTHILAKE, M.A.G.M.; DE KOKER, N.; FROST, D.J.: 13.-17.12.2010, AGU Fall Meeting, San Francisco, USA^{*4}: "Thermal conductivity measurements for silicate perovskite and ferropericlae: Implications for the lowermost mantle and D", Abstract DI11B-02, 2010
- MANTHILAKE, M.A.G.M.; MIYAJIMA, N.; HEIDELBACH, F.; FROST, D.J.: 13.-17.12.2010, AGU Fall Meeting, San Francisco, USA^{*4}: "The effect of aluminum and water on the development of orthopyroxene fabrics", Abstract DI13A-1859, 2010
- MANTOVANI, M.; ESCUDERO, A.; BECERRO, A.I.: 06.-11.06.2010, SEA-CSSJ-CMS, Trilateral Meeting on Clays, Madrid – Seville, Spain: "Kaolinite illitization at 300 °C with increasing pressure", Abstract Volume, 119-120
- MCCAMMON, C.: 09.02.2010, Ehime University, Geodynamics Research Center, Matsuyama, Japan: "Effect of spin transitions on properties and dynamics of the lower mantle"
- MCCAMMON, C.: 09.02.2010, Ehime University, Geodynamics Research Center, Matsuyama, Japan: "Transition metal chemistry and the Earth's interior"
- MCCAMMON, C.: 10.02.2010, Ehime University, Geodynamics Research Center, Matsuyama, Japan: "Oxygen fugacity and the Earth's interior"
- MCCAMMON, C.: 03.-05.03.2010, Ecole Normale Supérieure de Lyon, Biologie et Sciences de la Terre, Lyon, France: "Oxygen fugacity: Lecture and practical"
- MCCAMMON, C.: 10.-12.03.2010, 3. Berichtskolloquium of the DFG SPP 1236 'Structures and characteristics of crystals at extremely high pressures and temperatures', Oberursel, Germany: "Nuclear inelastic scattering of lower mantle minerals at high P,T"
- MCCAMMON, C.: 20.05.2010, University of Bristol, U.K.: "Tracing mantle properties and evolution through iron valence and spin state"
- MCCAMMON, C.; DUBROVINSKY, L.; GLAZYRIN, K.; NARYGINA, O.; WU, X.; KANTOR, I.; SERGUEEV, I.; CHUMAKOV, A.: 21.-27.08.2010, IMA2010, Budapest, Hungary^{*2}: "Nuclear resonance studies of lower mantle perovskite: spin state and elastic properties"
- MCCAMMON, C.A.; POTAPKIN, V.; CHUMAKOV, A.I.; CELSE, J.P.; RÜFFER, R.; SMIRNOV, G.; POPOV, S.L.; GLAZYRIN, K.; KANTOR, A.; KANTOR, I.; SERGUEEV, I.; BOFFA BALLARAN, T.; DUBROVINSKY, L.S.: 13.-17.12.2010, AGU Fall Meeting, San Francisco, USA^{*4}: "Iron spin transitions and elastic properties of (Mg,Fe)(Si,Al)O₃ perovskite using a newly developed synchrotron Mössbauer source and nuclear inelastic scattering", Abstract MR24A-03, 2010

- MIYAJIMA, N.; LANGENHORST, F.: 19.-22.09.2010, 88th Annual DMG Meeting, Münster, Germany^{*3}: "Fe L_{2,3}-edge energy-loss near-edge structure of high pressure minerals in a K-bearing MORB"
- MIYAJIMA, N.; WALTE, N.: 21.-27.08.2010, IMA2010, Budapest, Hungary^{*2}: "Burgers vector determination in deformed materials using the thickness-fringe method"
- MOOKHERJEE, M.; KEPPLER, H.; MANNING, C.E.; CARACAS, R.: 13.-18.06.2010, Goldschmidt 2010, Knoxville, USA: "Aluminate speciation in H₂O at high pressures and temperatures"
- MOOKHERJEE, M.; KARATO, S.: 11.-14.04.2010, EMPG XIII, Toulouse, France: "Solubility of water in pyrope-rich garnet at high pressure and temperature"
- MOOKHERJEE, M.; KEPPLER, H.; MANNING, C.E.; CARACAS, R.: 11.-14.04.2010, EMPG XIII, Toulouse, France: "*In situ* Raman spectroscopic study of Al₂O₃ speciation in H₂O-KOH solutions at high pressures and temperatures"
- MOOKHERJEE, M.: 01.10.2010, Ludwig-Maximilians-Universität, Department für Geo- und Umweltwissenschaften, München, Germany: "Energetics, Structure and Elasticity of subducted materials"
- MOOKHERJEE, M.; LITHGOW-BERTELLONI, C.: 11.-14.10.2010, CECAM Workshop 'Computational Mineral Physics: Application to Geophysics', Centre Européen de Calcul Atomique et Moléculaire, Zurich, Switzerland: "Energetics, structure and elasticity of subducted materials"
- MOOKHERJEE, M.: 18.11.2010, ETH Zurich, Institute of Geochemistry and Petrology, Zurich, Switzerland: "Fluids and melts in the Earth's interior"
- MOOKHERJEE, M.; FROST, D.: 13.-17.12.2010, AGU Fall Meeting, San Francisco, USA^{*4} (*invited*): "The composition of hydrous partial melt at 410 km: Geodynamic implications", Abstract MR44A-01, 2010
- MOOKHERJEE, M.; MANTHILAKE, M.A.G.M.; DE KOKER, N.; FROST, D.J.: 13.-17.12.2010, AGU Fall Meeting, San Francisco, USA^{*4}: "Thermal conductivity of serpentinite in subducting slabs: Measurements at high pressure and temperature", Abstract MR31A-1982, 2010
- NAKAJIMA, Y.; FROST, D.J.; RUBIE, D.C.: 14.-15.10.2010, Workshop for Extreme Conditions Research in a Large Volume Press at PETRA III, Lüneburg, Germany: "S, Si, and O partitioning between metal, lower-mantle minerals, and silicate melt during formation of the core"
- NAKAJIMA, Y.; FROST, D.J.; RUBIE, D.C.: 13.-17.12.2010, AGU Fall Meeting, San Francisco, USA^{*4}: "Si and O partitioning between metal and lower mantle minerals during formation of the core", Abstract DI41A-1929, 2010
- NI, H.; KEPPLER, H.; BEHRENS, H.: 13.-17.12.2010, AGU Fall Meeting, San Francisco, USA^{*4}: "Hydrous silicate melts in the Earth's asthenosphere: evidence from electrical conductivity measurements", Abstract DI31B-03, 2010
- NOVELLA, D.; KESHAV, S.: 11.-14.04.2010, EMPG XIII, Toulouse, France: "Silicate melt-carbonatite liquid immiscibility reconsidered in the system CaO-MgO-Al₂O₃-SiO₂-CO₂ at 2-3 GPa"

- OTSUKA, K.; LONGO, M.; MCCAMMON, C.A.; KARATO, S.: 13.-17.12.2010, AGU Fall Meeting, San Francisco, USA ^{*4}: "Role of ferric iron and protons in Mg-Fe interdiffusion in (Mg,Fe)O", Abstract V51A-2166, 2010
- OVSYANNIKOV, S.V.; SHCHENNIKOV, V.V.; SHVETSOVA, M.A.; POLIAN, A.; DUBROVINSKY, L.S.: 25.-29.07.2010, XLVIII European High Pressure Research Group Meeting, Uppsala, Sweden: "A high-pressure effect on the stoichiometry of Fe_{1-x}O wüstite"
- OVSYANNIKOV, S.V.; WU, X.; SHCHENNIKOV, V.V.; KARKIN, A.E.; TEPIKINA, Y.V.; MANTHILAKE, G.M.; DUBROVINSKAIA, N.; DUBROVINSKY, L.: 25.-29.07.2010, XLVIII European High Pressure Research Group Meeting, Uppsala, Sweden: "High-pressure high-temperature synthesis and characterization of Ti₂O₃ and some other sesquioxides"
- OVSYANNIKOV, S.V.; WU, X.; SHCHENNIKOV, V.V.; KARKIN, A.E.; TEPIKINA, Y.V.; MANTHILAKE, G.M.; DUBROVINSKAIA, N.; DUBROVINSKY, L. (2010): 01.-04.08.2010, 14th High-Pressure Semiconductor Physics Conference, Changchun, China: "HP-HT phases of sesquioxides and their properties: Ti₂O₃"
- OVSYANNIKOV, S.V.; SHCHENNIKOV, V.V.; SHVETSOVA, M.A.; DUBROVINSKY, L.S.; POLIAN, A.: 01.-04.08.2010, 14th High-Pressure Semiconductor Physics Conference, Changchun, China: "A high-pressure effect on the stoichiometry of Fe_{1-x}O wüstite: a thermoelectric power study"
- PAMATO, M.G.; BOFFA BALLARAN, T.; FROST, D.J.; TROTS, D.M.; KURNOSOV, A.; HEIDELBACH, F.; MIYAJIMA, N.: 13.-17.12.2010, AGU Fall Meeting, San Francisco, USA ^{*4}: "High pressure behaviour of hydrous aluminosilicate phases in the lower mantle", Abstract MR22A-02, 2010
- POLLOK, K.; HELDIGE, K.; PEIFFER, S.: 11.-14.04.2010, EMPG XIII, Toulouse, France: "Tracing the reaction pathway of iron sulphide formation by analytical TEM"
- POLLOK, K.: 16.-18.07.2010, Rundgespräch der Arbeitsgruppe geowissenschaftlicher Nachwuchs der DFG-Geokommision, Erfurt, Germany: "Mikrostruktur, Reaktivität und Raten: Fallstudien zur Alteration und Bildung von Monosulfiden"
- POLLOK, K.; HOPF, J.; HARRIES, D.; CHUST, T.; HOHELLA, M.F.; LANGENHORST, F.: 21.-27.08.2010, IMA2010, Budapest, Hungary ^{*2}: "Microbially enhanced dissolution of pyrrhotite polytypes: Surface roughness, reactivity and rates"
- POLLOK, K.; CHUST, T.; HARRIES, D.: 19.-22.09.2010, 88th Annual DMG Meeting, Münster, Germany ^{*3}: "From surface morphology to rates: An automated routine to evaluate converged roughness parameters of heterogeneous surfaces"
- POLLOK, K.; HALLBERG, K.: 19.-22.09.2010, 88th Annual DMG Meeting, Münster, Germany ^{*3}: "Biogenic sulfide formation in sediments from an abandoned copper mine: an example for the importance of nanoparticles to assess element mobility"
- POLLOK, K.; HARRIES, D.; HOPF, J.; ETZEL, K.; SCHEITER, D.; CHUST, T.; HOHELLA, M.F., JR.; HELDIGE, K.; PEIFFER, S.; HALLBERG, K.; LANGENHORST, F.: 26.-27.10.2010, 2. Statusseminar 'Mineral Surfaces – From atomic processes to industrial applications', Mainz, Germany: "Microstructural controls on monosulphide weathering and heavy metal release"

- POTAPKIN, V.; CHUMAKOV, A.; CELSE, J.-P.; RÜFFER, R.; SMIRNOV, G.V.; POPOV, S.L.; DUBROVINSKY, L.; MCCAMMON, C.: 02.07.2010, Nuclear Resonant Scattering at DESY: Past, Present, Future Workshop, Hamburg, Germany: "Synchrotron Mössbauer source"
- POTAPKIN, V.; CHUMAKOV, A.; RÜFFER, R.; SMIRNOV, G.V.; POPOV, S.L.; DUBROVINSKY, L.; MCCAMMON, C.: 25.-29.07.2010, XLVIII European High Pressure Research Group Meeting, Uppsala, Sweden: "Synchrotron Mössbauer source for high pressure studies at the ESRF"
- POTAPKIN, V.; CHUMAKOV, A.; RÜFFER, R.; SMIRNOV, G.V.; POPOV, S.L.; DUBROVINSKY, L.; MCCAMMON, C.: 29.08.-02.09.2010, European Crystallographic Meeting ECM-26 and 12th European Powder Diffraction Conference (EPDIC XII), Darmstadt, Germany: "Synchrotron Mössbauer source for geophysical studies at the ESRF"
- POTAPKIN, V.; CHUMAKOV, A.; RÜFFER, R.; SMIRNOV, G.V.; POPOV, S.L.; DUBROVINSKY, L.; MCCAMMON, C.: 06.-08.10.2010, ESRF Student and Science Day 2010, Grenoble, France: "Synchrotron Mössbauer source for high pressure studies at the ESRF"
- PRESCHER, C.; DUBROVINSKY, L.; MCCAMMON, C.: 25.-29.07.2010, XLVIII European High Pressure Research Group Meeting, Uppsala, Sweden: "Electronic transition(s) of Fe₃C observed with Mössbauer spectroscopy"
- RUBIE D.C.: 25.01.2010, Universität Freiburg, Institut für Geowissenschaften, Freiburg, Germany: "Formation of the Earth's core"
- RUBIE D.C.: 24.02.2010, University of Texas at Austin, Jackson School of Earth Sciences, Austin, USA: "Experimental studies of the early evolution of the Earth"
- RUBIE D.C.: 25.02.2010, University of Texas at Austin, Jackson School of Earth Sciences, Austin, USA: "Accretion and early differentiation of the Earth"
- RUBIE D.C.: 26.02.2010, University of Texas at Austin, Jackson School of Earth Sciences, Austin, USA: "Mechanisms and kinetics of mantle phase transformations"
- RUBIE, D.C.; FROST, D.J.; NIMMO, F.; O'BRIEN, D.P.; MANN, U.; PALME, H.: 01.-05.03.2010, 41st Lunar and Planetary Science Conference, The Woodlands, Texas, USA: "Accretion of volatile elements to the Earth and Moon", Abstract #1134
- RUBIE D.C.: 10.06.2010, ETH Zürich, Switzerland: "Accretion and early differentiation of the Earth"
- RUBIE, D.C.: 14.-15.10.2010, Workshop for Extreme Conditions Research in a Large Volume Press at PETRA III, Lüneburg, Germany: "Viscosity of melts at high pressure"
- RUBIE, D.C.; FROST, D.J.; NIMMO, F.; O'BRIEN D.P.; NAKAJIMA, Y.; VOGEL, A.; MANN, U.; PALME, H.: 27.-30.10.2010, Joint Meeting: 'Paneth Kolloquium' & 'The first 10 million years of the solar system', Nördlingen, Germany: "Heterogeneous accretion and core-mantle differentiation of the terrestrial planets"
- RUSKOV, T.; SPIROV, I.; GEORGIEVA, M.; YAMAMOTO, S.; GREEN, H.; MCCAMMON, C.; DOBRZHINetskAYA, L.: 21.-27.08.2010, IMA2010, Budapest, Hungary^{*2}: "Mössbauer spectroscopy studies of valence state of iron in a Tibetan chromite containing high-pressure mineral inclusions"

- RUSKOV, T.; SPIROV, I.; GEORGIEVA, M.; YAMAMOTO, S.; MCCAMMON, C.; GREEN, H.; DOBRZHINETSKAYA, L.: 13.-18.06.2010, Goldschmidt 2010, Knoxville, USA: "The valence state of iron in chromite from the Luobusa Massif of Tibet: Mössbauer spectroscopy studies"
- SAMUEL, H.; DEO, B.: 02.-07.05.2010, EGU 2010, Vienna, Austria^{*1} (*invited*): "The effect of continental lids on the long-term efficiency of mantle convective stirring", Geophysical Research Abstracts 12, EGU2010-6753, 2010
- SAMUEL, H.; DEO, B.: 02.-07.05.2010, EGU 2010, Vienna, Austria^{*1}: "Fast and accurate advection of sharp discontinuities in Geophysical flows using hybrid implicit surfaces", Geophysical Research Abstracts 12, EGU2010-6763, 2010
- SAMUEL, H.; EVONUK, M.: 07.-11.06.2010, CMG Workshop, Pisa, Italy: "Fast and accurate modeling of advection in geophysical flows with dynamic implicit surfaces"
- SAMUEL, H.; EVONUK, M.: 06.-08.10.2010, Geodynamics Workshop, Münster, Germany: "The numerical advection of discontinuous quantities in geophysical flows using particle level sets"
- SAMUEL, H.; ALEKSANDROV, V.; DEO, B.: 15.-17.11.2010, c2c Subduction Workshop, Mariánské Lázně, Czech Republic: "Mixing processes and mixing scales in the Earth's mantle"
- SAMUEL, H.; RUBIE, D.; MELOSH, J.: 13.-17.12.2010, AGU Fall Meeting, San Francisco, USA^{*4}: "Fragmentation of metal diapirs in terrestrial magma oceans", Abstract V44B-08, 2010
- SAMUEL, H.; ALEKSANDROV, V.; DEO, B.: 13.-17.12.2010, AGU Fall Meeting, San Francisco, USA^{*4}: "Continental lids and mantle convective stirring efficiency", Abstract DI52A-01, 2010
- SAMUEL, H.; ALEKSANDROV, V.; EVONUK, M.: 13.-17.12.2010, AGU Fall Meeting, San Francisco, USA^{*4}: "Modeling the advection of discontinuous quantities in geophysical flows using Particle Level Sets", Abstract DI51A-1860, 2010
- SHATSKIY, A.; LITASOV, K.; BORZDOV, Y.; KATSURA, T.; OHTANI, E.: 02.-07.05.2010, EGU 2010, Vienna, Austria^{*1}: "Incipient fluid migration through the deep mantle by dissolution-precipitation: crystal growth constraints", Geophysical Research Abstracts 12, EGU2010-7534, 2010
- SHATSKIY, A.; LITASOV, K.; YAMAZAKI, D.; KATSURA, T.; OHTANI, E.: 23.-28.05.2010, Japan Geoscience Union Meeting 2010, Chiba City, Japan: "Incipient fluid migration through the deep mantle by dissolution-precipitation: crystal growth constraints"
- SHATSKIY, A.; BORZDOV, Yu.M.; LITASOV, K.D.; OHTANI, E.; KHOKHRYAKOV, A.F.; PALYANOV, Yu.N.; KATSURA, T.: 20.-22.10.2010, The High Pressure Conference of Japan, Sendai, Japan: "Pressless split-sphere apparatus equipped with scaled-up Kawai-cell for mineralogical studies at 10-20 GPa"
- SHCHEKA, S.; KEPPLER, H.: 10.-12.03.2010, 3. Berichtskolloquium of the DFG SPP 1236 'Structures and characteristics of crystals at extremely high pressures and temperatures', Oberursel, Germany: "Noble gases in silicate perovskite: Solubility, dissolution mechanism and influence on the equation of state"

SHCHEKA, S.; KEPPLER, H.: 19.-22.09.2010, 88th Annual DMG Meeting, Münster, Germany^{*3}: "The origin of the terrestrial noble gas signature"

SHCHEKA, S.; KEPPLER, H.: 11.-14.04.2010, EMPG XIII, Toulouse, France: "Silicate perovskite – a reservoir of noble gases in the lower mantle"

SHCHEKA, S.; KEPPLER, H.: 13.-17.12.2010, AGU Fall Meeting, San Francisco, USA^{*4}: "Silicate perovskite and terrestrial noble gas signature", Abstract V53A-2231, 2010

SHEKHAR, S.; FROST, D.J.; WALTE, N.; MIYAJIMA, N.; HEIDELBACH, F.: 02.-07.05.2010, EGU 2010, Vienna, Austria^{*1}: "High pressure and temperature deformation experiments on San Carlos olivine and implications for upper mantle anisotropy", Geophysical Research Abstracts 12, EGU2010-13462, 2010

SINMYO, R.; HIROSE, K.; OHISHI, Y.: 13.-17.12.2010, AGU Fall Meeting, San Francisco, USA^{*4}: "Density profile of pyrolitic lower mantle", Abstract MR24A-05, 2010

SMITH, E.M.; KOPYLOVA, M.G.; DUBROVINSKY, L.S.: 10.-14.05.2010, GeoCanada 2010, Calgary, Canada: "X-ray diffraction study of the mineralogy of microinclusions in fibrous diamond"

SMYTH, J.R.; MIYAJIMA, N.; HUSS, G.R.; HELLEBRAND, E.; RUBIE, D.C.; FROST, D.J.: 13.-17.12.2010, AGU Fall Meeting, San Francisco, USA^{*4}: "Olivine-wadsleyite-pyroxene epitaxy: Element and volatile distributions at the 410 km discontinuity", Abstract MR22A-07, 2010

SOUGAWA, M.; SUMIYA, T.; TAKARABE, K.; MORI, Y.; OKADA, T.; GOTOU, H.; YAGI, T.; YAMAZAKI, D.; TOMIOKA, N.; KATSURA, T.: 20.-22.10.2010, The High Pressure Conference of Japan, Sendai, Japan: "Characterization and synthesis of carbon nitride"

STAGNO, V.; FROST, D.J.; MCCAMMON, C.A.: 02.-07.05.2010, EGU 2010, Vienna, Austria^{*1}: "The speciation of carbon in the Earth's mantle as a function of oxygen fugacity", Geophysical Research Abstracts 12, EGU2010-9806, 2010

STAGNO, V.; FROST, D.J.; MCCAMMON, C.A.: 13.-15.09.2010, 89th Meeting of the 'Societa' Italiana Mineralogia e Petrologia' (SIMP), Ferrara, Italy: "Carbon and carbonates in the Earth's mantle and implications for redox melting beneath mid-ocean ridges"

STAGNO, V.: 07.10.2010, Absolventenfeier des Elitenetzwerks Bayern, LMU, München, Germany: "Diamonds and carbonates in the Earth's interior: the deep carbon cycle"

STEINLE-NEUMANN, G.; DOLEJS, D.: 21.-27.08.2010, IMA2010, Budapest, Hungary^{*2}: "Thermodynamics of melting of Fe up to 100 GPa"

STEINLE-NEUMANN, G.: 14.-15.10.2010, Workshop for Extreme Conditions Research in a Large Volume Press at PETRA III, Lüneburg, Germany: "How does computational material science fit in with high pressure experiments?"

THOMAS, S.; JACOBSEN, S.D.; BINA, C.R.; GONCHAROV, A.F.; FROST, D.J.; MCCAMMON, C.A.: 13.-17.12.2010, AGU Fall Meeting, San Francisco, USA^{*4}: "The effect of temperature and pressure on optical absorption spectra of transition zone minerals – Implications for the radiative conductivity of the Earth's interior", Abstract DI51C-1884, 2010

- TIBBETTS, N.; BIZIMIS, M.; LONGO, M.; KESHAV, S.; SALTERS, V.; MCCAMMON, C.: 13.-18.06.2010, Goldschmidt 2010, Knoxville, USA: "Apparent oxygen fugacity structure beneath O'ahu, Hawai'i"
- TRONCHE, E.J.; PARKER, M.V.K.; VRIES, J.D.; WANG, Y.; SANEHIRA, T.; LI, J.; CHEN, B.; GAO, L.; KLEMME, S.; MCCAMMON, C.A.; WESTRENNEN, W.V.: 19.-22.09.2010, 88th Annual DMG Meeting, Münster, Germany^{*3}: "The thermal equation of state of FeTiO₃ ilmenite based on *in situ* X-ray diffraction at high pressures and temperatures"
- TROTS, D.M.; KURNOSOV, A.; BOFFA BALLARAN, T.; FROST D.J.: 21.-27.08.2010, 21.-27.08.2010, IMA2010, Budapest, Hungary^{*2}: "Single-crystal diffractometer with an ultrahigh intensity rotating anode X-ray source"
- TROTS, D.M.; KURNOSOV, A.; BOFFA BALLARAN, T.; VASYLECHKO, L.; BERKOWSKI, M.; FROST, D.J.: 29.08.-02.09.2010, European Crystallographic Meeting ECM-26 and 12th European Powder Diffraction Conference (EPDIC XII), Darmstadt, Germany: "Compressional behaviour of diomignite, Li₂B₄O₇"
- TSUNO, K.; FROST, D.J.; RUBIE, D.C.: 13.-17.12.2010, AGU Fall Meeting, San Francisco, USA^{*4} (*invited*): "Core-mantle partitioning of oxygen on Earth and Mars", Abstract MR14A-07, 2010
- URAKAWA, S.; MATSUBARA, R.; KATSURA, T.; WATANABE, T.; KIKEGAWA, T.: 23.-28.05.2010, Japan Geoscience Union Meeting 2010, Chiba City, Japan: "Melting relationships of the Ni-NiS system under pressure and the stability field of the Ni₃S"
- VAN MIERLO, W.L.; LANGENHORST, F.; MIYAJIMA, N.; FROST, D.; RUBIE, D.: 01.-02.06.2010, c2c Network Meeting, Trondheim, Norway: "Major element diffusion in garnets at high pressure"
- VAN MIERLO, W.L.; LANGENHORST, F.; MIYAJIMA, N.; FROST, D.; RUBIE, D.: 11.-14.04.2010, EMPG XIII, Toulouse, France: "Diffusion of the majorite component in Mg-majorite – pyrope garnet"
- VASYLECHKO, L.; PROTS, Y.; GRIN, Y.; TROTS, D.; MARGIOLAKI, I.: 05.-10.09.2010, 17th International Conference on Solid Compounds of Transition Elements, Annecy, France: "Anomalous thermal behaviour of YbNiGa and YbPdGa"
- VLCEK, V.; STEINLE-NEUMANN, G.; HOLBIG, E.: 29.08.-02.09.2010, European Crystallographic Meeting ECM-26 and 12th European Powder Diffraction Conference (EPDIC XII), Darmstadt, Germany: "Lattice dynamics of rutile and anatase: implications for phase stability"
- WANG, J.; BASS, J.; INOUE, T.; KATSURA, T.: 23.-28.05.2010, Japan Geoscience Union Meeting 2010, Chiba City, Japan: "Elastic properties of anhydrous and hydrous wadsleyite and ringwoodite at high pressures by Brillouin scattering"
- XU, J.; YAMAZAKI, D.; KATSURA, T.; WU, X.; REMMERT, P.; YURIMOTO, H.; CHAKRABORTY, S.: 23.-28.05.2010, Japan Geoscience Union Meeting 2010, Chiba City, Japan: "Si diffusion in single crystal of MgSiO₃ perovskite"
- YOSHINO, T.; KATSURA, T.; BABA, K.; UTADA, H.: 02.-07.05.2010, EGU 2010, Vienna, Austria^{*1}: "Laboratory-based conductivity structure in the mantle transition zone", Geophysical Research Abstracts 12, EGU2010-2361, 2010

YOSHINO, T.; KATSURA, T.; YAMAZAKI, D.; ITO, E.; SHAN, S.; GUO, X.; FUNAKOSHI, K.; HIGO, Y.: 23.-28.05.2010, Japan Geoscience Union Meeting 2010, Chiba City, Japan: "Effect of iron content on spin transition pressure of ferropericlasite"

YOSHINO, T.; LAUMONIER, M.; MCISAAC, E.; KATSURA, T.: 23.-28.05.2010, Japan Geoscience Union Meeting 2010, Chiba City, Japan: "Electrical conductivity of carbonatite-bearing peridotite"

YOSHINO, T.; ITO, E.; YAMAZAKI, D.; KATSURA, T.; SHAN, S.; GUO, X.; NISHI, M.; HIGO, Y.; FUNAKOSHI, K.: 20.-22.10.2010, The High Pressure Conference of Japan, Sendai, Japan: "Effect of iron content on spin transition pressure of ferropericlasite"

ZHANG, B.; YOSHINO, T.; MCCAMMON, C.; KATSURA, T.; WU, X.: 08.-12.08.2010, 2010 The Meeting of the Americas, Foz do Iguaçu, Brazil: "Effect of Al₂O₃ on the electrical conductivity of orthoenstatite and its implications for the electrical structure in the upper mantle"

*1 EGU: European Geosciences Union General Assembly 2010, 02.-07.05.2010, Vienna, Austria

*2 IMA: The 20th General Meeting of the International Mineralogical Association, 21.-27.08.2010, Budapest, Hungary

*3 DMG: 'From Dust to Dust', 88. Jahrestagung der Deutschen Mineralogischen Gesellschaft (88th Annual Meeting of the German Mineralogical Society), 19.-22.09.2010, Münster, Germany

*4 AGU: American Geophysical Union Fall Meeting, 13.-17.12.2010, San Francisco, USA

5.4 Lectures and seminars at Bayerisches Geoinstitut

AUDÉTAT, A., Bayerisches Geoinstitut, Bayreuth, Germany: "The behavior of molybdenum in magmatic and hydrothermal environments: evidence from nature and experiments", Ringvorlesung 21.06.2010

BACH, W., Universität Bremen, Fachbereich 5 Geowissenschaften, Bremen, Germany: "Is microbial life in basaltic ocean crust abundant? First insights, future studies, and some geochemical implications", 16.11.2010

BALI, E., Bayerisches Geoinstitut, Bayreuth, Germany: "The effect of H₂O-fluid on the trace element composition of arc magmas", 27.05.2010

BERNINI, D., Bayerisches Geoinstitut, Bayreuth, Germany: "Halogen and trace element behaviour in minerals and aqueous fluids in subduction zone", 25.11.2010

BEZACIER, L., Ecole Normale Supérieure, Lyon, France: "Elasticity of antigorite and glaucophane: anisotropy in the subduction zones", 28.04.2010

BREU, J., Anorganische Chemie I, Bayreuth, Germany: "Issues in nanotechnology", Ringvorlesung 21.06.2010

CHEMIA, Z., Geological Survey of Norway, Trondheim, Norway: "Thermal effects of metamorphic reactions in three-component slab", 08.07.2010

- DUBROVINSKY, L., Bayerisches Geoinstitut, Bayreuth, Germany: "Seismological signature of Earth spin transition zone", 14.01.2010
- DUBROVINSKY, L., Bayerisches Geoinstitut, Bayreuth, Germany: "High-pressure synthesis of novel superhard nanocrystalline materials", Ringvorlesung 17.05.2010
- EL GORESY, A., Bayerisches Geoinstitut, Bayreuth, Germany: "Forty years research on shocked Martian igneous rocks: discrepant equilibrium shock-pressure estimates and the resulting controversial radiometric ages", 18.03.2010
- ESCUADERO, A., Bayerisches Geoinstitut, Bayreuth, Germany: "Solubility of Al, Cr and Si in TiO₂ phases at high pressure and high temperature", 09.12.2010
- FEI, Y., Carnegie Institution of Washington, Geophysical Laboratory, Washington DC, USA: "Constraints on the chemistry and physical state of the terrestrial planetary cores", 10.05.2010
- FEI, Y., Carnegie Institution of Washington, Geophysical Laboratory, Washington DC, USA: "Advances in determining the composition and density of the Earth's Interior", 11.05.2010
- FENG, L., Chinese Academy of Sciences, Beijing, China: "Olivine-ringwoodite assemblages in Grove Mountains (Antarctica) meteorites: First evidence of multi shock events on L-chondritic parent body", 19.08.2010
- FROST, D., Bayerisches Geoinstitut, Bayreuth, Germany: "Magma oceans and melting in the Earth's deep interior", Ringvorlesung 21.06.2010
- FROST, D., Bayerisches Geoinstitut, Bayreuth, Germany: "Deep mantle melting", 02.12.2010
- GANSKOW, G., Bayerisches Geoinstitut, Bayreuth, Germany: "The effect of iron on the stability and water content of mantle silicates", 23.09.2010
- GOU, H., Rensselaer Polytechnic Institute, Mechanical, Aerospace & Nuclear Engineering, Troy, NY, USA: "Material behaviors under normal and extreme environments", 14.06.2010
- KATSURA, T., Bayerisches Geoinstitut, Bayreuth, Germany: "Electrical conduction of mantle minerals", Ringvorlesung 17.05.2010
- IRIFUNE, T., Ehime University, Geodynamics Research Center, Matsuyama, Japan: "Phase transitions and sound velocities of mantle and slab materials: implications for the composition of the mantle transition region" and "Recent progress in nano-polycrystalline diamond project: synthesis, physical properties, and applications", 01.09.2010
- JEANLOZ, R., University of California, Earth & Planetary Science, Berkeley, USA: "Earth to stars: Toward gigabar pressures and kilovolt chemistry", 24.02.2010
- JEANLOZ, R., University of California, Earth & Planetary Science, Berkeley, USA: "Shock waves and high pressures in Earth and planetary science", 25.02.2010
- JEGO, S., Academia Sinica, Taipei, Taiwan: "Solubility of gold in arc magmas: effects of redox state, sulfur, and pressure in hydrous intermediate silicate melts - Implications for ore-forming processes", 21.07.2010
- LONGO, M., Università degli Studi di Padova, Dipartimento di Geoscienze, Padova, Italy: "Iron oxidation state in garnets from upper mantle xenoliths in the Gibeon Kimberlite Province (Namibia) and implications for geothermobarometry", 24.06.2010
- MANTHILAKE, G., Bayerisches Geoinstitut, Bayreuth, Germany: "Thermal conductivity measurements for silicate perovskite and ferropericlase: Implications for the lowermost mantle and D'", 21.10.2010

- MARTIN, C., CNRS Nancy, France: "Hf and REE mobilization by fluids during HP-LT metamorphism", 11.05.2010
- MCCAMMON, C., Bayerisches Geoinstitut, Bayreuth, Germany: "Spotlight on Cr", 01.07.2010
- NAKAJIMA, Y., Bayerisches Geoinstitut, Bayreuth, Germany: "Element partitioning between metal, lower mantle minerals, and silicate melt during core formation", 04.11.2010
- NI, H., Bayerisches Geoinstitut, Bayreuth, Germany: "Electrical conductivity and diffusivity of silicate melts", 10.06.2010
- PALKE, A., Stanford University, Geological & Environmental Sciences Department, Stanford, USA: "Al and Fe substitution in MgSiO₃ perovskite: Paramagnetic interactions in NMR spectroscopy", 07.10.2010
- PAMATO, M.G., Bayerisches Geoinstitut, Bayreuth, Germany: "High pressure behaviour of hydrous Al phases of the deep mantle", 15.07.2010
- RUBIE, D., Bayerisches Geoinstitut, Bayreuth, Germany: "Accretion and early differentiation of the Earth", 20.05.2010
- SAMUEL, H., Bayerisches Geoinstitut, Bayreuth, Germany: "Modeling core formation in terrestrial magma oceans: Problems and solutions", 11.02.2010
- SAMUEL, H., Bayerisches Geoinstitut, Bayreuth, Germany: "The influence of material properties on the dynamics of mantle upwellings and downwellings", Ringvorlesung 17.05.2010
- SCHIAVI, F., Bayerisches Geoinstitut, Bayreuth, Germany: "A new moissanite cell apparatus for *in situ* observation of crystallizing melts at high temperature", 28.01.2010
- SCHMELING, H., Johann Wolfgang Goethe-Universität Frankfurt/M., Institut für Geowissenschaften, Geophysik, Frankfurt/M., Germany: "Role of melting processes in geodynamics: from continental rifting to mid-oceanic spreading and anomalous crust formation", 23.03.2010
- SEKINE, T., Okayama University, Institute for Study of the Earth's Interior, Misasa, Japan: "Earth and planetary materials evolution by shock wave", 26.08.2010
- SELF, S., U.S. Nuclear Regulatory Commission, Washington DC, USA; The Open University, Earth and Environmental Sciences, Milton Keynes, U.K.: "Volcanism and global sustainability", 11.10.2010
- SELF, S., U.S. Nuclear Regulatory Commission, Washington DC, USA; The Open University, Earth and Environmental Sciences, Milton Keynes, U.K.: "Flood basalt volcanism – mechanisms, volatile release, and environment impacts", 12.10.2010
- SENKER, J., Anorganische Chemie I, Bayreuth, Germany: "Solid-state NMR – principles and application", Ringvorlesung 17.05.2010
- SILVERA, I., Harvard University, Department of Physics, Cambridge, USA: "The solid hydrogen under pressure and the quest for metallic hydrogen", 22.07.2010
- SINMYO, R., Tokyo Institute of Technology, Department of Earth and Planetary Sciences, Tokyo, Japan: "Mg-Fe partitioning between lower mantle minerals: a laser-heated diamond anvil cell study", 21.01.2010

- SMITH, E., The University of British Columbia, Earth and Ocean Sciences, Vancouver, Canada: "The survival of brown colour in diamond during storage in the lithospheric mantle", 15.04.2010
- SOUSTELLE, V., Université Montpellier 2, Géosciences, Montpellier, France: "Effect of reactive melt/fluid percolation on deformation and consequences for seismic properties of the supra-subduction mantle", 28.10.2010
- STEINLE-NEUMANN, G., Bayerisches Geoinstitut, Bayreuth, Germany: "Spinels in general, and magnetite in particular", Ringvorlesung 21.06.2010
- TAJIMA, F., LMU München, Department für Geo- und Umweltwissenschaften, München, Germany: "Mineral physics implications for deep water transport with slab subduction and seismic evidence near the 660 km phase transformation depths", 29.04.2010
- UCHIDA, T., National Institute of Advanced Industrial Science and Technology, Osaka, Japan: "Computed microtomography using synchrotron X-ray radiation and electron microprobe", 19.10.2010
- VAN HUNEN, J., University of Durham, Department of Earth Sciences, Durham, U.K.: "The dynamics and consequences of dripping lithosphere", 18.11.2010
- VAN LICHTERVELDE, M., Universität Hannover, Institut für Mineralogie, Hannover, Germany: "Rare metal mineralizations in granites and pegmatites: from natural rocks to experimentation", 26.01.2010
- WANG, Y., University of Chicago, Argonne National Lab, Argonne, USA: "Large-volume high pressure at GSECARS", 07.04.2010
- WANG, Y., University of Chicago, Argonne National Laboratory, Argonne, USA: "Synchrotron based rheological studies on earth materials at high pressure and temperature", 08.04.2010
- WIGGINTON, N., Science Magazine, Washington DC, USA: "Scientific publishing from the inside out", 26.04.2010
- YANG, X., Bayerisches Geoinstitut, Bayreuth, Germany: "Electrical conductivity of lower crustal minerals", 11.11.2010
- YAMAZAKI, D., Okayama University, Institute for Study of the Earth's Interior, Misasa, Japan: "Pressure generation in a Kawai-type apparatus equipped with sintered diamond anvil", 12.10.2010
- ZUCCHINI, A., Università degli Studi di Perugia, Dipartimento di Scienze della Terra, Perugia, Italy: "Geochemical and mineralogical study of Dolomite samples", 16.09.2010

5.5 Conference organization

- 13.-18.06.2010, Goldschmidt Conference, Knoxville, USA: Symposium 03g: Geochemical Signatures of Mantle Redox Processes (A. KAVNER, C. McCAMMON, A. CAMPBELL)
- 21.-27.08.2010, International Mineralogical Association Meeting, Budapest, Hungary: Session DE42: Planetary Cores (G. STEINLE-NEUMANN, Y. FEI and E. OHTANI)
- 19.-22.09.2010, 88th Meeting of the German Mineralogical Society, Münster, Germany: Session 2.1: Environmental mineralogy and geochemistry (M. KERSTEN, K. POLLOK)

- 13.-17.12.2010, AGU Fall Meeting, San Francisco, USA: Mineral and Rock Physics Session MR13B/22A/31A: Stability, Rheology and Elasticity of Hydrous Phases: Geodynamical Implications (B. REYNARD, I. KATAYAMA, M. MOOKHERJEE)
- 13.-17.12.2010, AGU Fall Meeting, San Francisco, USA: Session MR11: Physical State of Planetary Cores (G. STEINLE-NEUMANN, Y. FEI, R. CARACAS)
- 06.-08.10.2010, Geodynamics Workshop, Münster, Germany: Convener for the session "Mantle dynamics" (H. SAMUEL)

6. Visiting scientists

6.1 Visiting scientists funded by the Bayerisches Geoinstitut

- ALEKSANDROV, V., Sofia University, Bulgaria: 11.-13.01.2010
- BEZACIER, L., Ecole Normale Supérieure, Laboratoire de Sciences de la Terre - UMR 5570, Lyon, France: 27.-30.04.2010
- CERANTOLA, V., Università degli Studi di Padova, Dipartimento di Geoscienze, Padova, Italy: 10.-12.01.2010
- DOLEJŠ, D., Charles University, Institute of Petrology and Structural Geology, Prague, Czech Republic: 16.-19.02.2010, 01.07.-31.08.2010
- FEI, H., Okayama University, Institute for Study of the Earth's Interior, Misasa, Japan: 01.-28.02.2010
- GOU, H., Rensselaer Polytechnic Institute, Mechanical, Aerospace & Nuclear Engineering, Troy, NY, USA: 11.-16.06.2010
- JEGO, S., Academia Sinica, Taipei, Taiwan: 20.-24.07.2010
- KUMAR, D., Jawaharlal Nehru Centre for Advanced Scientific Research, Bangalore, India: 31.01.-02.02.2010
- MARTIN, C., CNRS Nancy, France: 10.-13.05.2010
- OUSSADOU, M., Université des Sciences et de la Technologie Houari Boumedienne, Laboratoire de Physique des Matériaux, Algiers, Algeria: 01.-08.03.2010
- PALKE, A., Stanford University, Geological & Environmental Sciences Department, Stanford, USA: 06.09.-28.10.2010
- PALME, H., Forschungsinstitut und Naturmuseum Senckenberg, Sektion Meteoritenforschung, Frankfurt/M., Germany: 16.-17.08.2010
- REMMERT, P., Ruhr-Universität Bochum, Institut für Geologie, Mineralogie und Geophysik, Bochum, Germany: 25.-26.10.2010
- RIEDERER, M., Universität Würzburg, Julius-von-Sachs-Institut für Biowissenschaften, Würzburg, Germany: 28.07.2010
- ROSENTHAL, A., The Australian National University, Research School of Earth Sciences, Canberra, Australia: 29.06.2010
- SCHEITER, D., Universität Münster, Germany: 03.-04.06.2010
- SCHMELING, H., Johann Wolfgang Goethe-Universität, Inst. für Geowissenschaften, Geophysik, Frankfurt/M., Germany: 23.-24.03.2010
- SEKINE, T., Okayama University, Institute for Study of the Earth's Interior, Misasa, Japan: 26.-28.08.2010
- SINMYO, R., Tokyo Institute of Technology, Department of Earth and Planetary Sciences, Tokyo, Japan: 19.-25.01.2010
- SOUSTELLE, V., Université Montpellier 2, Géosciences, Montpellier, France: 27.-31.10.2010
- TAJIMA, F., LMU München, Department für Geo- und Umweltwissenschaften, München, Germany: 29.04.2010

VAN HUNEN, J., University of Durham, Department of Earth Sciences, Durham, U.K.: 17.-19.11.2010
VAN LICHTERVELDE, M., Universität Hannover, Institut für Mineralogie, Hannover, Germany: 25.-28.01.2010
WEIGEL, C., Université Montpellier 2, Laboratoire des Colloïdes, Verres et Nanomatériaux, Montpellier, France: 25.07.-01.08.2010
YAMAZAKI, D., Okayama University, Institute for Study of the Earth's Interior, Misasa, Japan: 10.-13.10.2010

6.2 Visiting scientists supported by other externally funded BGI projects

BACH, W., Universität Bremen, Fachbereich 5 Geowissenschaften, Bremen, Germany: 15.-17.11.2010 (ENB ^{*B})
CHEMIA, Z., Geological Survey of Norway, Trondheim, Norway: 04.-11.07.2010 (c2c ^{*A})
DMITRIEV, V., European Synchrotron Radiation Facility, Grenoble, France: 17.-19.03.2010 (IND ^{*E})
DOLEJŠ, D., Charles University, Institute of Petrology and Structural Geology, Prague, Czech Republic: 29.-30.03.2010 (c2c ^{*A})
FEI, Y., Carnegie Institution of Washington, Geophysical Laboratory, Washington DC, USA: 08.-12.05.2010 (ENB ^{*B})
JEANLOZ, R., University of California, Earth & Planetary Science, Berkeley, USA: 23.-28.02.2010 (ENB ^{*B})
MAIEROVA, P., Charles University Prague, Department of Geophysics, Prague, Czech Republic: 15.-17.06.2010 (c2c ^{*A})
NARYGINA, O., The University of Edinburgh, School of Physics and Astronomy, Edinburgh, U.K.: 15.-19.03.2010 (DFG ^{*C})
PARAKHONSKIY, G., A.V. Shubnikov Institute of Crystallography, Moscow, Russia: 25.-29.01.2010 (IND ^{*E})
POTAPKIN, V., European Synchrotron Radiation Facility, Grenoble, France: 02.-15.05.2010, 23.-30.11.2010 (DFG ^{*C})
PRADHAN, E., Institute of Technology, Mumbai, India: 23.02.-02.03.2010 (ENB ^{*B})
SELF, S., U.S. Nuclear Regulatory Commission, Washington DC, USA; The Open University, Earth and Environmental Sciences, Milton Keynes, U.K.: 10.-13.10.2010 (ENB ^{*B})
SILVERA, I., Harvard University, Department of Physics, Cambridge, USA: 21.-23.07.2010 (DFG ^{*C})
SPEZIALE, S., Helmholtz-Zentrum Potsdam, Deutsches GeoForschungsZentrum GFZ, Potsdam, Germany: 27.-29.09.2010 (ERC ^{*D})
WANG, Y., University of Chicago, Argonne National Laboratory, Chicago, USA: 05.-09.04.2010 (ENB ^{*B})

*A) **c2c: EU Marie Curie Research Training Network - the fate of subducted material**

*B) **ENB: International Graduate School under the Elitenetzwerk Bayern**

*C) **DFG: Deutsche Forschungsgemeinschaft**

*D) **ERC: European Research Council**

*E) **IND: Industrial Grant**

6.3 Visitors (externally funded)

ABRIKOSOV, I., Linköping University, Department of Physics, Chemistry, and Biology (IFM), Linköping, Sweden: 26.11.2010

ALMEEV, R., Universität Hannover, Institut für Mineralogie, Hannover, Germany: 14.12.2010

ANGEL, R., Virginia Polytechnic Institute and State University, Geosciences, Blacksburg, USA: 17.-18.05.2010

BORINSKI, S., Ruhr-Universität Bochum, Institut für Geologie, Mineralogie & Geophysik, Bochum, Germany: 16.-31.03.2010

BOTCHARNIKOV, R., Universität Hannover, Institut für Mineralogie, Hannover, Germany: 14.12.2010

BOYET, M., Muséum National d'Histoire Naturelle, Paris, France: 29.11.-02.12.2010

BROWN, D., University of Colorado at Boulder, Department of Geological Sciences, Boulder, USA: 08.02.-13.02.2010

BROWN, L., University of Massachusetts, Department of Geosciences, Amherst, USA: 16.-20.05.2010

BURLAKA, V., Universität Göttingen, Institut für Materialphysik, Göttingen, Germany: 15.-20.03.2010

BUSEMANN, H., University of Manchester, School of Earth, Atmospheric and Environmental Sciences, Manchester, U.K.: 09.-11.12.2010

CARACAS, R., Laboratoire de Sciences de la Terre, CNRS UMR5570, Ecole Normale Supérieure de Lyon, France: , 19.-29.07.2010, 22.-26.11.2010

CLAY, P., University of Manchester, School of Earth, Atmospheric and Environmental Sciences, Manchester, U.K.: 09.-11.12.2010

CORDIER, P., Université des Sciences et Technologies de Lille, Laboratoire de Structure et Propriétés de l'Etat Solide, Villeneuve d'Ascq, France: 19.-31.07.2010

DEFOUILLOY, C., Muséum National d'Histoire Naturelle, Paris, France: 27.09.-01.10.2010

DOBSON, D., University College London, Department of Earth Sciences, London, U.K.: 08.-14.09.2010

FABIAN, K., Geological Survey of Norway, Trondheim, Norway: 10.-13.03.2010

FORTUNATI, A., Università di Camerino, Dipartimento di Scienze della Terra, Camerino, Italy: 17.05.-08.06.2010

GALUSKIN, E., University of Silesia, Department of Geochemistry, Mineralogy and Petrography, Sosnowiec, Poland: 19.-20.07.2010

GALUSKINA, I., University of Silesia, Department of Geochemistry, Mineralogy and Petrography, Sosnowiec, Poland: 19.-20.07.2010

IRIFUNE, T., Ehime University, Geodynamics Research Center, Matsuyama, Japan: 28.08.-03.09.2010

KOZLENKO, D., Frank Laboratory of Neutron Physics, Joint Institute for Nuclear Research, Dubna, Russia: 02.-14.12.2010

KOZLOWSKA, M., AGH University of Science and Technology, Cracow, Poland: 17.-19.11.2010

MANG, C., Universität Heidelberg, Institut für Angewandte Geowissenschaften, Heidelberg, Germany: 12.-16.04.2010

MCCORMACK, R., University College London, Department of Earth Sciences, London, U.K.: 08.-15.03.2010, 25.-31.07.2010

MIKHAILOVA, D., Leibniz-Institut für Festkörper- und Werkstoffforschung, Dresden, Germany: 08.-15.11.2010

MOSTEFAOUI, S., Muséum National d'Histoire Naturelle, Paris, France: 28.11.-01.12.2010

ODÉN, M., Linköping University, Department of Physics, Chemistry, and Biology (IFM), Linköping, Sweden: 26.11.2010

OEHM, B., Universität Heidelberg, Institut für Angewandte Geowissenschaften, Heidelberg, Germany: 14.-16.04.2010

OTSUKA, K., Yale University, Department of Geology and Geophysics, New Haven, USA: 11.-24.04.2010

PIPPINGER, T., Universität Heidelberg, Mineralogisches Institut, Heidelberg, Germany: 22.-28.03.2010, 14.-15.07.2010, 04.-12.10.2010

POKROVSKI, G., Université de Toulouse, Experimental Geochemistry and Biogeochemistry, Toulouse, France: 07.-20.01.2010

ROUT, S., Universität Münster, Institut für Planetologie, Münster, Germany: 10.-11.11.2010

SARAPULOVA, A., Leibniz-Institut für Festkörper- und Werkstoffforschung, Dresden, Germany: 08.-15.11.2010

SCHOUWINK, P., Universität Heidelberg, Germany: 08.-11.06.2010

SCHUSTER, B., Gesellschaft für Schwerionenforschung mbH, Darmstadt, Germany: 20.-22.01.2010, 29.04.2010

SHEPHERD, H., CNRS Toulouse, Laboratoire de Chimie de Coordination, Toulouse, France: 15.-16.03.2010

SHUSHAKOVA, V., Universität Göttingen, Institut für Materialphysik, Göttingen, Germany: 15.-20.03.2010

SIMAK, S., Linköping University, Department of Physics, Chemistry, and Biology (IFM), Linköping, Sweden: 22.12.2010

SMYTH, J.R., University of Colorado at Boulder, Department of Geological Sciences, Boulder, USA: 25.01.-13.02.2010, 12.-23.07.2010

ŠPAČEK, P., Masaryk University, Institute of Physics of the Earth, Brno, Czech Republic: 01.-02.07.2010

SPIVAK, A., Institute of Experimental Mineralogy, Chernogolovka, Moscow region, Russia:
05.-31.07.2010, 16.11.-15.12.2010

TENNANT, C., University of Canterbury, Department of Chemistry, Christchurch, New
Zealand: 24.06.-20.07.2010

TRANQUIER, A., Ecole Normale Supérieure, Lyon, France: 27.09.-01.10.2010

UCHIDA, T., National Institute of Advanced Industrial Science and Technology, Osaka,
Japan: 19.10.2010

VOGEL, A.-K., Universität zu Köln, Institut für Geologie und Mineralogie, Köln, Germany:
06.04.-31.12.2010

WERNER, J., Leibniz-Institut für Festkörper- und Werkstofforschung, Dresden, Germany:
24.03.2010

WIGGINTON, N., Science Magazine, Washington DC, USA: 26.04.2010

WIRNHIER, E., LMU München, Lehrstuhl für Anorganische Festkörperchemie, München,
Germany: 11.-15.01.2010

WU, X., Beijing University, School of Earth and Space Sciences, Beijing, China: 01.-
21.08.2010

YAGI, T., University of Tokyo, Institute for Solid State Physics, Tokyo, Japan: 10.-
11.05.2010

YANG, Y., Beijing University, Department of Geology, Beijing, China: 16.04.-22.05.2010

ZIBERNA, L., Università degli Studi di Padova, Dipartimento di Geoscienze, Padova, Italy:
12.-26.05.2010

7. Additional scientific activities

7.1 Patent

KEPPLER, H.; WALTE, N. (2010): Hochtemperatur Moissanitsichtzelle. Patentschrift DE 10 2005 056 977 B4 des Deutschen Patentamtes

7.2 Theses

Ph.D. theses

GANSKOW, Geertje: The effect of iron on the stability, water storage capacity, and compressibility of mantle silicates – Implications to a hydrous Martian interior

NARYGINA, Olga: Investigation of the properties of iron-bearing alloys and silicates and their implications for the Earth's lower mantle and core

ZARECHNAYA, Evgeniya: The 5th element – a new high-pressure/high-temperature allotrope

M.Sc. theses

NOVELLA, Davide: Solidus reactions of model peridotite in the system CaO-MgO-Al₂O₃-SiO₂-CO₂-H₂O at 10-25 kbar

PAMATO, Martha: High-pressure behaviour of hydrous aluminous phases of the deep mantle

7.3 Honours and awards

KEPPLER, Hans was elected Fellow of the American Geophysical Union
received the Bowen Award 2010 of the American Geophysical Union

NARYGINA, Olga received the Bernd-Rendel Award of Deutsche Forschungsgemeinschaft (DFG)

RUBIE, David was honoured as the David Edwin Allday Lecturer, Jackson School of Earth Sciences, University of Texas at Austin, USA, February 2010

7.4 Editorship of scientific journals

HEIDELBACH, Florian Associate Editor "American Mineralogist"

KATSURA, Tomoo Associate Editor "Review of Geophysics"

KEPPLER, Hans Editorial Advisory Board "Elements"

Editorial Board "Contributions to Mineralogy and Petrology"

LANGENHORST, Falko	Associate Editor "Geochemistry/Chemie der Erde"
MCCAMMON, Catherine	Chief Editor "Physics and Chemistry of Minerals" Advisory Editor "Springer Briefs in Earth Sciences"
RUBIE, David	Editorial Board "Physics of the Earth and Planetary Interiors"

7.5 Membership of scientific advisory bodies

DUBROVINSKY, Leonid	Chair of SIG "Crystallography at extreme conditions" of the European Crystallography Union Member, Editorial Board of the Journal of High Pressure Research Member, Review Panel of Canadian Light Source Member, European High Pressure Research Group (EHPRG) Committee Member, Review Panel of SPRING8 Chair, Subcomission on Spectroscopy, Diffraction, and new Instrumentations in Mineral Physics of the International Mineralogical Association
FROST, Dan	Member of the council of the European Association of Geochemistry (EAG) for 3 years
KEPPLER, Hans	Member, Research Council of the German Mineralogical Society (Forschungskollegium Mineralogie der DMG) Member, Abraham Gottlob Werner Medal Committee, German Mineralogical Society (DMG) Member, Roebling Medal Committee, Mineralogical Society of America Chair, Goldschmidt Medal Committee, European Association of Geochemistry Member, American Geophysical Union Fellow Committee (VGP section) Member, Commission for Research of Bayreuth University (Präsidialkommission für Forschung und wissenschaftlichen Nachwuchs) Member, Advisory Board, Center of Extreme Conditions, Edinburgh Member, German National Academy of Sciences (Leopoldina) Member, Bavarian Academy of Sciences
LANGENHORST, Falko	President, German Mineralogical Society (DMG) Member, DFG-Senatskommission für geowissenschaftliche Gemeinschaftsforschung (Geokommission) Member, Academia Europaea

MCCAMMON, Catherine	<p>President Elect, Volcanology, Geochemistry & Petrology Section of the American Geophysical Union</p> <p>Member, Council of the American Geophysical Union</p> <p>Chairman, Fellows Committee of the Volcanology, Geochemistry & Petrology Section of the American Geophysical Union</p> <p>Member, Executive Committee of the Volcanology, Geochemistry & Petrology Section of the American Geophysical Union</p> <p>Member, Science Innovation Award Committee 2011 of the European Association of Geochemistry</p> <p>Member, Lecture Program Committee of the Mineralogical Society of America</p> <p>Member, Advisory Board of the Mössbauer Information Exchange</p> <p>Member, International Advisory Board of the Mössbauer Effect Data Center</p> <p>Chairman, Sub-committee "Earth's Deep Interior" of the Commission of the Physics of Minerals, International Mineralogical Association</p>
MCENROE, Suzanne	Member, Royal Norwegian Society of Sciences and Letters
RUBIE, David	Member of Forschungskollegium Physik des Erdkörpers (FKPE)

8. Scientific and Technical Personnel

Name		Position	Duration in 2010	Funding source
ALEKSANDROV, Vladislav	M.Sc.	Wiss. Mitarbeiter	from 15.05.	BGI/VP
AUDÉTAT, Andreas	Dr.	Akad. Rat z.A.		BGI
BALI, Enikő	Dr.	Wiss. Mitarbeiterin	to 31.08.	BGI/VP
BERNINI, Diego	Dipl.-Geol.	Wiss. Mitarbeiter	to 30.04.	EU
BÖHM, Ulrich		Mechaniker		BGI
BOFFA BALLARAN, Tiziana	Dr.	Akad. Rätin		BGI
BROCKMANN, Nicolas	Dipl.-Chem.	Wiss. Mitarbeiter		BGI/IGS ¹
BUCHERT, Petra		Fremdsprachen- sekretärin		BGI
CERANTOLA, Valerio	B.Sc.	stud. Hilfskraft	from 15.10.	DFG
CHANTEL, Julien	M.Sc.	Gastwissenschaftler	to 30.09.	EU
		Wiss. Mitarbeiter	from 11.10.	EU
CHEMIA, Zurab	Dr.	Gastwissenschaftler	to 31.01.	EU
CHUST, Thomas	Dipl. Geophys.	Wiss. Mitarbeiter		DFG
DE KOKER, Nico	Dr.	Gastwissenschaftler		EU
DITTMANN, Uwe		Präparator		BGI
DUBROVINSKY, Leonid	Apl. Prof. Dr.	Akad. Direktor		BGI
EL GORESY, Ahmed	Prof. Dr.			BGI/VP ²
ESCUADERO, Alberto	Dr.	Wiss. Mitarbeiter	to 28.02.	MICINN ³
			from 01.03.	BGI/VP
ETZEL, Katja	Dr.	Wiss. Mitarbeiterin	to 30.06.	BMBF
			15.09.-14.11.	BMBF
EVONUK, Martha	Dr.	Wiss. Mitarbeiterin	from 01.11.	DFG
FEI, Hongzhan	B.Sc.	Wiss. Mitarbeiter	from 15.04.	BGI/VP
FENG, Lu	B.Sc.	Stipendiatin	15.01.-15.09.	MPG
FISCHER, Heinz		Mechaniker		BGI
FISCHER, Nicole	ROI	Verwalt. Beamtin		BGI
FROST, Daniel	Dr.	Akad. Direktor		BGI
GANSKOW, Geertje	Dipl.-Geol.	Wiss. Mitarbeiterin	to 15.04.	BGI/IGS
			16.04.-30.06.	DFG ⁴
GIANNINI, Mattia	M.Sc.	Wiss. Mitarbeiter	from 15.02.	DFG
GLAZYRIN, Konstantin	Ing. Phys.	Wiss. Mitarbeiter		BGI/IGS
GOLLNER, Gertrud		Chem.-Techn. Assistentin		BGI
GREENBERG, Eran	M.Sc.	Wiss. Mitarbeiter	to 31.07.	DFG
HARRIES, Dennis	Dipl. Geowiss.	Wiss. Mitarbeiter	to 30.09.	BMBF/ DFG ⁴
			from 01.10.	BMBF

HASSANI SHABESTARI, Asiye Sadat	B.Sc.	stud. Hilfskraft	from 15.08.	DFG
HEIDELBACH, Florian	Dr.	Wiss. Mitarbeiter		BGI/IGS
HIRSEMANN, Dunja	Dipl.-Chem.	Wiss. Mitarbeiterin		BGI/IGS ⁵
HOPF, Juliane	Dipl.-Biol.	Wiss. Mitarbeiterin	to 31.10.	DFG
HUANG, Ruifang	B.Sc.	stud. Hilfskraft	from 01.08.	DFG ⁴
HUBER, Julia	CTA	Chem.-Techn. Assistentin	from 13.09.	BGI
KANTOR, Anastasia	Dr.	Wiss. Mitarbeiterin	from 24.11.	BMBF
KATSURA, Tomoo	Prof. Dr.		from 15.01.	BGI
KEPPLER, Hans	Prof. Dr.	Leiter		BGI
KESHAV, Shantanu	Dr.	Wiss. Mitarbeiter	to 10.07.	BGI/VP
KEYSSNER, Stefan	Dr.	Akad. Oberrat		BGI
KING, Scott	Prof. Dr.	Forschungspreisträger	19.05.-13.08.	AvH
KISON-HERZING, Lydia		Sekretärin		BGI
KLASINSKI, Kurt	Dipl.-Ing. (FH)	Techn. Angestellter		BGI
KRAUßE, Detlef	Dipl.-Inform. (FH)	Techn. Angestellter		BGI
KRIEGL, Holger		Haustechniker		BGI
KROPFGANS, Katja		Verwaltungs- angestellte	to 28.02.	BGI
KURNOSOV, Alexander	Dr.	Wiss. Mitarbeiter		EU
LANGENHORST, Falko	Prof. Dr.	Stellvertr. Leiter		BGI
LERCHBAUMER, Linda	Mag. rer. nat.	Wiss. Mitarbeiterin	to 10.03. 11.03.-31.05. 01.06.-30.09. from 01.10.	BGI/IGS DFG EXZ DFG
LI, Yuan	M.Sc.	Wiss. Mitarbeiter		BGI/IGS
LINHARDT, Sven		Elektrotechniker		BGI
LUNKENBEIN, Thomas	Dipl.-Chem.	Wiss. Mitarbeiter		BGI/IGS ⁵
MAIEROVA, Petra	M.Sc.	Gastwissenschaftlerin	from 08.09.	EU
MANNING, Craig	Prof. Dr.	Forschungspreisträger	01.07.-31.07.	AvH
MANTHILAKE, Geeth	Dr.	Wiss. Mitarbeiter		BGI/VP
MCCAMMON, Catherine	Dr.	Akad. Oberrätin		BGI
MCENROE, Suzanne	Dr.	Gastwissenschaftlerin	to 31.08.	EU
MIYAJIMA, Nobuyoshi	Dr.	Akad. Rat		BGI
MOOKHERJEE, Mainak	Dr.	Wiss. Mitarbeiter		BGI/VP
NAKAJIMA, Yoichi	Dr.	Wiss. Mitarbeiter		BGI/VP
NI, Huaiwei	Dr.	Wiss. Mitarbeiter		BGI/VP
NOVELLA, Davide	B.Sc. M.Sc.	stud. Hilfskraft Wiss. Mitarbeiter	to 31.03. from 16.04.	BGI BGI/IGS
OERTEL, Tina	Dipl.-Ing.	Wiss. Mitarbeiterin	11.01.-10.03. from 11.03.	BGI/VP ¹ BGI/IGS ¹

OUSSADOU, Mezhoura	M.Sc.	Gastwissenschaftlerin	from 01.06.	EU
OVSYANNIKOV, Sergey	Dr.	Forschungsstipendiat		AvH
PAMATO, Martha	B.Sc.	stud. Hilfskraft	to 30.04.	DFG ⁴
			01.05.-31.10.	DFG
	M.Sc.	Stipendiatin	from 01.11.	UB e.V.
PARAKHONSKIY, Gleb	M.Sc.	Wiss. Mitarbeiter	from 15.05.	DFG
PECHTOLD, Volker		Verwaltungs- angestellter	from 01.04.	
PESCE, Giacomo	B.Sc.	stud. Hilfskraft	15.10.-14.11.	BGI/HiWi
			from 15.11.	DFG
POLLOK, Kilian	Dr.	Akad. Rat a.Z.		BGI
POTZEL, Anke		Chem.-Techn. Assistentin		BGI
PRESCHER, Clemens	Dipl.-Min.	wiss. Mitarbeiter		BGI/IGS
RAMMING, Gerd		Elektroniker		BGI
RAUSCH, Oliver		Mechaniker		BGI
RUBIE, David C.	Prof. Dr.			EU
SAMUEL, Henri	Prof. Dr.	Juniorprofessor		Stiftung ⁶
SCHEITER, Daniel		Wiss. Mitarbeiter	from 25.08.	BMBF
SCHIAVI, Federica	Dr.	Wiss. Mitarbeiterin	to 30.11.	DFG
SCHMITT, Veronika	Dipl.-Min.	Wiss. Mitarbeiterin		BGI/IGS ⁵
SCHULZE, Hubert		Präparator		BGI
SHCHEKA, Svyatoslav	Dr.	Wiss. Mitarbeiter		DFG
SHEKHAR, Sushant	M.Sc.	Wiss. Mitarbeiter		BGI/IGS
SINMYO, Ryosuke	Dr.	Wiss. Mitarbeiter	from 01.07.	BGI/VP
SMITH, Evan	M.Sc.	Wiss. Mitarbeiter	15.01.-14.05.	DFG
STAGNO, Vincenzo	Dipl.-Geol.	Gastwissenschaftler	01.01.-31.03.	BGI/VP
		Wiss. Mitarbeiter	from 01.04.	DFG
STEINLE-NEUMANN, Gerd	Dr.	Akad. Rat		BGI
SUN, Wei	B.Sc.	stud. Hilfskraft	to 31.03.	BGI/VP
			from 01.04.	DFG
TROTS, Dmytro	Dr.	Wiss. Mitarbeiter		EU
ÜBELHACK, Stefan		Mechaniker		BGI
VAN MIERLO, Willem	M.Sc.	Gastwissenschaftler		EU
VLCEK, Vojtech	B.Sc.	stud. Hilfskraft	to 31.03.	DFG
			01.04.-30.06.	Studienb. ⁷
			from 01.07.	EU
WACK, Julia	Dipl.-Chem.	Wiss. Mitarbeiterin		BGI/IGS ⁵
WALTE, Nicolas	Dr.	Wiss. Mitarbeiter	to 31.01.	DFG
			from 01.07.	BMBF
WEI, Qingguo	B.Sc.	stud. Hilfskraft		DFG
YANG, Xiaozhi	Dr.	Forschungsstipendiat		AvH
ZARECHNAYA, Evgeniya	M.Sc.	Wiss. Mitarbeiterin	to 31.07.	DFG
ZUCCHINI, Azzurra	M.Sc.	Stipendiatin	13.06.-15.10.	Erasmus

Abbreviations/explanations:

AvH	Alexander von Humboldt Foundation
BGI	Staff Position of Bayerisches Geoinstitut
BGI/VP	Visiting Scientists' Program of Bayerisches Geoinstitut
BMBF	Federal Ministry of Education and Research
DFG	German Science Foundation
EXZ	Exzellenzinitiative der Universität Bayreuth
EU	European Union
IGS	International Graduate School under the Elitenetzwerk Bayern "Structure, Reactivity and Properties of Oxide Materials"
MICINN	Ministerio de Ciencia e Innovación, Gobierno de España
MPG	Max-Planck-Gesellschaft
UB e.V.	Universität Bayern e.V.

¹ Fraunhofer ISC Würzburg

² partially funded by the Visiting Scientists' Program of Bayerisches Geoinstitut

³ funded by the Spanish Ministry of Science

⁴ Leibniz award Prof. Langenhorst

⁵ Chair of Inorganic Chemistry I, Prof. Breu

⁶ Juniorprofessorship for Geodynamic Modeling funded by
Stifterverband für die Deutsche Wissenschaft

⁷ enrolment fee

Index

Adjaoud, O.	184
Aleksandrov, V.	24, 212
Aléon, J.	44
Ammann, M.W.	122
Audétat, A.	55, 77, 132, 135, 136, 206
Bali, E.	135
Beard, A.	122
Becerro, A.I.	170
Behrens, H.	143
Bernini, D.	72
Boffa Ballaran, T.	86, 88, 99, 101, 109, 110, 111, 115, 191, 197
Bons, P.	165
Boudouma, O.	51
Boyet, M.	46, 49
Brodholt, J.P.	122
Bull, J.	86
Burton, B.P.	184
Caillet Komorowski, C.	51
Caracas, R.	179, 199
Carroll, M.R.	145
Chantel, J.	31, 117
Charon, E.	44
Chemia, Z.	74
Chernyshov, D.	179
Chumakov, A.	119, 195
Chust, T.	208
Cordier, P.	159
Dang, N.T.	189
de Koker, N.	35
Deo, B.	24
Devouard, B.	49
Dmitriev, V.	179
Dobson, D.P.	122, 162
Dolejš, D.	36, 72, 74, 77
Dubrovinskaia, N.	99, 101, 177, 179, 182, 185, 193, 199, 202
Dubrovinsky, L.S.	83, 84, 95, 99, 101, 102, 106, 114, 119, 128, 149, 177, 179, 182, 185, 189, 193, 195, 199, 202
Dzierzanowski, P.	83
El Goresy, A.	44, 46, 49, 51, 173
Escudero, A.	92, 170

Etzel, K.	139
Filinchuk, Y.	179
Fortunati, A.	145
Franz, L.	68
Frost, D.J. 31, 33, 54, 55, 57, 62, 64, 67, 90, 94, 95, 99, 109, 110, 111, 115, 117, 120,	142, 152, 154, 159, 165, 191, 197, 203
Galuskin, E.V.	83
Galuskina, I.O.	83
Gannoun, A.	46, 49
Gazeev, V.M.	83
Giannini, M.	88
Glazyrin, K.	99, 101, 109, 114, 119, 128, 182, 193
Greenberg, E.	119
Hallberg, K.B.	80
Hanfland, M.	99, 101, 114, 179, 182, 193, 199
Harries, D.	52, 85, 172
Heidelberg, F.	110, 122, 152, 154, 156, 168
Hellebrand, E.	90
Hiraga, K.	173
Hirao, N.	173
Holbig, E.	130
Hopf, J.	138
Humayun, M.	51
Huss, G.	90
Irifune, T.	62, 160
Ito, E.	27
Jirák, Z.	189
Karato, S.	126
Katsura, T.	27
Keppler, H.	60, 72, 97, 125, 132, 135, 143, 145
Keshav, S.	147
Kimura, M.	173
King, S.D.	23
Klotz, S.	128
Kontny, A.	172
Kopylova, M.G.	84
Kozlenko, D.P.	189
Kurnosov, A.	99, 101, 109, 111, 115, 182, 191, 197
Kusz, J.	83
Langenhorst, F.	52, 70, 85, 88, 92, 120, 138, 172
Lerchbaumer, L.	206
Litvin, Yu.	149

Longo, M.	68, 126
Lowenstern, J.B.	77
Lukin, E.V.	189
Ma, C.	51
Maierová, P.	30
Malaspina, N.	70
Mang, Ch.	172
Mann, U.	54
Manthilake, M.A.G.M.	154, 203
Mantovani, M.	170
McCammon, C.A.	62, 64, 68, 86, 94, 106, 119, 125, 126, 195
McCormack, R.	122, 162
McKeegan, K.D.	44
Melosh, H.J.	40
Merlini, M.	99, 101, 109, 114, 179, 182, 193
Miletich, R.	114
Miyahara, M.	51, 173
Miyajima, N.	62, 90, 110, 120, 152, 154, 160, 162
Mookherjee, M.	31, 33, 38, 119
Mostefaoui, S.	46
Mussi, A.	159
Nagase, T.	173
Nakajima, Y.	54, 57, 95
Narygina, O.	119
Nestola, F.	68, 86
Ni, H.	125, 143
Nimis, P.	68
Nimmo, F.	54
Novella, D.	142, 147
O'Brien, D.P.	54
Ohishi, Y.	173
Ohtani, E.	173
Otsuka, K.	126
Ovsyannikov, S.V.	102, 185
Ozawa, S.	173
Palke, A.	94
Palme, H.	54, 55
Pamato, M.G.	110, 111
Parakhonskiy, G.	177
Pertsev, N.N.	83
Pippinger, T.	101, 114, 182
Poli, S.	70

Polian, A.	102
Pollok, K.	80, 85, 138, 139, 208
Popov, S.L.	195
Potapkin, V.	195
Prakapenka, V.B.	193
Prescher, C.	106
Prusik, K.	83
Robert, F.	51
Rubie, D.C.	40, 54, 55, 57, 90, 120, 165
Rüffer, R.	195
Sakai, T.	173
Samuel, H.	23, 24, 26, 40, 210, 212
Savenko, B.N.	189
Schouwink, P.	101, 114
Sergueev, I.	119
Shcheka, S.	60
Shchennikov, V.V.	102
Shekhar, S.	152
Shvetsova, M.A.	102
Sinmyo, R.	95, 119
Smirnov, G.V.	195
Smith, E.M.	84
Smyth, J.R.	90
Spacek, P.	168
Spivak, A.	149
Stagno, V.	62, 64, 67
Stebbins, J.F.	94
Steinle-Neumann, G.	30, 36, 38, 74, 98, 130, 184
Tang, Z.	98
Tange, Y.	62
Taniguchi, T.	162
Tennant, C.	86
Tomlinson, E.L.	84
Trots, D.M.	111, 115, 191, 197
van de Walle, A.	184
van Mierlo, W.	120
Vlcek, V.	130
Vogel, A.-K.	54, 55
Walte, N.	152, 156, 162, 165, 203
Wei, Q.	202
Wiedenbeck, M.	72
Wu, X.	185

Yamazaki, D.	27
Yang, X.-Z.	97, 125
Yoneda, A.	27
Yoshino, T.	27
Zarechnaya, E.	179
Zhang, L.	136
Zibera, L.	68